Signal Processing for Non-Gaussian Statistics: Clutter Distribution Identification and Adaptive Threshold Estimation

By

Justin G. Metcalf

Submitted to the graduate degree program in Department of Electrical Engineering and Computer Science and the Graduate Faculty of the University of Kansas in partial fulfillment of the requirements for the degree of
Doctor of Philosophy

Committee members

Dr. Shannon Blunt, Chairperson

Dr. Jun Huan

Dr. Tyrone Duncan

Dr. Jim Stiles

Dr. Lingjia Liu

Date defended: _____

The Dissertation Committee for Justin G. Metcalf certifies
that this is the approved version of the following dissertation :

Signal Processing for Non-Gaussian Statistics: Clutter Distribution Identification and Adaptive Threshold Estimation

Dr. Shannon Blunt, Chairperson

Date approved: _____

Abstract

We examine the problem of determining a decision threshold for the binary hypothesis test that naturally arises when a radar system must decide if there is a target present in a range cell under test. Modern radar systems require predictable, low, constant rates of false alarm (*i.e.* when unwanted noise and clutter returns are mistaken for a target). Measured clutter returns have often been fitted to heavy tailed, non-Gaussian distributions. The heavy tails on these distributions cause an unacceptable rise in the number of false alarms. We use the class of spherically invariant random vectors (SIRVs) to model clutter returns. SIRVs arise from a phenomenological consideration of the radar sensing problem, and include both the Gaussian distribution and most commonly reported non-Gaussian clutter distributions (*e.g.* K distribution, Weibull distribution).

We propose an extension of a prior technique called the Ozturk algorithm. The Ozturk algorithm generates a graphical library of points corresponding to known SIRV distributions. These points are generated from linked vectors whose magnitude is derived from the order statistics of the SIRV distributions. Measured data is then compared to the library and a distribution is chosen that best approximates the measured data. Our extension introduces a framework of weighting functions and examines both a distribution classification technique as well as a method of determining an adaptive threshold in data that may or may not belong to a known distribution. The extensions are then compared to neural networking techniques. Special attention is paid to producing a robust, adaptive estimation of the detection threshold. Finally, divergence measures of SIRVs are examined.

Acknowledgment

First and foremost, I would like to thank my wife, Miranda, for her loving support, encouragement, patience, and understanding through this journey. She provided a sea of calm when the difficulties of graduate school were at their rockiest. I would also like to thank Dr. Shannon Blunt for taking a chance on a Master's student who was struggling to apply an FIR filter. In particular, thanks for constantly encouraging me, supporting me, and imparting to me a love and appreciation of the philosophy of our discipline. I thank Dr. Braham Himed for his guidance, support, and for providing the genesis of this work. I would also like to thank the Air Force Research Labs Sensors Directorate for their financial support of this work. I would like to thank my son Mitchell, for the joy, wonder, and pride he has brought to my life. I also thank my daughter Rosalynn, who I get to meet as I start the next step in my journey. I would like to thank my parents, Jon and Tracy, and father-in-law Mitch for their unwavering support and encouragement. I would also like to thank my brother Jordan, and my sisters Brooke, Teri, and Kaylee. I hope you always embrace your dreams and the challenges life throws at you. I would like to thank Dr. Bryce Chriestenson for the help with the integration in Chapter 8 and the conversations on life, math, and school. I would like to thank all of the fellow graduate students who have worked alongside me. In particular, I would like to thank my officemates Cenk Sahin, John Jakabosky, Dr. Brian Cordill, and Paul Anglin. Our conversations and camaraderie were intellectually stimulating and endlessly entertaining. I would also like to thank my friend Jeff Beaver for his support and friendship through this challenging time. Last, but certainly not least, I would like to thank my committee, Dr. Stiles, Dr. Liu, Dr. Duncan, and Dr. Huan. Their advice and knowledge guided me to the final product. I would also like to thank them for their patience in wading through this dissertation.

Contents

List of Figures

List of Tables

Table 1: List of Acronyms

AMF	Adaptive matched filter
API	Adaptive piecewise integration
CA-CFAR	Cell averaging constant false alarm rate
CCM	Clairvoyantly known (true) covariant matrix
cdf	Cumulative distribution function
CFAR	Constant false alarm rate
CGM SIRV	Compound gamma modulated spherically invariant random vector
CLT	Central limit theorem
CNR	Clutter-to-noise ratio
COSMiC	Combined order statistics mapping in clutter
CPI	Coherent processing interval
CUT	Cell under test
CV	Cramer-Von Mises test
dB	decibel
DBM WSOS	Divide by mean weighted sum of order statistics
DBN	Deep belief network
DDT	Data-dependent threshold
EOA	Extended Ozturk Algorithm
FP	Fixed point
GIP	Generalized inner product
GLRT	Generalized likelihood ratio test
GM SIRV	Gamma modulated spherically invariant random vector
i.i.d.	Independent and identically distributed
INR	Interference-to-noise ratio
KASSPER	Knowledge aided sensor signal processing and expert reasoning
KL	Kullback-Leibler divergence

KS	Kolmogorov-Smirnov test
LRT	Likelihood ratio test
MCARM	Multichannel airborne radar measurements
MEC	Multivariate elliptically contoured
ML	Maximum likelihood
MMSE	Minimum mean square error
MoM	Method of moments
NAMF	Normalized adaptive matched filter
NHD	Non-homogeneity detector
NN	Neural network
NP	Neyman-Pearson
NSCM	Normalized sample covariance matrix
OS	Order statistics
pdf	Probability distribution function
PRF	pulse repetition frequency
RCS	Radar cross section
SAR	Synthetic aperture radar
SCM	Sample covariance matrix
SINR	Signal-to-interference-plus-noise ratio
SIRP	Spherically invariant random process
SIRV	Spherically invariant random vector
SNR	Signal-to-noise ratio
SSRV	Spherically symmetric random vector
STAP	Space-time adaptive processing
WSOS	Weighted sum of order statistics

Chapter 1

Introduction

The pioneers in statistical signal processing based much of their developments on models underpinned with assumptions of Gaussianity and stationarity [3, 4]. Quite often, these assumptions held up under the harsh lens of reality due to the applicability of the Central Limit Theorem [5]. However, as signal processing applications have increased in scope, power, and complexity, these two key assumptions have been found to be increasingly inaccurate (*e.g.* [1,4,6–8]). In the spirit of [4] and [1], this dissertation is an attempt to illuminate the consequences of, and provide tools to deal with, non-Gaussian and non-stationary environments encountered in radar signal processing.

In [4], Haykin lists five characteristics of modern signal processing algorithms, which are reproduced here:

1. *Prior information*, the extraction of which requires understanding the physical laws that govern the generation of signals of interest.

2. *Regularization*, which is achieved by embedding prior information in a computationally efficient manner into algorithmic design so as to stabilize the solution.

3. *Adaptivity*, which is made possible by learning from the operational environment so as to account for the unknown statistical structure of the environment and track its nonstationary behavior.

4. *Robustness*, which, in a deterministic sense, means that unavoidable disturbances (*e.g.*, errors due to choice of initial conditions, model mismatch, and use of finite-precision arithmetic) are not magnified by the algorithm. In a statistical sense, robustness means that the algorithm is insensitive to small deviations of the actual probability distribution from the probability distribution of the assumed model.

5. *Feedback*, a powerful engineering principle, the proper application of which has many beneficial effects (*e.g.*, improved convergence, reduced sensitivity to parameter variations, and improved robustness to the presence of unavoidable disturbances).

These characteristics are essential to translate algorithms which are attractive from a theoretic perspective into powerful sensor systems with practical use. In this dissertation we shall pay particular attention to the themes of prior information, adaptivity, and robustness in a hypothesis testing framework.

A statistical hypothesis test is designed to determine whether a sample of data is derived from a null distribution or an alternate distribution. There may be one (in the case of a binary hypothesis test) or many alternate hypotheses. The null distribution is considered to be the *default* distribution. There are two types of errors associated with a binary hypothesis test. A Type I error occurs when the null distribution is chosen but the data was generated by the alternate distribution. A Type II error occurs when the alternate hypothesis is chosen but the null hypothesis is true. The Neyman-Pearson (NP) criterion [9] is typically considered to be the theoretically optimal solution to a hypothesis test. The NP criterion is formed from the detection statistic which minimizes the Type I error. The NP threshold for this test statistic is then found such that a predetermined, fixed probability of Type II error occurs.

The usefulness of hypothesis tests crucially rests on the definition of the null and alternate hypotheses. When designing a signal processing algorithm, the principle of prior information must be effectively employed to define the hypothetical distributions. The NP criterion usually requires clairvoyant information about the hypothetical distributions (*e.g.* mean, variance). In practice, this information must be *adaptively* estimated from a set of sampled

data.

In this dissertation we shall apply novel innovations to the radar detection problem. The fundamental theory of radar detection and practical problems will be explored and developed. The need for adaptive and robust solutions will be developed and demonstrated throughout the rest of this dissertation.

1.1 Radar Clutter Classification

It is well known that the advent of radar detection proved to be of vital importance in a range of applications as early as World War II [10, 11]. However, the basic understanding of radar principles was known as early as 1886, when Hertz measured scattered electromagnetic radiation from objects to verify Maxwell's equations [10]. It took another two decades for the idea of using electromagnetic waves to detect ships and aircraft to be patented by Hülsmeyer [12]. Radar systems offer sensing capabilities in all environmental conditions, and have proven robust and popular for many uses over the last 75 years [10, 11].

While passive radar sensing modalities have shown promise (*e.g.* [13–15]), radar typically is an active sensor system. The radar transmits electromagnetic radiation into the environment and uses the received echoes to extract information about the illuminated area. In the radar literature, the object of interest is typically called a target, while unwanted echoes are termed clutter [11,16]. Clutter can be correlated with respect to both time [17] and space [18], and can also be thought of as interference. The terms clutter and interference will be used interchangeably throughout this dissertation. The designation of clutter is dependent on the desired application. For example, in an air traffic control scenario, passing aircraft would be the desired targets while received echoes from clouds and rain would be clutter. However, for a weather radar the reverse is true. For the purposes of this dissertation, clutter will be considered to come from ground or sea echoes.

Radar lends itself well to the realm of statistical signal processing, and the five principles

presented by Haykin in [4] are proving more important than ever. As the physical environment a radar must operate in is likely to change, the radar system must be adaptive and robust to non-stationarities. In addition, due to the ever increasing computational power available to system designers, digital signal processing algorithms are taking the center stage in current and future systems.

Taken to the extreme, the principles given in [4], when applied to radar signal processing, give rise to the idea of a "cognitive radar" [19–24]. A very closely related idea to cognitive radar is that of "knowledge-based" radar [21, 25]. The goal of these overlapping ideas is to provide a framework with which to imbue a form of artificial intelligence into the radar system. Put another way, these paradigms attempt to increase the number of parameters (*i.e.* degrees of freedom) over which the signal processing algorithms can adapt.

Knowledge based systems often consist of expert systems (*i.e.* rule based systems) that use information derived *a priori* by the radar engineers to optimize performance to the situation at hand. For example, a radar designer may pair geophysical location data (*e.g.* GPS sensor data) and previously measured covariance data to provide a more accurate covariance estimate based on the geography of the illuminated area [21, 25, 26]. Another example is tracking a target moving along a road. In this case, the radar may use *a priori* knowledge of the road's location and direction of travel in the Bayesian estimation of the movement/location of the target [25]. Finally, knowledge-based radar systems may incorporate learning through data fusion methods to allow different sensor systems or even platforms to exchange information about a scene and thereby inform their respective adaptive processing strategies [25].

In a cognitive framework, inspiration is often drawn from biological systems. For example, the sonar of bats or the visual processing power of the human brain can provide a model upon which to base an adaptive sensor system [19, 20, 27–29]. Promising results have been shown through adaptive cooperation between radar systems and adaption of transmitted waveforms (through the principle of feedback) [20, 24, 30–33]. However, these approaches often consider

the tracking of targets, or maximizing the detection probabilities (as expressed in terms of SNR or SINR). A radar system may be seen as a "system of systems". Each system is optimized to accomplish its goals under constraints set by the designers. Therefore, if the data output of one system is outside the parameters expected by the subsequent systems utilizing the data, performance of the entire system will necessarily degrade. For example, if the tracking algorithm is provided data from the detection algorithm with a greater number of false alarms than the former was designed to handle, false target tracks may occur. The problem of estimating a detection threshold from non-Gaussian data has been considered in many works (*e.g.* [7, 34–38] and references as a small sampling), and we will extend current methods to an adaptive framework. Here we have dual goals. When possible, we work in general terms so that these ideas and methods may be adapted and applied to other potential signal processing problems. When necessary, we delve into the implications and applications important to radar signal processing.

At the most basic level, radar engineers are tasked with optimizing the detection of targets while simultaneously suppressing the effects of noise and clutter. In a statistical sense, the radar must maximize the probability of detection (P_d) while minimizing the probability of false alarm (P_{fa}). The radar detection problem naturally takes the form of a hypothesis test [9]. Recall that the null hypothesis is the default hypothesis. For the radar detection problem, the null hypothesis, denoted as $\mathcal{H}_0$, hypothesizes that the received data is composed only of clutter and noise contributions. The alternate hypothesis, $\mathcal{H}_1$, then theorizes the data contains contributions from a target as well as clutter and noise. Therefore, the underlying statistics of the two distributions must be well known in order for the hypothesis test to provide meaningful results.

A primary focus of this dissertation is to find methods to classify sampled data as originating from theoretical and/or empirically measured distributions. In the context of the radar problem, we wish to find regions of relatively statistically homogeneous data. These regions will typically correspond to physical areas scanned by the radar. The measured data

should be statistically consistent, but some samples may have perturbations due to data from a different distribution, or deterministic-but-unknown data (*i.e.* a target). In other words, an ideal strategy for a radar system would be:

1. Separate the measured data into largely homogeneous blocks (*i.e.* non-homogeneity detection for clutter patches).

2. Find the theoretical distribution or empirically observed distribution to which the data most closely corresponds.

3. Determine the significance of this correspondence to provide a reliable and robust estimate in the distribution determination.

4. Search for deviations (*i.e.* targets) within the homogeneous blocks of measured data. Establish the confidence in the determination of a target.

In this dissertation we propose to implement a strategy using the representation of clutter data as spherically invariant random vectors (SIRVs) in conjunction with a novel distribution discrimination technique based on taking weighted sums of ordered statistics. It should be noted that errors due to receive chain non-linearities or waveform effects (*i.e.* range-Doppler ambiguities, pulse compression sidelobes, spectrum management, etc.) will not be considered. In addition, while significant work has been done in adaptively cancelling interference and enforcing Gaussianity on heterogeneous data, those results will not be discussed in this work [39, 40]. However, future work should incorporate the results of this dissertation with the results and strategies shown in [40] to provide a comprehensive approach in mitigating non-Gaussian clutter.

The remainder of the work presented here is organized as follows. A more in-depth discussion of radar detection and radar clutter is provided in Chapter 2 and the SIRV architecture is discussed in Chapters 3 and 4. A previous implementation of visual distribution identification using weighted sums of ordered statistics, as well as a new, generalized framework is

shown in Chapter 5. A more thorough examination of the proposed framework is found in Chapter 6. In Chapter 7 the application of neural networks to identify non-Gaussian distributions and estimate detection thresholds is considered. Chapter 8 examines definitions of various divergences, and explores the application of the Kullback-Leibler divergence. Finally, a summary of the work presented, proposals for future work, and the conclusions drawn from this work are presented in Chapter 9.

1.2 Mathematical Notation

Throughout this work scalars and random variables are given in lower-case, italic symbols. The corresponding vectors and random vectors are denoted in bold. Upper-case, bold letters correspond to matrices.

Chapter 2

Radar Detection

We consider the problem of using a radar to detect a discrete target. Naturally, the radar system must be designed to detect desired targets with a high probability while suppressing false alarms (*i.e.* claiming a target has been detected when there is no target present). However, the primary focus will be the signal processing behind current and classical radar detection strategies, paying particular attention to the assumptions and motivation that underpin their design and deployment.

Naturally, the information gleaned from the radar must be reliable. Variability in the false alarm rate could have disastrous implications for many radar applications. Therefore, the output of the radar signal processing must be designed to have a low, yet *constant* false alarm rate (CFAR). Also, the algorithms under consideration must also be designed to detect both large and small targets. The radar does not necessarily know *a priori* how large of an amplitude return a particular target will reflect. The magnitude of the return depends heavily on the distance, shape, orientation, and material composition of the target. For instance, a highly reflective object near to the radar will return a massive, easily recognized return. However, the reflected power received by the radar from the same target will be very small if the target is a great distance from the radar. The difference between the power of the largest detectable signal and the power of the smallest detectable signal of a radar

system is called the dynamic range. The ideal radar has both CFAR and a large dynamic range.

As mentioned previously, the radar detection problem naturally takes the form of the binary hypothesis test

$$\begin{aligned} \mathcal{H}_0 : &\quad \mathbf{y} = \mathbf{x} + \mathbf{u} \\ \mathcal{H}_1 : &\quad \mathbf{y} = \mathbf{s} + \mathbf{x} + \mathbf{u} \end{aligned} \tag{2.1}$$

where $\mathbf{y}$ is a length L received sampled signal vector at the radar receiver, $\mathbf{x}$ is the sampled clutter contribution, $\mathbf{u}$ is the sampled contribution due to thermal noise, and $\mathbf{s}$ is the signal contribution arising from the reflection of the radar waveform from the target. Unless noted otherwise, it is assumed that the received signal $\mathbf{y}$ has already been pulse compressed [11,16]. The radar transmits and receives in-phase and quadrature components, leading to complex sampled data [16]. For a successful test, the radar signal processor should choose $\mathcal{H}_0$ when no target is present and $\mathcal{H}_1$ when a target is present. A *miss* is defined as choosing $\mathcal{H}_0$ when a target is present (a Type I error), and a *false alarm* is defined as choosing $\mathcal{H}_1$ when $\mathcal{H}_0$ is true (a Type II error). This simplified model will be expanded and discussed in further detail in Section 2.2

The detection probability and false alarm probability are always dependent on the signal to interference-plus-noise ratio (SINR). Typically, false alarms come from one of two error sources. First, large spikes from thermal noise can be mistaken for a target. Thermal noise comes from the components of the physical radar system, as well as all objects illuminated by the radar [5, 10]. While thermal noise is unavoidable and uncorrelated, it is Gaussian distributed due to the Central Limit Theorem (CLT) [5]. Therefore, it lends itself well to closed form analysis. Second, unwanted echoes from radar clutter can cause a false alarm. The clutter echoes are typically of greater magnitude than the noise power. They are also much more difficult to characterize and mitigate. For these reasons, the physical phenomenon

governing clutter are discussed to illuminate the prior information available to radar signal processing designer. Once the prior information is established, common strategies for the mitigation of clutter in various scenarios will be discussed throughout the rest of this chapter.

2.1 General Clutter Mitigation Strategies

This section discusses general clutter mitigation strategies at a very high level. The succeeding sections then address more specific strategies and the mathematical assumptions that must be made to justify their use. The radar must have a good understanding of the magnitude and causes of the clutter encountered in order to mitigate it effectively and extract information on the desired target.

The magnitude of the clutter is highly dependent on the physical environment under observation and the characteristics of the particular radar. Clutter with large amplitudes typically comes from ground or sea echoes. These echoes may come from the mainlobe of the radar or the sidelobes [11]. Radar designers typically go to great lengths to suppress the sidelobes and increase the gain of the mainlobe of the radar system. For example, a radar system may use phased arrays and/or directional antennas [16]. However, even highly directional antennas and antenna arrays suffer from sidelobe contamination of the received signal [41]. Figure 2.1 illustrates a possible scenario for an airborne radar.

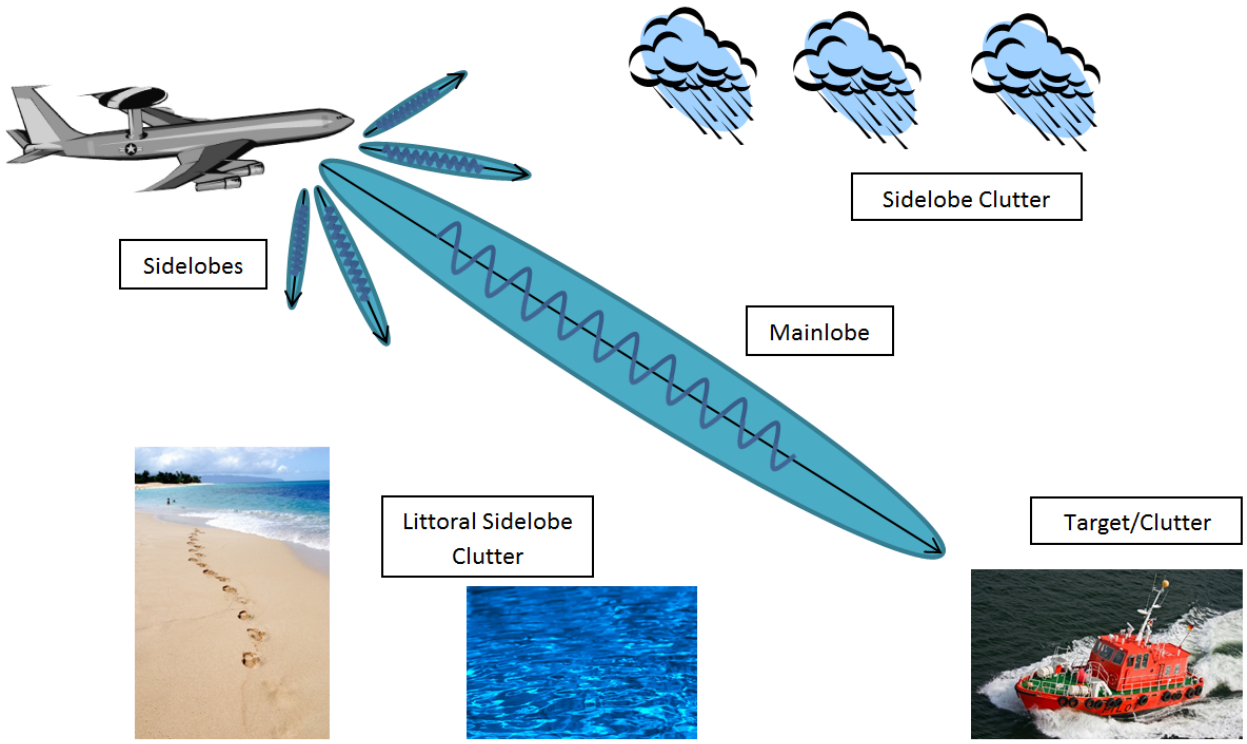

Figure 2.1: An example of an airborne radar

The physical environment produces clutter in two main categories: distributed and discrete clutter. The distributed clutter depends on the size of the illuminated area (determined by the mainlobe and sidelobe characteristics of the radar) and the radar cross-section (RCS) of the illuminated area. The RCS varies by terrain type and moisture level, among other factors [10, 16]. Discrete clutter arises from what are called specular reflections. Specular reflections are strong returns from sharp edges that resemble corner-reflectors or plate reflectors, and are typically found in man-made or maritime environments [11]. Notice that if the area illuminated by sidelobes and the mainlobe is reduced, the distributed clutter will be reduced correspondingly, but the discrete clutter returns may not be affected.

Due to the large magnitude of clutter returns, accurate target detection depends on effective clutter mitigation. The radar must find methods to *discriminate* between the clutter and a target. Radar systems can be designed to use spatial and temporal strategies to increase target detection capabilities. The particular strategy employed heavily depends

on the scenario the radar encounters (*i.e.* prior information must be employed). Various scenarios will be considered throughout the remainder of this chapter.

By transmitting a radar waveform multiple times, and coherently combining the resultant echoes, a radar may use temporal strategies to increase the likelihood of target detection. The rate at which these transmissions occur is known as the pulse repetition frequency (PRF), and the length of time for the transmission and reception of all pulses in a processing period is known as the coherent processing interval (CPI). The temporal strategy employed largely depends on the expected distribution and magnitude of the clutter statistics.

For a ground-based, air-looking radar (*i.e.* ground-to-air surveillance radar), the received signal has a very low clutter to noise ratio (CNR). The clutter contribution primarily arises from sidelobe clutter, which can be largely mitigated by sophisticated antenna design. If clutter is ignored or considered to be uncorrelated from pulse-to-pulse, a simple strategy is to coherently sum the received signal in the time domain [16]. The target echoes then coherently sum together while the uncorrelated noise does not. It can be shown that the signal-to-noise ratio increases by a factor of N, where N is the number of pulses in the CPI [9, 16]. A more sophisticated approach is to employ a CFAR Neyman-Pearson detector on individual pulses and use the resultant detection/no detection decision in a target tracking algorithm [9, 42]. In this case, the amplitude detection performed by the CFAR detector is designed to maximize the radar's ability to discriminate between target and clutter on an individual pulse basis, while the tracking algorithm attempts to provide further confidence through temporal diversity (*i.e.* multiple looks).

A radar may spatially filter the transmitted and received signals using mechanically (*e.g.* rotating) or electrically steered arrays of antennas [11]. This allows the radar to estimate the angle of arrival of a target. Also, a phased array of antennas allows the radar to use spatially adaptive processing to null strong clutter returns (*e.g.* ground returns for a ground-based, air-looking radar) [3, 43]. Of course, the spatially adaptive processing strategies are highly dependent on the statistical nature of the clutter, as well as the physical environment in

which the radar is operating.

For airborne or spaceborne applications, the mainbeam contains a large clutter contribution from ground or sea echoes. Therefore, it is highly likely that the return from a discrete target is much lower in power than the clutter. The large clutter return then causes the signal-to-interference-plus-noise ratio (SINR) to be much too low for the time domain, amplitude-based strategies to be employed (*e.g.*, [42], Chapter 16). The radar must utilize its prior information to discriminate between a possible target and the clutter in an adaptive, robust, and regularized clutter cancellation strategy.

If the target is moving, a radar may take advantage of the Doppler effect to separate the target from the clutter [16]. Doppler processing takes advantage of the temporal diversity afforded by the multiple pulses in a CPI in the frequency domain. The radar takes the Fast Fourier Transform (FFT) of the received pulses to find the Doppler spectrum of the environment. The Doppler spectrum of clutter largely depends on the motion of the clutter (*e.g.*, tree leaves blowing in the wind or waves in the ocean) and whether the radar system is itself in motion. If a target is traveling at a large radial velocity with respect to the radar, it is easily distinguished from the stationary ground clutter returns. Conversely, it is much more challenging to use Doppler processing to detect a slow moving target.

Finally, a radar may jointly take advantage of spatial and temporal adaptivity to more effectively cancel clutter returns through the use of space-time adaptive processing (STAP) [43]. In using spatial diversity afforded by an antenna array in conjunction with temporal diversity given by using multiple pulses over a CPI, target detection may be posed in a very high dimensional space. The subspace occupied by the target and the subspace of the clutter are theoretically separate. In addition, the clutter subspace occupies a smaller portion of the full space [43–45]. The nature of the clutter subspace is of course dependent on the statistical nature of the clutter. Therefore, the implementation and effectiveness of STAP also depends on the assumptions made about the environment, and how well those assumptions match to reality.

2.2 Radar Detection in Gaussian, Homogeneous Clutter

To create a realizable CFAR detector, the designer must have an accurate model for the target, noise, and clutter echoes. The radar system must also be capable of fitting the observed data to the model. In other words, the radar must be able to estimate noise and clutter distribution (*i.e.* the null distribution) parameters from measured data that is uncorrupted by possible targets. These estimates are then used to *adaptively* set detection thresholds based on the desired false alarm rate. In this section, the clutter is assumed to arise from a homogeneous, Gaussian process. The justification of this assumption, and the ensuing strategies derived are discussed in detail throughout the remainder of the section.

Early radar designers modeled the aggregated returns in each range cell as having been produced by a large number of elementary scatterers [7, 46]. Therefore, the Central Limit Theorem (CLT) may be invoked and the clutter statistics may be assumed to be complex Gaussian distributed. This model has many attractive properties. First, there is a sound phenomenological basis to this model, implying that it matches well to reality. Second, the thermal noise is well modeled by the Gaussian distribution, so the statistics of the clutter-plus-noise component are also Gaussian [5]. Third, a Gaussian distributed random variable is fully characterized by the first and second moments [5]. Finally the optimal CFAR detector for a target in the presence of Gaussian noise takes the familiar form of a whitening matched filter [9] compared to a data dependent threshold derived from an estimate of the noise power.

However, classical developments and strategic decisions depend largely on the *a priori* information that the radar signal processor is assumed to have. First, it is assumed throughout this section that the underlying null distribution does not change with respect to range or time (*i.e.* it is homogeneous). From a statistical standpoint, measured data vectors that do not contain a target are assumed to be independent and identically distributed (IID). As we are assuming the interference (clutter and noise) is homogeneous, the necessity for feedback is alleviated. However, *a priori* information must be exploited to form a robust,

adaptive, and regularized detector.

Revisiting the simple receive signal model presented in (2.1), first assume the received signal to be echoes from a single pulse incident on a single antenna. Let $\mathbf{y}$ be defined as a length L complex vector. The L samples are called *fast time* samples. Each individual sample corresponds to a physical range cell. The size of the range cell corresponding to each digital sample depends on multiple factors that will not be considered here, such as bandwidth and antenna beamwidth.

In the simplest case, the noise-plus-clutter contribution $\tilde{\mathbf{x}} = \mathbf{x} + \mathbf{u}$ is considered to be distributed as an uncorrelated, complex Gaussian random vector $\tilde{\mathbf{x}} \sim C\mathcal{N}(\mathbf{0}, \sigma_{\tilde{x}}^2\mathbf{I})$ where $\sigma_{\tilde{x}}^2$ is the variance of each null-distributed sample. Therefore, the amplitude (envelope) distribution is Rayleigh, the phase distribution is uniform over $(0, 2\pi)$, and the power distribution is exponential [42].

If the clutter magnitude is low with respect to the signal (*i.e.* an SINR > 0), the radar may use CFAR strategies based on the amplitude characteristics of the interference. Consider a window of data consisting of range cells in the received vector $\mathbf{y}$. The data in the window consists of received data that have been match filtered with the transmitted radar waveform, and the square magnitude of the result taken. The cell upon which the hypothesis test is conducted is known as the cell-under-test (CUT). This window is slid over the range data to test each cell for a target. The cells in front of the CUT are denoted lead cells, while the cells behind are called lagging cells.

Figure 2.2 illustrates an example CFAR processor. In this CFAR processor, α is chosen to provide the desired probability of false alarm and $g(f_{lag}, f_{lead})$ provides an estimate of the clutter power. However, the guard cells, labeled 'G', are not used to estimate the clutter power. The data dependent threshold, T, is then compared to the cell under test to determine whether a target is present or not.

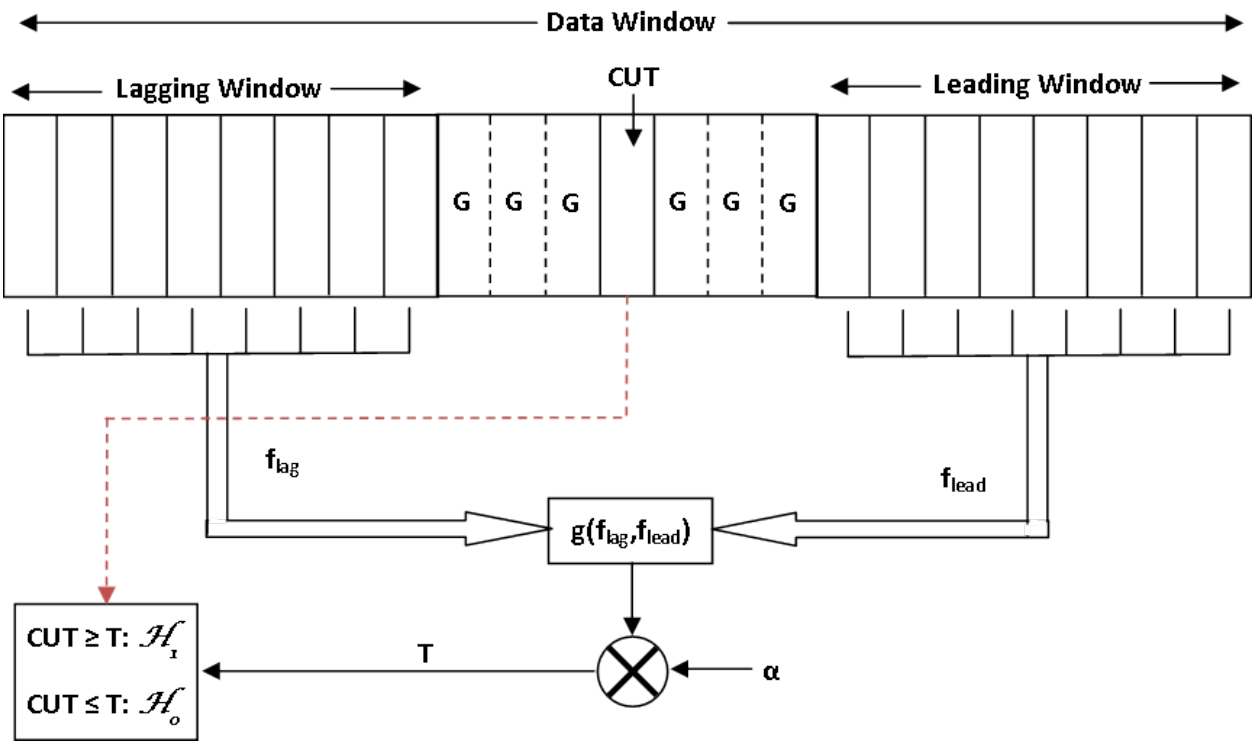

Figure 2.2: An example CFAR detector

The most popular CFAR strategy is known as the cell-averaging CFAR (CA-CFAR) [42]. The average power of the interference is estimated from leading and lagging cells. Due to the assumption of the interference as a complex Gaussian distribution, the estimate of the exponentially distributed power samples corresponds to the variance of the power. This power estimate is used in a *data dependent threshold* (DDT) to compare against for the hypothesis test. This DDT provides adaptivity, robustness, and regularity to the detection statistic. Most importantly, as long as the homogeneous Gaussian assumption holds, this CFAR detector requires no *a priori* knowledge of the clutter power.

However, the DDT produces a slightly higher threshold than the optimal Neyman-Pearson threshold, which leads to a loss in detection probability. This loss is called the CFAR loss, and plots of CFAR loss for the CA-CFAR are shown in [42]. Using a larger data window decreases the CFAR loss by improving the estimate of the clutter power. However, by increasing the size of the data window, there is a correspondingly increasing chance that

the clutter power may not be homogeneous. In addition, there is a higher probability that a target may lie in the data window, corrupting the power estimate. Therefore, a trade-off occurs between data homogeneity and CFAR loss from the selection of the data window size. Typically, range cells adjacent to the CUT are designated as guard cells. The estimated power of the guard cells are discarded to prevent the returns from an extended target (*i.e.* a target that extends into multiple range cells) from corrupting the estimate. Using guard cells reduces the number of samples used to produce the DDT, leading to a slightly increased CFAR loss.

The CA-CFAR detection statistic depends on a large SINR. Depending on the number of samples used to form the power estimate, the SINR should be larger than 10-15 dB to yield a high probability of detection with low probability of false alarm [42]. Therefore, in the example of an airborne or space born radar system with a great deal of mainlobe clutter, the radar will need to use clutter cancellation techniques.

Beginning with the groundbreaking work of Reed, Mallot, and Brennan (RMB) [47], radar engineers began to develop elegant analyses of adaptive array based detection algorithms. The RMB technique separated the measured data into primary (*i.e.* cell under test, possibly containing a target) and secondary (target free) range cells. The secondary data is then used to estimate the space-time covariance matrix, which is used to form a whitening filter. While [47] examined the problem from an SNR perspective, Kelly expanded the analysis in his famous generalized likelihood ratio test (GLRT) [48]. In a GLRT, the secondary data is used to form a maximum likelihood [49] estimate of the null hypothesis. The covariance matrix estimated from the secondary data is assumed to hold for the primary data, and a maximum likelihood estimate for the alternate hypothesis is formed. The GLRT detection statistic is then the ratio between the maximum likelihood estimates of the two hypotheses, whereas the traditional likelihood ratio test (LRT) is formed as the ratio between the clairvoyantly known distributions of the hypotheses. Assuming homogeneous, target-free training data, the GLRT is known to be CFAR and asymptotically optimal, in the sense

that it maximizes the probability of detection. The optimal decision boundary is defined by the Neyman-Pearson criterion if the distributions are clairvoyantly known. The GLRT can be computationally expensive, which led to the development of the adaptive matched filter (AMF) implementation [50]. The AMF requires lower computation, but suffers a penalty in SNR. It is important to note that the performance of both the GLRT and the AMF suffer when the assumption of homogeneity and/or Gaussianity is not valid [51].

2.3 Radar Detection in Non-Gaussian, Non-Homogenous Clutter

Early on, it was expected that increasing the range resolution of a radar system would decrease the magnitude of the clutter. Instead, an increase in "spikes" in the clutter data was observed [7]. As noted earlier, while the contribution of the distributed clutter will necessarily be reduced as the range resolution increases, the contribution of discrete clutter will not necessarily be reduced as expected. These clutter spikes correspond to a heavier tailed amplitude distribution.

In addition, particularly for airborne applications, the homogeneous nature of the clutter is not assured. For example, the radar may encounter a road in the midst of farmland, or be flying along a coast (*i.e.* a littoral region). If the range cells adjacent to the CUT are not drawn from the same distribution, the covariance estimate will necessarily be flawed. This *model mismatch* can lead to decreased detection and prevent CFAR from being achieved.

Signal processing algorithms derived from the classical STAP architecture rely on stationary, homogeneous, and Gaussian clutter to optimally detect targets and maintain CFAR. However, empirical measurements have long shown that the Gaussian model may not fit measured amplitude statistics [1]. For many years, observed and modeled data have been fitted to the Weibull [52–54], log-normal [54–57] and K [53–55, 58, 59] distributions. These distributions have heavier tails than the Gaussian distribution, leading to an increase in false

alarms if not accounted for. These measurements are highly dependent on multiple variables such as grazing angle, sea state, range resolution, etc. [17, 18, 60]. Therefore, it is apparent that modern radar signal processing algorithms must be able to determine statistically homogeneous blocks of range data, and to robustly fit the data to a distribution.

One approach is to use feedback to determine the distributions present in heterogeneous data, and then adapt the algorithms to the encountered data. In other words, the signal processing algorithm must adaptively group contiguous range cells into clutter "patches" that are statistically homogeneous. Segmenting data into contiguous regions and finding the boundaries separating those regions is intuitively similar to problems encountered in an image processing or computer vision framework. The similarities to image processing are especially clear when operating in a synthetic aperture radar (SAR) framework [61]. For a traditional pulse Doppler approach, the work in [62] provides an intriguing *ad hoc* approach based on an image processing framework. Unfortunately, the approach taken in [62] depends heavily on parameters that must be defined by the user. Also, while the algorithm appears to function well in non-Gaussian clutter scenarios, there was no formal verification or analysis performed to characterize its robustness.

Another promising avenue of research focuses on methods to provide the signal processor with *a priori* environmental knowledge. The most prominent effort was the DARPA knowledge aided sensor signal processing and expert reasoning (KASSPER) program [26, 63]. Of course, the reliability and accuracy of the *a priori* environmental knowledge must be considered, and the impact of possible model mismatch addressed. Here we consider the means to allow the radar to adaptively assimilate environmental information. However, before this learning process can be defined, the concept of spherically invariant random vectors (SIRVs) must be developed in Chapter 3.

Chapter 3

Spherically Invariant Random Processes - Background

In order to design a robust radar detector, the statistics of the radar clutter must be accurately characterized. It has been suggested that a *good* statistical model for clutter must satisfy two requirements [64]:

1. The amplitude statistics of a single pulse are accurately modeled.

2. The correlation between the pulses in a CPI are accurately modeled.

However, it has been established that it is possible to have two arbitrary probability density functions (pdfs) that satisfy these requirements yet still have different optimal Neyman-Pearson detectors [65]. Further, these detectors can be very sensitive to a mismatch between the assumed and actual models. Therefore, it is necessary to further constrain the clutter modeling problem. Here we propose constraints based on the physics encountered in radar sensing.

The clutter model should be general enough to be robust to the widely varying operational parameters of a typical airborne radar (*e.g.* altitude, grazing angle, terrain type, etc.), yet specific enough to allow a useful characterization of the clutter statistics. Here a

third qualification will be added to the list from [64]: a good radar clutter model should have a sound *phenomenological* basis. By adhering to a phenomenological structure, signal processing algorithms based on the clutter model should prove to be robust and able to adapt to scenarios encountered after deployment. As mentioned previously, early clutter models assumed the clutter to be Gaussian distributed. From a phenomenological standpoint, the Gaussian assumption for the clutter amplitude distribution is derived from the Central Limit Theorem (CLT). Unfortunately measured data is often reported to be distributed according to a non-Gaussian distribution [52–59].

Therefore, a radar clutter model should be formulated from a sound phenomenological basis and fully capture amplitude statistics of a multivariate, non-Gaussian distribution. Defining the pdf of multivariate non-Gaussian random distributions can be a very difficult task. In many cases, there is no unique closed form expression for the pdf [65]. It was noticed that several non-Gaussian distributions (*e.g.* Weibull, K distribution, Student t distribution, Generalized Cauchy [66, 67]) that had been empirically fit to observed radar data belonged to the class of random processes called spherically invariant random processes (SIRPs) [8].

A vector sample from a SIRP is by definition a spherically invariant random vector (SIRV). SIRVs have been historically studied under many guises, such as multivariate elliptically contoured (MEC), Gaussian mixtures, compound Gaussian distributions, Rayleigh mixtures, symmetric distributions, and sub-Gaussian alpha-stable distributions [68]. Several of the monikers listed provide key insights into the properties of these random vectors. For example, contours of constant probability take the form of ellipses. Also, SIRVs may be modeled as a Gaussian random vector modulated by a positive random variable. Further, the random vector is fully characterized by a mean, covariance matrix, and a characteristic function. These properties, among others, are explored in more detail in this chapter.

Recall that the assumption of a large number of independent scatterers in a range cell leads to the Gaussian distribution via application of the CLT. However, by assuming the number of elementary scatterers to be a random variable, the SIRV architecture can be

derived as a scattering phenomenon [7, 55]. This version of the CLT applies even when the expected value of the number of scatters is very large. From an intuitive perspective, the CLT may be applied to each range cell, providing locally Gaussian statistics. However, the power varies from range cell to range cell, which is accounted for via the modulating positive random variable [1]. In the radar community, the Gaussian component is often called speckle, while the modulated power component is denoted as the texture parameter [34]. Therefore, the SIRV architecture fits the radar clutter problem both from an empirical and physics based approach.

While SIRVs are a natural fit to many sources of impulsive, non-Gaussian noise, they are often omitted from analysis of robust estimators [69]. Multivariate SIRV distributions often do not have a closed form solution for problems of interest (*e.g.* cdf). To deal with the mathematical intractability of this useful framework, we use Monte Carlo techniques to estimate the true distributions when necessary.

The remainder of this chapter develops the framework and lists various useful properties of the SIRV/SIRP architecture. The notation and terminology used in the SIRV literature can vary from author to author. Care must be taken when comparing or attempting to duplicate results in papers from different authors. Oftentimes transformations will be required in order for the pdfs to match. Therefore, this chapter provides a cohesive, unifying framework from a radar signal processing perspective. This framework is used extensively in future chapters.

3.1 Real SSRVs and SIRVs

The early work by Kingman [70, 71] and Yao [72] considered the case of real-valued SIRVs. First, Kingman defined a spherically symmetric random vector (SSRV) $\mathbf{x}$ to be a length L random vector with a radially dependent pdf [70] of the form

$$f_{\mathbf{X}}(\mathbf{x}) = kh_L(\mathbf{x}^T\mathbf{x}) \tag{3.1}$$

where $(\bullet)^T$ denotes the transpose operation. The value k is a normalizing constant to ensure the pdf integrates to a probability of 1, while the non-negative, real, monotonically decreasing function $h_L(\bullet)$ is arbitrary to each SSRV.

The representation theorem for SSRVs [71, 72], as stated in [1], is given as

Theorem 1 *If a random vector* $\mathbf{x} = [x_1 x_2 \dots x_L]^T$ *is an SSRV* $\forall L > 0$*, then there exists a non-negative random variable* d *such that the random variables* $x_i (i = 1, 2, \dots, L)$ *conditioned on* $D = d$ *are independent, identically distributed (i.i.d.), Gaussian random variables with zero mean and variance equal to* $2d$*.*

For the purposes of this dissertation, let

$$v \equiv \sqrt{2d} \equiv \sqrt{\tau}. \tag{3.2}$$

In the literature pdfs are commonly reported in the form of v or τ, so this notation is used to be flexible in defining properties and pdfs. From Theorem 1, the pdf of $\mathbf{x}$ conditioned on v is given as

$$f_{\mathbf{X}|V}(\mathbf{x}|v) = (2\pi)^{-L/2} v^{-L} \exp(-\frac{\mathbf{x}^T\mathbf{x}}{2v^2}). \tag{3.3}$$

The pdf $f_V(v)$ is known as the characteristic pdf. Using the law of total probability, the pdf of the SSRV $\mathbf{x}$ is

$$f_{\mathbf{X}}(\mathbf{x}) = (2\pi)^{-L/2} \int_0^\infty v^{-L} \exp(-\frac{\mathbf{x}^T\mathbf{x}}{2v^2}) f_V(v) \mathrm{d}v. \tag{3.4}$$

Note that (3.3) and (3.4) corresponds to the product

$$\mathbf{x} = \mathbf{z}v \tag{3.5}$$

where $\mathbf{z}$ is a length L Gaussian random vector with zero mean and identity covariance matrix. Therefore, an SSRV is equivalent to a multivariate white Gaussian random vector modulated by a non-negative random variable. The Gaussian distribution is then an example

of an SSRV. For a Gaussian distribution, the characteristic pdf is

$$f_V(v) = \delta(v-1) \tag{3.6}$$

where $\delta(\bullet)$ is the Dirac delta function [1].

Note that the contours of constant probability for the pdf of an SSRV are circles. Of more practical interest are spherically *invariant* random variables (SIRVs), which have elliptical contours of constant probability. SIRVs are formed through a linear transformation as given by [1, 73]:

Theorem 2 *If a random vector* $\mathbf{x}$ *is an SSRV with characteristic pdf* $f_V(v)$*, then the deterministic linear transformation*

$$\mathbf{y} = \mathbf{A}\mathbf{x} + \mu \tag{3.7}$$

results in $\mathbf{y}$ *being an SIRV with mean vector* μ *and covariance matrix* $\mathbf{\Sigma} = \mathbf{A}\mathbf{A}^T$*.*

Note that it is required that $\mathbf{A}\mathbf{A}^T$ result in a non-singular matrix. As a consequence of Theorem 2, the linear transformation of any SIRV results in another SIRV possessing the same characteristic pdf. This result is known as the closure property of SIRVs [72, 74]. A detailed proof of Theorem 2 is available in [1]. The closure property becomes very useful when generating arbitrary SIRV distributions.

Upon inspection, it is apparent that a SIRV results from the modulation of a colored Gaussian vector with the nonnegative random variable v. It shall be assumed without loss of generality that $E[v^2] = 1$. The joint pdf of $\mathbf{y}$ can expressed using the quadratic form

$$q = (\mathbf{y}-\mu)^T\mathbf{\Sigma}^{-1}(\mathbf{y}-\mu) \tag{3.8}$$

as

$$f_{\mathbf{Y}}(\mathbf{y}) = (2\pi)^{-L/2}|\mathbf{\Sigma}|^{-1/2}h_L(q) \tag{3.9}$$

where

$$h_L(q) = \int_0^\infty v^{-L} \exp(-\frac{q}{2v^2}) f_V(v) \mathrm{d}v \tag{3.10}$$

and $|\mathbf{\Sigma}|$ is the determinant of the covariance matrix.

It can be seen from the closure property and equations (3.9) and (3.10) that any SIRV is completely characterized with a mean vector, covariance matrix, and characteristic pdf. Therefore, the bulk of the developments in this dissertation are concerned with using the quadratic form defined in (3.8). The pdf $f_Q(q)$ is found to be [66]

$$f_Q(q) = \frac{1}{2^{\frac{L}{2}}\Gamma(\frac{L}{2})} q^{\frac{L}{2}-1} h_L(q) u(q) \tag{3.11}$$

where $u(q)$ is the unit step function and $\Gamma(\bullet)$ is the Eulero-Gamma function.

SIRVs may be decomposed into generalized spherical coordinates $r \in (0, \infty), \theta \in (0, 2\pi)$, and $\phi_k \in (0, \pi)$, for $k = 1, ..., L-2$ [74]. This representation, as stated in [1], is given by the theorem:

Theorem 3 *When the components of the random vector* $\mathbf{x} = [x_1, \ldots, x_L]^T$ *are represented in the generalized spherical coordinates given by*

$$\begin{aligned}
x_1 &= r\cos(\phi_1) \\
x_k &= r\cos(\phi_k) \prod_{i=1}^{k-1} \sin(\phi_i) \quad (1 < k < L-2) \\
x_{L-1} &= r\cos(\theta) \prod_{i=1}^{L-2} \sin(\phi_i) \\
x_L &= r\sin(\theta) \prod_{i=1}^{L-2} \sin(\phi_i),
\end{aligned} \tag{3.12}$$

$\mathbf{x}$ *is an SSRV if and only if* r, θ, *and* ϕ_k *are mutually and statistically independent random*

variables having pdfs of the form

$$f_R(r) = \frac{r^{L-1}}{2^{\frac{L}{2}-1}\Gamma\frac{L}{2}} h_L(r^2)u(r) \tag{3.13}$$

and

$$f_{\Phi_k}(\phi_k) = \frac{\Gamma(\frac{L-k+1}{2})}{\sqrt{\pi}\Gamma(\frac{L-k}{2})} \sin^{L-1-k}(\phi_k)[u(\phi_k) - u(\phi_k - \pi)]$$
$$f_\Theta(\theta) = (2\pi)^{-1}[u(\theta) - u(\theta - 2\pi)] \tag{3.14}$$

where $\Gamma(\bullet)$ *is the Eulero Gamma function and* $u(\bullet)$ *is the unit step function.* The proof of Theorem 3 is given in [1].

It is often useful to transform from the envelope random variable r to the closely related quadratic form Q, and vice versa. This transformation is given as

$$q = g(r) = r^2. \tag{3.15}$$

It is clear from (3.11) and (3.13) that $q \geq 0$ and $r \geq 0$. Therefore,

$$r = g^{-1}(q) = \sqrt{q} \tag{3.16}$$

has only one root and

$$\left| \frac{\mathrm{d}g^{-1}(q)}{\mathrm{d}q} \right| = \frac{1}{2\sqrt{q}}. \tag{3.17}$$

From (3.13), (3.16), and (3.17), the pdf of (3.11) is derived as [5]

$$\begin{aligned} f_Q(q) &= f_R(g^{-1}(q)) \left| \frac{\mathrm{d}g^{-1}(q)}{\mathrm{d}q} \right| \\ &= \frac{(\sqrt{q})^{L-1}}{2^{\frac{L}{2}-1}\Gamma(\frac{L}{2})} h_L((\sqrt{q})^2) \frac{1}{2\sqrt{q}} \\ &= \frac{q^{\frac{L-1}{2}} q^{-\frac{1}{2}}}{2^{\frac{L}{2}-1} 2\Gamma(\frac{L}{2})} h_L(q) \\ &= \frac{q^{\frac{L}{2}-1}}{2^{\frac{L}{2}}\Gamma(\frac{L}{2})} h_L(q). \end{aligned} \tag{3.18}$$

The reverse transformation given by (3.16) also holds.

The function $h_L(q)$ possesses a useful recurrence relation. Let q be replaced by the dummy variable w. From [1]

$$\begin{aligned} h_{2L+1}(w) &= (-2)^L \frac{\mathrm{d}^L h_1(w)}{\mathrm{d}w^L} \\ h_{2L+2}(w) &= (-2)^L \frac{\mathrm{d}^L h_2(w)}{\mathrm{d}w^L}. \end{aligned} \tag{3.19}$$

Therefore, it is possible to generate arbitrary order pdfs for SIRV models, provided the function $h_L(q)$ is known for orders h_1 and h_2. This recurrence relationship will be used later for maximum likelihood estimation of the covariance matrix [75].

It should be noted that as a consequence of (3.5) SIRVs are by nature non-ergodic. Each sample vector generated from a SIRP will have a different instantiation of the random variable V. It can be easily shown that if and only if a SIRV is ergodic, V is a constant and that SIRV is generated by a Gaussian distribution.

3.2 Complex SIRVs

A length L zero-mean complex SIRV $\mathbf{y} = \mathbf{y}_c + j\mathbf{y}_s$ has in-phase components $\mathbf{y}_c = [y_{c,1}, y_{c,2}, \ldots, y_{c,L}]$ and quadrature components $\mathbf{y}_s = [y_{s,1}, y_{s,2}, \ldots, y_{s,L}]$. The necessary and sufficient conditions

for $\mathbf{y}$ to be admissible as a SIRV are [76]

$$\mathrm{E}[\mathbf{y}_c] = E[\mathbf{y}_s] = 0, \tag{3.20}$$

$$\mathbf{\Sigma}_{cc} = \mathbf{\Sigma}_{ss} \tag{3.21}$$

and

$$\mathbf{\Sigma}_{cs} = -\mathbf{\Sigma}_{sc} \tag{3.22}$$

where

$$\begin{aligned} \mathbf{\Sigma}_{cc} &= \mathrm{E}[\mathbf{y}_c\mathbf{y}_c^T] \qquad \mathbf{\Sigma}_{ss} = \mathrm{E}[\mathbf{y}_s\mathbf{y}_s^T] \\ \mathbf{\Sigma}_{cs} &= \mathrm{E}[\mathbf{y}_c\mathbf{y}_s^T] \qquad \mathbf{\Sigma}_{sc} = \mathrm{E}[\mathbf{y}_s\mathbf{y}_c^T]. \end{aligned} \tag{3.23}$$

The properties of (3.20), (3.21), and (3.22) imply that complex valued SIRVs are members of the strongly circular class of complex random vectors [76, 77]. Using (3.20), (3.21), and (3.22), the covariance matrix of $\mathbf{y}$ is given as

$$\mathbf{\Sigma} = 2[\mathbf{\Sigma}_{cc} + j\mathbf{\Sigma}_{sc}]. \tag{3.24}$$

It is required that the covariance matrix $\mathbf{\Sigma}$ be nonnegative definite Hermitian. As the complex valued SIRVs are assumed to be zero mean, the quadratic form for the SIRV, using the covariance matrix of (3.24), is

$$q = \mathbf{y}^H\mathbf{\Sigma}^{-1}\mathbf{y} \tag{3.25}$$

where $(\bullet)^H$ denotes the complex conjugate transpose, or Hermitian operation. The pdf of $\mathbf{y}$ is then

$$f_{\mathbf{Y}}(\mathbf{y}) = (\pi)^{-L}|\mathbf{\Sigma}|^{-1}h_{2L}(q) \tag{3.26}$$

where

$$h_{2L}(q) = \int_0^\infty v^{-2L} \exp(-\frac{q}{v^2}) f_V(v) \mathrm{d}v \tag{3.27}$$

and $f_V(v)$ is the characteristic pdf of the SIRV. The pdf for the quadratic form given in (3.11) becomes

$$f_Q(q) = \frac{1}{\Gamma(L)} q^{L-1} h_{2L}(q) u(q) \tag{3.28}$$

Note that the formulation for $\mathbf{y}$ given in (3.25) is identical to the product

$$\mathbf{Y} = \tilde{\mathbf{z}} v \tag{3.29}$$

where $\tilde{\mathbf{z}}$ is a zero-mean complex Gaussian random vector with covariance matrix given by (3.24).

3.3 Optimal Detection in SIRV Clutter

Optimal detection in SIRV clutter is very similar to detection in Gaussian distributed clutter. Both rely on a whitening matched filter to maximize SNR and a data dependent threshold (DDT) to minimize false alarms. This section follows developments presented in [78], which provides the optimal Neyman-Pearson detector for SIRV clutter. However, the optimal detector is shown to depend on clairvoyant knowledge of the SIRV characteristic PDF. Therefore, subsequent developments in this area are oriented at finding suboptimal detectors for SIRV clutter (*e.g.* [34, 78]).

Recalling the hypothesis test given in (2.1), assume that the clutter power is much greater than the noise power, allowing the latter to be ignored. The hypothesis test is then given as

$$\begin{aligned} \mathcal{H}_0 : &\quad \mathbf{y} = \mathbf{x} \\ \mathcal{H}_1 : &\quad \mathbf{y} = \mathbf{s} + \mathbf{x} \end{aligned} \tag{3.30}$$

where $\mathbf{y}$ is the complex valued, length L received sampled signal vector at the radar, $\mathbf{x}$ is the sampled clutter contribution, and $\mathbf{s}$ is the signal contribution arising from the reflection of the radar waveform from the target. It is often assumed that

$$\mathbf{s} = \gamma \mathrm{e}^{j\phi}\mathbf{p} \tag{3.31}$$

where $\gamma \mathrm{e}^{j\phi}$ is the complex amplitude associated with the target response and $\mathbf{p}$ is the Doppler steering vector associated with the target. The quadratic form for each hypothesis is then

$$\begin{aligned} q_1 &= (\mathbf{y}-\mathbf{s})^H \boldsymbol{\Sigma}^{-1}(\mathbf{y}-\mathbf{s}) \\ q_0 &= \mathbf{y}^H \boldsymbol{\Sigma}^{-1}\mathbf{y}. \end{aligned} \tag{3.32}$$

For this derivation, the clutter is assumed to have been generated by the process

$$\mathbf{x} = \sqrt{\tau}\tilde{\mathbf{z}} \tag{3.33}$$

where $\tilde{\mathbf{z}}$ is a zero mean, complex Gaussian random process and τ is the modulating random variable. For $i = 0, 1$ the pdf of each hypothesis is

$$\begin{aligned} f_i(\mathbf{y}) &= \frac{1}{(2\pi)^L |\boldsymbol{\Sigma}|} \int_0^\infty \frac{1}{\tau^L} \exp\left(-\frac{q_i}{2\tau}\right) f_\tau(\tau) \mathrm{d}\tau \\ &= \frac{h_{2L}(q_i)}{(2\pi)^L |\boldsymbol{\Sigma}|} \end{aligned} \tag{3.34}$$

where

$$h_{2L}(q_i) = \int_0^\infty \frac{1}{\tau^L} \exp\left(-\frac{q_i}{2\tau}\right) f_\tau(\tau) \mathrm{d}\tau. \tag{3.35}$$

Therefore, the Likelihood Ratio Test (LRT) is

$$\begin{aligned}\Lambda(\mathbf{y}) &= \frac{f_1(\mathbf{y})}{f_0(\mathbf{y})} \\ &= \frac{\int_0^\infty \frac{1}{\tau^L}\exp\left(-\frac{q_1}{2\tau}\right) f_\tau(\tau)\mathrm{d}\tau}{\int_0^\infty \frac{1}{\tau^L}\exp\left(-\frac{q_0}{2\tau}\right) f_\tau(\tau)\mathrm{d}\tau} \\ &= \frac{h_{2L}(q_1)}{h_{2L}(q_0)}. \end{aligned} \tag{3.36}$$

From (3.36), the optimal NP detector is seen to be

$$\frac{h_{2L}(q_1)}{h_{2L}(q_0)} \underset{\mathcal{H}_0}{\overset{\mathcal{H}_1}{\gtrless}} \mathrm{e}^{\mathcal{T}} \tag{3.37}$$

where $\mathcal{T}$ is the threshold determined to provide an acceptable level of false alarm by the system designer. Notice that (3.37) may be put into the form

$$h_{2L}(q_1) \underset{\mathcal{H}_0}{\overset{\mathcal{H}_1}{\gtrless}} \mathrm{e}^{\mathcal{T}} h_{2L}(q_0). \tag{3.38}$$

As previously stated (and can be seen by inspection of (3.35)), $h_{2L}(q)$ is a monotonically decreasing function in q. Therefore, the inverse $h_{2L}^{-1}(q)$ exists. The NP detector may then be given as

$$h_{2L}^{-1}(\mathrm{e}^{\mathcal{T}} h_{2L}(q_0)) \underset{\mathcal{H}_0}{\overset{\mathcal{H}_1}{\gtrless}} q_1. \tag{3.39}$$

Define the quantity

$$f_{\mathrm{opt}}(q_0, \mathcal{T}) = \frac{1}{2}(q_0 - h_{2L}^{-1}(\mathrm{e}^{\mathcal{T}} h_{2L}(q_0))). \tag{3.40}$$

Adding the quantity $2f_{\mathrm{opt}}(q_0, \mathcal{T}) - q_1$ to both sides, (3.39) takes the form

$$q_0 - q_1 \underset{\mathcal{H}_0}{\overset{\mathcal{H}_1}{\gtrless}} 2f_{\mathrm{opt}}(q_0, \mathcal{T}). \tag{3.41}$$

Expanding the quadratic form of the signal present hypothesis ($\mathcal{H}_1$) given in (3.32),

$$\begin{aligned} q_1 &= (\mathbf{y}-\mathbf{s})^H \boldsymbol{\Sigma}^{-1}(\mathbf{y}-\mathbf{s}) \\ &= \mathbf{y}^H \boldsymbol{\Sigma}^{-1}\mathbf{y} - 2\mathrm{Re}\left\{\mathbf{s}^H \boldsymbol{\Sigma}^{-1}\mathbf{y}\right\} + \mathbf{s}^H \boldsymbol{\Sigma}^{-1}\mathbf{s} \\ &= q_0 - 2\mathrm{Re}\left\{\mathbf{s}^H \boldsymbol{\Sigma}^{-1}\mathbf{y}\right\} + \mathbf{s}^H \boldsymbol{\Sigma}^{-1}\mathbf{s}. \end{aligned} \tag{3.42}$$

Substituting (3.42) for q_1 in (3.41) yields

$$\mathrm{Re}\left\{\mathbf{s}^H \boldsymbol{\Sigma}^{-1}\mathbf{y}\right\} \underset{\mathcal{H}_0}{\overset{\mathcal{H}_1}{\gtrless}} f_{\mathrm{opt}}(q_0, \mathcal{T}) + \frac{1}{2}\mathbf{s}^H \boldsymbol{\Sigma}^{-1}\mathbf{s}. \tag{3.43}$$

From (3.43) it is observed that the optimum NP detector for SIRV distributed clutter takes the form of a whitening matched filter compared to a data dependent threshold. Crucially, this data dependent threshold depends on both the signal and the inverse of the function $h_{2L}(q)$.

For the special case of Gaussian distributed clutter, it can be shown that [78]

$$h_{2L}(q) = \frac{\exp(-\frac{q}{2\sigma^2})}{\sigma^{2L}} \tag{3.44}$$

where σ^2 is the variance of the Gaussian SIRV. From (3.44), $2f_{\mathrm{opt}}(q_0, \mathcal{T})$ may be derived as

$$\begin{aligned} 2f_{\mathrm{opt}}(q_0, \mathcal{T}) &= q_0 + 2\sigma^2 \ln\left[\mathrm{e}^{\mathcal{T} - \frac{q_0}{2\sigma^2}}\right] \\ &= 2\sigma^2 \mathcal{T}. \end{aligned} \tag{3.45}$$

Using (3.45) in (3.41), the optimal NP detector for Gaussian clutter is

$$q_0 - q_1 \underset{\mathcal{H}_0}{\overset{\mathcal{H}_1}{\lessgtr}} 2\sigma^2 \mathcal{T}. \tag{3.46}$$

Comparing (3.46) to (3.43) illustrates the influence of the modulating random variable of

a SIRV. For the Gaussian case, this random variable is actually the delta function. Therefore, the threshold for a constant false alarm rate only depends on the variance of the SIRV. However, for a general SIRV the optimal threshold depends on the variance as well as complete characterization of the SIRV. In the literature, attempts have been made to approximate $h_{2L}^{-1}(q)$ using quadratic [78] and linear [34] fitting techniques.

In order to further illuminate the problem, [78] considered another form of an optimal detector. This alternate derivation focuses on the modulating random variable rather than the function $h_{2L}(q)$. First, [78] introduced the transformation

$$\tau = \frac{1}{\alpha} \tag{3.47}$$

where the pdf of α is

$$f_\alpha(\alpha) = \frac{1}{\alpha^2} f_\tau(\frac{1}{\alpha}). \tag{3.48}$$

Using the transformed characteristic variable, the function $h_{2L}(q_i)$ becomes

$$h_{2L}(q_i) = \int_0^\infty \alpha^L \exp\left(-\frac{q_i}{2}\alpha\right) f_\alpha(\alpha) \mathrm{d}\alpha \tag{3.49}$$

and the pdf for each hypothesis is still given as (3.34). The conditional mean estimate of α is also the minimum mean squared error (MMSE) estimate, and may be expressed as [78]

$$\begin{aligned} \mathrm{E}\left[\alpha|\frac{q_i}{2}\right] &= \frac{1}{h_{2L}(q_i)} \int_0^\infty \alpha^{L+1} \exp\left(-\frac{q_i}{2}\alpha\right) f_\alpha(\alpha) \mathrm{d}\alpha \\ &= \frac{-2}{h_{2L}(q_i)} \frac{\mathrm{d}h_{2L}(q_i)}{\mathrm{d}(q_i)} \\ &= -2\frac{\mathrm{d}}{\mathrm{d}q_i} \ln h_{2L}(q_i). \end{aligned} \tag{3.50}$$

Therefore, taking the natural log of the LRT results in

$$\begin{aligned}\ln\frac{f_1(\mathbf{y})}{f_0(\mathbf{y})} &= \ln\frac{h_{2L}(q_1)}{h_{2L}(q_0)} \\ &= \int_{q_1/2}^{q_0/2} \mathrm{E}\left[\alpha|s\right] \mathrm{d}s. \end{aligned} \tag{3.51}$$

The LRT can then be expressed as

$$\Lambda(\mathbf{y}) = \exp\left(\int_{q_1/2}^{q_0/2} \mathrm{E}\left[\alpha|s\right] \mathrm{d}s\right). \tag{3.52}$$

For the case of Gaussian noise, the LRT becomes [78]

$$\Lambda(\mathbf{y}) = \exp\left(\int_{q_1/2}^{q_0/2} \frac{1}{\sigma_x^2} \mathrm{d}s\right). \tag{3.53}$$

where σ^2 is the variance of the Gaussian noise.

The structure of (3.52) and (3.53) show that the estimator correlator structure provides an optimal detection structure [79]. Additionally, this derivation crucially rests on the MMSE estimation of the transformed modulating variable, α. This estimation is difficult to implement in practice, but suggests a line of reasoning from which to derive suboptimal implementations, such as maximum likelihood (ML), generalized likelihood ratio test (GLRT) and maximum *a posteriori* (MAP) methods [78]. The intuition developed in this section will serve as an inspiration in future developments to derive novel methods to discriminate and identify an underlying SIRV distribution based on sampled data.

3.4 Generating SIRVs

When evaluating signal processing algorithms, it is useful to implement the algorithms on simulated data. However, generating multivariate, non-Gaussian random data is rarely a straightforward endeavor. This section will examine two general methods of generating

SIRV data depending on whether or not the characteristic pdf $f_V(v)$ of the desired SIRV is known [80].

When generating random variables, there are four common methods. First, common distributions (*e.g.* uniform, Gaussian, gamma) are often available from software packages (*e.g.* Matlab). Second, the desired distribution may be formed from a linear transformation of an available distribution. The transformation method will be employed in Section 4.1 to generate K distributed random vectors. Third, if the cdf of the desired pdf has a known inverse, the desired distribution may be obtained from uniformly distributed variables [81]. Let y be the desired data distribution, with pdf $p(y)$. The cdf is then given as

$$F_Y(y) = \int_{-\infty}^{y} p(y')\mathrm{d}y'. \tag{3.54}$$

If $z \sim U(0,1)$, data distributed according to the desired distribution is generated as

$$y = F^{-1}(z). \tag{3.55}$$

Finally, if the inverse of the cdf is not known, knowledge of the pdf allows for the generation of the random variables through the use of the 'Rejection Method' [1, 80–82].

The Rejection method requires the generation of two random variables. First, let u_1 be a random variable drawn from distribution $f_{U_1}(u_1)$ that can be readily simulated via a software package (*e.g.* uniform, gamma distributed). It is required that $f_{U_1}(u_1) = 0$ everywhere $f_R(r) = 0$. Second, let u_2 be a uniformly distributed random variable with support $(0,1)$. Third, let a be a positive lower bound such that

$$\frac{f_{U_1}(u_1)}{f_R(u_1)} \geq a > 0 \quad \text{for every } u_1. \tag{3.56}$$

The Rejection Method for generating random variables from the pdf of r as given in [1] is

1. Generate u_1 and u_2.

2. If $u_2 \leq a\frac{f_R(u_1)}{f_{U_1}(u_1)}$, then $u_1 = r$.

3. Otherwise reject u_1.

The proof for this method is given in Appendix B of [1].

Clearly, the accuracy of this method depends on the selection of the bound a. While the form given in Step 2 above is convenient to the proof given in [1], it is not necessarily amenable to determining a convenient value for a. A more intuitive approach is given in [81]. For convenience, define a scaling factor k to be large enough that

$$kf_{U_1}(u_1) \geq f_R(r). \tag{3.57}$$

Figure 3.1 illustrates the inequality of (3.57) for two arbitrary distributions.

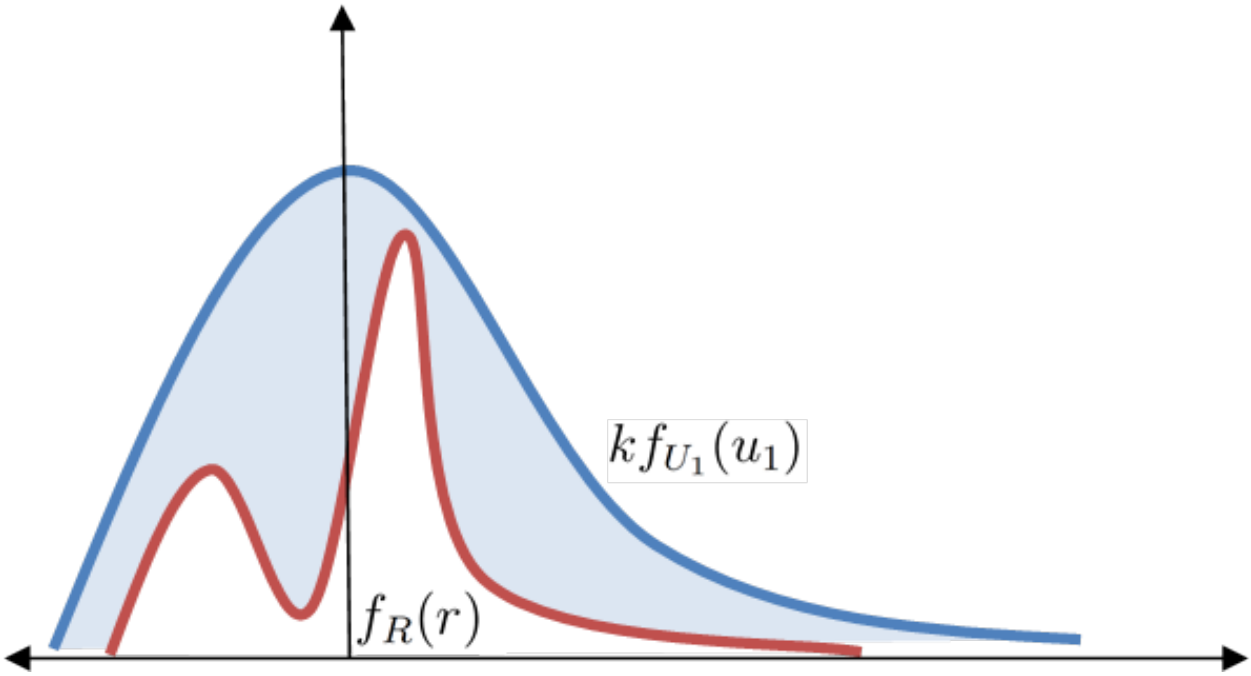

Figure 3.1: Rejection Method Example

As it is assumed that data distributed according to $f_{U_1}(u_1)$ may be readily obtained, the Rejection Method works by discarding points falling within the shaded area of Figure 3.1. The distribution $f_{U_1}(u_1)$ is used to sample within the same *range* as the desired pdf. The

random variable u_2 is then used to reject points that are not contained within the desired pdf. The steps of the rejection method then become

1. Generate u_1
2. Generate $u_2 \sim U(0, kf_{U_1}(u_1))$.
3. If $u_2 \leq f_R(u_1)$, then $u_1 = r$.
4. Otherwise reject u_1.

These steps are illustrated by Figure 3.2.

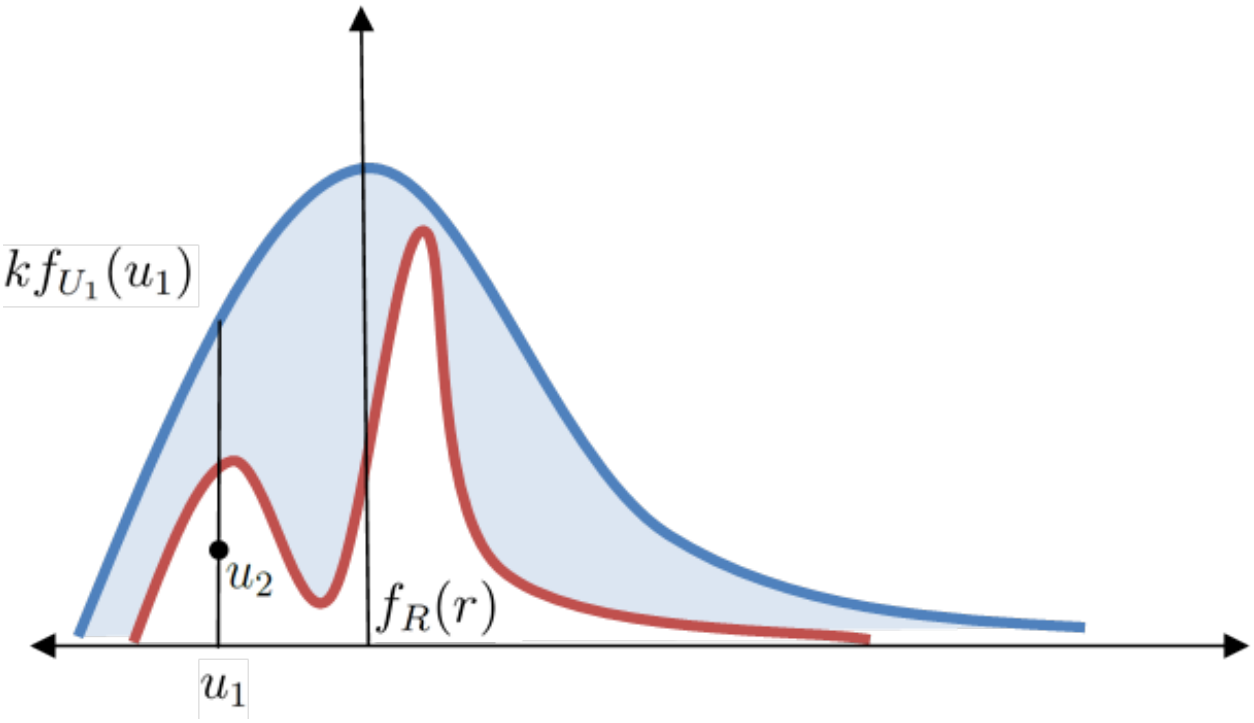

Figure 3.2: Rejection Method Example

The combination of u_1 and u_2 provide a uniform sampling of the area under the curve $kf_{U_1}(u_1)$ [81].

A straightforward implementation of the Rejection Method is to use the uniform distribution as the bounding distribution. Let the interval $(0, c)$ be approximately the range of

$f_R(r)$ and set k to be the maximum value of the desired pdf $f_R(r)$. Therefore, $u_1 \sim U(0, c)$ and $u_2 \sim U(0, k)$. Notice that

$$\frac{f_{U_1}(u_1)}{f_R(u_1)} \geq \frac{1}{ck} \tag{3.58}$$

Therefore, from (3.56) and (3.58), a possible bound is

$$a = \frac{1}{ck}. \tag{3.59}$$

Clearly, if the true domain of $f_R(r)$ is greater than c, the Rejection Method will result in data that is not precisely distributed according to the desired distribution. Similarly, if the pdf $f_R(r)$ approaches infinity at some point, the uniform distribution may be a poor choice as a bounding distribution. The Rejection method will be used in Section 4.2 to generate Weibull distributed random vectors, and these issues will be explored in more detail there.

3.4.1 Generating SIRV Data when the Characteristic pdf is Known

If $f_V(v)$ is known, the SIRV data may be generated using (3.5) (if real) or (3.29) (if complex) and (3.7) to achieve any length vector with any arbitrary covariance structure and mean vector. However, note that it was assumed in this chapter that $E[v^2] = 1$. It is often simpler to generate a random variable t with the properties $E[t^2] = a^2$. The random variable v is then obtained as $v = \frac{t}{a}$. Therefore, to generate SIRV data with an arbitrary distribution, one must be able to generate a Gaussian random vector $\mathbf{z}$ and the random variable v or t. The correlation and mean of SIRV can then be set with the desired correlation matrix $\mathbf{A}$ and mean vector $\mathbf{b}$. The general process is shown by Figure 3.3.

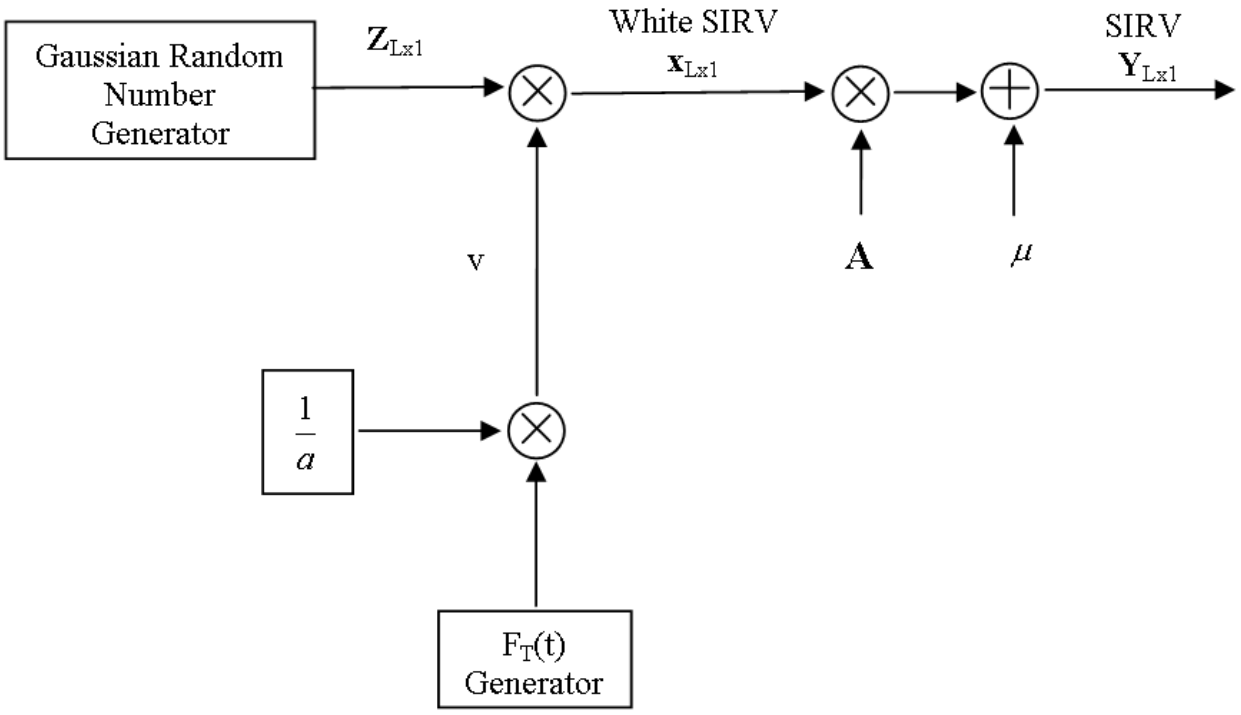

Figure 3.3: Generation of Arbitrary SIRV Data with Known Characteristic pdf

As the desired covariance matrix $\mathbf{\Sigma}$ should be known, the correlation matrix $\mathbf{A}$ can be formed from the eigendecomposition of $\mathbf{\Sigma}$ as

$$\mathbf{A} = \mathbf{Q}^T \mathbf{\Lambda}^{\frac{1}{2}} \tag{3.60}$$

where $\mathbf{Q}$ is the $L \times L$ matrix of eigenvectors and $\mathbf{\Lambda}$ are the corresponding eigenvalues. Note that if a complex SIRV is desired, the generated Gaussian vector $\mathbf{z}$ should be complex and the correlation matrix is formed from the complex conjugate transpose of the eigenvectors.

3.4.2 Generating SIRV Data when the Characteristic pdf is Unknown

If the characteristic pdf is not known in closed form, SIRV data may be generated by taking advantage of the spherical coordinates defined in (3.12). There are several important properties of (3.12) that should be noted. First, the pdfs of θ and ϕ_k are unchanged between

SIRVs of the same dimension. Second, the distribution envelope function $f_R(r)$ changes both with the the SIRV type and SIRV length (assuming a white SIRV). Finally, it can be seen that for a real, white, SIRV [1]

$$r^2 = \sum_{k=1}^{L} x_k^2 = \mathbf{X}^T\mathbf{X}. \tag{3.61}$$

Therefore, r is the ℓ_2 *norm* of the SIRV. Each element of the SIRV vector is generated by multiplying a random variable from the norm pdf and a random phase. As the phase is unchanged between white SIRVs, a white SIRV may be transformed into a different type of white SIRV by dividing by the current norm of the SIRV and multiplying by the desired norm. As the Gaussian distribution is readily available on most software packages (*e.g.* Matlab), it is a logical distribution with which to start. Further shaping of the white SIRV to generate data with a specified mean vector and covariance matrix are then performed as specified in Section 3.4.1. The generation technique for SIRVs when the characteristic pdf is not known is summarized as [1]:

1. Generate a white, zero mean Gaussian random vector with identity covariance matrix, denoted as $\mathbf{z}$.
2. Compute the norm of $\mathbf{z}$ as $r_Z = ||\mathbf{z}|| = \sqrt{\mathbf{z}^T\mathbf{z}}$. Note that $E[r_Z] = \sqrt{L}$.
3. Generate the desired norm of the SIRV $\mathbf{x}$, $r_X = ||\mathbf{x}|| = \sqrt{\mathbf{x}^T\mathbf{x}}$.
4. Generate $\mathbf{x}$ as $\mathbf{x} = \mathbf{z}\frac{r_X}{r_Z}$.

These steps result in a white SIRV $\mathbf{x}$. The arbitrary SIRV $\mathbf{x}$ may then be manipulated to have the desired covariance structure and mean vector as discussed in Section 3.4.1. Using this method requires the generation of random variables from the arbitrary pdf given by (3.14) for the desired SIRV.

3.5 The K Distribution

This section provides background information on the K distribution. The pdfs corresponding to common forms of the K distribution are presented, and proofs are offered to illuminate the intuition and development of the K distribution.

The K Distribution has been shown empirically and analytically to be a good fit to radar clutter in certain scenarios [7,53–55,58,59,83]. In addtion, the K distribution is admissible as a SIRP [1]. The envelope of the K distribution is parameterized both by a shape parameter and a scale parameter b. The shape parameter is typically denoted as α or ν [1,84]. The shape parameter defines how "heavy tailed" the distribution becomes. For very small values of ν, the data is very heavy tailed. However, as $\nu \to \infty$ the K distribution becomes Gaussian [75]. The amplitude pdf of the K distribution is given as [1, 75]

$$\begin{aligned} f_R(r) &= \frac{2b}{\Gamma(\nu)} \left(\frac{br}{2} \right)^{\nu} \mathrm{K}_{\nu-1}(br) \\ &= \frac{b^{\nu+1} r^{\nu}}{2^{\nu-1}\Gamma(\nu)} \mathrm{K}_{\nu-1}(br) \end{aligned} \tag{3.62}$$

where $\mathrm{K}_{\nu}(\bullet)$ is the modified Bessel function of the second kind of order ν, which gives the distribution its name. The function $h_L(q)$ of the K distribution is [1]

$$h_L(q) = \frac{b^L}{\Gamma(\nu)} \frac{(b\sqrt{q})^{\nu-\frac{L}{2}}}{2^{\nu-1}} K_{\frac{L}{2}-\nu}(b\sqrt{q}). \tag{3.63}$$

Therefore, from (3.11) and (3.63), the quadratic form of the pdf for real valued samples is

derived as

$$\begin{aligned} f_Q(q) &= \frac{q^{\frac{L}{2}-1}}{2^{\frac{L}{2}}\Gamma(\frac{L}{2})} h_L(q) \\ &= \frac{q^{\frac{L}{2}-1}}{2^{\frac{L}{2}}\Gamma(\frac{L}{2})} \frac{b^L}{\Gamma(\nu)} \frac{(b\sqrt{q})^{\nu-\frac{L}{2}}}{2^{\nu-1}} K_{\frac{L}{2}-\nu}(b\sqrt{q}) \\ &= \frac{b^{\nu+\frac{L}{2}} q^{\frac{\nu}{2}+\frac{L}{4}-1}}{\Gamma(\frac{L}{2})\Gamma(\nu)2^{\frac{L}{2}+\nu-1}} K_{\frac{L}{2}-\nu}(b\sqrt{q}). \end{aligned} \tag{3.64}$$

For L complex valued samples, the pdf of (3.64) becomes

$$f_Q(q) = \frac{b^{\nu+L} q^{\frac{\nu+L}{2}-1}}{\Gamma(L)\Gamma(\nu)2^{L+\nu-1}} K_{L-\nu}(b\sqrt{q}) \tag{3.65}$$

Figure 3.4 plots the cdf for the quadratic form of a complex K distributed SIRV with $L = 4$ samples per vector. The curves for $\nu = 0.05$ and $\nu = 100$ in particular illustrate the heavy tailed nature of the K distribution.

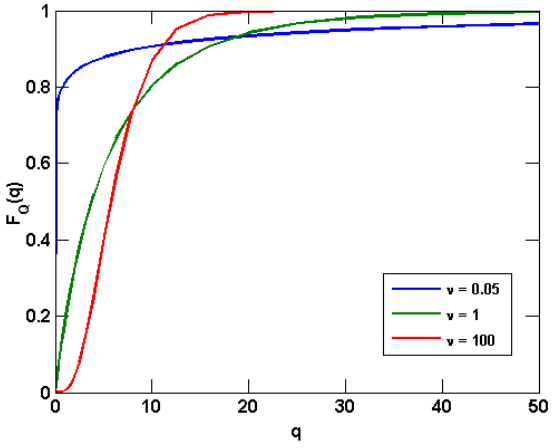

Figure 3.4: cdfs of the K distribution for increasing shape parameter

While there are many methods of deriving the K distribution, for the purposes of this work the method given in [8] provides the most illumination. The K distribution arises when the modulating random variable V is a generalized χ distribution with unit root mean square

value (RMS) (*i.e.* $E[v^2] = 1$). The pdf of V is given as [8]

$$f_V(v) = \frac{2v^{2\alpha-1}}{\Gamma(\alpha)}\alpha^{\alpha}\exp(-\alpha v^2)u(v) \tag{3.66}$$

where α is the shape parameter of the generalized χ distribution. To avoid confusion between the sample random variable v and the shape parameter notation ν that is used throughout this work, we will use $\alpha \equiv \nu$ for the majority of this derivation. In other contexts, the modulating variable for the K distribution is sometimes reported as [1]

$$f_V(v) = \frac{2b}{\Gamma(\alpha)2^{\alpha}}(bv)^{2\alpha-1}\exp\left(-\frac{b^2v^2}{2}\right)u(v) \tag{3.67}$$

where b is the scale parameter. Note that (3.66) is obtained from (3.67) by setting

$$b = \sqrt{2\nu}. \tag{3.68}$$

By normalizing the scale parameter with respect to the shape parameter, the modulating variable is normalized to unit variance. When thought of in context of modeling clutter, (3.66) results in the power (*i.e.* variance) of the K distributed SIRV being determined by the covariance structure of the complex Gaussian component of the SIRV. This restriction allows for easier comparison between SIRV distributions, so we will use (3.66) rather than the more general (3.67).

To establish that (3.66) is the modulating variable of the K distributed SIRV, we will

show that substituting (3.66) in (3.10) results in (3.63). Substituting (3.66) in (3.10) yields

$$\begin{aligned}
h_L(q) &= \int_0^\infty v^{-L}\exp(-\frac{q}{2v^2})\frac{2v^{2\alpha-1}}{\Gamma(\alpha)}\alpha^\alpha\exp(-\alpha v^2)\mathrm{d}v \\
&= \frac{1}{\Gamma(\alpha)}\int_0^\infty 2v^{2\alpha-L-1}\alpha^\alpha\exp\left(-\alpha v^2-\frac{q}{2v^2}\right)\mathrm{d}v \\
&= \frac{1}{\Gamma(\alpha)}\int_0^\infty 2(\alpha v^2)^\alpha v^{-L-1}\exp\left(-\alpha v^2-\frac{q}{2v^2}\right)\frac{\alpha v}{\alpha v}\mathrm{d}v \\
&= \frac{1}{\Gamma(\alpha)}\int_0^\infty (\alpha v^2)^\alpha\frac{v^{-L-2}}{\alpha}\exp\left(-\alpha v^2-\frac{q}{2v^2}\right)2\alpha v\frac{\alpha^{L/2}}{\alpha^{L/2}}\mathrm{d}v \\
&= \frac{1}{\Gamma(\alpha)}\int_0^\infty (\alpha v^2)^\alpha(\alpha v^2)^{-L/2-1}\alpha^{L/2}\exp\left(-\alpha v^2-\frac{q}{2v^2}\right)2\alpha v\mathrm{d}v. \qquad (3.69)
\end{aligned}$$

Introducing the change of variables

$$\begin{aligned}
t &= \alpha v^2 \\
\mathrm{d}t &= 2\alpha v \qquad (3.70)
\end{aligned}$$

into (3.69) results in

$$\begin{aligned}
h_L(q) &= \frac{1}{\Gamma(\alpha)}\int_0^\infty t^\alpha t^{-L/2-1}\alpha^{L/2}\exp\left(-t-\frac{q\alpha}{2t}\right)\mathrm{d}t \\
&= (2^{1-\alpha/2+L/4}(\alpha q)^{\alpha/2-L/4})(2^{-1+\alpha/2-L/4}(\alpha q)^{-\alpha/2+L/4})\frac{\alpha^{L/2}}{\Gamma(\alpha)}\int_0^\infty t^{\alpha-L/2-1}\exp\left(-t-\frac{q\alpha}{2t}\right)\mathrm{d}t \\
&= \frac{\alpha^{L/2}}{\Gamma(\alpha)}(2^{1-\alpha/2+L/4}(\alpha q)^{\alpha/2-L/4})\frac{(\sqrt{\alpha q/2})^{L/2-\alpha}}{2}\int_0^\infty t^{\alpha-L/2-1}\exp\left(-t-\frac{q\alpha}{2t}\right)\mathrm{d}t. \qquad (3.71)
\end{aligned}$$

From [85], the modified Bessel function of the second kind can be given as

$$K_\beta(xz) = \frac{z^\beta}{2}\int_0^\infty \exp\left[-\frac{x}{2}(t+\frac{z^2}{t})\right]t^{-\beta-1}\mathrm{d}t. \qquad (3.72)$$

Letting

$$\begin{aligned}\beta &= \frac{L}{2} - \alpha \\ x &= 2 \\ z &= \sqrt{\frac{q\alpha}{2}}\end{aligned} \tag{3.73}$$

and substituting the values in (3.73) into (3.72),

$$\begin{aligned}K_{\frac{L}{2}-\alpha}(2\sqrt{\frac{q\alpha}{2}}) &= \frac{(2\sqrt{\frac{q\alpha}{2}})^{L/2-\alpha}}{2}\int_0^\infty \exp\left[-\frac{2}{2}(t+\frac{\frac{q\alpha}{2}}{t})\right] t^{-L/2+\alpha-1}\mathrm{d}t \\ \implies K_{\frac{L}{2}-\alpha}(\sqrt{2q\alpha}) &= \frac{(\sqrt{\frac{q\alpha}{2}})^{L/2-\alpha}}{2}\int_0^\infty \exp\left[-t-\frac{q\alpha}{2t})\right] t^{\alpha-L/2-1}\mathrm{d}t.\end{aligned} \tag{3.74}$$

Substituting the result of (3.74) into (3.71) yields

$$\begin{aligned}h_L(q) &= \frac{\alpha^{L/2}}{\Gamma(\alpha)}(2^{1-\alpha/2+L/4}(\alpha q)^{\alpha/2-L/4})K_{\frac{L}{2}-\alpha}(\sqrt{2q\alpha}) \\ &= \frac{2^{1-\alpha/2+L/4}\alpha^{L/2+\alpha/2-L/4}q^{\alpha/2-L/4}}{\Gamma(\alpha)}K_{\frac{L}{2}-\alpha}(\sqrt{2q\alpha}) \\ &= \frac{2^{1-\alpha/2+L/4}\alpha^{\alpha/2+L/4}q^{\alpha/2-L/4}}{\Gamma(\alpha)}K_{\frac{L}{2}-\alpha}(\sqrt{2q\alpha}).\end{aligned} \tag{3.75}$$

To finish the derivation, substitute (3.68) into (3.63), which results in

$$\begin{aligned}h_L(q) &= \frac{(2\nu)^{L/2}(\sqrt{2\nu q})^{\nu-L/2}2^{1-\nu}}{\Gamma(\nu)}K_{\frac{L}{2}-\nu}(\sqrt{2q\nu}) \\ &= \frac{2^{1-\nu/2+L/4}\nu^{\nu/2+L/4}q^{\nu/2-L/4}}{\Gamma(\nu)}K_{\frac{L}{2}-\nu}(\sqrt{2q\nu}).\end{aligned} \tag{3.76}$$

Recalling that $\alpha \equiv \nu$, (3.75) is clearly equivalent to (3.76), establishing the generalized χ distribution as the modulating variable for K distributed SIRVs.

In the case of the K distribution, the random variable V is readily obtained from the

Gamma distribution, defined as [86]

$$f_{T'}(t') = \frac{t'^{\nu-1}}{\beta^{\nu}\Gamma(\nu)}\exp(-\frac{t'}{\beta}) \quad t > 0 \tag{3.77}$$

where $\nu > 0$ is the desired shape parameter and $\beta > 0$ is the scale parameter. For our purposes the scale parameter is set to 1, yielding

$$f_{T'}(t') = \frac{t'^{\nu-1}}{\Gamma(\nu)}\exp(-t') \quad t > 0. \tag{3.78}$$

Gamma distributed random variables are typically available on mathematical software packages (*e.g.* the function *gamrnd* in Matlab). The random variable T is then obtained from the transformation

$$\begin{aligned} T &= g(T') \\ &= \frac{\sqrt{2T'}}{b} \\ &= \sqrt{\frac{2T'}{2\nu}} \\ &= \sqrt{\frac{T'}{\nu}}. \end{aligned} \tag{3.79}$$

where b is the normalized scale parameter. As $t' > 0$,

$$t' = g^{-1}(t) = t^2\nu \tag{3.80}$$

has one root and

$$\left|\frac{\mathrm{d}g^{-1}(t)}{\mathrm{d}t}\right| = 2t\nu. \tag{3.81}$$

From (3.78), (3.80), and (3.81) the pdf of T is found to be [5]

$$\begin{aligned} f_T(t) &= f_{T'}(g^{-1}(t)) \left| \frac{\mathrm{d}g^{-1}(t)}{\mathrm{d}t} \right| \\ &= \frac{(t^2\nu)^{\nu-1}}{\Gamma(\nu)} \exp(-t^2\nu) 2t\nu \\ &= \frac{2t^{2\nu-1}\nu^{\nu}}{\Gamma(\nu)} \exp(-t^2\nu). \end{aligned} \tag{3.82}$$

As the pdf of (3.82) is equivalent to (3.66), transforming Gamma distributed random variables according to (3.79) yields generalized χ distributed random variables.

It should be noted that the Laplace distribution is a special case of the K distribution. Laplace distributed SIRVs can be generated from (3.78) and (3.79) by setting $\nu = 1$ [1].

When measured data has been fitted to the K distribution, the shape parameter can be obtained from the envelope pdf via the method of moments (MoM) technique [87]. Using the scale parameter definition of (3.68) in (3.62), the n^{th} moment of the envelope pdf is given by [87]

$$\begin{aligned} E\left\{r^n\right\} &= m_R(n) \\ &= \left(\frac{2}{b}\right)^n \frac{\Gamma\left(\nu + \frac{n}{2}\right) \Gamma\left(1 + \frac{n}{2}\right)}{\Gamma(\nu)}. \end{aligned} \tag{3.83}$$

The estimate of the n^{th} moment is can be found from M amplitude samples of data $\mathbf{y} = [y_1, y_2, \ldots, y_M]$ as

$$\hat{m}_R(n) = \frac{1}{M} \sum_{i=1}^{M} |y_i|^n. \tag{3.84}$$

The shape parameter can then be estimated from the equation [87]

$$\frac{m_R(2)}{[m_R(1)]^2} = \frac{\hat{m}_R(2)}{[\hat{m}_R(1)]^2}. \tag{3.85}$$

Using (3.85) in (3.83) the estimate $\hat{\nu}$ is found by solving for ν in [87]

$$\frac{4}{\pi}\frac{\nu\Gamma^2(\nu)}{\Gamma^2\left(\nu+\frac{1}{2}\right)} - \frac{\hat{m}_R(2)}{[\hat{m}_R(1)]^2} = 0. \tag{3.86}$$

3.6 The Weibull Distribution

In 1951 Waloddi Weibull introduced the distribution that now bears his name [88]. While Weibull noted that his distribution did not have much theoretical relation to the problems he was examining, it did provide a very good empirical fit to measured data. However, it can be shown that the Rayleigh distribution is a special case of the more general Weibull pdf [89]. Therefore, when early radar engineers noticed that the Rayleigh distribution appeared to be a poor fit to measured radar amplitude data under certain circumstances, the Weibull distribution was a natural hypothesis to explore [52, 89]. Later efforts used the theory of SIRVs to provide a theoretical relationship between the Weibull distribution and radar clutter [8, 66]. The Weibull distribution is commonly reported with a shape parameter, $\nu > 0$, and scale parameter, $b > 0$. The Weibull envelope pdf may be given as [1, 7, 46, 66]

$$f_R(r) = b\nu r^{\nu-1}\exp(-br^{\nu}). \tag{3.87}$$

However, the form the scale parameter takes varies from author to author. Two other common forms are [17, 52, 90, 91]

$$f_R(r) = \frac{\nu}{a}\left(\frac{r}{a}\right)^{\nu-1}\exp\left(-\left(\frac{r}{a}\right)^{\nu}\right) \tag{3.88}$$

and [89]

$$f_R(r) = \frac{\nu r^{\nu-1}}{c}\exp\left(-\frac{r^{\nu}}{c}\right). \tag{3.89}$$

From(3.87), (3.88), and (3.89) it is clear that

$$b \equiv \left(\frac{1}{a}\right)^{\nu} \equiv \frac{1}{c}. \tag{3.90}$$

The scale parameter may also be normalized by dividing measured values by the median value, r_{median}. If

$$r' = \frac{r}{r_{\text{median}}}, \tag{3.91}$$

then it can be shown that [89, 92]

$$f_{R'}(r') = \ln(2)\nu(r')^{\nu-1}\exp\left(-\ln(2)(r')^{\nu}\right) \tag{3.92}$$

where $\ln(\bullet)$ denotes the natural logarithm. The normalization of (3.91) does not appear in the more recent literature (*e.g.* [17, 90]), and depends highly on the *a priori* assumption that the data is Weibull distributed. In practical systems, the Weibull distribution is only a hypothesis which must be confirmed over other hypothetical distributions. Therefore, for a unified, flexible framework we will not employ this normalization technique. The Weibull distribution is also sometimes reported using its cdf, given as [17]

$$F_R(r) = 1 - \exp\left(-br^{\nu}\right). \tag{3.93}$$

The cdf is needed to implement various goodness-of-fit tests, such as the Kolmogorov–Smirnov (KS) and Cramer-Von Mises (CV) tests, which have been used successfully to fit measured radar data to the Weibull distribution [17, 93].

While the shape parameter for the Weibull distribution may take on any real, positive value, the Weibull distribution cannot be classified as a SIRV for shape parameters greater than 2 [1,7,46,66]. However, lower shape parameters cause the Weibull distribution to exhibit heavier tails. Further, it can be shown that when $\nu = 1$ the Weibull distribution coincides with the exponential distribution, and for $\nu = 2$ the Weibull distribution is equivalent to

the Rayleigh distribution. Therefore, while shape parameters greater than $\nu = 2$ have been reported (*e.g.* [89]), those values will not cause an increase in false alarms relative to the assumption of complex Gaussian clutter (*i.e.* Rayleigh envelope).

The function $h_{2L}(q)$ for the Weibull distribution can be shown to be [1]

$$h_{2L}(q) = \sum_{k=1}^{L} C_k q^{\frac{k\nu}{2}-L} \exp\left(-b\sigma_y^{\nu} q^{\frac{\nu}{2}}\right) \tag{3.94}$$

where σ_y^2 is the variance of the individual samples, and

$$C_k = \sum_{m=1}^{k} (-1)^{m+L} 2^L \frac{\left(b\sigma_y^{\nu}\right)^k}{k!} \begin{pmatrix} k \\ m \end{pmatrix} \frac{\Gamma\left(1+\frac{m\nu}{2}\right)}{\Gamma\left(1+\frac{m\nu}{2}-L\right)}. \tag{3.95}$$

The quadratic form of the complex Weibull distribution with arbitrary dimensionality L can then be formed from (3.11), (3.94), and (3.95) as

$$f_Q(q) = \frac{1}{2^L \Gamma(L)} q^{L-1} \sum_{k=1}^{L} C_k q^{\frac{k\nu}{2}-L} \exp\left(-b\sigma_y^{\nu} q^{\frac{\nu}{2}}\right) \tag{3.96}$$

3.7 The Pareto Distribution

The Pareto distribution has been attracting interest in recent years as a good fit to measured sea clutter [94,95]. Recent work has characterized CFAR detectors for both univariate Pareto distributed data [96] and multivariate Pareto distributed data [97].

The modulating random variable V of the Pareto SIRV is known and may be generated by transforming Gamma distributed random variables. The Gamma pdf from equation (3.78) may be restated as [97]

$$f_T(t) = \frac{\lambda^{\alpha}}{\Gamma(\alpha)} t^{\alpha-1} \exp(\lambda v) \tag{3.97}$$

where λ is the scale parameter of the Gamma distribution (the inverse of the previous definition in (3.78)) and α is the shape parameter. Samples of the modulating random

variable V with desired shape parameter β may be generated from Gamma distributed random variables with shape $\alpha = \beta + 1$ and scale $\lambda = \beta$. This choice of λ and α is to ensure that $E[v^2] = 1$. The resulting random variable are then raised to the power $t^{-1/2}$ resulting in

$$\begin{aligned} f_V(v) &= 2v^{-3} f_T(v^{-2}) \\ &= 2v^{-3} \frac{\beta^{\beta+1}}{\Gamma(\beta+1)} v^{-2\beta} \exp(-\beta v^{-2}) \\ &= \frac{2\beta^{\beta}}{\Gamma(\beta)} \frac{\exp(-\beta/v^2)}{v^{2\beta+3}} \quad v \geq 0, \beta \geq 1. \end{aligned} \tag{3.98}$$

To provide a unified framework for the other distributions with shape parameters (*e.g* K, Weibull), we now change the designation of the shape parameter from β to ν. The use of β was done to clarify the results of (3.98). For a complex, length L Pareto distributed SIRV the function $h_{2L}(q)$ is found from (3.98) to be [97]

$$h_{2L}(q) = \frac{\Gamma(L+\nu+1)}{\Gamma(\nu+1)} \frac{\nu^{(\nu+1)}}{(q+\nu)^{(L+\nu+1)}}. \tag{3.99}$$

From (3.28) and (3.99), the pdf for the quadratic form of the complex Pareto SIRV is

$$f_Q(q) = \frac{\Gamma(L+\nu+1)\,\nu^{(\nu+1)}}{\Gamma(L)\Gamma(\nu+1)} \frac{q^{L-1}}{(q+\nu)^{(L+\nu+1)}}. \tag{3.100}$$

3.8 The Lognormal Distribution

The lognormal distribution is so named due to its relation to the normal distribution. Taking the natural logarithm of a lognormal distributed random variable results in a random variable that follows the normal, or Gaussian distribution. The lognormal distribution has been fit to measured data, especially sea clutter [54, 55, 57]. However, unlike the other distributions under consideration here, the lognormal distribution is not admissable as a SIRV [1]. Here we define the pdfs of the univariate and multivariate lognormal distributions.

Given a real valued, normally distributed random variable $p \sim \mathcal{N}(\mu, \sigma^2)$ with mean μ and variance σ^2, a real valued, univariate lognormal distributed random variable can be obtained by taking the exponential of p as [56]

$$r = \exp(p). \tag{3.101}$$

The lognormal random variable r then follows the pdf

$$f_R(r) = \frac{1}{\sqrt{(2\pi)}\sigma r}\exp\left(-\frac{\ln^2(r/m)}{2\sigma^2}\right) \tag{3.102}$$

where m is the median value of r, given as $m = \exp(\mu)$ and σ is now referred to as the "logarithmic standard deviation" of r [56]. Here we follow the convention of [56] and consider the Gaussian random variables to be zero mean, leading to the median value of r having the value $m = \exp(0) = 1$.

Complex valued lognormal distributed random variables may similarly be formed from complex valued Gaussian random variables. In general, define the complex valued Gaussian random variable z formed from two zero-mean real valued Gaussian random variables as

$$z = x + jy. \tag{3.103}$$

The complex valued lognormal distributed random variable w is then formed by taking the complex exponential of z, defined as [56]

$$w = u + jv = \text{cexp}(z) = [\exp(x)]\,[\cos(y) + j\sin(y)]\,. \tag{3.104}$$

The expected value of w is then [56]

$$E[w] = \exp\left(\frac{\sigma_x^2 - \sigma_y^2}{2}\right)[\cos(\sigma_{xy}) + j\sin(\sigma_{xy})]\,. \tag{3.105}$$

By requiring x and y to be uncorrelated i.i.d. random variables, the expected value of w is found from (3.105) to be

$$E[w] = \exp(0)\left[\cos(0) + j\sin(0)\right] = 1. \tag{3.106}$$

A length L uncorrelated, zero mean multivariate lognormal distributed vector with power P may be generated from a length L zero mean, unit variance, complex Gaussian random vector $\mathbf{z}$ as [56]

$$\mathbf{w} = \text{cexp}\left(\mathbf{z}\sqrt{\ln(1+P)}\right) - \mathbf{1}. \tag{3.107}$$

where $\mathbf{1}$ is a length L vector of ones (the expected value found in (3.106)). To create multivariate lognormal data with an arbitrary covariance matrix $\mathbf{\Sigma}$, form a matrix

$$\mathbf{\Sigma}' = \ln\left(\mathbf{1} + \mathbf{\Sigma}\right). \tag{3.108}$$

The shaping matrix $\mathbf{A}$ is formed from the eigendecomposition of $\mathbf{\Sigma}'$ as was shown in equation (3.60). Inserting the shaping matrix into (3.107) yields

$$\mathbf{w} = \text{cexp}\left(\mathbf{A}\mathbf{z}\right) - \mathbf{1}. \tag{3.109}$$

Chapter 4

Spherically Invariant Random Processes - New Work

In Chapter 5 we create a library of test statistics based on SIRV distributions. As a first step toward creating this library, in this chapter we extend the results of Chapter 3 to the simulation of several distributions belonging to the SIRV class of random vectors. First, we examine the K distribution. Second, the practical problems of simulating Weibull distributed data is discussed, and a solution is developed. Finally, we propose two new arbitrary SIRV distributions based on using Gamma distributed random variables to modulate a complex Gaussian random vector.

4.1 Examining the K Distribution

This section examines the simulation of the K distribution and verifies the accuracy of the simulation algorithm. While shape parameter $0.3 \leq \nu \leq 0.8$ are commonly reported [17, 18, 87], shape parameters up to $\nu = 100$ have also been measured [18]. Recall that smaller shape values correspond to "spikier" clutter (*i.e.* more outliers in the measured data).

The methods described in this chapter were implemented in Matlab. To generate the

histograms in all figures in this chapter 10^7 points were generated in a Monte Carlo fashion, and 10^3 bins were used to generate the histogram. The vector samples were formed from $L = 4$ complex samples with a covariance matrix of linearly decreasing correlation. In other words,

$$E[y, y-\tau] = \begin{cases} 1 - \frac{\tau}{L}, & \tau < L \\ 0, & \text{otherwise.} \end{cases} \tag{4.1}$$

The true (*i.e.* clairvoyantly known) inverse covariance matrix is used to form the quadratic form q.

It is instructive to examine the modulating random variable V for the K distribution. Recall from (3.6) that in the Gaussian case the random variable V becomes an impulse at $V = 1$. Also, it is expected that as the shape parameter goes to infinity, the K distribution tends to the Gaussian distribution. Figure 4.1 shows the analytical pdf of $f_V(v)$ for the K distribution for increasing values of ν.

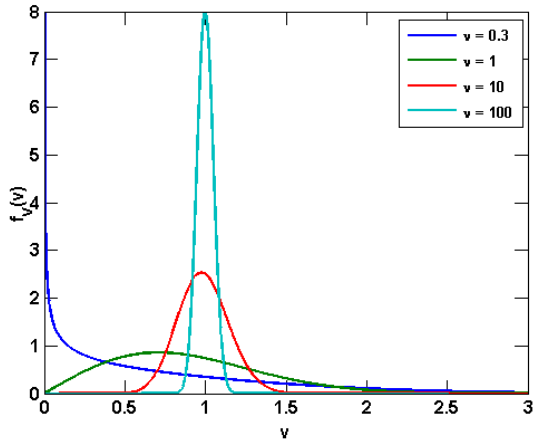

Figure 4.1: pdf of $f_V(v)$ for increasing shape parameter

The convergence of $f_V(v)$ to an impulse function can be seen in Figure 4.1, illustrating the behavior of the random variable as the shape parameter increases. In order to estimate a threshold for a Neyman-Pearson test, the effect of the random variable V must be well understood.

The behavior of the K distribution changes rapidly at low values of ν, but slowly at large

values. In order to clarify the behavior of the distribution, we examine the K distribution for three different regimes. These regimes are classified by a range of values of the shape parameter. We define low shape parameter regime to be from $0 < \nu < 0.5$, the medium regime to exist from $0.5 < \nu \leq 5$, and the large shape parameter regime to be for values $\nu > 5$. The low and medium regimes are the most commonly encountered in practice [17, 18, 87]. Examples of the pdfs and cdfs for these regimes are shown to illustrate the behavior of the distribution as a function of shape parameter, and we examine the impact on detector threshold levels and corresponding false alarm rates.

As the K distribution is heavier tailed than the (default) Gaussian distribution, the Neyman-Pearson threshold to achieve an acceptable level of false alarm will be greater than the threshold for the Gaussian assumption. This difference will be shown as

$$\begin{aligned} \Delta_{\text{thresh}}(\text{dB}) &\doteq 10\log_{10}\left(\frac{\sigma_y^2\mathcal{T}_K}{\sigma_y^2\mathcal{T}_G}\right) \\ &= 10\log_{10}\left(\frac{\mathcal{T}_K}{\mathcal{T}_G}\right) \end{aligned} \tag{4.2}$$

where σ_y^2 is the common variance (*i.e.* power) of the individual samples, $\mathcal{T}_K$ is the threshold for the K distribution producing a desired probability of false alarm, and $\mathcal{T}_G$ is the corresponding threshold for a Gaussian distributed random vector. Therefore, Δ_{thresh} expresses the threshold for the K distribution in terms of multiples of the Gaussian threshold for the same clutter power. Use of a threshold derived from the Gaussian assumption will lead to an increased P_{fa} in heavier tailed clutter. Therefore, we examine the P_{fa} resulting from using $\mathcal{T}_G$ when K distributed clutter is present. As there are no closed form solutions available for the thresholds for multivariate K distributed clutter, we use Monte Carlo simulations to estimate the thresholds. In order the obtain the thresholds, 10^8 Monte Carlo runs were performed, with a desired $P_{fa} = 10^{-6}$.

Figures 4.2a-4.3b illustrate the behavior of the K distribution for two values of ν in the low shape parameter regime. To verify the accuracy of the simulation procedure described in

Section 3.4.1 and the characteristic pdf generation method given in Section 3.5, the analytic pdf is plotted with the histogram in Figures 4.2a and 4.2b. Figures 4.3a and 4.3b show pdfs and cdfs, respectively, of the K distribution for several shape parameters.

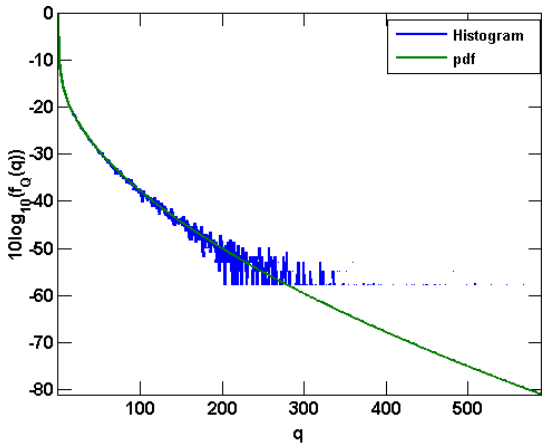

(a) Histogram and analytic pdf for Q, $\nu = 0.3$

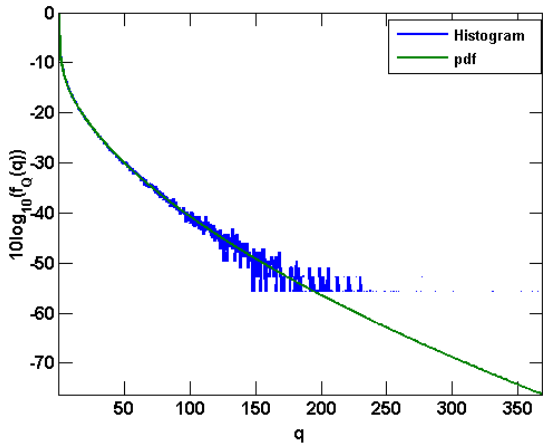

(b) Histogram and analytic pdf for Q, $\nu = 0.5$

Figure 4.2: Analytic and simulated pdf for K distribution for low values of ν

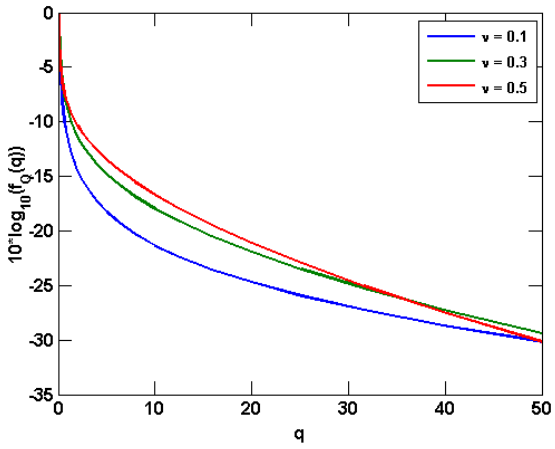

(a) Analytic pdf for Q, small shape parameters

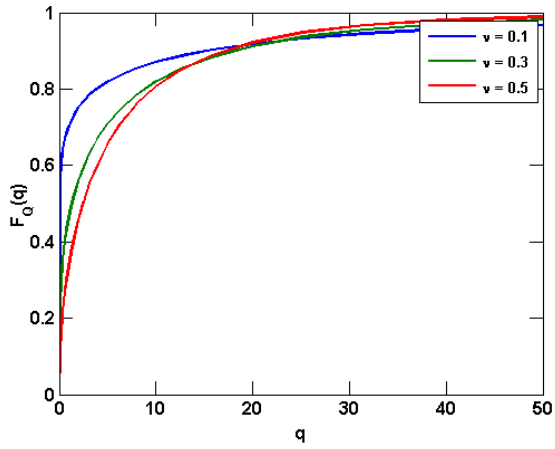

(b) Analytic cdf for Q, small shape parameters

Figure 4.3: Comparing K distribution pdfs and cdfs for small values of ν

While there is some difference between the analytic curve and histogram values in Figures 4.2a and 4.2b, the deviations are at areas of very low probability. Some variance is to be expected as the probability of an event approaches the inverse of the number of Monte Carlo trial runs. Figures 4.4a and 4.4b illustrate the impact of K distributed values on

the Neyman-Pearson hypothesis test. Figure 4.4a shows the increase in threshold over the Gaussian assumption, as defined in (4.2). Figure 4.4b shows the increase in false alarm resulting in applying a threshold derived from the Gaussian assumption to data that is K distributed. In other words, Figure 4.4b shows the penalty associated with *model mismatch*.

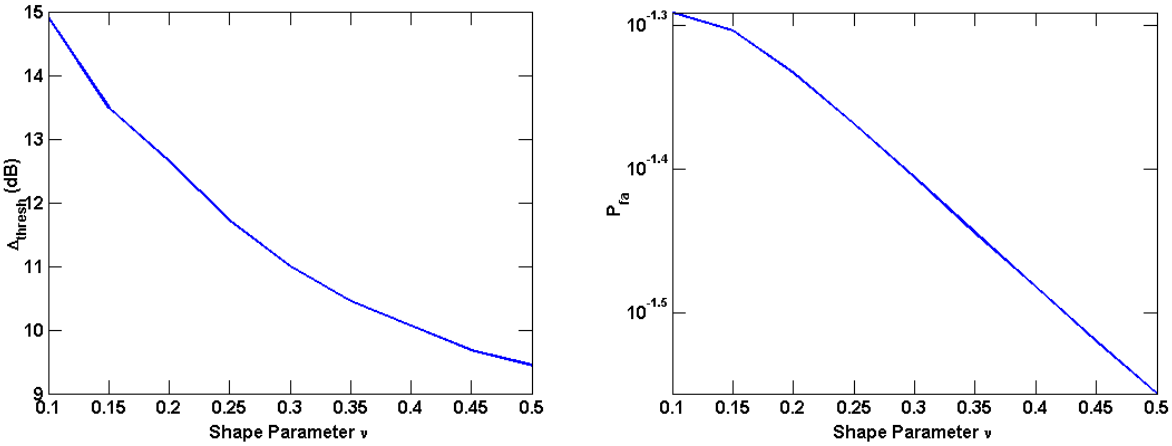

(a) Increased NP threshold for K distributed data for small values of ν

(b) Increased false alarm for K distributed data for small values of ν

Figure 4.4: Impact of K distribution for small values of ν on NP test

Recall that the threshold is derived for a desired $P_{fa} = 10^{-6}$. Therefore, Figure 4.4b show a great increase in false alarms when an incorrect model assumption is made. Figures 4.4a and 4.4b illustrate the consequences of using traditional, Gaussian based methods in impulsive clutter.

Figures 4.5a-4.6b explore the pdf and cdf of the K distribution for medium shape values. These shape values may still be encountered in practice (*e.g.*, [17, 18]),but are less heavy tailed than the pdfs shown in Figures 4.2a-4.3b. Once more, the efficacy of the simulation strategy is shown by the close match of the analytical pdfs and the histograms in Figures 4.5a and 4.5b.

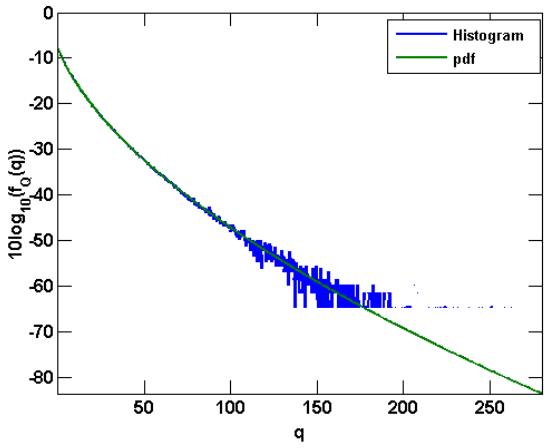

(a) Histogram and analytic pdf for Q, $\nu = 1$

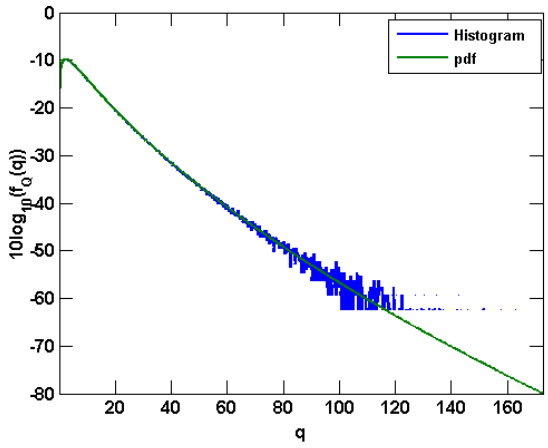

(b) Histogram and analytic pdf for Q, $\nu = 2$

Figure 4.5: Analytic and simulated pdf for K distribution for medium values of ν

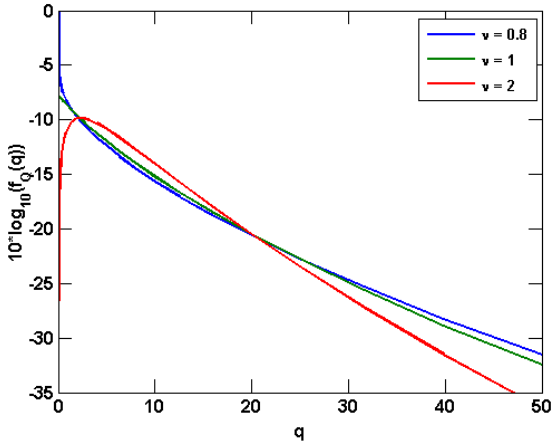

(a) Analytic pdf for Q, medium shape parameters

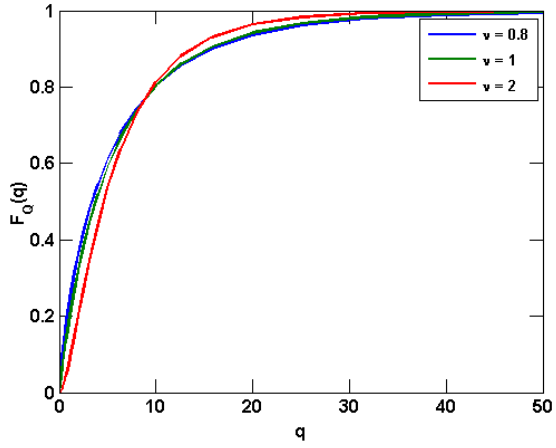

(b) Analytic cdf for Q, medium shape parameters

Figure 4.6: Comparing pdfs and cdfs of the K distribution for medium values of ν

Figures 4.7a-4.7b show that K distributed clutter with medium shape values results in an appreciable increase in false alarms with respect to the Gaussian assumption.

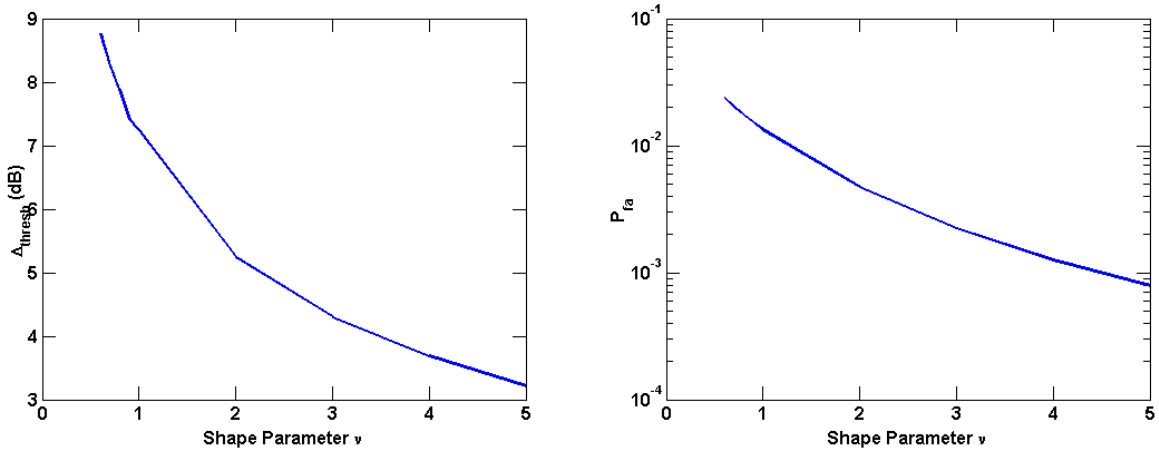

(a) Increased NP threshold for K distributed data for medium values of ν

(b) Increased false alarm for K distributed data for medium values of ν

Figure 4.7: Impact of K distribution for medium values of ν on NP test

Comparing Figures 4.6a-4.7b to 4.3a-4.4b, the K distribution appears to more sensitive low values of ν (*i.e.* $\nu < 1$). The increasing lack of sensitivity becomes apparent in Figures 4.8a-4.8b, which show the pdf and cdf for the K distribution for large values of ν.

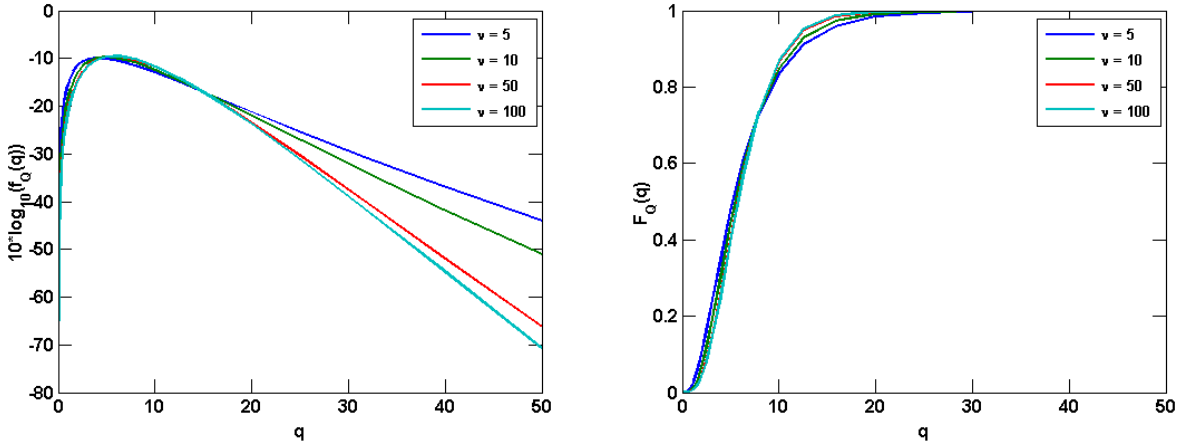

(a) Analytic pdf for Q, large shape parameters

(b) Analytic cdf for Q, large shape parameters

Figure 4.8: Comparing pdfs and cdfs of the K distribution for large values of ν

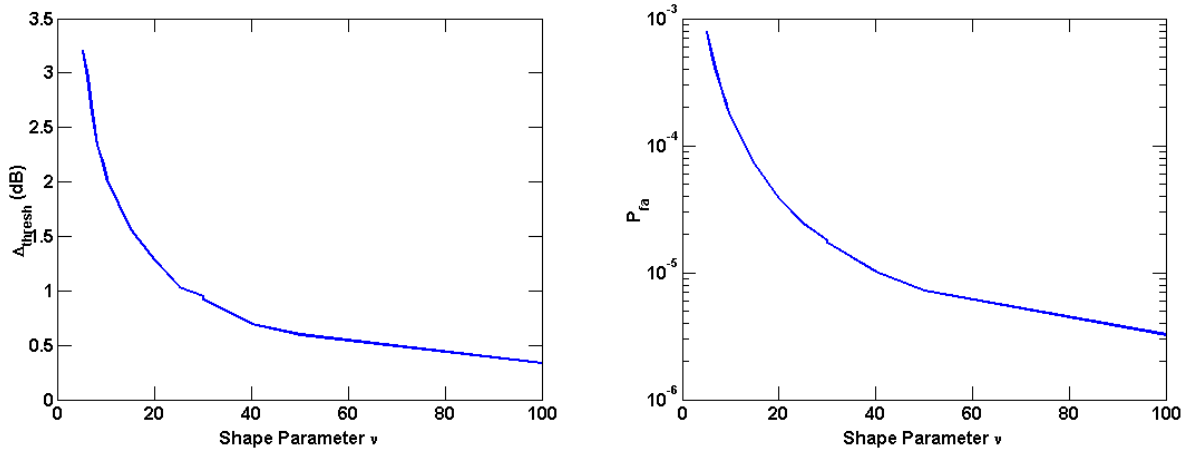

(a) Increased NP threshold for K distributed data for large values of ν

(b) Increased false alarm for K distributed data for large values of ν

Figure 4.9: Impact of K distribution for large values of ν on NP test

As shown in Figure 4.9a, the true threshold for K distributed data approaches the Gaussian threshold for large values of the shape parameter. For the large shape parameter regime the model mismatch only produces mildly elevated rates of false alarm.

The figures in this section suggest that the K distribution is primarily of interest for low values of shape parameters. This section serves as a first attempt at this understanding the K distribution, and the effects of the shape parameter and modulating variable on the final pdf. The analytical pdfs and derived thresholds will be used in later sections to compare K distributed data to other SIRV distributions. Finally, the simulation techniques for generating K distributed data using (3.79) and the gamma distribution were verified.

4.2 Examining the Weibull Distribution

In Section 3.5 the K distribution was explored using both the shape parameter and the modulating random variable, V. Unfortunately, the modulating variable for the Weibull distribution is not known [1, 8]. Without knowledge of V, the ℓ_2 norm of the Weibull distribution may be used to generate multivariate Weibull distributed data as described in Section 3.4.2. The general expression for the ℓ_2 norm of a real valued SIRV is given by (3.13).

From (3.13), (3.94), and (3.95) the envelope function for the complex Weibull distribution is given as

$$\begin{aligned} f_R(r) &= \frac{r^{2L-1}}{2^{L-1}\Gamma(L)} h_{2L}(r^2) \\ &= \frac{r^{2L-1}}{2^{L-1}\Gamma(L)} \sum_{k=1}^{L} C_k (r^2)^{\frac{k\nu}{2}-L} \exp\left(-b\sigma_y^{\nu}(r^2)^{\frac{\nu}{2}}\right) \\ &= \frac{1}{2^{L-1}\Gamma(L)} \sum_{k=1}^{L} C_k r^{k\nu-2L+2L-1} \exp\left(-b\sigma_y^{\nu} r^{\nu}\right) \\ &= \frac{1}{2^{L-1}\Gamma(L)} \sum_{k=1}^{L} C_k r^{k\nu-1} \exp\left(-b\sigma_y^{\nu} r^{\nu}\right) \end{aligned} \tag{4.3}$$

It is a standard assumption that each element has unit variance (*i.e.* $\sigma_y^2 = 1$). This assumption can be verified by comparing (3.87) to (3.95) and (4.3). We assume unit variance for each element in the SIRV, but this assumption can be readily modified through use of a shaping covariance matrix as shown in (3.60).

Here we use the Rejection Method implemented with two Uniform distributions to generate random data distributed according to (4.3). Recall that the Rejection Method requires the maximum range of the desired pdf, denoted as c, and the maximum value of the pdf, denoted as k. In order to find the maximum value of the pdf, we take the derivative of (4.3) after substituting $\sigma_y^2 = 1$, which results in

$$\begin{aligned} \frac{\mathrm{d}}{\mathrm{d}r} f_R(r) &= \frac{\mathrm{d}}{\mathrm{d}r} \left(\frac{1}{2^{L-1}\Gamma(L)} \sum_{k=1}^{L} C_k r^{k\nu-1} \exp\left(-br^{\nu}\right) \right) \\ &= \frac{1}{2^{L-1}\Gamma(L)} \sum_{k=1}^{L} C_k (k\nu-1) r^{k\nu-2} \exp\left(-br^{\nu}\right) + C_k r^{k\nu-1} \exp\left(-br^{\nu}\right) \left(-br^{\nu-1}\right) \\ &= \frac{\exp\left(-br^{\nu}\right)}{2^{L-1}\Gamma(L)} \sum_{k=1}^{L} C_k (k\nu-1) r^{k\nu-2} - C_k b r^{(k+1)\nu-2}. \end{aligned} \tag{4.4}$$

Recalling that SIRVs are unimodal [1] and setting (4.4) equal to 0 gives location of k as the

solution to the root finding problem

$$\sum_{k=1}^{L} C_k(k\nu - 1)r^{k\nu-2} - C_k b r^{(k+1)\nu-2} = 0. \tag{4.5}$$

As an example, consider the single sample case (*i.e.* $L = 1$). From (3.95),

$$\begin{aligned} C_1 &= (-1)^{1+1}2^1 \frac{(b)^1}{1!} \begin{pmatrix} 1 \\ 1 \end{pmatrix} \frac{\Gamma\left(1+\frac{\nu}{2}\right)}{\Gamma\left(1+\frac{\nu}{2}-1\right)} \\ &= 2b\frac{\Gamma\left(1+\frac{\nu}{2}\right)}{\Gamma\left(\frac{\nu}{2}\right)} \\ &= 2b\frac{\frac{\nu}{2}\Gamma\left(\frac{\nu}{2}\right)}{\Gamma\left(\frac{\nu}{2}\right)} \\ &= b\nu. \end{aligned} \tag{4.6}$$

Substituting (4.6) into (4.5) yields

$$\begin{aligned} & C_1(\nu-1)r^{\nu-1} - C_1 r^{(1+1)\nu-2} = 0 \\ \Longrightarrow\ & b\nu(\nu-1)r^{\nu-2} = b^2\nu r^{2\nu-2} \\ \Longrightarrow\ & r^{2\nu-2-\nu+2} = \frac{b\nu(\nu-1)}{b^2\nu} \\ \Longrightarrow\ & r^{\nu} = \frac{\nu-1}{b} \\ \Longrightarrow\ & r = \sqrt[\nu]{\frac{\nu-1}{b}}. \end{aligned} \tag{4.7}$$

Examination of (4.3) and (4.7) reveals that the maximum pdf value is $f_R(0) = \infty$ when $\nu \leq 1$. Therefore, as a rule k can be found by root finding methods commonly implemented in software such as Matlab or Mathematica for $\nu > 1$. However, for values of $\nu \leq 1$ an approximate value of k must be chosen such that the resultant pdf is approximately equal to the desired pdf.

Therefore, it is important to develop a procedure that can generate complex multivariate

data that is approximately Weibull distributed. Later developments will require the generation of data for varying shape parameters, so special attention must be paid to creating a general procedure that is amenable to automation. We rely on numerical integration of the pdf given in (4.3) to yield the cdf. The cdf will then be used to select the values of b and k to be used in the Rejection Method.

As an example, consider a dimension $L = 4$ complex Weibull SIRV with desired $b = 1, \nu = 0.3$. Caution must be taken when estimating the cdf of the distribution, as the pdf goes to infinity rapidly as $r \to 0$. In addition, as the Weibull distribution is heavy tailed for small values of ν, there is probability mass for large magnitude events that must be accounted for. Therefore, we use a logarithmic scaling of r to reduce the computational demands of the integration and allow for a large range of values of r. A common method approximates the function between integration points as rectangular area (*i.e.* the integral is approximated by a Riemmanian sum) over the pdf [98]. Here we suggest two alternate procedures: trapezoidal integration and adaptive piecewise integration (API).

The trapezoidal rule gives a linear interpolation between two points, approximating the local area of the function as a trapezoid [99]. The linear interpolation provides a local, first order approximation of the function between each integration points. Therefore, for an equal number of integration points, the trapezoidal rule provides a more accurate numerical integration when compared to the rectangular (*i.e.* zero order) approximation given by the Riemmanian sum.

In contrast to the trapezoidal and rectangular rules, adaptive quadrature rules attempt to satisfy the condition

$$\epsilon \approx \left| Q - \int_a^b f(x)\mathrm{d}x \right| \tag{4.8}$$

where ϵ is the magnitude of the error between the true integral and the estimate

$$Q \approx \int_a^b f(x)\mathrm{d}x. \tag{4.9}$$

The adaptive quadrature rule then recursively subdivides the interval $[a, b]$ until the error between the approximation and the true integral satisfies a user defined bound [99, 100]. In local adaptive quadrature integration, the error condition must be met for each subdivision, while in global adaptive quadrature integration an error bound must be met over the entire integration area. Adaptive quadrature rules provide methods to automatically integrate well behaved functions, and the only user defined variable needed is the maximum magnitude of error. The user defined magnitude of error also allows for greater ease in reproducing results. However, the implementation of such rules are more complex than trapezoidal integration.

Rather than derive and implement our own adaptive quadrature integrator, we use the Matlab *integral* function. The *integral* function is a globally adaptive quadrature technique. However, the *integral* function is not capable of integrating the PDF of the Weibull distribution for small shape parameters due to large changes in the pdf over small steps in r. Therefore, we still must manually divide the region of integration into smaller pieces to be fed into the integral function. We call this approach the adaptive piecewise integration (API) approach.

Figures 4.10a and 4.10b show the result of using rectangular numerical integration, trapezoidal numerical integration, and API to examine the cdf of the Weibull distribution. In Figure 4.10a the integration is carried over a spacing of 2 logarithmic units between samples, while Figure 4.10b uses a stepsize of 0.2 logarithmic units.

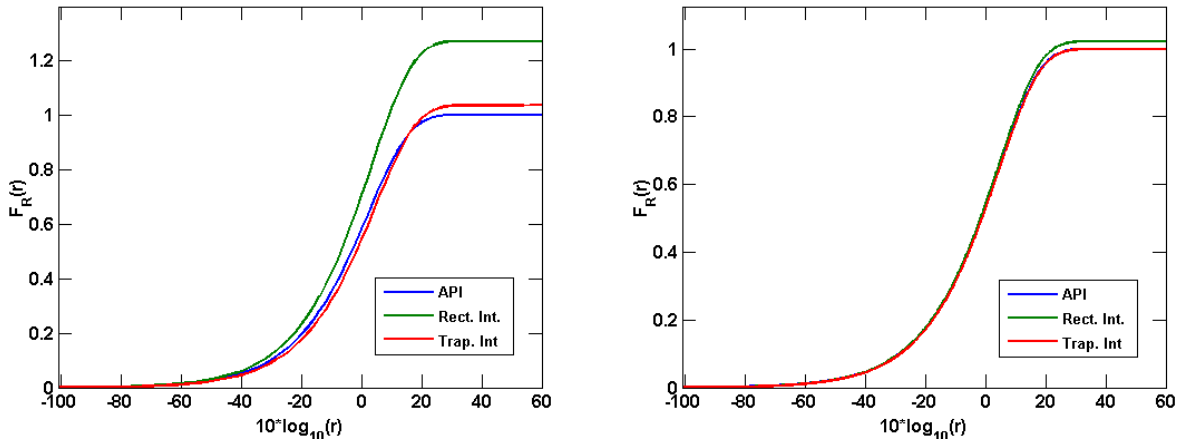

(a) Comparing numerical integration techniques with insufficient sample support

(b) Comparing numerical integration techniques with insufficient sample support

Figure 4.10: Examples of numerical integration of the cdf of the Weibull SIRV

Upon examination of Figures 4.10a and 4.10b, it is clear that only the trapezoidal and API techniques should be used. However, the trapezoidal rule depends on sufficiently small sample spacing to yield accurate results, while the adaptive technique only requires that the rate of change between samples be small enough that the algorithm can function. In either case, as the behavior of the pdf becomes less extreme with increasing shape parameter, an automated cdf generation algorithm may be formed that uses parameters defined by a worst case shape parameter. Therefore, the pdf for any shape parameter greater than the worst case will integrate properly. Due to its flexibility and the ability to define an error bound of the integration, we will use the API method for the remainder of this work with the default global error bound of $\epsilon < 10^{-10}$.

Now that the cdf can be found, we will use the left and right tails of the cdf to determine appropriate bounding constants for the Rejection method. As a first approximation, we will consider the appropriate bounds on a cdf to occur when

$$1 - F_R(c) \leq 10^{-4} \tag{4.10}$$

and

$$F_R(k) \leq 10^{-4}. \tag{4.11}$$

Continuing with the example of a complex Weibull SIRV of length $L = 4$ with scale parameter $b = 1$ and shape parameter $\nu = 0.3$, the conditions of (4.10) and (4.11) are shown in Figure 4.11a, while the resulting values of the maximum pdf value and the pdf value at the maximum range are shown in Figure 4.11b.

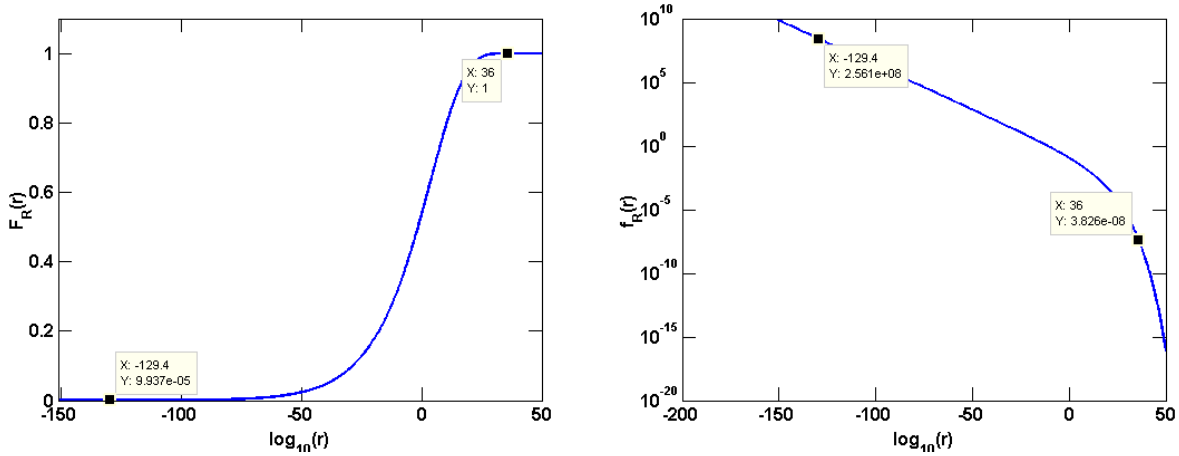

(a) $F_R(c)$ and $F_R(k)$ for $b = 1, \nu = 0.3$

(b) $f_R(c)$ and $f_R(k)$ for $b = 1, \nu = 0.3$

Figure 4.11: Finding approximate values of c and k with the estimated CDF of a Weibull distribution for $\nu = 0.3$

From Figures 4.11a and 4.11b, to satisfy the constraint of (4.11) the maximum pdf value is $k = 2.58 \times 10^8$. While shape parameters as low as $\nu = 0.3$ have been reported in the literature [90], the Rejection Method using the uniform distribution as a bounding distribution is not feasible. In future work, we will attempt to find a distribution that provides a tighter bound. A tradeoff must be made for $\nu \leq 1$ between accuracy of the resultant pdf and number of points that will be rejected. This tradeoff is more clear when examining the difference between the envelope pdf for $\nu = 0.7$ and $\nu = 0.8$.

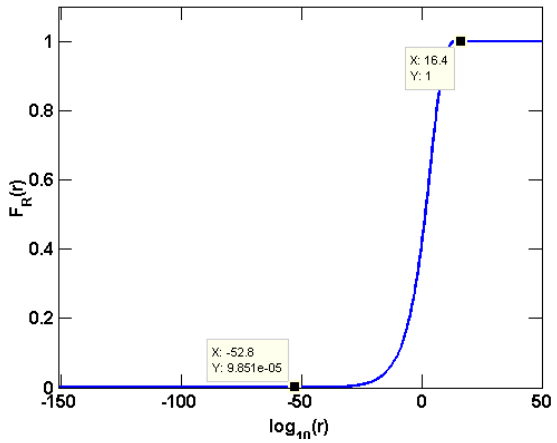

(a) $F_R(c)$ and $F_R(k)$ for $b = 1, \nu = 0.7$

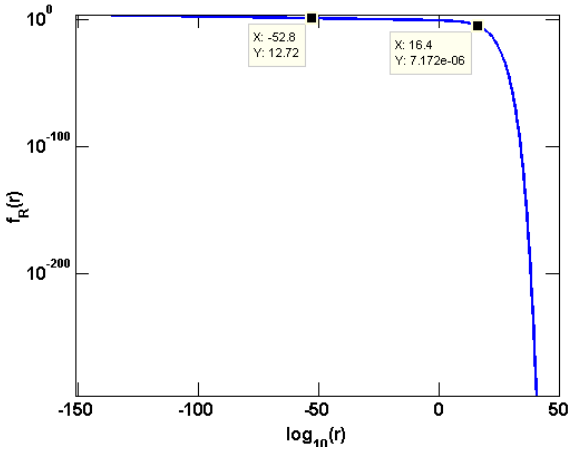

(b) $f_R(c)$ and $f_R(k)$ for $b = 1, \nu = 0.7$

Figure 4.12: Finding approximate values of c and k with the estimated CDF of a Weibull distribution for $\nu = 0.7$

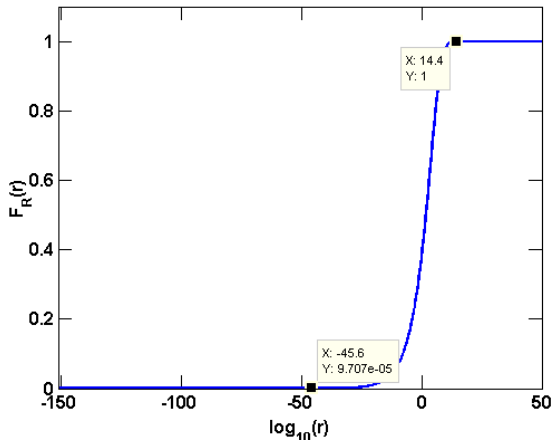

(a) $F_R(c)$ and $F_R(k)$ for $b = 1, \nu = 0.8$

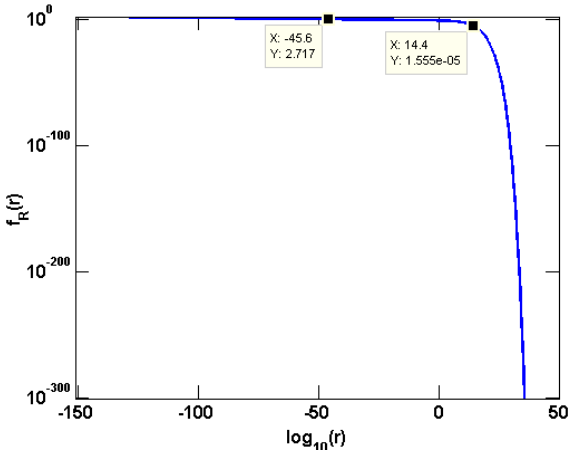

(b) $f_R(c)$ and $f_R(k)$ for $b = 1, \nu = 0.8$

Figure 4.13: Finding approximate values of c and k with the estimated CDF of a Weibull distribution for $\nu = 0.8$

Using the values for c and k determined in Figures 4.12a and 4.13a, 10^5 samples were generated according to the Rejection method. The probability of a sample being accepted as fitting (4.3) when $\nu = 0.7$ is found to be $P_{accept} \approx 7.5 \times 10^{-4}$, while for $\nu = 0.8$, $P_{accept} \approx 9.3 \times 10^{-3}$. Therefore, there is approximately an order of magnitude more samples rejected for $\nu = 0.7$ as compared to $\nu = 0.8$. Due to the excessive calculations required to generate Weibull envelope data with low shape parameters, for the present work we limit our examination to

values of $\nu \geq 0.8$.

However, for values $1 < \nu \leq 2$, the maximum pdf value may be found explicitly through root finding methods. As an example, Figures 4.14a and 4.14b show the pertinent points for $\nu = 1.01$.

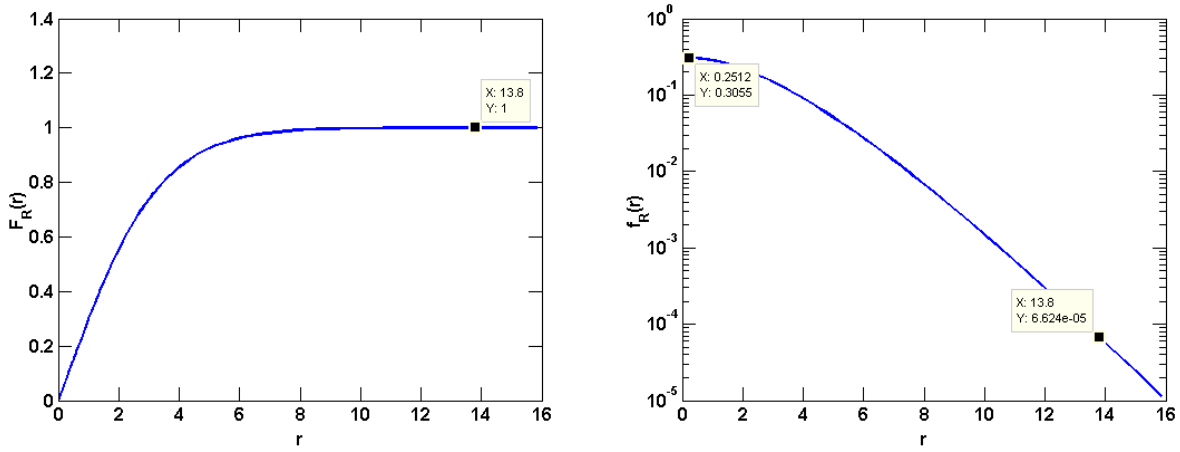

(a) $F_R(c)$ and $F_R(k)$ for $b = 1, \nu = 1.01$

(b) $f_R(c)$ and $f_R(k)$ for $b = 1, \nu = 1.01$

Figure 4.14: Finding approximate values of c and k with the estimated CDF of a Weibull distribution for $\nu = 1.01$

While the maximum value of the pdf is bounded in this region, the range of the pdf is still infinite. Therefore, the maximum value for the range of the pdf must still be found from (4.10) or simply set to where (4.11) is satisfied for all values of ν in this region. In other words, we use a common lower bound, which becomes increasingly tight as the shape parameter increases.

To evaluate the Rejection Method for both regions, Monte Carlo simulations were run for $\nu = 0.9$ and $\nu = 1.1$. Each simulation generated 10^8 Weibull envelope random variables. For $\nu = 0.9$, the maximum pdf value that satisfies (4.11) is $k = 0.8153$, reached at $r = 1.05 \times 10^{-4}$. The maximum range, satisfying (4.10), is reached at $r = 20$. Figures 4.15a shows the analytic pdf and the histogram of the resultant data. Figure 4.15a likewise gives the cdf for both the analytic function and the empirical estimate given by the histogram.

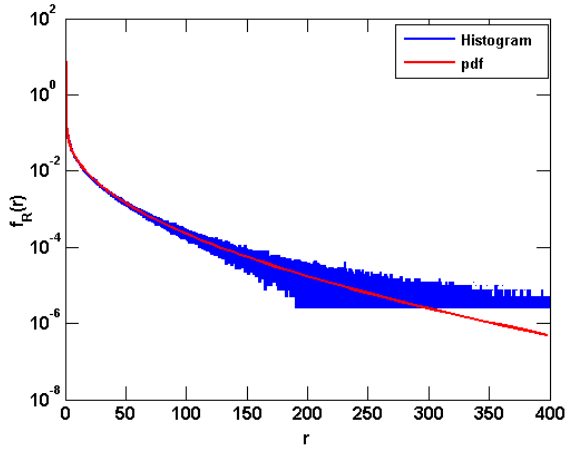

(a) Histogram and analytic pdf for the Weibull envelope with $b = 1, \nu = 0.9$

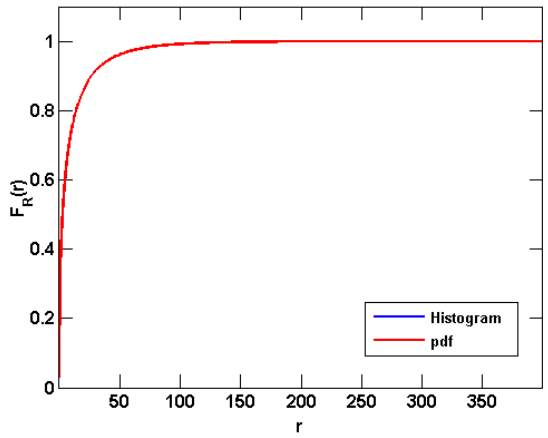

(b) Histogram and analytic cdf for the Weibull envelope with $b = 1, \nu = 0.9$

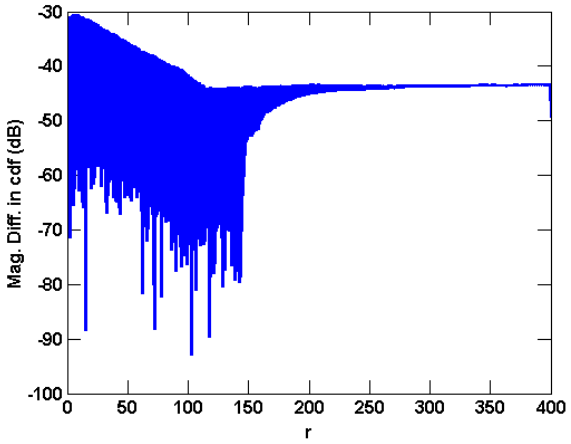

(c) Magnitude difference between estimated and analytic cdf in log scale $b = 1, \nu = 0.9$

Figure 4.15: Comparing analytic and simulated distributions of the Weibull envelope for $\nu = 0.9$

Note that the while the numerical limitations of the histogram are apparent for low probability events, the empirical and analytic cdfs appear identical. To better quantify the accuracy of the rejection method, Figure 4.15c gives the magnitude difference between the empirical cdf and the analytic cdf in log scale. The magnitude difference is given by

$$\Delta_{cdf} = 10\log_{10}\left(\left|F(r) - \hat{F}(r)\right|\right) \tag{4.12}$$

where $F(r)$ is the analyic cdf and $\hat{F}(r)$ is the empirical cdf. Comparing Figures 4.15a and

4.15c shows that the difference is greatest in the region where the pdf has the greatest probability, and then levels off in the tail of the distribution.

For $\nu = 1.1$, the maximum range satisfying (4.10) is reached at $r = 10.96$. However, as $\nu > 1$ the maximum value of the pdf is found explicitly. The histogram and analytic pdf are compared in Figure 4.16a and the emperical and analytic cdfs are compared in Figure 4.16b.

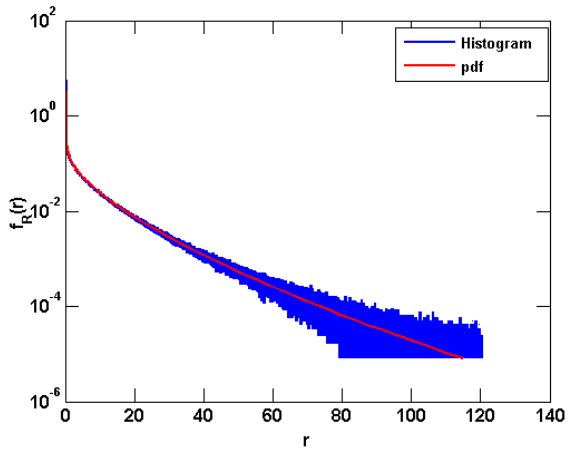

(a) Histogram and analytic pdf for the Weibull envelope with $b = 1, \nu = 1.1$

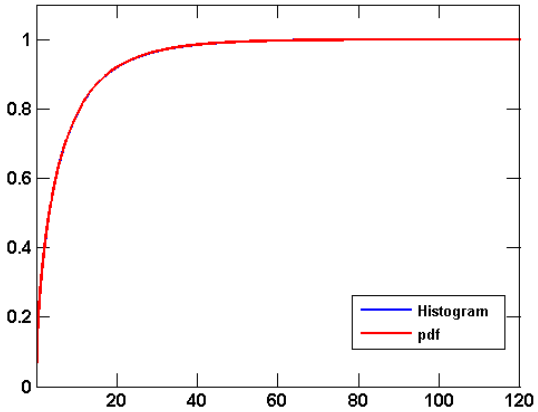

(b) Histogram and analytic cdf for the Weibull envelope with $b = 1, \nu = 1.1$

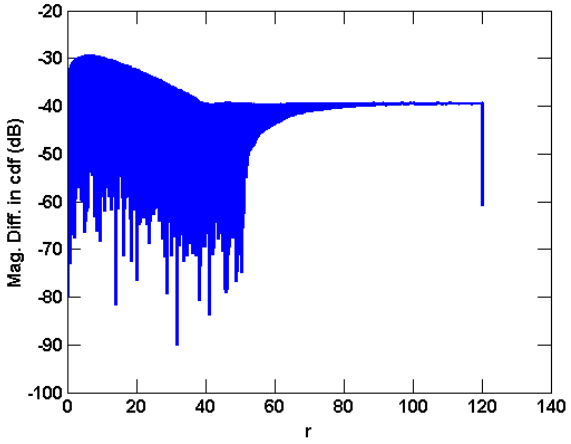

(c) Magnitude difference between estimated and analytic cdf in log scale $b = 1, \nu = 1.1$

Figure 4.16: Comparing analytic and simulated distributions of the Weibull envelope for $\nu = 1.1$

Comparing Figure 4.16c to Figure 4.15c, the empirical cdf appears to be a good estimate of the analytical cdf when (4.10) and (4.11) are satisfied.

After establishing the validity of the Rejection Method, we now implement the technique discussed in Section 3.4.2. For the Weibull pdf, a complex SIRV is generated by [1]:

1. Generate a white, zero mean Gaussian random vector with identity covariance matrix, denoted as $\mathbf{Z}$ and desired length L.

2. Compute the norm of $\mathbf{Z}$ as $R_Z = ||\mathbf{Z}|| = \sqrt{\mathbf{Z}^T\mathbf{Z}}$. Note that $E[R_Z] = \sqrt{L}$.

3. Generate the desired norm of via the Rejection Method, equations (4.3), (4.10), and (4.11), and the resulting Uniform distributed random variables.

4. Generate $\mathbf{X}$ as $\mathbf{X} = \mathbf{Z}\frac{R_X}{R_Z}$.

We used this procedure to generate 10^8 complex Weibull distributed SIRV variables of length $L = 4$, with shape and scale parameters $\nu = b = 1$. The histogram of the quadratic form of these random vectors is then compared to the analytic pdf in Figure 4.17a. The resulting empirical cdf is compared to the analytic cdf in Figure 4.17b.

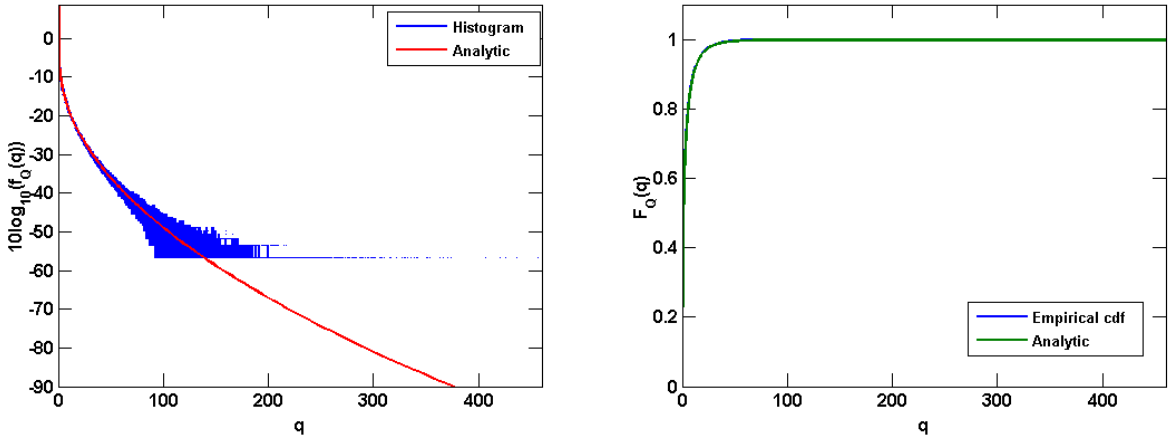

(a) Histogram and analytic pdf for quadratic form of complex Weibull SIRV with $b = 1, \nu = 1$

(b) Empirical and analytic cdf for quadratic form of complex Weibull SIRV with $b = 1, \nu = 1$

Figure 4.17: Comparing analytic and simulated distributions of a complex Weibull SIRV for $\nu = 1$

The cdfs in Figure 4.17b verifies the generation of the complex Weibull SIRV, even though the modulating random variable is *not* known.

For radar detection, the heavy tailed nature of the clutter gives rise to a necessarily increased threshold to maintain a constant, acceptable probability of false alarm. The decibel scale change in threshold (as compared to Gaussian distributed data) for the complex Weibull distribution is given in Figure 4.18 for valid shape parameters (*i.e.* $\nu \leq 2$).

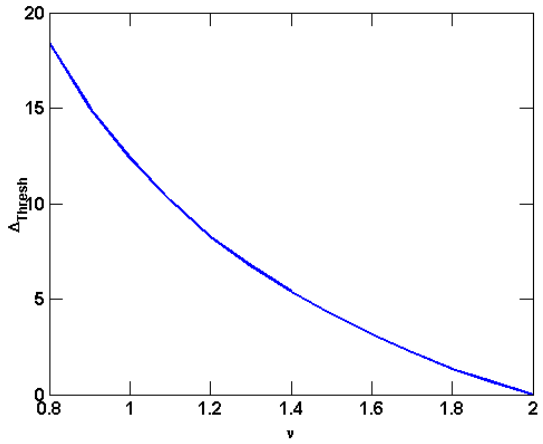

Figure 4.18: Δ_{thresh} in log scale for the Weibull distribution for increasing shape parameter

The delta threshold in Figure 4.18 is calculated according to (4.2). As expected, the Weibull distribution is equal to the Rayleigh distribution for $\nu = 2$, yielding a $\Delta_{\text{thresh}}(\text{dB}) = 0$. However, the threshold rises rapidly as the shape parameter decreases, modeling more impulsive clutter.

4.3 Examining the Pareto Distribution

Figures 4.19a and 4.19b show the pdf and cdf of quadratic form of the Pareto distribution for length $L = 4$ vectors. Note from Figure 4.19b the cdfs of the $\nu = 2.35$ and $\nu = 70$ case appear to be very close. However heavy tail of the lower shape parameter is apparent in Figure 4.19a.

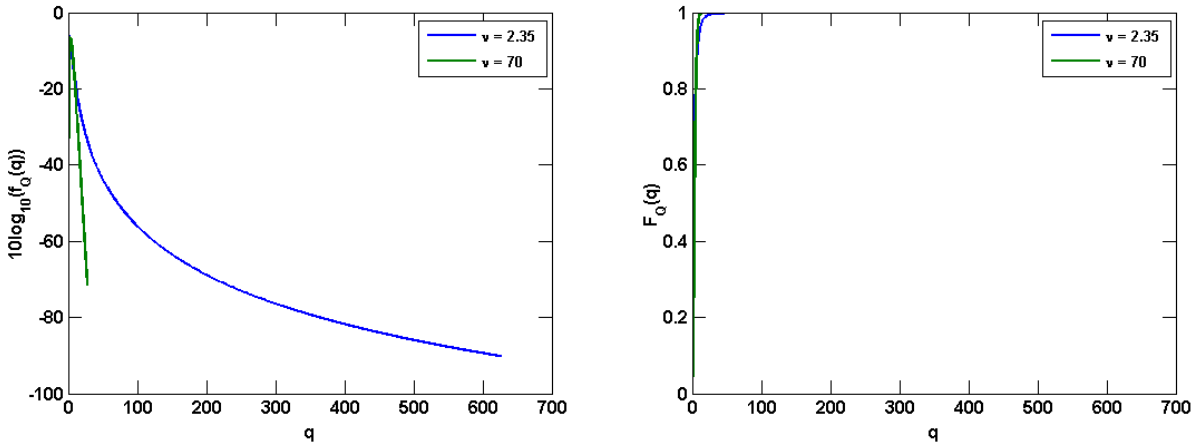

(a) pdf of the quadratic form of complex Pareto data (b) cdf of the quadratic form of complex Pareto data

Figure 4.19: pdf and cdf of quadratic form of Pareto clutter

Next we examine the impact Pareto distributed data has on threshold and probability of false alarm. Using the metric of (4.2), the decibel difference in threshold required to maintain a probability of false alarm of 10^{-5} for Pareto clutter over Gaussian clutter is shown in Figure 4.20a. The increased false alarm caused by Pareto clutter when the threshold for Gaussian clutter is used is shown in Figure 4.20b.

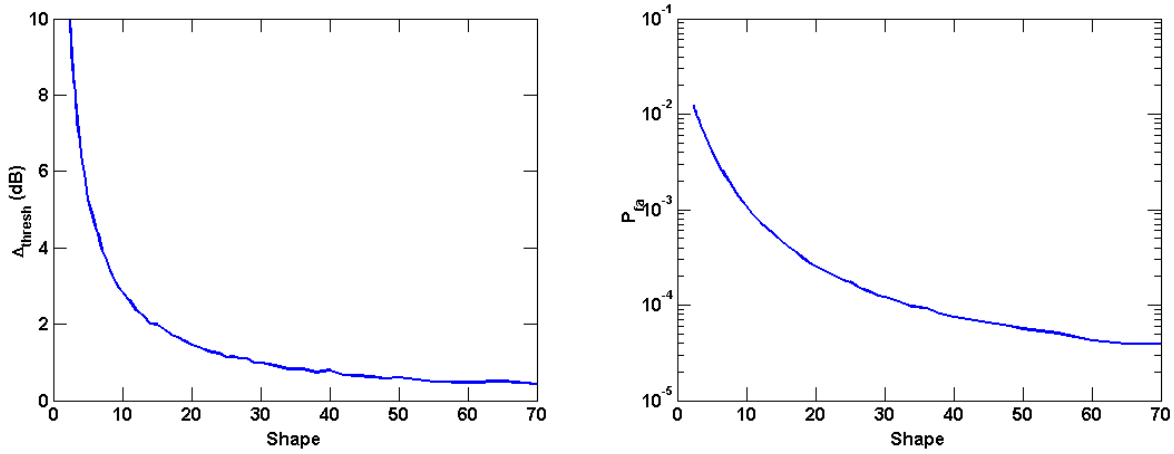

(a) Δ_{thresh} (dB) for the Pareto distribution (b) Increased P_{fa} for Pareto data

Figure 4.20: Consequences of Pareto clutter

4.4 Examining the Lognormal Distribution

Here we consider lognormal random vectors of length L. As the lognormal pdf is not a SIRV, we note that the generalized inner product (GIP) possesses the same form as the quadratic form of a SIRV [101–103]. Therefore, we form the generalized inner product of 10^7 length $L = 4$ lognormal random vectors. The empirical pdf of (3.109) was generated with 10^7 samples and is shown in Figure 4.21a, while the corresponding empirical cdf is shown in Figure 4.21b.

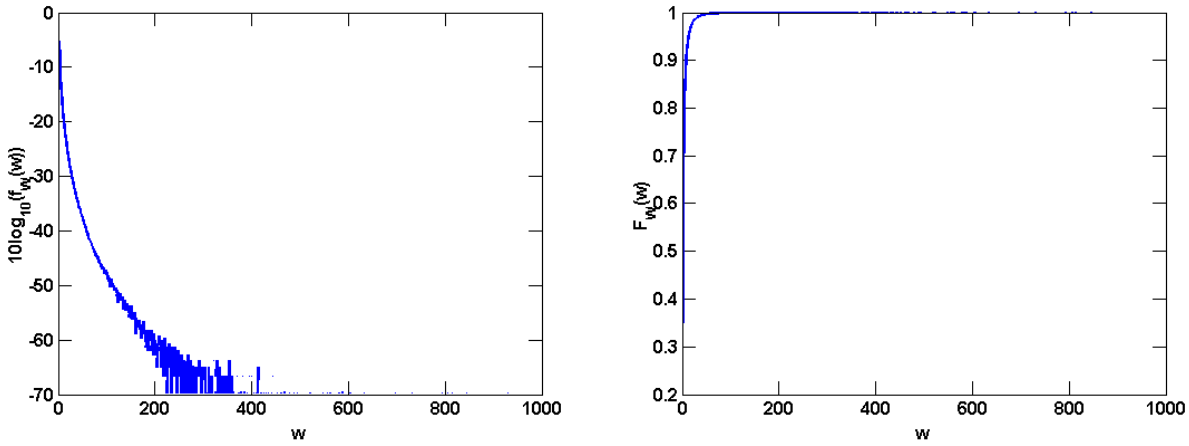

(a) Empirical pdf of GIP of complex lognormal data (b) Empirical cdf of GIP of complex lognormal data

Figure 4.21: Empirical pdf and cdf of the GIP of complex lognormal data for length $L = 4$ vectors

Note that the lognormal distribution does not have a shape parameter. For the case of length $L = 4$ complex samples per vector, the threshold in lognormal clutter is 10.2 dB greater than the threshold needed in complex Gaussian clutter to maintain a probability of false alarm of 10^{-5}. If the threshold for Gaussian clutter is used (corresponding to a desired $P_{fa} = 10^{-5}$) but lognormal clutter is present, the resulting P_{fa} is 2.91×10^{-2}.

4.5 Gamma Modulated SIRV

In order to provide a more extensive library of readily generated SIRVs, we propose a Gamma modulated (GM) SIRV. In other words, a potential modulating random variable $f_V(v)$ is distributed as

$$f_{V'}(v') = \frac{v'^{\alpha-1}}{\Gamma(\alpha)}\exp(-v') \quad v > 0. \tag{4.13}$$

where α is the shape parameter and we once again set the scale parameter equal to 1 [86]. The Gamma distribution is commonly found in software packages, so the GM SIRV is amenable to generation and simulation. The expected value and variance of a Gamma distribution with unit scale parameter is [86]

$$E[V'] = Var[V'] = \alpha. \tag{4.14}$$

Therefore, the normalizing constant to achieve $E[V^2] = 1$ is

$$\begin{aligned}\sqrt{E[V'^2]} &= \sqrt{Var[V'] + E[V']^2} \\ &= \sqrt{\alpha + (\alpha)^2}.\end{aligned} \tag{4.15}$$

For the GM SIRV, the normalizing transformation is given as

$$\begin{aligned}v &= g(v') \\ &= \frac{v'}{\sqrt{\alpha^2 + \alpha}},\end{aligned} \tag{4.16}$$

the inverse transformation is

$$\begin{aligned}v' &= g^{-1}(v) \\ &= v\sqrt{\alpha^2 + \alpha},\end{aligned} \tag{4.17}$$

and

$$\left|\frac{\mathrm{d}g^{-1}(v)}{\mathrm{d}v}\right| = \sqrt{\alpha^2+\alpha}. \tag{4.18}$$

From (4.13), (4.17) and (4.18), the pdf for the scaled Gamma distribution is [5]

$$\begin{aligned} f_V(v) &= f_{V'}(g^{-1}(v))\left|\frac{\mathrm{d}g^{-1}(v)}{\mathrm{d}v}\right| \\ &= \frac{\left[(\sqrt{\alpha^2+\alpha})v\right]^{\alpha-1}}{\Gamma(\alpha)}\exp\left[-(\sqrt{\alpha^2+\alpha})v\right]\sqrt{\alpha^2+\alpha} \\ &= \frac{(\alpha^2+\alpha)^{\frac{\alpha}{2}}v^{\alpha-1}}{\Gamma(\alpha)}\exp\left[-(\sqrt{\alpha^2+\alpha})v\right]. \end{aligned} \tag{4.19}$$

From (3.10),

$$\begin{aligned} h_L(q) &= \int_0^\infty v^{-L}\exp\left(-\frac{q}{2v^2}\right)f_V(v)\mathrm{d}v \\ &= \int_0^\infty v^{-L}\exp\left(-\frac{q}{2v^2}\right)\frac{(\alpha^2+\alpha)^{\frac{\alpha}{2}}v^{\alpha-1}}{\Gamma(\alpha)}\exp\left[-(\sqrt{\alpha^2+\alpha})v\right]\mathrm{d}v \\ &= \frac{(\alpha^2+\alpha)^{\frac{\alpha}{2}}}{\Gamma(\alpha)}\int_0^\infty v^{\alpha-L-1}\exp\left(-(\sqrt{\alpha^2+\alpha})v-\frac{q}{2v^2}\right)\mathrm{d}v. \end{aligned} \tag{4.20}$$

From (3.11) and (4.20), the pdf of the GM SIRV for real data is

$$\begin{aligned} f_Q(q) &= \frac{q^{\frac{L}{2}-1}}{2^{\frac{L}{2}}\Gamma(\frac{L}{2})}h_L(q) \\ &= \frac{(\alpha^2+\alpha)^{\frac{\alpha}{2}}q^{\frac{L}{2}-1}}{2^{\frac{L}{2}}\Gamma(\frac{L}{2})\Gamma(\alpha)}\int_0^\infty v^{\alpha-L-1}\exp\left(-(\sqrt{\alpha^2+\alpha})v-\frac{q}{2v^2}\right)\mathrm{d}v \end{aligned} \tag{4.21}$$

while for complex data

$$f_Q(q) = \frac{(\alpha^2+\alpha)^{\frac{\alpha}{2}}q^{L-1}}{2^L\Gamma(L)\Gamma(\alpha)}\int_0^\infty v^{\alpha-2L-1}\exp\left(-(\sqrt{\alpha^2+\alpha})v-\frac{q}{2v^2}\right)\mathrm{d}v. \tag{4.22}$$

As the integral in (4.20) does not have a clear closed form solution, the pdf of this SIRV must be estimated through Monte Carlo simulation.

We used Monte Carlo simulation to generate 10^6 instantiations of the GM SIRV and used

a histogram to generate the cdf for the GM SIRV for several shape parameters. The cdf for the GM SIRV is shown in Figure 4.22 for shape parameters $\alpha = 0.5, 5, 20$.

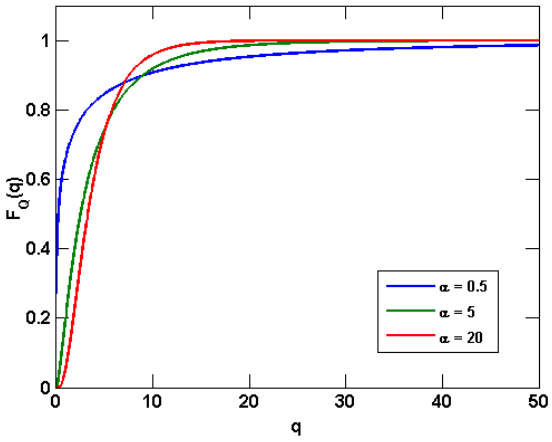

Figure 4.22: cdfs of the GM SIRV distribution

Note the heavy tail of the GM SIRV for low shape parameters. The heavy tail causes the detection threshold required to assure an arbitrary level of false alarms to rise with respect to the threshold in Gaussian clutter. The change in threshold for GM clutter to Gaussian clutter is quantified by (4.2). Figure 4.23a plots the value of (4.2) as the shape parameter of the modulating Gamma RV is varied. When a threshold derived from Gaussian clutter is assumed, yet GM distributed clutter is encountered, the model mismatch will cause an increase in false alarms. Figure 4.23b shows the P_{fa} under this scenario for varying values of the Gamma shape parameter and a desired $P_{Fa} = 10^{-6}$.

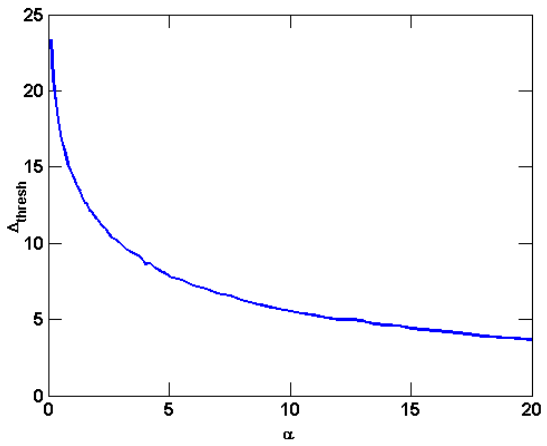

(a) Δ_{thresh} (dB) for the GM SIRV as a function of shape parameter

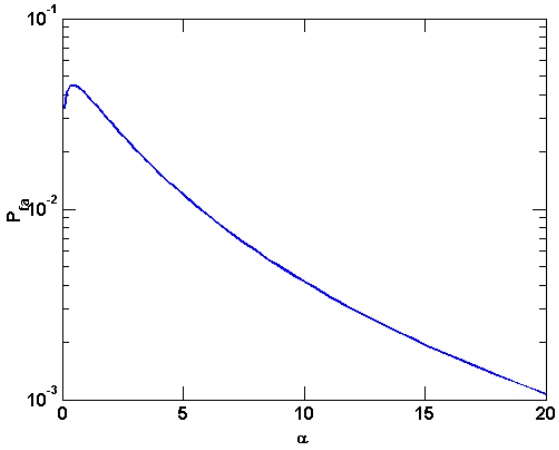

(b) P_{fa} for the GM SIRV as a function of shape parameter

Figure 4.23: Threshold and P_{fa} properties of the GM SIRV

4.6 Compound Gamma Modulated SIRV

Another possible SIRV can be formed from a modulating random variable resulting from the product of two standard Gamma distributed random variables. We denote this SIRV a compound Gamma modulated (CGM) SIRV. Let

$$f_X(x) = \frac{x^{\alpha_1 - 1}}{\Gamma(\alpha_1)} \exp(-x), \quad x > 0 \tag{4.23}$$

and

$$f_Y(y) = \frac{y^{\alpha_2 - 1}}{\Gamma(\alpha_2)} \exp(-y), \quad x > 0 \tag{4.24}$$

where $\alpha_1, \alpha_2 > 0$ are the respective shape parameters. The pdf of a product of two random variables $V = XY$ can be given as [104]

$$f_V(v) = \int_{-\infty}^{\infty} f_{X,Y}\left(x, \frac{v}{x}\right) \frac{1}{|x|} \mathrm{d}x. \tag{4.25}$$

As $X, Y > 0$ and are independent, (4.25) becomes

$$\begin{aligned} f_V(v) &= \int_0^\infty f_X(x) f_Y\left(\frac{v}{x}\right) \frac{1}{x} \mathrm{d}x \\ &= \int_0^\infty \frac{x^{\alpha_1 - 1}}{\Gamma(\alpha_1)} \exp\left(-x\right) \frac{\left(\frac{v}{x}\right)^{\alpha_2 - 1}}{\Gamma(\alpha_2)} \exp\left(-\left(\frac{v}{x}\right)\right) \frac{1}{x} \mathrm{d}x \\ &= \int_0^\infty \frac{x^{\alpha_1 - 1} x^{-\alpha_2 + 1} v^{\alpha_2 - 1}}{\Gamma(\alpha_1)\Gamma(\alpha_2)} \exp\left(-x - \left(\frac{v}{x}\right)\right) \frac{1}{x} \mathrm{d}x \\ &= \int_0^\infty \frac{x^{\alpha_1 - \alpha_2 - 1} v^{\alpha_2 - 1}}{\Gamma(\alpha_1)\Gamma(\alpha_2)} \exp\left(-x - \left(\frac{v}{x}\right)\right) \mathrm{d}x. \end{aligned} \tag{4.26}$$

To simplify (4.26), first note that

$$\begin{aligned} f_V(v) &= \int_0^\infty \frac{x^{\alpha_1 - \alpha_2 - 1} v^{\alpha_2 - 1}}{\Gamma(\alpha_1)\Gamma(\alpha_2)} \exp\left(-x - \left(\frac{v}{x}\right)\right) \mathrm{d}x \\ &= \frac{v^{\alpha_2 - 1}}{\Gamma(\alpha_1)\Gamma(\alpha_2)} \int_0^\infty x^{\alpha_1 - \alpha_2 - 1} \exp\left(-x - \left(\frac{v}{x}\right)\right) \mathrm{d}x \\ &= \frac{v^{\alpha_2 - 1}}{\Gamma(\alpha_1)\Gamma(\alpha_2)} \frac{2}{2} v^{\frac{\alpha_1}{2} - \frac{\alpha_1}{2}} \int_0^\infty x^{\alpha_1 - \alpha_2 - 1} \exp\left(-x - \left(\frac{v}{x}\right)\right) \mathrm{d}x \\ &= \frac{2 v^{\frac{\alpha_2 + \alpha_1}{2} - 1}}{\Gamma(\alpha_1)\Gamma(\alpha_2)} \frac{v^{\frac{\alpha_2 - \alpha_1}{2}}}{2} \int_0^\infty x^{\alpha_1 - \alpha_2 - 1} \exp\left(-x - \left(\frac{v}{x}\right)\right) \mathrm{d}x \end{aligned} \tag{4.27}$$

Next, recall (3.72), and let

$$\begin{aligned} \beta &= \alpha_2 - \alpha_1 \\ x &= 2 \\ z &= \sqrt{v} \end{aligned} \tag{4.28}$$

leads to a modified Bessel function of the second kind of the form

$$\begin{aligned} K_\beta(xz) &= \frac{z^\beta}{2}\int_0^\infty \exp\left[-\frac{x}{2}(t+\frac{z^2}{t})\right] t^{-\beta-1}\mathrm{d}t \\ \implies K_{\alpha_2-\alpha_1}(2\sqrt{v}) &= \frac{\sqrt{v}^{\alpha_2-\alpha_1}}{2}\int_0^\infty \exp\left[-\frac{2}{2}\left(t+\frac{v}{t}\right)\right] t^{-(\alpha_2-\alpha_1)-1}\mathrm{d}t \\ \implies K_{\alpha_2-\alpha_1}(2\sqrt{v}) &= \frac{v^{\frac{\alpha_2-\alpha_1}{2}}}{2}\int_0^\infty \exp\left[-t-\frac{v}{t}\right] t^{\alpha_1-\alpha_2-1}\mathrm{d}t. \end{aligned} \tag{4.29}$$

Substituting (4.29) into (4.27) results in

$$\begin{aligned} f_V(v) &= \frac{2v^{\frac{\alpha_2+\alpha_1}{2}-1}}{\Gamma(\alpha_1)\Gamma(\alpha_2)}\frac{v^{\frac{\alpha_2-\alpha_1}{2}}}{2}\int_0^\infty x^{\alpha_1-\alpha_2-1}\exp\left(-x-\left(\frac{v}{x}\right)\right)\mathrm{d}x \\ &= \frac{2v^{\frac{\alpha_2+\alpha_1}{2}-1}}{\Gamma(\alpha_1)\Gamma(\alpha_2)}K_{\alpha_2-\alpha_1}(2\sqrt{v}). \end{aligned} \tag{4.30}$$

The similarity of (4.30) to (3.62) is unsurprising, as the K distribution is often derived as the product of two correlated Gamma distributions, particularly in SAR applications (*e.g.* [83] and references therein).

The function $h_L(q)$ is found by plugging the results of (4.30) into (3.10), yielding

$$\begin{aligned} h_L(q) &= \int_0^\infty v^{-L}\exp(-\frac{q}{2v^2})f_V(v)\mathrm{d}v \\ &= \int_0^\infty v^{-L}\exp\left(-\frac{q}{2v^2}\right)\frac{2v^{\frac{\alpha_2+\alpha_1}{2}-1}}{\Gamma(\alpha_1)\Gamma(\alpha_2)}K_{\alpha_2-\alpha_1}(2\sqrt{v})\mathrm{d}v \\ &= \frac{2}{\Gamma(\alpha_1)\Gamma(\alpha_2)}\int_0^\infty v^{\frac{\alpha_2+\alpha_1}{2}-L-1}\exp\left(-\frac{q}{2v^2}\right)K_{\alpha_2-\alpha_1}(2\sqrt{v})\mathrm{d}v. \end{aligned} \tag{4.31}$$

The pdf for real valued CGM SIRV data is then found from (3.11) and (4.31) to be

$$\begin{aligned} f_Q(q) &= \frac{1}{2^{\frac{L}{2}}\Gamma(\frac{L}{2})}q^{\frac{L}{2}-1}h_L(q) \\ &= \frac{q^{\frac{L}{2}-1}}{2^{\frac{L}{2}-1}\Gamma(\frac{L}{2})\Gamma(\alpha_1)\Gamma(\alpha_2)}\int_0^\infty v^{\frac{\alpha_2+\alpha_1}{2}-L-1}\exp\left(-\frac{q}{2v^2}\right)K_{\alpha_2-\alpha_1}(2\sqrt{v})\mathrm{d}v \end{aligned} \tag{4.32}$$

and the pdf for complex valued CGM SIRV data is

$$f_Q(q) = \frac{q^{L-1}}{2^{L-1}\Gamma(L)\Gamma(\alpha_1)\Gamma(\alpha_2)} \int_0^\infty v^{\frac{\alpha_2+\alpha_1}{2}-2L-1} \exp\left(-\frac{q}{2v^2}\right) K_{\alpha_2-\alpha_1}(2\sqrt{v})\mathrm{d}v \tag{4.33}$$

We used Monte Carlo simulation to generate 10^6 instantiations of the CGM SIRV and used a histogram to generate the cdf for the CGM SIRV for several shape parameters. For illustrative purposes, we used identically distributed Gamma random variables (*i.e.* each Gamma distribution has the same shape parameter). The cdf for the CGM SIRV is shown in Figure 4.24 for shape parameters $\alpha_1 = \alpha_2 = 1, 5, 50$.

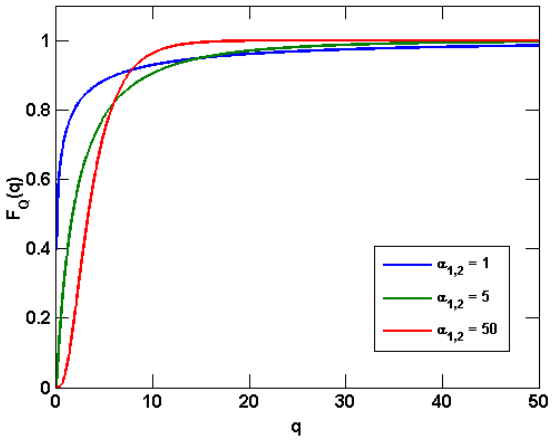

Figure 4.24: cdfs of the CGM SIRV distribution

Note the heavy tail of the CGM SIRV for low shape parameters. As the CGM SIRV distribution is characterized by two shape parameters, we show the change in threshold defined by (4.2) for varying values of α_1 and α_2 in Figure 4.25. Two features are apparent. First, the threshold is maximized along the ridge defined by $\alpha_1 = \alpha_2$. As one holds α_1 constant and increases α_2 (or vice versa), the threshold decreases. Second, comparing Figure 4.23a to Figure 4.25, for arbitrary shape parameters the CGM SIRV appears to result in a higher threshold than the GM SIRV.

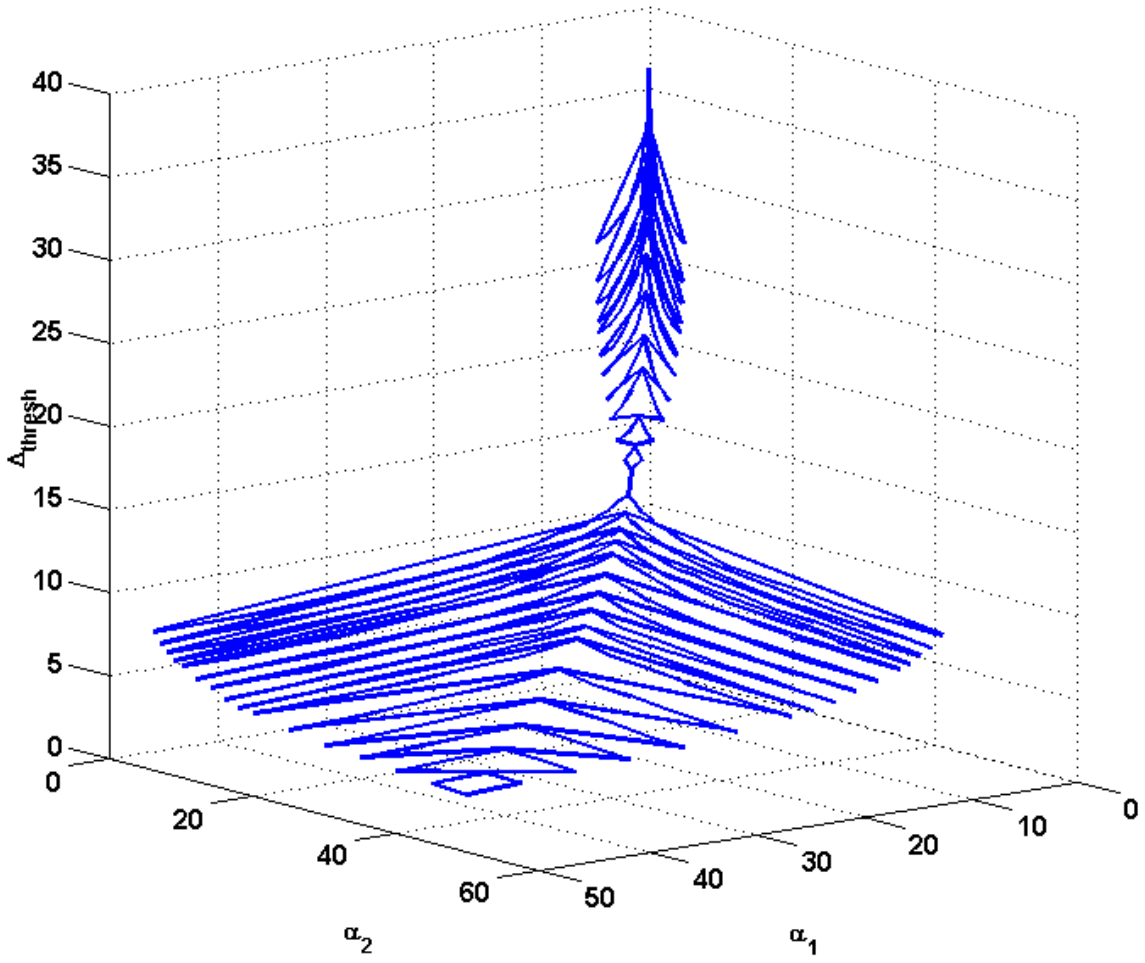

Figure 4.25: Δ_{thresh} (dB) for the CGM SIRV as a function of shape parameter

Figure 4.26 shows the P_{fa} for CGM clutter when the clutter is incorrectly assumed to be Gaussian distributed. The threshold is derived from a desired $P_{fa} = 10^{-6}$. For illustrative purposes, we limit the plot to the $\alpha_1 = \alpha_2$ ridge, which was established to be the "worst case" threshold via examination of Figure 4.25.

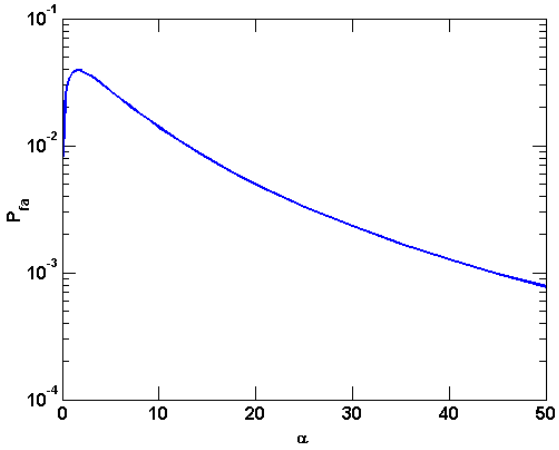

Figure 4.26: P_{fa} for the CGM SIRV as a function of shape parameter

4.7 Limitations of SIRVs

There have been multiple concerns raised about the utility of SIRVs in modeling non-Gaussian radar clutter. First, care must be taken when generating simulated radar clutter. For example, there has been recent work in modeling VHF SAR forest clutter with SIRVs [105]. Due to the high range resolution of the SAR system, SIRV distributed scatterers provide a good model to measured results. However, it was noted in [105] that the SAR processing induced spatial correlation between range cells. A naive application of SIRV theory can lead to simulated clutter that bears little similarity to measured results. Therefore, both the spatial and temporal correlation must be accounted for in certain applications. The problem of incorporating radar system sampling effects into clutter generation is outside the scope of this work, but provides a promising area of future research.

Several members of the audience had constructive feedback after the presentation of [2]. There is some skepticism in the community as to the "fit" of measured data to the proposed distributions. Recall that SIRVs are all related to the Gaussian distribution, and differ only in distribution of the modulating random variable. Therefore, it is possible that there may be *ambiguities* in terms of different SIRVs with respect to the tails of the distributions. This concept of ambiguity between distributions is central throughout this work.

In a similar vein, most studies on fitting SIRV clutter focus on fitting measured data to one or two known distributions. However, this parametric fitting of data presupposes that the true distribution of the data comes from a set of known distributions. Therefore, we ignore the possibility of an unknown distribution being the actual distribution of the measured data. However, the SIRV model was shown in [7,46] to derive from a modification of the central limit theorem based on the theory of electromagnetic scattering. Based on this justification we may hypothesize that any unknown distributions may fit to the SIRV class of random vectors. This line of reasoning raises the question of whether we can use our knowledge of various SIRV distributions to successfully estimate the detection threshold (*i.e.* tail) of an unknown distribution. After all, the purpose of using parametric models is to maximize our probability of detection for a given false alarm rate. For the purposes of a radar receiver, if a clutter model is incorrect, but yields a correct threshold, any system using the output of the detector (*e.g.* tracker, target identifier) does not care about the distribution used by the detector. This theme will be explored in more detail in Chapters 6-8.

Chapter 5

Distribution Estimation using Combinations of Order Statistics

This chapter examines the use of ordered statistics to explore both parametric and non-parametric distribution identification techniques. Consider N variables, $X_1, \ldots, X_N$, which are assumed to be IID with pdf $f_X(x)$. The ordered statistics $X_{(1)}, \ldots, X_{(N)}$ are formed by sorting the random variables by increasing magnitude as [106]

$$X_{(1)} \leq X_{(2)} \leq \cdots \leq X_{(N)}. \tag{5.1}$$

Individual order statistics are often used in many non-parametric and parametric applications. For example, the minimum ($X_{(1)}$), maximum ($X_{(N)}$), and median ($X_{(N/2)}$) are often used to provide context to sampled data. The pdf of the i^{th} order statistic from a distribution with cdf $F(x)$ is given as

$$f_{(i)}(x) = \frac{1}{B(i, n-i+1)} F^{i-1}(x)[1-F(x)]^{n-i} f(x) \tag{5.2}$$

where $B(a,b)$ is the Beta function defined as

$$B(a,b) = \int_0^1 t^{a-1}(1-t)^{b-1}\mathrm{d}t \quad a>0, b>0. \tag{5.3}$$

Order statistics are often invoked to provide robustness to data processing techniques, especially with respect to outliers in measured data [107]. For example, the median filter (*i.e.* the output of the filter is the median of a sliding window of data) is effective at smoothing data but preserves edges or impulses better than conventional low pass finite impulse response (FIR) filters [108], [107, Chapter 21]. Radar signal processing engineers have long used order statistics in various ways to reduce false alarms (*e.g.* [42], [107, Chapter 23]). The remainder of this chapter is concerned with the application of order statistics for distribution identification of non-Gaussian radar clutter. The first section explores a prior technique known as the Ozturk algorithm, and we apply the algorithm to measured radar data. The subsequent sections provide our extensions to the Ozturk algorithm and explore their applicability to radar signal processing. Finally, we culminate in a proposed design to fuse multiple test statistics with the goal of classifying an underlying clutter statistic and adaptively estimating a detection threshold.

5.1 The Ozturk Goodness-of-Fit Algorithm

Goodness-of-fit algorithms are a class of techniques that determine whether measured data fits hypothesized distributions. Classical order statistic based techniques use quantiles of the cdf of a distribution, or require the hypothesized distributions to be of the location/scale type [107, Chapter 16]. For the latter methods, the distributions may be discriminated by the actual locations of the individual order statistics or the spacing between the order statistics [107, Chapter 17].

A graphical goodness-of-fit algorithm based on ordered statistics was developed in a series of papers [109–112] and refined to consider SIRV clutter in [1]. This algorithm will be denoted

as the Ozturk alorithm for the remainder of this work. Originally, the Ozturk algorithm was developed to assess the normality (*i.e.* Gaussianity) of a distribution. In subsequent developments, the Ozturk algorithm was altered to provide a method of efficiently comparing sampled data to a library of known distributions and determining the distribution that the sampled data most closely resembles. This section describes the method and reasoning behind the Ozturk algorithm. The intuition gathered from this algorithm gives rise to the novel methods presented and tested in the subsequent sections.

The Ozturk algorithm uses the Gaussian distribution as the null hypothesis and attempts to develop a *distance* measure on a two dimensional space relative to the Gaussian distribution for a group of other distributions. Therefore, measured data could be easily (*i.e.* with low computational cost) projected onto this space and the nearest known point determined. A key benefit of this approach is to change the distribution identification problem from a hypothesis test to a hypothesis *suggestion*. Recall that SIRV distributions are all Gaussian distributions that have been modulated by a random variable. Therefore, the fact that the Ozturk algorithm attempts to measure distance between a candidate distribution and the Gaussian distribution indicates that it may be well suited to identifying SIRV distributions.

To implement the Ozturk algorithm, one constructs a set of vectors associated with the order statistics of a distribution. As the algorithm operates in two dimensions, denoted as U and V, each vector may be described by a magnitude and angle. The set of angles ϕ_i used are common to all distributions. However, the magnitude of each vector is generated from the studentized order statistics [106] of the individual distribution. These vectors are then linked head-to-tail. The endpoint of the linked vectors is the discriminating statistic of the algorithm.

To develop the vector magnitudes of a SIRV distribution, consider a series of N sampled, zero mean, independent and identically distributed (i.i.d.) length L vectors $\mathbf{y}_1, \mathbf{y}_2, \ldots \mathbf{y}_N$

with covariance $\mathbf{\Sigma}$ and the corresponding quadratic forms

$$\begin{aligned} q_1 &= \mathbf{y}_1^H \mathbf{\Sigma}^{-1} \mathbf{y}_1 \\ q_2 &= \mathbf{y}_2^H \mathbf{\Sigma}^{-1} \mathbf{y}_2 \\ &\vdots \\ q_N &= \mathbf{y}_N^H \mathbf{\Sigma}^{-1} \mathbf{y}_N. \end{aligned} \tag{5.4}$$

The quadratic samples are then sorted as

$$q_{(1)} \leq q_{(2)} \leq \cdots \leq q_{(N)}. \tag{5.5}$$

The sample mean of the quadratic samples is found as

$$\bar{q} = \frac{1}{N} \sum_{i=1}^{N} q_i \tag{5.6}$$

and the sample variance of the quadratic samples is

$$\hat{\sigma}^2 = \frac{1}{N-1} \sum_{i=1}^{N} (q_i - \bar{q})^2. \tag{5.7}$$

The studentized order statistics are obtained as [106]

$$z_{(i)} = \frac{q_{(i)} - \bar{q}}{\hat{\sigma}} \tag{5.8}$$

In other words, studentization enforces a zero mean, unit variance constraint on the sampled data.

To create angles $\phi_1, \phi_2, \ldots \phi_N$, the Ozturk algorithm uses the expected value of the N

order statistics of the standard Normal distribution given as

$$m_{(i)} = E[x_{(i)}], \quad i = 1, \ldots, N \tag{5.9}$$

where $x \sim \mathcal{N}(0, 1)$. The angles $\phi_1, \phi_2, \ldots \phi_N$ are then generated as

$$\phi_i = \pi\Phi(m_{(i)}), \quad i = 1, \ldots, N \tag{5.10}$$

where $\Phi(\bullet)$ is the cdf of the standard normal distribution.

Finally, the vectors whose length is given by $|z_{(i)}|$ and whose angle with respect to the V axis is ϕ_i are linked. Starting at $(0, 0)$, the coordinates of the endpoint of each vector is given by

$$\begin{aligned} U_k &= \frac{1}{k}\sum_{i=1}^{k} \cos(\phi_i)|z_{(i)}| \\ V_k &= \frac{1}{k}\sum_{i=1}^{k} \sin(\phi_i)|z_{(i)}| \\ k &= 1, \ldots, N. \end{aligned} \tag{5.11}$$

The endpoint (U_N, V_N) for each distribution is then plotted. Figure 5.1 illustrates the Ozturk algorithm for a candidate distribution and the null (Gaussian) distribution.

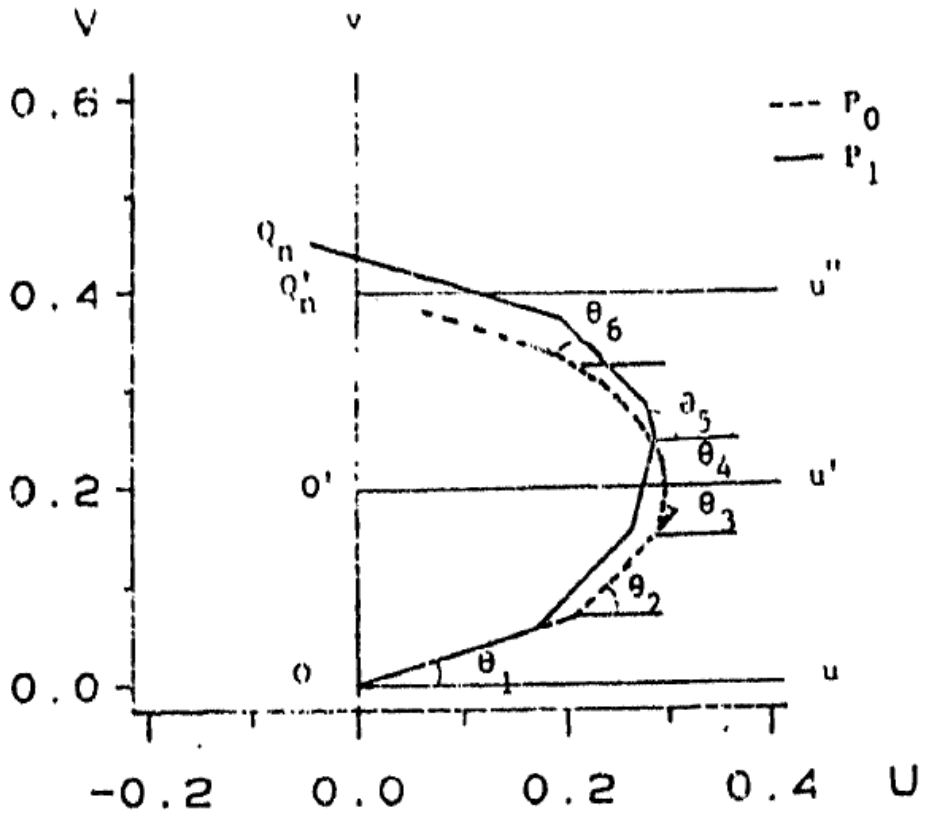

Figure 6.1: Linked Vector Chart:Dashed lines P_0= Null Linked Vectors, Solid Lines P_1= Sample Linked Vectors

Figure 5.1: Illustration of linked vectors (reprinted from [1])

Note that the number of data points used to form the order statistics must be known *a priori*. However, it is possible to form a library of distribution plots offline to be deployed according to need. An example library was generated in [1]. A visual representation of the library is shown in Figure 5.2.

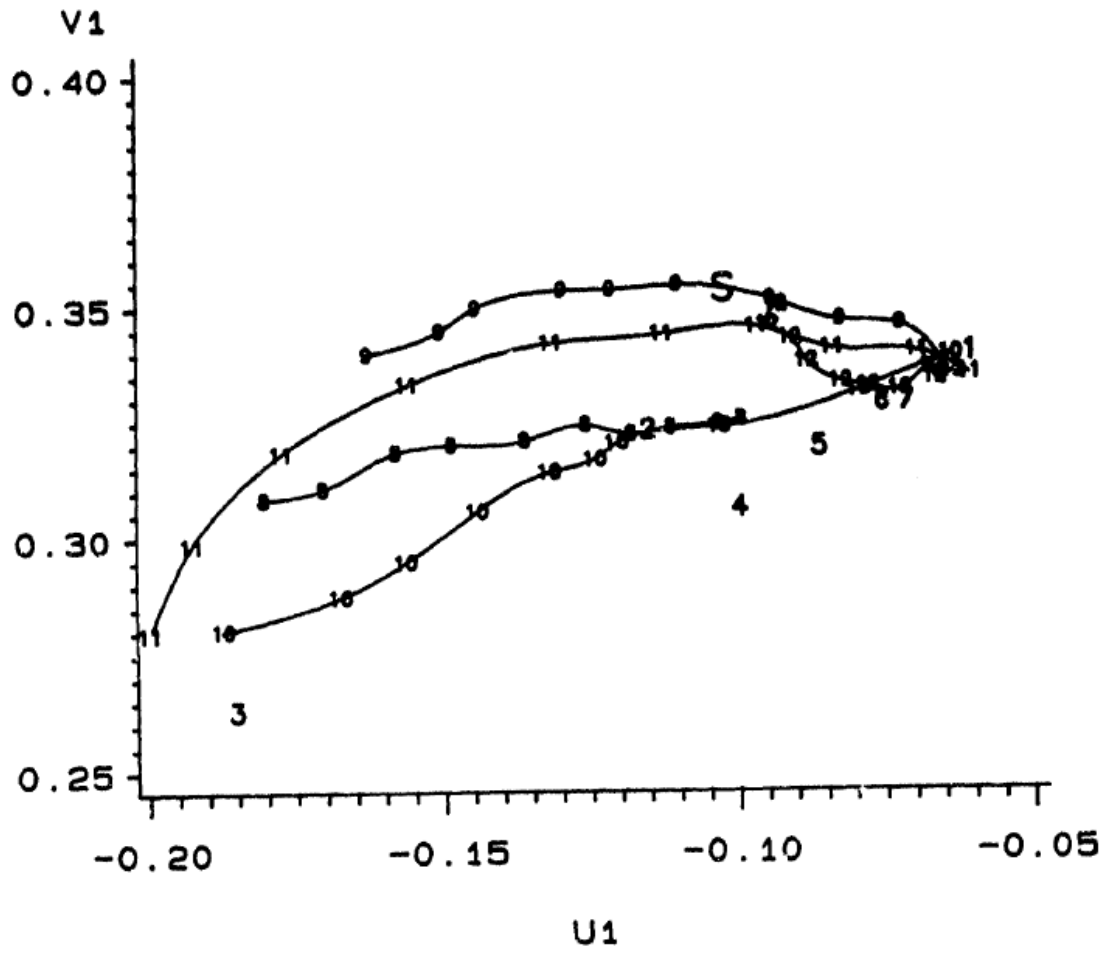

Figure 7.2: Identification Chart for SIRVs (n=2000, N=4) 1 = Gaussian, 2 = Laplace, 3 = Cauchy, 4, 5, 6, 7 = Student-t, 8 = K-distribution, 9 = Chi, 10 = Generalized Rayleigh, 11 = Weibull, 12 = Rician

Figure 5.2: Library of endpoints for SIRV identification (reprinted from [1])

The lines in Figure 5.2 are formed by distributions with shape parameters. Note that all distributions converge to the Gaussian distribution on the right for some value of their shape parameter (*i.e.* $\nu = 2$ for the Weibull distribution and $\nu = \infty$ for the K distribution).

The Ozturk algorithm was implemented and tested in a Monte Carlo fashion on real valued K distributed SIRV data. Each length $L = 16$ SIRV was given a zero mean vector and covariance matrix structured so that $\sigma^2_{y_i y_j} = E[Y_i Y_j]^2 = \frac{L-|i-j|}{L}$ (*i.e.* linearly decreasing covariance). There were $N = 16$ samples to generate the ordered statistics, and 100,000 Monte

Carlo runs were performed. Figure 5.3a shows the null distribution and the K distribution for shape parameters $\nu = 0.5, 1$.

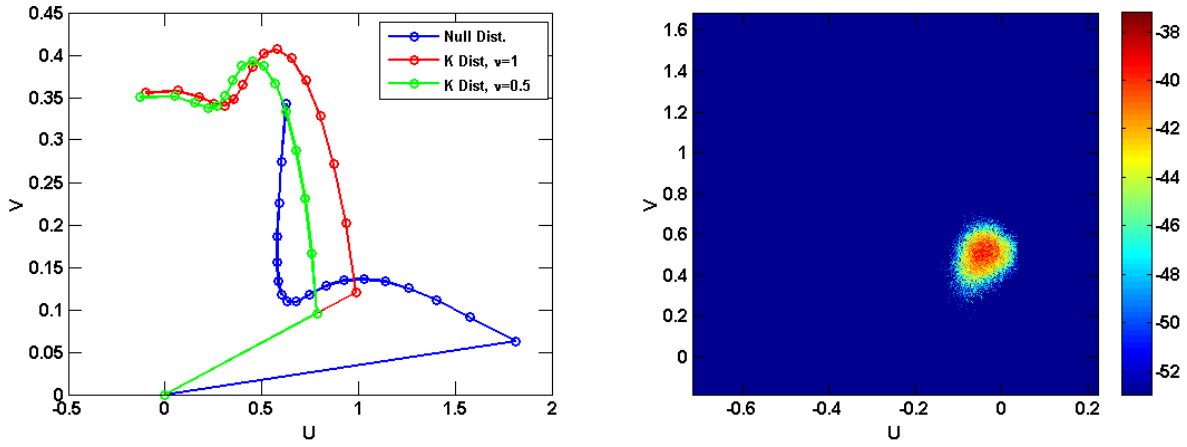

(a) Ozturk algorithm example library

(b) Graphical pdf of K endpoint distribution

Figure 5.3: Implementation of the Ozturk algorithm

Each circle of Figure 5.3a corresponds to the average endpoints generated for each linked vector. Figure 5.3b shows the distribution of the endpoint of a K distributed variable with shape parameter $\nu = 1$. Unlike the other figures, 200,000 Monte Carlo simulations were run to generate Figure 5.3b, but all other pertinent variables were held constant. The pdf is given in $10\log_{10}(f_{U,V}(u, v))$.

It was asserted in [1] that the Ozturk algorithm was scale invariant. Due to the non-ergodicity of a SIRV (caused by the modulating random variable), the true covariance matrix and the sample covariance matrix of a SIRV will differ by a scale factor [75]. The scaling factor will tend toward unity as the number of samples used to construct the sample covariance matrix goes to infinity. The property of scale invariance allows the Ozturk algorithm to be well suited to identifying SIRV distributions from limited data samples. Figures 5.4a and 5.4b illustrate the scale invariance of the Ozturk algorithm.

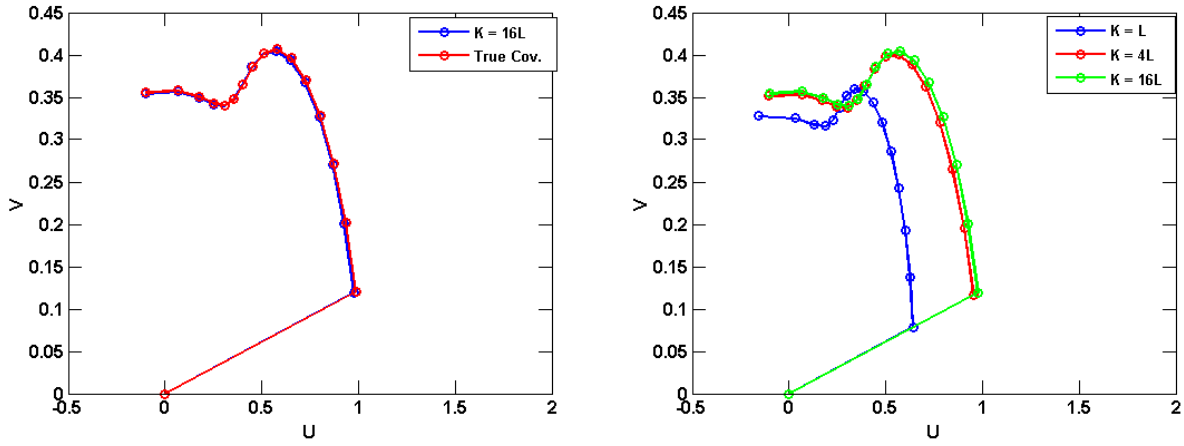

(a) Sample cov. matrix v. true cov. matrix

(b) Effect of increasing sample size

Figure 5.4a shows the linked vectors generated when the true covariance matrix is known, and when $K = 16L = 256$ vectors were used to generate the sample covariance matrix. Figure 5.4b shows the effect of increasing the number of samples used to estimate the covariance matrix. Notice that while using $K = L = 16$ sample vectors does not appear to produce accurate results, the endpoint for $K = 4L$ and $K = 16L$ sample vectors produce very similar results. Therefore, the Ozturk algorithm should perform well even with limited sample support. Note in practical STAP systems, the Reed, Mallett, Brennan (RMB) rule states that a system will suffer a detection loss of approximately 3 dB if $K = 2L$ samples are used to estimate the sample covariance matrix [47]. The RMB rule will be explored in future work.

5.1.1 Applying the Ozturk Algorithm

As a proof of concept, we implemented the Ozturk algorithm with an initial library consisting of the K distribution and the Gaussian distribution (*i.e.* the null hypothesis in terms of distribution identification). These average endpoints are then compared to measured endpoints from the multichannel airborne radar measurement (MCARM) program [113]. The MCARM program used an L band radar operating at 1240 MHz. The MCARM radar transmits a 50.4 μs linear frequency modulated waveform with a pulse compression ratio of 63. This

waveform is transmitted from an 11×11 planar array mounted on the side of a BAC1-11 aircraft. For further details on the MCARM program, see [75, 113–115] and the references contained therein.

While multiple channels of data are provided by the MCARM data files, this early implementation of the Ozturk algorithm does not support data from multiple antennas. Therefore, for this proof of concept we only consider the data from the first antenna. We implemented the Ozturk algorithm for the complex Gaussian distribution as well as complex K distributed data, with shape parameter $0.3 \leq \nu \leq 4$ by steps of 0.1. The MCARM data files provide measurements for a coherent processing interval of 128 pulses and 630 range cells. For this initial implementation we divide the measurements of each range cell into 8 measurements of $L = 16$ consecutive pulses. A sliding window is formed consisting of 10 range cells, for a sample matrix of dimension 16×80. The sample covariance matrix is estimated from this $K \times 5L$ matrix. The 80 vectors are "compressed" into their quadratic using the inverse of the sample covariance matrix. The endpoint is formed as discussed in Section 5.1. Each new endpoint is formed by sliding the window one range cell farther from the radar, until the final range cell is reached.

Figure 5.5 shows the output of the Ozturk algorithm when applied to MCARM data file rd050465. The blue line shows the path formed by endpoints of K distributed data. Notice that the shape parameter of the K distribution is increasing smoothly from left to right, and tends toward the Gaussian endpoint at the far right. The individual circles represent endpoints of the Ozturk algorithm as applied to the sliding window. This experiment serves as a conceptual illustration of the Ozturk algorithm, and establishes the applicability of the Ozturk algorithm to real data.

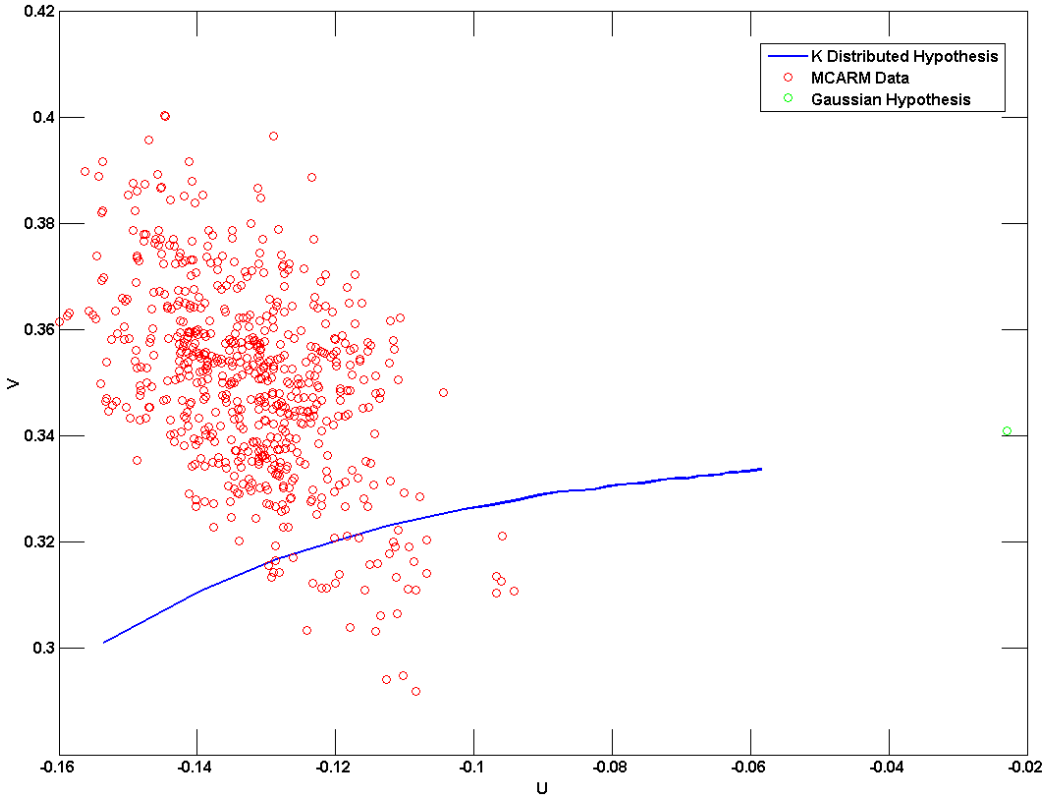

Figure 5.5: Implementation of Ozturk algorithm on MCARM data file rd050465

In the future we will modify the assumption of 8 individual SIRVs per CPI. The "sampling" rate of the modulating variable will be allowed to vary. Further, Figure 5.5 shows the need to expand the library of SIRVs from the K distribution. We will investigate the expansion of the library, as well as the expansion of the basic principles of the Ozturk algorithm, in the subsequent sections.

5.2 Weighted Sums of Ordered Statistics

In this section we expand on the Ozturk algorithm and generalize it by introducing a new framework of combining ordered statistics through weighted sums. Most of the reasoning in this section is focused on development of intuition for the Ozturk algorithm, as well as

extending this intuition to new methods. The Ozturk algorithm was developed to provide a one-to-one mapping from the space of order statistics to a two-dimensional space. This space was designed to provide a distance metric between distributions. While not addressed in the publications, clearly such a strategy wishes to maximize the distance between distributions in order to provide an accurate classifier. Here we introduce new weighting functions, and consider the use of non-studentized data. Finally, we address the applicability of identifying distributions with limited sample support and the correlation between the sums given by different weighting functions.

It should be noted that for the Ozturk algorithm, the endpoint of the linked vectors provides the discriminating data point of interest. Throughout this work we continue to use this terminology, despite removing the vector notation and intuition established in Section 5.1. First, we use this notation for consistencies sake. Second, in future work we will revisit the physical interpretation of linked vectors in a modified form. The future work is discussed in section 9.2.

Define a weighted sum of ordered statistics (WSOS) as

$$U(\mathbf{X}) = \sum_{i=1}^{N} a_i X_{(i)}. \tag{5.12}$$

If the ordered statistics are not first studentized, (5.11) becomes a special case of (5.12). Upon closer inspection of (5.10), the expectation yields

$$\begin{aligned} \phi_i &= \pi\Phi(m_{(i)}), \quad i = 1, \ldots, N \\ &= \pi\frac{i}{N+1}, \quad i = 1, \ldots, N. \end{aligned} \tag{5.13}$$

In other words, the series $\phi_1, \ldots, \phi_N$ corresponds to a uniform sampling of $(0, \pi)$. Therefore, the weightings in (5.11) correspond to a cosine weighting and a sine weighting with argument given by the series (5.13).

For the Ozturk algorithm, the quadratic values have been studentized. As the ordered

statistics are positive before studentizing, the minimum values will tend towards the negative of the mean of the quadratic values, scaled by the square root of their variance. However, the Ozturk algorithm takes the magnitude of the studentized statistics, causing the new values associated with the minimum measured values to become positive, yet close to the scaled mean. Similarly, the statistics that were close to the mean will be close to zero.

This exploration causes one to consider the selection of the sine and cosine as weightings. With an argument uniformly distributed $(0, \pi)$, the sine function provides very low weights to extreme values of the distribution (*i.e.* order statistics near the minimum and maximum are weighted close to zero). However, the values near the median are weighted strongly. Therefore, the sine function at this interval *emphasizes* the median values and *deemphasizes* the values at the tails of the distribution. An example of sine weightings is shown in Figure 5.6a. For the Ozturk algorithm, this weighting will provide information to the difference between the mean and the median of a distribution. If the data is not studentized, the sine appears to simply emphasize the median values.

However, the cosine function over the same interval gives positive weight to minimum values, negative weight to maximum values, and very little weight to statistics near the median of the distribution. The cosine weighting, as applied in the Ozturk algorithm, would appear to provide a measure of the separation between the mean and the tails of a distribution.

Just as using both weightings of studentized and non-studentized order statistics provide two different data points for each observation, increasing the number of weightings considered can cast the distribution identification problem into a higher order dimensional space. Therefore, it becomes instructive to examine different possible weightings.

Figure 5.6a shows the weights supplied by using a uniform spacing of the open interval $(0, 1)$ parameterized by the variable t. As mentioned previously, the sine weights provide smaller weight to the extremes of the ordered samples symmetrically around the median. However, the sine squared weightings provide even less weight to the samples farther from the median. In other words, the shaping is sharper around the median.

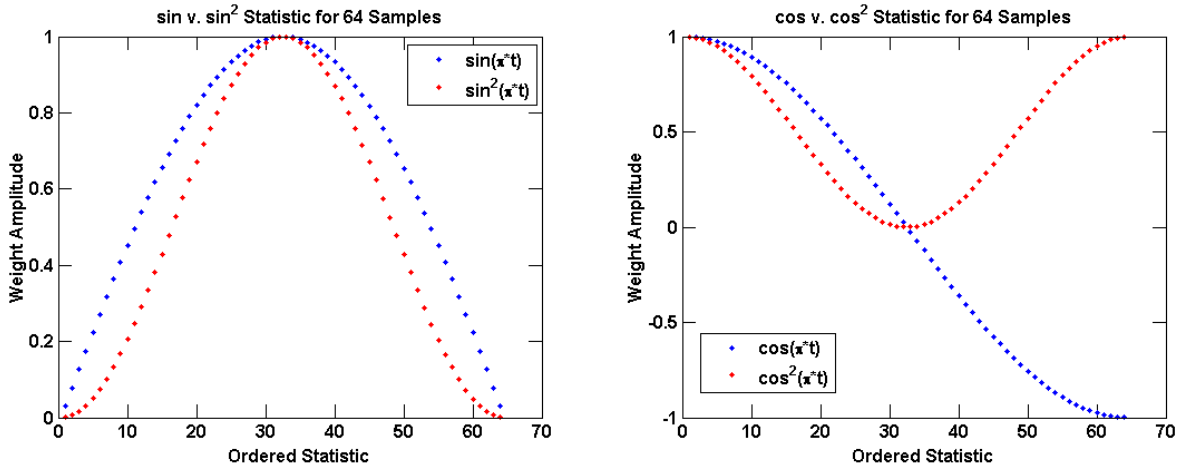

(a) Weights of sine v. sine^2

(b) Weights of cosine v. cosine^2

Figure 5.6: Comparing sine and cosine derived weightings

Figure 5.6b shows the weightings for the cosine and cosine squared functions. The cosine weighting was discussed previously. However, the cosine squared weighting over the $(0, \pi)$ interval appears to provide approximately an inverse weighting to the sine or sine squared weightings. In other words the extremes (maximum and minimum) are weighted heavily, while the median statistic is given zero weight.

Thus far, the weightings discussed have been derived from trigonometric functions. One may also consider hyperbolic functions. However, while the selection of the interval $(0, \pi)$ appears to be a logical interval over which to evaluate trigonometric functions, no such interval appears immediately obvious for the hyperbolic functions. Therefore, as a first attempt, we use a uniform sampling of the open interval $(0, 1)$, which may be expressed as $\frac{\phi_i}{\pi}$. Figure 5.7a shows the weights provided by the hyperbolic sine and square of the hyperbolic sine functions. Likewise, Figure 5.7b shows the weights provided by the hyperbolic cosine and square of the hyperbolic cosine functions. Finally, Figure 5.7c shows the weights provided by the hyperbolic tangent and square of the hyperbolic tangent functions.

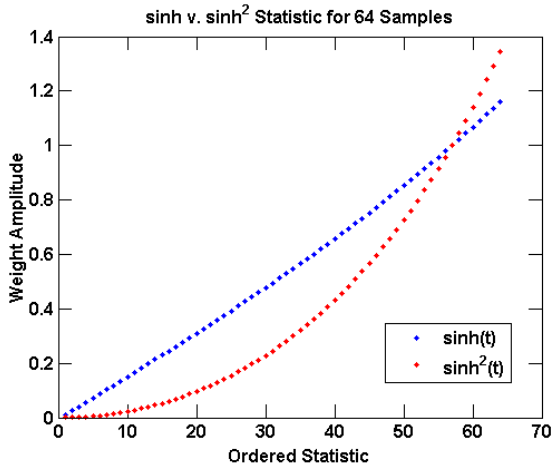

(a) Weights of sinh v. sinh squared

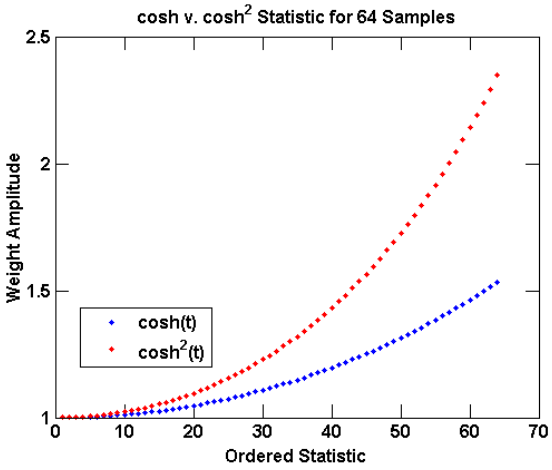

(b) Weights of cosh v. cosh squared

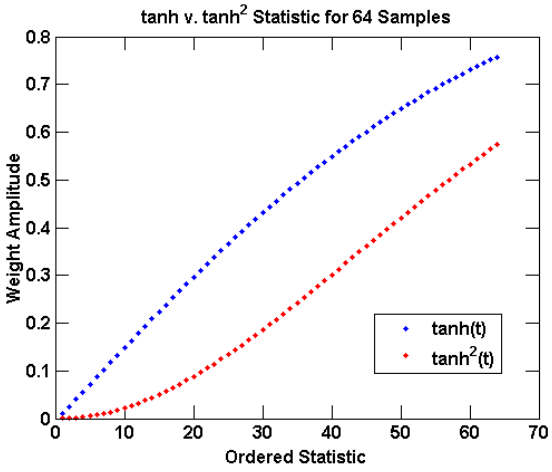

(c) Weights of tanh v. tanh squared

Figure 5.7: Comparing sinh, cosh, and tanh derived weightings

While the shape of the curve corresponding to each weighting function is different, all the weightings for the hyperbolic function provide increasing weights as the order of the statistic increases. While the weightings for the trigonometric functions are all bound $-1 \leq a_i \leq 1$, no such strict bounding is common to all hyperbolic functions. It may be necessary to consider normalization procedures when hyperbolic functions are used to generate weightings.

In order to explore the weighting schemes presented, consider the order statistics formed by examining instantiations of a dimension $L = 64$ complex K distributed SIRV with shape parameter $\nu = 1$ and scale parameter $b = 1.5$. The simulated pdf and cdf of the quadratic form q of this random vector is shown in Figures 5.8a and 5.8b. Note that unless the Ozturk

method is specified, all figures in this section make use of non-studentized order statistics, and no normalization is performed on any of the endpoint statistics.

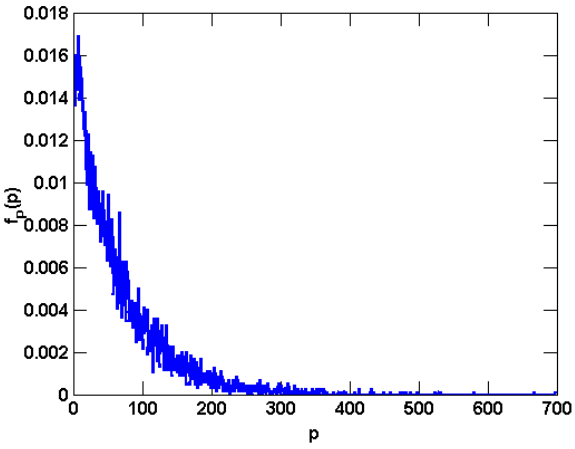

(a) pdf of K Distributed SIRV with $L = 64, \nu = 1, b = 1.5$

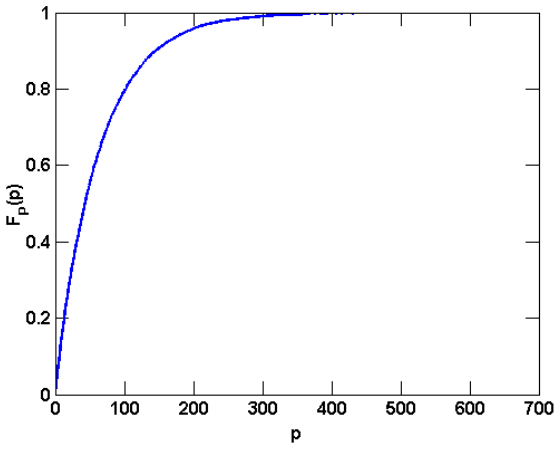

(b) cdf of K Distributed SIRV with $L = 64, \nu = 1, b = 1.5$

Figure 5.8: pdf and cdf of example K distributed SIRV

Clearly, the number of samples N used to form ordered statistics will influence the final value of the weighted sum. It is expected that as the number of samples increases, the better approximation to the underlying quadratic PDF will be given. Therefore, the variance of the WSOS should be lower and the separation between the endpoints of different weighting methods should be greater. Note that in practice N samples are used to estimate the common covariance matrix $\hat{\mathbf{\Sigma}}$. Therefore, for a full rank estimation of the covariance matrix, in a general application it is common to require $N \geq L$.

First, Figures 5.9a and 5.10b considers the sine and sine squared weightings for $N = L, 4L = 64, 256$.

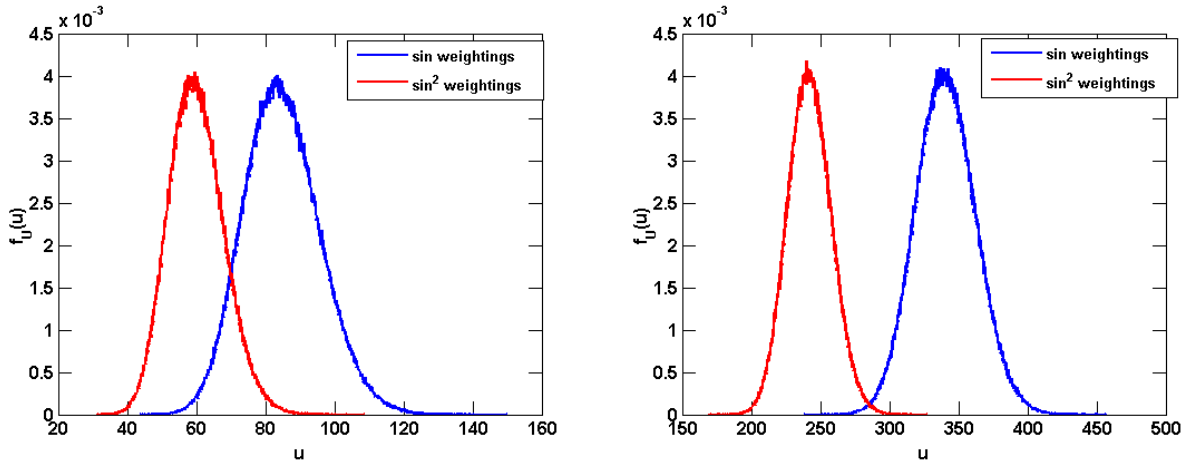

(a) $N = L$ (b) $N = 4L$

Figure 5.9: Endpoint distribution for sin and $\sin^2$

The histogram of the WSOS for each of these weightings is shown. Examining Figure 5.6a, the two weighting functions are of similar and weight the median value identically. Therefore, it is expected that the pdfs of these WSOS overlap a great deal. However, when the number of samples is increased to $N = 4L = 256$, the pdfs are well separated.

Next Figures 5.10a and 5.10b examine the cosine and cosine squared weightings

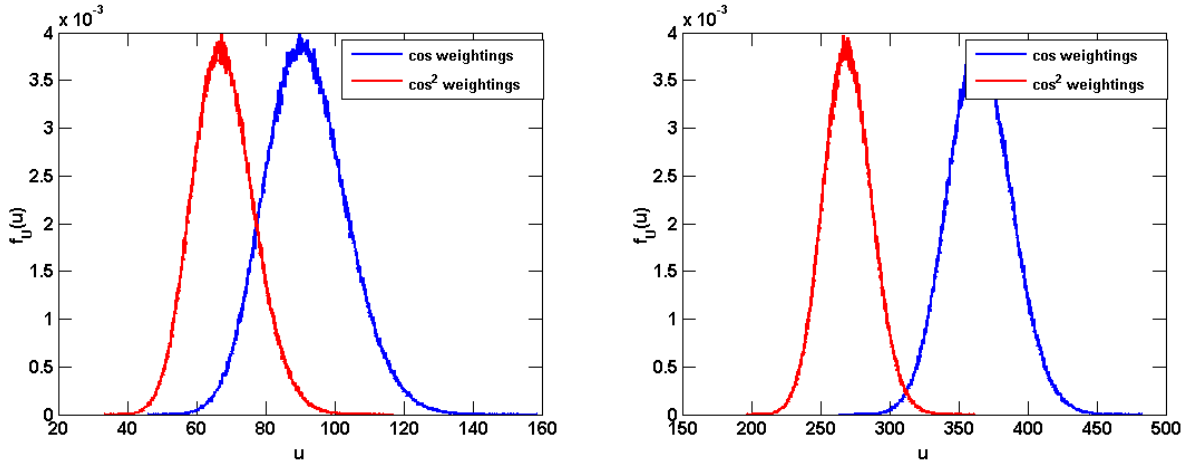

(a) $N = L$ (b) $N = 4L$

Figure 5.10: Endpoint distribution for cos and $\cos^2$

While it is not immediately obvious from Figure 5.6b, these two pdfs do not appear well separated for $N = L$. However, just as with the sine and sine squared WSOS pdfs, increasing

the number of samples allows one to clearly discriminate between the two pdfs.

The hyperbolic cosh and tanh functions, along with their respective squares, appear to provide well separated WSOS. This separation is illustrated in Figures 5.11a through 5.11d.

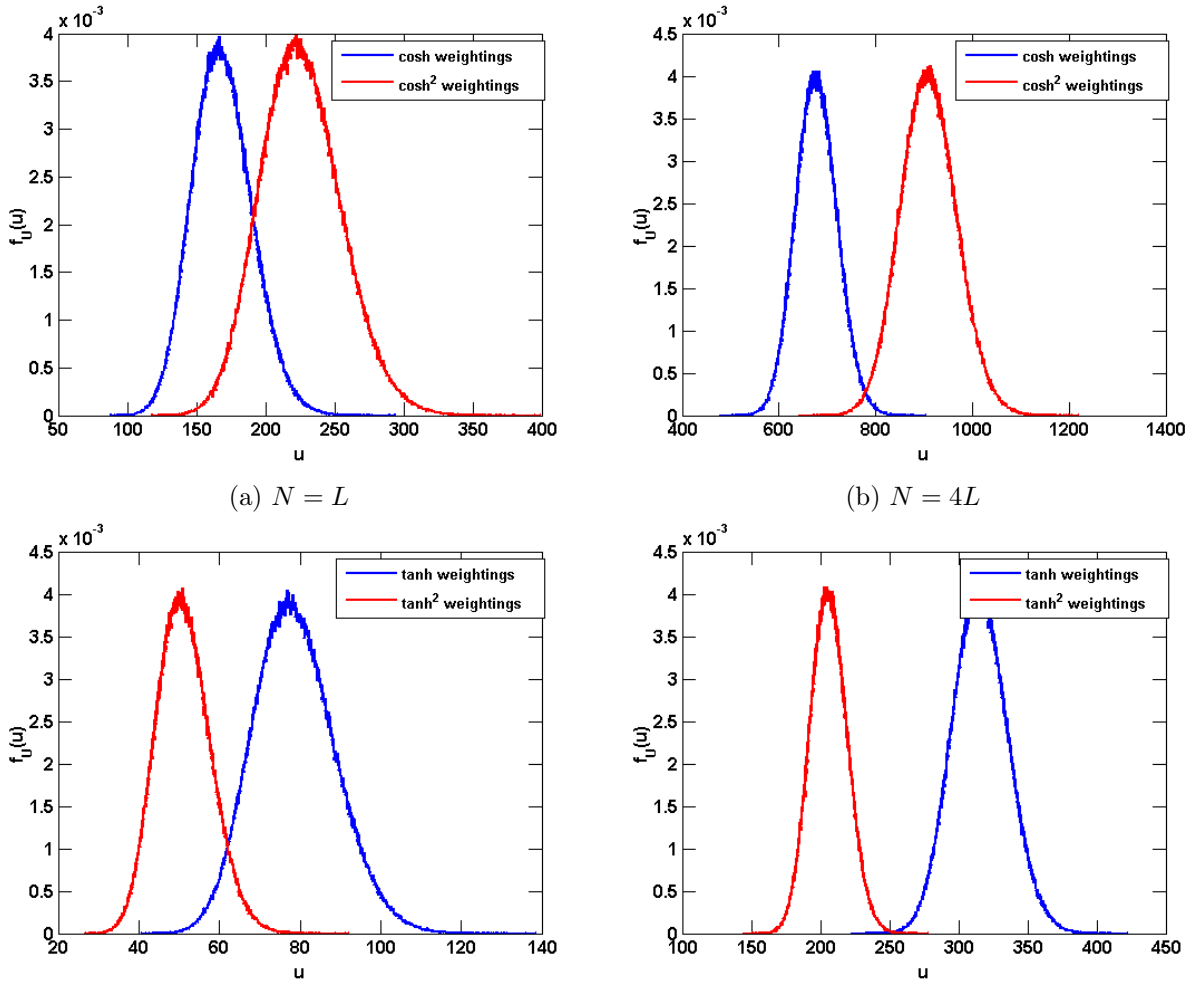

(a) $N = L$ (b) $N = 4L$

(c) $N = L$ (d) $N = 4L$

Figure 5.11: Endpoint distribution for cosh, $\cosh^2$, tanh, and $\tanh^2$

However, the sinh and sinh squared functions do not appear to be well separated, as shown in Figures 5.12a and 5.12b.

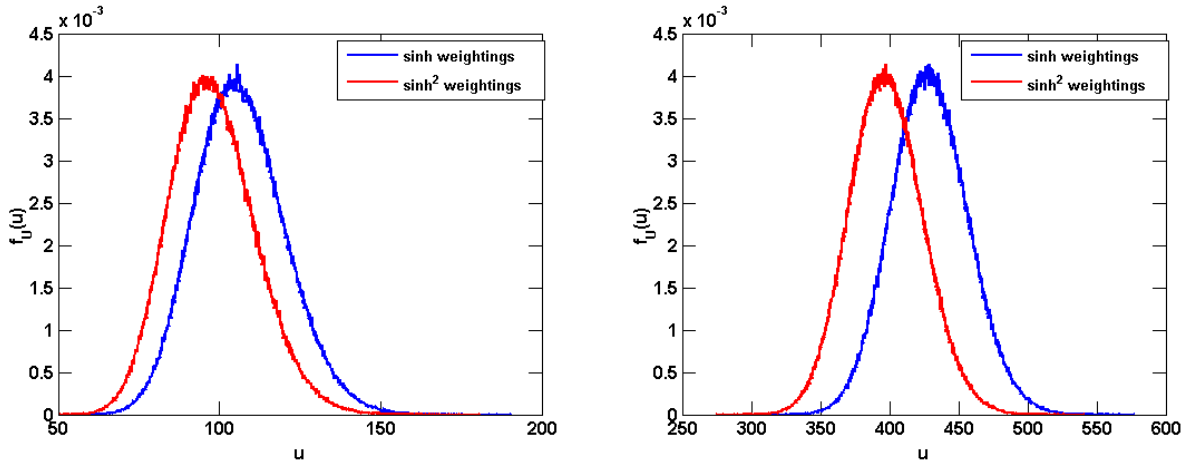

(a) $N = L$ (b) $N = 4L$

Figure 5.12: Endpoint distribution for sinh and sinh^2

While examining the univariate distributions of the WSOS is illustrative, it is also instructive to examine the bivariate distribution for pairs of WSOS. Figures 5.13a through 5.13d show the bivariate distributions of four pairs of WSOS for the $N = L$ case.

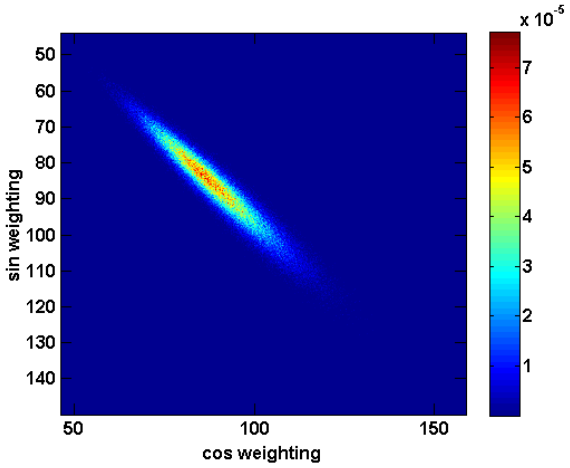

(a) Endpoint distribution of cos and sin WSOS

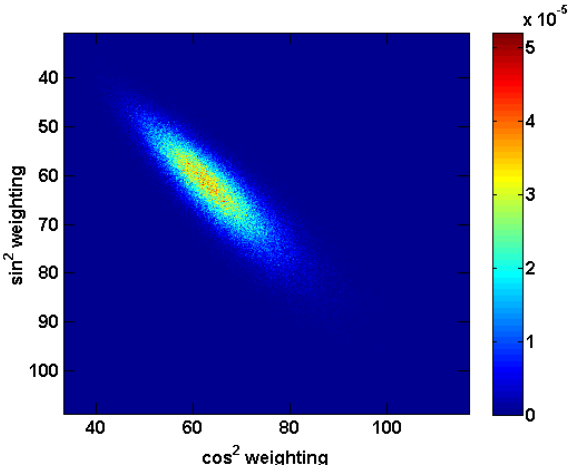

(b) Endpoint distribution of $\cos^2$ and $\sin^2$ WSOS

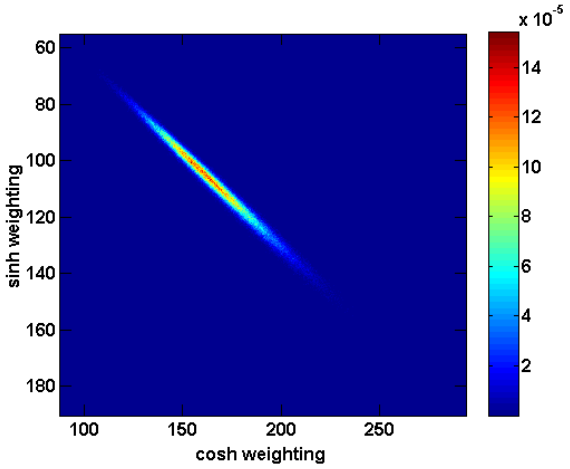

(c) Endpoint distribution of cosh and sinh WSOS

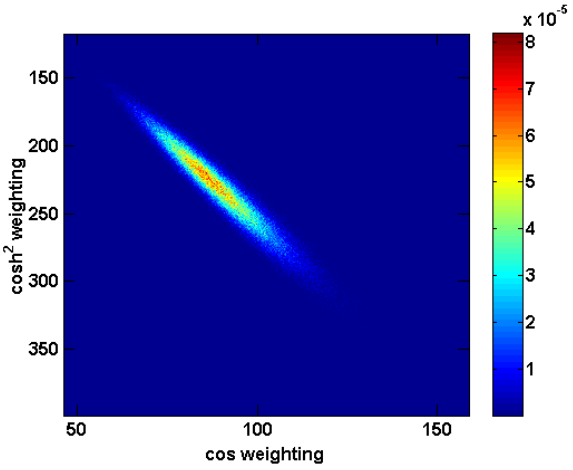

(d) Endpoint distribution of cos and $\cosh^2$ WSOS

Figure 5.13: Endpoint distributions for pairs of weighting functions with K distributed data

Note that Figure 5.13a is equivalent to the Ozturk algorithm except for the scaling factor $\frac{1}{N}$ and the lack of studentization. The ridge in Figure 5.13a shows some correlation between the cosine and sine weightings. However, Figure 5.13b appears to have much less correlation between the two functions. This lack of correlation could be predicted from Figures 5.6a and 5.6b, where the cosine squared and sine squared weightings appear to weight opposite areas of the pdf highly. Therefore, the cosine squared and sine squared weightings used in conjunction should be better at identifying K distributed data using the WSOS method than if they were used separately. In addition, of the four pairings considered here, they appear to yield the most information. Notice that the cosh and sinh WSOS are very highly correlated.

Finally, the cosine and cosh squared weightings appear to have a similar distribution to the cosine and sine WSOS.

This section explored a generalized form of the Ozturk algorithm with non-studentized data. The weighting functions were expanded to additional trigonometric and hyperbolic functions in an effort to provide diversity. Finally, the correlation between WSOS for different weighting functions was shown.

5.3 Scaled Weighted Sums of Ordered Statistics

Section 5.2 generalized the Ozturk algorithm to a weighted sum of ordered statistics with non-studentized data. Now we propose a new set of weighted sums of ordered statistics (WSOS) that are scaled based on the sampled data. These new methods are the studentized WSOS, the divide by mean (DBM) WSOS, and an extension of the Ozturk algorithm to arbitrary weightings, denoted as the extended Ozturk algorithm (EOA).

Note from (5.8) the data is studentized by subtracting the sample mean and scaling the result by the sample standard deviation. Therefore, the studentized order statistics are forced to zero mean, unit variance. In (5.11), the Ozturk algorithm takes the additional step of taking the absolute value of the resulting order statistics. In the context of the Ozturk algorithm, this step corresponds to assigning the magnitude of a vector. We propose using the studentized order statistics without taking the absolute value.

We re-define the Ozturk order statistics as

$$z_{\mathrm{Oz},(i)} = \left| \frac{q_{(i)} - \bar{q}}{\hat{\sigma}} \right| \tag{5.14}$$

where $q_{(i)}$ are the ordered, quadratic samples defined in (5.5), $\bar{q}$ is the sample mean of the quadratic samples defined in (5.6), and $\hat{\sigma}$ is the sample standard deviation defined in (5.7).

The studentized order statistics are denoted as

$$z_{\text{Stud},(i)} = \frac{q_{(i)} - \bar{q}}{\hat{\sigma}}. \tag{5.15}$$

Noting that the quadratic samples q_i are power estimates, we take inspiration from the classic CFAR detector and propose scaling the order statistics by the sample mean [42]. The divide by mean (DBM) order statistics are defined as

$$z_{\text{DBM},(i)} = \frac{q_{(i)}}{\bar{q}}. \tag{5.16}$$

The three variants of scaled WSOS can then be formed from the 10 proposed weighting functions given in Section 5.2 and the three scaled order statistics given in (5.14), (5.15), and (5.16). The general WSOS given in Section 5.2 may be thought of as a constant scaling of 1 over all samples.

5.4 Combined Order Statistics Modeled in Clutter

The methods presented in this chapter are based on a general statistical premise: determining the underlying distribution of sampled SIRV data. However, in the context of radar detection, the underlying distribution of clutter is by definition a means to an end: the detection of a target with a constant, predictable probability of false alarm. The threshold for detection is determined from the tail of the clutter distribution. Therefore, we examine the possibility of mapping directly from endpoint space to a detection threshold for each of the four frameworks discussed.

Recalling the characteristics of [4], by modeling the radar clutter as a SIRV we have used the principle of prior information. Using the sample covariance matrix with small sample support allows the methods we have presented to adapt to temporal non-stationarities between coherent processing intervals. The remainder of this section will emphasize the

principle of robustness. By using multiple scalings and weighting functions, we provide a diverse range of possible endpoints. As we are attempting to model clutter, and use a framework of combinations of order statistics to determine the clutter distribution and/or a detection threshold, we denote the combined algorithm the Combined Order Statistics Modeled in Clutter (COSMiC) algorithm.

In the spirit of the Ozturk algorithm, we examine the correlation between endpoints for several pairs of weightings for each of the scaled WSOS and the non-scaled WSOS. Then, we examine the thresholds for each expected endpoint location. Clearly, for the purposes of radar detection we desire a one-to-one (*i.e.* bijective) mapping between endpoint and detection threshold. The threshold "space" will be quantified by the change in threshold with respect to Gaussian distributed clutter. This quantification is calculated via (4.2). By looking at *pairs* of endpoints we increase measurement diversity and introduce the possibility of two beneficial yet differing goals. First, if the location of the endpoints for two different functions are tightly correlated (*i.e.* the location of the endpoint for one weighting function tells us where the endpoint will land for a different weighting function), those weighting functions and the corresponding weighting algorithm are good candidates for a *robust* estimator. However, if the average endpoints are in each weighting "space" are different as a function of source (SIRV) distribution, the algorithm (*e.g.* WSOS, DBM, Studentized, EOA) and weighting functions used are good candidates for a distribution classifier. This second goal was the goal of the original Ozturk algorithm. The distinction between these two goals, as well as candidate methods for each goal, are examined in this section.

In general, the COSMiC goals may be expressed via the flowcharts shown in Figures 5.14a and 5.14b.

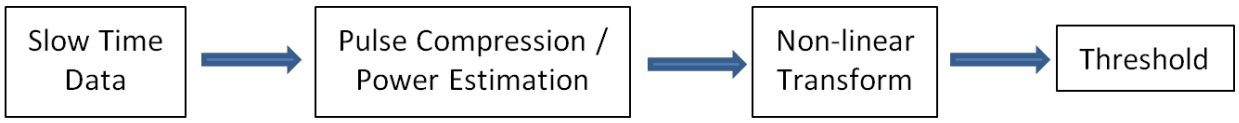

(a) Flowchart for Threshold Identification

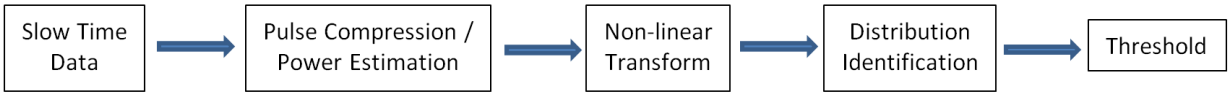

(b) Flowchart for Distribution Identification and Threshold Identification

Figure 5.14: COSMiC Flowcharts

The non-linear transform used will be varied in this section. As an example, the non-linear transform for a WSOS is shown in Figure 5.15

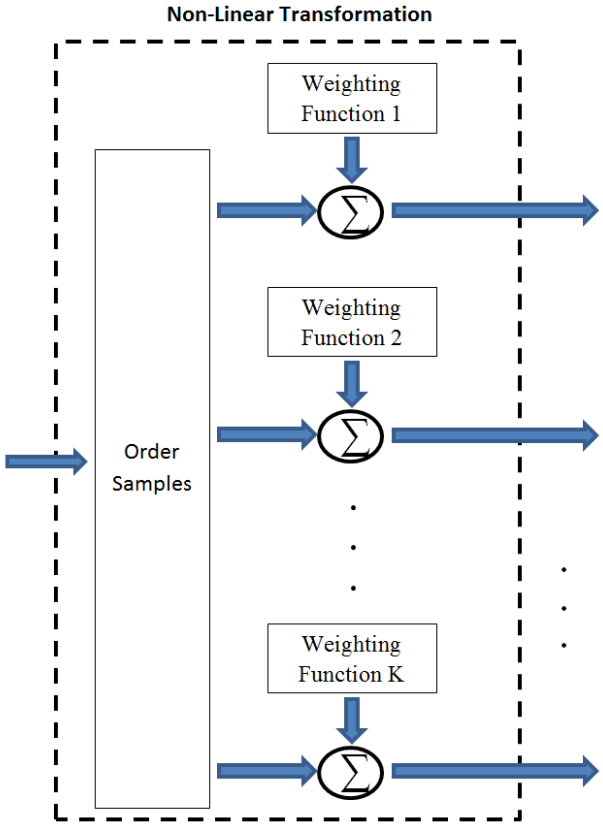

Figure 5.15: Example non-linear transform: weighted sum of order statistics

As a proof of concept, we simulated a limited library of SIRVs to model potential clutter distributions. The distributions modeled are the K, Weibull, Gamma Modulated (GM), and Compound Gamma Modulated (CGM) distributions. These distributions are discussed in

detail in Chapters 3 and 4. Each endpoint was found through Monte Carlo simulation of 10^6 complex SIRVs, each of dimension $L = 4$. We use $N = 4L = 16$ order statistics of the quadratic form of the SIRV to form each endpoint. The clairvoyantly known covariance matrix was used to form each quadratic sample. The thresholds were all found by Monte Carlo simulation of 10^8 quadratic samples of the SIRV, with a desired $P_{fa} = 10^{-6}$. In forming all WSOS, we divide the final sum (*i.e.* endpoint) by N to reduce the scale of the endpoint space, and provide continuity to the previous work in [1, 109–112].

In this section we denote the "best" weighting function/algorithm combinations to be the mappings with the least ambiguities. We examine two types of plots. First, we look at the relation of the average endpoint locations for pairs of weighting functions. The endpoints are parametrized twice. First, they are parametrized by distribution (the four previously mentioned). Second, each distribution is parametrized by shape parameter(s). For a robust estimator, the two dimensional endpoints will ideally trace either a straight line or a curve with little to no variance. For a distribution classifier, the endpoints should trace separate "paths" of endpoints. Each of these paths should consist of points from a single distribution with a varying shape parameter. Note that points from multiple paths could share a common threshold (*i.e.* distribution tail). The second type of plot is a mapping from "endpoint space" to "threshold space". In other words, for each of the distributions simulated we estimated the change in threshold for a CFAR radar above the threshold one would use in Gaussian clutter. For each weighting function/algorithm pair examined we then plot the endpoints of each distribution with respect to the change in threshold. A "good" mapping is one where distributions with similar endpoints also possess similar thresholds. If a point in endpoint space corresponds to multiple thresholds, there is an ambiguity at that location in endpoint space. A "tight" mapping is considered to be a point in endpoint space where the difference in threshold for close points is on the order of ϵ dB, where ϵ is defined by the user. The concepts of "good" pairs of weighting functions and processing algorithms will be examined in the context of the plots given in the rest of this section.

To begin, Figures 5.16a-5.16d examine examine the sine and cosine pairing. As mentioned previously, each endpoint corresponds to one of four distributions with a varying shape parameter (and threshold). Figure 5.16a shows the library of average endpoints for the WSOS algorithm. For the WSOS algorithm with sine and cosine weighting functions, the path of the endpoints for the distributions in this library appear to trace an arc from left to right (*i.e.* lower values of the each endpoint correspond to distributions with greater thresholds). The top right endpoint is equivalent to the Gaussian distribution (Weibull with shape $\nu = 2$). The sine and cosine functions appear to correlate fairly tightly, but there is variance around the arc traced. The variance appears to be primarily caused by the Weibull distributed values. Therefore, the WSOS algorithm with sine and cosine weightings is a candidate for a robust estimator to determine the threshold for SIRV data. Depending on the variance in endpoint values, it may also be a candidate to determine whether sample data fits a Weibull distribution or a SIRV distribution derived from a transformed Gamma modulating random variable (*e.g.* K, GM, CGM).

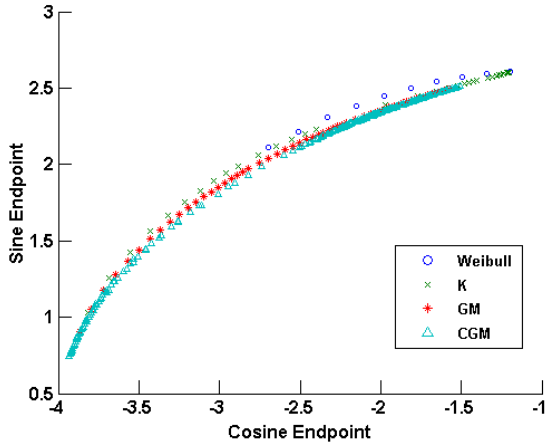

(a) Endpoint distribution of cosine and sine WSOS

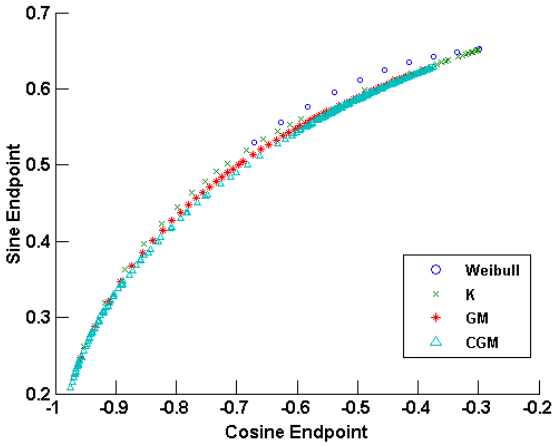

(b) Endpoint distribution of cosine and sine DBM WSOS

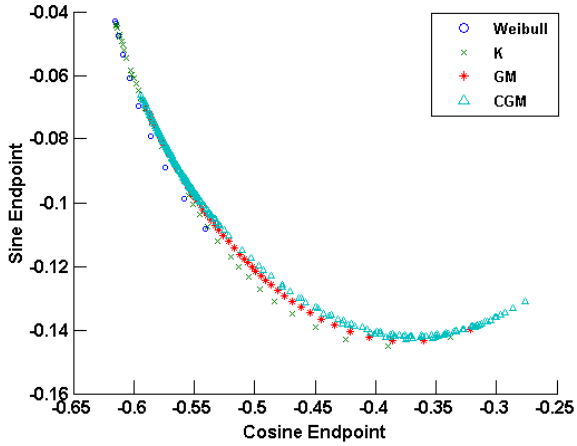

(c) Endpoint distribution of cosine and sine Studentized WSOS

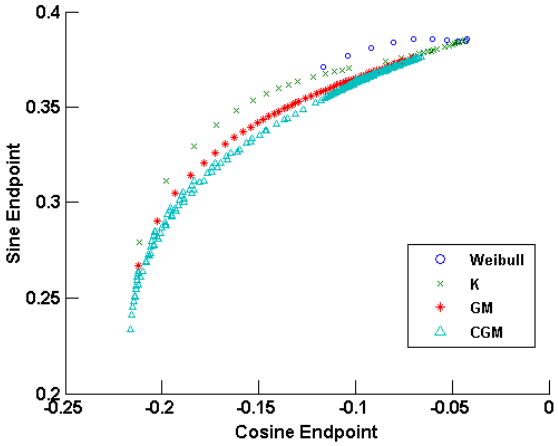

(d) Endpoint distribution of cosine and sine EOA

Figure 5.16: COSMiC endpoint distributions, cosine v. sine

Figure 5.16b shows the endpoint distribution for the DBM algorithm with the sine and cosine function weightings. The endpoint arc and slight variance appear similar to the results for the WSOS algorithm shown in Figure 5.16a. Therefore, the DBM method and WSOS may be used in tandem to produce a robust estimate. Figure 5.16c shows the endpoint distribution for the Studentized WSOS using the sine and cosine weighting functions. Unlike the WSOS and DBM methods, the Studentized method produces endpoints with increasing thresholds corresponding to decreasing sine values and increasing cosine values. The Gaussian threshold is at the top left of the arc. In addition, the endpoint distribution has an ambiguity when

the sine weighting function is used. Because of this ambiguity, the Studentized WSOS with the sine weighting function may not a good candidate to explore or exploit compared to the methods explored in this analysis. Figure 5.16d gives a library of endpoints corresponding to the original Ozturk algorithm. Unlike the other three methods, the EOA provides a clear distinction between the individual distributions making up the library. However, this implies that the EOA may not yield a bijective mapping from endpoint space to threshold space.

Next we examine the individual endpoints given by the cosine weighting function and the corresponding changes in thresholds.

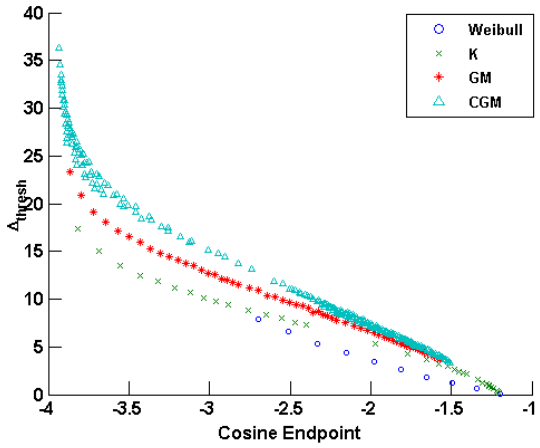

(a) Endpoint distribution of cosine v. threshold for WSOS

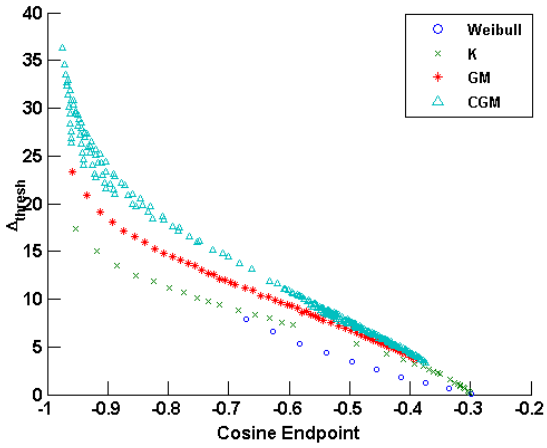

(b) Endpoint distribution of cosine v. threshold for DBM WSOS

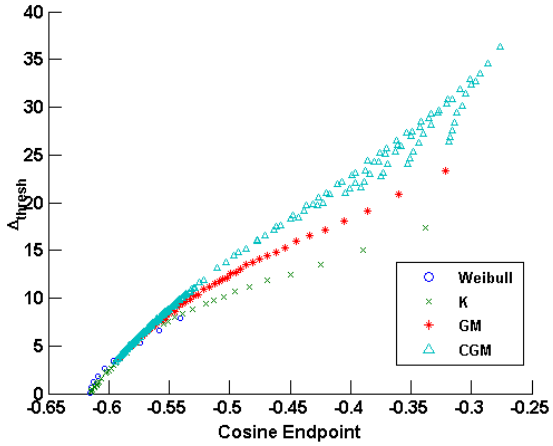

(c) Endpoint distribution of cosine v. threshold for Studentized WSOS

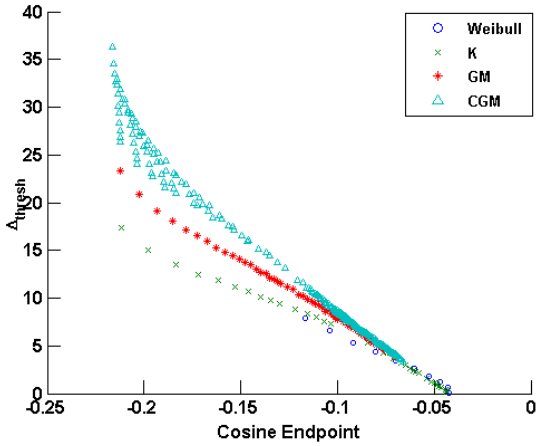

(d) Endpoint distribution of cosine v. threshold for EOA

Figure 5.17: COSMiC endpoint distributions for cosine v. threshold

It is immediately apparent that there are ambiguities between the endpoint space and the Δ_{thresh} for all methods. In other words, points falling close to each other in endpoint space correspond to distributions with very different tails (and therefore different thresholds). In the context of the radar detection problem, this ambiguity is problematic. However, as a practical matter, in this work we concentrate on changes in threshold less than 10 dB. As the threshold has a direct relation to the probability of detecting a target when a target is present, a 10 dB loss of detection will likely compromise the functionality of a typical radar. In future work, we will examine the endpoint location of measured radar data. If these measurements suggest higher thresholds are needed, the limit of a 10 dB change in threshold will be re-examined.

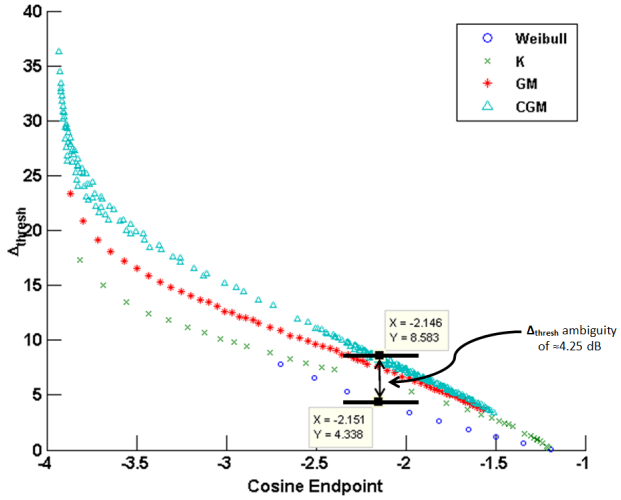

Figure 5.18: Ambiguity for cosine v. threshold

Figure 5.17a shows the cosine endpoint and the corresponding change in threshold for the WSOS method. The ambiguity in Figure 5.17a is highlighted in Figure 5.18. Figure 5.17b shows the cosine endpoint and change in threshold for the DBM method. As with Figures 5.16a and 5.16b suggest, the results for the WSOS and DBM methods are similar up to a scaling factor for the endpoint. Intuitively, this makes sense as the divide by mean (DBM) method is dividing by the mean of a series of power estimates arising from identically distributed data. Therefore, in the expectation, these points should be identical up to a

scale factor. However, in practice this scaling may prove to make the estimate more robust. The robustness of the DBM method, and the improvement offered by combining the two methods, will be explored in future work. Similarity aside, neither the WSOS nor DBM method appears to provide an unambiguous mapping into threshold space with the cosine weighting function. However, for changes in threshold below 5 dB, the Studentized WSOS and EOA provide a tight mapping between cosine endpoint space and threshold space.

Next, Figures 5.19a-5.19d show the relation between the sine endpoint and the change in threshold for the four methods. Figures 5.19a and 5.19b illustrate the scaling difference between the WSOS and the DBM methods. However, unlike the cosine endpoint, the mapping between sine endpoint space and threshold space appears to be tight for low changes in threshold ($\Delta_{\text{thresh}} < 5$ dB). Figure 5.19c gives the mapping between sine endpoint space and the change in threshold for the Studentized WSOS method. The ambiguity shown in Figure 5.16c is apparent in Figure 5.19c. However, the ambiguous endpoints are in the endpoint space we are not interested in. In addition, the mapping between endpoint space is tight for values $\Delta_{\text{thresh}} < 5$. Figure 5.19d shows the results for the sine endpoint when the EOA is used. When the modulating random variable of the underlying SIRV distribution is derived from the Gamma distribution (*i.e.* K distribution, GM, CGM), there is a tight mapping from sine endpoint space to values of $\Delta_{\text{thresh}} < 11$ dB. However, the sine endpoint ambiguously maps to a higher threshold for a Weibull distributed SIRV than for the Gamma derived SIRVs.

Therefore, when combining the sine and cosine weightings the EOA (in this case identical to the original Ozturk algorithm) provides the best distribution discrimination. For the individual endpoints, the Studentized WSOS and EOA methods provide the best (least ambiguous) mapping into the threshold space.

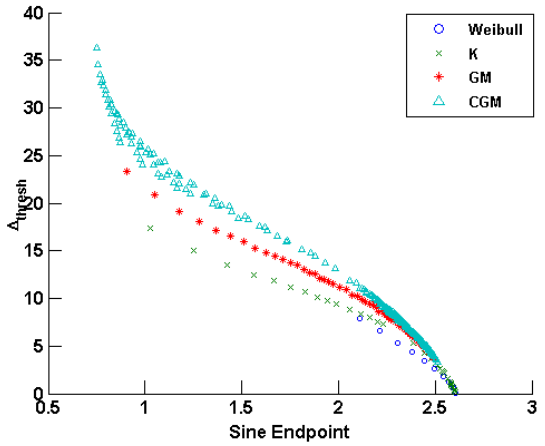

(a) Endpoint distribution of sine v. threshold for WSOS

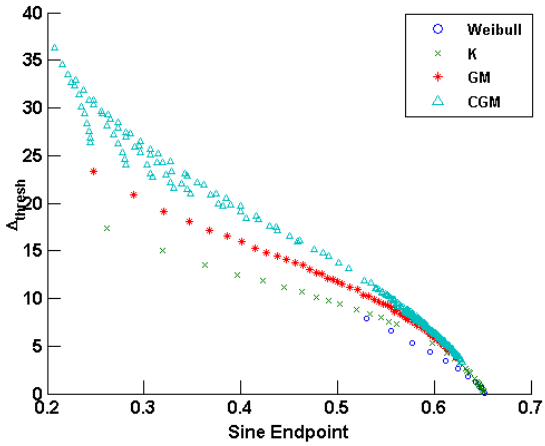

(b) Endpoint distribution of sine v. threshold for DBM WSOS

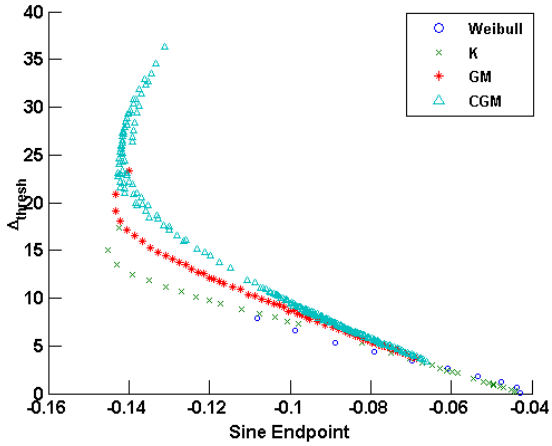

(c) Endpoint distribution of sine v. threshold for Studentized WSOS

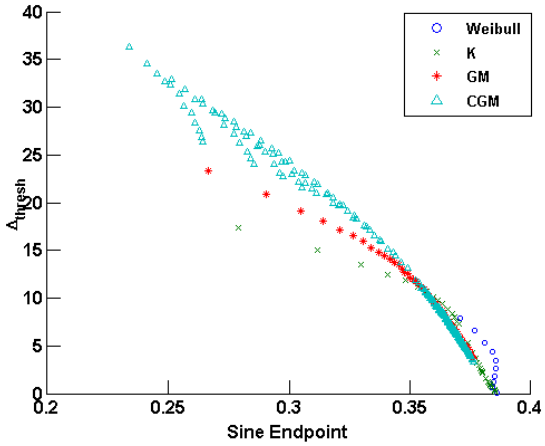

(d) Endpoint distribution of sine v. threshold for EOA

Figure 5.19: COSMiC endpoint distributions for sine v. threshold

Next, we examine the combination of the sine squared and cosine squared weighting functions for the four methods. Figures 5.20a and 5.20b show results of the WSOS and DBM methods, respectively. As expected, they differ only by a scale factor. There appears to be a linear, perfectly correlated relationship between the cosine squared endpoint and the sine squared endpoint for the WSOS and DBM methods.

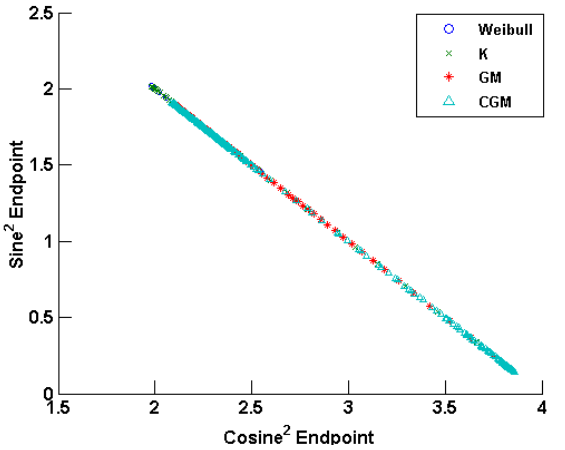

(a) Endpoint distribution of cosine squared and sine squared WSOS

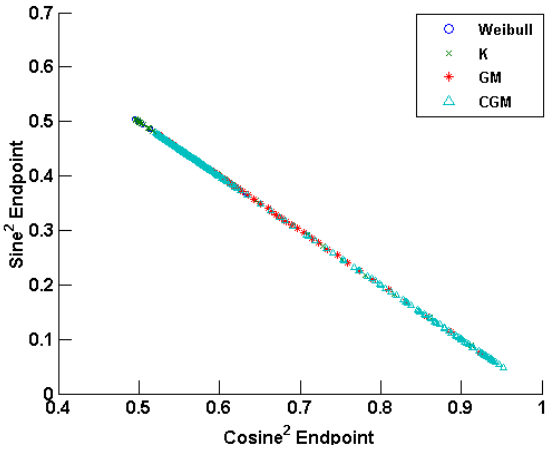

(b) Endpoint distribution of cosine squared and sine squared DBM WSOS

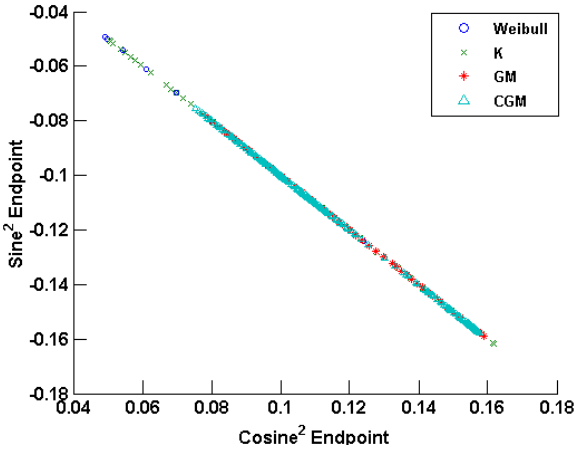

(c) Endpoint distribution of cosine squared and sine squared Studentized WSOS

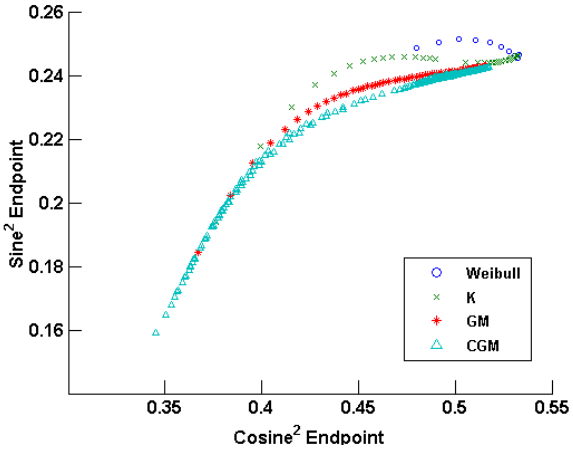

(d) Endpoint distribution of cosine squared and sine squared EOA

Figure 5.20: COSMiC endpoint distributions, sine squared v. cosine squared

Like the WSOS and DBM methods, Figure 5.20c shows that the Studentized WSOS method also results in a linear, perfectly correlated relationship between the sine squared weighting function and the cosine squared weighting function. In addition, visual inspection of the upper left of the endpoint space (*i.e.* the largest sine squared values and smallest cosine squared values) shows that in this case the distributions with lower thresholds are "spread" out. In other words, for samples produced by a K distribution or Weibull distribution with large shape values the cosine squared and sine squared weighting functions used in conjunction with the Studentized WSOS method separate the endpoints. However, the

Weibull and K endpoints are still interspersed, so this method may not be used to distinguish between distributions. However, Figure 5.20d shows the distribution discrimination capabilities of the Ozturk algorithm apply to the new weighting functions.

Figures 5.21a-5.21d show the cosine squared endpoint with respect to change in threshold for the four methods. Examining Figures 5.21a and 5.21b, the cosine squared weighting function does not appear to be better than cosine weighting function or sine weighting function at determining threshold unambigously when the WSOS or DBM methods are used.

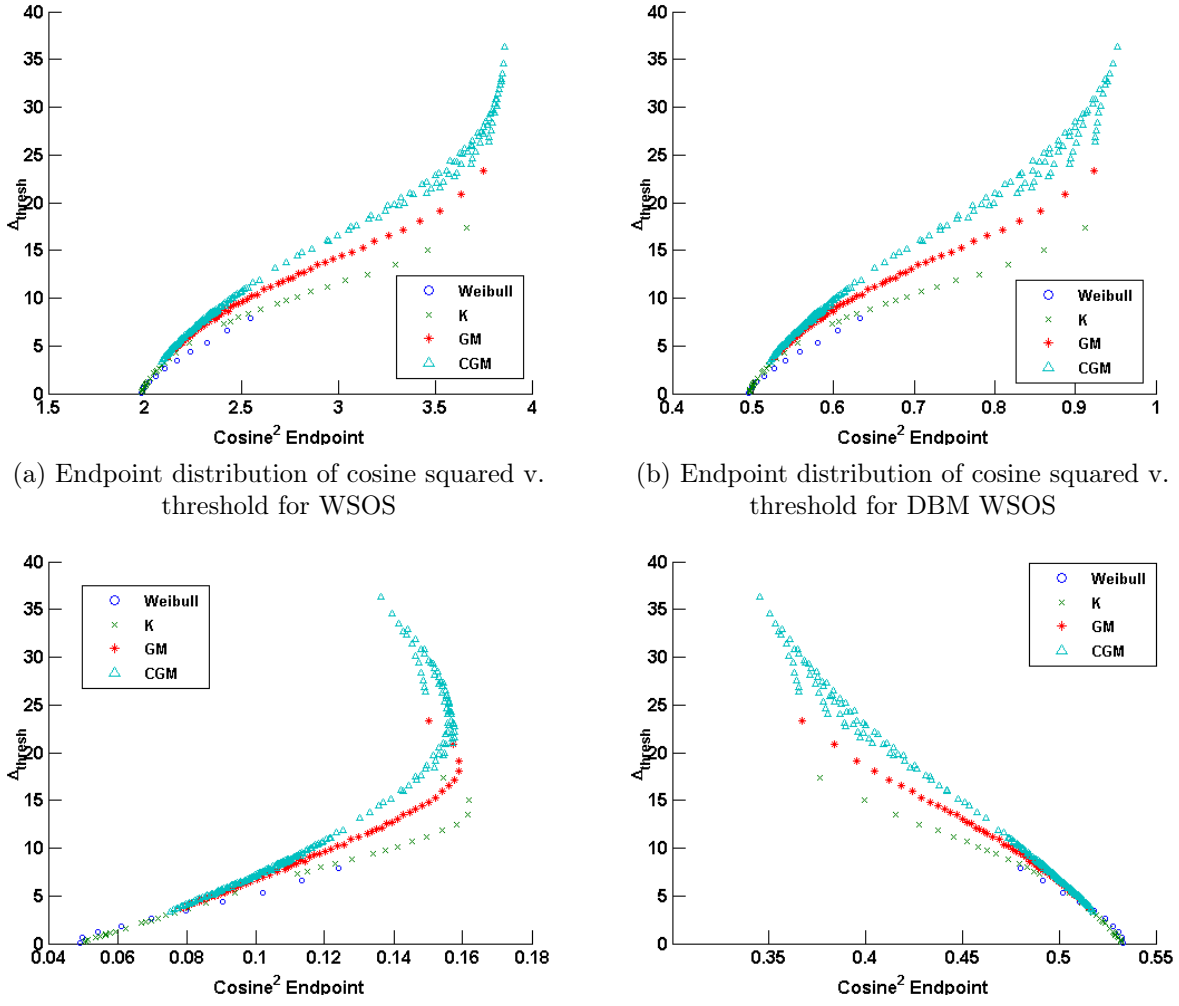

(a) Endpoint distribution of cosine squared v. threshold for WSOS

(b) Endpoint distribution of cosine squared v. threshold for DBM WSOS

(c) Endpoint distribution of cosine squared v. threshold for Studentized WSOS

(d) Endpoint distribution of cosine squared v. threshold for EOA

Figure 5.21: COSMiC endpoint distributions for cosine squared v. threshold

However, the Studentized WSOS method, as shown in Figure 5.21c, produces a similar ambiguity for high threshold distributions as was seen for the sine weighting function was used for the same method. The Studentized WSOS method with the cosine squared weighting function gives a tight approximation of the threshold for $\Delta_{\text{thresh}} < 5$ dB. The spreading of low threshold distributions is also apparent in Figure 5.21c. As the Weibull and K distribution are both commonly measured, the pairing of the cosine squared weighting function and the Studentized WSOS is a promising technique and will be investigated further with measured data. Figure 5.21d shows the effectiveness of the EOA method for mapping distributions with $\Delta_{\text{thresh}} < 8$ dB to an endpoint generated with the cosine squared weighting function.

Figures 5.22a-5.22d show the change in threshold when the sine squared weighting function is used for the four different methods. By comparing Figures 5.22a-5.22c to Figures 5.21a-5.21c, the suitability of the sine squared weighting function in mapping from endpoint space to threshold space appears to be approximately equivalent to the cosine squared threshold for the WSOS, DBM, and Studentized WSOS methods. For both weighting functions the mapping appears to have have a low amount of ambiguity for $\Delta_{\text{thresh}} < 5$. Unlike the cosine squared weighting function, higher threshold distributions map to smaller valued endpoints when the sine squared weighting function is used (*i.e.* the "direction" of travel when increasing threshold is reversed). Also, as can be seen in Figures 5.22c and 5.21c, the ambiguity for high threshold distributions appears to be complimentary to the cosine squared weighting when the Studentized WSOS method is used. As a result, the ambiguity is identically "folded" into the line of endpoints seen in Figure 5.20c when the cosine squared and sine squared weighting functions are used in conjunction.

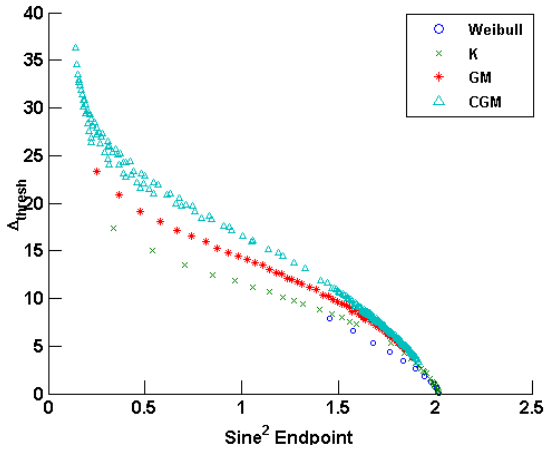

(a) Endpoint distribution of sine squared v. threshold for WSOS

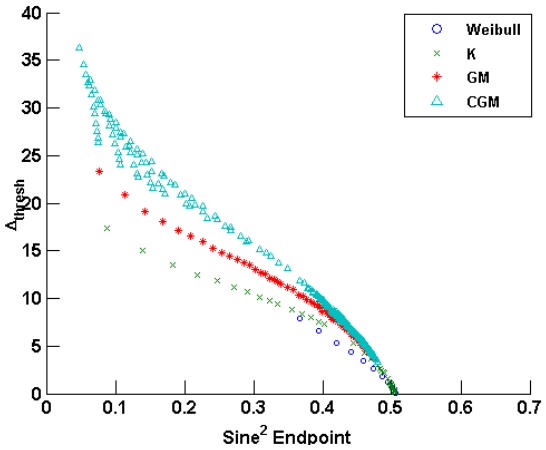

(b) Endpoint distribution of sine squared v. threshold for DBM WSOS

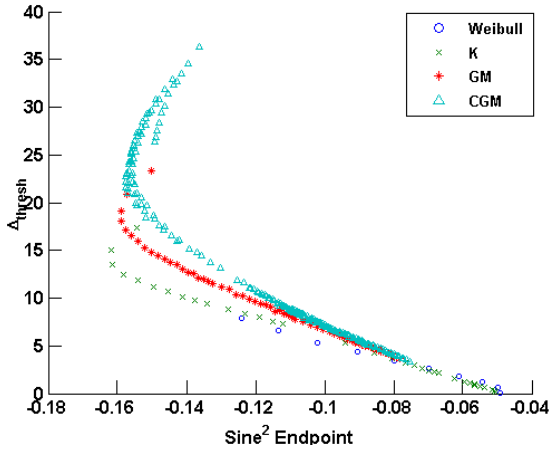

(c) Endpoint distribution of sine squared v. threshold for Studentized WSOS

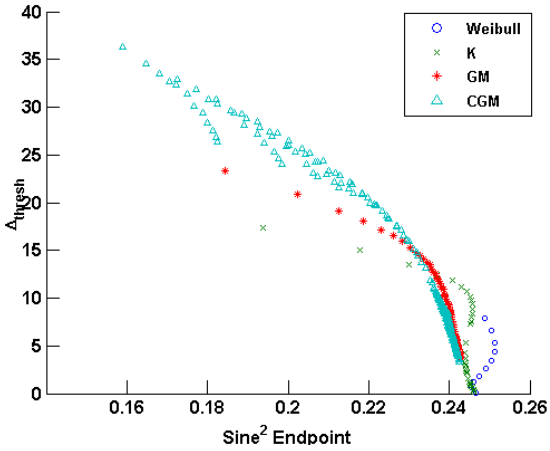

(d) Endpoint distribution of sine squared v. threshold for EOA

Figure 5.22: COSMiC endpoint distributions for sine squared v. threshold

From Figure, 5.22d, the EOA method yields highly ambiguous results when the sine squared weighting is used. Figure 5.20d shows the separation of distributions when the EOA is used with *both* the cosine squared and sine squared weightings. Therefore, while the sine squared weighting has value in the EOA framework, it should only be used together with another weighting function.

Up to this point, we have examined the endpoints resulting from trigonometric weighting functions used with our four methods of weighting. Now, we examine the pairing of the hyperbolic functions sinh and cosh. Figures 5.23a-5.23d show the endpoints for the four

methods. The WSOS, DBM, and Studentized WSOS methods have no apparent ambiguity between the two weighting functions. Therefore, it appears that the sinh and cosh weighting functions are well suited to be combined in a robust estimator. However, upon examination of Figure 5.23c the line formed by the two endpoint locations for the Studentized WSOS method has some curvature for distributions with low thresholds.

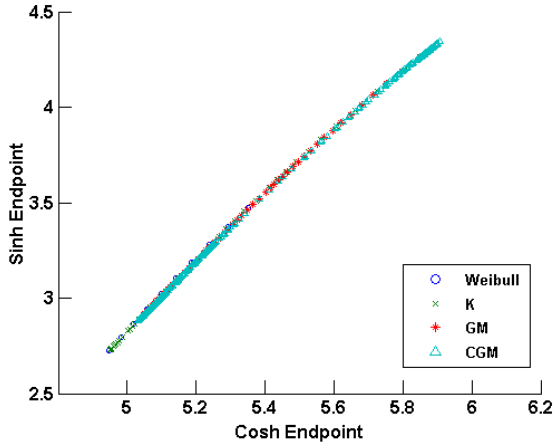

(a) Endpoint distribution of cosh and sinh WSOS

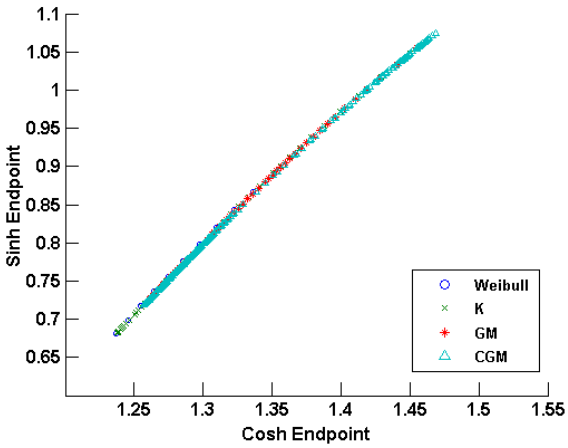

(b) Endpoint distribution of cosh and sinh DBM WSOS

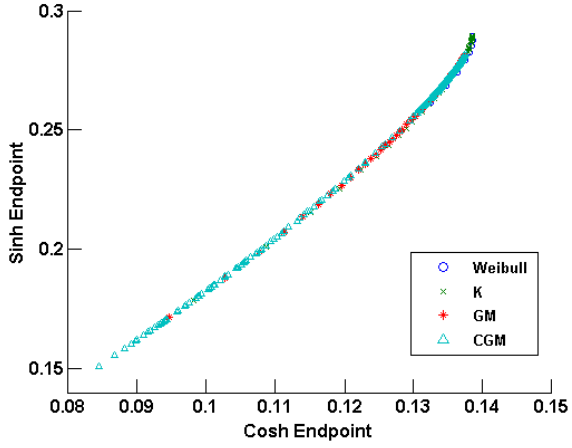

(c) Endpoint distribution of cosh and sinh Studentized WSOS

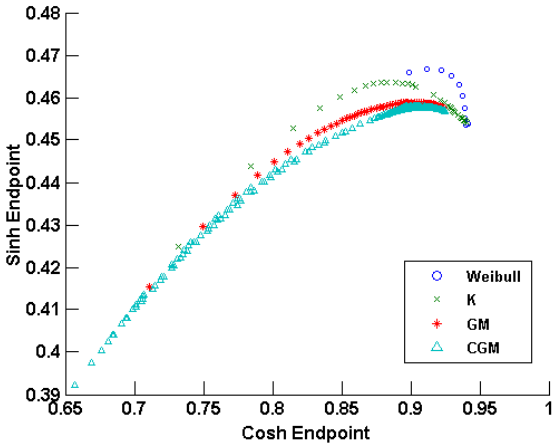

(d) Endpoint distribution of cosh and sinh EOA

Figure 5.23: COSMiC endpoint distributions, cosh v. sinh

Figure 5.23d reinforces the suitability of the EOA method for classifying distributions.

Next, Figures 5.24a-5.24d examine change in threshold as a function of the cosh weighting function endpoint location for the four methods. From Figures 5.24a-5.24b, the cosh

weighting function applied with the WSOS and DBM methods does not give a tight, unambiguous mapping from endpoint space to threshold space. However, Figure 5.24c shows the Studentization WSOS method yields a very tight mapping from endpoint space to threshold space. The cosh weighting function used with the Studentization WSOS method appears to provide one of the least ambiguous mappings between endpoint space and threshold space for $\Delta_{\text{thresh}} < 10$ dB.

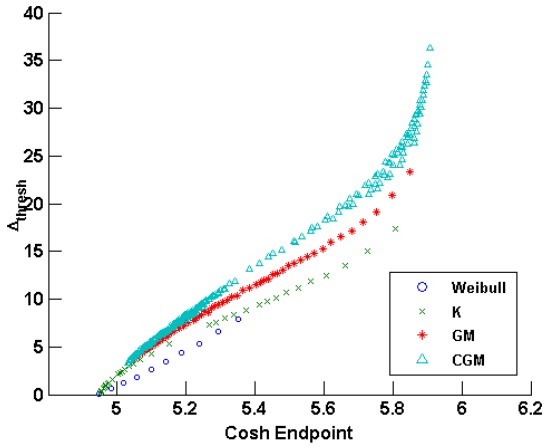

(a) Endpoint distribution of cosh v. threshold for WSOS

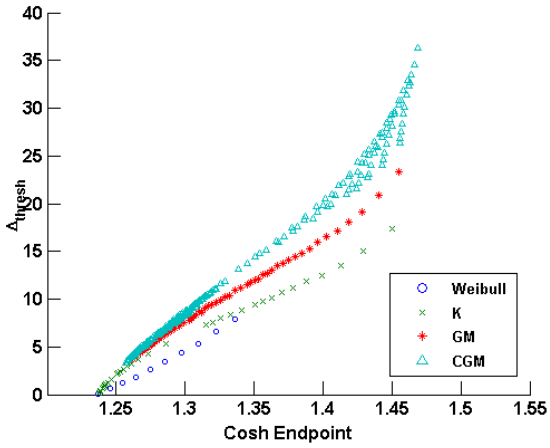

(b) Endpoint distribution of cosh v. threshold for DBM WSOS

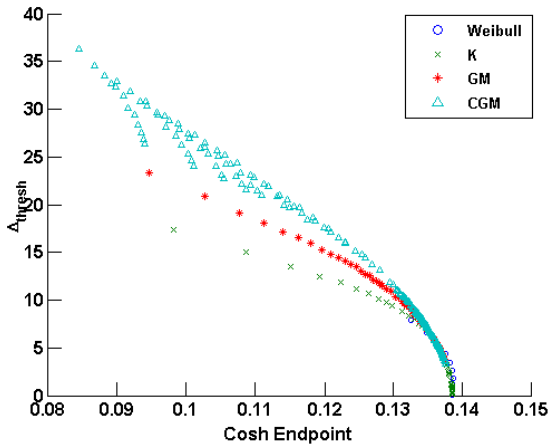

(c) Endpoint distribution of cosh v. threshold for Studentized WSOS

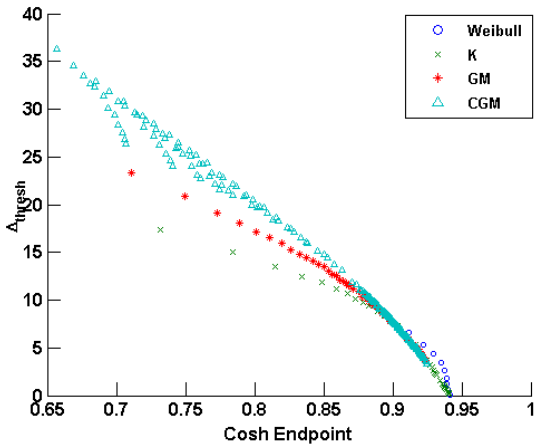

(d) Endpoint distribution of cosh v. threshold for EOA

Figure 5.24: COSMiC endpoint distributions for cosh v. threshold

When the cosh weighting function is used with the EOA, the Weibull distribution appears to introduce a slight ambiguity in the mapping with respect to the other three (Gamma

modulating RV derived) distributions.

Figures 5.25a-5.25d illustrate the endpoint to threshold mapping for the sinh weighting function and the four methods. The WSOS and DBM methods provide very ambiguous mappings between endpoint space and threshold space. Those methods should not be used for that purpose. However, like the cosh weighting function, the Studentization WSOS used with the sinh weighting function provides a low amount of ambiguity when mapping between endpoint space and threshold space.

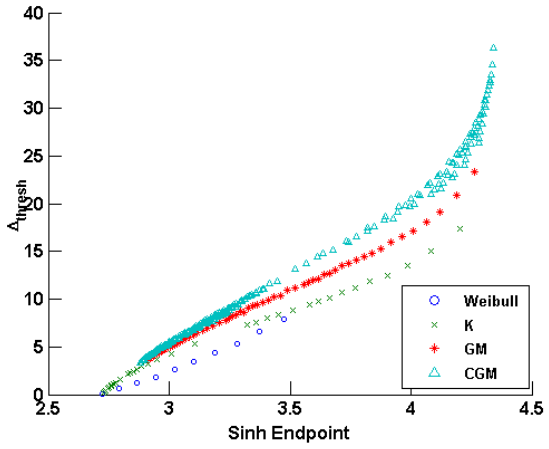

(a) Endpoint distribution of sinh v. threshold for WSOS

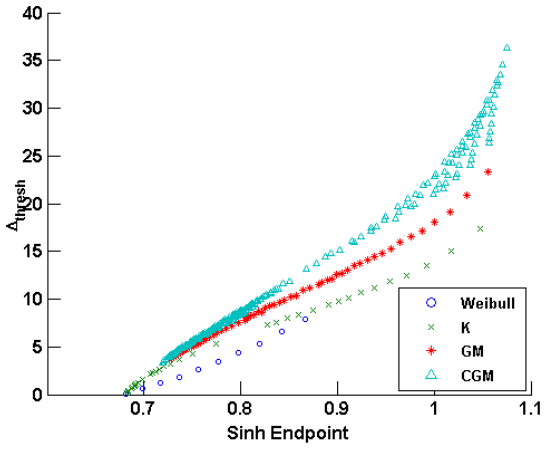

(b) Endpoint distribution of sinh v. threshold for DBM WSOS

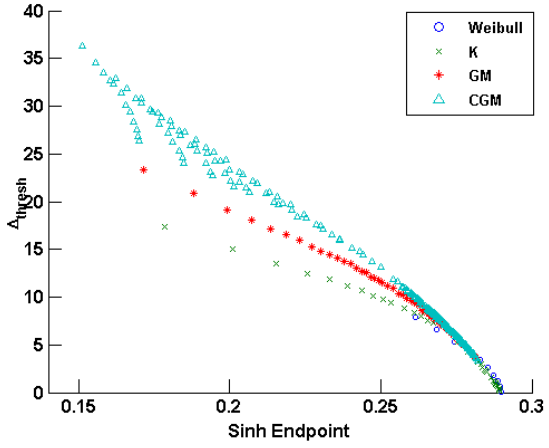

(c) Endpoint distribution of sinh v. threshold for Studentized WSOS

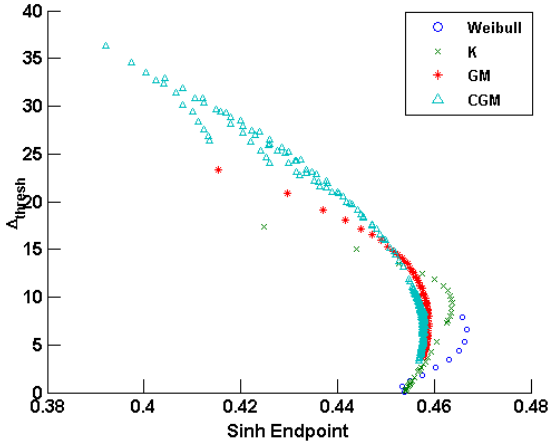

(d) Endpoint distribution of sinh v. threshold for EOA

Figure 5.25: COSMiC endpoint distributions for sinh v. threshold

Figure 5.25d shows that the EOA yields a highly ambiguous mapping between endpoint

space and threshold space.

Finally, we examine the pairing of the hyperbolic weighting function tanh and the trigonometric weighting function sine. Figures 5.26a-5.26d show the endpoint pairs for the four methods. The WSOS and DBM methods appear to have some ambiguity in the sine dimension. This ambiguity can also be seen in the sine-cosine pairing in Figures 5.16a-5.16c. An additional ambiguity in the sine dimension shows up in the upward curve at the left of Figure 5.26c for the Studentized WSOS method for high threshold distributions.

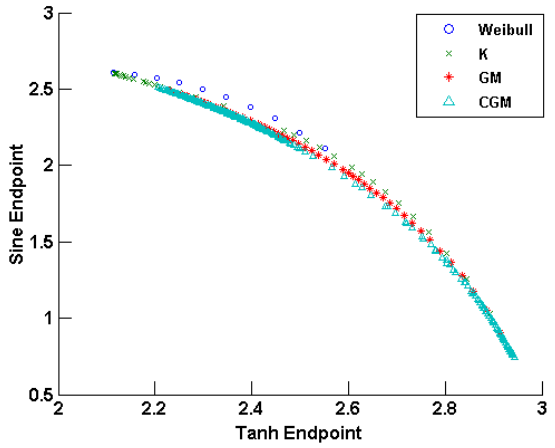

(a) Endpoint distribution of tanh and sine WSOS

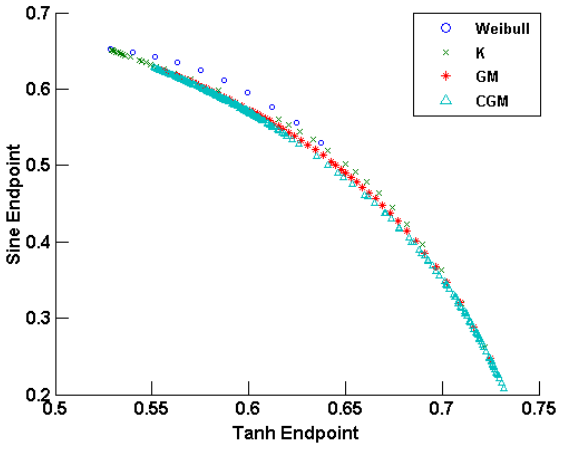

(b) Endpoint distribution of tanh and sine DBM WSOS

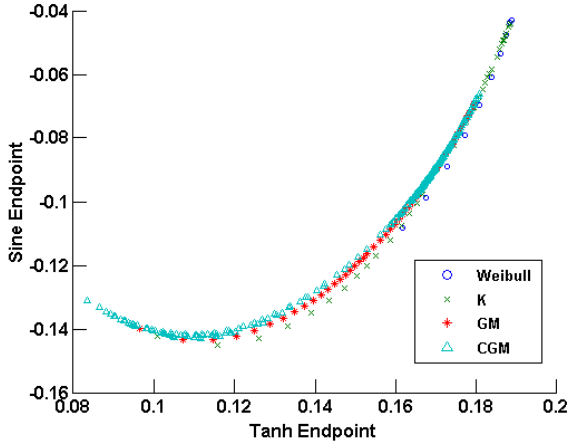

(c) Endpoint distribution of tanh and sine Studentized WSOS

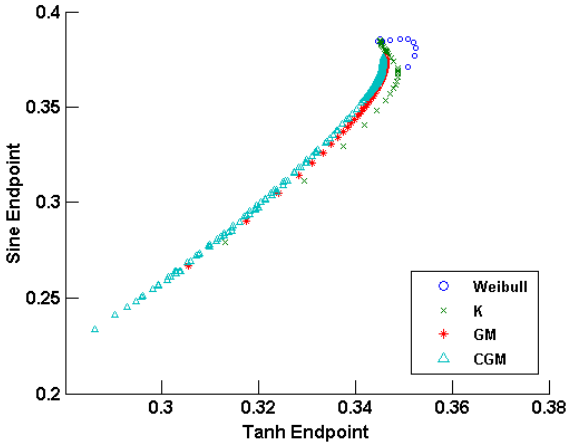

(d) Endpoint distribution of tanh and sine EOA

Figure 5.26: COSMiC endpoint distributions, tanh v. sine

Figure 5.26d shows clear "tracks" for each of the distributions when the EOA method is

used.

Figures 5.27a-5.27d show the mapping from the endpoint space of the tanh weighting function to threshold space. The WSOS, DBM, and EOA methods all produce ambiguous mappings. However, the Studentization WSOS provides little ambiguity when $\Delta_{\text{thresh}} < 5$ dB.

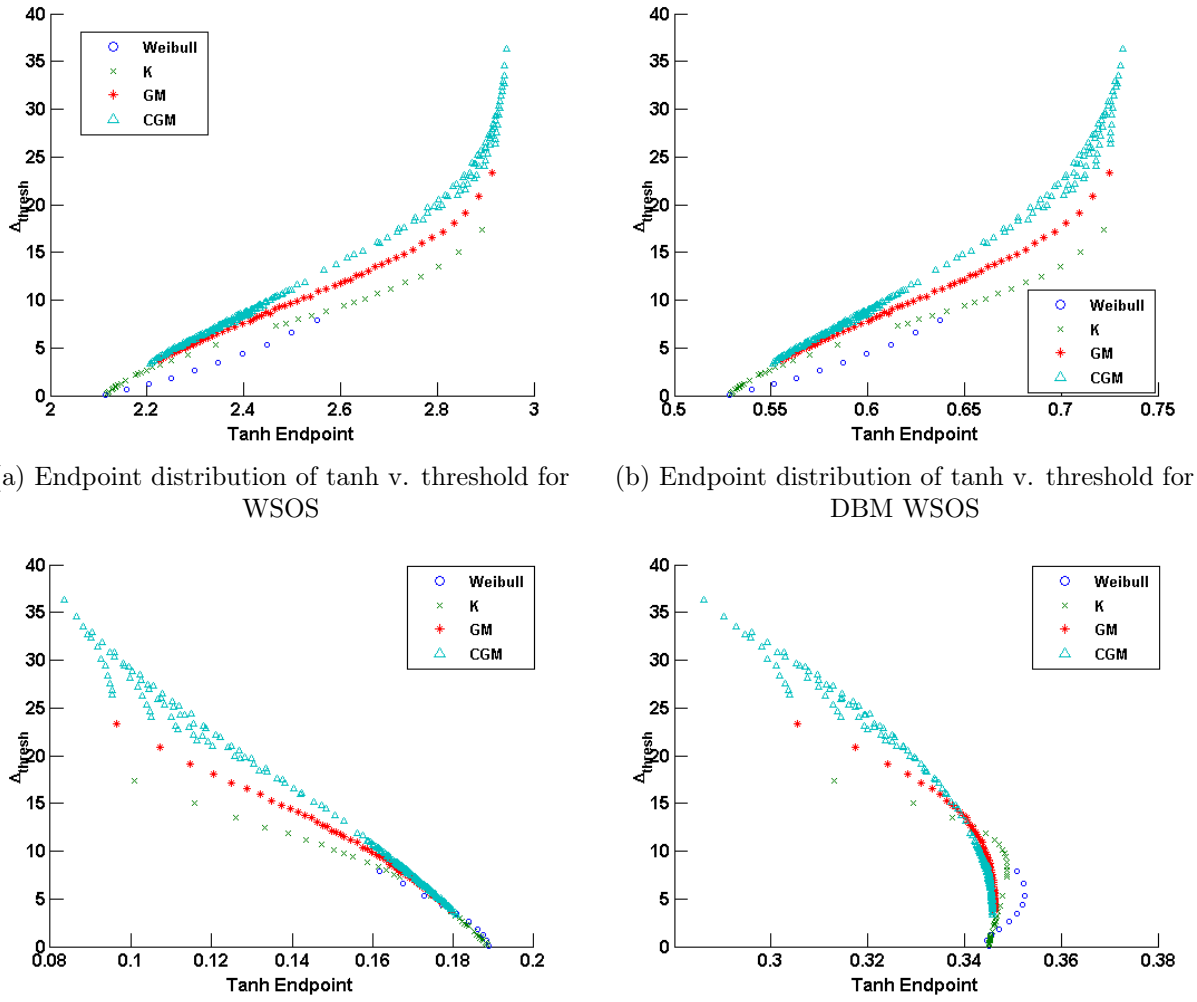

(a) Endpoint distribution of tanh v. threshold for WSOS

(b) Endpoint distribution of tanh v. threshold for DBM WSOS

(c) Endpoint distribution of tanh v. threshold for Studentized WSOS

(d) Endpoint distribution of tanh v. threshold for EOA

Figure 5.27: COSMiC endpoint distributions for tanh v. threshold

EOA is good when using pairs of weighting functions at distribution classification. WSOS and DBM appear good in most cases for robust estimation when multiple weightings are used. Studentization WSOS is best for mapping from endpoint space to threshold space. Of the

weighting functions considered in this analysis, the Studentization WSOS mapping from endpoint space to threshold space is best for the cosine, cosh, and sinh weighting functions.

The EOA appears to be an effective distribution classifier, at least when it is employed with all pairs of weighting functions considered so far. Examining the endpoint vs. threshold plots, each pair considered appears to have one member that maps endpoint to threshold with a low amount of ambiguity and one that maps with high ambiguity. This complementary pairing seems to give the diversity needed to distinguish between distribution endpoints. The implications of this combination will be considered when designing the overall COSMiC algorithm.

It should be noted that the sine weighting function appears to provide the worst (*i.e.* most ambiguous) mapping between endpoints and threshold. Because of this ambiguity, we do not recommend using the sine weighting function to establish the location of endpoints for the goal of robust estimation. However, the ambiguity of the sine weighting function provides benefits when considering the distribution classification problem.

When a measured endpoint falls in a location with an ambiguity in threshold space (depending on underlying SIRV distribution), the radar designer can make an informed decision on how to set the threshold. If the probability of false alarm must be constricted, the upper threshold can be chosen. This decision trades off improved detection performance for the possibility of a higher false alarm rate. However, the knowledge of the spread may also be used to set the threshold to the minimum value given by the library (*i.e.* maximizing P_d) and the algorithms in the system meant to mitigate the inevitable false alarms (*e.g.* the tracking algorithm) can be informed of the variable false alarm rate. Clearly, this is not a desirable scenario. However, in such a situation, to preserve a minimum level of functionality the system designer may be forced to accept a higher false alarm rate. The tradeoffs between detection and false alarm will be explored further in the context of the COSMiC algorithm framework.

Chapter 6

Developing the COSMiC Algorithm

In Chapter 5 the individual pieces combined order statistics mapping in clutter (COSMiC) algorithm were proposed. As was noted in Section 4.4, the quadratic form of a SIRV is identical to the generalized inner product (GIP) [101–103]. Therefore, hereafter the two terms are used interchangeably. For the purposes of the COSMiC algorithm, this equivalence allows us to treat the lognormal distribution in the same manner as the SIRV distributions under consideration. This chapter expands on and clarifies the concepts explored in Chapter 5.

The two metrics examined in this chapter are distribution identification and threshold estimation. Generally speaking, the original Ozturk algorithm was proposed to offer a hypothesis suggestion of the distribution most likely to fit the data. However, there are no claims made to the optimality of the algorithm. Armed with a hypothesis suggestion, a detector may select a distribution specific detection metric (*e.g.* maximum likelihood). However, we also explore the possibility of directly estimating the proper detection threshold for a set probability of false alarm. In other words, we will propose that the nearest two endpoints with known thresholds in the COSMiC library may be used to directly estimate the threshold of a measured sample. These two metrics will be described in more detail in Section 6.1, and form the basis of the evaluation conducted in Sections 6.2-6.3.

The rest of the chapter is as follows. The first section provides a formal statement of the COSMiC algorithm. The second section describes the first evaluation of the COSMiC algorithm, which was presented in [2]. The third section delves into a comprehensive examination of the performance of pairs of weighting functions in the COSMiC framework in conjunction with a full library of proposed distributions. Finally, a discussion of the results is presented and a conclusion is given.

6.1 Formal COSMiC Statement

For clarity, here we restate some of the work that was developed in Chapter 5. This section will provide a concise, unified definition of two proposed COSMiC algorithms. Various pieces of the COSMiC algorithms are then examined in the succeeding sections. The two proposed COSMiC algorithms are separated by the desired output. In the spirit of the original Ozturk algorithm, the first COSMiC algorithm provides a distribution suggestion, as well as an estimate of the shape parameter of the distribution (if applicable). The second COSMiC algorithm provides the threshold estimate associated with the distribution/shape parameter estimate of the first COSMiC algorithm.

Both COSMiC algorithms begin with a data pre-processing step. As we are considering a radar application, the slow-time data of interest consists of a set of N length L complex vectors $\mathbf{x}_i$. This set corresponds to the measurements of N i.i.d. range cells over L pulses. The value of the modulating random variable of each SIRV is assumed to be constant over the coherent processing interval (*i.e.* over the L pulses). To form the generalized inner product (GIP), or quadratic form of each vector the temporal covariance matrix must be estimated from the N samples. For the purposes of this work we will compare the use of the true covariance matrix, or clairvoyant covariance matrix (CCM), and the sample covariance

matrix (SCM). The SCM is formed as

$$\hat{\mathbf{\Sigma}} = \frac{1}{N}\sum_{i=1}^{N} \mathbf{x}_i \mathbf{x}_i^H. \tag{6.1}$$

It should be noted that estimation of the covariance matrix of SIRVs is not straightforward. The different instantiations of the modulating random variable over the training data causes each random vector to be scaled differently. Informal examination of this problem has implied that the sample covariance matrix tends to over estimate the clutter power, leading to over-nulled clutter. The consequences of this result will be shown in Sections 6.3 and 6.4. The maximum likelihood estimation of the covariance matrix requires knowledge of both the distribution and shape parameter [75,114]. However, the expectation-maximization (EM) algorithm used in [75, 114] appears to require larger values of L than are used here. The numerical instability caused by low sample support leads to the EM algorithm producing far worse estimates of the covariance matrix than the SCM method. Other methods of covariance matrix estimation were compared in [87], but the SCM provided the best results.

The block diagram of the data pre-processing step is shown in Figure 6.1.

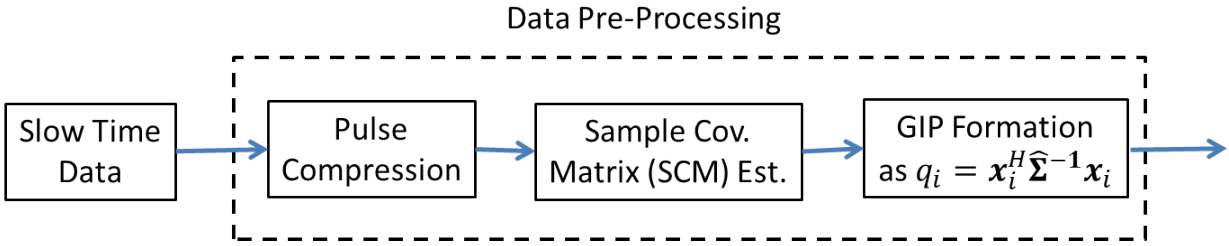

Figure 6.1: Data pre-processing block diagram

Both proposed algorithms use the same set of four methods proposed in Chapter 5. Each method performs the weighted sum of the transformed, ordered GIP statistics. The exploration in Chapter 5 was focused on the expected endpoints of the methods and the thresholds associated with each endpoint. In this chapter, we examine the performance of the methods. All four methods begin with forming the order statistics of the set of GIPs.

The GIP of the sampled vectors is defined as

$$q_i = \mathbf{x}_i^H \hat{\mathbf{\Sigma}}^{-1} \mathbf{x}_i. \tag{6.2}$$

The order statistics of $\mathbf{q}$ are then sorted such that $q_{(1)} \leq q_{(2)} \leq \cdots \leq q_{(N)}$. The four methods are distinguished by transforming the order statistics, and then performing a weighted sum

$$U(\mathbf{q}) = \sum_{i=1}^{N} a_i z_{(i)}(q_{(i)}) \tag{6.3}$$

where $z_{(i)}$ are the transformed order statistics and a_i are the N weights. The ten current weights under consideration are formed from the trigonometric functions cosine and sine, the hyperbolic functions cosh, sinh, and tanh, as well as their respective squares. The trigonometric weights are parameterized uniformly on the open interval $(0, \pi)$, and the hyperbolic functions are parameterized uniformly on the open interval $(0, 1)$.

The first method is designated the weighted sum of order statistics (WSOS). In this case, the order statistics are not transformed but are denoted

$$z_{\mathrm{WSOS},(i)}(q_{(i)}) = q_{(i)}. \tag{6.4}$$

The second method is the divide by mean (DBM) method. The DBM method finds the sample mean of the GIPs as

$$\bar{q} = \frac{1}{N} \sum_{i=1}^{N} q_i \tag{6.5}$$

and forms the transformed order statistics by dividing the order statistics by the sample mean as

$$z_{\mathrm{DBM},(i)}(q_{(i)}) = \frac{q_{(i)}}{\bar{q}}. \tag{6.6}$$

In the expectation, the WSOS and DBM are identical, but not necessarily for sample data. The third method is the studentized method, where the GIPs are scaled to be zero mean

and unit variance. Defining the sample variance to be

$$\hat{\sigma}^2 = \frac{1}{N-1}\sum_{i=1}^{N}(q_i - \bar{q})^2 \tag{6.7}$$

the studentized order statistics are then

$$z_{\mathrm{Stud},(i)}(q_{(i)}) = \frac{q_{(i)} - \bar{q}}{\hat{\sigma}}. \tag{6.8}$$

The final method under consideration is the extended Ozturk algorithm (EOA). The EOA order statistics are formed by taking the absolute value of the studentized order statistics, expressed as

$$z_{\mathrm{EOA},(i)}(q_{(i)}) = |z_{\mathrm{Stud},(i)}|. \tag{6.9}$$

For each method we form a library of endpoints. Each endpoint is formed by taking the expected value of the weighted sum of the transformed order statistics of various distributions. The endpoints of a distribution with a shape parameter form a curve in the endpoint space. Therefore, each distribution/shape (if applicable) pair is associated with ten endpoint values for each method. The associated threshold of each endpoint is calculated for the desired probability of false alarm. In all cases throughout this chapter 10^6 Monte Carlo trials were used to find the expected endpoint. The desired probability of false alarm was set to 10^{-5}.

The first COSMiC algorithm under consideration is intended to identify the distribution of the sample data, along with any applicable shape parameter. In the context of a detection scenario, a successful distribution identification by the COSMiC framework would allow a detector to employ a strategy optimized for that particular distribution (*e.g.* maximum likelihood). This scenario is considered for the K distribution in Section 6.2. For this algorithm, the pre-processed data is fed into the four methods. A number of weighted sums is then calculated for each method, and the results fed into a fusion algorithm. The output

of the fusion algorithm is then the most likely distribution present. These basic steps are illustrated in Figure 6.2.

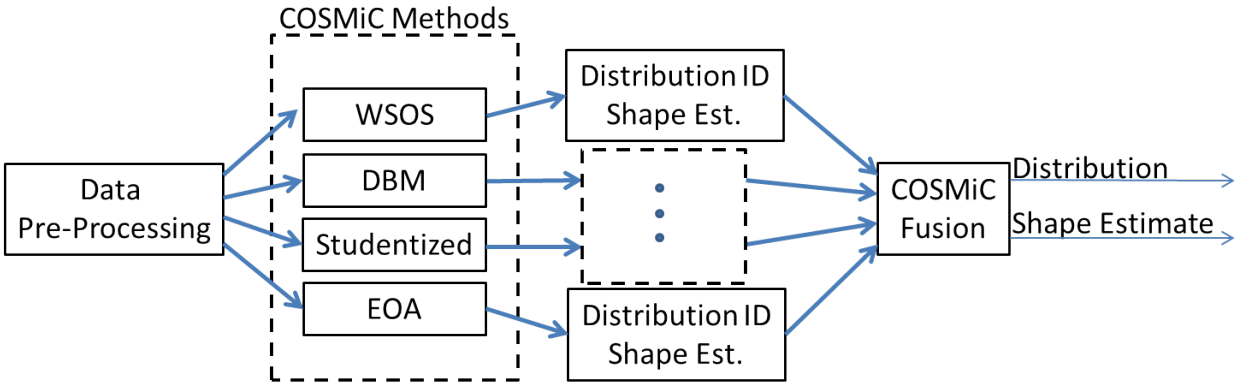

Figure 6.2: COSMiC distribution identification block diagram

Each method should use the best weightings to identify the distribution associated with the input data. To do this, the endpoint of the sample data with respect to the best K weightings is calculated. The Euclidean distance to the nearest known endpoint in the K dimensional endpoint space is found, and the associated distribution/shape parameter is then the given as the output of the method.

A key question is how many weightings should be used to estimate the distribution. The original Ozturk algorithm used a pair of weightings (specifically, the sine and cosine). The use of several pairs of weightings was explored in Section 5.4, as was the behavior of the endpoints for the single weighting case. Do more endpoints provide diversity to improve the estimate? Also, it should be determined which weightings provide the best discrimination between distributions. These two questions will be addressed in more detail in Sections 6.2-6.4. The fusion of the outputs of each method is also an open question, but is beyond the scope of this work. The fusion algorithm will be explored in future work.

The second algorithm to be considered is estimating the threshold of the data. If the identified distribution does not possess a shape parameter (*e.g.* Gaussian, lognormal), the second algorithm merely reports the known threshold associated with the identified distribution. Here we wish to preserve the computational simplicity of the original Ozturk algorithm,

and maintain the use of look-up tables. If the identified distribution does possess a shape parameter, the threshold must then be determined from the estimated shape parameter and the pre-calculated shape parameters. However, here we must consider the idea of "distance" in the endpoint space. Through experimentation, we have determined that the endpoint space is symmetric, but not necessarily linear. Due to the non-linearity of the space, we have no formal basis with which to compare the distance between distributions in endpoint space. We assume that the sampling between shape parameters if fine enough that the distance between calculated endpoints belonging to the same distribution may be approximated as linear. However, we do not assume that the number of distributions in our library is sufficient to make the same assumption.

Therefore to estimate the threshold of a sample endpoint, we consider a linear distance between the nearest known endpoint, and the second nearest known endpoint belonging to the same distribution as the first. All considered SIRVs possess the property that the tail of the distribution gets heavier (*i.e.* a higher threshold) as the shape parameter decreases. Therefore, for the remainder of the discussion we designate the known endpoint with the smaller shape parameter (and therefore larger threshold) to be ν_1 and the second endpoint to be ν_2. This notation establishes the relationship $\nu_2 \geq \hat{\nu} \geq \nu_1$. As we have assumed sufficient sampling in ν to approximate the distance in endpoint space to be linear, we further assume that the sampling in threshold $\mathcal{T}$ to be linear. Under these two assumptions, we may determine the estimated threshold based on the interpolated distance between shape and threshold as

$$\hat{\mathcal{T}} = \frac{\hat{\nu} - \nu_1}{\nu_2 - \nu_1}(\mathcal{T}_2 - \mathcal{T}_1) + \mathcal{T}_1 \tag{6.10}$$

where $\hat{\mathcal{T}}$ is the estimated threshold. The flowchart of the threshold estimating COSMiC algorithm is shown in Figure 6.3. As is the case with the distribution identification case, the fusion algorithm is outside the scope of this work and will be addressed in future work.

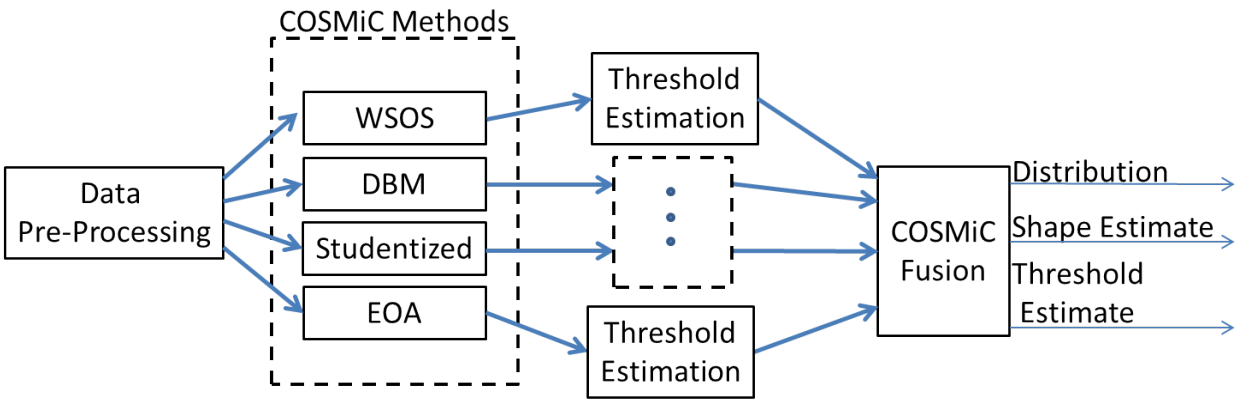

Figure 6.3: COSMiC threshold estimation block diagram

Recall from Chapter 3 that SIRVs provide a robust, general statistical model for clutter returns. However, as was discussed in Section 4.7, to date the literature is focused on fitting measured data to known distributions, most of which belong to the SIRV class. It is important to consider the possibility that there exists distribution(s) that are unknown to researchers, but fit measured data better than the available models. Due to the relation between the SIRV formulation, the central limit theorem, and electromagnetic scattering theory [7] we view the class of SIRVs to be an attractive architecture to use as a general model of radar clutter. Viewing the class of SIRVs as a whole provides the flexibility to account for unknown clutter distributions.

When considering the possibility of unknown distributions, one immediately faces the question of how to test against the unknown. For an initial approach, we use a series of "excised" COSMiC libraries. In other words, we excise knowledge of each distribution under consideration, and then test sample data from the excised distribution. This formulation applies only to the threshold estimation algorithm. By testing on data from a distribution not in our library, we can examine the accuracy of our methods for the commonly encountered clutter distributions. Further, we may explore how closely we can infer the tail of an unknown distributions from a collection of known distributions. This initial examination provides insight on how our methods may work when an unknown SIRV distribution is the best fit for measured data.

6.2 Initial COSMiC Evaluation

The initial examination of the COSMiC algorithm was shown in [2]. Here we restate the results of [2] to preface the more detailed examination conducted in Sections 6.3 and 6.4. The work in [2] provides a small scale implementation of the distribution identification and threshold estimation EOA transformation method discussed in Section 6.1.

The scope of implementation was limited with respect to the COSMiC algorithm in several ways. First, only the extended Ozturk algorithm (EOA) was examined. Second, the endpoint library only contained the K, Weibull, and lognormal distributions. The Gaussian distribution was included by virtue of including the Weibull distribution with shape parameter of $\nu = 2$. The distributions selected are the most commonly encountered distributions in the literature, making them ideal choices for an introduction to this initial implementation of the EOA method. Finally, with respect to Chapter 5, the K and Weibull distributions were limited to shape parameters greater that $\nu = 0.3$ and $\nu = 1.1$ respectively. The increase in the lower limit of the shape parameter was done to restrict the tail under examination such that the difference in threshold needed to maintain a $P_{fa} = 10^{-5}$ was approximately 10 dB or less. Recall from Chapter 5 that lower shape parameters were associated in a non-linear fashion with a rapidly increasing threshold. We use the $\Delta_{\text{thresh}} = 10$ dB (for an identical clutter power) as a cut-off to maintain realism. As any increase in threshold causes a corresponding loss in detection, we assume that any loss of more than 10 dB to be unrealistic.

As with the examples considered here, the EOA library formed in [2] used collections of $N = 16$ length $L = 4$ complex vectors. Several pairs of endpoints were considered. The choice of endpoints was informed by the examinations shown in Section 5.4. First, the distribution identification capabilities were examined. Figures 6.4a and 6.4b (reprinted from [2]) show the classification accuracies as a function of shape parameter for the cosine and sine pairs of weightings (*i.e.* the original Ozturk algorithm) and the cosine and cosine^2 weightings.

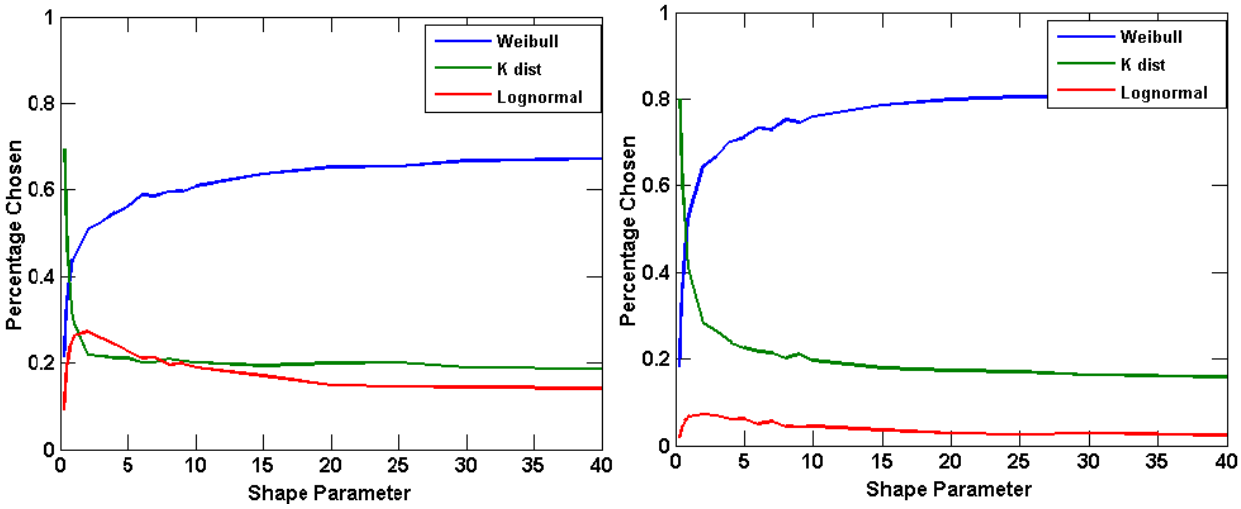

(a) Misclassification of K data for cosine, sine weightings

(b) Misclassification of K data for cosine, cosine^2 weightings

Figure 6.4: Using the EOA to classify K data as a function of shape (reprinted from [2])

It is clear that the distribution classification accuracy is very poor for medium to large shape values. Note that as the shape parameter increases, both the Weibull and K tend towards Gaussian. This coincidence implies that it may be difficult to distinguish between K, Weibull, and Gaussian data for large shape parameters. However, in this case the consequences of misclassification decrease due to similarly valued tails of the distributions for those shape parameters. However, if K data is mistaken as lognormal data at a high shape parameter, it would lead to the detection threshold being set too high and cause a large loss in detection. Finally, notice that the (cosine, cosine^2) pair of weightings provide better accuracy when compared to the original (sine, cosine) set of weightings.

Next, the problem of threshold estimation was considered, the process of which is detailed in Section 6.1. Figure 6.5a shows the error in threshold estimation as a function of shape parameter when K data is fed into the EOA method, while Figure 6.5b shows the same with Weibull distributed data. The error in threshold is defined as the ratio of true threshold of the data divided by the estimated threshold. The average over 10^5 Monte Carlo trials was found and the decibel difference is shown.

The endpoints corresponding to four pairs of weightings are considered, as well as the

combination of all ten weightings. The latter case is denoted as the "All Statistics" line. Note that an error in threshold greater than zero corresponds to an equal loss in detection capability, and an error in threshold less than zero corresponds with a non-linear increase in false alarm. To provide a comparison to the EOA technique, we also compare the performance of the EOA method to the traditional method of moments (MoM) technique for the K distributed data.

Recall from equations (3.83)-(3.86) in Section 3.5 that the MoM provides a maximum likelihood estimate of the shape parameter ν of the K distribution. Therefore, for comparison, the error in threshold is shown when the same test data is assumed to be *a priori* known to be K distributed, and the shape parameter estimated according to the MoM. In other words, the maximum likelihood estimation given knowledge of the distribution but not the shape parameter.

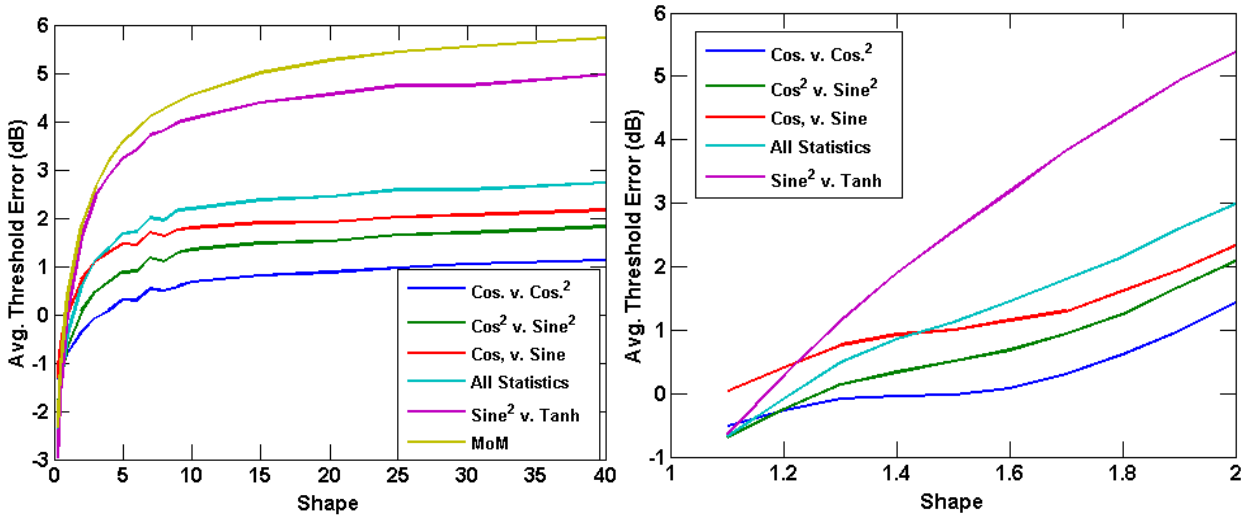

(a) Threshold estimation of K data

(b) Threshold estimation of Weibull data

Figure 6.5: Using the EOA to estimate threshold as a function of shape (reprinted from [2])

However, despite possessing more prior information and using an optimal shape estimator, it is clear from Figure 6.5a that the MoM technique performs worse than any of the EOA weighting pairs considered. Recall that we used set of $N = 16$ length $L = 4$ vectors for each sample. The MoM estimator then has four independent values of the modulating

random variable with which to estimate the shape parameter, and only 48 quadratic samples overall. Further, the MoM is a closed form solution. Therefore, while the shape estimate is on average more accurate for the MoM than the EOA output, the estimate suffers from numerical instability caused by extremely low sample support. Recall from Section 4.1 that the shape to threshold mapping is highly non-linear. Therefore, an occasional outlier caused by numerical instability may have a far greater effect on the average threshold error than a generally less accurate, but more stable output (given by the EOA).

Note that for the parameters considered, the lognormal distribution has a threshold of ≈ 9.5 dB more than the threshold needed for K data with shape parameter $\nu = 40$. However, it the thresholds of lognormal and K data are approximately equal for $\nu = 0.3$. Therefore, when K data with a high shape parameter is misclassified as lognormal by the EOA the resulting threshold is biased, causing a detection loss. Conversely, when low parameter K data is misclassified as lognormal by the EOA, there is little to no penalty in threshold. It should also be observed that the EOA formulation causes a "clipping" for K data with the minimum shape parameter of $\nu = 0.3$. As there is no distribution in the library with a greater threshold, any K data with low shape parameter that is misclassified as Weibull, or has an over estimated shape parameter will result in a lower than desired threshold error. By removing unlikely data points, the flexibility of the EOA has been reduced. This problem might be alleviated by allowing for more data points in the library. Despite this source of error, the lowest average threshold error for K distributed data is only at -3 dB. Therefore, in the presence of extreme K distributed clutter, the EOA produces an average threshold error of -3 dB compared to the -10 dB error resulting from the default assumption of complex Gaussian clutter.

Figure 6.5b shows the error in estimated threshold when Weibull data is fed into the EOA method. The non-linearity in threshold was also shown for the Weibull distribution in Section 4.2. For a shape parameter of $\nu = 1.1$ the corresponding threshold is ≈ 7.3 dB greater than the threshold for complex Gaussian data. The EOA algorithm is capable of an

average detection loss of ≈ 1 dB when $\nu = 2$ (*i.e.* when complex Gaussian data is present), and a threshold within 1 dB when at the extreme case of $\nu = 1.1$.

It was hypothesized that when the data is misclassified, the incorrect distribution could have a similar tail (and therefore threshold) to the correct distribution. This robustness is illustrated in Figures 6.5a and 6.5b. In addition, it is clear for both K and Weibull distributed data that the increased diversity offered by using all statistics at once does not necessarily improve the threshold estimation. The performance of the threshold estimation algorithm depends heavily on the pairs of weightings used, with the (sine^2, tanh) pair of weightings uniformly producing the worst results for the five sets of weightings considered. For both the Weibull and K distributions the (cosine, cosine^2) pair of weightings provides the best results, with an average threshold error of $\approx \pm 1$ dB despite a change in true threshold of 7.3 and 10 dB, respectively.

In addition to the findings above, we include here results that were omitted from [2] due to length limitations. Comparing Figures 6.4a-6.4b and 6.5a-6.5b, misclassifying high shape parameter K and Weibull data as lognormal produces a large bias to the average threshold. In addition, it has been established that the lognormal distribution is not admissable as a SIRV [1]. Therefore, as the K and Weibull distributions are the most commonly reported SIRV clutter distributions, we removed the lognormal distribution from the library and generated the average threshold error. The results of the EOA with only K and Weibull data in the library is shown in Figures 6.6a and 6.6b.

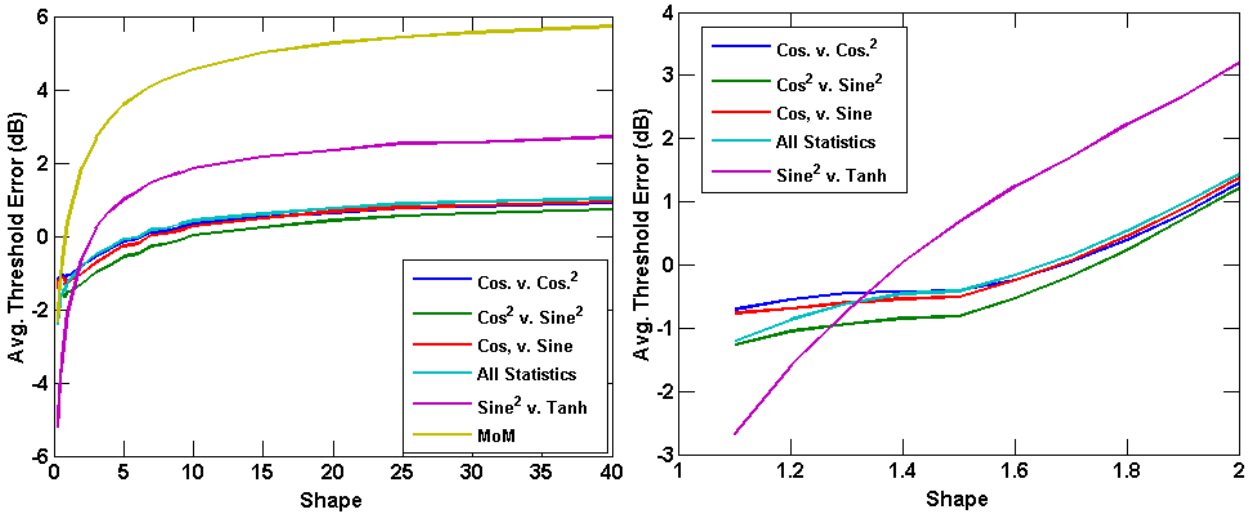

(a) Threshold estimation of K data for cosine, sine weightings

(b) Threshold estimation of K data for cosine, cosine^2 weightings

Figure 6.6: Using the EOA to classify K data as a function of shape with lognormal distribution omitted from library

Note that the (sine^2, tanh) pair of weightings appeared the be selecting the lognormal the distribution the most for both Weibull and K data. From Figure 6.6a, we see that the estimation of high shape parameter clutter is greatly improved when the bias induced by data misclassified as lognormal is eliminated. In addition, the low shape parameter data is improved for all weighting combinations other than the (sine^2, tanh) pair for K distributed data.

6.3 Evaluating Pairs of Weightings in COSMiC

Here we attempt a comprehensive examination COSMiC when pairs of weightings are used to establish endpoints. An expanded library of distributions is used to exhaustively search for the most effective pairs of weightings to use in conjunction with the four considered transformation methods. The efficacy of the weighting pairs/transformation method combinations is established via their accuracy in identifying distributions and estimating thresholds.

The discussion in Section 6.2 used a limited library for the initial exploration of the extend Ozturk algorithm (EOA). To provide a more thorough analysis, for the remainder of

this chapter we consider an expanded library. In addition to the K, Weibull, and lognormal distributions, we also include the Pareto distribution of Sections 3.7 and 4.3, as well as the gamma modulated (GM) distribution of Section 4.5. While the compound gamma modulated (CGM) was examined in Chapter 5, it is omitted here. The CGM distribution was suggested to improve the sampling of the distribution class of SIRVs. However, from the examination conducted in Chapter 5, the combination of the sampling of the CGM in endpoint space and the dual parameter formulation of the CGM are not compatible with the shape parameter estimation (and therefore threshold estimation) algorithm established in Section 6.1. As with the library used in Section 6.2, only distribution/shape parameter combinations with a difference in threshold $\Delta_{\text{thresh}} < 10$ dB compared to the complex Gaussian threshold (for a similar clutter power and probability of false alarm) are considered.

While the complex Gaussian distribution is implicitly considered in Section 6.2 as a special case of the Weibull distribution, throughout the rest of this Chapter we consider it explicitly. It should be emphasized that the complex Gaussian distribution is the default distribution of choice, and measurements have established the Gaussian as the proper fit for the majority of radar clutter. We must pay special attention to the implications of incorrectly choosing a heavier tailed distribution in place of the Gaussian, and the corresponding loss in detection power caused by such a choice.

In order to provide a comprehensive search, both Sections 6.3.1 and 6.3.2 used 10^4 Monte Carlo trials for all possible weighting combinations. It should be noted that the ordering of the weighting pairs considered did not matter, yielding symmetrical results. Therefore, only half of the total combinatoric possibilities (45 of the 90 possible) were considered. After the exhaustive search was conducted, the top ten performing pairs for each metric were selected, and an additional 10^5 Monte Carlo trials were conducted to verify the results.

6.3.1 Distribution Identification

First we examine the distribution identification capabilities of the transformation methods for each distribution. Tables 6.1-6.3 show the top pair of weightings for each transformation method (*i.e.* the pair of weightings that most often chooses the true distribution of the data). When the true distribution possesses a shape parameter, the accuracy is averaged over all shape parameters. For reference, the top ten weighting pairs for each input distribution/transformation method combination are available in Appendix A.1. For this section, the clairvoyant covariance matrix (CCM) is used to provide a bound on the theoretical performance of the distribution identification capabilities of each transformation method. For this examination, we ignore the estimated shape parameter corresponding to distribution choice.

Table 6.1 shows the accuracy of the top weighting pairs for the WSOS, or when there is no transformation performed on the order statistics of the GIP. When Gaussian data is fed into the WSOS library, the majority of the time Gaussian or Weibull is selected as the generating distribution. This result is not surprising based on the convergence of the Weibull distribution with the Gaussian. However, when K distributed data is present, the WSOS overwhelmingly chooses the Weibull distribution from the library. In fact the WSOS method is more likely to choose Weibull as the distribution when K data is present than when Weibull data is present. In addition, when Pareto data is present the Weibull distribution is chosen 7.5% more than the Pareto distribution. Therefore, it appears that the WSOS is strongly biased to the Weibull distribution.

	Weightings		Percentage Chosen					
True Dist.	1	2	Gaussian	K	Weibull	Pareto	Lognormal	Gamma Mod.
Gaussian	cosh	$\cosh^2$	48.1	5.2	44.2	2.5	0.0	0.0
K	cos	$\cos^2$	0.1	3.2	93.8	0.6	2.0	0.2
Weibull	sine	$\sin^2$	4.5	11.5	65.4	12.9	2.6	3.1
Pareto	$\cos^2$	sine	17.2	9.1	39.2	31.7	1.7	1.2
lognormal	$\cos^2$	sine	5.9	14.0	23.9	40.9	10.2	5.1

Table 6.1: Distribution identification percentages of top WSOS COSMiC weighting pairs

Next, Table 6.2 shows the distribution identification accuracy of the top pairs of weightings when the Studentization transformation method is used. In general, the Studentization method appears more accurate than the WSOS method, and does not possess the same bias towards the Weibull distribution. However, the Studentization method performs worse than the WSOS method with lognormal data, yielding only a 10.2% success rate.

	Weightings		Percentage Chosen					
True Dist.	1	2	Gaussian	K	Weibull	Pareto	Lognormal	Gamma Mod.
Gaussian	$\cosh^2$	sinh	60.8	10.8	5.7	19.0	0.2	3.6
K	$\cosh^2$	sinh	36.2	23.8	8.4	21.2	0.3	10.1
Weibull	sine	sine^2	25.7	13.8	45.7	9.0	2.1	3.7
Pareto	$\cosh^2$	sinh	42.6	18.4	5.9	24.0	0.3	8.8
lognormal	cos	$\cos^2$	6.2	40.7	39.6	4.8	2.8	5.9

Table 6.2: Distribution identification percentages of top Studentized COSMiC weighting pairs

Finally, the EOA method does appear to produce the best results of the three methods under consideration. While the probability of correctly identifying Gaussian, Weibull, and Pareto distributed data is slightly lower than the WSOS method, the improved accuracy for K and lognormal data more than makes up for those slight decreases in accuracy.

	Weightings		Percentage Chosen					
True Dist.	1	2	Gaussian	K	Weibull	Pareto	Lognormal	Gamma Mod.
Gaussian	cos	$\cos^2$	46.6	2.2	37.6	11.8	0.8	1.1
K	tanh	$\tanh^2$	17.8	20.4	37.9	15.4	3.2	5.4
Weibull	sinh	$\sinh^2$	12.3	13.3	54.5	13.4	2.8	3.7
Pareto	sine	sine^2	17.2	5.9	38.0	26.8	8.1	4.0
lognormal	$\cos^2$	sine	5.1	22.0	29.4	11.7	23.9	7.8

Table 6.3: Distribution identification percentages of top EOA COSMiC weighting pairs

Notice that the average accuracy examined in Tables 6.1-6.3 does not take into account the shape parameter of the distribution under test. In other words, one would expect high shape parameter K, Weibull, and Pareto data to be often mistaken for Gaussian data (or one another). Therefore, Figures 6.7a-6.9c examine the accuracy of the top two weighting

functions for each distribution/transformation method pair, with the second most accurate weighting pair shown as a dotted line. The overall accuracy percentages for the second best pair of weighting functions (as are shown in Tables 6.1-6.3 for the top pair of weighting functions) are available in Appendix A.1.

Figures 6.7a-6.7c show the distribution identification accuracy for the top two pairs of weighting functions when K distributed data is fed into libraries derived from the WSOS, Studentization, and EOA transformations. First, notice that for the WSOS transformation the distribution identification accuracy was better for very low values of the shape parameter, but the Weibull distribution was primarily chosen for all shape parameter values. Also, the top two weighting pairs yield virtually identical results for both the WSOS and Studentization methods. As was the case with the weighting pairs examined in Section 6.2, the Studentized and EOA methods provide accurate classification only at the low shape parameter values. At medium to high shape values, the Gaussian, Weibull, and Pareto distributions all are incorrectly chosen at much higher rates than the K distribution. Only the EOA method has a significant difference in performance between the top two weightings. However, the difference in performance only relates to the rates of incorrect classifications, not the rate of correct classification.

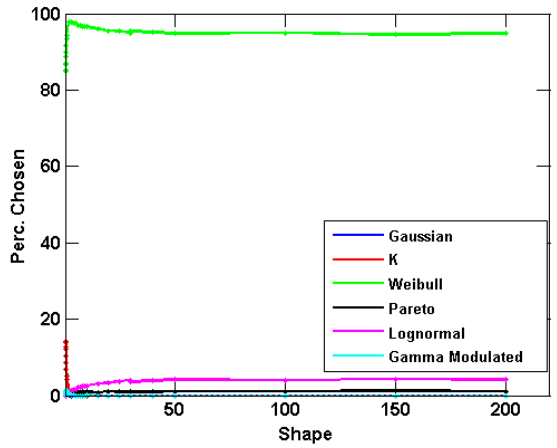

(a) WSOS, (cosine, cosine^2) (solid) vs. (cosine, sine) (dotted)

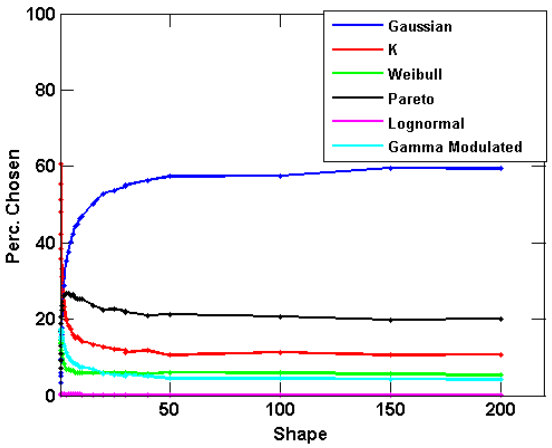

(b) Studentized, (cosh^2, sinh) (solid) vs. (cosh^2, sinh^2) (dotted)

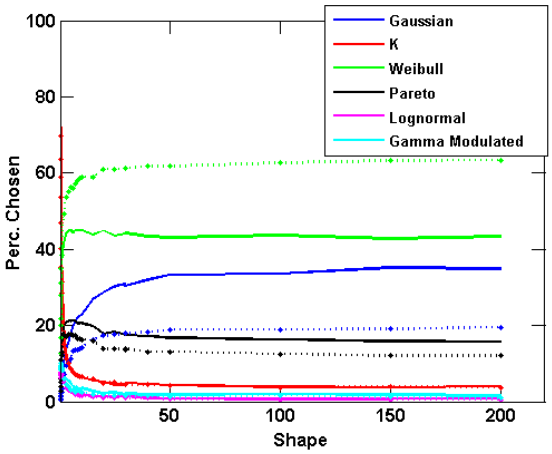

(c) EOA, (tanh, tanh^2) (solid) vs. (sinh, sinh^2) (dotted)

Figure 6.7: COSMiC distribution identification v. shape parameter for K distributed data for top pairs

Figure 6.8a-6.8c then show the distribution identification accuracy for the top two weighting pairs of the three transformation methods under consideration when Weibull distributed data is present. As was noted in Table 6.1, the WSOS method tends to identify most data as Weibull data. However, it should be noted that as the shape parameter increases, all three methods increasingly select the Gaussian distribution. The K distribution is the most commonly incorrectly chosen distribution for low shape parameter data.

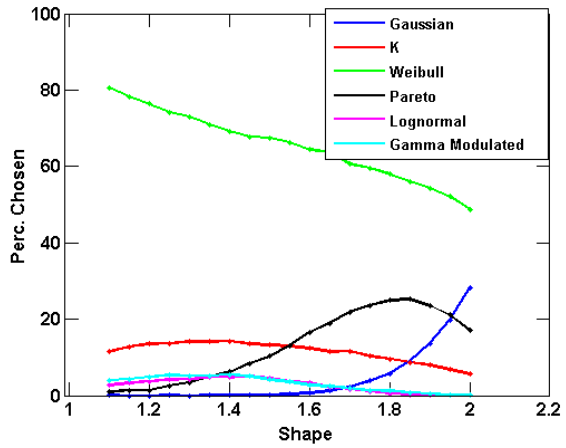

(a) WSOS, (sine, sine^2) (solid) vs. (sine, cosh) (dotted)

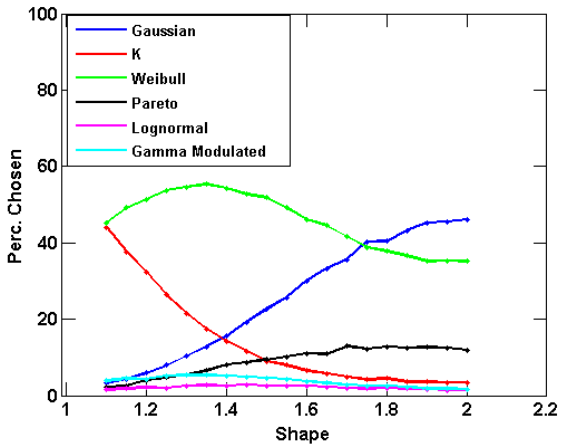

(b) Studentized, (sine, sine^2) (solid) vs. (sine, cosh) (dotted)

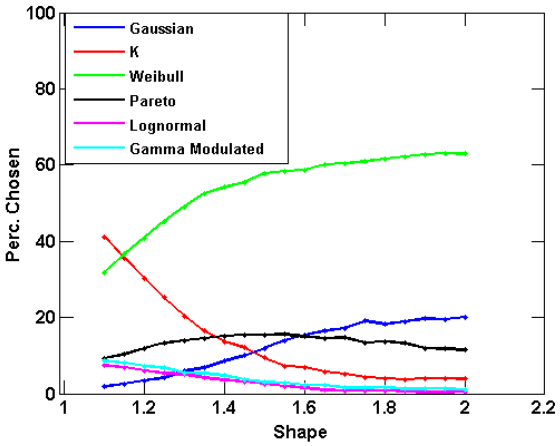

(c) EOA, (sinh, sinh^2) (solid) vs. (sinh, tanh) (dotted)

Figure 6.8: COSMiC distribution identification v. shape parameter for Weibull distributed data for top pairs

Finally, Figures 6.9a-6.9c show the inaccuracy of all three methods when Pareto data is present. The best method for correctly identifying Pareto data is the WSOS, but all methods only correctly identify the distribution approximately 20% of the time for large shape parameters.

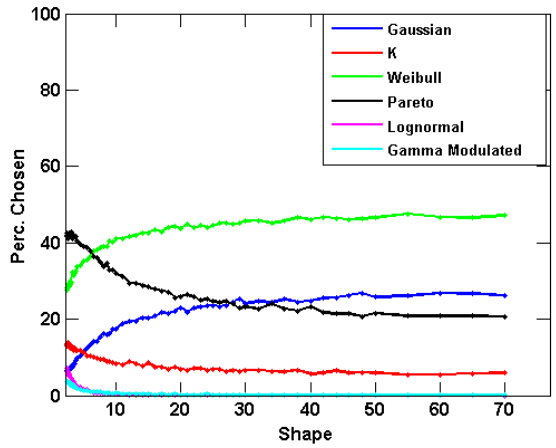

(a) WSOS, ($\cos^2$, sine) (solid) vs. ($\cos^2$, sine^2) (dotted)

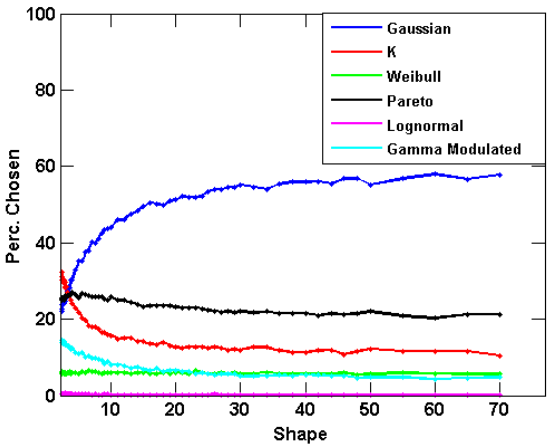

(b) Studentized, ($\cosh^2$, sinh) (solid) vs. ($\cosh^2$, $\sinh^2$) (dotted)

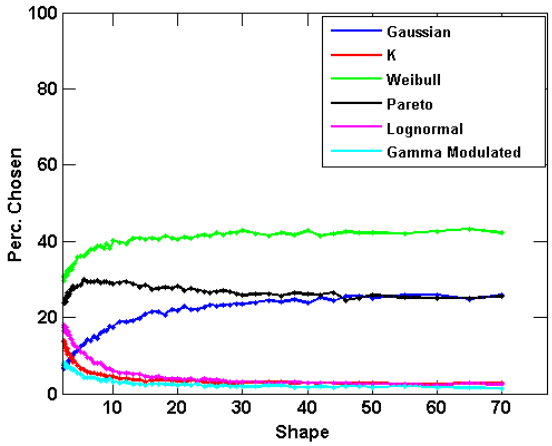

(c) EOA, (sine, sine^2) (solid) vs. (sine, cosh) (dotted)

Figure 6.9: COSMiC distribution identification v. shape parameter for Pareto distributed data for top pairs

In conclusion, when using pairs of weightings none of the four methods appears to be particularly accurate at correctly identifying the distributions under consideration. It should be particularly noted that for large shape parameter values, the distributions appear to become very difficult to separate. Intuitively, this difficulty makes sense based on the relation between the SIRV distributions and the Gaussian distribution.

It should be noted that the divide by mean (DBM) method was not discussed here. First, the DBM method is proposed to help with scaling inconsistencies in sampled data. As here we only considered the sample covariance matrix, some of those sampling problems

are alleviated. Second, the universal poor performance implies that the COSMiC algorithm is not appropriate for distribution identification with the selected parameters, at least when two weighting pairs are used. Therefore, due to the close relationship between the DBM and WSOS methods and in the interest of brevity we do not expand the distribution identification analysis to the DBM method.

6.3.2 Threshold Estimation - Identifying Top Weightings

Section 6.2 established the efficacy of the EOA method to closely approximate the true threshold of measured data for a variety of shape parameters of the K and Weibull distributions. Here we identify the top pairs of weightings for each distribution/transformation method combination. The impact of each of these choices in weighting pairs is then examined in detail in Section 6.3.3. The DBM method is examined in Section 6.3.3 with the weightings established for the WSOS method.

Each row of Tables 6.4-6.6 corresponds to the pair of weighting functions that provide the lowest average threshold error for each of the five distributions considered. Note that in the case of the K, Weibull, and Pareto distributions this average is taken first over the Monte Carlo trials and second over the shape parameter. Each distribution then has a pair of columns associated with it. The first column gives the overall rank (out of the 45 possible combinations) as a function of the average threshold error. The second column for each distribution reports the average decibel difference in threshold between the estimated threshold and the true threshold for the distribution with a desired $P_{fa} = 10^{-5}$.

Table 6.4 gives the threshold estimation error for the top five pairs of weights for the WSOS method. The WSOS method yields an average of ≈ 1 dB threshold error for Gaussian, Weibull, and Pareto distributed data. Unfortunately, the K and Lognormal distributions have a large amount of error regardless of the weighting pair chosen. However, the types of error for the K and Lognormal distributions are different. In this case, the threshold for the K distribution is overestimated, resulting in a detection loss. In contrast, the threshold

for the Lognormal distributed data is underestimated, leading to an increased false alarm rate. Note that the (sine, $\tanh^2$) pairing is universally the second worst weighting to use for the other four distributions. As the Lognormal is not a SIRV, this fact leads us to ignore the (sine, $\tanh^2$) pairing in the subsequent analysis, as it does not appear to be suitable for general use. Note that the (cos, $\tanh^2$) pairing yields an average threshold error ≈ 0.66 dB lower than the (sine, $\tanh^2$) error for Lognormal distributed data, implying that it is a suitable replacement weighting pair.

Weightings		Gaussian		K		Weibull		Pareto		Lognormal	
1	2	Rank	Error	Rank	Error	Rank	Error	Rank	Error	Rank	Error
cos	$\tanh^2$	1	0.83 dB	2	4.2 dB	14	1.16 dB	37	2.74 dB	30	-2.16 dB
cos	sine^2	11	1.07 dB	1	3.9 dB	32	1.62 dB	6	-0.44 dB	9	-3.33 dB
$\sinh^2$	$\tanh^2$	7	0.92 dB	8	5.3 dB	1	0.91 dB	20	-0.9 dB	19	-4.77 dB
$\cos^2$	$\cosh^2$	33	1.76 dB	20	6.28 dB	5	1.03 dB	1	-0.30 dB	23	-5.02 dB
sine	$\tanh^2$	44	4.43 dB	44	6.67 dB	44	3.16 dB	44	3.19 dB	1	-1.50 dB

Table 6.4: Summary of top WSOS COSMiC weighting pairs

Table 6.5 shows the average threshold error for the top weighting pairs when the Studentized transformation method is used. Note that the top two weighting pairs for the Gaussian, K, Weibull, and Pareto distributions are equivalent (albeit with a flipped order for the K distribution). In general, the Studentized weighting pairs give a more accurate threshold for the K distribution and less accurate (greater) threshold for the Gaussian distribution. Also, the threshold accuracy for the Pareto distribution depends little on the weighting pair choice, with a deviation between the first and fortieth weighting of 0.6 dB. Similarly, the difference in average threshold error for when Lognormal distributed data is present is 0.74 dB less for the forty first weighting pair versus the best weighting pair.

Weightings		Gaussian		K		Weibull		Pareto		Lognormal	
1	2	Rank	Error	Rank	Error	Rank	Error	Rank	Error	Rank	Error
sinh	tanh	1	2.92 dB	2	1.75 dB	2	1.09 dB	1	1.32 dB	35	-2.56 dB
cosh	sinh	2	3.02 dB	1	1.75 dB	1	1.07 dB	2	1.34 dB	41	-2.62 dB
sinh	tanh	1	2.92 dB	2	1.75 dB	2	1.09 dB	1	1.32 dB	35	-2.56 dB
sinh	tanh	1	2.92 dB	2	1.75 dB	2	1.09 dB	1	1.32 dB	35	-2.56 dB
$\cos^2$	sine^2	37	3.47 dB	40	2.53 dB	40	2.00 dB	40	1.92 dB	1	-1.88 dB

Table 6.5: Summary of top Studentized COSMiC weighting pairs

Finally, Table 6.6 gives the average threshold error for the top weighting pairs when the EOA transformation method is used. Similarly to the Studentized method, two weighting pairs are the top two performers for the four SIRV distributions, with the order being switched for the Gaussian distribution. However, the average error is much higher than when the Studentized transformation method is used.

Weightings		Gaussian		K		Weibull		Pareto		Lognormal	
1	2	Rank	Error	Rank	Error	Rank	Error	Rank	Error	Rank	Error
cos	$\cos^2$	1	3.19 dB	2	2.26 dB	2	1.64 dB	2	1.74 dB	26	-2.00 dB
$\cos^2$	$\tanh^2$	2	3.27 dB	1	2.11 dB	1	1.47 dB	1	1.69 dB	40	-2.35 dB
$\cos^2$	$\tanh^2$	2	3.27 dB	1	2.11 dB	1	1.47 dB	1	1.69 dB	40	-2.35 dB
$\cos^2$	$\tanh^2$	2	3.27 dB	1	2.11 dB	1	1.47 dB	1	1.69 dB	40	-2.35 dB
sine^2	$\sinh^2$	39	7.92 dB	39	5.70 dB	39	5.28 dB	39	5.55 dB	1	-0.70 dB

Table 6.6: Summary of top Extended Ozturk COSMiC weighting pairs

6.3.3 Threshold Estimation - Evaluating Robustness of COSMiC Methods

In Section 6.3.2 the top pairs of weightings were found for the various distribution/transformation method combinations using an exhaustive search of all combinations of weightings with 10^4 Monte Carlo trials per candidate pair. Here we evaluate the top weightings using 10^5 Monte Carlo runs under different conditions. First, we consider the impact of an unknown distribution on the COSMiC algorithm. To simulate this condition, we sequentially

excise a single distribution from the library and examine the resulting estimated threshold error. Second, we consider the impact of the sample covariance matrix (SCM). The SCM is a poor approximation to the clairvoyant covariance matrix (CCM) for SIRVs, due to the scaling errors caused by the separate instantiations of the modulating random variable in each training data vector.

Each subsection examines one of the five clutter distributions observed in literature: Gaussian, K, Weibull, Pareto, and Lognormal. Note that the library consists of a sixth distribution, the gamma modulated (GM), but this distribution is included only to provide diversity to the library. Each distribution has a table corresponding to three transformation methods: WSOS, Studentization, and the EOA. The results of the DBM method are included in the WSOS tables, albeit only with the SCM incorporated into the generalized inner products (GIPs). All threshold error differences are given in decibel scale. The final two columns provide the dB difference between the threshold error when the clairvoyant covariance matrix (CCM) and SCM are used.

6.3.3.1 Gaussian Data

Table 6.7 shows the threshold error when Gaussian data is fed into the WSOS transformation method using the CCM and SCM, and the DBM transformation method with the SCM. For this case, it is clear that the WSOS method is superior to the DBM method. It is noted in Section 6.1 that informal observations of the SCM generated with non-Gaussian SIRV data tended to result in an overestimate the power. Due to the matrix inverse in the GIP, this overestimate causes an over-nulling of the clutter. However, for the case of the Gaussian distribution this behavior is not due to the scaling problems inherent in SIRVs. As the number of vectors used to estimate the SCM increases, the SCM converges to the true CCM. That being said, the slightly increased over-nulling is apparent in Table 6.7 through examination of the difference between the CCM and SCM errors.

For all COSMiC transformation/weighting pairs the Gaussian threshold is always over-

estimated, as no other distribution in the library possesses a lighter tail. However, by over-nulling the clutter, the estimated distribution (when not correctly determined to be Gaussian) is estimated to have a lighter tail than when the ideal CCM is used. Therefore, the error induced by the SCM counteracts the error inherent in estimating the edge case that is the Gaussian distribution.

Weightings		Clairvoyant Cov. Matrix		Sample Cov. Matrix		SCM - DBM Weightings		Δ Clair, SCM	
1	2	Full Lib.	Excised Lib.	Full Lib.	Excised Lib.	Full Lib.	Excised Lib.	Δ WSOS	Δ DBM
cos	$\tanh^2$	0.81	0.81	0.4	0.4	9.82	9.82	-0.41	9.01
cos	sine^2	1.04	1.04	0.35	0.35	0.92	0.92	-0.69	-0.12
$\sinh^2$	$\tanh^2$	0.93	0.93	0.27	0.26	2.92	2.92	-0.66	1.99
$\cos^2$	$\cosh^2$	1.78	1.78	0.32	0.32	9.13	9.13	-1.45	7.36

Table 6.7: Average Threshold Error (dB) when Gaussian distributed data is fed into the WSOS and DBM weightings

Tables 6.8 and 6.9 show the threshold error when the Studentized and EOA methods are used, respectively. Both methods produce more error for the Gaussian distribution than the WSOS method.

Weightings		Clairvoyant Cov. Matrix		Sample Cov. Matrix		
1	2	Full Lib.	Excised Lib.	Full Lib.	Excised Lib.	Δ Clair, SCM
sinh	tanh	2.84	2.84	1.39	1.39	-1.45
cosh	sinh	2.93	2.93	1.61	1.61	-1.33
$\cos^2$	sine^2	3.41	3.63	2.07	2.46	-1.34

Table 6.8: Average Threshold Error (dB) when Gaussian distributed data is fed into the Studentized weightings

Weightings		Clairvoyant Cov. Matrix		Sample Cov. Matrix		
1	2	Full Lib.	Excised Lib.	Full Lib.	Excised Lib.	Δ Clair, SCM
cos	$\cos^2$	3.10	3.11	1.62	1.65	-1.47
$\cos^2$	$\tanh^2$	3.17	3.17	1.61	1.61	-1.56
sine^2	$\sinh^2$	7.95	7.95	7.26	7.26	-0.69

Table 6.9: Average Threshold Error (dB) when Gaussian distributed data is fed into the EOA weightings

6.3.3.2 K Data

Table 6.10 shows the average threshold error when K data is fed into the WSOS and DBM libraries. Note that the impact of the SCM matrix estimation error is much greater (over 4 dB) than what was shown for Gaussian data in Section 6.3.3.1. This result illustrates the complications implicit in covariance matrix estimation for SIRV distributed data. Note that for the WSOS method on average there is a 4-6.3 dB detection loss if the covariance matrix is known, but an increase of false alarm resulting in a threshold 0.8-1.4 dB too low if the covariance matrix must be estimated. However, this trend does not hold for the DBM method.

Weightings		Clairvoyant Cov. Matrix		Sample Cov. Matrix		SCM - DBM Weightings		Δ Clair, SCM	
1	2	Full Lib.	Excised Lib.	Full Lib.	Excised Lib.	Full Lib.	Excised Lib.	Δ WSOS	Δ DBM
cos	$\tanh^2$	4.19	4.19	-0.79	-0.25	6.80	6.74	-4.99	2.61
cos	sine^2	3.92	3.92	-0.93	-0.61	-1.89	-1.89	-4.85	-5.81
$\sinh^2$	$\tanh^2$	5.27	5.27	-1.40	-1.27	0.21	0.21	-6.67	-5.06
$\cos^2$	$\cosh^2$	6.28	6.28	-1.41	-1.31	6.37	6.37	-7.68	0.09

Table 6.10: Average Threshold Error (dB) when K distributed data is fed into the WSOS and DBM weightings

As Table 6.10 only illustrates the average performance over all considered shape parameters, Figures 6.10a-6.10d show the threshold error for various scenarios for the WSOS method as a function of shape parameter. Figure 6.10a shows the effect of excising the K distribution from the library when the covariance matrix is known. For the K distribution, there is no discernible effect. Likely this effect stems from the bias that the WSOS method has towards selecting the Weibull distribution (as established in Section 6.3.1). Figure 6.10b shows the impact of using the SCM versus the CCM when the K distribution is in the library, while Figure 6.10c shows the same when the K distribution is excised from the library. Finally, Figure 6.10d shows the average threshold error when the full library with the CCM is used versus when the excised library with the SCM is used. This last scenario is the most interesting, as it represents an ideal case where the distribution is known versus a "worst

case" scenario where the true distribution is unknown and the covariance matrix must be estimated. In this case the (cosine, $\tanh^2$) and (cosine, $\sin^2$) pairs both provide very stable, accurate results in the worst case scenario over all shape parameters.

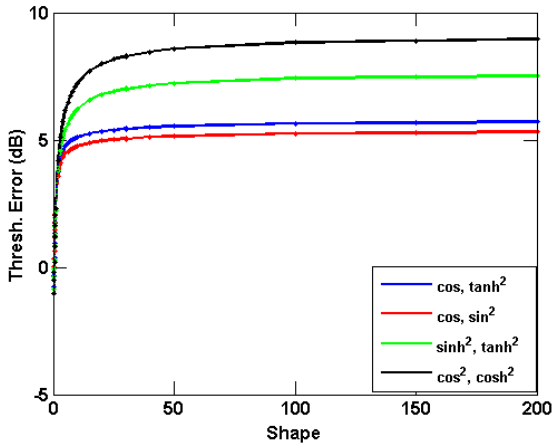

(a) Full Lib. w/CCM (solid) vs. Excised Lib. w/CCM (dotted)

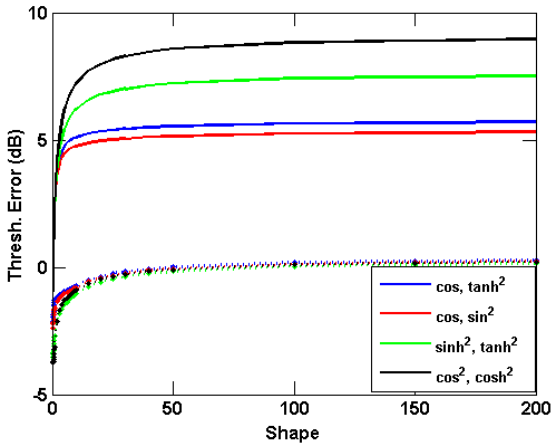

(b) Full Lib. w/ CCM (solid) vs. Full Lib. w/ SCM (dotted)

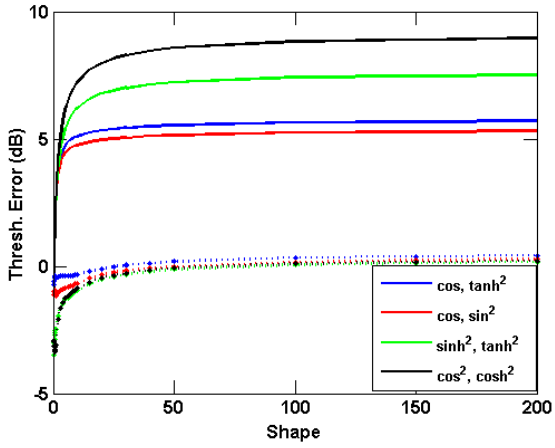

(c) Excised Lib. w/CCM (solid) vs. Excised Lib. w/ SCM (dotted)

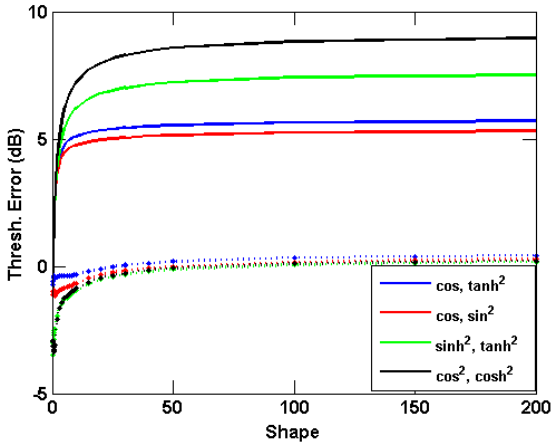

(d) Full Lib. w/CCM (solid) vs. Excised Lib. w/SCM (dotted)

Figure 6.10: Threshold estimation error (dB) using WSOS with K distributed data

Next, Figures 6.11a-6.11d show the same results as Figures 6.10a-6.10d, except the DBM method is used instead of the WSOS method. Once more, excising the K distribution from the library has little to no effect. However, the (cos, $\tanh^2$) weighting pair gives a higher threshold when the SCM is used, while the threshold for the ($\cos^2$, $\cosh^2$) weighting pair varies little whether the CCM or SCM is used. This behavior appears to be unique to the

DBM method. In all cases, the DBM method performs worse than the WSOS method at low shape parameters. For high shape parameters, the (cosine, sine^2) weighting pair performs very well if the SCM is used.

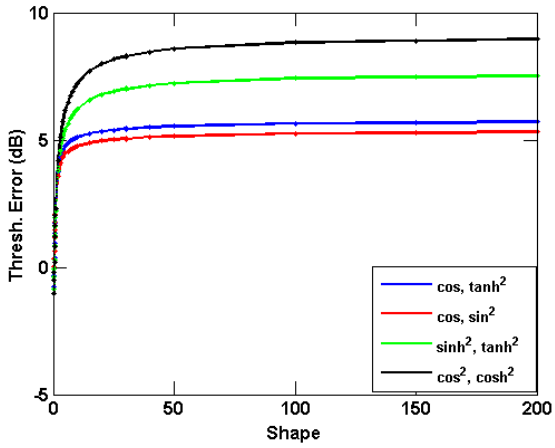

(a) Full Lib. w/CCM (solid) vs. Excised Lib. w/CCM (dotted)

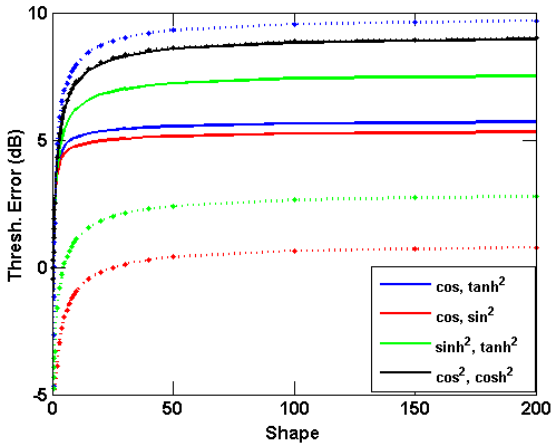

(b) Full Lib. w/ CCM (solid) vs. Full Lib. w/ SCM (dotted)

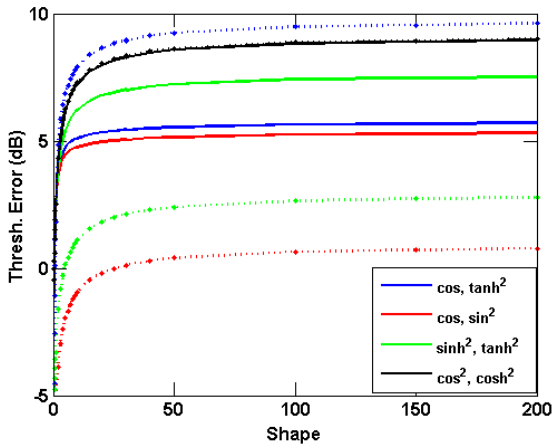

(c) Excised Lib. w/CCM (solid) vs. Excised Lib. w/ SCM (dotted)

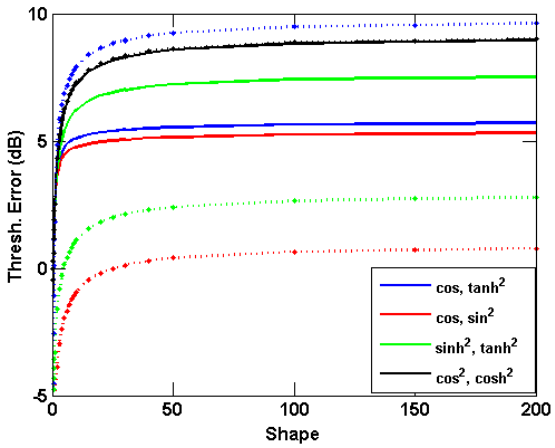

(d) Full Lib. w/CCM (solid) vs. Excised Lib. w/SCM (dotted)

Figure 6.11: Threshold estimation error (dB) using DBM with K distributed data

Next we examine the threshold error when the Studentization method is used. Note that the difference for using the SCM versus the CCM is still greater than any noticed for Gaussian data in Section 6.3.3.1, but less than the differences noted when K data is fed into the WSOS or DBM method. The overall error is low, but varies by less than a tenth of a dB whether or not the K distribution is included in the library. Note that the (cosine^2,

sine^2) weighting pair gives the best results when the covariance matrix is unknown, but the worst threshold estimation error when the covariance matrix is known. Also, the difference between the thresholds found using the CCM versus the SCM is on average ≈ 0.6 dB closer for the (cosine^2, sine^2) pair than the other two weighting pairs.

Weightings		Clairvoyant Cov. Matrix		Sample Cov. Matrix		
1	2	Full Lib.	Excised Lib.	Full Lib.	Excised Lib.	Δ Clair, SCM
sinh	tanh	1.75	1.84	-1.03	-1.01	-2.78
cosh	sinh	1.74	1.82	-0.97	-0.96	-2.71
cos^2	sine^2	2.51	2.56	0.37	0.39	-2.15

Table 6.11: Average Threshold Error (dB) when K distributed data is fed into the Studentized weightings

Figures 6.12a-6.12d examine the impact of using the SCM and excised libraries as compared to the CCM and full libraries when the Studentization method is employed. As was seen in Table 6.11, there is little difference between using the full or the excised library. However, when the (cosine^2, sine^2) pair of weightings are used in conjunction with the SCM, the resulting average threshold is ≈ 0.5 dB greater than the other two weightings at high shape parameters, but up to 3.1 dB closer to the true threshold for the lowest of shape parameters. The former difference translates directly to detection loss, while the latter difference occurs where the true threshold is 10 dB greater than the threshold needed in Gaussian clutter of equal power. Therefore the (cosine^2, sine^2) weighting pair allows for improved performance in heavy tailed K distributed clutter at the cost of negligible degradation in detection loss at lighter tailed clutter, compared to the other weighting pairs. For this reason, the (cosine^2, sine^2) weighting pair is the best pair to use with the Studentization method when K distributed data is encountered.

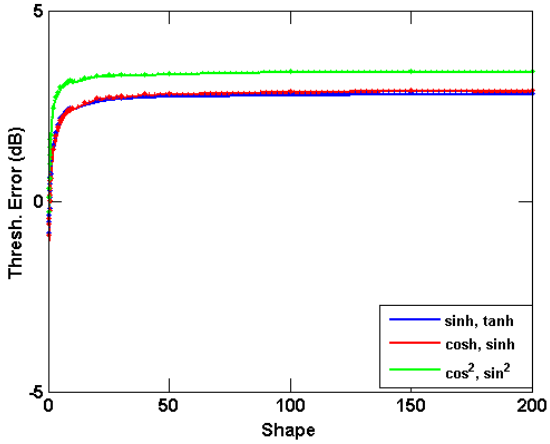

(a) Full Lib. w/CCM (solid) vs. Excised Lib. w/CCM (dotted)

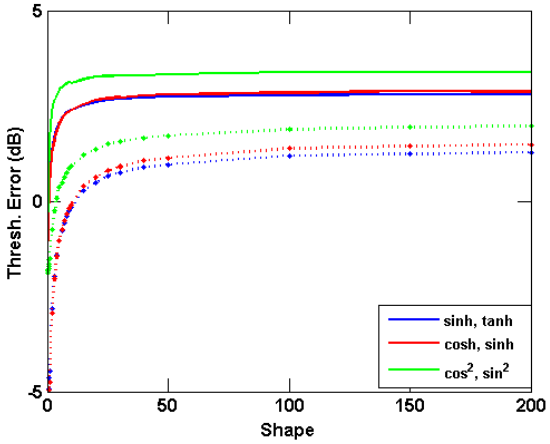

(b) Full Lib. w/ CCM (solid) vs. Full Lib. w/ SCM (dotted)

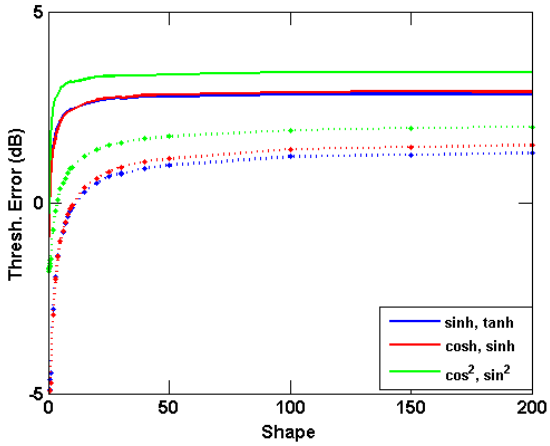

(c) Excised Lib. w/CCM (solid) vs. Excised Lib. w/ SCM (dotted)

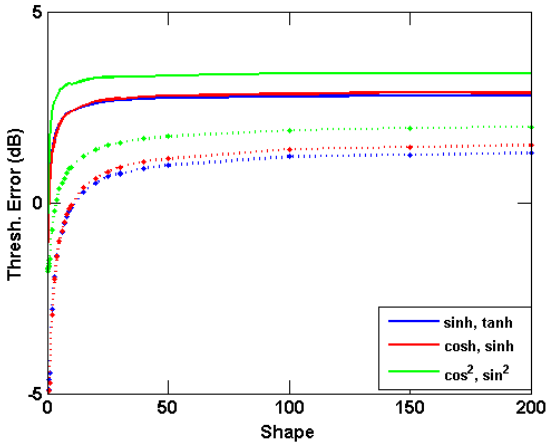

(d) Full Lib. w/CCM (solid) vs. Excised Lib. w/SCM (dotted)

Figure 6.12: Threshold estimation error (dB) using Studentized method with K distributed data

Finally we examine the EOA method. Note that on average, the EOA method produces worse threshold estimates compared to the Studentization method. Once more, excising the K distribution from the library makes minimal difference in estimated threshold. However, the (sine^2, sinh^2) threshold estimate is only reduced by ≈ 1 dB on average when the SCM is used.

Weightings		Clairvoyant Cov. Matrix		Sample Cov. Matrix		
1	2	Full Lib.	Excised Lib.	Full Lib.	Excised Lib.	Δ Clair, SCM
cos	$\cos^2$	2.25	2.29	-0.37	-0.35	-2.62
$\cos^2$	$\tanh^2$	2.10	2.11	-0.73	-0.72	-2.83
sine^2	$\sinh^2$	5.69	5.69	4.77	4.77	-0.93

Table 6.12: Average Threshold Error (dB) when K distributed data is fed into the EOA weightings

Figures 6.13a-6.13d illustrate the results of Table 6.12 as a function of shape parameter. Note that while the (sine^2, $\sinh^2$) weighting pair provides an accurate threshold estimate at low shape parameter values, it suffers more than a 7 dB loss over the optimal threshold at high shape parameter values. However, the other weighting pairs will cause a sharp increase in false alarm rates at low shape parameters.

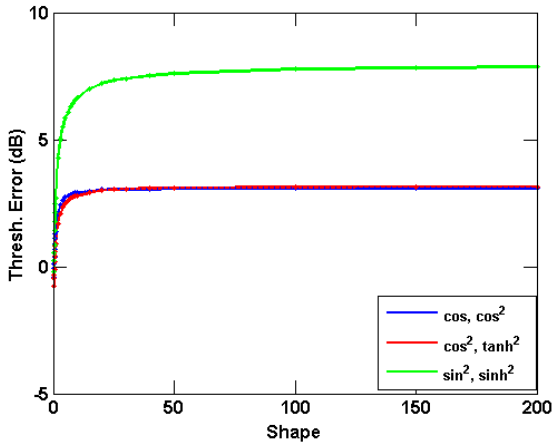

(a) Full Lib. w/CCM (solid) vs. Excised Lib. w/CCM (dotted)

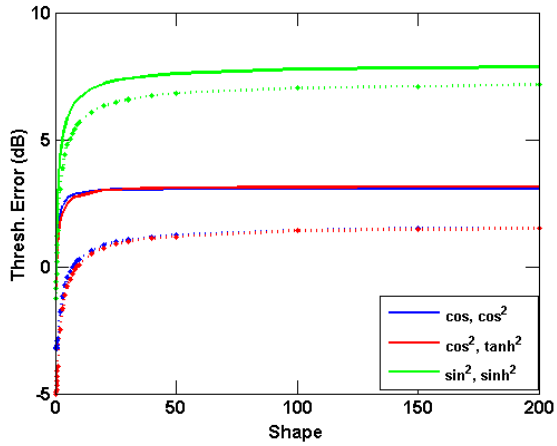

(b) Full Lib. w/ CCM (solid) vs. Full Lib. w/ SCM (dotted)

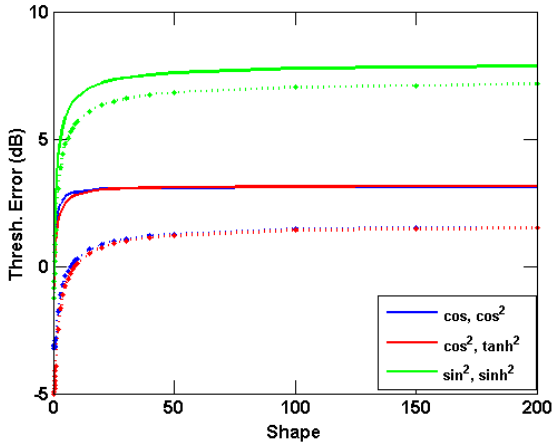

(c) Excised Lib. w/CCM (solid) vs. Excised Lib. w/ SCM (dotted)

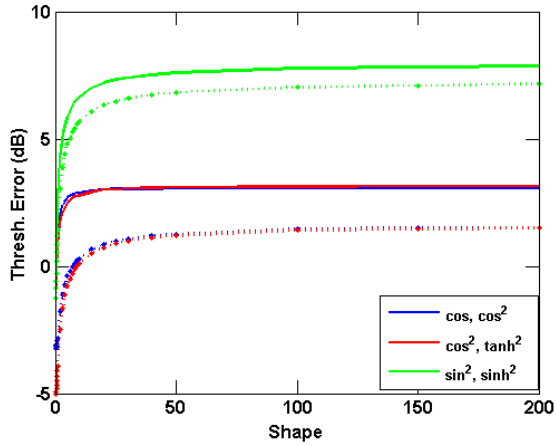

(d) Full Lib. w/CCM (solid) vs. Excised Lib. w/SCM (dotted)

Figure 6.13: Threshold estimation error (dB) using EOA method with K distributed data

Overall the WSOS with (cosine, tanh^2) and (cosine, sine^2) weightings and Studentization method with (cosine^2, sine^2) weightings provide the closest approximation to the true threshold when K data is present and the SCM is used. It is not recommended to use the DBM or EOA method when K data is present.

6.3.3.3 Weibull Data

Here we examine the thresholds estimated by the four COSMiC transformation methods when Weibull distributed data is present. Table 6.13 shows the average threhold estimation

error for the WSOS and DBM methods, averaged over shape parameters $1.1 \leq \nu \leq 2$ (note that the value of $\nu = 2$ is equivalent to the Gaussian distribution). It is established in Section 6.3.1 that the WSOS method tends to select the Weibull distribution. As a consequence, Table 6.13 shows a large discrepancy in values shown for the full library and excised library when the true covariance matrix is used. However, the impact of leaving the Weibull distribution out of the library is heavily dependent on the pair of weightings chosen.

Weightings		Clairvoyant Cov. Matrix		Sample Cov. Matrix		SCM - DBM Weightings		Δ Clair, SCM	
1	2	Full Lib.	Excised Lib.	Full Lib.	Excised Lib.	Full Lib.	Excised Lib.	Δ WSOS	Δ SCM
cos	$\tanh^2$	1.16	3.44	-0.34	-0.34	6.46	6.37	-1.50	5.30
cos	sine^2	1.61	2.10	-0.82	-0.44	-2.19	-3.09	-2.44	-3.80
$\sinh^2$	$\tanh^2$	0.91	2.89	-1.53	-0.71	-0.04	-3.09	-2.45	-0.95
$\cos^2$	$\cosh^2$	1.03	3.77	-1.83	-0.90	5.92	4.36	-2.86	4.89

Table 6.13: Average Threshold Error (dB) when Weibull distributed data is fed into the WSOS and DBM weightings

Figures 6.14a-6.14d show the results of Table 6.13 for the WSOS transformation method as a function of shape parameter. It is important to remember that the ideal threshold as a function of shape parameter is not linear. The threshold at $\nu = 1.1$ is approximately 7.6 dB greater than the threshold of the Gaussian threshold. By examination of Figures 6.14a-6.14d, when the thresholds resulting from the excised library are worse than the full library when the true covariance matrix is known. However, when the WSOS transformation method is used with the SCM, the excised library achieves threshold estimates closer to the true value than the full library over the full range of shape parameters. In addition, the four weighting pairs under consideration produce closer (*i.e.* more robust) results than when the full library is used. If the true covariance matrix could be accurately estimated, the WSOS technique is capable of giving average threshold results of $\approx \pm 1$ dB over the range of shape parameters.

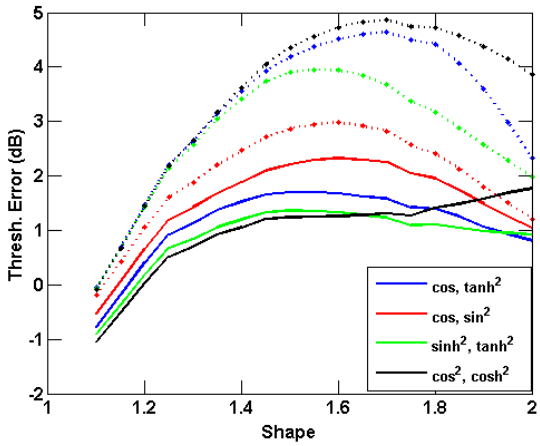

(a) Full Lib. w/CCM (solid) vs. Excised Lib. w/CCM (dotted)

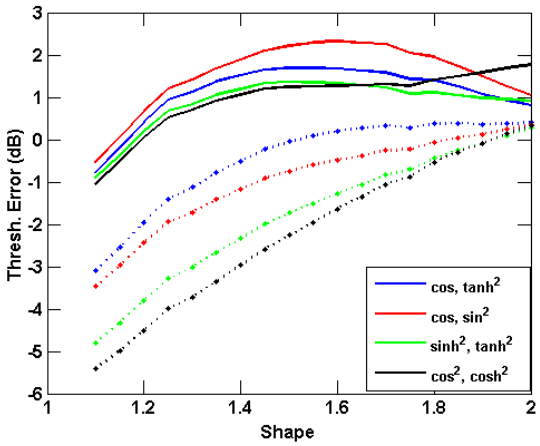

(b) Full Lib. w/ CCM (solid) vs. Full Lib. w/ SCM (dotted)

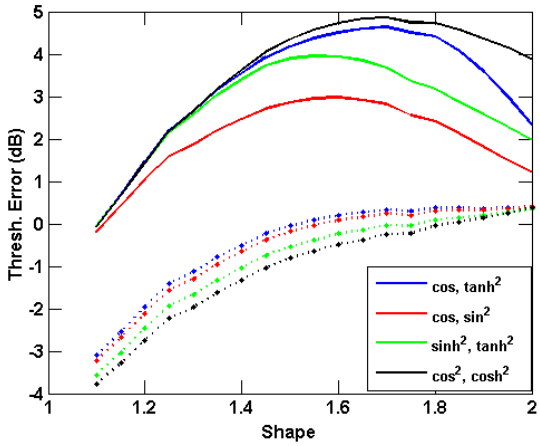

(c) Excised Lib. w/CCM (solid) vs. Excised Lib. w/ SCM (dotted)

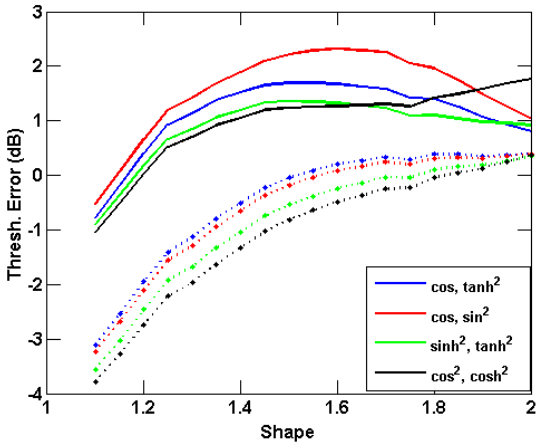

(d) Full Lib. w/CCM (solid) vs. Excised Lib. w/SCM (dotted)

Figure 6.14: Threshold estimation error (dB) using WSOS with Weibull distributed data

Next Figure 6.15a-6.15d shows the corresponding results when the DBM method is used. It is clear that the WSOS method is superior to the DBM method. Both the use of the SCM and the excised library prompt large swings in the estimated threshold from the optimum levels.

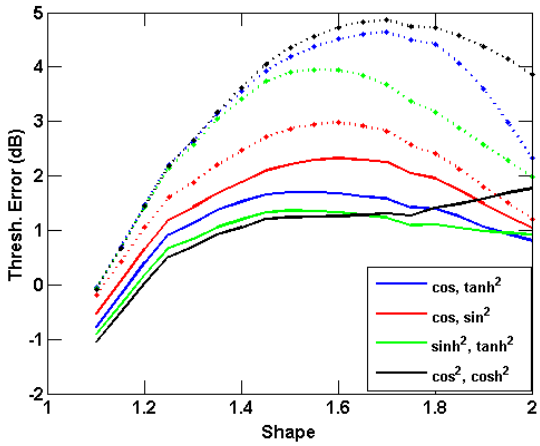

(a) Full Lib. w/CCM (solid) vs. Excised Lib. w/CCM (dotted)

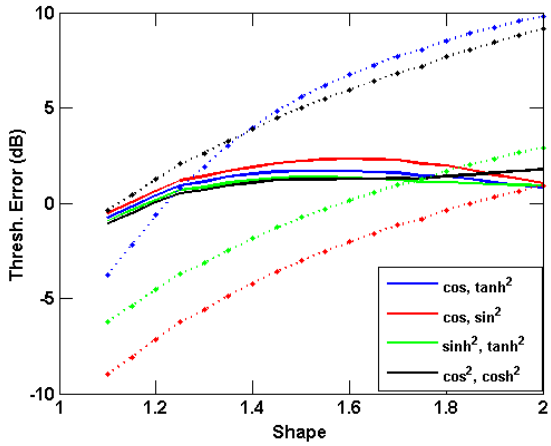

(b) Full Lib. w/ CCM (solid) vs. Full Lib. w/ SCM (dotted)

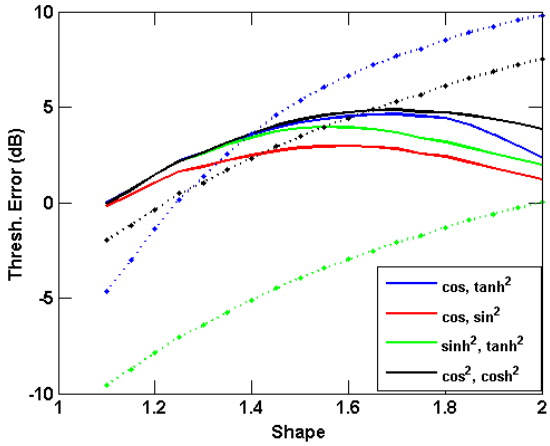

(c) Excised Lib. w/CCM (solid) vs. Excised Lib. w/ SCM (dotted)

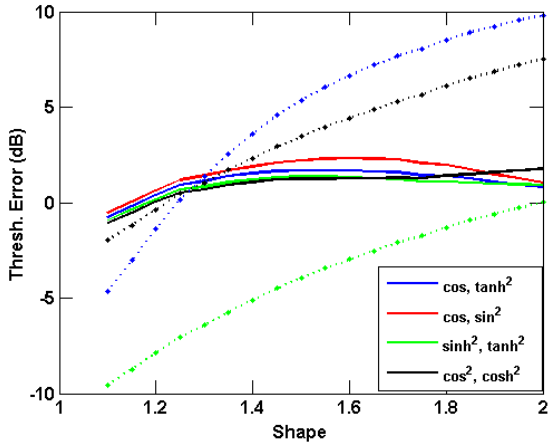

(d) Full Lib. w/CCM (solid) vs. Excised Lib. w/SCM (dotted)

Figure 6.15: Threshold estimation error (dB) using DBM with Weibull distributed data

Table 6.14 then examines the average accuracy of the Studentization transformation method. On the surface the Studentization transformation method appears to offer excellent accuracy that varies little whether or not the excised library or SCM is used, but only when considering the average threshold estimate over the range of shape parameters.

Weightings		Clairvoyant Cov. Matrix		Sample Cov. Matrix		
1	2	Full Lib.	Excised Lib.	Full Lib.	Excised Lib.	Δ Clair, SCM
sinh	tanh	1.07	0.73	-1.89	-2.12	-2.96
cosh	sinh	1.06	0.74	-1.78	-1.98	-2.84
$\cos^2$	sine^2	2.00	2.13	-0.55	-0.37	-2.55

Table 6.14: Average Threshold Error (dB) when Weibull distributed data is fed into the Studentized weightings

However, Figures 6.16a-6.16d show the accuracy of the Studentization method as a function of shape parameter. It can be seen from examining the plots in Figures 6.16a-6.16d that the average values for the excised and when the SCM is used do not convey the behavior for the different shape parameters. In general, the threshold given is not accurate for the Studentized transformation method. Only the (cosine, sine^2) weighting pair yields adequate accuracy when the SCM is used.

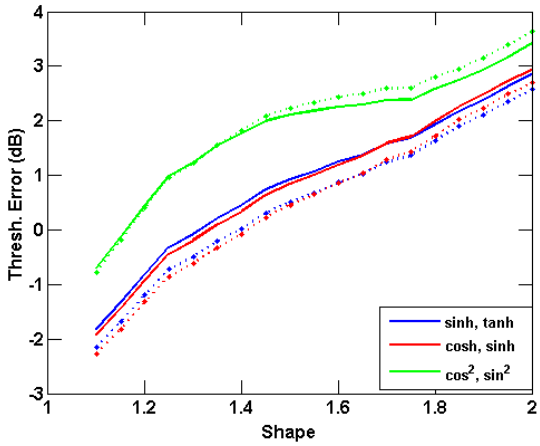

(a) Full Lib. w/CCM (solid) vs. Excised Lib. w/CCM (dotted)

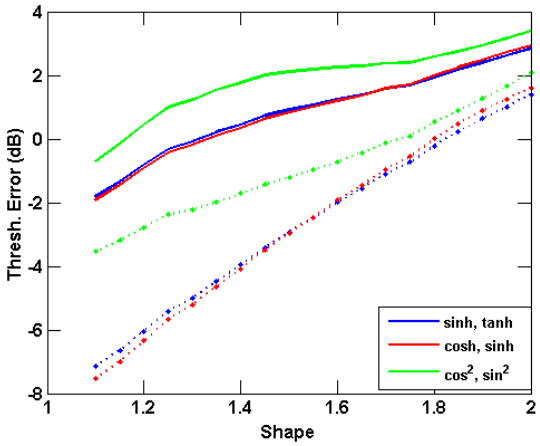

(b) Full Lib. w/ CCM (solid) vs. Full Lib. w/ SCM (dotted)

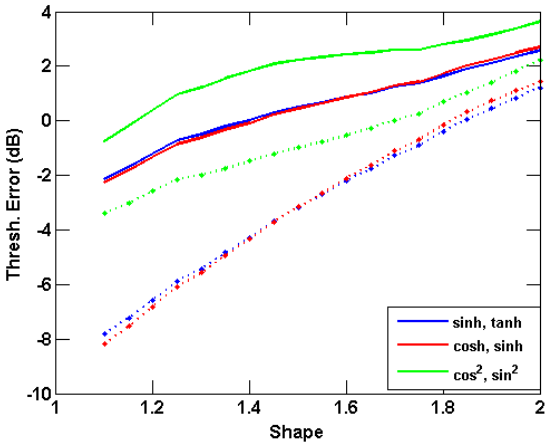

(c) Excised Lib. w/CCM (solid) vs. Excised Lib. w/ SCM (dotted)

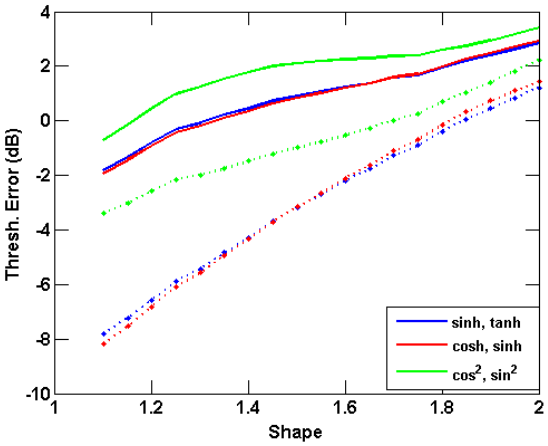

(d) Full Lib. w/CCM (solid) vs. Excised Lib. w/SCM (dotted)

Figure 6.16: Threshold estimation error (dB) using Studentized method with Weibull distributed data

Table 6.15 examines the last transformation method under discussion, the EOA. From the

average values given, only the weighting pair appears to be inappropriate for consideration. Recall that the EOA for the Weibull distribution was considered for a limited library in Section 6.3.1.

Weightings		Clairvoyant Cov. Matrix		Sample Cov. Matrix		
1	2	Full Lib.	Excised Lib.	Full Lib.	Excised Lib.	Δ Clair, SCM
cos	$\cos^2$	1.63	1.27	-1.26	-1.64	-2.89
$\cos^2$	$\tanh^2$	1.46	1.16	-1.59	-1.98	-3.06
sine^2	$\sinh^2$	5.28	5.42	4.15	4.25	-1.13

Table 6.15: Average Threshold Error (dB) when Weibull distributed data is fed into the EOA weightings

The results of Table 6.15 are show as a function of shape parameter in Figures 6.17a-6.17d. The (sine^2, $\sinh^2$) weighting pair is the only pair that gives adequate threshold estimation performance at low values of the shape parameter. However, we do not consider the ≈ 7 dB detection loss when Gaussian data is present to be acceptable.

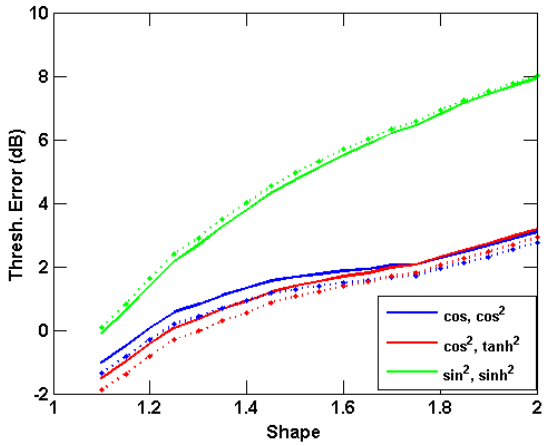

(a) Full Lib. w/CCM (solid) vs. Excised Lib. w/CCM (dotted)

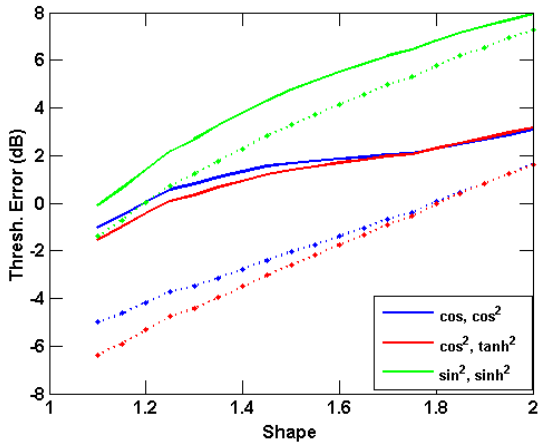

(b) Full Lib. w/ CCM (solid) vs. Full Lib. w/ SCM (dotted)

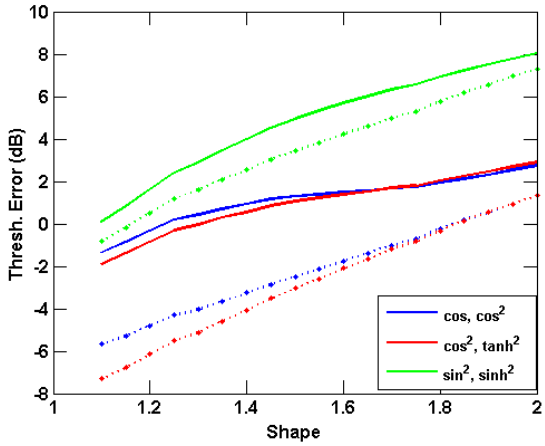

(c) Excised Lib. w/CCM (solid) vs. Excised Lib. w/ SCM (dotted)

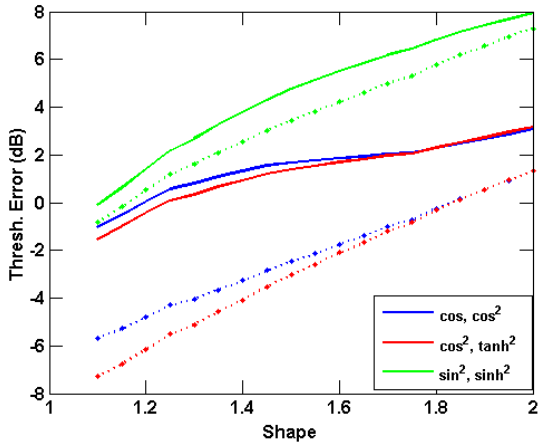

(d) Full Lib. w/CCM (solid) vs. Excised Lib. w/SCM (dotted)

Figure 6.17: Threshold estimation error (dB) using EOA method with Weibull distributed data

Examination of Tables 6.13-6.15 and Figures 6.14a-6.17d suggests that the weighting pair (cosine, sine^2) used in conjunction with the Studentization transformation method is the only acceptable COSMiC method for setting a threshold in complex Weibull distributed clutter.

6.3.3.4 Pareto Data

Table 6.16 shows the average threshold error for the WSOS and DBM transformation methods when Pareto data is present. With the exception of the (cosine^2, cosh^2) weighting pair, both the WSOS and DBM methods underestimate the true threshold. Therefore, the Pareto data will cause more false alarms when the WSOS and DBM transformation methods are used.

Weightings		Clairvoyant Cov. Matrix		Sample Cov. Matrix		SCM - DBM Weightings		Δ Clair, SCM	
1	2	Full Lib.	Excised Lib.	Full Lib.	Excised Lib.	Full Lib.	Excised Lib.	Δ WSOS	Δ SCM
cos	tanh^2	-1.19	-1.35	-1.87	-2.01	6.97	6.97	-0.68	8.15
cos	sine^2	-0.44	-1.01	-1.88	-2.12	-1.94	-1.94	-1.45	-1.50
sinh^2	tanh^2	-0.90	-1.14	-2.09	-2.26	0.09	0.09	-1.18	1.00
cos^2	cosh^2	-0.30	-0.51	-1.94	-2.25	6.30	6.30	-1.64	6.60

Table 6.16: Average Threshold Error (dB) when Pareto distributed data is fed into the WSOS and DBM weightings

Figures 6.18a-6.18d show the results of Table 6.16 as a function of shape parameter. Note that when that the difference between the excised library and full library when the SCM is used is approximately 0.5 dB (at the lowest shape pameter value) to less than a few hundredths of a dB. The difference between the threshold estimate for the full library with true clairvoyant covariance matrix and the excised library with the SCM ranges between a 1.95 - 0.5 dB difference (with relation to the increasing shape parameter).

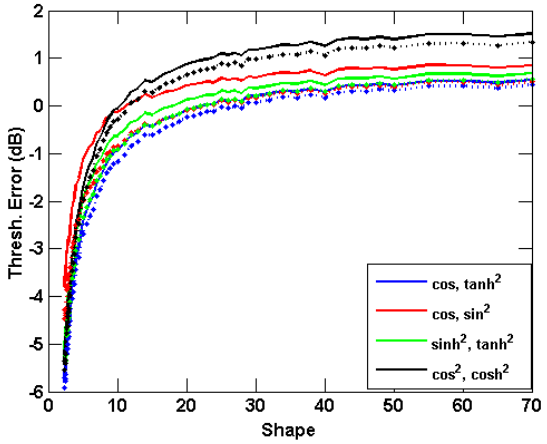

(a) Full Lib. w/CCM (solid) vs. Excised Lib. w/CCM (dotted)

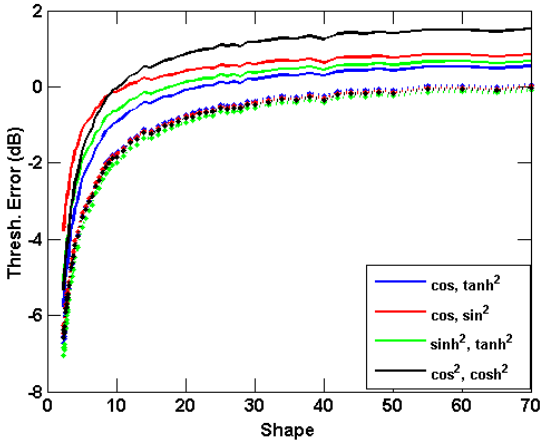

(b) Full Lib. w/ CCM (solid) vs. Full Lib. w/ SCM (dotted)

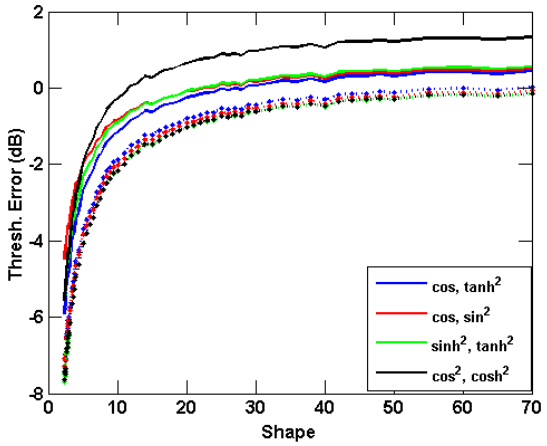

(c) Excised Lib. w/CCM (solid) vs. Excised Lib. w/ SCM (dotted)

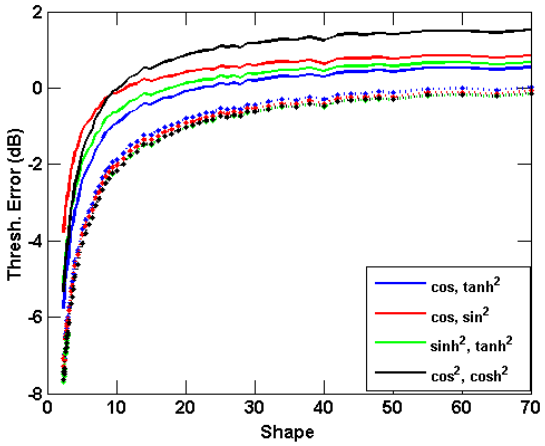

(d) Full Lib. w/CCM (solid) vs. Excised Lib. w/SCM (dotted)

Figure 6.18: Threshold estimation error (dB) using WSOS with Pareto distributed data

Figures 6.19a-6.19d show the average threshold estimation accuracy when the DBM method is used with Pareto data. Note that unlike the WSOS method, when the SCM is used the (cosine, $\tanh^2$) and (cosine^2, $\cosh^2$) weighting pairs produce much different results compared to the (cosine, sine^2) and ($\sinh^2$, $\tanh^2$) weighting pairs. In particular, the former are more accurate for low shape parameter values and result in large amounts of detection loss for high shape parameter values. Meanwhile, the latter result in very low thresholds for low shape parameter data but accurate thresholds for high shape parameter data.

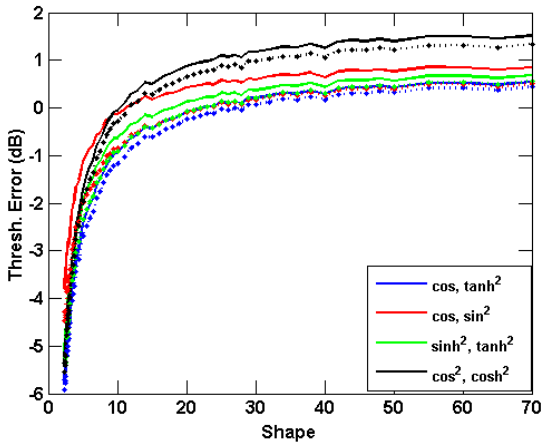

(a) Full Lib. w/CCM (solid) vs. Excised Lib. w/CCM (dotted)

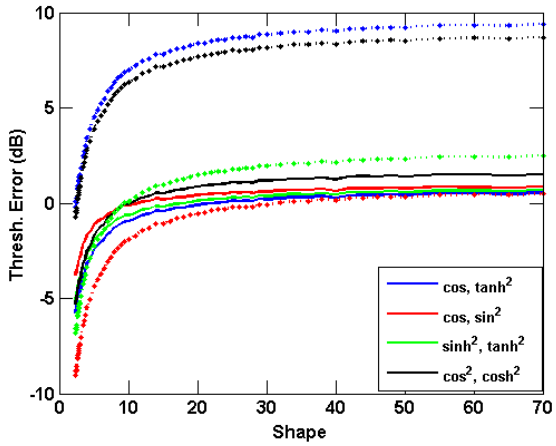

(b) Full Lib. w/ CCM (solid) vs. Full Lib. w/ SCM (dotted)

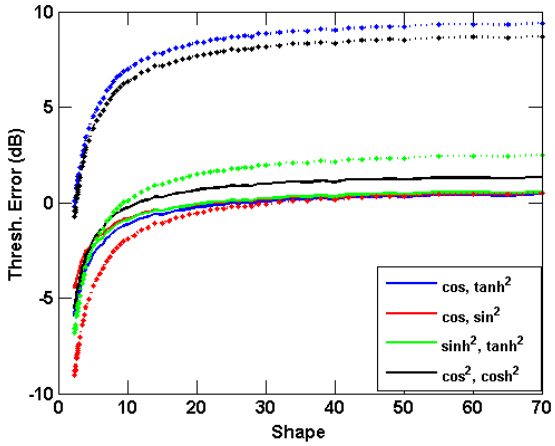

(c) Excised Lib. w/CCM (solid) vs. Excised Lib. w/ SCM (dotted)

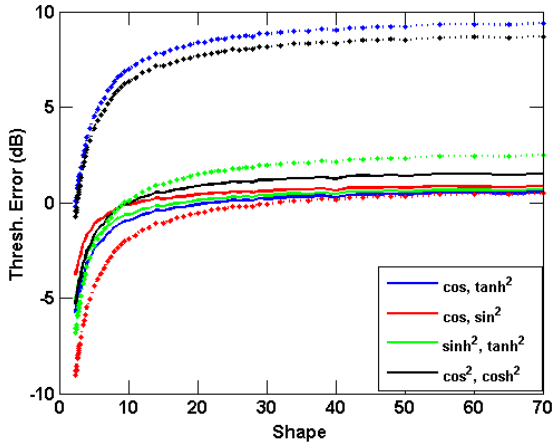

(d) Full Lib. w/CCM (solid) vs. Excised Lib. w/SCM (dotted)

Figure 6.19: Threshold estimation error (dB) using DBM with Pareto distributed data

Next, Table 6.17 shows results that are on average between 1 and 2 dB off of optimal threshold values when the Studentized transformation method is used. There appears to be just over a 2 dB difference when the SCM is used, with little difference when the excised library is used.

Weightings		Clairvoyant Cov. Matrix		Sample Cov. Matrix		
1	2	Full Lib.	Excised Lib.	Full Lib.	Excised Lib.	Δ Clair, SCM
sinh	tanh	1.33	1.14	-1.04	-1.23	-2.37
cosh	sinh	1.35	1.12	-0.93	-1.19	-2.27
$\cos^2$	sine^2	1.93	1.71	-0.08	-0.26	-2.01

Table 6.17: Average Threshold Error (dB) when Pareto distributed data is fed into the Studentized weightings

Figures 6.20a-6.20d then clarify the results of Table 6.17 by showing the average threshold error as a function of shape parameter. The (sinh, tanh) and (cosh, sinh) pairs yield virtually the same results (compared to each other) for all cases. However, when the SCM is used, the (cosine^2, sine^2) weighting pair produces better results at lower shape parameters, but suffers detection loss relative to the other two pairs at higher shape parameter values.

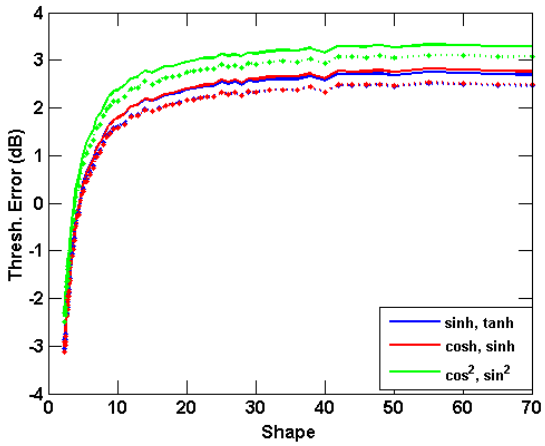

(a) Full Lib. w/CCM (solid) vs. Excised Lib. w/CCM (dotted)

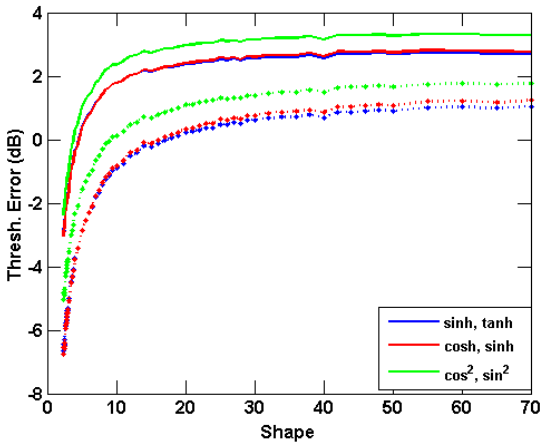

(b) Full Lib. w/ CCM (solid) vs. Full Lib. w/ SCM (dotted)

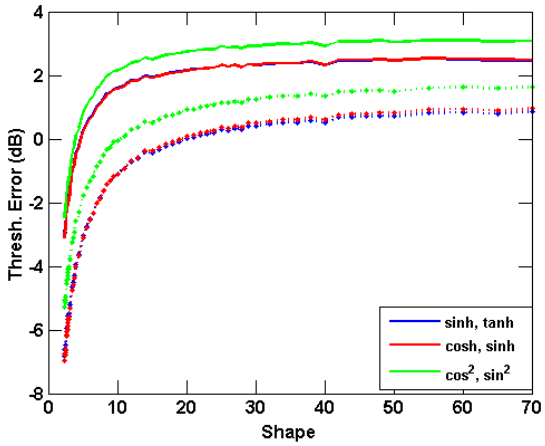

(c) Excised Lib. w/CCM (solid) vs. Excised Lib. w/ SCM (dotted)

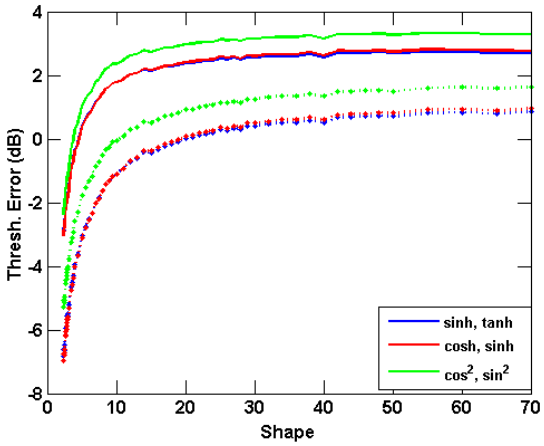

(d) Full Lib. w/CCM (solid) vs. Excised Lib. w/SCM (dotted)

Figure 6.20: Threshold estimation error (dB) using Studentized method with Pareto distributed data

The last method under consideration is the EOA transformation method. Comparing Table 6.17 to Table 6.18, the top two weighting pairs for the EOA method seem similar to the top two pairs for the Studentized transformation method. However, the last pair suffers a large detection loss compared to the last pair of the Studentized weighting. Recall that the last pair for both weighting methods was chosen in Section 6.3.2 to provide the lowest threshold error for the Lognormal distribution.

Weightings		Clairvoyant Cov. Matrix		Sample Cov. Matrix		
1	2	Full Lib.	Excised Lib.	Full Lib.	Excised Lib.	Δ Clair, SCM
cos	$\cos^2$	1.74	1.42	-0.65	-0.82	-2.39
$\cos^2$	$\tanh^2$	1.69	1.35	-0.78	-1.08	-2.47
sine^2	$\sinh^2$	5.55	5.60	4.69	4.69	-0.86

Table 6.18: Average Threshold Error (dB) when Pareto distributed data is fed into the EOA weightings

The accuracy of the threshold estimation shown in Table 6.18 is given as a function of shape parameter in Figures 6.21a-6.21d. The top two weightings result in a comparable accuracy to the top two weightings for the Studentized method. However, the (sine^2, $\sinh^2$) weighting pair results in a very large detection loss for high shape parameter values. Therefore, the (sine^2, $\sinh^2$) weighting pair should not be used in conjunction with the EOA method.

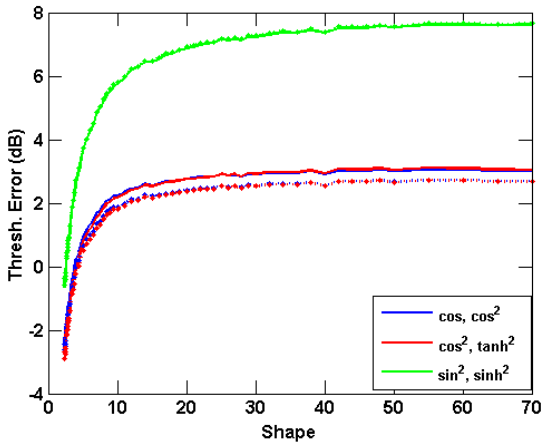

(a) Full Lib. w/CCM (solid) vs. Excised Lib. w/CCM (dotted)

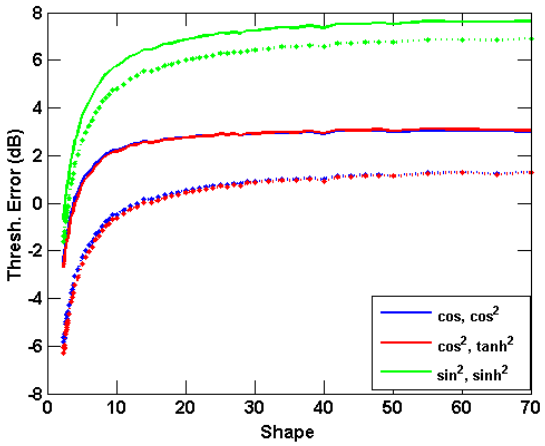

(b) Full Lib. w/ CCM (solid) vs. Full Lib. w/ SCM (dotted)

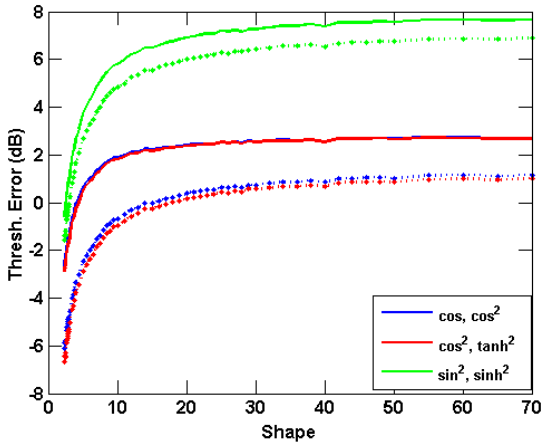

(c) Excised Lib. w/CCM (solid) vs. Excised Lib. w/ SCM (dotted)

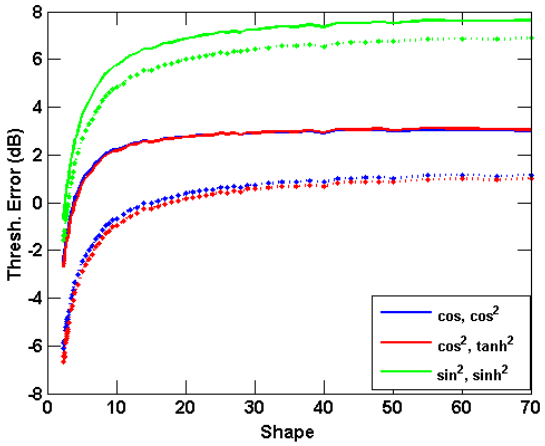

(d) Full Lib. w/CCM (solid) vs. Excised Lib. w/SCM (dotted)

Figure 6.21: Threshold estimation error (dB) using EOA method with Pareto distributed data

In general, the Studentized method provides the most accurate threshold estimates, with (cosine^2, sine^2) offering best low shape parameter results and the (sinh, tanh) and (cosh, sinh) weighting pairs offering the best high shape parameter results. The top two weighting pairs for the EOA transformation method provide comparable results to the Studentized method.

6.3.3.5 Lognormal Data

Note that for the parameters under consideration, the Lognormal distribution requires a threshold 10 dB greater than the threshold needed for the same probability of false alarm in complex Gaussian noise. Table 6.19 shows the average estimated threshold error for Lognormal clutter when the WSOS and DBM methods are used to estimate the threshold. When the DBM method is used, both the (cosine, $\tanh^2$) and (cosine^2, $\cosh^2$) weighting combinations yield very accurate threshold estimates.

Weightings		Clairvoyant Cov. Matrix		Sample Cov. Matrix		SCM - DBM Weightings		Δ Clair, SCM	
1	2	Full Lib.	Excised Lib.	Full Lib.	Excised Lib.	Full Lib.	Excised Lib.	Δ WSOS	Δ SCM
cos	$\tanh^2$	-5.58	-5.62	-6.42	-6.43	-0.50	-0.50	-0.84	5.09
cos	sine^2	-3.36	-3.57	-5.79	-5.92	-9.30	-9.30	-2.43	-5.94
$\sinh^2$	$\tanh^2$	-4.82	-4.88	-6.51	-6.52	-7.04	-7.04	-1.68	-2.22
cos^2	$\cosh^2$	-5.04	-5.12	-5.64	-5.81	-0.88	-0.88	-0.61	4.15

Table 6.19: Average Threshold Error (dB) when Lognormal distributed data is fed into the WSOS and DBM weightings

Next the performance of the Studentized transformation method is examined in Table 6.20. Despite the difference in performance between the WSOS and Studentized methods when the true covariance matrix is used, the Studentized method has an average threshold error equal to or better than the WSOS method. However, the top two DBM weighting pairs outperform all three of the Studentized pairs.

Weightings		Clairvoyant Cov. Matrix		Sample Cov. Matrix		
1	2	Full Lib.	Excised Lib.	Full Lib.	Excised Lib.	Δ Clair, SCM
sinh	tanh	-2.58	-2.59	-6.00	-6.01	-3.42
cosh	sinh	-2.64	-2.65	-6.15	-6.17	-3.51
cos^2	sine^2	-1.90	-1.90	-4.15	-4.15	-2.25

Table 6.20: Average Threshold Error (dB) when Lognormal distributed data is fed into the Studentized weightings

Finally, Table 6.21 shows the average threshold error when the EOA transformation method is applied to Lognormal data. In this case, the (sine^2, $\sinh^2$) pairing is the best choice whether or not the covariance matrix is known.

Weightings		Clairvoyant Cov. Matrix		Sample Cov. Matrix		
1	2	Full Lib.	Excised Lib.	Full Lib.	Excised Lib.	Δ Clair, SCM
cos	$\cos^2$	-2.02	-2.10	-4.97	-5.01	-2.95
$\cos^2$	$\tanh^2$	-2.35	-2.41	-5.66	-5.74	-3.31
sine^2	$\sinh^2$	-0.72	-0.80	-1.52	-1.58	-0.80

Table 6.21: Average Threshold Error (dB) when Lognormal distributed data is fed into the EOA weightings

Overall, when Lognormal data is present, the EOA transformation method and weighting pair (sine^2, $\sinh^2$) offers the best results when the covariance matrix is known, but also the second best accuracy when the sample covariance matrix is used. However, if the sample covariance matrix is used the (cosine^2, $\cosh^2$) and (cosine, $\tanh^2$) weightings work best when transformed via the DBM method.

6.4 Evaluating Triplets of Weightings in COSMiC

Section 6.3 considered the use of pairs of weighting functions in conjunction with four transformation methods to identify the distribution and threshold associated with various distributions. This section considers the extension from pairs of weighting functions to triplets of weighting functions. In other words, does the addition of a weighting function provide diversity and improve the results established in Section 6.3? Experimentation showed that the underlying endpoint space is symmetric. Therefore, with 10 candidate weighting functions, only 120 combinations of triplets of weightings needed to be considered (versus the 45 pairs of weightings considered).

Section 6.4.1 examines the problem of distribution identification, while Sections 6.4.2-6.4.3.5 examine the utility of using triplets of weightings to estimate the threshold in the presence of the distributions under test.

6.4.1 Distribution Identification with Triplets of Weightings

The distribution identification accuracy of the proposed transformation methods (excepting the DBM method) when three weightings are used to form the endpoint is shown in Tables 6.22-6.24. Comparing Tables 6.22-6.24 to Tables 6.1-6.3 it appears that the use of triplets of weightings actually slightly degrades the distribution identification capabilities of all three transformation methods when compared to using pairs of weightings.

	Weightings			Percentage Chosen					
True Dist.	1	2	3	Gaussian	K	Weibull	Pareto	Lognormal	Gamma Mod.
Gaussian	$sine^2$	cosh	$cosh^2$	49.1	5.0	43.3	2.5	0.0	0.1
K	$sinh^2$	tanh	$tanh^2$	0.1	3.1	96.6	0.0	0.0	0.2
Weibull	sine	$sine^2$	cosh	12.7	18.7	64.9	2.0	0.1	1.6
Pareto	cos	cos^2	sine	24.6	8.5	38.9	24.2	1.3	2.5
Lognormal	cos	cos^2	sine	12.6	8.3	27.6	34.5	6.7	10.3

Table 6.22: Distribution identification percentages of top WSOS COSMiC weighting triplets

	Weightings			Percentage Chosen					
True Dist.	1	2	3	Gaussian	K	Weibull	Pareto	Lognormal	Gamma Mod.
Gaussian	sinh	$sinh^2$	tanh	45.8	3.5	35.3	12.3	1.3	1.7
K	cos	cos^2	sine	22.2	22.1	41.4	8.6	2.1	3.7
Weibull	$sine^2$	cosh	$cosh^2$	24.6	13.8	47.6	8.4	1.9	3.6
Pareto	cos^2	sine	$sine^2$	26.3	11.8	42.5	11.8	3.0	4.6
Lognormal	cos^2	sine	$sine^2$	5.0	41.9	38.5	4.9	3.4	6.3

Table 6.23: Distribution identification percentages of top Studentized COSMiC weighting triplets

	Weightings			Percentage Chosen					
True Dist.	1	2	3	Gaussian	K	Weibull	Pareto	Lognormal	Gamma Mod.
Gaussian	$sinh^2$	tanh	$tanh^2$	42.9	2.8	39.9	12.3	0.9	1.2
K	$sinh^2$	tanh	$tanh^2$	21.3	18.6	41.5	11.4	3.0	4.2
Weibull	cosh	$cosh^2$	sinh	16.9	9.4	51.9	13.1	4.5	4.1
Pareto	cos^2	sine	$sine^2$	20.0	7.2	38.4	22.8	7.2	4.4
Lognormal	cos	cos^2	sine	5.6	30.7	31.7	10.9	12.8	8.3

Table 6.24: Distribution identification percentages of top EOA COSMiC weighting triplets

The distribution identification performance as a function of shape paramter is shown for the two triplets of weightings with the highest identification accuracy when K, Weibull, and Pareto distributed data is present is shown in Figures 6.22a-6.24c. In light of the decreased performance of the triplets when compared to using pairs of weightings, the results are presented without further comment.

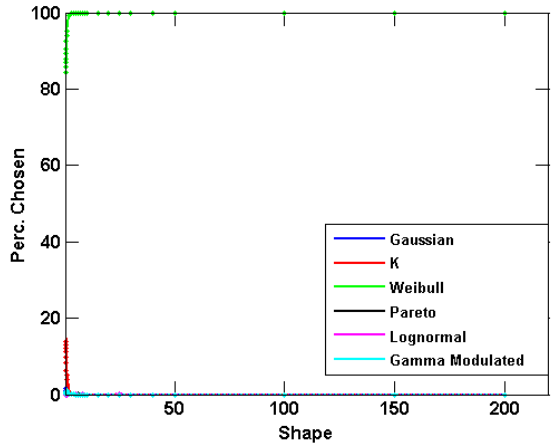

(a) (sinh^2, tanh, tanh^2) (solid) vs. (cosh^2, sinh, sinh^2) (dotted)

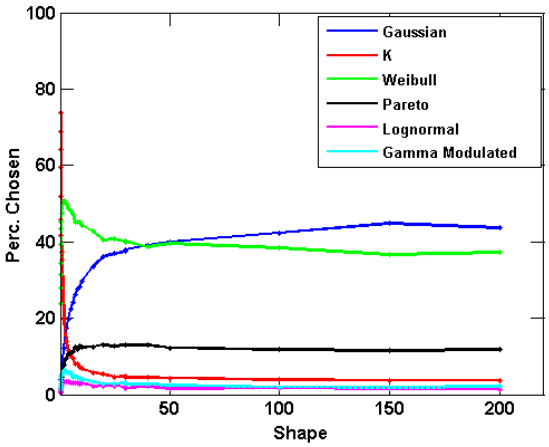

(b) (cos, cos^2, sine) (solid) vs. (cos, cos^2, sine^2) (dotted)

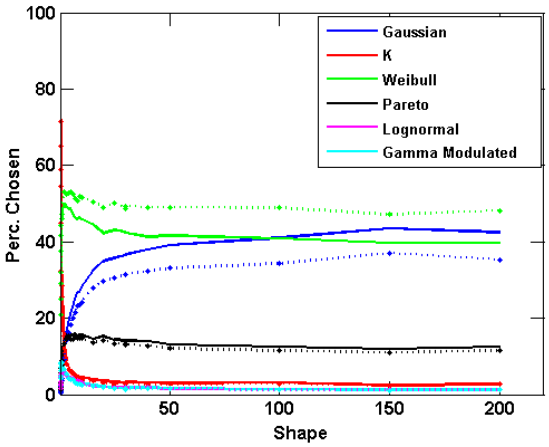

(c) (sinh^2, tanh, tanh^2) (solid) vs. (cosh^2, sinh, sinh^2) (dotted)

Figure 6.22: COSMiC distribution identification vs. shape parameter for Weibull distributed data for top triplets

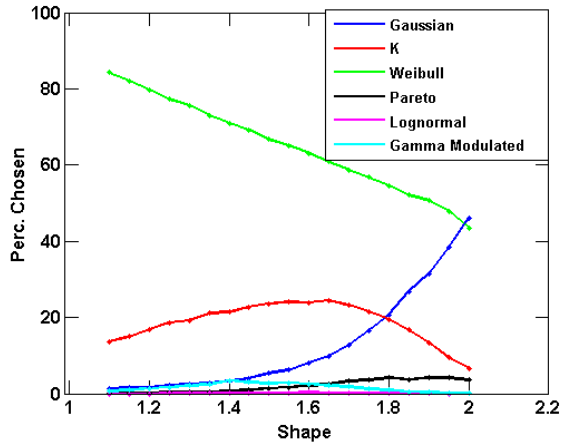

(a) (sine, sine^2, cosh) vs. (sine, sine^2, cosh^2) (solid) (dotted)

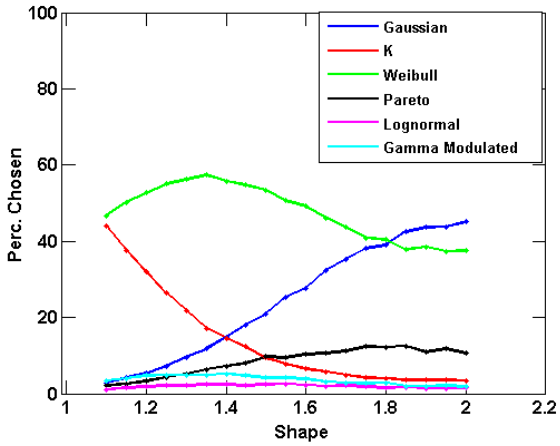

(b) (sine^2, cosh, cosh^2) (solid) vs. (sine^2, cosh, sinh) (dotted)

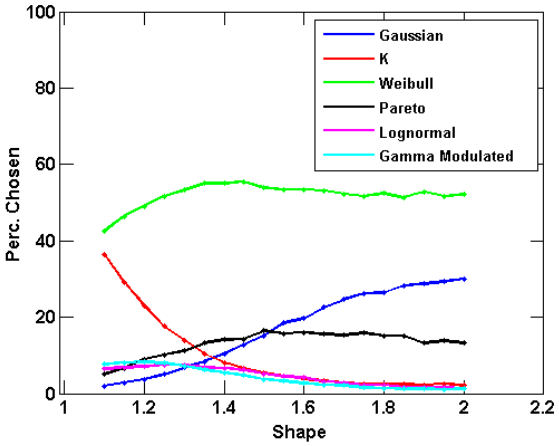

(c) (cosh, cosh^2, sinh) (solid) vs. (cosh, cosh^2, sinh^2) (dotted)

Figure 6.23: COSMiC distribution identification vs. shape parameter for Weibull distributed data for top triplets

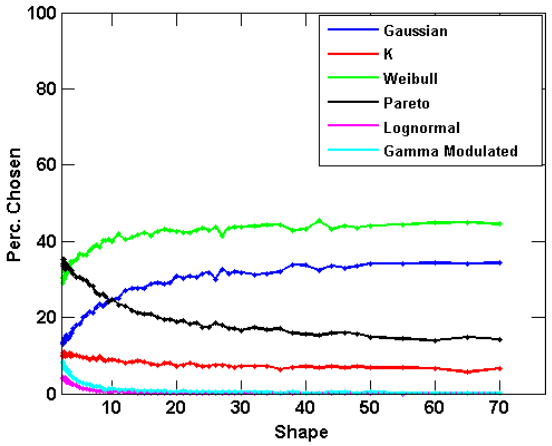

(a) (cos, $\cos^2$, sine) (solid) vs. (cos, $\cos^2$, sine^2) (dotted)

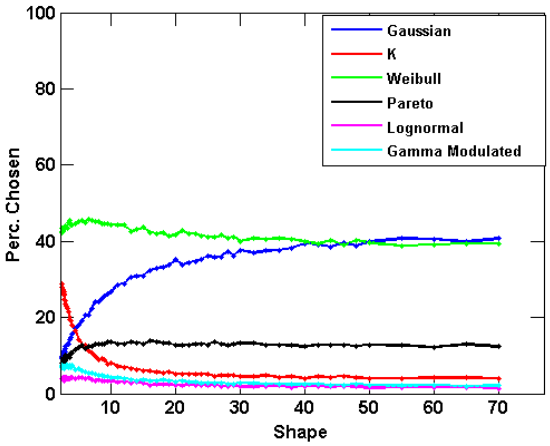

(b) ($\cos^2$, sine, sine^2) (solid) vs. ($\cos^2$, sine, cosh) (dotted)

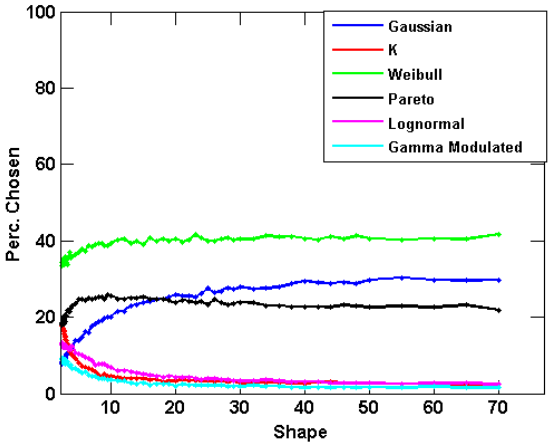

(c) ($\cos^2$, sine, sine^2) (solid) vs. ($\cos^2$, sine, cosh) (dotted)

Figure 6.24: COSMiC distribution identification v. shape parameter for Pareto distributed data for top triplets

6.4.2 Threshold Estimation - Identifying Top Triplet Weightings

The most accurate (averaged over all values of shape parameter) triplet of weighting functions is reported for each distribution/transformation combination in the same manner as was shown in Section 6.3.2. Despite the degradation noted in distribution identification, comparing Tables 6.4 and 6.5 to Tables 6.25 and 6.26, respectively, shows that for the WSOS and Studentization transformation methods the use of triplets of weightings provides a slight improvement in threshold estimation accuracy when compared to using pairs of weightings.

However, comparing Tables 6.6 and 6.27, only the Lognormal distribution has an improved threshold estimate when the EOA transformation method is used with triplets of weightings. In addition, the top pairs of weightings are present in one or more of the top triplets of weightings for each method. Therefore, addition of the third weighting function only offers a slight improvement, if any, over the pair of weightings. This result implys that there is little new information gained by adding the third endpoint.

Weightings			Gaussian		K		Weibull		Pareto		Lognormal	
1	2	3	Rank	Error	Rank	Error	Rank	Error	Rank	Error	Rank	Error
cos	$\sinh^2$	$\tanh^2$	1	0.76 dB	2	4.94 dB	33	1.14 dB	114	-1.17 dB	92	-5.46 dB
cos	sine^2	$\tanh^2$	26	1.04 dB	1	4.40 dB	101	1.56 dB	26	-0.54 dB	12	-3.41 dB
$\cos^2$	cosh	$\cosh^2$	88	1.35 dB	90	6.52 dB	1	1.01 dB	54	-0.70 dB	86	-5.30 dB
$\cos^2$	sine^2	$\tanh^2$	107	1.73 dB	46	6.29 dB	96	1.48 dB	1	0.06 dB	11	-3.25 dB
sine	sine^2	tanh	119	4.68 dB	119	6.67 dB	119	3.22 dB	119	3.02 dB	1	-1.40 dB

Table 6.25: Summary of top WSOS weighting triplets

Weightings			Gaussian		K		Weibull		Pareto		Lognormal	
1	2	3	Rank	Error	Rank	Error	Rank	Error	Rank	Error	Rank	Error
cos	sinh	$\tanh^2$	1	2.77 dB	1	1.64 dB	1	0.98 dB	1	1.27 dB	119	-2.61 dB
cos	sinh	$\tanh^2$	1	2.77 dB	1	1.64 dB	1	0.98 dB	1	1.27 dB	119	-2.61 dB
cos	sinh	$\tanh^2$	1	2.77 dB	1	1.64 dB	1	0.98 dB	1	1.27 dB	119	-2.61 dB
cos	sinh	$\tanh^2$	1	2.77 dB	1	1.64 dB	1	0.98 dB	1	1.27 dB	119	-2.61 dB
$\cos^2$	$\cosh^2$	$\sinh^2$	114	3.54 dB	116	2.37 dB	116	1.86 dB	112	1.91 dB	1	-1.86 dB

Table 6.26: Summary of top studentized weighting triplets

Weightings			Gaussian		K		Weibull		Pareto		Lognormal	
1	2	3	Rank	Error	Rank	Error	Rank	Error	Rank	Error	Rank	Error
cos	$\cos^2$	$\tanh^2$	1	3.28 dB	1	2.28 dB	1	1.74 dB	1	1.81 dB	70	-1.90 dB
cos	$\cos^2$	$\tanh^2$	1	3.28 dB	1	2.28 dB	1	1.74 dB	1	1.81 dB	70	-1.90 dB
cos	$\cos^2$	$\tanh^2$	1	3.28 dB	1	2.28 dB	1	1.74 dB	1	1.81 dB	70	-1.90 dB
cos	$\cos^2$	$\tanh^2$	1	3.28 dB	1	2.28 dB	1	1.74 dB	1	1.81 dB	70	-1.90 dB
sine^2	$\sinh^2$	$\tanh^2$	114	7.94 dB	115	5.70 dB	115	5.32 dB	114	5.57 dB	1	-0.67 dB

Table 6.27: Summary of top extended Ozturk weighting triplets

6.4.3 Threshold Estimation with Triplets of Weightings - Evaluating Robustness of COSMiC Methods

Sections 6.4.3.1-6.4.3.5 follow in the footsteps of Sections 6.3.3.1-6.3.3.5 by showing the accuracy of the threshold estimate produced by the pairing of the various weighting triplets/transformation methods when the test data is distributed according to the candidate distributions. The numerical results are reported in the tables and figures, while the analysis is primarily concerned with the comparison to the corresponding scenario when a pair of weightings is used. In other words, for each case what is the benefit of using the third weighting function?

6.4.3.1 Gaussian Data

Compared to the results in Section 6.3.3.1, when Gaussian data is present there is little to no increase in average threshold estimate error offered by using the third weightings.

Weightings			Clairvoyant Cov. Matrix		Sample Cov. Matrix		SCM - DBM Weightings		Δ Clair, SCM	
1	2	3	Full Lib.	Excised Lib.	Full Lib.	Excised Lib.	Full Lib.	Excised Lib.	Δ WSOS	Δ DBM
cos	$\sinh^2$	$\tanh^2$	0.83	0.83	0.35	0.36	9.82	9.82	-0.47	8.99
cos	sine^2	$\tanh^2$	1.02	1.02	0.34	0.34	0.92	0.92	-0.68	-0.10
$\cos^2$	cosh	$\cosh^2$	1.69	1.70	0.55	0.56	0.00	0.02	-1.14	-1.68
$\cos^2$	sine^2	$\tanh^2$	1.40	1.40	0.33	0.33	7.50	7.50	-1.07	6.10
sine	sine^2	tanh	4.72	4.72	0.64	0.64	0.00	0.92	-4.08	-4.72

Table 6.28: Average Threshold Error (dB) when Gaussian distributed data is fed into the WSOS and DBM weightings

Weightings			Clairvoyant Cov. Matrix		Sample Cov. Matrix		
1	2	3	Full Lib.	Excised Lib.	Full Lib.	Excised Lib.	Δ Clair, SCM
cos	sinh	$\tanh^2$	2.86	2.86	1.52	1.52	-1.34
$\cos^2$	$\cosh^2$	$\sinh^2$	3.37	3.44	2.02	2.15	-1.35

Table 6.29: Average Threshold Error (dB) when Gaussian distributed data is fed into the Studentized weightings

Weightings			Clairvoyant Cov. Matrix		Sample Cov. Matrix		
1	2	3	Full Lib.	Excised Lib.	Full Lib.	Excised Lib.	Δ Clair, SCM
cos	$\cos^2$	$\tanh^2$	3.19	3.22	1.70	1.77	-1.49
$\sin e^2$	$\sinh^2$	$\tanh^2$	7.96	7.97	7.29	7.29	-0.68

Table 6.30: Average Threshold Error (dB) when Gaussian distributed data is fed into the EOA weightings

6.4.3.2 K Data

Comparing Tables 6.10 and 6.31 the weighting pairs (cosine, $\tanh^2$) and ($\sinh^2$, $\tanh^2$) were combined into the triplet (cosine, $\sinh^2$, $\tanh^2$). The resultant combination yields decreased performance when the SCM is used for the WSOS transformation method due to the inclusion of the $\sinh^2$ weighting, and greatly decreased performance of the DBM method due to the inclusion of the cosine weighting. This example shows that the disadvantages of different weightings can be combined to form a triplet that performs worse than the separate pairs of weightings. Therefore, rather than introducing diversity in the form additional endpoints to a single set of weightings, it may be more effective to incorporate multiple pairs of weightings. This concept should be explored in future work.

Weightings			Clairvoyant Cov. Matrix		Sample Cov. Matrix		SCM - DBM Weightings		Δ Clair, SCM	
1	2	3	Full Lib.	Excised Lib.	Full Lib.	Excised Lib.	Full Lib.	Excised Lib.	Δ WSOS	Δ DBM
cos	$\sinh^2$	$\tanh^2$	4.96	4.96	-0.89	-0.38	6.74	6.68	-5.85	1.78
cos	$\sin e^2$	$\tanh^2$	4.42	4.42	-0.93	-0.60	-1.91	-1.91	-5.35	-6.33
$\cos^2$	cosh	$\cosh^2$	6.30	6.31	-0.99	-0.84	-2.40	-2.40	-7.29	-8.70
$\cos^2$	$\sin e^2$	$\tanh^2$	6.52	6.52	-1.19	-1.04	4.74	4.74	-7.71	-1.79
sine	$\sin e^2$	tanh	6.67	6.68	-0.95	-0.79	-2.78	-2.78	-7.62	-9.45

Table 6.31: Average Threshold Error (dB) when K distributed data is fed into the WSOS and DBM weightings

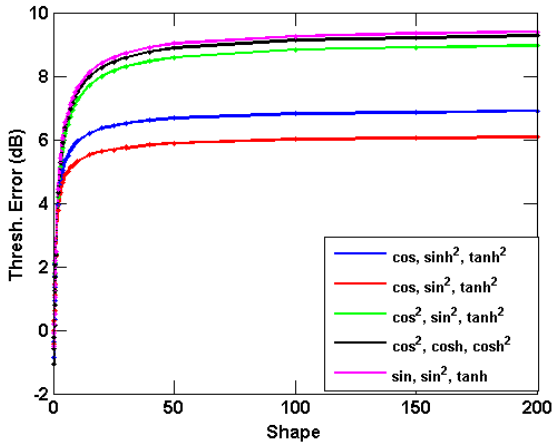

(a) Full Lib. w/CCM (solid) vs. Excised Lib. w/CCM (dotted)

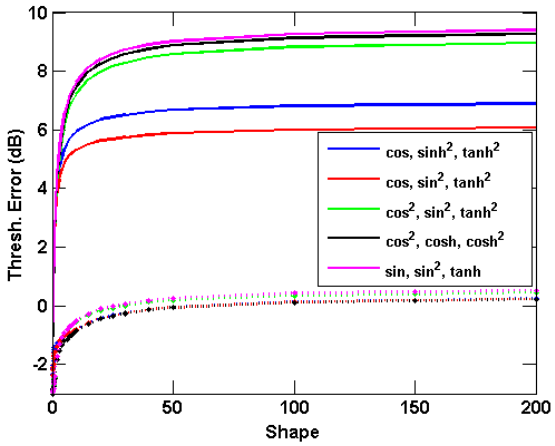

(b) Full Lib. w/ CCM (solid) vs. Full Lib. w/ SCM (dotted)

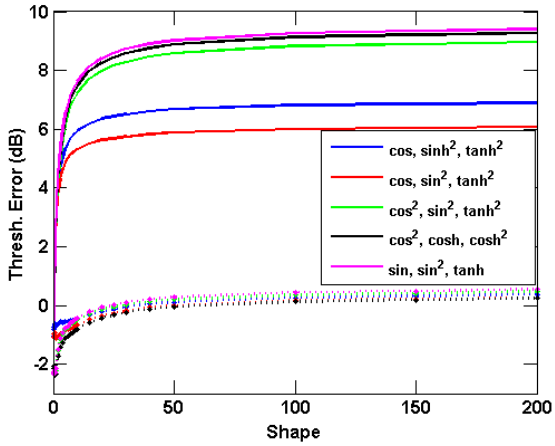

(c) Excised Lib. w/CCM (solid) vs. Excised Lib. w/ SCM (dotted)

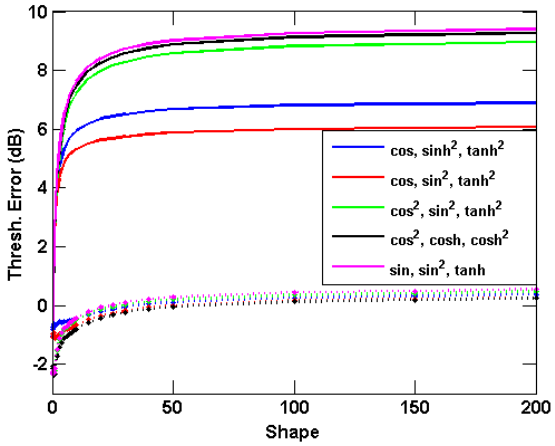

(d) Full Lib. w/CCM (solid) vs. Excised Lib. w/SCM (dotted)

Figure 6.25: Threshold estimation error (dB) using WSOS with K distributed data

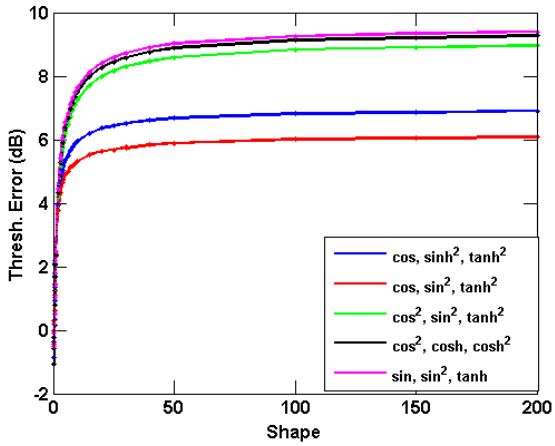

(a) Full Lib. w/CCM (solid) vs. Excised Lib. w/CCM (dotted)

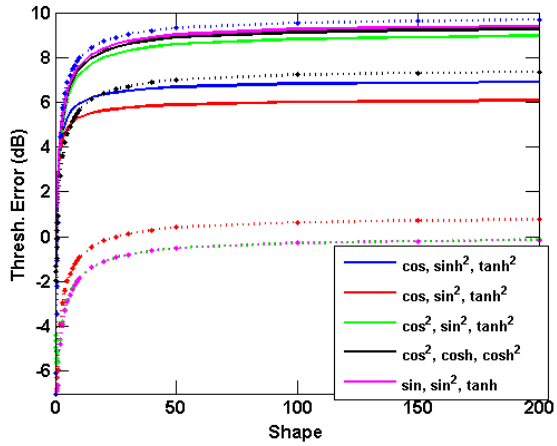

(b) Full Lib. w/ CCM (solid) vs. Full Lib. w/ SCM (dotted)

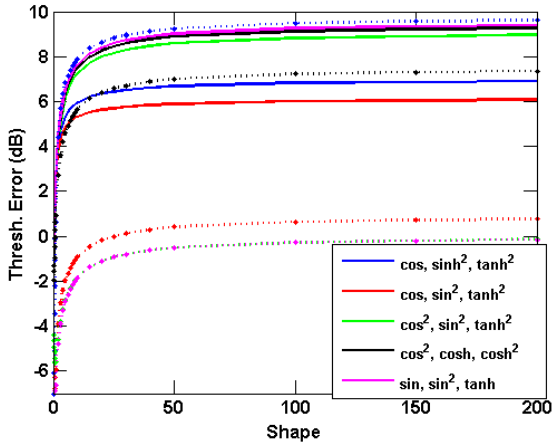

(c) Excised Lib. w/CCM (solid) vs. Excised Lib. w/ SCM (dotted)

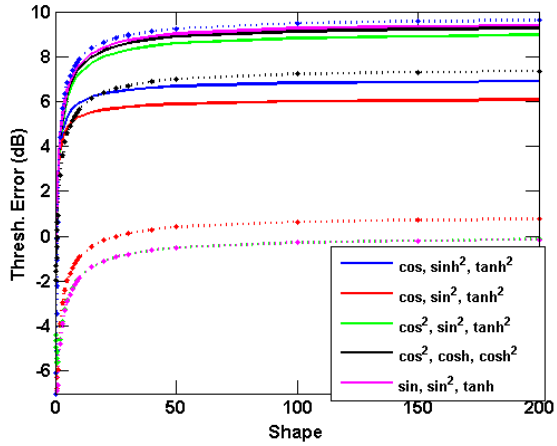

(d) Full Lib. w/CCM (solid) vs. Excised Lib. w/SCM (dotted)

Figure 6.26: Threshold estimation error (dB) using DBM with K distributed data

For the Studentized method, the ($\cos^2$, $\cosh^2$, $\sinh^2$) triplet provides a quarter of a decibel of improvement over the best weighting pair when the SCM is used. However, at the lowest shape parameter, if the SCM is used both the full and excised libraries produce a threshold $\approx$ 0.5 dB lower than that of the best weighting pair. Therefore, in general the weighting pairs are better than the triplets of weightings in this case.

Weightings			Clairvoyant Cov. Matrix		Sample Cov. Matrix		
1	2	3	Full Lib.	Excised Lib.	Full Lib.	Excised Lib.	Δ Clair, SCM
cos	sinh	$\tanh^2$	1.67	1.77	-1.05	-0.99	-2.72
$\cos^2$	$\cosh^2$	$\sinh^2$	2.41	2.50	0.07	0.11	-2.34

Table 6.32: Average Threshold Error (dB) when K distributed data is fed into the Studentized weightings

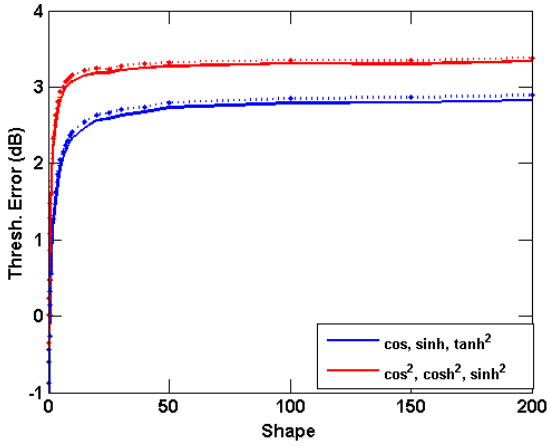

(a) Full Lib. w/CCM (solid) vs. Excised Lib. w/CCM (dotted)

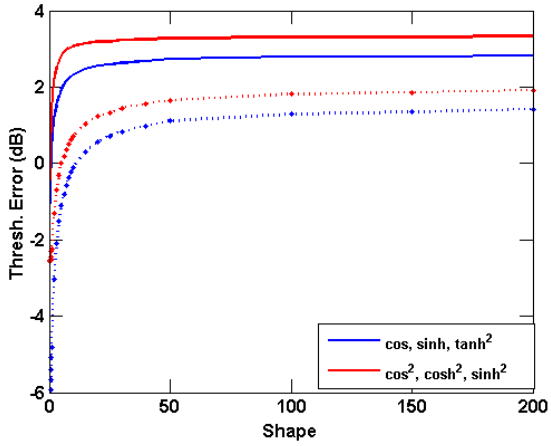

(b) Full Lib. w/ CCM (solid) vs. Full Lib. w/ SCM (dotted)

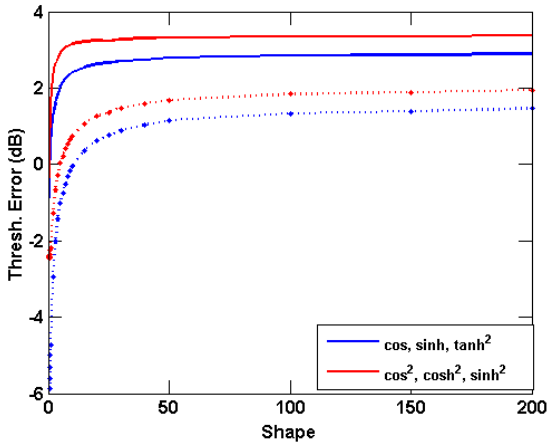

(c) Excised Lib. w/CCM (solid) vs. Excised Lib. w/ SCM (dotted)

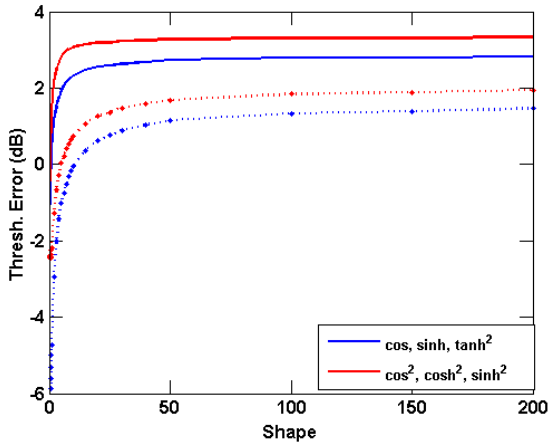

(d) Full Lib. w/CCM (solid) vs. Excised Lib. w/SCM (dotted)

Figure 6.27: Threshold estimation error (dB) using Studentized method with K distributed data

The EOA method produces similar results for the top pairs of weightings and the top triplets of weightings. The results for the (cosine, $\cos^2$, $\tanh^2$) triplet yields an average

threshold of ≈ 0.1 dB more than the average threshold for the (cosine, cosine^2) weighting pair for all values of the shape parameter.

Weightings			Clairvoyant Cov. Matrix		Sample Cov. Matrix		
1	2	3	Full Lib.	Excised Lib.	Full Lib.	Excised Lib.	Δ Clair, SCM
cos	$\cos^2$	$\tanh^2$	1.67	1.77	-1.05	-0.99	-2.72
$\sin e^2$	$\sinh^2$	$\tanh^2$	2.41	2.50	0.07	0.11	-2.34

Table 6.33: Average Threshold Error (dB) when K distributed data is fed into the EOA weightings

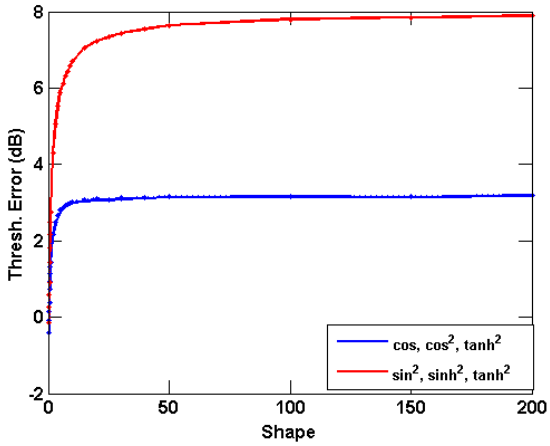

(a) Full Lib. w/CCM (solid) vs. Excised Lib. w/CCM (dotted)

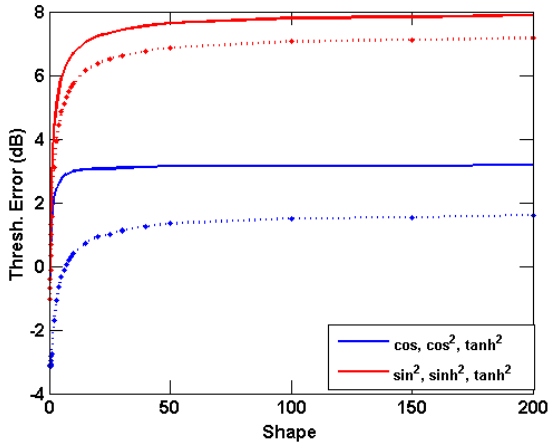

(b) Full Lib. w/ CCM (solid) vs. Full Lib. w/ SCM (dotted)

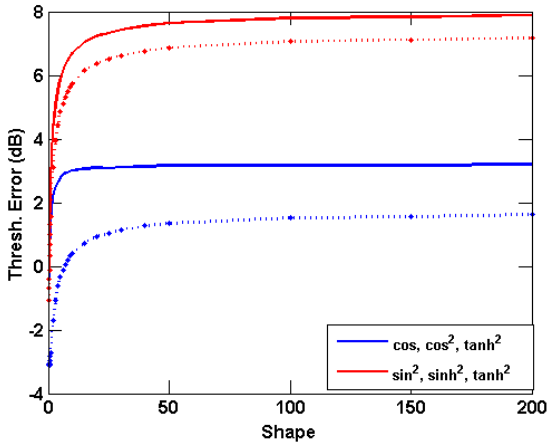

(c) Excised Lib. w/CCM (solid) vs. Excised Lib. w/ SCM (dotted)

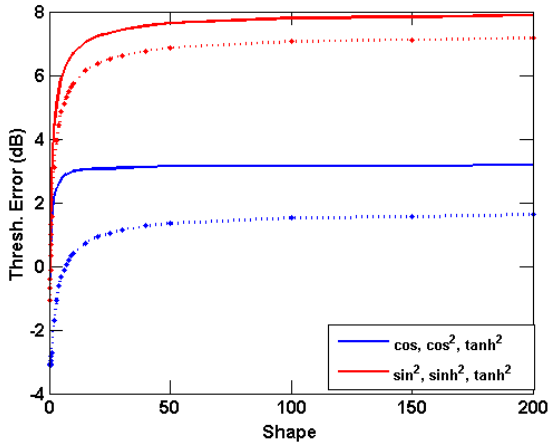

(d) Full Lib. w/CCM (solid) vs. Excised Lib. w/SCM (dotted)

Figure 6.28: Threshold estimation error (dB) using EOA method with K distributed data

6.4.3.3 Weibull Data

Upon examination of the average errors in threshold estimate given in Table 6.34, it appears that there is no advantage to using triplets of weighting functions rather than pairs of weighting functions when the WSOS transformation method is employed and Weibull data is present.

Weightings			Clairvoyant Cov. Matrix		Sample Cov. Matrix		SCM - DBM Weightings		Δ Clair, SCM	
1	2	3	Full Lib.	Excised Lib.	Full Lib.	Excised Lib.	Full Lib.	Excised Lib.	Δ WSOS	Δ DBM
cos	$\sinh^2$	$\tanh^2$	1.13	3.63	-0.47	-0.45	6.25	6.02	-1.60	5.12
cos	sine^2	$\tanh^2$	1.55	2.16	-0.83	-0.44	-2.22	-3.09	-2.39	-3.77
$\cos^2$	cosh	$\cosh^2$	1.47	1.86	-1.35	-1.32	-2.91	-2.97	-2.82	-4.38
$\cos^2$	sine^2	$\tanh^2$	0.98	3.90	-1.51	-0.87	4.37	4.77	-2.50	3.39
sine	sine^2	tanh	3.21	1.90	-1.19	-1.30	-3.09	-3.09	-4.40	-6.29

Table 6.34: Average Threshold Error (dB) when Weibull distributed data is fed into the WSOS and DBM weightings

However, when the threshold error is shown as a function of shape parameter, it is apparent that Table 6.34 does not tell the entire story. Comparing Figures 6.29a-6.29d with Figures 6.14a-6.14d, the use of weighting triplets appears to mitigate the wide swings in threshold estimation error (as a function of shape parameter) that arise when the SCM is used with the WSOS transformation method. In particular, the triplets of weightings tend not to overestimate the threshold. However, the underestimation of the threshold error will cause an increase in false alarms. It should be noted that the false alarms resulting from this increase will be less than the false alarms the detector would experience if the threshold for Gaussian data is used when Weibull clutter is present (*i.e.* the traditional radar assumption). Despite the improvement in performance over using pairs of weighting functions, the top triplets for the WSOS transformation method still provide worse threshold estimates than the top pair for the Studentization method when Weibull data is present.

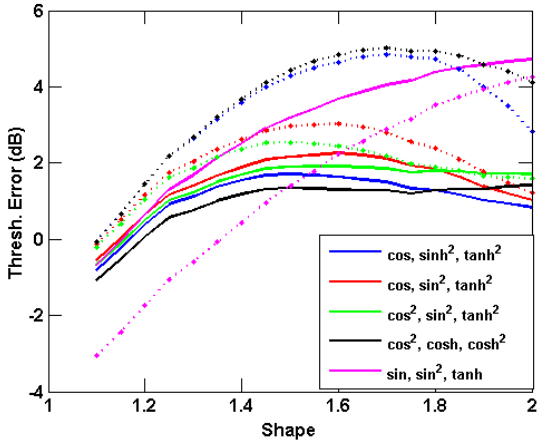

(a) Full Lib. w/CCM vs. Excised Lib. w/CCM (dotted)

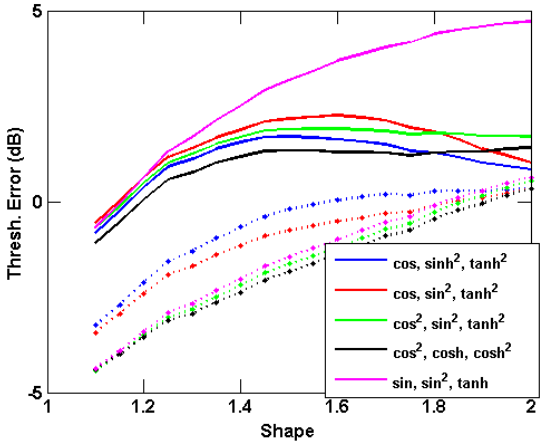

(b) Full Lib. w/ CCM vs. Full Lib. w/ SCM (dotted)

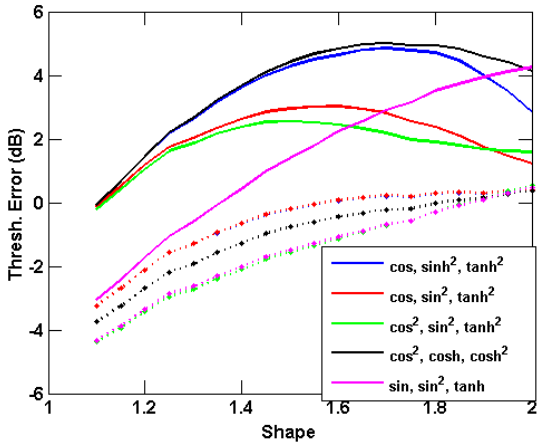

(c) Excised Lib. w/CCM vs. Excised Lib. w/ SCM (dotted)

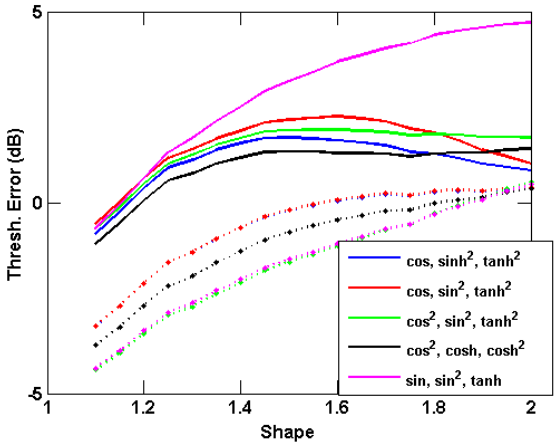

(d) Full Lib. w/CCM vs. Excised Lib. w/SCM (dotted)

Figure 6.29: Threshold estimation error (dB) using WSOS with Weibull distributed data

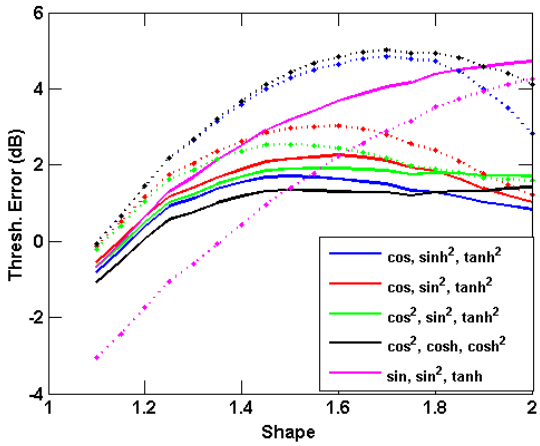

(a) Full Lib. w/CCM vs. Excised Lib. w/CCM (dotted)

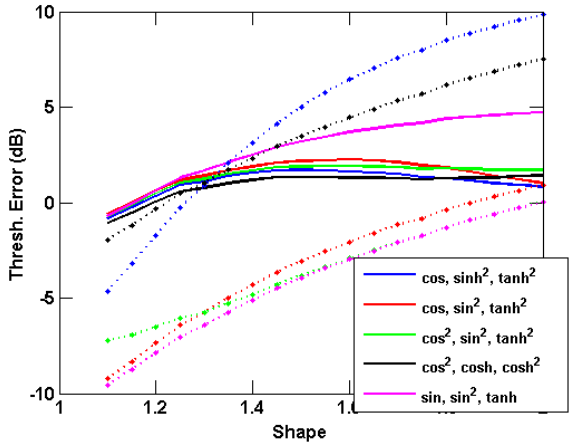

(b) Full Lib. w/ CCM vs. Full Lib. w/ SCM (dotted)

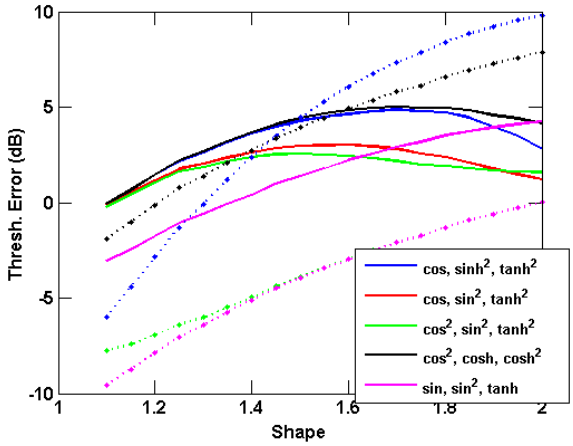

(c) Excised Lib. w/CCM vs. Excised Lib. w/ SCM (dotted)

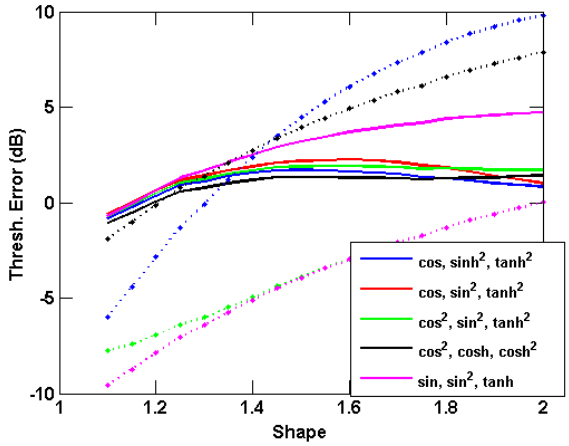

(d) Full Lib. w/CCM vs. Excised Lib. w/SCM (dotted)

Figure 6.30: Threshold estimation error (dB) using DBM with Weibull distributed data

Table 6.35 summarizes the average threshold error for the top triplets of weightings for the Studentization transformation method. There is a slight improvement ($\approx$ 0.1 dB) in using the triplet weightings as compared to the top pairs of weightings. Recall that the Studentized method was the best transformation method for the Weibull distribution when the weighting pairs were used in Section 6.3.3.3.

Weightings			Clairvoyant Cov. Matrix		Sample Cov. Matrix		
1	2	3	Full Lib.	Excised Lib.	Full Lib.	Excised Lib.	Δ Clair, SCM
cos	sinh	$\tanh^2$	0.97	0.87	-1.86	-1.95	-2.83
$\cos^2$	$\cosh^2$	$\sinh^2$	1.83	1.36	-0.79	-1.36	-2.62

Table 6.35: Average Threshold Error (dB) when Weibull distributed data is fed into the Studentized weightings

However, examination of Figures 6.31a-6.31d shows that the impact of the sample covariance matrix overwhelms the slight advantage gained through use of the extra weighting. Therefore, it does not appear that the Studentized method benefits from the use of three weighting functions as compared to two.

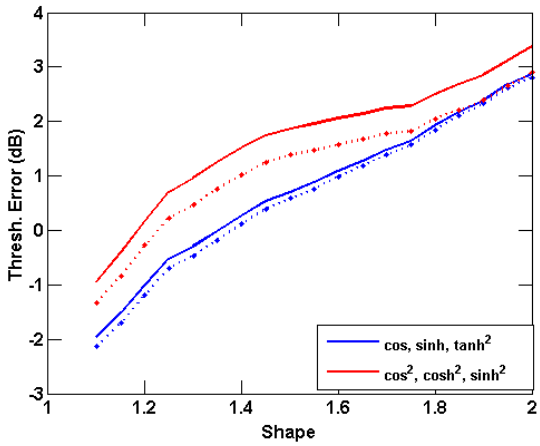

(a) Full Lib. w/CCM vs. Excised Lib. w/CCM (dotted)

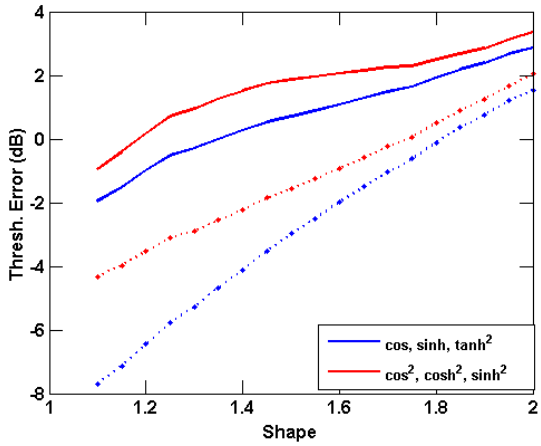

(b) Full Lib. w/ CCM vs. Full Lib. w/ SCM (dotted)

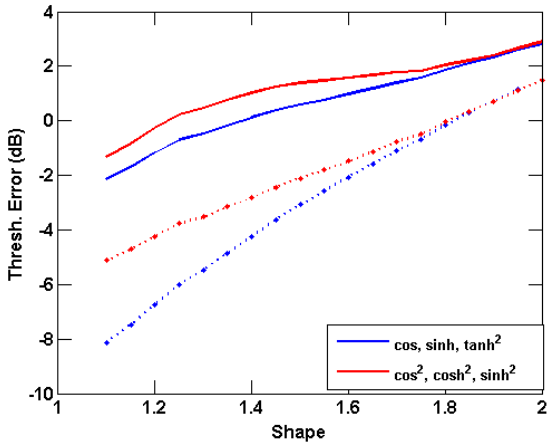

(c) Excised Lib. w/CCM vs. Excised Lib. w/ SCM (dotted)

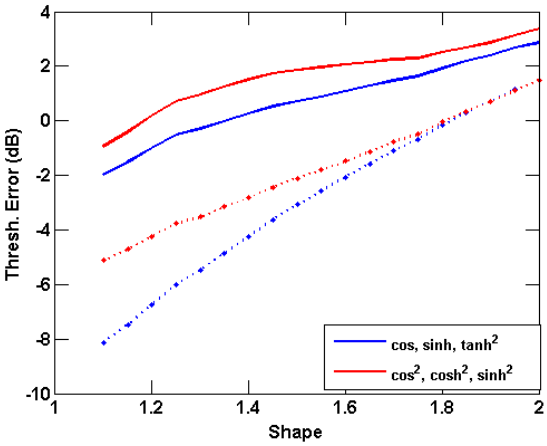

(d) Full Lib. w/CCM vs. Excised Lib. w/SCM (dotted)

Figure 6.31: Threshold estimation error (dB) using Studentized method with Weibull distributed data

Examining Tables 6.15 and 6.36 shows that when the CCM is used, there is a slight improvement (≈ 0.07 dB) when the (cos, $\cos^2$, $\tanh^2$) triplet of weightings is used compared to when the weighting pair (cos, $\cos^2$) is employed. However, this slight improvement comes at the cost of a performance degradation when compared to the estimate given by the weighting pair ($\cos^2$, $\tanh^2$). The top weighting triplet does perform better than either pair when the SCM is used, but the average threshold error is only reduced by < 0.1 dB.

Weightings			Clairvoyant Cov. Matrix		Sample Cov. Matrix		
1	2	3	Full Lib.	Excised Lib.	Full Lib.	Excised Lib.	Δ Clair, SCM
cos	$\cos^2$	$\tanh^2$	1.70	1.34	-1.17	-1.59	-2.88
sine^2	$\sinh^2$	$\tanh^2$	5.31	5.49	4.20	4.39	-1.12

Table 6.36: Average Threshold Error (dB) when Weibull distributed data is fed into the EOA weightings

Figures 6.32a-6.32d then illustrate the results of Table 6.36 as a function of shape parameter. Once more, comparing Figures 6.32a-6.32d to Figures 6.17a-6.17d there is no real improvement in performance given by adding an extra weighting function.

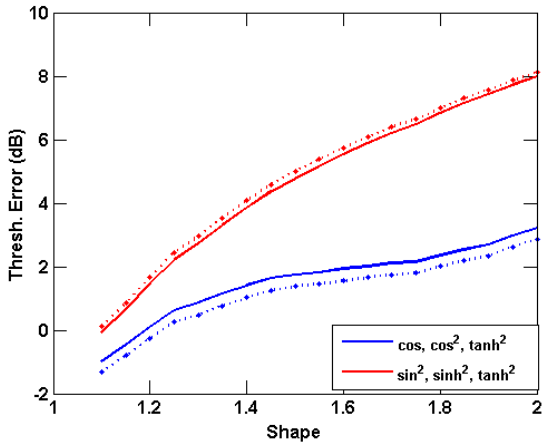

(a) Full Lib. w/CCM vs. Excised Lib. w/CCM (dotted)

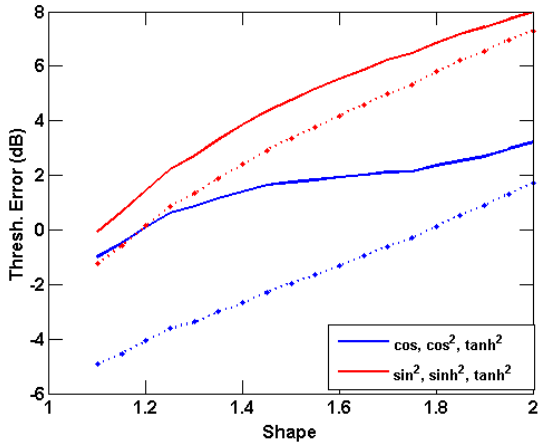

(b) Full Lib. w/ CCM vs. Full Lib. w/ SCM (dotted)

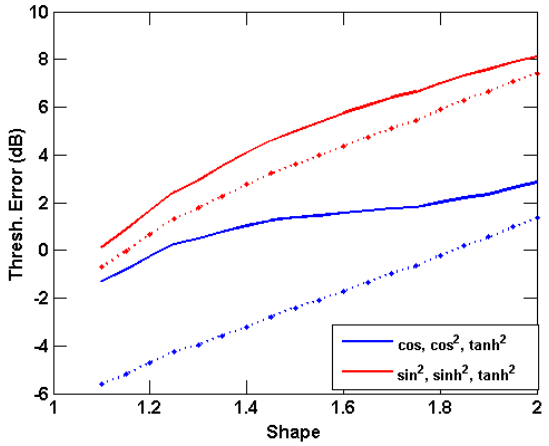

(c) Excised Lib. w/CCM vs. Excised Lib. w/ SCM (dotted)

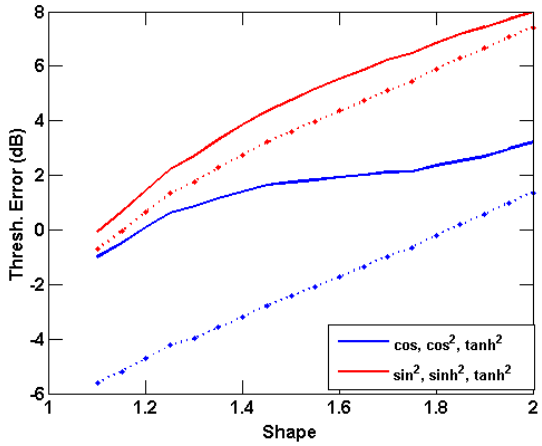

(d) Full Lib. w/CCM vs. Excised Lib. w/SCM (dotted)

Figure 6.32: Threshold estimation error (dB) using EOA method with Weibull distributed data

In general, if Weibull data is present the addition of the extra weighting function does not greatly improve the threshold estimation accuracy if the covariance matrix is known. For certain transformation methods (*e.g.* the EOA) the estimation accuracy improves by a small amount for select situations. However, this marginal improvement does not necessarily justify the increased complexity or computational cost caused by the additional weighting function.

On the other hand, if the covariance matrix is not known, there is a significant advantage

to using the triplets of weightings with the WSOS transformation method. Unfortunately, this added advantage does not result in superior average threshold estimates when compared to the (cosine, sine^2) weighting pair transformed via the Studentization method. Therefore, it is not necessary to use triplets of weighting functions when Weibull data is present.

6.4.3.4 Pareto Data

It is apparent from comparing Tables 6.37 and 6.16 that the addition of the cosh weighting function to the weighting pair (cosine^2, cosh^2) leads to a small improvement (up to 0.3 dB depending on the scenario) in the threshold estimates given when the WSOS transformation method is used. However the DBM performance changes from an average detection loss of 6.3 dB to an average threshold estimate error of -2.84 dB (*i.e.* an underestimate). Therefore, the DBM method used with a pair of weighting functions causes an average detection loss, but when a triplet of weightings are employed the loss becomes an average increase in the probability of false alarm.

Weightings			Clairvoyant Cov. Matrix		Sample Cov. Matrix		SCM - DBM Weightings		Δ Clair, SCM	
1	2	3	Full Lib.	Excised Lib.	Full Lib.	Excised Lib.	Full Lib.	Excised Lib.	Δ WSOS	Δ DBM
cos	sinh^2	$\tanh^2$	-1.18	-1.32	-1.95	-2.07	6.95	6.95	-0.76	8.14
cos	sine^2	$\tanh^2$	-0.53	-1.05	-1.90	-2.13	-1.94	-1.94	-1.36	-1.40
$\cos^2$	cosh	cosh^2	0.07	-0.48	-1.61	-2.01	-2.84	-2.84	-1.68	-2.90
$\cos^2$	sine^2	$\tanh^2$	-0.70	-0.88	-1.91	-2.21	4.65	4.65	-1.21	5.35
sine	sine^2	tanh	3.04	2.60	-1.58	-1.93	-2.86	-2.86	-4.62	-5.89

Table 6.37: Average Threshold Error (dB) when Pareto distributed data is fed into the WSOS and DBM weightings

Comparing Figures 6.33a-6.33d to Figures 6.18a-6.18d, there is little change in behaviour of the average threshold estimate as a function of shape parameter between the top triplets of weightings and the top pairs of weightings when the WSOS transformation method is used.

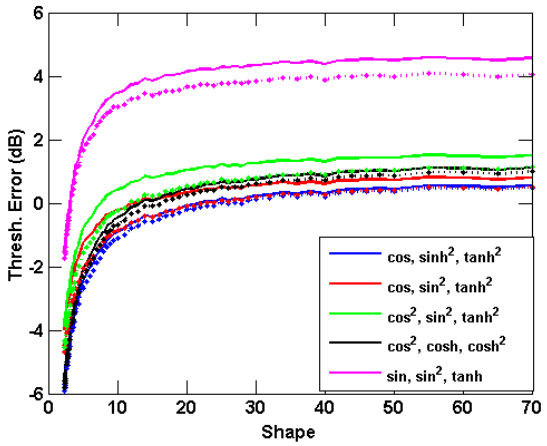

(a) Full Lib. w/CCM vs. Excised Lib. w/CCM (dotted)

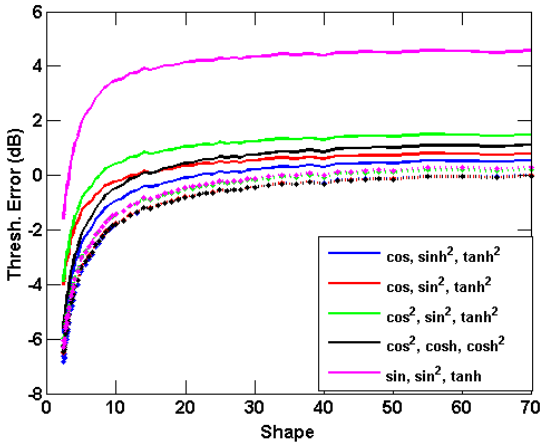

(b) Full Lib. w/ CCM vs. Full Lib. w/ SCM (dotted)

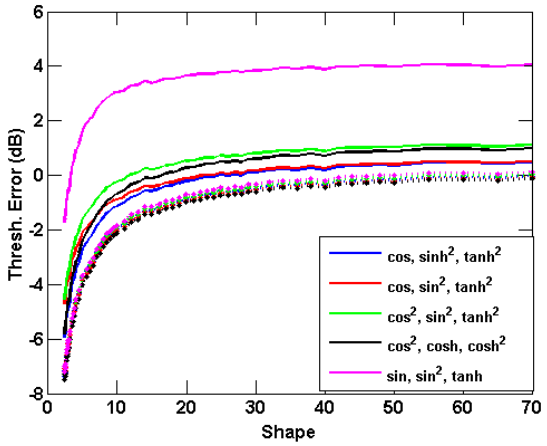

(c) Excised Lib. w/CCM vs. Excised Lib. w/ SCM (dotted)

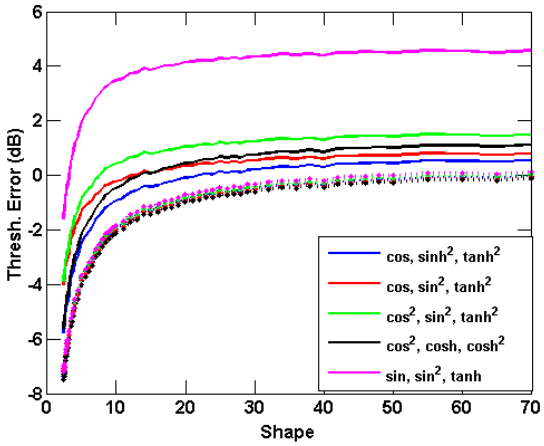

(d) Full Lib. w/CCM vs. Excised Lib. w/SCM (dotted)

Figure 6.33: Threshold estimation error (dB) using WSOS with Pareto distributed data

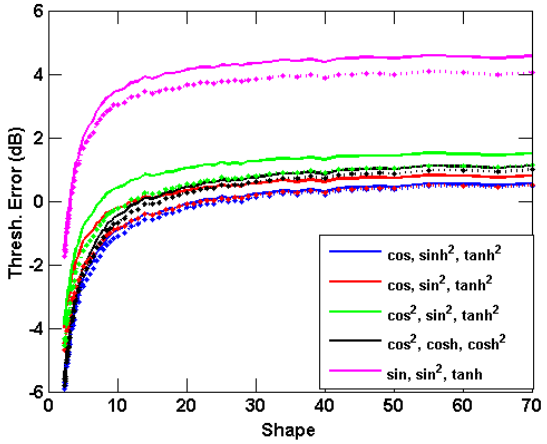

(a) Full Lib. w/CCM vs. Excised Lib. w/CCM (dotted)

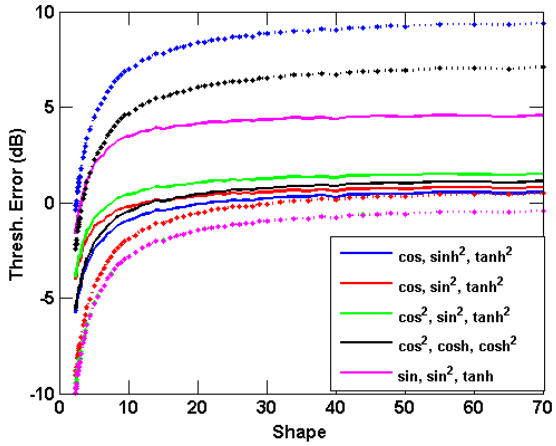

(b) Full Lib. w/ CCM vs. Full Lib. w/ SCM (dotted)

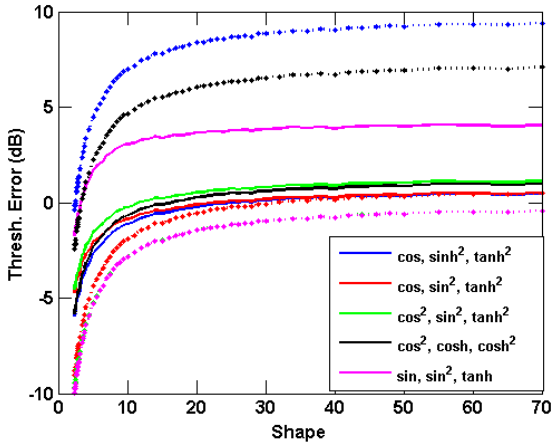

(c) Excised Lib. w/CCM vs. Excised Lib. w/ SCM (dotted)

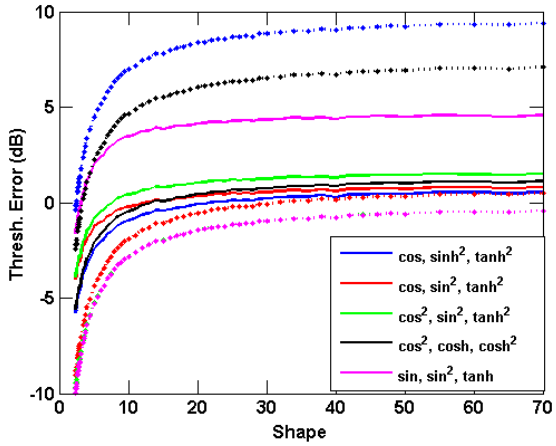

(d) Full Lib. w/CCM vs. Excised Lib. w/SCM (dotted)

Figure 6.34: Threshold estimation error (dB) using DBM with Pareto distributed data

Table 6.38 shows the average threshold error for the top triplets of weightings when the Studentization transformation method is used. From comparing Table 6.38 to Table 6.17, note that the top triplet weightings are not formed from "merging" the top pairs of weightings. However, the final performance is still very close.

Weightings			Clairvoyant Cov. Matrix		Sample Cov. Matrix		
1	2	3	Full Lib.	Excised Lib.	Full Lib.	Excised Lib.	Δ Clair, SCM
cos	sinh	$\tanh^2$	1.27	1.07	-1.01	-1.24	-2.28
$\cos^2$	$\cosh^2$	$\sinh^2$	1.90	1.71	-0.28	-0.37	-2.18

Table 6.38: Average Threshold Error (dB) when Pareto distributed data is fed into the Studentized weightings

Comparing Figures 6.35a-6.35d to Figures 6.20a-6.20d, the average threshold error as a function of shape parameter when the triplets of weightings are used in conjunction with the Studentization method is very close to the performance when the top pairs of weightings are used. However, there is no real improvement to make up for the increased complexity added by the use of the extra weighting function.

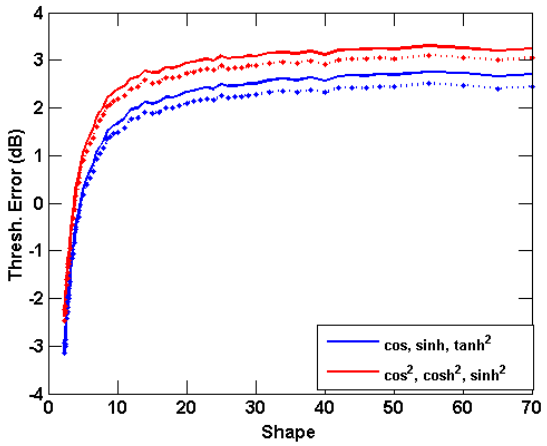

(a) Full Lib. w/CCM vs. Excised Lib. w/CCM (dotted)

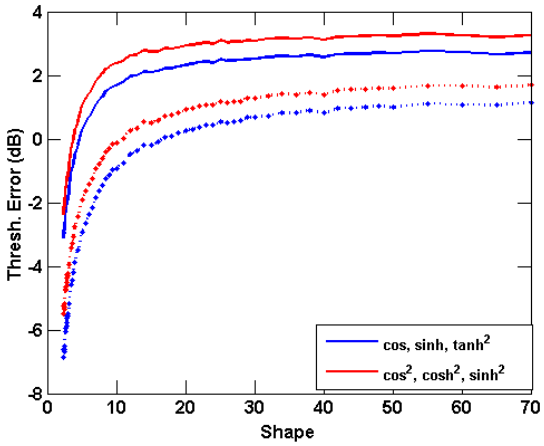

(b) Full Lib. w/ CCM vs. Full Lib. w/ SCM (dotted)

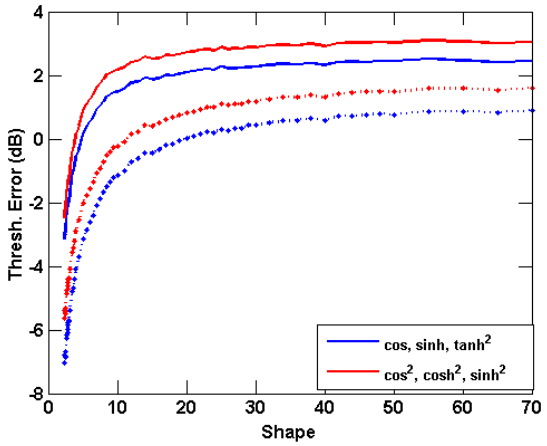

(c) Excised Lib. w/CCM vs. Excised Lib. w/ SCM (dotted)

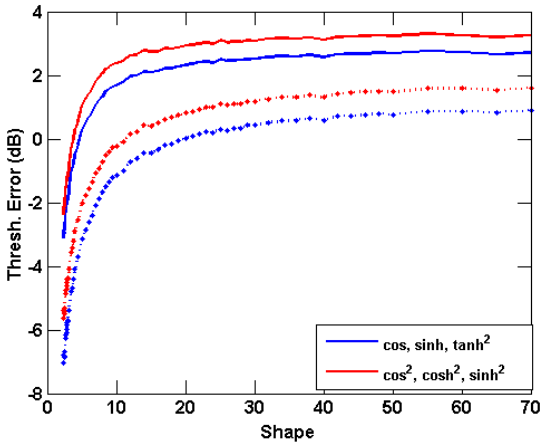

(d) Full Lib. w/CCM vs. Excised Lib. w/SCM (dotted)

Figure 6.35: Threshold estimation error (dB) using Studentized method with Pareto distributed data

In contrast to the Studentization method, comparing Tables 6.39 and 6.18 shows that the top two triplets of weighting functions for the EOA transformation method are combinations of the top three pairs of weighting functions. However, the merging of the top pairs into triplets of weighting functions actually slightly degrades the average threshold estimate.

Weightings			Clairvoyant Cov. Matrix		Sample Cov. Matrix		
1	2	3	Full Lib.	Excised Lib.	Full Lib.	Excised Lib.	Δ Clair, SCM
cos	$\cos^2$	$\tanh^2$	1.81	1.49	-0.58	-0.76	-2.38
sine^2	$\sinh^2$	$\tanh^2$	5.58	5.62	4.72	4.71	-0.86

Table 6.39: Average Threshold Error (dB) when Pareto distributed data is fed into the EOA weightings

Figures 6.36a-6.36d show the average threshold error for the top triplets of weighting functions used in conjunction with the EOA transformation method as a function of shape parameter when Pareto distributed data is present. Compared to Figures 6.21a-6.21d, the error yielded by the triplets is similar, if slightly greater.

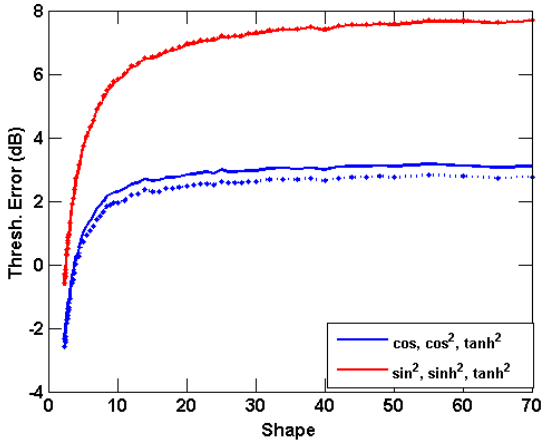

(a) Full Lib. w/CCM vs. Excised Lib. w/CCM (dotted)

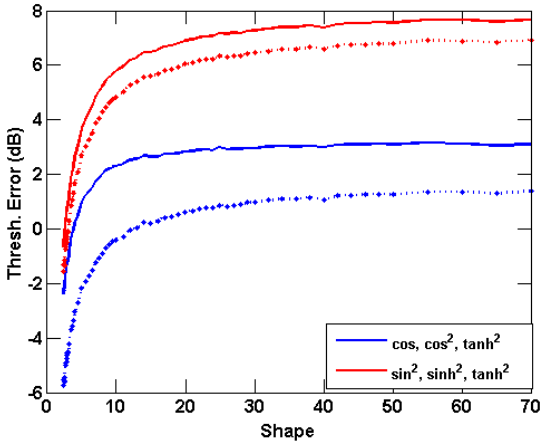

(b) Full Lib. w/ CCM vs. Full Lib. w/ SCM (dotted)

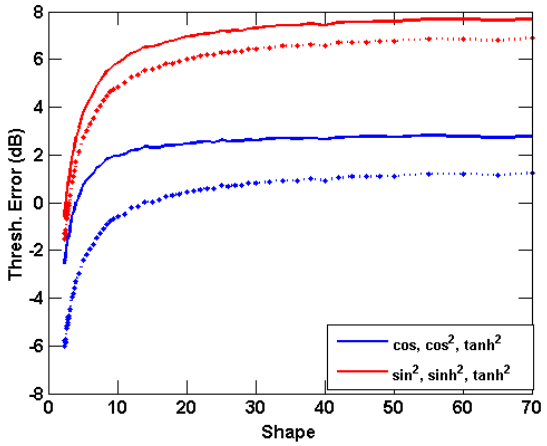

(c) Excised Lib. w/CCM vs. Excised Lib. w/ SCM (dotted)

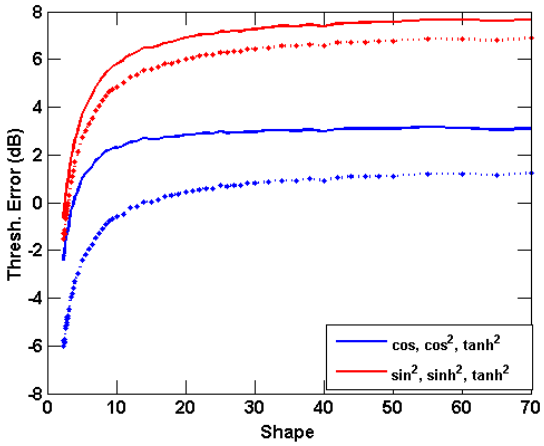

(d) Full Lib. w/CCM vs. Excised Lib. w/SCM (dotted)

Figure 6.36: Threshold estimation error (dB) using EOA method with Pareto distributed data

Using triplets of weightings instead of pairs of weightings resulted in a slight increase in threshold estimation accuracy when the WSOS transformation method was employed. However, the top pair of weighting functions combined with the Studentization method still gives the best threshold estimate for Pareto data when compared to all other transformation methods and weighting function combinations. Examination of the Studentization method shows that there are not necessarily superior weighting functions, as the top triplets were different than the top pairs. However, the top triplets of the EOA method *were* combinations

of the top three pairs of weightings. Therefore, more work is needed to isolate the effects of the individual weightings.

6.4.3.5 Lognormal Data

Table 6.40 shows the average threshold error in the estimates for the Lognormal distribution when the WSOS and DBM transformation methods are used and the endpoints are generated from triplets of weighting functions. Comparing the results to Table 6.19, most of the average threshold estimates given by the triplets yield little improvement to actual degradation relation to the top weighting pairs. However, the (sine, sine^2, tanh) triplet provides an excellent estimate when the true covariance matrix is known.

Weightings			Clairvoyant Cov. Matrix		Sample Cov. Matrix		SCM - DBM Weightings		Δ Clair, SCM	
1	2	3	Full Lib.	Excised Lib.	Full Lib.	Excised Lib.	Full Lib.	Excised Lib.	Δ WSOS	Δ DBM
cos	sinh^2	$\tanh^2$	-5.57	-5.64	-6.49	-6.52	-0.77	-0.77	-0.92	4.80
cos	sine^2	$\tanh^2$	-3.58	-3.78	-5.79	-5.91	-9.31	-9.31	-2.21	-5.73
$\cos^2$	cosh	$\cosh^2$	-3.34	-3.54	-5.30	-5.45	-9.48	-9.48	-1.96	-6.14
$\cos^2$	sine^2	$\tanh^2$	-5.30	-5.38	-5.60	-5.74	-2.62	-2.62	-0.30	2.68
sine	sine^2	tanh	-1.48	-1.79	-5.42	-5.56	-10.22	-10.22	-3.94	-8.74

Table 6.40: Average Threshold Error (dB) when Lognormal distributed data is fed into the WSOS and DBM weightings

In contrast, as Table 6.41 shows, there is no benefit to using triplets of weightings instead of pairs of weightings when the Studentization method is employed.

Weightings			Clairvoyant Cov. Matrix		Sample Cov. Matrix		
1	2	3	Full Lib.	Excised Lib.	Full Lib.	Excised Lib.	Δ Clair, SCM
cos	sinh	$\tanh^2$	-2.68	-2.68	-6.30	-6.31	-3.62
$\cos^2$	$\cosh^2$	sinh^2	-1.96	-2.00	-4.64	-4.67	-2.69

Table 6.41: Average Threshold Error (dB) when Lognormal distributed data is fed into the Studentized weightings

Finally, the average threshold error estimates for the EOA method are shown in Table 6.42. There is a slight (< 0.1 dB) improvement in average threshold estimate for using triplets of weightings versus using pairs of weightings with the EOA method. Overall, the

EOA method gives the best average threshold estimates for the Lognormal distributed data whether pairs or triplets of weighting functions are used.

Weightings			Clairvoyant Cov. Matrix		Sample Cov. Matrix		
1	2	3	Full Lib.	Excised Lib.	Full Lib.	Excised Lib.	Δ Clair, SCM
cos	$\cos^2$	$\tanh^2$	-1.97	-2.05	-4.89	-4.94	-2.92
sine^2	$\sinh^2$	$\tanh^2$	-0.70	-0.77	-1.45	-1.50	-0.75

Table 6.42: Average Threshold Error (dB) when Lognormal distributed data is fed into the EOA weightings

6.5 Discussion of COSMiC Results

This chapter provided an initial exploration of the two COSMiC algorithms: distribution identification and threshold estimation. These algorithms are designed to aid a cognitive radar in adapting to commonly encountered non-Gaussian clutter distributions. In particular, the non-Gaussian distributions examined were largely chosen from the spherically invariant random vector (SIRV) class, with the exception of the Lognormal distribution.

Each algorithm has four constituent transformations of order statistics. These transformations are the weighted sum of order statistics (WSOS), divide by mean (DBM), Studentization, and Extended Ozturk Algorithm (EOA). Applying each transformation to the order statistics of a set of power estimates (via the quadratic form or generalized inner product (GIP) of a complex random vector) yields a set of endpoints that can be parametrized by the combination of the weighting function(s) used and the distribution/shape parameter of the underlying data. This set of endpoints is collected into a series of libraries. Each endpoint in the libraries is addressed via the dimensionality of the endpoint. The dimensionality of the endpoint corresponds to the number of weighting functions used to form the endpoint. Here only the performances of the individual transformations were considered, leaving the fusion stage of the algorithm to future work.

6.5.1 Discussion of Distribution Identification

In the context of this chapter, the distribution identification algorithm performed poorly. In particular, increasing the number of weightings used to form the endpoint did not correspond to an increased accuracy in distribution identification. However, in Chapter 5 it was shown that the libraries formed by each transformation method resulted in unique, separated curves associated with each distribution.

Recall that in all test cases in this chapter, the quadratic form of length $L = 4$ complex random vectors were grouped into sets of $N = 4L = 16$. In addition, note that individual SIRV distributions (with the same dimensionality) are only separated by the form of the modulating random variable. Thus, both the number of draws of the modulating random variable and the number of random vectors used to estimate the covariance matrix were low. Therefore, the scenarios examined were in a low sample support regime. In this context, it appears that the distribution identification algorithm requires a larger sample support than was examined.

It should be emphasized that discriminating between different SIRV distributions is inherently ambiguous. As each multivariate distribution is uniquely identified by the modulating random variable v and the dimensionality L, the SIRV can be compressed to the scalar, quadratic form with no loss in information. In addition, many SIRVs (*e.g.* K, Pareto, Weibull) possess shape parameters with infinite support. Therefore, it is inevitable that the tails of the SIRVs overlap for some values of the shape parameters. Note that the value of shape parameter where the overlap occurs also depends on the desired probability of false alarm. This ambiguity is exploited by the the threshold estimation COSMiC algorithm, but is a hindrance when trying to determine which SIRV generated a set of test data. Proper characterization of the ambiguity between SIRVs will be a focus of future work.

Recall that in Chapter 5 the endpoints reported for each library corresponded to an average of endpoints generated via Monte Carlo. Therefore, to parallel that approach, consider the prospect of increasing the number of sets of order statistics collected from one set to K

sets. In such a scenario, the GIP for NK range cells would be generated, and K sets of N order statistics would be generated. For each transformation method and set of weightings used, K endpoints would be generated and averaged together. The estimated distribution could then be estimated from each transformation method.

Such a scheme necessarily introduces a trade space between the size of the order statistic set used to generate the endpoints and the number of sets collected (*i.e.* independent endpoints generated). This approach raises a number of interesting questions. For instance, would a library formed from the total number of order statistics (*i.e.* NK) yield better results than averaging the K endpoints generated from sets of N order statistics? Of course, the NK samples correspond to power estimates from range cells. Each estimate is assumed to be drawn from a homogeneously distributed region. Due to the need for homogeneity, there is a limit in the number of available range cells.

One solution is to generate a single library with a minimum number (N) of required homogeneous range cells. Suppose there are J available homogeneous range cells to form an estimate. The available range cells could be arranged into $K = \left\lfloor \frac{J}{N} \right\rfloor$ groups (*i.e.* the floor of the ratio). The endpoints generated from each group could then be averaged together, yielding a flexible estimate based on available data. However, in such a framework the detection and impact of non-homogeneous data would have to be considered.

Increased sample support in the number of samples in the random vector (*i.e.* slow time samples) may also help the performance of the distribution identification COSMiC algorithm. However, it should be noted that increasing the number of slow time samples implicitly requires an increase in the number of range cells (*i.e.* fast time samples) available. The additional range cells are needed due to the increased dimensionality of the needed covariance matrix estimate. Once more, care must be taken to ensure homogeneous data.

6.5.2 Discussion of Threshold Estimation

Overall, the threshold estimation COSMiC algorithm was much more effective than the distribution identification COSMiC algorithm. As a detection threshold is the integral of the tail of a null distribution, the threshold estimation algorithm can exploit the ambiguity between tails of SIRVs. A key finding of this chapter is that all of the average estimates given by the various combinations of transformation method/weighting pairs examined provide some improvement in the rate of false alarms for heavy tailed clutter.

However, the key metric used to evaluate the transformation methods and choices of weighting functions was the robustness of the estimate. In other words, a desirable transformation method/weighting pair provides an accurate threshold in both spiky and Gaussian or near-Gaussian distributed clutter. The library format used necessarily introduces an estimation bias. There are no distributions reported with a lighter tail than the Gaussian distribution. Therefore, in the presence of high shape parameter (*i.e.* near-Gaussian) clutter, a misestimate of the shape parameter will more likely produce a threshold estimate higher than the true threshold, rather than lower. This threshold estimate is further biased by the non-linear relationship between the shape parameter and the detection threshold (see Chapters 3 and 4 for more details). In addition, when Gaussian data is present, if any endpoint in the library is chosen other than the Gaussian endpoint the resulting threshold estimate will be too high (and therefore result in a detection loss).

Conversely, the heavy tailed Lognormal distribution (which is not a SIRV) suffers from the opposite problem. Recall that for the parameters used (*i.e.* $L = 4$ length vector) the Lognormal distribution requires a detection threshold ≈ 10 dB greater than the threshold in Gaussian clutter to maintain an identical probability of false alarm $P_{fa} = 10^{-5}$. In addition, the Lognormal distribution is the distribution with the heaviest tail in the library. Note that the library was thus limited to restrict the considered distributions to those that may be realistically encountered by a radar system. Due to this limitation, if the library chooses any other endpoint the resultant threshold estimate will be lower than the true threshold.

Therefore, in the absence of a perfect identification any threshold estimate for the Lognormal will necessarily be biased towards a lower threshold than the true threshold. While this trend is problematic, the Lognormal distribution is not a SIRV. Due to the physical justification for the SIRV architecture, there remains the possibility of an undiscovered SIRV distribution that has an instantiation with a similar or identical tail to the Lognormal distribution. If such a SIRV exists, distribution fitting techniques may provide equally good fits for measured data to the Lognormal distribution and the SIRV distribution.

It was noted that the use of the sample covariance matrix had a large impact on the threshold estimate. The nature of the impact was varied, but with the exception of the Gaussian distribution, it was largely negative. Therefore, an important point of future research is to investigate and incorporate more effective covariance matrix estimation techniques. It was noted that the expectation-maximization (EM) algorithm of [75, 114] was informally attempted, but the results were omitted. The selection of length $L = 4$ SIRVs resulted in too few samples with which to estimate the modulating random variable. Therefore, the EM did not work effectively. In the future, the number of slow-time samples will be increased so that the EM method may be incorporated.

The choice of weighting functions and transformation method proved crucial for each of the distributions examined. However, it was noted that increasing the number of weightings from two to three did not necessarily correspond to an increase in threshold estimation accuracy. Further, the accuracy of the estimate varied from distribution to distribution. The best transformation methods and weighting pairs for each distribution are given in Table 6.43.

Distribution	Transformation Method	Weighting Pair
Gaussian	WSOS	(cos, $\tanh^2$)
		(cos, sine^2)
		(sinh, $\tanh^2$)
	Studentization	($\cos^2$, sine^2)
K	WSOS	(cos, $\tanh^2$)
		(cos, sine^2)
	Studentization	($\cos^2$, sine^2)
Weibull	Studentization	($\cos^2$, sine^2)
Pareto	Studentization	($\cos^2$, sine^2)
Lognormal	EOA	(sine^2, $\sinh^2$)
	DBM	($\cos^2$, $\cosh^2$)
		(cos, $\tanh^2$)

Table 6.43: Summary of the best COSMiC transformation methods and weightings

Therefore, in general, for SIRV clutter the Studentization method used in conjunction with the ($\cos^2$, sine^2) appears to be the best overall transformation method and weighting pair combination with which to estimate the threshold.

Note that for the Gaussian distribution, the Studentization method used in conjunction with the ($\cos^2$, sine^2) weighting pair results in a detection loss of 3.41 dB when the clairvoyant covariance matrix is used and 2.07 dB when the sample covariance matrix is used. This detection loss corresponds to an additional 2.6 dB detection loss compared to the WSOS transformation with the (cos, $\tanh^2$) weighting pair and clairvoyant covariance matrix, or an additional 1.5 dB detection loss in the same case but with the sample covariance matrix.

For the Lognormal distribution, this case results in a threshold estimate 1.9 dB below the optimal threshold when the clairvoyant covariance matrix is used and 4.15 dB below the optimal threshold the sample covariance matrix is used. Note that in this case the optimal threshold is 10 dB above that of the Gaussian distribution. Therefore, in contrast to the default, non-cognitive/knowledge aided approach, the Studentization transformation method and($\cos^2$, sine^2) weighting function pair still results in a useful estimate.

For all distributions, the threshold estimate given by each transformation method and

weighting pair did not change dramatically if the distribution was removed from the library. In fact, the use of the sample covariance matrix had a far greater impact on the threshold estimate. Therefore, it is concluded that the library contained sufficient distributions to infer the tail of an encountered distribution that was not in the library. This encouraging result indicates that the COSMiC algorithm has the potential to form the basis for a cognitive radar detector.

There appears to be little to no benefit to using more than two weighting functions to generate an endpoint. Notice that there are few degrees of freedom available to the SIRV class. Therefore, it is logical to encounter rapidly diminishing returns from adding degrees of freedom (*i.e.* additional dimensionality from multiple weighting functions) to the library. However, there may be additional effective weightings that were not explored here (*e.g.* logarithmic weighting functions). Therefore, the relationship between the information gained from using a particular weighting function and the tail of the pdf of the SIRV should be explored (see Chapter 5 for a high level discussion of this topic).

These initial results are based on examining a large range of possible shape parameters. These shape parameters were chosen for their relation to the required detection threshold values. However, this wide range of shape parameters is a primary source of difficulty in estimating the threshold. Note that the selected shape parameters may not be realistic. In particular, the shape parameters used here for the K and Weibull distributions have all been measured in real data. However, the threshold needed depends on the dimensionality of the SIRV, as well as the shape parameter. Therefore, without taking into account the dimensionality of the measured data, it is difficult to make an accurate comparison to the range of measured results and the simulated results. The selection of realistic shape parameters, and the corresponding impact on the COSMiC algorithms, should be explored in future work.

6.6 Conclusions

This chapter laid out a formal definition for two COSMiC algorithms: distribution identification and threshold estimation. Each algorithm consisted of a group of four libraries formed from a known set of distributions. Each endpoint is generated by passing candidate data from each distribution through non-linear, order statistic based transformations that are then compressed to a single point through a weighted sum. The endpoints in the library are formed by finding the expected value of the generated endpoints via Monte Carlo simulation. To evaluate the algorithms, the impact of the type and number of weighting distributions were considered along with the different types of transformation methods.

Ultimately the results of this chapter are mixed. The inherent ambiguity between SIRVs was exploited by the threshold estimation algorithm, but caused problems for the distribution identification algorithm. Therefore, under the assumptions and parameters used here the distribution identification COSMiC algorithm was not effective. However, the threshold estimation COSMiC algorithm proved effective in forming accurate thresholds over a wide range of distributions. It appears that the choice of weighting function impacts the performance of the algorithm more than the number of weighting functions used (*i.e.* the dimensionality of the library).

In addition, it was shown that the threshold for a distribution that was *not* in the library could be inferred based on the behaviour of the other distributions in the library. This inference capability provides a potential foundation upon which to build a cognitive radar detector.

Further work is needed in improving the estimate of the covariance matrix, as well as characterizing the impact made by using an estimated covariance matrix. In addition, the scenarios examined here made use of extremely low sample support. The sample support should be varied to properly characterize the impact at various sample support regimes. Also, more work is needed to examine the impact of the weighting functions and to find better methods with which to select effective weighting functions. Finally, the overall COSMiC

algorithm should fuse of the results of the individual transformation methods. The fusion of the output of the different libraries should be considered in future work.

These conclusions will be restated in Chapter 9.

Chapter 7

Neural Network Approaches

In many respects, the human brain is unmatched as a pattern recognition machine. Naturally, researchers have long been interested in emulating the structure of the brain in order to improve machine based pattern recognition. The neural network is an early, prominent example of brain inspired processing [81, 116–120]. A neural network is formed as a directed graph. The nodes of the graph are neurons, which are connected by weighted links. Neural networks are commonly used to perform pattern recognition, function approximation, and control applications [116].

At the heart of the neural network is the model of the neuron. In general, the output of a neuron is equal to the sum of weighted inputs passed through a non-linear activation function. The graphical model of the k^{th} neuron of a neural network is shown in Figures 7.1a and 7.1b. The inputs are denoted as the length L vector $\mathbf{q}$, with the corresponding weight vector $\mathbf{w}_k$. The scalar w_{k0} is the bias term for the neuron.

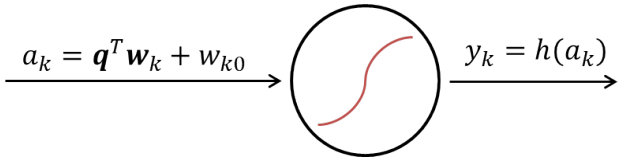

(a) Simple perceptron model

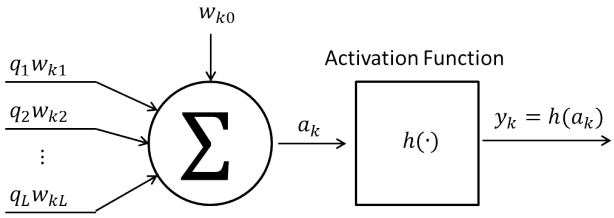

(b) Expanded perceptron model

Figure 7.1: Simple and expanded perceptron models

The earliest neuron model was called the McCulloch-Pitts model [116, 117], which was based on a hard limiting threshold activation function. Mathematically, this activation function is equivalent to the Heavyside step function

$$y_k = \begin{cases} 1 & \text{if } a_k \geq 0, \\ 0 & \text{if } a_k < 0. \end{cases} \tag{7.1}$$

The first neural "network" was Rosenblatt's perceptron, which consisted of a single McCulloch-Pitts neuron [116, 119, 120]. The perceptron proved useful in attacking binary classification problems [116, 121]. However, the two classes must be linearly separable. In other words, consider data $\mathbf{x}$ which has been generated by one of two classes. Rosenblatt's perceptron can be trained to form a decision hyperplane of the form

$$\sum_{i=1}^{L} w_i x_i + b = 0. \tag{7.2}$$

If the boundary separating the two classes of data cannot be expressed in the form of (7.2), then the perceptron cannot correctly classify the data. A classic example of such a non-linearly separable problem is the XOR function. As such, a single perceptron cannot be trained to mimic the XOR function. The shortfalls of the perceptron were pointed out in

the well known work [121], which was largely responsible for holding back interest in neural network research until the 1980s [116].

The next big improvement to neural networks was the multilayer perceptron model. As the name suggests, a multilayer neural network possesses one or more "hidden" layers of neurons in addition to an input and output layer. A simple example of a multilayer neural network is shown in Figure 7.2. Note the superscripts for each weight correspond to the layer in the neural network.

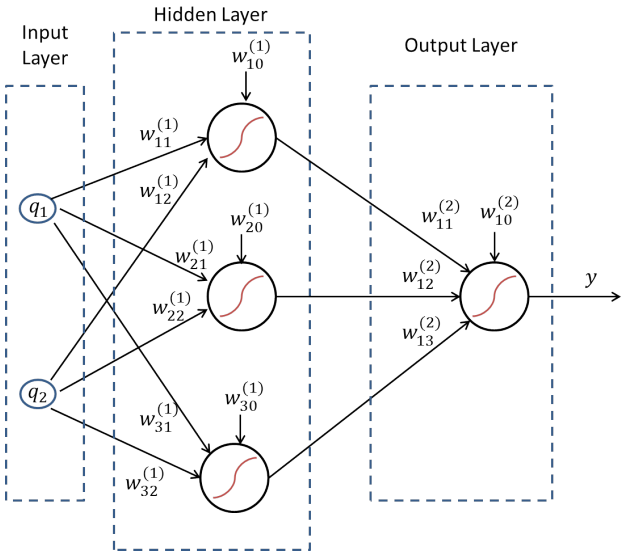

Figure 7.2: Example multilayer perceptron neural network

Generally, the output of the k^{th} output neuron of a 2 layer neural network is given as

$$y_k(\mathbf{q}, \mathbf{w}) = \sigma\left(\sum_{j=1}^{M} w_{kj}^{(2)} h\left(\sum_{i=1}^{L} w_{ji}^{(1)} q_i + w_{j0}^{(1)}\right) + w_{k0}^{(2)}\right) \tag{7.3}$$

where $\sigma(\bullet)$ is the activation function of the output neuron and $h(\bullet)$ is the activation function of the neurons in the hidden layer.

While Rosenblatt's perceptron used the Heavyside function as the activation function, the multilayer perceptron model requires the activation functions to be differentiable. The smooth analogue to the hard limiting threshold is the sigmoid function. A sigmoid function is "a strictly increasing function that exhibits a graceful balance between linear and non-

linear behavior." [116]. One of the most common sigmoids is the logistic sigmoid, defined as [81, 116])

$$\phi(a) = \frac{1}{1 + \exp(-ac)}, \tag{7.4}$$

where c is a slope parameter. The hyperbolic tangent function is also commonly used as a sigmoid function [81, 116]. It can be shown that the tanh is a rescaled and biased form of the logistic sigmoid [116]. The tanh sigmoid allows for negative outputs from the activation function, which can offer an advantage over the logistic sigmoid [116].

In order to provide a correct output, the weights of the neural network must be trained. Neural networks can be easily trained if the training data is labelled. In other words, if a set of training data is available along with the corresponding desired output of the neural network. The classic technique of training a multilayer neural network is the backpropogation algorithm, which utilizes the optimization technique of gradient descent [81, 116]). Backpropogation is computationally efficient, but may be slow to converge [81, 116]).

Care must be taken when using a neural network. In their most common form, neural networks are fully connected directed graphs. For a large network, the number of connections correspond to the amount of training data needed. The computation cost of the backpropagation algorithm is linear with respect to the number of weights in the network, and is therefore considered efficient [116]. However, depending on the network architecture, the number of weights in the network can increase rapidly in relation to the number of neurons in the network. In situations where training data is scarce, the training the network may be infeasible. Conversely, neural networks can suffer from the problem of "over fitting" or "overtraining" [116]. An overtrained neural network essentially perfectly maps the input training data to the desired output, rather than learning the desired generalized mapping. Put another way, the network memorizes the answers to the test, without understanding the questions asked. In such a case, the network will likely produce incorrect outputs when data that is not in the training set is fed into the network.

Chapter 6 considered two challenges related to a cognitive radar. First, in the presence

of possibly non-Gaussian clutter, can the underlying distribution of the data be estimated? Second, can the detection threshold for a Neyman-Pearson hypothesis test be set by inference determined from a library of known distributions. These two problems are denoted as the distribution identification and threshold estimation problems, respectively. Chapters 3 and 4 illustrated the applicability of spherically invariant random vectors (SIRVs) to modelling radar clutter, and several candidate distributions were examined. From the results of those chapters, the distributions considered here largely belong to the SIRV class, with the exception of the Lognormal distribution.

Neural networks are an attractive solution to both of these problems. Note that there is an essentially infinite amount of labelled data available via simulation (see Chapters 3 and 4 for details). For the distribution identification problem, we only consider a small number of classes (six) to distinguish between. Therefore, for the distribution identification neural network, the output can be a binary valued vector. Finally, for the threshold estimation problem the neural network requires only a single real valued output neuron.

The rest of the chapter is as follows. Section 7.1 discusses the Matlab specific implementation details pertaining to the neural networks used. Section 7.2 shows the results for the multilayer perceptron neural networks, and Section 7.3 provides the conclusions. As a supplement, in Appendix B, the concept of deep neural networks is introduced and applied to the problem of threshold estimation. The results of Appendix B are also discussed in Section 7.3.

7.1 Implementation Details

This work is focussed on exploring methods to improve detection in non-Gaussian clutter. As such, the neural networks used were generated via the Matlab Neural Networking Toolbox, rather than developed from scratch. In particular, the networks were trained with a combination of CPU parallel processing as well as GPU parallel processing. However, due

to the lack of availability of a Jacobian calculation function on the GPUs, Matlab used the Scaled Conjugate Gradient training method rather than the default Levenberg-Marquardt training method. All sigmoid functions were set to the default of the tanh function.

Note that the neural network toolbox automatically pre-processes the inputs to the neural network by normalizing them. This prevents the sigmoids from saturating, which slows the convergence of the training by reducing the training gradient [122]. In addition, the Neural Networking Toolbox provides methods to prevent overtraining. Matlab randomly divides the input training data into training, validation, and testing subsets [122]. The test subset is not used by Matlab, but can be used to compare models. The training subset is used to train the weights of the neural network, while the validation data is used to prevent overtraining. For all networks developed here, the default ratios of 70% training data, 15% validation data, and 15% test data were used.

For each scenario considered (*i.e.* distribution identification or threshold estimation), a number of neural networks were trained and examined. The input data consists of a collection of $N = 16$ length $L = 4$ (resulting in $N = 4L$) complex valued vectors that are compressed into their quadratic form and fed into $N = 16$ input neurons. These parameters were chosen to correspond to those used in Chapter 6. For each scenario, individual neural networks were trained with varying numbers of neurons in the hidden layer and numbers of training samples used. In addition, the impact of using ordered training data was considered. For each test, a total of 18 neural networks were trained and examined.

The first neural network parameter examined is the number of hidden neurons. The number of hidden neurons in a neural network impacts the degrees of freedom associated with the network, as well as the number of training samples required to properly train the network. Recall that SIRVs are formed by modulating a Gaussian distributed random vector with a positive random variable. Therefore, the individual SIRV distributions are entirely differentiated by the pdf of the modulating random variable. In addition, the distribution identification neural networks are required to distinguish between six different distributions,

while the threshold estimation neural networks must map the input data to a scalar output. Therefore, the number of hidden neurons needed is expected to be small. For each scenario, neural networks with 10, 20, and 30 hidden neurons were trained.

Next, the number of training samples was varied. An increased number of samples can result in improved performance, at the price of increased training time/computational cost. Note that we are relying on the cross-validation procedures of Matlab's Neural Networking Toolbox to prevent overtraining. To choose the number of training samples to use, the number of input/output mappings required of the final neural network must be considered. The networks must be able to characterize four distributions (K, Weibull, Pareto, and Gamma Modulated) with shape parameters and two distributions without a shape parameter (the Gaussian and Lognormal distributions). These shape parameters have infinite support, with $0 \leq \nu \leq \infty$ for the K, Pareto, and Gamma Modulated distributions and $0 \leq \nu \leq 2$ for the Weibull distribution. Therefore, data associated with a relevant subset of the shape parameter values should be used to properly train the networks.

The shape parameter governs the behaviour of the tail of a distribution. Smaller values of the shape parameter yield a heavy tail, while the SIRV distributions approach the Gaussian distribution as the shape parameter approaches infinity (for the K, Pareto, and Gamma Modulated distributions) or 2 (for the Weibull distribution). Therefore, to maintain a desired false alarm rate, the threshold must be set very high for low shape parameter values and low for large shape parameter values. However, as was examined in Chapters 3 and 4, the threshold varies non-linearly with shape parameter. At low shape parameter values, the threshold is highly sensitive to the shape parameter. However, as the shape parameter increases the threshold asymptotically approaches the threshold needed for the Gaussian distribution. The exact nature of the shape parameter v. threshold curve is dependent on the distribution. Therefore, here we sampled the shape parameter more densely in the high threshold region and sparsely in the asymptotic, low threshold region.

The number and value of the shape parameters used for each distribution was identical

to those used in the COSMiC methods of Chapter 6. For each value of the size of the neural network (*i.e.* number of hidden neurons), three neural networks were trained with a variable number of samples: $10^2, 10^3$, and 10^4 for each distribution/shape parameter pair. The total number of training samples used for each distribution is equal to the number of training samples per input/output mapping (*i.e.* $10^2, 10^3, 10^4$)) times the number of shape parameters considered for the distribution, shown in Table 7.1. Note that each training sample consists of $N = 16$ values of the quadratic form of a length $L = 4$ complex random vector.

Distribution	Number of values of Shape Parameter Examined
Gaussian	1
K	28
Weibull	19
Pareto	65
Lognormal	1
Gamma Modulated	39
Total distribution/shape parameter pairs: 153	
Total training samples used: $153 \times (10^2, 10^3, 10^4)$	

Table 7.1: Number of shape parameter values by distribution used to train neural networks

In Chapters 5 and 6 the COSMiC algorithm used ordered data. Ordering the input data induces an extra structure, and is a form of pre-processing. Therefore, neural networks were trained with both raw data and data vectors that were sorted.

The training parameters examined are summarized in Table 7.2.

Number of hidden neurons	Number of training samples	Ordered
10, 20, 30	$153\times(10^2, 10^3, 10^4)$	Yes,No
Total neural networks trained per scenario: 18		

Table 7.2: Neural network training parameters summary

7.2 Neural Network Implementation

The neural networks examined here have a pass through input layer followed by two layers of neurons: the hidden layer and the output layer. Two applications of neural networks are considered. First, in Section 7.2.1 a set of neural networks are trained to identify the distribution that is most likely to have generated a set of sample data. This problem is analogous to the classic problem of training a neural network classifier. Therefore, the terms distribution classification and distribution identification will be used interchangeably throughout the rest of this work. Second, in Section 7.2.2 a set of neural networks are trained to directly map input data to a detection threshold based on training data generated from the six candidate distributions. In both cases the shape parameters of the distributions (when applicable) are varied to provide a thorough examination of the desired test space.

7.2.1 Distribution Classification with Neural Networks

The set of distribution classification neural networks examined here are differentiated by the number of hidden neurons contained within the neural network, the number of training samples used, and whether the input data is ordered or not. The general construction of a distribution classification (*i.e.* distribution identification) neural network is shown in Figure 7.3.

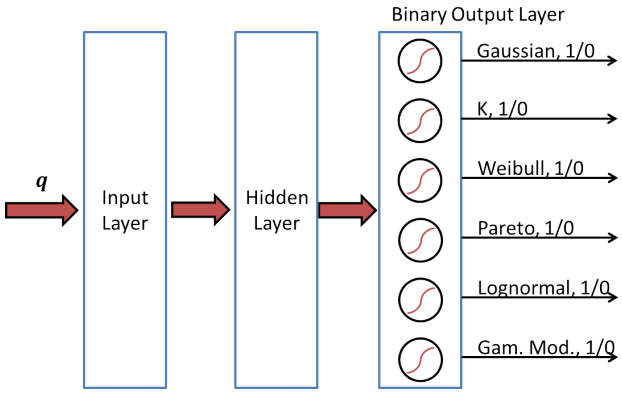

Figure 7.3: Distribution identification neural network

Note that as a distribution classifier, the output layer provides a vector of six binary values. The desired value is a vector of all zeros except for a single output equal to one corresponding to the distribution that best fits the input data. For example, if the K distribution is the generating distribution for a set of sample data, the desired output layer response (according to the ordering established in Figure 7.3) would be [010000]. In practice, the output neurons provide a continuous response. Therefore, the chosen distribution was selected as the distribution associated with the neuron possessing the largest output.

Note that the Gamma modulated (GM) distribution is included in the training data but not in the test data. The GM distribution was hypothesized in Chapter 4 to help fill out the SIRV distribution space. Therefore, to maintain a comparison between the neural network results and the COSMiC based results of Chapter 6 the GM distribution is included as training. However, it is important to remember that the GM distribution has not been measured in practice. As such, it is not included in the test data.

Each neural network was tested with 10^5 sets of sample data. Note that each set of sample data consists of $N = 16$ scalar values generated from the generalized inner product (or quadratic form) of a length $L = 4$ complex random vector. The generalized inner product (GIP) of the test data was formed from both a clairvoyantly known covariance matrix (CCM) and the sample covariance matrix (SCM). Tables 7.3-7.12 summarize the accuracy given by each of the neural networks in classifying each distribution. Two tables are given for each

distribution. The first table summarizes the classification accuracy where the input data is unordered. The second table provides the results when the training and test data are ordered (*i.e.* sorted into order statistics). Both sets of tables are formatted such that the leftmost column corresponds to the number of neurons in the hidden layer. The next column shows the number of training samples used per distribution/shape parameter pair. Finally, six columns corresponding to each of the candidate distributions in the output layer are given. The percentage of data classified by each neural network to belong to a particular distribution is shown in the corresponding column. Note that there are two numbers in the columns associated with a distribution. The first number is the percentage of data classified to that distribution when the CCM is used to form the GIP. The number in parentheses is the percentage of data classified to the corresponding distribution when the SCM is used to form the GIP.

First, Tables 7.3 and 7.4 show the classification accuracy of the neural networks when the test data is Gaussian distributed. Note that none of neural networks that were trained successfully identify the test data as Gaussian distributed. The neural networks overwhelmingly chose Pareto as the distribution with the best fit. The neural networks chose K, Weibull, or GM as the originating distribution at a low rate. The ratio of data classified as belonging to a distribution other than Pareto is increased when the data is ordered, or when the unordered data is passed through a network with 30 hidden neurons. Note that the majority of the test data (65/153 sets of training samples) was Pareto distributed. In addition, it has been shown that at high values of the shape parameter, the tail of the SIRV distributions with a shape parameter approach that of the Gaussian distribution, introducing an ambiguity. It is encouraging that the heavy-tailed, non-SIRV Lognormal distribution is never chosen to be the generating distribution for Gaussian distributed test data.

		Percentage Chosen					
Num. HNs	Samp. Support	Gaussian	K	Weibull	Pareto	Lognormal	Gamma Mod.
10	10^2	0.0 (0.0)	0.0 (0.0)	0.0 (0.0)	100.0 (100.0)	0.0 (0.0)	0.0 (0.0)
10	10^3	0.0 (0.0)	0.1 (0.0)	0.0 (0.0)	99.9 (100.0)	0.0 (0.0)	0.0 (0.0)
10	10^4	0.0 (0.0)	0.1 (0.0)	0.0 (0.0)	99.9 (100.0)	0.0 (0.0)	0.0 (0.0)
20	10^2	0.0 (0.0)	0.4 (0.0)	0.1 (0.0)	99.0 (99.9)	0.0 (0.0)	0.5 (0.1)
20	10^3	0.0 (0.0)	0.4 (0.0)	0.2 (0.1)	99.0 (99.9)	0.0 (0.0)	0.4 (0.0)
20	10^4	0.0 (0.0)	0.1 (0.0)	0.0 (0.0)	99.9 (100.0)	0.0 (0.0)	0.0 (0.0)
30	10^2	0.0 (0.0)	0.8 (0.0)	0.0 (0.0)	98.4 (99.9)	0.0 (0.0)	0.7 (0.1)
30	10^3	0.0 (0.0)	0.3 (0.0)	0.1 (0.0)	99.1 (99.9)	0.0 (0.0)	0.5 (0.1)
30	10^4	0.0 (0.0)	0.3 (0.0)	0.1 (0.0)	99.0 (99.9)	0.0 (0.0)	0.5 (0.1)

Table 7.3: Distribution identification percentages of Neural Networks for unordered Gaussian Distributed data

		Percentage Chosen					
Num. HNs	Samp. Support	Gaussian	K	Weibull	Pareto	Lognormal	Gamma Mod.
10	10^2	0.0 (0.0)	0.5 (0.0)	0.1 (0.0)	99.8 (99.9)	0.0 (0.0)	0.6 (0.1)
10	10^3	0.0 (0.0)	0.3 (0.0)	0.1 (0.0)	99.1 (99.9)	0.0 (0.0)	0.5 (0.1)
10	10^4	0.0 (0.0)	0.3 (0.0)	0.1 (0.0)	99.1 (99.9)	0.0 (0.0)	0.6 (0.1)
20	10^2	0.0 (0.0)	0.3 (0.0)	0.1 (0.0)	99.2 (99.9)	0.0 (0.0)	0.4 (0.0)
20	10^3	0.0 (0.0)	0.3 (0.0)	0.1 (0.0)	99.1 (99.9)	0.0 (0.0)	0.5 (0.1)
20	10^4	0.0 (0.0)	0.4 (0.0)	0.2 (0.1)	99.0 (99.9)	0.0 (0.0)	0.4 (0.0)
30	10^2	0.0 (0.0)	0.4 (0.0)	0.0 (0.0)	99.1 (99.9)	0.0 (0.0)	0.5 (0.0)
30	10^3	0.0 (0.0)	0.3 (0.0)	0.2 (0.1)	99.1 (99.9)	0.0 (0.0)	0.5 (0.1)
30	10^4	0.0 (0.0)	0.3 (0.0)	0.1 (0.1)	99.1 (99.9)	0.0 (0.0)	0.5 (0.1)

Table 7.4: Distribution identification percentages of Neural Networks for ordered Gaussian Distributed data

Next Table 7.5 shows the average distribution identification percentages when unordered K distributed data is fed into the set of neural networks. From Table 7.5, when the CCM is employed the number of training samples used has a greater impact on the classification accuracy than the number of hidden neurons. However, when the SCM is employed the majority of the samples are misclassified as belonging to the Pareto and GM distributions. In this case, an increased number of hidden neurons reduces the misclassification rate.

		Percentage Chosen					
Num. HNs	Samp. Support	Gaussian	K	Weibull	Pareto	Lognormal	Gamma Mod.
10	10^2	2.4 (0.0)	70.9 (0.0)	0.2 (0.0)	26.4 (100.0)	0.0 (0.0)	0.0 (0.0)
10	10^3	0.0 (0.0)	90.7 (0.0)	0.0 (0.0)	9.3 (100.0)	0.0 (0.0)	0.0 (0.0)
10	10^4	0.0 (0.0)	90.6 (0.0)	0.0 (0.0)	9.4 (100.0)	0.0 (0.0)	0.0 (0.0)
20	10^2	0.0 (0.0)	85.9 (5.5)	5.9 (9.6)	3.0 (66.0)	0.0 (0.0)	5.3 (18.9)
20	10^3	0.0 (0.0)	87.1 (1.9)	5.8 (19.2)	2.3 (66.1)	0.0 (0.0)	4.7 (12.8)
20	10^4	0.0 (0.0)	90.6 (0.0)	0.0 (0.0)	9.4 (100.0)	0.0 (0.0)	0.0 (0.0)
30	10^2	0.0 (0.0)	83.9 (2.7)	4.9 (3.8)	4.2 (66.0)	0.0 (0.0)	6.9 (27.4)
30	10^3	0.0 (0.0)	87.1 (4.9)	5.4 (13.2)	2.3 (66.0)	0.0 (0.0)	5.2 (15.9)
30	10^4	0.0 (0.0)	87.0 (5.4)	5.5 (15.2)	2.3 (65.9)	0.0 (0.0)	5.2 (13.5)

Table 7.5: Distribution identification percentages of Neural Networks for unordered K Distributed data

The results of Table 7.5 are expanded as a function of shape parameter in Figures 7.4a-7.4d. Figures 7.4a-7.4c show the average correct classification percentage as a function of shape parameter for neural network with 10,20, and 30 hidden neurons, respectively. Figure 7.4d shows the result of the best performing neural network. The best performing neural network is determined as the network yielding the highest average classification accuracy. Note that the accuracy is based on the results when the CCM is used to form the GIP. In addition, the accuracy is determined by first averaging the correct classification rate over all training samples, and then averaging that result over all the shape parameters that were examined. For the K distribution, the best neural network was formed from 10 hidden neurons, and trained with 10^4 training samples per shape parameter value. Surprisingly, the classification was the least accurate at low shape parameter values. Based on the threshold ambiguity plots shown in Section 5.4, it has thus far been assumed that the SIRVs become less difficult to discriminate as their tails get heavier.

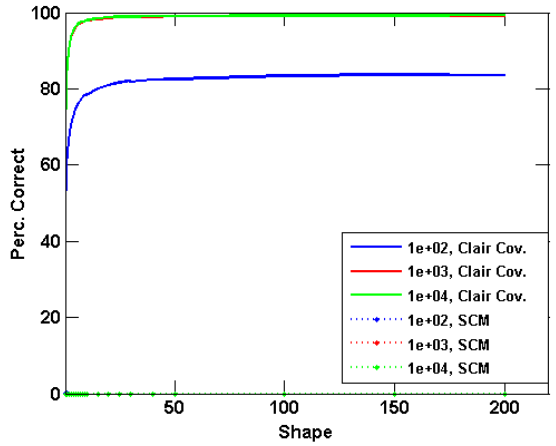

(a) Percentage correct identification for varying training sample support w/CCM (solid) and SCM (dotted) with 10 hidden neurons

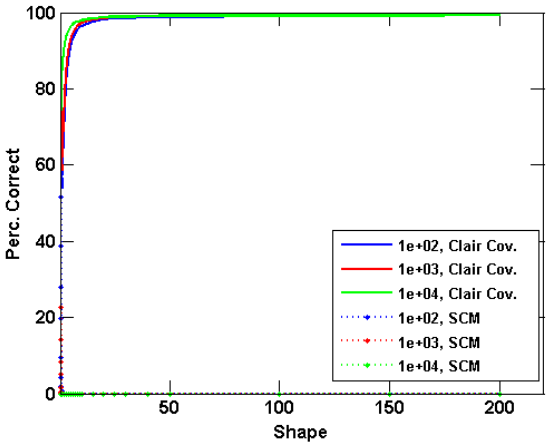

(b) Percentage correct identification for varying training sample support w/CCM (solid) and SCM (dotted) with 20 hidden neurons

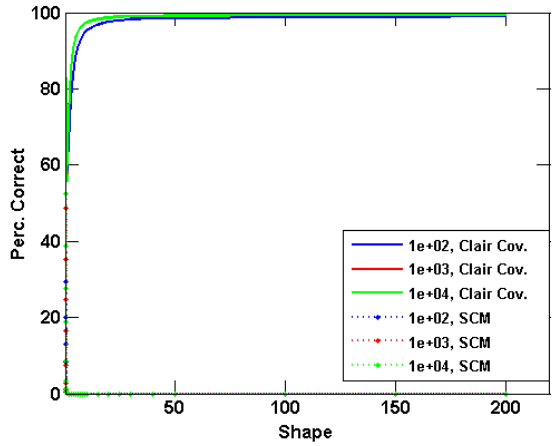

(c) Percentage correct identification for varying training sample support w/CCM (solid) and SCM (dotted) with 30 hidden neurons

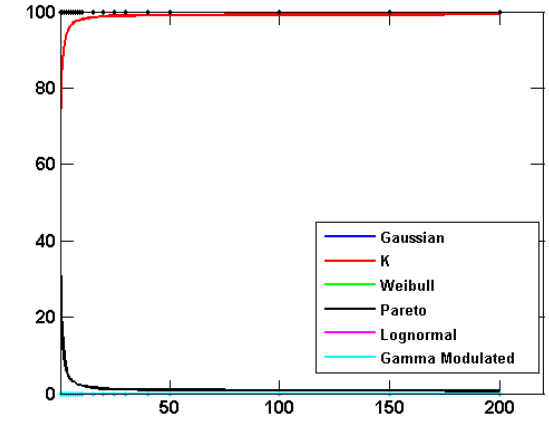

(d) Distribution identification w/CCM (solid) and SCM (dotted) for a neural network with 10 hidden neurons, 10^4 training samples

Figure 7.4: Distribution identification by neural networks for unordered K distributed data

Next Table 7.6 shows the average distribution identification percentages when ordered K distributed test data is processed through the corresponding neural networks. Note that in comparison with Table 7.5 the ordering of the data clearly reduces impact of the number of hidden neurons and the number of training samples required when the CCM is used. However, when the SCM is used, the number of samples correctly classified is only slightly increased. Meanwhile, in comparison to the unordered case the distributions mistakenly assigned to the data trend towards the Weibull and GM distributions when fewer neurons

or training samples are used.

		Percentage Chosen					
Num. HNs	Samp. Support	Gaussian	K	Weibull	Pareto	Lognormal	Gamma Mod.
10	10^2	0.0 (0.0)	85.8 (5.2)	6.1 (6.8)	3.0 (65.5)	0.0 (0.0)	5.1 (22.4)
10	10^3	0.0 (0.0)	87.3 (5.6)	4.4 (4.8)	2.4 (65.9)	0.0 (0.0)	5.9 (23.7)
10	10^4	0.0 (0.0)	87.8 (5.2)	4.9 (15.1)	2.4 (66.0)	0.0 (0.0)	5.0 (13.7)
20	10^2	0.0 (0.0)	86.6 (4.3)	5.2 (11.5)	2.9 (66.2)	0.0 (0.0)	5.2 (18.0)
20	10^3	0.0 (0.0)	87.1 (3.9)	5.9 (17.8)	2.4 (66.0)	0.0 (0.0)	4.6 (12.2)
20	10^4	0.0 (0.0)	86.7 (4.6)	6.0 (16.3)	2.4 (66.0)	0.0 (0.0)	4.9 (13.2)
30	10^2	0.0 (0.0)	84.4 (1.8)	6.0 (5.3)	3.2 (66.5)	0.0 (0.0)	6.4 (26.4)
30	10^3	0.0 (0.0)	87.4 (4.2)	5.5 (16.2)	2.2 (66.0)	0.0 (0.0)	4.8 (13.6)
30	10^4	0.0 (0.0)	87.1 (5.1)	6.0 (16.3)	2.2 (65.8)	0.0 (0.0)	4.7 (12.7)

Table 7.6: Distribution identification percentages of Neural Networks for ordered K Distributed data

Figures 7.5a-7.5c show the results for the correct classification of K distributed data summarized in Table 7.6 as a function of shape parameter. Figure 7.5d then shows the best performing CCM case, which was the neural network with 10 hidden neurons trained with 10^4 training samples per distribution/shape parameter pair.

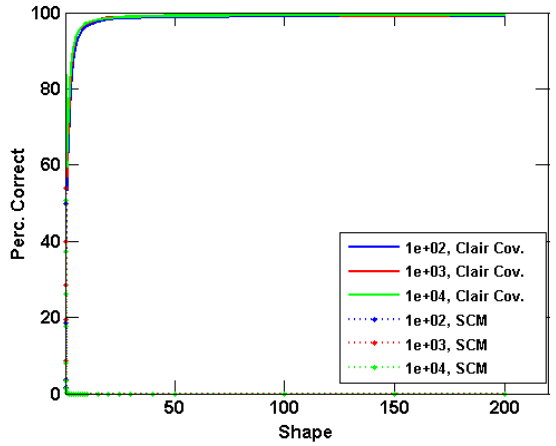

(a) Percentage correct identification for varying training sample support w/CCM (solid) and SCM (dotted) with 10 hidden neurons

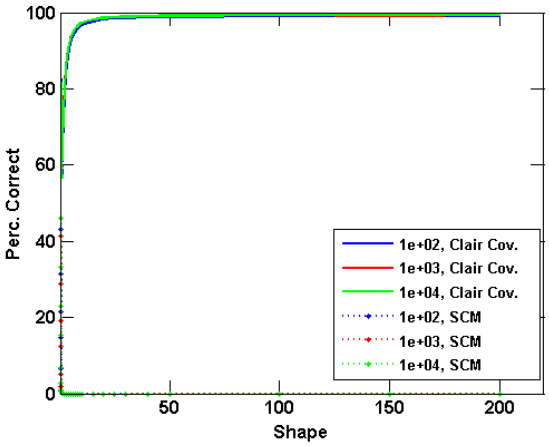

(b) Percentage correct identification for varying training sample support w/CCM (solid) and SCM (dotted) with 20 hidden neurons

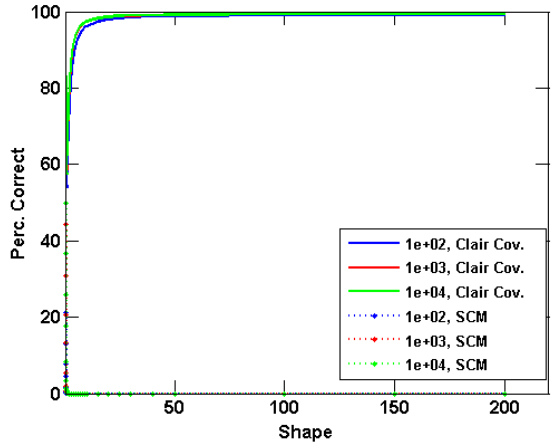

(c) Percentage correct identification for varying training sample support w/CCM (solid) and SCM (dotted) with 30 hidden neurons

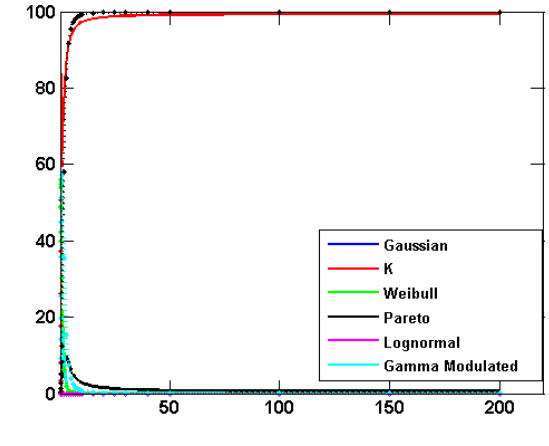

(d) Distribution identification w/CCM (solid) and SCM (dotted) for a neural network with 10 hidden neurons, 10^4 training samples

Figure 7.5: Distribution identification by neural networks for ordered K distributed data

Table 7.7 shows the average distributions chosen by each neural network when the test data is unordered and Weibull distributed. Note that unlike the K distribution, the Weibull data was still selected when the SCM was used. In addition, increasing the number of hidden neurons in the neural network positively influenced the classification accuracy when the SCM was used. Also, while the Pareto and GM distributions were often chosen regardless of which covariance matrix was employed, the K distribution was often chosen if the true covariance matrix was known. Finally, when 10 hidden neurons were used, the neural networks did not

converge to a solution that would choose the Weibull distribution regardless of the number of training samples used.

		Percentage Chosen					
Num. HNs	Samp. Support	Gaussian	K	Weibull	Pareto	Lognormal	Gamma Mod.
10	10^2	0.0 (0.0)	12.9 (0.0)	0.1 (0.0)	86.6 (100.0)	0.0 (0.0)	0.0 (0.0)
10	10^3	0.0 (0.0)	21.2 (0.0)	0.0 (0.0)	78.8 (100.0)	0.0 (0.0)	0.0 (0.0)
10	10^4	0.0 (0.0)	21.1 (0.0)	0.0 (0.0)	78.9 (100.0)	0.0 (0.0)	0.0 (0.0)
20	10^2	0.0 (0.0)	12.2 (1.0)	22.7 (19.8)	36.2 (46.8)	0.0 (0.0)	28.9 (32.4)
20	10^3	0.0 (0.0)	12.5 (0.1)	28.5 (33.0)	35.0 (45.6)	0.0 (0.0)	24.0 (21.3)
20	10^4	0.0 (0.0)	21.0 (0.0)	0.0 (0.0)	79.0 (100.0)	0.0 (0.0)	0.0 (0.0)
30	10^2	0.0 (0.0)	11.8 (0.4)	18.3 (10.2)	37.6 (48.2)	0.0 (0.0)	32.4 (41.1)
30	10^3	0.0 (0.0)	12.6 (0.8)	24.4 (26.3)	35.7 (45.9)	0.0 (0.0)	27.3 (27.0)
30	10^4	0.0 (0.0)	12.6 (0.9)	27.2 (32.3)	35.2 (45.2)	0.0 (0.0)	25.0 (21.5)

Table 7.7: Distribution identification percentages of Neural Networks for unordered Weibull Distributed data

Next, Figures 7.6a-7.6c illustrate the classification accuracy of the neural networks of Table 7.7 as a function of shape parameter. In particular, the positive impact of additional training samples is clearly shown in the results of Figures 7.6b and 7.6c. Each increase in training sample support led to an increase in distribution classification accuracy, with the exception of the case in Figure 7.6b with 10^4 training samples. The training of the network in Figure 7.6b appears to have not converged to a usable solution. Note that when the SCM is used the classification accuracy appears to improve at low values of the shape parameter, but decrease at medium to high values of the shape parameter.

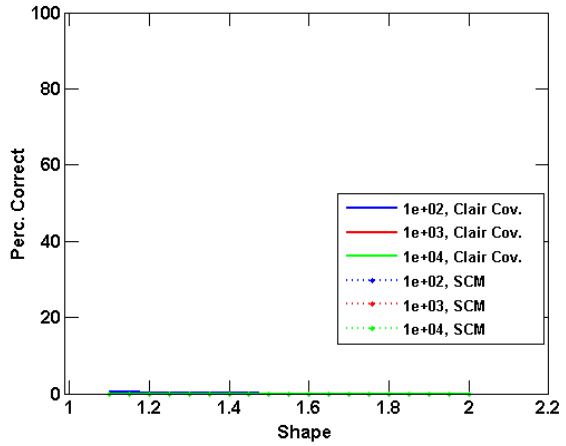

(a) Percentage correct identification for varying training sample support w/CCM (solid) and SCM (dotted) with 10 hidden neurons

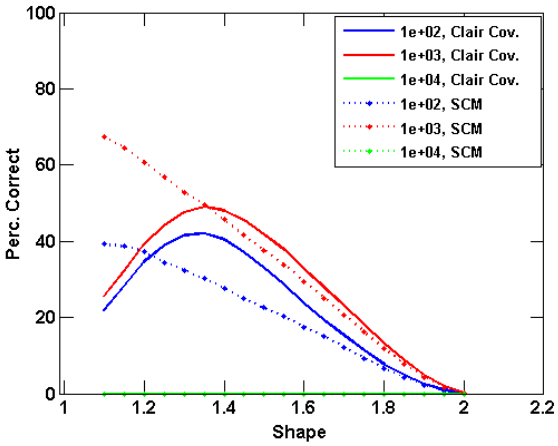

(b) Percentage correct identification for varying training sample support w/CCM (solid) and SCM (dotted) with 20 hidden neurons

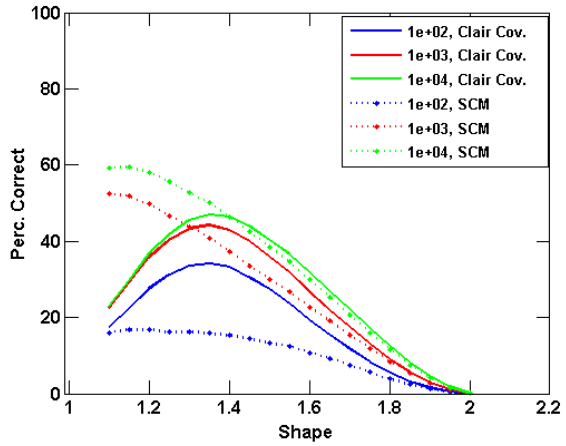

(c) Percentage correct identification for varying training sample support w/CCM (solid) and SCM (dotted) with 30 hidden neurons

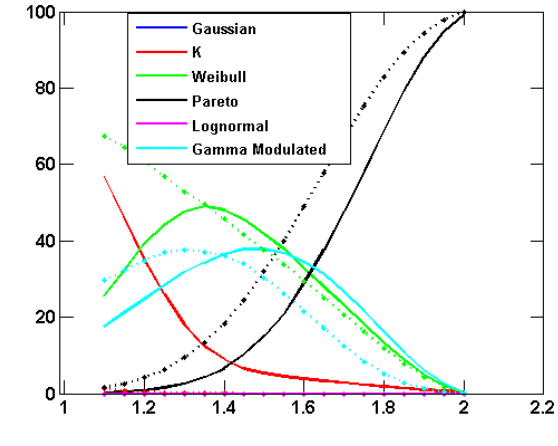

(d) Distribution identification w/CCM (solid) and SCM (dotted) for a neural network with 20 hidden neurons, 10^3 training samples

Figure 7.6: Distribution identification by neural networks for unordered Weibull distributed data

Figure 7.6d shows the best neural network for classifying Weibull data with the CCM, which occurs when a network with 20 hidden neurons is trained with 10^3 samples. Once more, the classification accuracy is highest when the shape parameter is low. The K distribution is often incorrectly chosen when the CCM is used and the shape parameter is low. The GM distribution is primarily chosen for medium values of the shape parameter, while the network increasingly picks the Pareto distribution as the shape parameter increases.

Next Table 7.8 considers the impact of ordering the input data to the distribution classification neural networks when Weibull test data is examined. Immediately apparent is the performance of the neural networks with 10 hidden neurons. The ordering allows them to successfully identify $\approx 20 - 25\%$ of the samples as belonging to the Weibull distribution. However, the highest classification percentages are still $\approx 29\%$.

		Percentage Chosen					
Num. HNs	Samp. Support	Gaussian	K	Weibull	Pareto	Lognormal	Gamma Mod.
10	10^2	0.0 (0.0)	12.7 (1.0)	22.0 (14.9)	35.2 (45.3)	0.0 (0.0)	30.1 (38.8)
10	10^3	0.0 (0.0)	13.5 (1.0)	19.1 (13.7)	35.5 (45.9)	0.0 (0.0)	32.0 (39.4)
10	10^4	0.0 (0.0)	13.3 (0.8)	25.6 (30.7)	35.7 (46.0)	0.0 (0.0)	25.4 (22.4)
20	10^2	0.0 (0.0)	12.5 (0.7)	23.5 (24.0)	37.0 (47.1)	0.0 (0.0)	27.0 (28.2)
20	10^3	0.0 (0.0)	12.3 (0.5)	28.7 (33.4)	35.4 (45.3)	0.0 (0.0)	23.7 (20.8)
20	10^4	0.0 (0.0)	12.2 (0.7)	28.8 (33.4)	34.7 (44.6)	0.0 (0.0)	24.4 (21.3)
30	10^2	0.0 (0.0)	10.6 (0.2)	22.2 (14.8)	37.7 (49.9)	0.0 (0.0)	29.5 (35.2)
30	10^3	0.0 (0.0)	12.7 (0.5)	28.0 (32.7)	34.8 (45.2)	0.0 (0.0)	24.4 (21.6)
30	10^4	0.0 (0.0)	12.3 (0.8)	28.8 (33.4)	34.9 (44.8)	0.0 (0.0)	24.1 (20.9)

Table 7.8: Distribution identification percentages of Neural Networks for ordered Weibull Distributed data

Figures 7.7a-7.7c show the classification accuracy of Table 7.8 as a function of shape parameter. When compared to Figures 7.6b and 7.6c, it is clear that the performance for the networks with 20 and 30 hidden neurons converge to similar solutions after 10^3 training samples are used. Consequently, there is little difference in performance between the networks trained with 10^3 and 10^4 samples. However, when examining Figure 7.6a, the network trained with 10^3 samples actually had a lower accuracy than the network trained with 10^2 training samples. Therefore, it is apparent that the convergence of the neural network training algorithms is not guaranteed to behave in a monotonic fashion with respect to training sample support.

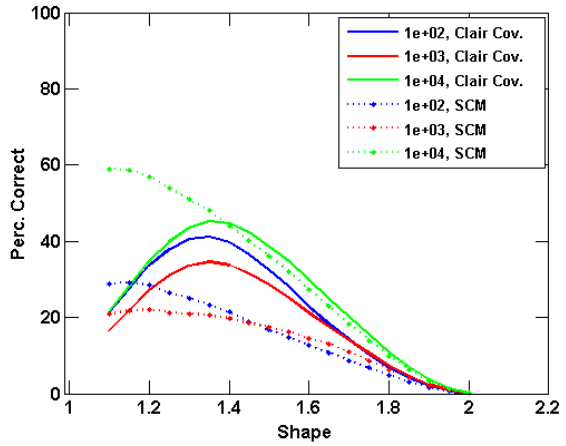

(a) Percentage correct identification for varying training sample support w/CCM (solid) and SCM (dotted) with 10 hidden neurons

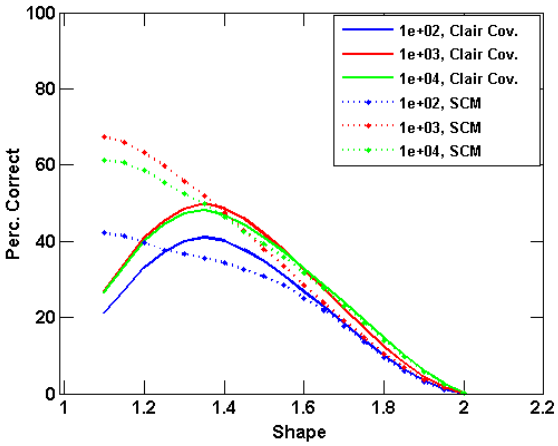

(b) Percentage correct identification for varying training sample support w/CCM (solid) and SCM (dotted) with 20 hidden neurons

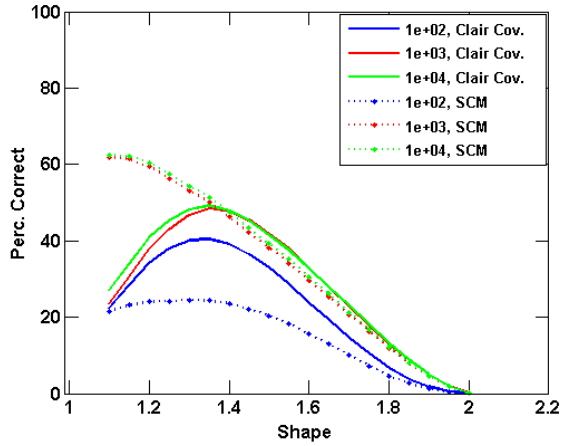

(c) Percentage correct identification for varying training sample support w/CCM (solid) and SCM (dotted) with 30 hidden neurons

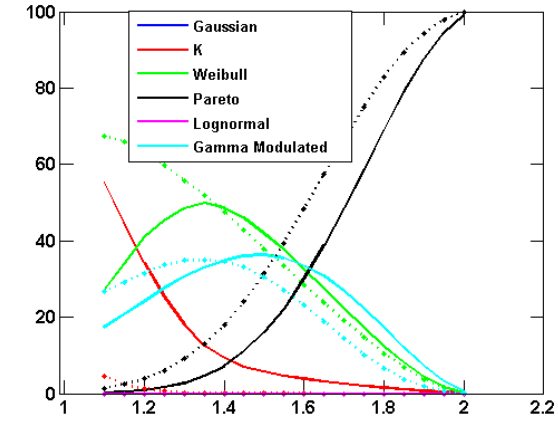

(d) Distribution identification w/CCM (solid) and SCM (dotted) for a neural network with 20 hidden neurons, 10^3 training samples

Figure 7.7: Distribution identification by neural networks for ordered Weibull distributed data

The behaviour of Figure 7.7d is virtually identical to the behaviour of Figure 7.6d, and occurs for the same number of hidden neurons and training samples. Therefore, from comparing Figures 7.6a-7.6d to Figures 7.7a-7.7d, it appears that ordering the data reduces the training and adaptivity requirements (*i.e.* the number of hidden neurons required), but does not necessarily yield a better performing neural network than was found with the unordered data.

Next, Table 7.9 examines the identification accuracy of the neural networks when unordered Pareto distributed test data is present. As might be expected from the previous results shown in this section, the neural networks select the Pareto distribution for the majority of the test samples. The K and GM distributions are the most often incorrectly selected distributions.

		Percentage Chosen					
Num. HNs	Samp. Support	Gaussian	K	Weibull	Pareto	Lognormal	Gamma Mod.
10	10^2	0.0 (0.0)	1.2 (0.0)	0.0 (0.0)	98.8 (100.0)	0.0 (0.0)	0.0 (0.0)
10	10^3	0.0 (0.0)	1.9 (0.0)	0.0 (0.0)	98.1 (100.0)	0.0 (0.0)	0.0 (0.0)
10	10^4	0.0 (0.0)	1.9 (0.0)	0.0 (0.0)	98.1 (100.0)	0.0 (0.0)	0.0 (0.0)
20	10^2	0.0 (0.0)	0.4 (0.0)	0.3 (0.1)	90.1 (97.3)	0.0 (0.0)	9.2 (2.6)
20	10^3	0.0 (0.0)	0.5 (0.0)	0.5 (0.2)	90.7 (97.5)	0.0 (0.0)	8.6 (2.3)
20	10^4	0.0 (0.0)	1.8 (0.0)	0.0 (0.0)	98.2 (100.0)	0.0 (0.0)	0.0 (0.0)
30	10^2	0.0 (0.0)	0.5 (0.0)	0.2 (0.0)	88.9 (97.1)	0.0 (0.0)	10.3 (2.9)
30	10^3	0.0 (0.0)	0.5 (0.0)	0.2 (0.1)	90.5 (97.4)	0.0 (0.0)	8.8 (2.5)
30	10^4	0.0 (0.0)	0.5 (0.0)	0.4 (0.2)	90.3 (97.3)	0.0 (0.0)	8.9 (2.5)

Table 7.9: Distribution identification percentages of Neural Networks for unordered Pareto Distributed data

Figures 7.8a-7.8d reinforce the conclusions of Table 7.9. The K distribution is most often selected for extremely low values of the shape parameter.

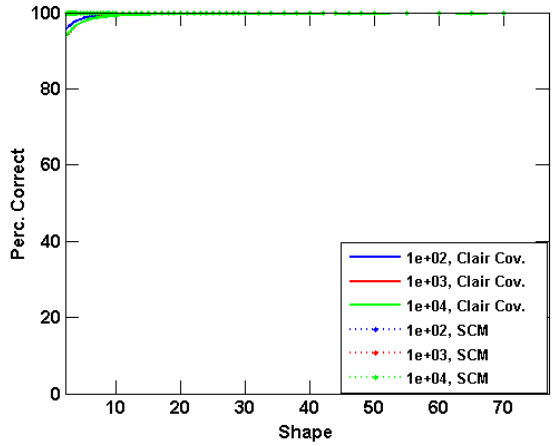

(a) Percentage correct identification for varying training sample support w/CCM (solid) and SCM (dotted) with 10 hidden neurons

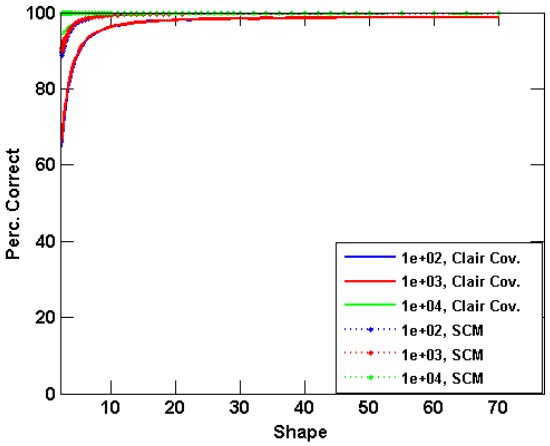

(b) Percentage correct identification for varying training sample support w/CCM (solid) and SCM (dotted) with 20 hidden neurons

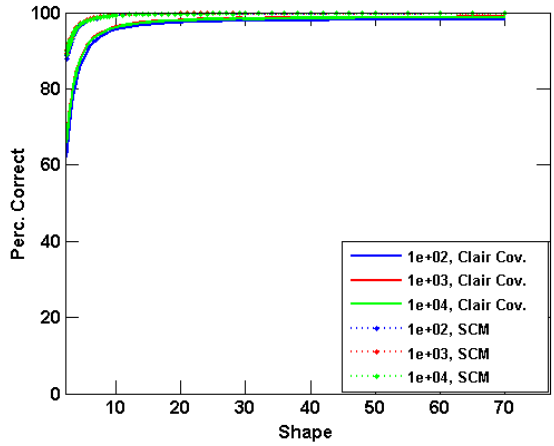

(c) Percentage correct identification for varying training sample support w/CCM (solid) and SCM (dotted) with 30 hidden neurons

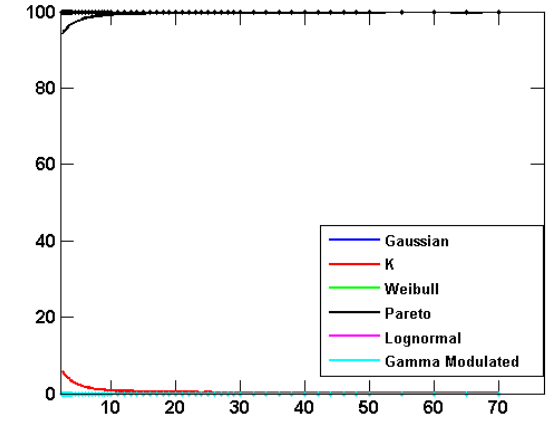

(d) Distribution identification w/CCM (solid) and SCM (dotted) for a neural network with 20 hidden neurons, 10^4 training samples

Figure 7.8: Distribution identification by neural networks for unordered Pareto distributed data

When the Pareto test data is ordered and the CCM is used the accuracy of all the neural networks actually declines, as shown in Table 7.10. The number of samples incorrectly classified as belonging to the K distribution also declines, while the number of samples incorrectly classified as GM increases. However, when the SCM is used, the number of incorrect classifications declines to $\approx 2.5\%$.

		Percentage Chosen					
Num. HNs	Samp. Support	Gaussian	K	Weibull	Pareto	Lognormal	Gamma Mod.
10	10^2	0.0 (0.0)	0.5 (0.0)	0.3 (0.0)	89.7 (96.9)	0.0 (0.0)	9.5 (3.0)
10	10^3	0.0 (0.0)	0.4 (0.0)	0.2 (0.1)	90.4 (97.4)	0.0 (0.0)	8.9 (2.6)
10	10^4	0.0 (0.0)	0.5 (0.0)	0.3 (0.1)	90.3 (97.4)	0.0 (0.0)	8.9 (2.5)
20	10^2	0.0 (0.0)	0.4 (0.0)	0.4 (0.2)	90.6 (97.4)	0.0 (0.0)	8.6 (2.4)
20	10^3	0.0 (0.0)	0.5 (0.0)	0.3 (0.1)	90.7 (97.5)	0.0 (0.0)	8.6 (2.4)
20	10^4	0.0 (0.0)	0.5 (0.0)	0.5 (0.3)	90.4 (97.4)	0.0 (0.0)	8.6 (2.2)
30	10^2	0.0 (0.0)	0.4 (0.0)	0.4 (0.1)	89.2 (97.5)	0.0 (0.0)	10.0 (2.5)
30	10^3	0.0 (0.0)	0.5 (0.0)	0.4 (0.2)	90.3 (97.4)	0.0 (0.0)	8.8 (2.4)
30	10^4	0.0 (0.0)	0.5 (0.0)	0.4 (0.2)	90.2 (97.3)	0.0 (0.0)	9.0 (2.5)

Table 7.10: Distribution identification percentages of Neural Networks for ordered Pareto Distributed data

Figures 7.9a-7.9d follow directly from Table 7.10. The GM distribution is incorrectly chosen largely for low values of the shape parameter.

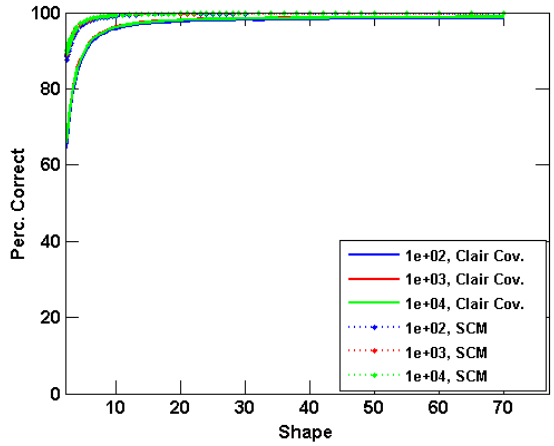

(a) Percentage correct identification for varying training sample support w/CCM (solid) and SCM (dotted) with 10 hidden neurons

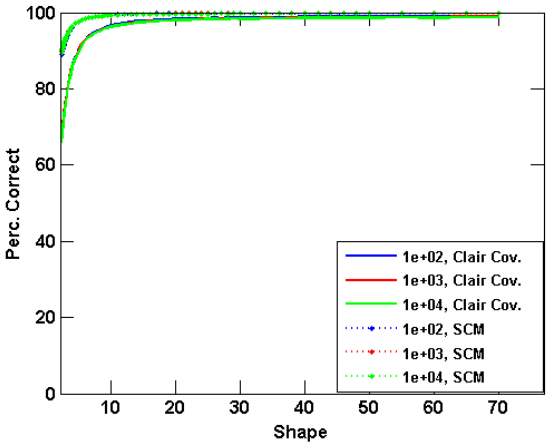

(b) Percentage correct identification for varying training sample support w/CCM (solid) and SCM (dotted) with 20 hidden neurons

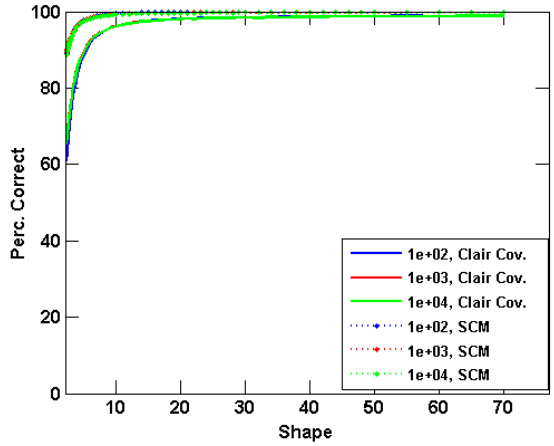

(c) Percentage correct identification for varying training sample support w/CCM (solid) and SCM (dotted) with 30 hidden neurons

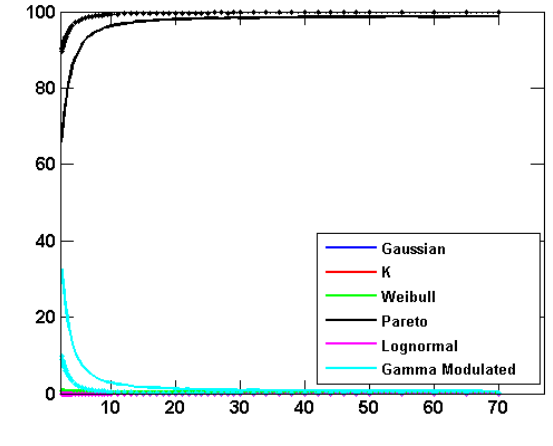

(d) Distribution identification w/CCM (solid) and SCM (dotted) for a neural network with 20 hidden neurons, 10^4 training samples

Figure 7.9: Distribution identification by neural networks for ordered Pareto distributed data

Finally, Tables 7.11 and 7.12 show the classification accuracy for unordered and ordered Lognormal distributed test data, respectively. None of the neural networks ever correctly chose the Lognormal distribution. If the CCM is used, the distribution chosen the most often is the Pareto, but the GM distribution is chosen between $\approx 32 - 42\%$ of the time by some of the neural networks operating on unordered data, and all of the networks trained with ordered data. However, when the SCM is used, $> 90\%$ of the test data is classified as

Pareto.

		Percentage Chosen					
Num. HNs	Samp. Support	Gaussian	K	Weibull	Pareto	Lognormal	Gamma Mod.
10	10^2	0.3 (0.0)	5.7 (0.0)	0.0 (0.0)	94.0 (100.0)	0.0 (0.0)	0.0 (0.0)
10	10^3	0.0 (0.0)	8.4 (0.0)	0.0 (0.0)	91.6 (100.0)	0.0 (0.0)	0.0 (0.0)
10	10^4	0.0 (0.0)	8.1 (0.0)	0.0 (0.0)	91.9 (100.0)	0.0 (0.0)	0.0 (0.0)
20	10^2	0.0 (0.0)	0.7 (0.0)	0.2 (0.0)	63.3 (88.9)	0.0 (0.0)	35.8 (11.1)
20	10^3	0.0 (0.0)	0.6 (0.0)	0.3 (0.1)	65.5 (90.6)	0.0 (0.0)	33.7 (9.3)
20	10^4	0.0 (0.0)	8.0 (0.0)	0.0 (0.0)	92.0 (100.0)	0.0 (0.0)	0.0 (0.0)
30	10^2	0.0 (0.0)	0.6 (0.0)	0.3 (0.0)	59.0 (87.7)	0.0 (0.0)	40.2 (12.3)
30	10^3	0.0 (0.0)	0.6 (0.0)	0.2 (0.0)	65.6 (90.1)	0.0 (0.0)	33.6 (9.9)
30	10^4	0.0 (0.0)	0.6 (0.0)	0.2 (0.1)	65.2 (89.9)	0.0 (0.0)	34.1 (10.0)

Table 7.11: Distribution identification percentages of Neural Networks for unordered Lognormal Distributed data

		Percentage Chosen					
Num. HNs	Samp. Support	Gaussian	K	Weibull	Pareto	Lognormal	Gamma Mod.
10	10^2	0.0 (0.0)	0.8 (0.0)	0.4 (0.0)	64.1 (88.5)	0.0 (0.0)	34.8 (11.5)
10	10^3	0.0 (0.0)	0.6 (0.0)	0.2 (0.0)	65.7 (90.0)	0.0 (0.0)	33.6 (9.9)
10	10^4	0.0 (0.0)	0.7 (0.0)	0.2 (0.1)	66.5 (90.1)	0.0 (0.0)	32.6 (9.8)
20	10^2	0.0 (0.0)	0.7 (0.0)	0.3 (0.1)	63.9 (89.0)	0.0 (0.0)	35.2 (10.8)
20	10^3	0.0 (0.0)	1.0 (0.0)	0.2 (0.1)	66.7 (90.7)	0.0 (0.0)	32.2 (9.2)
20	10^4	0.0 (0.0)	0.6 (0.0)	0.3 (0.2)	64.6 (90.2)	0.0 (0.0)	34.5 (9.6)
30	10^2	0.0 (0.0)	0.8 (0.0)	0.5 (0.0)	56.5 (88.3)	0.0 (0.0)	42.2 (11.6)
30	10^3	0.0 (0.0)	0.8 (0.0)	0.3 (0.1)	64.7 (89.9)	0.0 (0.0)	34.2 (10.0)
30	10^4	0.0 (0.0)	0.8 (0.0)	0.2 (0.1)	63.7 (89.2)	0.0 (0.0)	35.3 (10.7)

Table 7.12: Distribution identification percentages of Neural Networks for ordered Lognormal Distributed data

The distribution identification performance of the neural networks is difficult to quantify. It is probable that the division of training data caused the neural networks to be biased towards selecting the Pareto distribution. However, for the Weibull distribution the Pareto was often chosen when the shape parameter is large, where the Weibull approaches the Gaussian. It is important to note that none of the distributions successfully identified the Gaussian or Lognormal distributions as the best fit to test data (even if they were).

In addition, the networks needed at least 20 hidden neurons to converge to the most accurate set of solutions. Increasing the number of hidden neurons from 20 to 30 appeared to help mitigate the impact of the SCM, but had no net benefit if the CCM was used. However, in many cases the test and training data needed to be ordered for the neural networks with 10 hidden neurons to achieve any positive results.

When the SCM was used, the networks displayed a strong bias towards the Pareto distribution. This was especially prominent for the K distribution. However, the networks were largely accurate in classifying K distributed data if the CCM was used. This bias was also shown for Weibull data with large shape parameter values.

It should also be noted that care must be taken when training the neural networks. Only one neural network was trained for each scenario. However, the neural networks do not always converge to a usable solution. Nor do they behave in a monotonic fashion with respect to the training parameters. For instance, consider the Weibull networks with 10 hidden neurons that were trained with ordered data. The networks trained with 10^2 and 10^4 training samples per distribution/shape parameter pair both exhibited a higher classification accuracy than the network trained with 10^3 training samples.

The neural networks were effective at classifying test data to the source distribution if the covariance matrix was known and the distribution under test was one of the SIRVs with a shape parameter. In particular, if the CCM was used with unordered data there was only marginal improvement beyond using 20 hidden neurons and 10^3 training samples. In addition, the use of ordered data clearly reduced the needed number of hidden neurons and training samples.

However, the distribution identification neural networks largely chose the Pareto distribution if the SCM was used. Increasing the number of hidden neurons in the network also improved classification accuracy when the SCM was used, leaving open the possibility of increased accuracy if additional hidden neurons are added to the neural network compared to the cases considered here. However, this is a low sample support case. Increased sample

support would correspond to more input neurons (*i.e.* data) and a better covariance matrix estimate. Given the performance when the CCM is used, improved covariance matrix estimation techniques would also increase the performance of the distribution identification neural network.

7.2.2 Threshold Estimation

The next series of neural networks examined are trained to directly estimate the thresholds for all of the distributions under consideration. The parameters of the neural network (*i.e.* the number of hidden neurons, number of training samples, ordering of the training data) is described in Section 7.1. The general network architecture implemented here is shown in Figure 7.10.

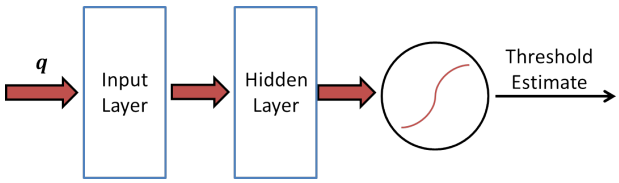

Figure 7.10: Threshold estimation neural network

Unlike the distribution identification neural networks shown in Section 7.2.1, here there are two measures of accuracy. First, the neural networks are evaluated by the average threshold estimation accuracy (once more the impact of using the SCM is considered). Second, a set of neural networks is formed with identical parameters where the distribution under test is excised from the training data. This second formulation is examined in an attempt to quantify the robustness of the estimation capabilities of the trained networks. In addition, by excising the distribution under test we provide a proxy for measuring the threshold estimation accuracy when the neural network encounters a distribution outside the training set (*i.e.* an unknown distribution).

The summary of the results of all the tests run are presented in Tables 7.13-7.17. The two leftmost columns of each table shows the number of hidden neurons and training samples

used to construct the neural network under test. The rest of the table is split into two sections, corresponding to the neural networks that were trained and tested with unordered data and those that were trained and tested with ordered data. The first column in each section shows the average threshold estimation accuracy (averaged over the test data and then averaged over all tested shape parameters, if applicable) for the neural networks trained with the distribution under test in the training data. The number outside the parentheses gives the accuracy when the clairvoyantly known true covariance matrix (CCM) is used to form the generalized inner product (GIP), while number in parentheses gives the average accuracy when the sample covariance matrix (SCM) is used instead. The second column gives the same results as the first column, except the neural networks used to provide that data were trained with a data set which had the distribution under test excised. Finally, the third column provides the change (in dB) made by using the SCM instead of the SCM. In this case, the number in parentheses corresponds to the networks trained with the excised data set, while the numbers outside the parentheses was generated by the networks trained with the full data set.

7.2.2.1 Threshold Estimation of Gaussian Data with Neural Networks

The first distribution under test is the Gaussian distribution. The accuracy of the average threshold estimates generated by each of the neural networks for the Gaussian distribution is shown in Table 7.13. From Table 7.13, when the data is unordered the network needs at least 20 hidden neurons to converge to an effective solution. Note that we are defining an effective solution to be a solution giving the best average error (which occurs for multiple networks). However, when 30 hidden neurons are used, the number of training samples does not have a great impact on the threshold estimate. The neural network corresponding to 20 hidden neurons trained with 10^4 training samples per distribution/shape parameter pair failed for both the full training set and the excised training set (note the full training set consisted of 153×10^4 training samples while the excised training set was a subset of 152×10^4 of those

training samples).

However, it is important to note that the use of the SCM degraded the average estimate by ≈ 1 dB for all cases with an effective solution. In addition, when the data was ordered all of the networks converged to solutions that gave approximately the same estimate accuracy. Therefore, once more ordering is shown to reduce the requirements of both the number of hidden neurons and number of training samples.

		Unordered Data			Ordered Data		
HN	Samples	Full	Excised	Δ_{full} (Δ_{excised})	Full	Excised	Δ_{full} (Δ_{excised})
10	10^2	5.3 (5.3)	5.5 (5.5)	0.0 (0.0)	3.2 (2.3)	3.1 (2.1)	-0.9 (-1.0)
10	10^3	5.5 (5.5)	5.1 (5.0)	0.0 (0.0)	3.1 (2.2)	3.2 (2.3)	-1.0 (-0.9)
10	10^4	5.5 (5.5)	5.7 (5.6)	0.0 (0.0)	3.0 (2.1)	3.1 (2.1)	-0.9 (-1.9)
20	10^2	3.3 (2.4)	3.2 (2.3)	-0.9 (-0.9)	3.5 (2.7)	3.2 (2.3)	-0.8 (-0.9)
20	10^3	3.3 (2.4)	3.4 (2.5)	-0.9 (-0.9)	3.3 (2.5)	3.2 (2.4)	-0.8 (-0.9)
20	10^4	5.5 (5.4)	5.6 (5.6)	0.0 (0.0)	3.1 (2.1)	3.2 (2.3)	-1.0 (-0.9)
30	10^2	3.1 (2.1)	3.2 (2.3)	-1.0 (-0.9)	3.4 (2.6)	3.2 (2.3)	-0.8 (-0.9)
30	10^3	3.1 (2.2)	3.3 (2.5)	-0.9 (-0.8)	3.5 (2.8)	3.2 (2.3)	-0.7 (-0.9)
30	10^4	3.2 (2.3)	3.2 (2.3)	-0.9 (-0.9)	3.2 (2.2)	3.2 (2.3)	-0.9 (-0.9)

Table 7.13: Average Threshold Error (dB) when Gaussian data is fed into single layer neural networks

7.2.2.2 Threshold Estimation of K Data with Neural Networks

Table 7.14 summarizes the average threshold accuracy given by the neural networks under consideration when K distributed test data is applied. When looking at the averages over shape parameter shown in Table 7.14, it appears that the number of hidden neurons and number of training samples used to form the neural network (for the parameters tested) make little difference when K distributed data is included in the training data. However, there is no clear trend that can be extrapolated when the K distributed data is excised from the training data. In addition, excising the K distributed data causes an ≈ 2 dB degradation in the average threshold estimate.

		Unordered Data			Ordered Data		
HN	Samples	Full	Excised	Δ_{full} (Δ_{excised})	Full	Excised	Δ_{full} (Δ_{excised})
10	10^2	2.6 (2.7)	4.1 (2.7)	0.0 (-1.4)	2.4 (2.3)	3.7 (2.3)	-0.1 (-1.5)
10	10^3	2.7 (2.8)	4.6 (2.9)	0.1 (-1.7)	2.4 (2.3)	3.1 (2.4)	-0.1 (-0.6)
10	10^4	2.8 (2.7)	3.6 (2.6)	-0.1 (-1.0)	2.4 (2.2)	3.0 (1.9)	-0.2 (-1.1)
20	10^2	2.3 (2.4)	2.0 (2.1)	0.0 (0.0)	2.4 (2.6)	3.7 (1.9)	0.2 (-1.8)
20	10^3	2.3 (2.5)	1.7 (2.4)	0.2 (0.7)	2.4 (2.5)	5.6 (1.9)	0.2 (-3.6)
20	10^4	2.8 (2.8)	4.0 (2.7)	-0.1 (-1.3)	2.4 (2.2)	3.7 (1.9)	-0.2 (-1.8)
30	10^2	2.4 (2.3)	3.2 (2.2)	-0.2 (-1.0)	2.4 (2.5)	3.5 (2.0)	0.1 (-1.5)
30	10^3	2.4 (2.2)	4.7 (2.0)	-0.2 (-2.7)	2.2 (2.6)	4.1 (2.0)	0.4 (-2.1)
30	10^4	2.4 (2.3)	4.4 (2.0)	-0.1 (-2.4)	2.4 (2.3)	3.9 (1.9)	-0.1 (-2.0)

Table 7.14: Average Threshold Error (dB) when K data is fed into single layer neural networks

Next, Figures 7.11a-7.11c show the average estimates as a function of shape parameter for the networks trained with the full set of unordered data while Figures 7.12a-7.12c show the same results for the networks trained with the ordered data. For both of these cases, the robustness to the SCM that was given in Table 7.14 is clearly illustrated. However, when shown as a function of shape parameter, the average threshold error is shown to be highly dependent on shape parameter. In other words, the threshold error is ≈ -4 dB for low shape parameter values, but ≈ 5 dB for high shape parameters. Therefore, the overall average accuracy listed in Table 7.14 is shown to be an artifact of the sampling of the shape parameter, rather than a representative average error.

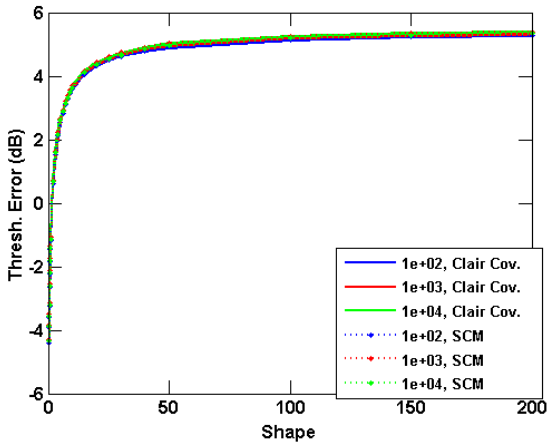

(a) Threshold error (in dB) for varying training sample support w/CCM (solid) and SCM (dotted) with 10 hidden neurons

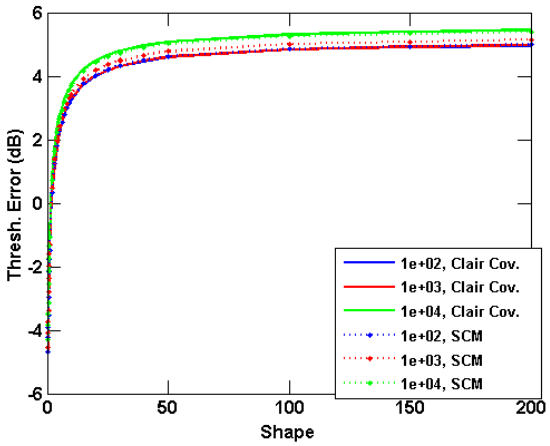

(b) Threshold error (in dB) for varying training sample support w/CCM (solid) and SCM (dotted) with 20 hidden neurons

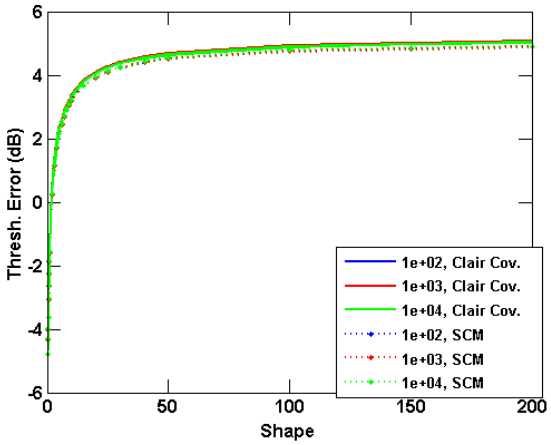

(c) Threshold error (in dB) for varying training sample support w/CCM (solid) and SCM (dotted) with 30 hidden neurons

Figure 7.11: Threshold estimation by neural networks for unordered K distributed data

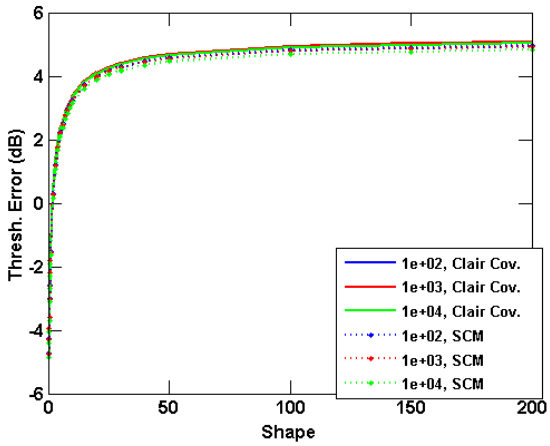

(a) Threshold error (in dB) for varying training sample support w/CCM (solid) and SCM (dotted) with 10 hidden neurons

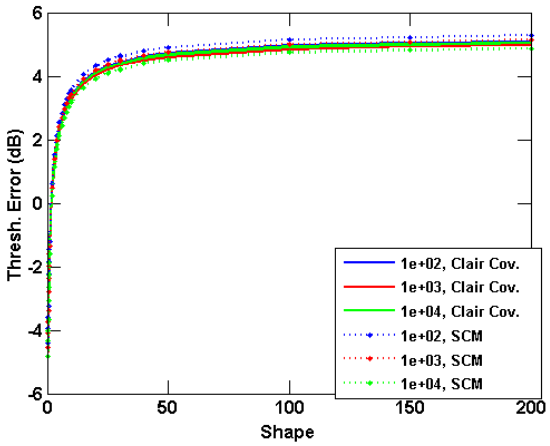

(b) Threshold error (in dB) for varying training sample support w/CCM (solid) and SCM (dotted) with 20 hidden neurons

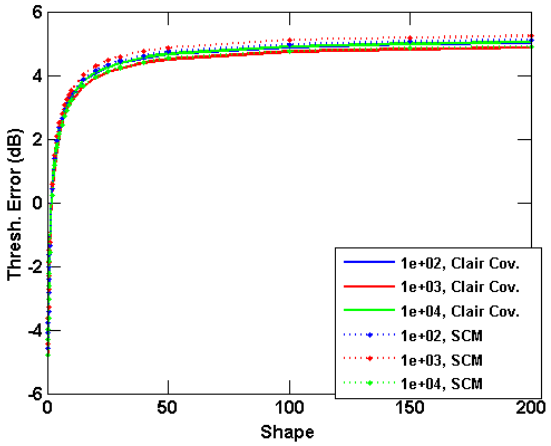

(c) Threshold error (in dB) for varying training sample support w/CCM (solid) and SCM (dotted) with 30 hidden neurons

Figure 7.12: Threshold estimation by neural networks for ordered K distributed data

Next, Figures 7.13a-7.13c and Figures 7.14a-7.14c show the average threshold estimate error as a function of shape parameter for neural networks trained without the K distribution in the data set. Figures 7.13a-7.13c show the results for the networks trained and tested with unordered data, while Figures 7.14a-7.14c show the average error when the training and test data is ordered.

The behaviour of the average threshold error as a function of shape parameter for Figures 7.13a-7.14c is similar to that seen in Figures 7.11a-7.12c. However, the greater impact of the

SCM that was shown in Table 7.14 is also clear.

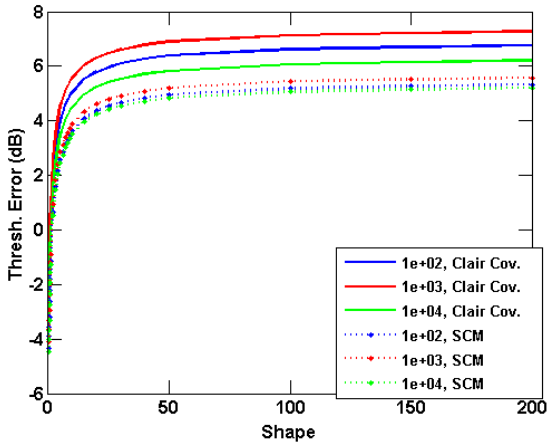

(a) Threshold error (in dB) for varying training sample support w/CCM (solid) and SCM (dotted) with 10 hidden neurons

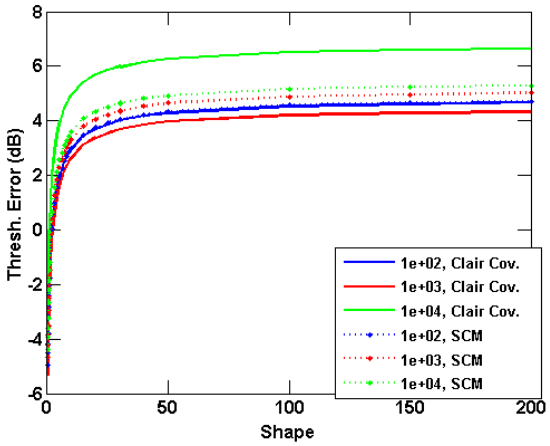

(b) Threshold error (in dB) for varying training sample support w/CCM (solid) and SCM (dotted) with 20 hidden neurons

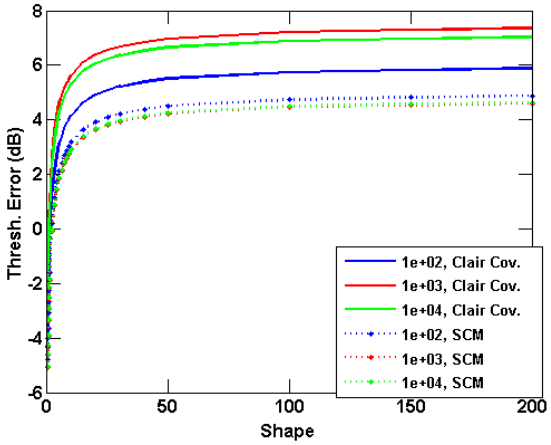

(c) Threshold error (in dB) for varying training sample support w/CCM (solid) and SCM (dotted) with 30 hidden neurons

Figure 7.13: Threshold estimation by neural networks for unordered K distributed data, K data not included in training data

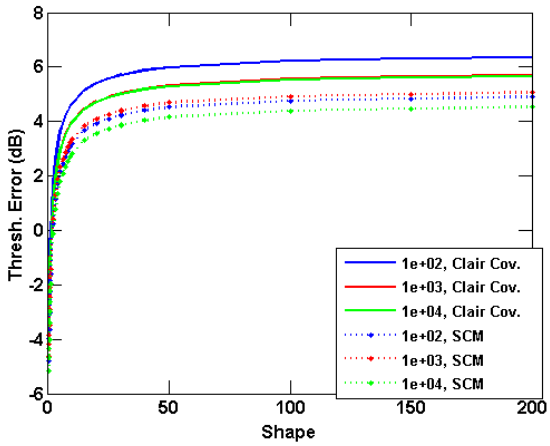

(a) Threshold error (in dB) for varying training sample support w/CCM (solid) and SCM (dotted) with 10 hidden neurons

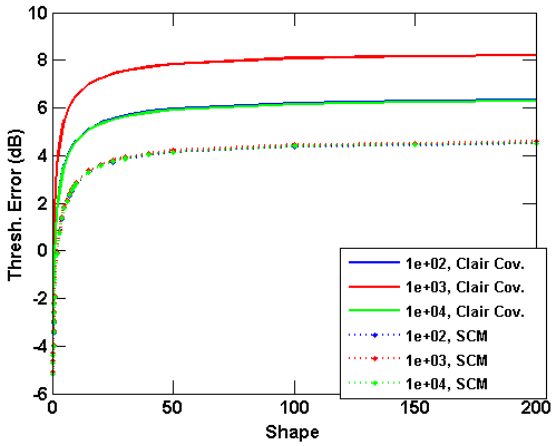

(b) Threshold error (in dB) for varying training sample support w/CCM (solid) and SCM (dotted) with 20 hidden neurons

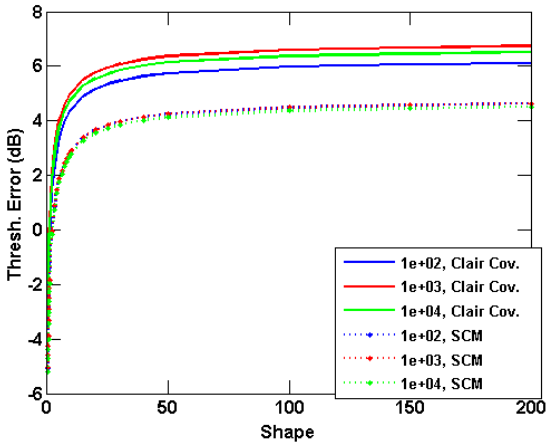

(c) Threshold error (in dB) for varying training sample support w/CCM (solid) and SCM (dotted) with 30 hidden neurons

Figure 7.14: Threshold estimation by neural networks for ordered K distributed data, K data not included in training data

7.2.2.3 Threshold Estimation of Weibull Data with Neural Networks

Table 7.15 summarizes the average threshold error when Weibull test data is fed into the threshold estimating neural networks. It is interesting to note that the networks using unordered data actually produced worse results when 30 hidden neurons were used, as opposed to 10 or 20. However, this degradation was only on the order of 0.5 dB. Also, the neural networks operating on ordered data all largely produced the same average results, all of

which were equivalent to the neural networks with 30 hidden neurons using unordered data. Once more, using the SCM had negligible impact ($< 1dB$).

		Unordered Data			Ordered Data		
HN	Samples	Full	Excised	Δ_{full} (Δ_{excised})	Full	Excised	Δ_{full} (Δ_{excised})
10	10^2	2.5 (2.3)	2.5 (2.5)	-0.2 (0.0)	3.0 (2.3)	3.3 (2.8)	-0.7 (-0.5)
10	10^3	2.5 (2.4)	2.5 (2.5)	0.0 (0.0)	3.0 (2.3)	3.3 (2.7)	-0.7 (-0.6)
10	10^4	2.4 (2.4)	2.8 (2.8)	0.0 (0.0)	3.0 (2.2)	3.3 (2.7)	-0.8 (-0.6)
20	10^2	3.0 (2.4)	3.2 (2.6)	-0.6 (-0.6)	3.1 (2.6)	3.2 (2.6)	-0.5 (-0.6)
20	10^3	3.1 (2.6)	3.3 (2.8)	-0.5 (-0.5)	3.2 (2.6)	3.3 (2.8)	-0.6 (-0.5)
20	10^4	2.5 (2.4)	2.6 (2.7)	-0.1 (0.0)	3.0 (2.3)	3.4 (2.8)	-0.7 (-0.6)
30	10^2	3.0 (2.2)	3.3 (2.9)	-0.7 (-0.4)	3.1 (2.5)	3.3 (2.9)	-0.6 (-0.4)
30	10^3	3.0 (2.3)	3.3 (2.8)	-0.7 (-0.5)	3.1 (2.6)	3.3 (2.8)	-0.5 (-0.5)
30	10^4	3.0 (2.3)	3.3 (2.8)	-0.7 (-0.5)	3.0 (2.3)	3.3 (2.7)	-0.7 (-0.6)

Table 7.15: Average Threshold Error (dB) when Weibull data is fed into single layer neural networks

Figures 7.15a-7.18c show the results for Table 7.15 as a function of shape parameter. The results for all cases are universally negative. The one positive result is the constant low impact of the SCM. However, all cases provide an estimate that is ≈ 4 dB below the optimal threshold for low shape parameter Weibull data while suffering a detection loss of ≈ 6 dB for data with a tail equal to the Gaussian distribution. The neural network parameters examined all have very little impact on the final estimate, nor does removing the Weibull distribution from the training data appreciably change the average error of the estimate.

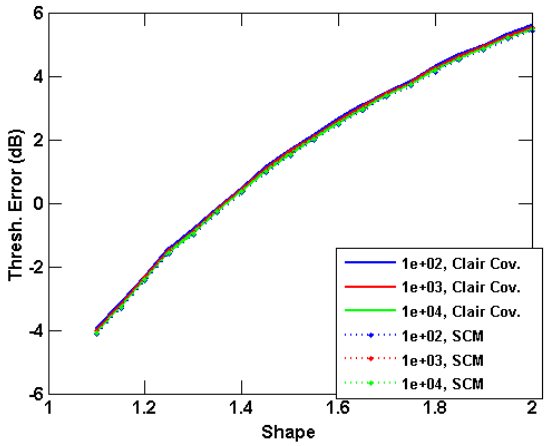

(a) Threshold error (in dB) for varying training sample support w/CCM (solid) and SCM (dotted) with 10 hidden neurons

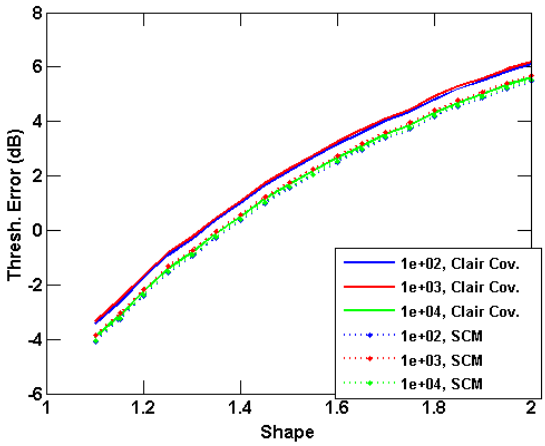

(b) Threshold error (in dB) for varying training sample support w/CCM (solid) and SCM (dotted) with 20 hidden neurons

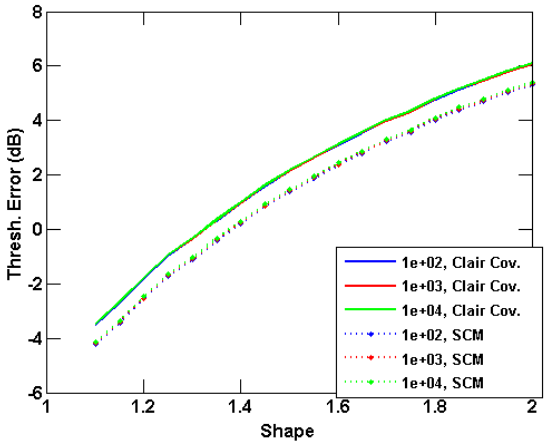

(c) Threshold error (in dB) for varying training sample support w/CCM (solid) and SCM (dotted) with 30 hidden neurons

Figure 7.15: Threshold estimation by neural networks for unordered Weibull distributed data

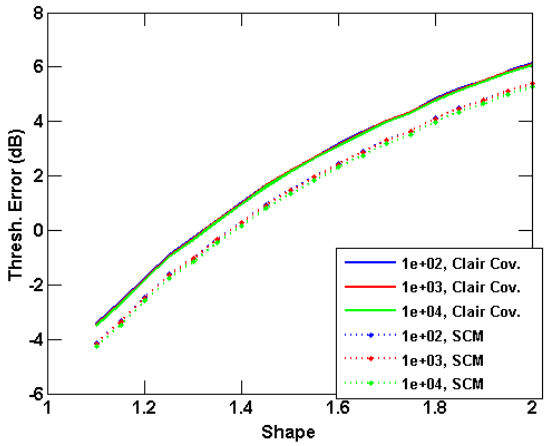

(a) Threshold error (in dB) for varying training sample support w/CCM (solid) and SCM (dotted) with 10 hidden neurons

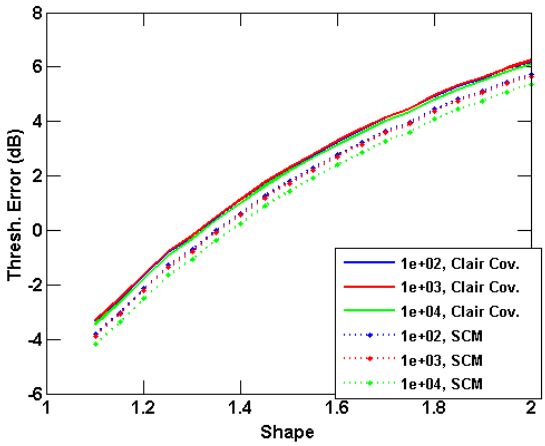

(b) Threshold error (in dB) for varying training sample support w/CCM (solid) and SCM (dotted) with 20 hidden neurons

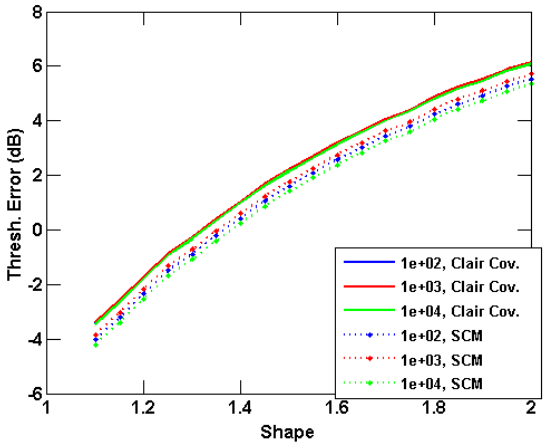

(c) Threshold error (in dB) for varying training sample support w/CCM (solid) and SCM (dotted) with 30 hidden neurons

Figure 7.16: Threshold estimation by neural networks for ordered Weibull distributed data

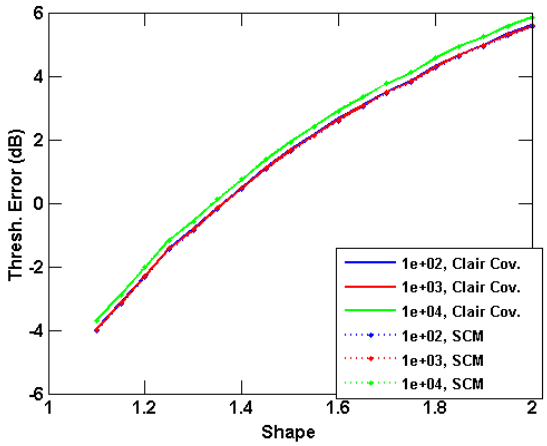

(a) Threshold error (in dB) for varying training sample support w/CCM (solid) and SCM (dotted) with 10 hidden neurons

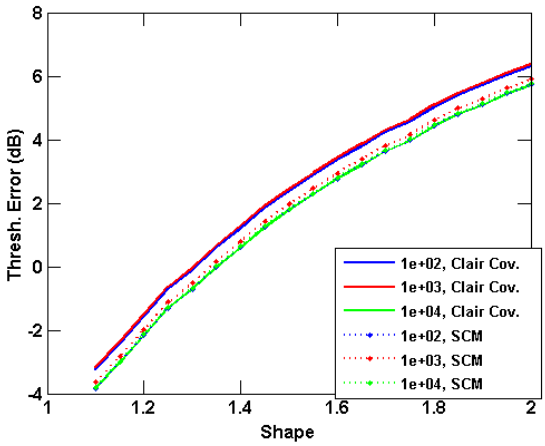

(b) Threshold error (in dB) for varying training sample support w/CCM (solid) and SCM (dotted) with 20 hidden neurons

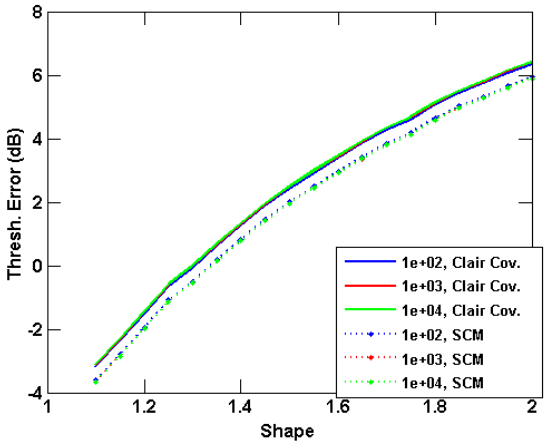

(c) Threshold error (in dB) for varying training sample support w/CCM (solid) and SCM (dotted) with 30 hidden neurons

Figure 7.17: Threshold estimation by neural networks for unordered Weibull distributed data, Weibull data not included in training data

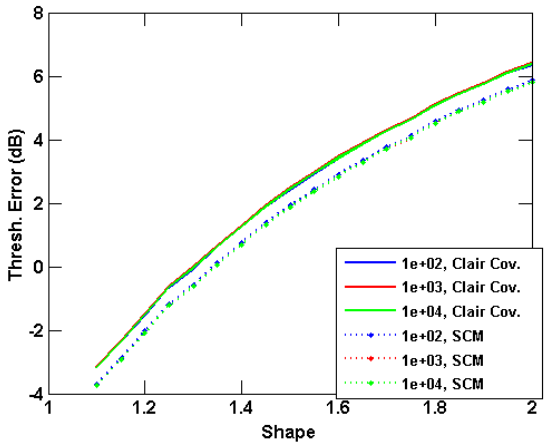

(a) Threshold error (in dB) for varying training sample support w/CCM (solid) and SCM (dotted) with 10 hidden neurons

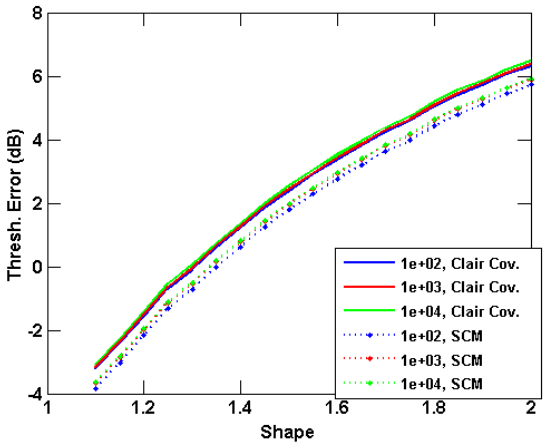

(b) Threshold error (in dB) for varying training sample support w/CCM (solid) and SCM (dotted) with 20 hidden neurons

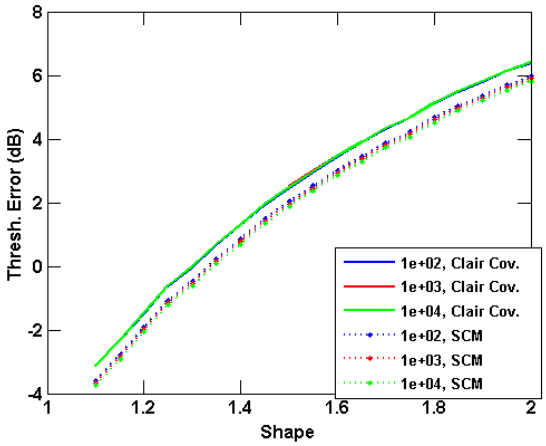

(c) Threshold error (in dB) for varying training sample support w/CCM (solid) and SCM (dotted) with 30 hidden neurons

Figure 7.18: Threshold estimation by neural networks for ordered Weibull distributed data, Weibull data not included in training data

7.2.2.4 Threshold Estimation of Pareto Data with Neural Networks

Table 7.16 shows the average threshold estimate error when Pareto distributed data is tested with the generated neural networks. The results shown in Table 7.16 show little variance among the various parameters considered. Note that the SCM has a slightly greater impact than was seen in Sections 7.2.2.1-7.2.2.3, but its use only results in estimates differing by ≈ 1 dB from the estimates generated by the CCM.

		Unordered Data			Ordered Data		
HN	Samples	Full	Excised	Δ_{full} (Δ_{excised})	Full	Excised	Δ_{full} (Δ_{excised})
10	10^2	2.6 (2.4)	2.9 (2.9)	-0.1 (0.0)	1.8 (0.5)	1.1 (0.1)	-1.3 (-0.9)
10	10^3	2.7 (2.6)	2.8 (2.9)	0.0 (0.0)	1.7 (0.4)	1.1 (0.2)	-1.3 (-0.9)
10	10^4	2.6 (2.6)	2.9 (2.9)	0.0 (0.0)	1.8 (0.3)	1.0 (-0.1)	-1.5 (-1.1)
20	10^2	1.8 (0.6)	0.8 (-0.3)	-1.2 (-1.1)	1.9 (0.9)	0.9 (-0.2)	-1.0 (-1.1)
20	10^3	1.8 (0.7)	1.0 (-0.1)	-1.1 (-1.1)	1.8 (0.7)	1.1 (0.1)	-1.1 (-1.0)
20	10^4	2.7 (2.6)	3.0 (3.0)	-0.1 (0.0)	1.8 (0.4)	1.0 (0.0)	-1.3 (-1.1)
30	10^2	1.8 (0.4)	1.1 (0.1)	-1.3 (-1.0)	1.8 (0.7)	1.5 (0.4)	-1.1 (-1.1)
30	10^3	1.7 (0.4)	1.0 (-0.2)	-1.3 (-1.1)	1.9 (0.9)	1.1 (0.0)	-1.0 (-1.1)
30	10^4	1.8 (0.5)	0.9 (-0.2)	-1.3 (-1.2)	1.8 (0.5)	1.0 (-0.1)	-1.3 (-1.1)

Table 7.16: Average Threshold Error (dB) when Pareto data is fed into single layer neural networks

Once more, as was seen in Sections 7.2.2.2 and 7.2.2.3, Figures 7.19a-7.22c show the poor threshold estimate given by the neural network for Pareto distributed data as a function of shape parameter. Any altering of most of the neural network parameters had little effect. However, Figures 7.21c and 7.22c show that when the Pareto distribution is omitted from the training data and 30 hidden neurons are used, the networks provide a slightly improved estimate for high shape parameter data. The improvement is on the order of ≈ 2 dB.

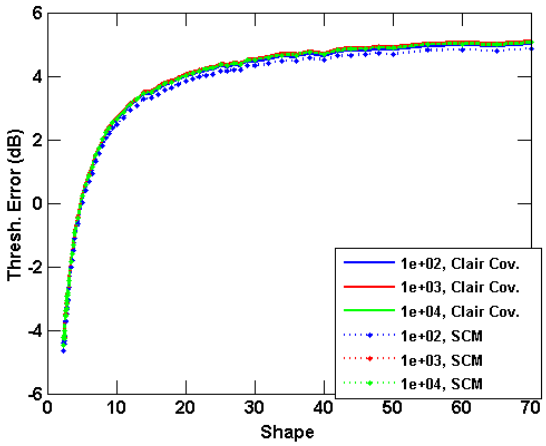

(a) Threshold error (in dB) for varying training sample support w/CCM (solid) and SCM (dotted) with 10 hidden neurons

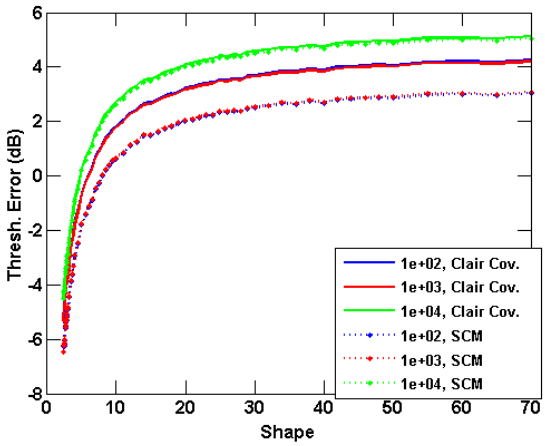

(b) Threshold error (in dB) for varying training sample support w/CCM (solid) and SCM (dotted) with 20 hidden neurons

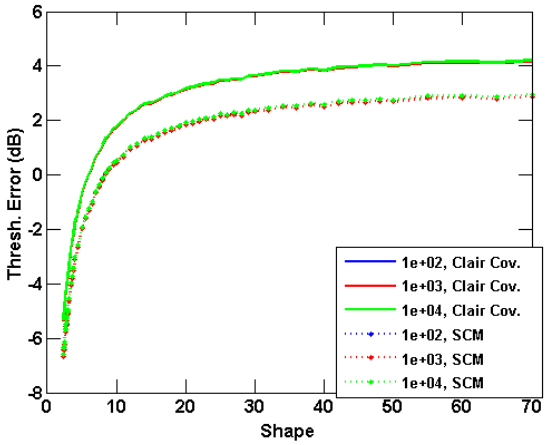

(c) Threshold error (in dB) for varying training sample support w/CCM (solid) and SCM (dotted) with 30 hidden neurons

Figure 7.19: Threshold estimation by neural networks for unordered Pareto distributed data

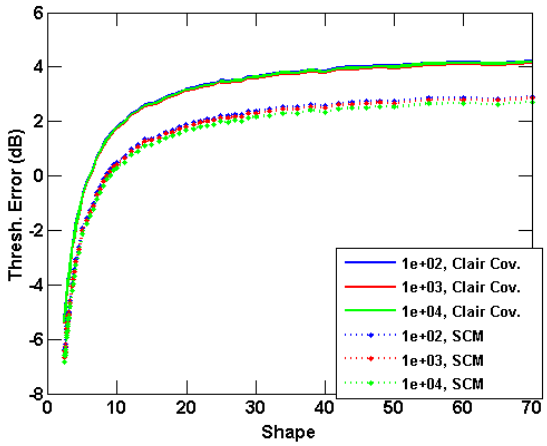

(a) Threshold error (in dB) for varying training sample support w/CCM (solid) and SCM (dotted) with 10 hidden neurons

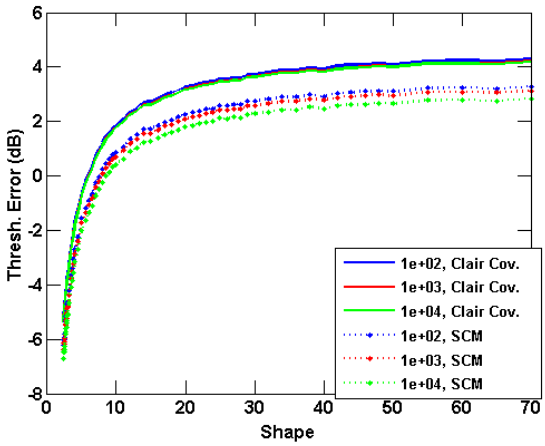

(b) Threshold error (in dB) for varying training sample support w/CCM (solid) and SCM (dotted) with 20 hidden neurons

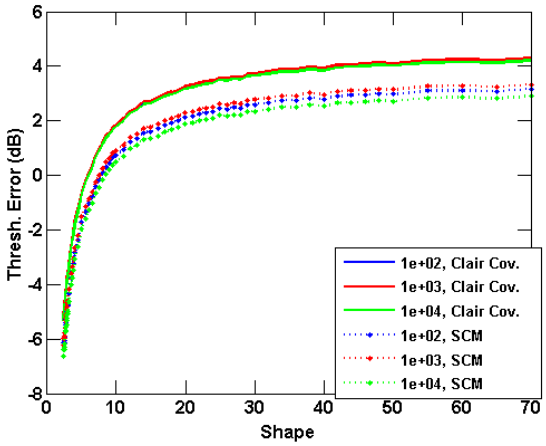

(c) Threshold error (in dB) for varying training sample support w/CCM (solid) and SCM (dotted) with 30 hidden neurons

Figure 7.20: Threshold estimation by neural networks for ordered Pareto distributed data

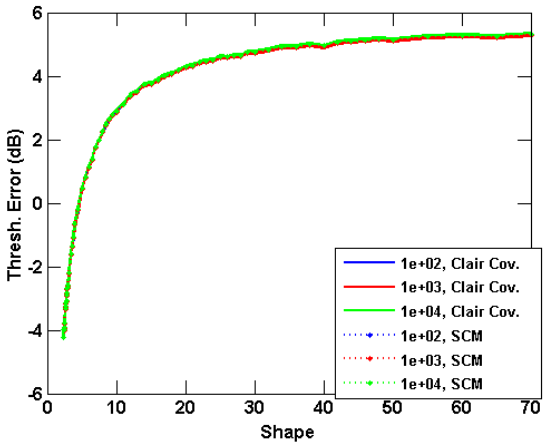

(a) Threshold error (in dB) for varying training sample support w/CCM (solid) and SCM (dotted) with 10 hidden neurons

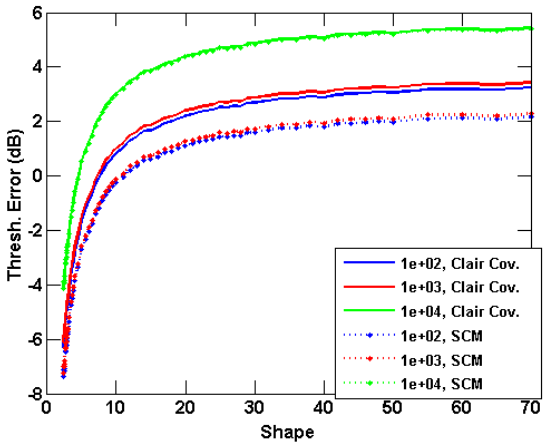

(b) Threshold error (in dB) for varying training sample support w/CCM (solid) and SCM (dotted) with 20 hidden neurons

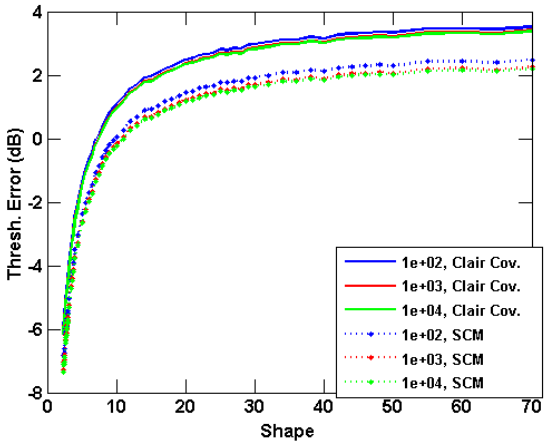

(c) Threshold error (in dB) for varying training sample support w/CCM (solid) and SCM (dotted) with 30 hidden neurons

Figure 7.21: Threshold estimation by neural networks for unordered Pareto distributed data, Pareto data not included in training data

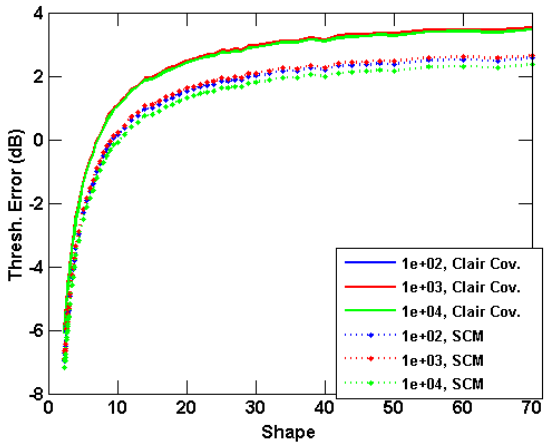

(a) Threshold error (in dB) for varying training sample support w/CCM (solid) and SCM (dotted) with 10 hidden neurons

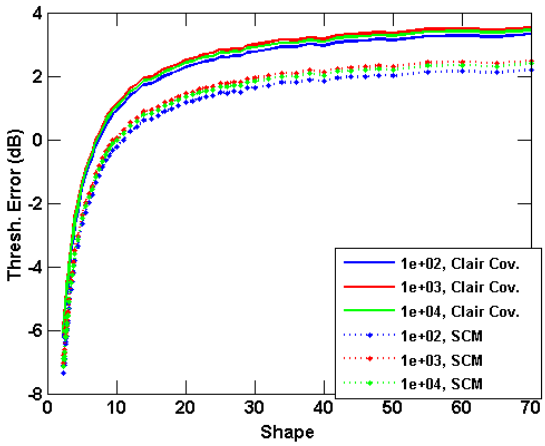

(b) Threshold error (in dB) for varying training sample support w/CCM (solid) and SCM (dotted) with 20 hidden neurons

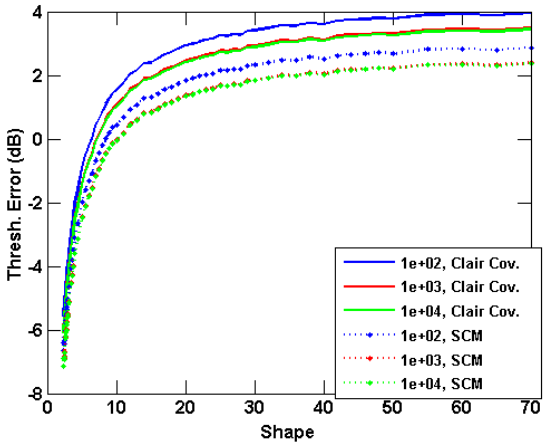

(c) Threshold error (in dB) for varying training sample support w/CCM (solid) and SCM (dotted) with 30 hidden neurons

Figure 7.22: Threshold estimation by neural networks for ordered Pareto distributed data, Pareto data not included in training data

7.2.2.5 Threshold Estimation of Lognormal Data with Neural Networks

Table 7.17 shows the accuracy of the set of neural networks in estimating the threshold of Lognormal distributed test data. The estimate error does not change appreciably if the Lognormal distribution is omitted from the distribution. However, the Lognormal distribution is the distribution with the heaviest tail out of the tested distributions. Note that the average accuracy is approximately the same as is seen for the smallest shape parameters of the

K, Weibull, and Pareto distributions (*i.e.* the closest comparable distributions examined). Also, the SCM has the largest effect on the average threshold estimate when compared to the results shown in Tables 7.13-7.16.

		Unordered Data			Ordered Data		
HN	Samples	Full	Excised	Δ_{full} (Δ_{excised})	Full	Excised	Δ_{full} (Δ_{excised})
10	10^2	-4.4 (-4.8)	-4.7 (-4.8)	-0.4 (-0.1)	-3.5 (-5.4)	-3.9 (-5.4)	-1.8 (-1.5)
10	10^3	-4.6 (-4.7)	-4.2 (-4.6)	-0.1 (-0.4)	-3.6 (-5.4)	-3.8 (-5.4)	-1.8 (-1.6)
10	10^4	-4.7 (-4.7)	-4.8 (-4.9)	0.0 (-0.1)	-3.4 (-5.5)	-3.6 (-5.5)	-2.1 (-1.9)
20	10^2	-3.6 (-5.3)	-3.7 (-5.5)	-1.7 (-1.8)	-3.8 (-5.2)	-3.9 (-5.4)	-1.3 (-1.6)
20	10^3	-3.8 (-5.3)	-3.8 (-5.4)	-1.5 (-1.5)	-3.8 (-5.3)	-3.7 (-5.4)	-1.5 (-1.7)
20	10^4	-4.4 (-4.7)	-4.7 (-4.8)	-0.2 (-0.1)	-3.5 (-5.4)	-3.9 (-5.4)	-1.9 (-1.5)
30	10^2	-3.6 (-5.4)	-3.9 (-5.5)	-1.8 (-1.6)	-3.8 (-5.4)	-3.8 (-5.4)	-1.6 (-1.7)
30	10^3	-3.6 (-5.4)	-3.7 (-5.5)	-1.8 (-1.7)	-3.9 (-5.2)	-3.7 (-5.4)	-1.4 (-1.7)
30	10^4	-3.6 (-5.3)	-3.7 (-5.4)	-1.7 (-1.6)	-3.6 (-5.4)	-3.8 (-5.4)	-1.8 (-1.6)

Table 7.17: Average Threshold Error (dB) when lognormal data is fed into single layer neural networks

7.2.2.6 Conclusions

In conclusion, the distribution with the most accurate threshold estimate is the Gaussian distribution. The threshold estimates for distributions possessing shape parameters were highly dependent on the shape parameter of the test data. In addition, the estimates were universally $\approx$ 4 dB too low for the shape parameters corresponding to the heaviest tail (which require thresholds $\approx$ 10 dB greater than the Gaussian distribution) and suffered from a detection loss of 4-6 dB for the distributions approaching the Gaussian (*i.e.* with high shape parameters). However, the estimates were robust to the SCM and largely did not vary with respect to number of hidden neurons or training samples. In summation, for the parameters considered here, on the whole neural networks are not a good fit for directly estimating the detection threshold for this group of distributions.

7.3 Conclusions

The neural networks examined here struggled with the ambiguities inherent in the distributions considered. However, Section 7.2.1 showed that a simple feedforward multilayer perceptron network with one hidden layer could potentially distinguish SIRV distributions with large shape parameters.

In particular, applying neural networks to the distribution identification/classification task showed promise. However there were two primary sources of error. First, using the sample covariance matrix estimate greatly disrupted the ability of the neural networks to classify the test data to the correct distribution. Second, the networks had problems identifying light tailed SIRV distributions (*i.e.* distributions whose tail approaches that of the Gaussian). This error was evident when Gaussian data or high shape parameter Weibull distributed data was tested. However, in these cases data was often assigned to the Pareto distribution, which was possibly over-represented in the training data.

In Appendix C research is presented on the maximal scale invariant test statistic for SIRV distributions. However, the maximum estimation of the covariance matrix needed to implement the test statistic of (C.9) requires the distribution and shape parameter of the SIRV to which the data belongs. As such a neural network with the capability to efficiently identify the generating SIRV distribution of test data could be coupled with a distribution specific shape parameter estimator. This processing chain would allow the test statistic of (C.9) to be optimally implemented. This technique was informally attempted, although the results are not shown. The sample support under consideration was not sufficient to provide numerically stable estimates of the covariance matrix.

In addition, increased sample support would likely improve performance of the neural network. It was shown that only ≈ 20 hidden neurons are needed to successfully perform distribution identification if the covariance matrix is known. However, if the sample covariance matrix is used, an additional 10 hidden neurons improve the accuracy of the classifier. Therefore, as in practice the covariance matrix is never known, in future work the sample

support and number of hidden neurons should be increased when attempting to generate a distribution classification neural network.

For both the distribution identification and threshold estimation neural networks, it was shown that pre-processing the sample data by ordering it did not necessarily improve the accuracy of the output of the neural network. However, ordering the data aided in the convergence of the neural network training. In particular, consistent results were found for all three sizes of neural networks considered and the number of training samples needed to converge to the best found solution was reduced. Without ordering, some neural networks failed to converge to a successful output.

It was confirmed that the performance of the neural network was not heavily dependent on the number of hidden neurons. Increasing the number of hidden neurons from 20 to 30 did not improve performance in the majority of situations examined when the true covariance matrix was used. However, when the sample covariance matrix was employed, increasing the number of hidden neurons to 30 appeared to provide robustness to the estimate.

The threshold estimates that were given by the neural networks considered in Section 7.2.2 were accurate when averaged over the values of shape parameter. However, when examined as a function of shape parameter, the threshold estimate was highly inaccurate. Two different approaches based on a deep network architecture are considered in Appendix B. However, neither of these approaches improves on the results shown in Section 6.3.3. In general, it appears that the threshold estimating neural networks were biased towards estimating a threshold close to the average threshold of the training data (*i.e.* the true threshold, averaged over all shape parameters and distributions). Therefore, the nature of the threshold estimate error given by the neural networks depended on the relationship between the shape parameter and threshold for each SIRV distribution under test.

To improve the results shown here, scenarios with greater sample support should be considered. The increased sample support should increase the accuracy of the neural network due to the availability of more information, as well as increase the quality of the data through

a more accurate covariance matrix estimate.

In addition, a "bootstrapping" approach to covariance matrix estimation should be considered. In this approach, the output of the distribution identification neural network is used to inform the covariance matrix estimation technique shown in [75, 114]. The improved covariance matrix estimate is then fed into the distribution identification neural network to ensure that the hypothesized distribution is unchanged If a different distribution was chosen by the neural network, repeat the process until convergence.

A new threshold estimation neural network should be examined. More precisely, a neural network with a discrete number of outputs corresponding to "steps" in threshold magnitude should be formed. These steps should be formed to conform to mission needs. For instance, the output layer could consist of 11 output neurons corresponding to an increased threshold (above that needed in the presence of Gaussian distributed clutter) of $0, 1, \ldots, 10$ dB. In such a case, the training data would need to be segmented to ensure an equal amount of samples correspond to each step, or output neuron. The deep approaches considered in Appendix B should also be examined using this new threshold estimation architecture.

Finally, the deep belief network (DBN) is a popular form of deep network [116, 123]. This important technique uses unsupervised learning to form the bottom layers of the deep network, along with supervised learning to fine tune the parameters. This training process helps prevent the DBN from becoming stuck in solutions corresponding to local minima [123].

Overall, the neural network based techniques show much promise in mitigating SIRV clutter, and may form a strong foundation upon which to build a cognitive radar. However, more work is needed to explore their capabilities in this arena.

Chapter 8

Divergences

At the heart of the radar detection problem is a binary question: is a target present or absent in a cell under test. To provide statistical meaning, the question is typically posed as a binary hypothesis test. In order for the hypothesis test to produce accurate detections, the underlying distributions of each hypothesis must be accurately represented. In Chapter 5 a novel approach was presented to provide a method of transforming and separating distributions into subspaces. The question naturally arises, how does one define *distances* between distributions? To address the utility of the COSMiC algorithm, how does one address the notion of distance in the endpoint space? This chapter provides a brief discussion of work to illuminate these questions. The Bregman divergence and the f divergence are defined and briefly discussed, and the Kullback-Leibler divergence is shown and explored.

8.1 The Bregman Divergence

The Bregman divergence was first conceived in 1967 as a method of convex optimization [124]. Let the function $\phi : \mathbb{R}^L \mapsto \mathbb{R}$ be a strictly convex differentiable function. Then the Bregman divergence $d_\phi : \mathbb{R}^L \times \mathbb{R}^L \mapsto [0, \infty)$ is given as [124, 125]

$$d_\phi(\mathbf{x}, \mathbf{y}) = \phi(\mathbf{x}) - \phi(\mathbf{y}) - \langle \mathbf{x} - \mathbf{y}, \nabla\phi(\mathbf{y}) \rangle \tag{8.1}$$

where $\langle \mathbf{x}, \mathbf{y} \rangle$ is the inner product and $\nabla\phi(\mathbf{y})$ is the gradient of ϕ, evaluated at $\mathbf{y}$.

The squared Euclidean distance is a classic example of a Bregman divergence. For the squared Euclidean distance, the function $\phi(\mathbf{x}, \mathbf{x}) = \langle \mathbf{x}, \mathbf{x} \rangle$. Using this definition in (8.1),

$$\begin{aligned} d_\phi(\mathbf{x}, \mathbf{y}) &= \phi(\mathbf{x}) - \phi(\mathbf{y}) - \langle \mathbf{x} - \mathbf{y}, \nabla\phi(\mathbf{y}) \rangle \\ &= \langle \mathbf{x}, \mathbf{x} \rangle - \langle \mathbf{y}, \mathbf{y} \rangle - \langle \mathbf{x} - \mathbf{y}, \nabla\phi(\mathbf{y}) \rangle \\ &= \langle \mathbf{x}, \mathbf{x} \rangle - \langle \mathbf{y}, \mathbf{y} \rangle - \langle \mathbf{x} - \mathbf{y}, 2\mathbf{y} \rangle \\ &= \mathbf{x}^T\mathbf{x} - \mathbf{y}^T\mathbf{y} - 2\mathbf{x}^T\mathbf{y} + 2\mathbf{y}^T\mathbf{y} \\ &= \mathbf{x}^T\mathbf{x} - 2\mathbf{x}^T\mathbf{y} + \mathbf{y}^T\mathbf{y} \\ &= ||\mathbf{x} - \mathbf{y}||^2. \end{aligned} \tag{8.2}$$

The general class of Bregman divergences encompass a number of commonly used divergence functions, such as the Itakura-Saito distance, Kullback-Leibler divergence, Mahalanobis distance, and the generalized I-divergence [125–128].

The Bregman divergence is unique in that it is minimized by the conditional expectation. Further, if a function is minimized by the conditional expectation (*e.g.* mean squared error), it is a Bregman divergence [129]. Finally, the Bregman divergence possesses a dual convex function, obtained using the gradient of ϕ. The divergence between transformed points does not vary in this dual space, allowing for further versatility when using a Bregman divergence [130].

8.2 The f Divergence

The f divergence is another class of divergence, discovered by Csiszar [131] and Ali and Silvey [132]. For continuous random variables, the f divergence is defined as [133]

$$D_f(P, Q) = \int \frac{\mathrm{d}Q}{\mathrm{d}\mu} f\left(\frac{\mathrm{d}P/\mathrm{d}\mu}{\mathrm{d}Q/\mathrm{d}\mu}\right) \mathrm{d}\mu \tag{8.3}$$

for convex $f : (0, \infty) \mapsto \mathbb{R}$ where μ is a σ-finite measure.

The f divergence between probabilities $\mathbf{x}$ and $\mathbf{y}$, $D_f(\mathbf{x} : \mathbf{y})$ possesses the property of information monoticity. In other words, when transforming distributions $\mathbf{x} \mapsto \mathbf{x}'$ and $\mathbf{y} \mapsto \mathbf{y}'$

$$D_f(\mathbf{x} : \mathbf{y}) \geq D_f(\mathbf{x}' : \mathbf{y}'). \tag{8.4}$$

8.3 The Kullback-Leibler Divergence

The Kullback-Leibler (KL) divergence is a useful measure of distance between distributions. The KL divergence between distributions $p(\mathbf{x})$ and $q(\mathbf{x})$ is defined as [134, 135]

$$D(P, Q) = \int p(\mathbf{x}) \log \frac{p(\mathbf{x})}{q(\mathbf{x})} \tag{8.5}$$

where $\mathbf{x} \in \mathbb{R}^L$. From inspection of (8.5), it can be seen that the KL divergence is the expectation of the log likelihood of $p(\mathbf{x})$ and $q(\mathbf{x})$, evaluated over the distribution $p(\mathbf{x})$. The KL divergence is [134]

1. Asymmetric: $D(P, Q) \neq D(Q, P)$.

2. Nonnegative: $D(P, Q) \geq 0$, reaching equality for identical distributions, so $D(P, P) = 0$.

The KL divergence can be used to explore the consequences of distribution mismatch in the context of a hypothesis test. In other words, consider a sample vector $\mathbf{x}$, a null hypothesis $f_H(\mathbf{x})$, and an alternate hypothesis (*i.e.* target present) $f_A(\mathbf{x})$. By taking the natural logarithm of the likelihood ratio test, the log-likelihood test is given as

$$\begin{aligned} \Lambda &= \Lambda(\mathbf{x}) \\ &= \log \frac{f_A(\mathbf{x})}{f_H(\mathbf{x})}. \end{aligned} \tag{8.6}$$

The Neyman-Pearson criterion is satisfied when the probability P_A is maximized for a threshold u such that $P_H(\Lambda > u) = \alpha$ where α is chosen to give an acceptable level of probability of false alarm. However, if an incorrect null hypothesis $f_Q(\mathbf{x})$ is used, the incorrect log-likelihood test is given as

$$\begin{aligned}\tilde{\Lambda} &= \tilde{\Lambda}(\mathbf{x}) \\ &= \log\frac{f_A(\mathbf{x})}{f_Q(\mathbf{x})}.\end{aligned} \tag{8.7}$$

It can be shown that [134]

$$P_A(\Lambda > u) - P_A(\tilde{\Lambda} > u) \geq e^u[P_H(\Lambda > u) - P_H(\tilde{\Lambda} > u)]. \tag{8.8}$$

Integrating over all possible thresholds of u from $-\infty$ to ∞ yields the loss of power of the test [134]

$$\begin{aligned}\Delta_{\text{power}} &= \int (\Lambda - \tilde{\Lambda}) f_H(\mathbf{x}) \mathrm{d}\mathbf{x} \\ &= D(P_H, P_Q) \geq 0.\end{aligned} \tag{8.9}$$

Therefore, the KL divergence between the correct and incorrect null hypothesis is equal to the overall loss of power of the hypothesis test caused by the incorrect assumption.

It was established in [136] that the KL divergence is the only divergence to intersect the f divergence and Bregman divergence classes under linear constraints. Those results were extended to prove that the KL divergence is the only divergence to belong to both classes under nonlinear constraints [130]. In particular, the f divergence $f(t) = t\ln t$ forms the KL divergence. Therefore, the KL divergence possesses all of the advantageous properties discussed in Sections 8.1 and 8.2. As such, the KL divergence is the focus of the remainder of this chapter.

8.4 Kullback-Leibler divergence from the Gaussian distribution

In Chapter 3 the spherically invariant class of random vectors (SIRVs) was introduced as a physically and mathematically justified model for radar clutter. In addition, it was established that SIRVs are formed by modulating a Gaussian distributed random vector with a positive random variable. In Chapter 5.2 the Ozturk algorithm was introduced and expanded on. The goal of the Ozturk algorithm was to create a unique graphical "distance" between various known non-Gaussian SIRV distributions and the Gaussian distribution. Here we take a divergence based approach (namely the Kullback-Leibler divergence) to provide an expression of the distance between arbitrary SIRV distributions and the Gaussian distribution.

First, recall equation (3.28), restated here:

$$f_Q(q) = \frac{1}{2^L \Gamma(L)} q^{L-1} h_{2L}(q) u(q). \tag{8.10}$$

For the Gaussian distribution, $h_{2L}(q)$ is

$$h_{2L}(q) = \exp(-q). \tag{8.11}$$

Therefore, from (8.5), (8.10) and (8.11), the KL divergence between the quadratic forms of

the Gaussian distribution and any arbitrary SIRV distribution S is

$$\begin{aligned} D(G,S) &= \int_0^\infty f_G(q)\ln\frac{f_G(q)}{f_S(q)}\mathrm{d}q \\ &= \int_0^\infty \frac{1}{2^L\Gamma(L)}q^{L-1}\exp(-q)\ln\frac{\frac{1}{2^L\Gamma(L)}q^{L-1}\exp(-q)}{\frac{1}{2^L\Gamma(L)}q^{L-1}h_{2L}(q)}\mathrm{d}q \\ &= \frac{1}{2^L\Gamma(L)}\int_0^\infty q^{L-1}\exp(-q)\ln\frac{\exp(-q)}{h_{2L}(q)}\mathrm{d}q \\ &= \frac{1}{2^L\Gamma(L)}\int_0^\infty q^{L-1}\exp(-q)\left[\ln(\exp(-q)) - \ln(h_{2L}(q))\right]\mathrm{d}q \\ &= \frac{1}{2^L\Gamma(L)}\int_0^\infty q^{L-1}\exp(-q)\left[-q - \ln(h_{2L}(q))\right]\mathrm{d}q \end{aligned} \tag{8.12}$$

where $f_G(q)$ is the pdf of the quadratic form of the Gaussian distribution, ln is the natural logarithm, $f_S(q)$ is the pdf of the quadratic form of an arbitrary SIRV, and $h_{2L}(q)$ is the function associated with the SIRV S, defined in (3.27). The Gamma function is defined as [98, 99]

$$\Gamma(x) = \int_0^\infty \exp(-t)t^{x-1}\mathrm{d}t \tag{8.13}$$

and possesses the relation for integer L [99]

$$\Gamma(L+1) = L! \tag{8.14}$$

where $(\bullet)!$ denotes the factorial operation. Using the linearity of the integral operation and

the definitions of (8.13) and (8.14), the KL divergence of (8.12) becomes

$$\begin{aligned} D(G,S) &= \int_0^\infty f_G(q)\ln\frac{f_G(q)}{f_S(q)}\mathrm{d}q \\ &= \frac{1}{2^L\Gamma(L)}\int_0^\infty q^{L-1}\exp(-q)\left[-q-\ln(h_{2L}(q))\right]\mathrm{d}q \\ &= \frac{1}{2^L\Gamma(L)}\left[\int_0^\infty -q^L\exp(-q)\mathrm{d}q - \int_0^\infty q^{L-1}\exp(-q)\ln(h_{2L}(q))\mathrm{d}q\right] \\ &= \frac{1}{2^L\Gamma(L)}\left[-\Gamma(L+1) - \int_0^\infty q^{L-1}\exp(-q)\ln(h_{2L}(q))\mathrm{d}q\right] \\ &= \frac{1}{2^L\Gamma(L)}\left[-L! - \int_0^\infty q^{L-1}\exp(-q)\ln(h_{2L}(q))\mathrm{d}q\right]. \end{aligned} \tag{8.15}$$

Therefore, the KL divergence between the Gaussian SIRV and different SIRVs solely depends on the integral in (8.15).

8.4.1 KL divergence between the Gaussian and Pareto distributions

Upon examination of the SIRV pdfs explored in Chapter 3, the pdf of the Pareto function is the only pdf with a closed form. Therefore, the Pareto distribution is a convenient distribution with which to study the KL divergence of equation (8.15). Recall from (3.99) that the function $h_{2L}(q)$ of the Pareto distribution is

$$h_{2L}(q) = \frac{\Gamma\left(L+\nu+1\right)}{\Gamma\left(\nu+1\right)}\frac{\nu^{(\nu+1)}}{(q+\nu)^{(L+\nu+1)}}. \tag{8.16}$$

For notational convenience, define the values

$$\alpha = L+\nu+1 \tag{8.17}$$

and

$$\beta = \frac{\Gamma(\alpha)\nu^{\nu+1}}{\Gamma(\nu+1)}. \tag{8.18}$$

Note that both α and β are non-zero, positive real numbers. Combining (8.15) - (8.18) and invoking the linearity of the integration operator yields

$$\begin{aligned}
D(G,P) &= \frac{1}{2^L\Gamma(L)}\left[-L! - \int_0^\infty q^{L-1}\exp(-q)\ln(h_{2L}(q))\mathrm{d}q\right] \\
&= \frac{1}{2^L\Gamma(L)}\left[-L! - \int_0^\infty q^{L-1}\exp(-q)\ln\left(\frac{\Gamma\left(L+\nu+1\right)}{\Gamma\left(\nu+1\right)}\frac{\nu^{(\nu+1)}}{(q+\nu)^{(L+\nu+1)}}\right)\mathrm{d}q\right] \\
&= \frac{1}{2^L\Gamma(L)}\left[-L! - \int_0^\infty q^{L-1}\exp(-q)\ln\left(\frac{\beta}{(q+\nu)^\alpha}\right)\mathrm{d}q\right] \\
&= \frac{1}{2^L\Gamma(L)}\left[-L! - \int_0^\infty q^{L-1}\exp(-q)\left[\ln\beta - \ln\left((q+\nu)^\alpha\right)\right]\mathrm{d}q\right] \\
&= \frac{1}{2^L\Gamma(L)}\left[-L! - \left(\ln\beta\int_0^\infty q^{L-1}\exp(-q)\mathrm{d}q - \alpha\int_0^\infty q^{L-1}\exp(-q)\ln(q+\nu)\mathrm{d}q\right)\right].
\end{aligned} \tag{8.19}$$

Applying the definitions (8.13) and (8.14) to (8.19) results in

$$\begin{aligned}
D(G,P) &= \frac{1}{2^L\Gamma(L)}\left[-L! - \int_0^\infty q^{L-1}\exp(-q)\ln(h_{2L}(q))\mathrm{d}q\right] \\
&= \frac{1}{2^L\Gamma(L)}\left[-L! - \left(\ln\beta\int_0^\infty q^{L-1}\exp(-q)\mathrm{d}q - \alpha\int_0^\infty q^{L-1}\exp(-q)\ln(q+\nu)\mathrm{d}q\right)\right] \\
&= \frac{1}{2^L\Gamma(L)}\left[-L! - \left(\ln\beta\Gamma(L) - \alpha\int_0^\infty q^{L-1}\exp(-q)\ln(q+\nu)\mathrm{d}q\right)\right] \\
&= \frac{1}{2^L\Gamma(L)}\left[\alpha\int_0^\infty q^{L-1}\exp(-q)\ln(q+\nu)\mathrm{d}q - L! - \ln\beta(L-1)!\right].
\end{aligned} \tag{8.20}$$

The divergence of (8.20) then requires evaluation of the integral

$$\int_0^\infty q^{L-1}\exp(-q)\ln(q+\nu)\mathrm{d}q \tag{8.21}$$

where L is the integer length of the SIRV, ν is the non-zero, positive, real-valued shape parameter. The integration of (8.21) can be evaluated via integration by parts as

$$\int_0^\infty q^{L-1}\exp(-q)\ln(q+\nu)\mathrm{d}q = \int_0^\infty u\mathrm{d}v = [uv]_0^\infty - \int_0^\infty v\mathrm{d}u \tag{8.22}$$

where

$$u = \ln(q + \nu), \tag{8.23}$$

$$\mathrm{d}u = \frac{1}{q + \nu}\mathrm{d}q, \tag{8.24}$$

and

$$\mathrm{d}v = q^{L-1}\exp(-q)\mathrm{d}q. \tag{8.25}$$

The integral of (8.22) is solved in four stages. First, the indefinite integral of (8.25) is determined. Second, the product uv must be evaluated at the limit $q \to \infty$. Third, the product uv must be evaluated at the limit $q \to 0$. Fourth, the integral $\int_0^\infty v\mathrm{d}u$ is found. The four parts are then combined to form the final value.

First, the indefinite integral

$$\int q^{L-1}\exp(-q)\mathrm{d}q \tag{8.26}$$

can be evaluated using integration by parts. Let

$$\begin{aligned}\int q^{L-1}\exp(-q)\mathrm{d}q &= \int m\mathrm{d}n \\ &= mn - \int n\mathrm{d}m\end{aligned} \tag{8.27}$$

where

$$m = q^{L-1}, \tag{8.28}$$

$$\mathrm{d}n = \exp(-q)\mathrm{d}q, \tag{8.29}$$

$$\mathrm{d}m = (L-1)q^{L-2}\mathrm{d}q, \tag{8.30}$$

and n is readily found as

$$n = \int \mathrm{d}n = \int \exp(-q)\mathrm{d}q = -\exp(-q). \tag{8.31}$$

Therefore, from (8.28) - (8.31), (8.27) becomes

$$\begin{aligned}\int q^{L-1}\exp(-q)\mathrm{d}q &= \int m\mathrm{d}n \\ &= mn - \int n\mathrm{d}m \\ &= -q^{L-1}\exp(-q) - (-1)\int \exp(-q)(L-1)q^{L-2}\mathrm{d}q \\ &= -q^{L-1}\exp(-q) + (L-1)\int q^{L-2}\exp(-q)\mathrm{d}q. \end{aligned} \tag{8.32}$$

Applying a similar integration by parts as (8.28) -(8.31) to (8.32) yields

$$\begin{aligned}\int q^{L-1}\exp(-q)\mathrm{d}q &= -q^{L-1}\exp(-q) + (L-1)\int q^{L-2}\exp(-q)\mathrm{d}q \\ &= -q^{L-1}\exp(-q) + (L-1)\left[-q^{L-2}\exp(-q) - \int(-1)\exp(-q)(L-2)q^{L-3}\mathrm{d}q\right] \\ &= -\exp(-q)\left(q^{L-1} + (L-1)q^{L-2}\right) + (L-1)(L-2)\int q^{L-3}\exp(-q)\mathrm{d}q \\ &= -\exp(-q)(L-1)!\left(\frac{1}{(L-1)!}q^{L-1} + \frac{1}{(L-2)!}q^{L-2}\right) + \frac{1}{(L-3)!}\int q^{L-3}\exp(-q)\mathrm{d}q. \end{aligned} \tag{8.33}$$

Repeating the integration by parts an additional $L-3$ times gives the result

$$\begin{aligned} v &= \int q^{L-1}\exp(-q)\mathrm{d}q \\ &= -\exp(-q)(L-1)!\sum_{i=0}^{L-1}\frac{q^{L-i-1}}{(L-i-1)!}. \end{aligned} \tag{8.34}$$

Therefore, combining (8.23) and (8.34) results in

$$[uv]_0^\infty = \left[-\ln(q+\nu)\exp(-q)(L-1)!\sum_{i=0}^{L-1}\frac{q^{L-i-1}}{(L-i-1)!}\right]_0^\infty. \tag{8.35}$$

The next step is to find the limit of (8.35) as $q \to \infty$. First, note that if the limit exists, then the limit of a sum is equal to the sum of the limits [98]. Therefore, we consider the first

term in the sum and find the limit

$$\lim_{q\to\infty} -\ln(q+\nu)\exp(-q)(L-1)!\frac{q^{L-1}}{(L-1)!} = \lim_{q\to\infty} -\ln(q+\nu)\exp(-q)q^{L-1}. \tag{8.36}$$

Note that (8.36) is an indeterminate limit. Therefore, arrange (8.36) as

$$\lim_{q\to\infty} -\ln(q+\nu)\exp(-q)q^{L-1} = (-1)\lim_{q\to\infty}\frac{\ln(q+\nu)q^{L-1}}{\exp(q)} \tag{8.37}$$

which is of the indeterminate form $\frac{\infty}{\infty}$. This indeterminate form allows the application of L'Hôpital's rule [98] to (8.37), which gives

$$(-1)\lim_{q\to\infty}\frac{\ln(q+\nu)q^{L-1}}{\exp(q)} \overset{\text{L'Hôp.}}{\to} (-1)\lim_{q\to\infty}\frac{\frac{1}{q+\nu}q^{L-1}+\ln(q+\nu)(L-1)q^{L-2}}{\exp(q)} \tag{8.38}$$

where $\to^{\text{L'Hôp.}}$ indicates the application of L'Hôpital's rule. Invoking the linearity of the limit operation, the first part of the sum in (8.38) may be examined separately as

$$\begin{aligned}\lim_{q\to\infty}\frac{\frac{1}{q+\nu}q^{L-1}}{\exp(q)} &= \lim_{q\to\infty}\frac{q^{L-1}}{\exp(q)(q+\nu)} \\ &\overset{\text{L'Hôp.}}{\to} \lim_{q\to\infty}\frac{(L-1)q^{L-2}}{\exp(q)(q+\nu)+\exp(q)} \\ &= \lim_{q\to\infty}\frac{(L-1)q^{L-2}}{\exp(q)(q+\nu+1)}.\end{aligned} \tag{8.39}$$

Equation (8.39) is still in the indeterminate form $\frac{\infty}{\infty}$. However, after applying L'Hôpital's rule $L-2$ additional times, (8.39) becomes

$$\lim_{q\to\infty}\frac{(L-1)!}{\exp(q)(q+\nu+L-1)} = 0. \tag{8.40}$$

Substituting (8.40) into (8.38) yields

$$(-1)\lim_{q\to\infty}\frac{\frac{1}{q+\nu}q^{L-1}+\ln(q+\nu)(L-1)q^{L-2}}{\exp(q)} = (-1)\lim_{q\to\infty}\frac{\ln(q+\nu)(L-1)q^{L-2}}{\exp(q)}. \tag{8.41}$$

Repeating equations (8.38)-(8.41) $L-2$ times results in

$$\begin{aligned}(-1)\lim_{q\to\infty}\frac{\ln(q+\nu)q^{L-1}}{\exp(-q)} &= -(L-1)!\lim_{q\to\infty}\frac{\ln(q+\nu)}{\exp(q)}\\ &\overset{\text{L'Hôp.}}{\to} -(L-1)!\lim_{q\to\infty}\frac{\frac{1}{(q+\nu)}}{\exp(q)}\\ &= -(L-1)!\lim_{q\to\infty}\frac{1}{\exp(q)(q+\nu)}\\ &= 0. \end{aligned} \tag{8.42}$$

Note the only difference between the elements of the sum of (8.35) is degree of the polynomial q^{L-i-1} and the constant $\frac{(L-1)!}{(L-i-1)!}$. Upon the examination of the (8.36)-(8.42), the degree of the polynomial q^{L-i-1} only alters the number of times L'Hôpital's rule must be invoked to find the limit of 0, while the constant multiplicative factor has no impact on a limit of 0. Therefore,

$$uv|_{\infty} = 0. \tag{8.43}$$

Next, the limit of (8.35) as $q \to 0$ is found as

$$\begin{aligned}uv|_0 &= \lim_{q\to 0} -\ln(q+\nu)\exp(-q)(L-1)!\sum_{i=0}^{L-1}\frac{q^{L-i-1}}{(L-i-1)!}\\ &= -\ln(\nu)(L-1)!\frac{1}{(L-L-1+1)!}\\ &= -\ln(\nu)(L-1)!. \end{aligned} \tag{8.44}$$

Therefore, from (8.43) and (8.44),

$$[uv]_0^{\infty} = 0-(-1)\ln(\nu)(L-1)! = \ln(\nu)(L-1)!. \tag{8.45}$$

The second part to be evaluated is found from (8.22), (8.24) and (8.34) as

$$\begin{aligned}\int_0^\infty v\mathrm{d}u &= \int_0^\infty \left(-\exp(-q)(L-1)!\sum_{i=0}^{L-1}\frac{q^{L-i-1}}{(L-i-1)!}\right)\left(\frac{1}{q+\nu}\mathrm{d}q\right)\\ &= -(L-1)!\int_0^\infty \frac{\exp(-q)}{q+\nu}\sum_{i=0}^{L-1}\frac{q^{L-i-1}}{(L-i-1)!}\mathrm{d}q\\ &= -\sum_{i=0}^{L-1}\frac{(L-1)!}{(L-i-1)!}\int_0^\infty \frac{\exp(-q)q^{L-i-1}}{(q+\nu)}\mathrm{d}q. \end{aligned} \tag{8.46}$$

Next, perform the substitution $x = q + \nu$ to (8.46), resulting in

$$\begin{aligned}\int_0^\infty v\mathrm{d}u &= -\sum_{i=0}^{L-1}\frac{(L-1)!}{(L-i-1)!}\int_0^\infty \frac{\exp(-q)q^{L-i-1}}{(q+\nu)}\mathrm{d}q\\ &= -\sum_{i=0}^{L-1}\frac{(L-1)!}{(L-i-1)!}\int_\nu^\infty \frac{\exp(-(x-\nu))}{x}(x-\nu)^{L-i-1}\mathrm{d}x\\ &= -\sum_{i=0}^{L-1}\frac{(L-1)!}{(L-i-1)!}\exp(\nu)\int_\nu^\infty \exp(-x)x^{-1}(x-\nu)^{L-i-1}\mathrm{d}x. \end{aligned} \tag{8.47}$$

The Binomial theorem is defined as [98]

$$\begin{aligned}(x+y)^n &= x^n + \binom{n}{1}x^{n-1}y + \binom{n}{2}x^{n-2}y^2 + \cdots + \binom{n}{k}x^{n-k}y^k + \cdots + \binom{n}{n-1}xy^{n-1} + y^n\\ &= \sum_{k=0}^{n}\binom{n}{k}x^{n-k}y^k, \end{aligned} \tag{8.48}$$

where $\binom{n}{k}$ is the binomial coefficient, defined as

$$\binom{n}{k} = \frac{n!}{k!(n-k)!}. \tag{8.49}$$

Applying the Binomial theorem to (8.47) gives

$$\begin{aligned}
\int_0^\infty v\mathrm{d}u &= -\sum_{i=0}^{L-1} \frac{(L-1)!}{(L-i-1)!} \exp(\nu) \int_\nu^\infty \exp(-x) x^{-1} (x-\nu)^{L-i-1} \mathrm{d}x \\
&= -\sum_{i=0}^{L-1} \frac{(L-1)! \exp(\nu)}{(L-i-1)!} \int_\nu^\infty \exp(-x) x^{-1} \sum_{k=0}^{L-i-1} \binom{L-i-1}{k} x^{L-i-k-1} (-\nu)^k \mathrm{d}x \\
&= -\sum_{i=0}^{L-1} \frac{(L-1)! \exp(\nu)}{(L-i-1)!} \sum_{k=0}^{L-i-1} \binom{L-i-1}{k} (-\nu)^k \int_\nu^\infty \exp(-x) x^{L-i-k-2} \mathrm{d}x \\
&= -(L-1)! \sum_{i=0}^{L-1} \frac{\exp(\nu)}{(L-i-1)!} \sum_{k=0}^{L-i-1} \binom{L-i-1}{k} (-\nu)^k \Gamma(L-i-k-1, \nu) \\
&= -J(L,\nu)(L-1)!. \qquad (8.50)
\end{aligned}$$

where $\Gamma(s,\nu)$ is the upper incomplete Gamma function, defined as [137, 138]

$$\Gamma(s,\nu) = \int_\nu^\infty t^{s-1} \exp(-t) \mathrm{d}t \qquad (8.51)$$

and the function $J(L,\nu)$ has been introducted for notational convenience.

It should be noted that the function $J(L,\nu)$ may be problematic to numerically evaluate. The last term of the inner sum (*i.e.* when $k = L-i-1$) results in

$$\binom{L-i-1}{k} (-\nu)^k \Gamma(L-i-k-1,\nu)\Big|_{k=L-i-1} = (-\nu)^{L-i-1} \Gamma(0,\nu). \qquad (8.52)$$

The value of the incomplete Gamma function of (8.52) can be defined as the continued fraction [138, 139]

$$\Gamma(0,x) = \cfrac{\exp(-x)}{x+1-\cfrac{1}{x+3-\cfrac{4}{x+5-\cfrac{9}{x+7+\ldots}}}} \qquad (8.53)$$

or computed as a numerical integral. However, some software packages (*e.g.* Matlab and Octave) implement the incomplete Gamma function in the normalized form [140, 141]

$$\Gamma(a,x) = \frac{1}{\Gamma(a)} \int_x^\infty \exp(-t) t^{a-1} \mathrm{d}t. \tag{8.54}$$

The formulation of (8.54) cannot evaluate (8.52) as $\Gamma(0) = \infty$. Therefore, care should be taken when implementing (8.50) in software.

The integral of (8.22) is now found by substituting (8.45) and (8.50) into (8.22) as

$$\begin{aligned}
\int_0^\infty q^{L-1} \exp(-q) \ln(q+\nu) \mathrm{d}q &= \int_0^\infty u \mathrm{d}v \\
&= [uv]_0^\infty - \int_0^\infty v \mathrm{d}u \\
&= \ln(\nu)(L-1)! - (-1) J(L,\nu)(L-1)! \\
&= (L-1)!(\ln(\nu) + J(L,\nu))
\end{aligned} \tag{8.55}$$

Finally, the KL divergence between the Gaussian and Pareto distributions for arbitrary SIRV length L and Pareto shape parameter ν is found by substituting (8.55) into (8.20), resulting in

$$\begin{aligned}
D(G,P) &= \frac{1}{2^L \Gamma(L)} \left[\alpha \int_0^\infty q^{L-1} \exp(-q) \ln(q+\nu) \mathrm{d}q - L! - \ln\beta (L-1)! \right] \\
&= \frac{1}{2^L \Gamma(L)} \left[\alpha (L-1)! \left(\ln(\nu) + J(L,\nu) \right) - L! - \ln\beta (L-1)! \right] \\
&= \frac{(L-1)!}{2^L \Gamma(L)} \left[\alpha \left(\ln(\nu) + J(L,\nu) \right) - \frac{L!}{(L-1)!} - \ln\beta \right] \\
&= 2^{-L} \left[\alpha \left(\ln(\nu) + J(L,\nu) \right) - L - \ln\beta \right] \\
&= 2^{-L} \left[(L+\nu+1) \left(\ln(\nu) + J(L,\nu) \right) - L - \ln \frac{\Gamma(L+\nu+1)\nu^{\nu+1}}{\Gamma(\nu+1)} \right] \\
&= 2^{-L} \left[(L+\nu+1) \left(\ln(\nu) + J(L,\nu) \right) - L - (\nu+1)\ln(\nu) - \ln \frac{\Gamma(L+\nu+1)}{\Gamma(\nu+1)} \right] \\
&= 2^{-L} \left[(L+\nu+1) J(L,\nu) + L\ln(\nu) - L - \ln \frac{\Gamma(L+\nu+1)}{\Gamma(\nu+1)} \right].
\end{aligned} \tag{8.56}$$

To speed up numerical computation, (8.56) may be reduced using the relationship [99]

$$\Gamma(x+1) = x\Gamma(x) \tag{8.57}$$

as

$$\begin{aligned}
D(G,P) &= 2^{-L}\left[(L+\nu+1)J(L,\nu) + L\ln(\nu) - L - \ln\frac{\Gamma(L+\nu+1)}{\Gamma(\nu+1)}\right] \\
&= 2^{-L}\left[(L+\nu+1)J(L,\nu) + L\ln(\nu) - L - \ln\frac{(L+\nu)\Gamma(L+\nu)}{\Gamma(\nu+1)}\right] \\
&= 2^{-L}\left[(L+\nu+1)J(L,\nu) + L\ln(\nu) - L - \ln\frac{\prod_{i=0}^{L-1}(L+\nu-i)\Gamma(\nu+1)}{\Gamma(\nu+1)}\right] \\
&= 2^{-L}\left[(L+\nu+1)J(L,\nu) + L\ln(\nu) - L - \ln\prod_{i=0}^{L-1}(L+\nu-i)\right] \\
&= 2^{-L}\left[(L+\nu+1)J(L,\nu) + L(\ln(\nu)-1) - \sum_{i=0}^{L-1}\ln(L+\nu-i)\right].
\end{aligned} \tag{8.58}$$

Even with the relatively simple form of the function $h_{2L}(q)$ of the Pareto distribution, the KL divergence of (8.56) is not a simple matter. However, even with the care required in evaluating (8.50), the divergence of (8.56) and (8.58) can be readily evaluated by numerical means. Figure 8.1 shows the evaluation of (8.58) for $0.1 \leq \nu \leq 100$ and $L = 4$ in decibel scale. As is expected, the KL divergence smoothly decreases with increasing shape parameter. By definition, the KL divergence approaches zero as $\nu \to \infty$.

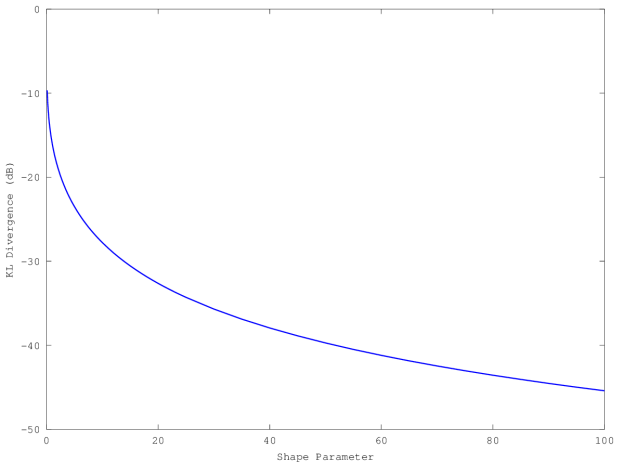

Figure 8.1: Kullback-Leibler divergence (in dB) between Gaussian and Pareto distributions for vector length $L = 4$

8.4.2 KL divergence between the Gaussian and K distributions

Recall the general Kullback-Leibler (KL) divergence between the Gaussian distribution and an arbitrary SIRV is found in (8.15) to only depend on the function $h_{2L}(q)$. The function $h_L(q)$ for real valued K distributed data was given in equation (3.76), repeated here

$$h_L(q) = \frac{2^{1-\nu/2+L/4}\nu^{\nu/2+L/4}q^{\nu/2-L/4}}{\Gamma(\nu)}K_{\frac{L}{2}-\nu}(\sqrt{2q\nu}). \tag{8.59}$$

For complex valued K distributed data, the function $h_{2L}(q)$ is found from (8.59) to be

$$\begin{aligned} h_{2L}(q) &= \frac{2^{1-\nu/2+L/2}\nu^{\nu/2+L/2}q^{\nu/2-L/2}}{\Gamma(\nu)}K_{L-\nu}(\sqrt{2q\nu}) \\ &= \frac{2^{1+(L-\nu)/2}\nu^{(\nu+L)/2}q^{(\nu-L)/2}}{\Gamma(\nu)}K_{L-\nu}(\sqrt{2q\nu}). \end{aligned} \tag{8.60}$$

Substituting (8.60) into (8.15) gives the KL divergence between the Gaussian and K distributions the form

$$
\begin{aligned}
D(G,K) &= \int_0^\infty f_G(q)\ln\frac{f_G(q)}{f_K(q)}\mathrm{d}q \\
&= \frac{1}{2^L\Gamma(L)}\left[-L! - \int_0^\infty q^{L-1}\exp(-q)\ln(h_{2L}(q))\mathrm{d}q\right] \\
&= \frac{1}{2^L\Gamma(L)}\left[-L! - \int_0^\infty q^{L-1}\exp(-q)\ln\left(\frac{2^{1+(L-\nu)/2}\nu^{(\nu+L)/2}q^{(\nu-L)/2}}{\Gamma(\nu)}K_{L-\nu}(\sqrt{2q\nu})\right)\mathrm{d}q\right] \\
&= \frac{1}{2^L\Gamma(L)}\left[-L! - \ln\left(\frac{2^{1+(L-\nu)/2}\nu^{(\nu+L)/2}}{\Gamma(\nu)}\right)\int_0^\infty q^{L-1}\exp(-q)\mathrm{d}q\right. \\
&\qquad\left. - \int_0^\infty q^{L-1}\exp(-q)\ln\left(q^{(\nu-L)/2}K_{L-\nu}(\sqrt{2q\nu})\right)\mathrm{d}q\right] \\
&= 2^{-L}\left[-\frac{L!}{\Gamma(L)} - \frac{\Gamma(L)}{\Gamma(L)}\ln\left(\frac{2^{1+(L-\nu)/2}\nu^{(\nu+L)/2}}{\Gamma(\nu)}\right)\right. \\
&\qquad\left. -\frac{1}{\Gamma(L)}\int_0^\infty q^{L-1}\exp(-q)\ln\left(q^{(\nu-L)/2}K_{L-\nu}(\sqrt{2q\nu})\right)\mathrm{d}q\right] \\
&= 2^{-L}\left[\ln\left[\Gamma(\nu)\right] - L - \ln\left(2^{1+(L-\nu)/2}\nu^{(\nu+L)/2}\right) - \frac{1}{\Gamma(L)}\int_0^\infty q^{L-1}\exp(-q)\ln\left(q^{(\nu-L)/2}\right)\mathrm{d}q\right. \\
&\qquad\left. -\frac{1}{\Gamma(L)}\int_0^\infty q^{L-1}\exp(-q)\ln\left(K_{L-\nu}(\sqrt{2q\nu})\right)\mathrm{d}q\right] \\
&= 2^{-L}\left[\beta - \frac{1}{\Gamma(L)}\left(\frac{\nu-L}{2}\int_0^\infty q^{L-1}\exp(-q)\ln\left(q\right)\mathrm{d}q\right.\right. \\
&\qquad\left.\left. + \int_0^\infty q^{L-1}\exp(-q)\ln\left(K_{L-\nu}(\sqrt{2q\nu})\right)\mathrm{d}q\right)\right] \qquad (8.61)
\end{aligned}
$$

where the term

$$
\begin{aligned}
\beta &= \ln\left[\Gamma(\nu)\right] - L - \ln\left(2^{1+(L-\nu)/2}\nu^{(\nu+L)/2}\right) \\
&= \ln\left[\Gamma(\nu)\right] - L - \left(1+\frac{L-\nu}{2}\right)\ln 2 - \frac{\nu+L}{2}\ln\nu \qquad (8.62)
\end{aligned}
$$

was introduced for notational convenience.

Therefore, two integrals in (8.61) need to be solved to find the KL divergence between the quadratic forms of the Gaussian and K distributions. First, note that due to the inclusion

of the modified Bessel function of the second kind, the integral

$$\int_0^\infty q^{L-1}\exp(-q)\ln\left(K_{L-\nu}(\sqrt{2q\nu})\right)\mathrm{d}q \tag{8.63}$$

is not mathematically tractable. Therefore, we turn our attention to solving

$$\int_0^\infty q^{L-1}\exp(-q)\ln\left(q\right)\mathrm{d}q. \tag{8.64}$$

First, decompose the integral of (8.64) into the parts

$$u = q^{L-1}\ln q, \tag{8.65}$$

$$\begin{aligned}\mathrm{d}u &= \left[(L-1)q^{L-2}\ln q + q^{L-2}\right]\mathrm{d}q \\ &= q^{L-2}\left[(L-1)\ln q + 1\right]\mathrm{d}q,\end{aligned} \tag{8.66}$$

$$\mathrm{d}v = \exp(-q)\mathrm{d}q, \tag{8.67}$$

and

$$v = -\exp(-q). \tag{8.68}$$

Therefore, from the integration by parts definition of $\int_0^\infty u\mathrm{d}v = [uv]_0^\infty - \int_0^\infty v\mathrm{d}u$, the quantity

$$[uv]_0^\infty = \left[\left(q^{L-1}\ln q\right)\left(-\exp(-q)\right)\right]_0^\infty \tag{8.69}$$

must be evaluated. First, the limit

$$\begin{aligned}\lim_{q\to\infty} -q^{L-1}\ln q\exp(-q) &= \lim_{q\to\infty} -(L-1)!\frac{\ln q}{\exp(q)} \\ &= -(L-1)!\lim_{q\to\infty}\frac{1}{q\exp(q)} \\ &= 0 \end{aligned} \tag{8.70}$$

is found in a similar manner as (8.36)-(8.40) in Section 8.4.1. Second, note that

$$\begin{aligned}\lim_{q\to 0} -q^{L-1}\ln q\exp(-q) &= \lim_{q\to 0} -\frac{q^{-L}q^{L}\ln q}{q^{-L}\exp(q)} \\ &= \lim_{q\to 0} -\frac{\ln q}{q^{-L}\exp(q)} \\ &= \frac{\infty}{\infty}. \end{aligned} \tag{8.71}$$

Therefore, applying L'Hôpital's rule [98] to (8.71) yields

$$\begin{aligned}\lim_{q\to 0} -\frac{\ln q}{q^{-L}\exp(q)} &\overset{\text{L'Hôp.}}{\to} \lim_{q\to 0}\frac{-\frac{1}{q}}{-L\left(q^{-(L+1)}\exp(q)+q^{-L}\exp(q)\right)} \\ &= \lim_{q\to 0}\frac{1}{q^{-1}\exp(q)\left(q^{-L}-Lq^{-(L+1)}\right)} \\ &= \lim_{q\to 0}\frac{q^{L+2}}{\exp(q)\left(q-L\right)} \\ &= 0. \end{aligned} \tag{8.72}$$

Therefore, from (8.65)-(8.72), equations (8.69) and (8.64) are shown to be

$$\begin{aligned}[uv]_0^\infty &= \left[\left(q^{L-1}\ln q\right)\left(-\exp(-q)\right)\right]_0^\infty \\ &= [0-0] = 0, \end{aligned} \tag{8.73}$$

and

$$\begin{aligned}\int_0^\infty q^{L-1}\exp(-q)\ln(q)\,\mathrm{d}q &= \int_0^\infty u\mathrm{d}v = [uv]_0^\infty - \int_0^\infty v\mathrm{d}u \\ &= 0 - \int_0^\infty v\mathrm{d}u \\ &= -\int_0^\infty (-\exp(-q))\left(q^{L-2}\left[(L-1)\ln q + 1\right]\mathrm{d}q\right) \\ &= \int_0^\infty \exp(-q)q^{L-2}\left[(L-1)\ln q + 1\right]\mathrm{d}q \\ &= (L-1)\int_0^\infty \exp(-q)q^{L-2}\ln q\mathrm{d}q + \int_0^\infty \exp(-q)q^{L-2}\mathrm{d}q \\ &= \Gamma(L-1) + (L-1)\int_0^\infty \exp(-q)q^{L-2}\ln q\mathrm{d}q, \end{aligned} \tag{8.74}$$

respectively. Taking advantage of the recursive nature of (8.74) equations (8.65)-(8.74) may then be applied a total of $L-1$ times, yielding

$$\begin{aligned}&\int_0^\infty q^{L-1}\exp(-q)\ln(q)\,\mathrm{d}q = \Gamma(L-1) + (L-1)\int_0^\infty \exp(-q)q^{L-2}\ln q\mathrm{d}q \\ &= \Gamma(L-1) + (L-1)\Gamma(L-2) + (L-1)(L-2)\Gamma(L-4)\cdots + (L-1)\ldots(L-L+3)\Gamma(L-L+2) \\ &\quad + (L-1)(L-2)\ldots(L-L+3)(L-L+2)\Gamma(L-L+1) - (L-1)!\gamma \end{aligned} \tag{8.75}$$

where γ is the Euler-Mascheroni constant [142, 143]

$$\begin{aligned}\gamma &= -\int_0^\infty \exp(-x)\ln x\mathrm{d}x \\ &\approx 0.5772\ldots \end{aligned} \tag{8.76}$$

Equation (8.75) may then be simplified to

$$
\begin{aligned}
&\int_0^\infty q^{L-1}\exp(-q)\ln(q)\,\mathrm{d}q \\
&= \Gamma(L-1) + (L-1)\Gamma(L-2) + (L-1)(L-2)\Gamma(L-3)\cdots + (L-1)\ldots(L-L+3)\Gamma(L-L+2) \\
&\quad + (L-1)(L-2)\ldots(L-L+3)(L-L+2)\Gamma(L-L+1) - (L-1)!\gamma \\
&= (L-2)! + (L-1)(L-3)! + (L-1)(L-2)(L-4)! + \ldots(L-1)\cdots + (L-L-3)1! \\
&\quad + (L-1)(L-2)\ldots(L-L+3)(L-L+2)0! - (L-1)!\gamma \\
&= (L-1)!\left[-\gamma + \frac{(L-2)!}{(L-1)!} + \frac{(L-1)(L-3)!}{(L-1)!} + \frac{(L-1)(L-2)(L-4)!}{(L-1)!} + \ldots\right. \\
&\quad \left. + \frac{(L-1)\ldots(L-L-3)}{(L-1)!} + \frac{(L-1)(L-2)\ldots(L-L+3)(L-L+2)}{(L-1)!}\right] \\
&= (L-1)!\left[-\gamma + \frac{1}{L-1} + \frac{(L-3)!}{(L-2)!} + \frac{(L-4)!}{(L-3)!} + \cdots + \frac{1}{(L-L+2)!} + \frac{1}{(L-L+1)!}\right] \\
&= (L-1)!\left[-\gamma + \frac{1}{L-1} + \frac{1}{L-2} + \frac{1}{L-3} + \cdots + \frac{1}{2} + \frac{1}{1}\right] \\
&= (L-1)!\left[-\gamma + \sum_{i=1}^{L-1}\frac{1}{L-i}\right]. \qquad (8.77)
\end{aligned}
$$

Therefore, substituting (8.61) into (8.77), the Kullback-Leibler divergence between the

quadratic forms of the Gaussian and K distributions can be expressed as

$$
\begin{aligned}
D(G,K) &= \int_0^\infty f_G(q)\ln\frac{f_G(q)}{f_K(q)}\mathrm{d}q \\
&= 2^{-L}\left[\beta - \frac{1}{\Gamma(L)}\left(\frac{\nu-L}{2}\int_0^\infty q^{L-1}\exp(-q)\ln(q)\,\mathrm{d}q\right.\right. \\
&\qquad \left.\left. + \int_0^\infty q^{L-1}\exp(-q)\ln\left(K_{L-\nu}(\sqrt{2q\nu})\right)\mathrm{d}q\right)\right] \\
&= 2^{-L}\left[\beta - \frac{1}{\Gamma(L)}\left(\frac{\nu-L}{2}(L-1)!\left[-\gamma + \sum_{i=1}^{L-1}\frac{1}{L-i}\right]\right.\right. \\
&\qquad \left.\left. + \int_0^\infty q^{L-1}\exp(-q)\ln\left(K_{L-\nu}(\sqrt{2q\nu})\right)\mathrm{d}q\right)\right] \\
&= 2^{-L}\left[\beta - \frac{(L-1)!}{(L-1)!}\frac{\nu-L}{2}\left[-\gamma + \sum_{i=1}^{L-1}\frac{1}{L-i}\right]\right. \\
&\qquad \left. - \frac{1}{\Gamma(L)}\int_0^\infty q^{L-1}\exp(-q)\ln\left(K_{L-\nu}(\sqrt{2q\nu})\right)\mathrm{d}q\right] \\
&= 2^{-L}\left[\beta + \frac{\nu-L}{2}\left[\gamma - \sum_{i=1}^{L-1}\frac{1}{L-i}\right] - \frac{1}{\Gamma(L)}\int_0^\infty q^{L-1}\exp(-q)\ln\left(K_{L-\nu}(\sqrt{2q\nu})\right)\mathrm{d}q\right],
\end{aligned}
\tag{8.78}
$$

where β is defined in (8.62). Two unsuccessful efforts were made to evaluate the integral in (8.63) using the Octave software package [144]. It was noted in Chapter 4 that care must be taken when evaluating the modified Bessel function of the second kind due to numerical instability. The Octave function *quadgk* performs a numerical integration using Gauss-Konrod quadrature [144, 145]. This function produced the results shown in Section 8.4.1 (namely the integration of the incomplete Gamma function of (8.50)). However, *quadgk* could not converge to a solution to (8.63). The Octave function *quadcc* numerically integrates an integral using doubly adaptive Clenshaw-Curtis quadrature [144]. However, the *quadcc* function similarly failed. Therefore, at this time more examination is needed of (8.61) to facilitate a numerically stable equation to solve the KL divergence between the Gaussian and K distributions.

8.5 Conclusions

In this chapter the Bregman divergence and f divergence were defined and explored. In particular, it was noted that the Kullback-Leibler (KL) divergence is the only divergence to belong to both the Bregman and f classes of divergence. Because of this unique advantage, the KL divergence was selected to characterize the divergence between the Gaussian distribution and the class of spherically invariant random vectors (SRIVs) of which the Gaussian is a member. The KL divergence between the Gaussian distribution and an arbitrary SIRV was shown, and the KL divergence between the Gaussian and Pareto distributions was derived. However, the KL divergence between the Gaussian and K distributions was found to be numerically unstable. Therefore, the KL divergence offers intriguing capabilities as a measure of distance between SIRV distributions, but more work is needed to explore the problems with numerical stability in evaluating the KL divergence. It has been noted that most SIRVs do not possess closed form pdfs [69], which makes evaluating the KL divergence between SIRVs a challenging problem in need of further exploration.

Chapter 9

Conclusions and Future Work

9.1 Summary

The defining feature of a cognitive radar is its ability to adapt in an intelligent manner to unexpected circumstances. In particular, the clutter environment encountered by a radar may not fit the commonly assumed Gaussian distribution. Here the question of setting a detection threshold for a desired probability of false alarm in non-Gaussian data with an unknown distribution was considered. To this end, a series of knowledge aided, machine learning based approaches were examined. These approaches focused on the related problems of identifying a distribution from a set on non-Gaussian sample data and estimating the proper detection threshold directly from the sample data.

Chapter 2 examined the problem of radar detection. Radar clutter was mathematically and physically defined. In addition, the impact of radar clutter on radar detection was explored. Finally, a number of current problems facing advanced radar detectors was discussed.

In Chapter 3 the characterization of the non-Gaussian clutter environment was considered via exploration of commonly measured clutter distributions. It was established that the spherically invariant random vector (SIRV) architecture was physically, empirically, and mathematically justified to be a general model for non-Gaussian clutter. Also, the close

relationship between non-Gaussian SIRVs and the Gaussian distribution (which is a member of the SIRV class) was illustrated. It was shown that a SIRV can be compressed into a quadratic form, allowing the random vector to be fully characterized by a normalized random variable. Optimal detection in SIRV clutter was defined and explored. However, it was noted that the Lognormal distribution has been empirically fitted to measured data. Therefore, despite not belonging to the class of SIRVs, the Lognormal distribution was included as a candidate distribution.

The distributions introduced in Chapter 3 were examined more closely in Chapter 4. The pdfs of the distriubutions were shown, and simulated data was generated from each distribution. In addition, the simulated data was used to generate detection thresholds for desired probabilities of false alarm. The difference in detection threshold for non-Gaussian distributions and the Gaussian distribution for a desired probability of false alarm (defined as Δ_{thresh}) was shown. For SIRVs with a shape parameter, the dependence of Δ_{thresh} on shape parameter was shown. The candidate clutter distributions were expanded to include two original distributions, the Gamma modulated (GM) and compound Gamma modulated (CGM) distributions. These two new distributions were defined and explored. Finally, some potential limitations of modeling radar clutter with SIRVs were briefly discussed.

The prior work denoted as the Ozturk algorithm (after its lead author) was described and investigated in Section 5.1 of Chapter 5. The Ozturk algorithm was intended to find a graphical distance between the Gaussian distribution and various SIRV distributions. In particular, the Ozturk algorithm operates via a non-linear transformation of a set of order statistics of the quadratic form of the SIRVs. The Ozturk algorithm forms a library of known distributions where each each distribution/shape parameter pair is mapped to an endpoint generated by taking the expected value of the transformation. Candidate data undergoes the same transformation, and the resultant endpoint is compared to the endpoints in the library. The Ozturk algorithm then returns a distribution *suggestion* corresponding to the known distribution/shape parameter pair whose endpoint is closest to the endpoint of the measured

data. An initial library consisting of the K and Gaussian distributions was constructed using the Ozturk algorithm. The Ozturk algorithm was then applied to a set of measured data and the generated endpoints were compared to the initial library. However, the endpoints from the measured data largely deviated from the endpoints in the library, implying that a larger set of candidate distributions was required to fill out the endpoint space.

In Section 5.2 a generalization of the Ozturk algorithm was considered, namely the weighted sum of order statistics (WSOS). The impact of weighting a set of order statistics was briefly explored through the consideration of a set of ten weights: sine, cosine, cosh, sinh, tanh, and their respective squares. Note that the sine and cosine were the original weighting functions used in the Ozturk algorithm. It was then shown that using a sample covariance matrix (SCM) could have an impact on the location of the endpoints generated via the various weighting functions. The pdfs of various pairs of endpoints were shown for K distributed data.

Section 5.3 unified the framework developed in Sections 5.1 and 5.2. In addition, two new non-linear transformations of order statistics were introduced: the divide-by-mean (DBM) and Studentization transformation methods. Due to the introduction of additional weightings and the generalization of the framework, when the transformation used by the Ozturk algorithm was utilized in the context of the new framework, it was designated the extended Ozturk algorithm (EOA).

To conclude Chapter 5, Section 5.4 introduced two combined order statistics modelled in clutter (COSMiC) algorithms and considered aspects of the behaviour of the constituent weighted transforms. The goal of the first COSMiC algorithm is to identify the generating distribution of a set of sample data. This algorithm has the same goal as the Ozturk algorithm, but is distinguished by the use of additional transformations and weighting pairs. The second algorithm attempts to directly infer a detection threshold by associating a precomputed detection threshold to each distribution/shape parameter pair in the various libraries. The second algorithm then returns a hypothesized threshold determined from the

endpoints in the library closest to the endpoint generated by the candidate data.

The initial exploration of the COSMiC algorithm in Section 5.4 began with the implementation of four libraries associated with the different transformation methods. Each library had a series of endpoints generated for the ten weighting functions. Each weighting function was applied to data derived from four distributions: Weibull, K, GM, and CGM. Finally, for each of these distributions the shape parameter was varied to encompass both exceptionally heavy tailed data (*i.e.* $\Delta_{\text{thresh}} \approx 35dB$) and relatively light tailed data (*i.e.* $\Delta_{\text{thresh}} < 1dB$).

With the generated libraries in hand, two types of plots were shown. First, the average endpoints for several selected pairs of weighting functions were shown for each of the transformation methods (and all distribution/shape parameter pairs). These plots illustrated the theoretical distribution identification capability of each transformation method. It was noted that other than the EOA method, the other three transformation methods did not appear to provide separation between the different distributions. Next, for each of the weighting functions considered, the Δ_{thresh} was shown for each distribution/shape parameter pair as a function of the endpoint. These plots illustrated an ambiguity in endpoint space for realistic points (*i.e.* $\Delta_{\text{thresh}} < 10dB$). In other words, distributions with similar thresholds resulted in similar endpoints. This verified that the COSMiC structure could be used to directly map sample data to a detection threshold.

Chapter 6 began with a formal definition of the COSMiC algorithms. Block diagrams illustrating the flow of data through the different processing blocks making up each of the COSMiC algorithms were shown. It was noted that the fusion of the output of the libraries associated with each transformation would be needed. While the fusion algorithm is considered to be outside the scope of this work, its construction should be informed by the results presented here.

An initial implementation of the EOA was presented in [2]. The results of [2] were shown in Section 6.2 and discussed. For brevity, only the EOA transformation was considered in [2]. In addition, a reduced library consisting only of the Weibull, K, and Lognormal distributions

was used. Note that the Gaussian distribution was also included, but as a special case of the Weibull distribution (the Weibull and Gaussian distributions are equivalent when the shape parameter f the Weibull $\nu = 2$). It was shown that at the sample support levels considered (length $L = 4$ complex random vectors, $N = 4L = 16$ order statistics used to calculate each endpoint) the distribution identification algorithm performed poorly. For low shape parameter values, K distributed data was correctly identified with high probability, but was incorrectly attributed to the Weibull distribution for medium to high shape parameter values (*i.e.* as the tail became lighter).

However, it was shown that for certain selections of pairs of weighting functions, the threshold estimate was very accurate (within ≈ 1 dB in many cases) over a wide variety of shape parameters. It was also noted that using the optimal estimate (in a maximum likelihood sense) for the K shape parameter resulted in a less accurate threshold estimate compared to the EOA. This was due to the low sample support used, which caused the maximum likelihood estimate of the K shape parameter to have an increased number of outlier estimates with respect to the EOA. As the detection threshold for K distributed data is highly non-linear with respect to the shape parameter, these outliers biased the average threshold estimate. It was also noted that the choice of weighting functions greatly influenced the results. In addition, the case where all weighting functions were used to create a ten-dimensional endpoint produced an average threshold estimate worse than the the average estimate generated by several pairs of weighting functions (*i.e.* two-dimensional endpoints).

While not appearing in [2], results were also shown for the threshold estimation with only the K and Weibull distributions in the library (*i.e.* removing the Lognormal distribution). The resulting estimates were more accurate than when the Lognormal distribution was in the library.

A new library was introduced in Section 6.3. This library is also used for Section 6.4. The new library consisted of the Gaussian, K, Weibull, Pareto, Logormal, and GM distributions. The shape parameters for each distribution where chosen to provide a smooth continuum of

detection thresholds such that $0 < \Delta_{\text{thresh}} \leq 0$.

Section 6.3.1 then conducted an exhaustive search of all pairs of weighting functions to find the pairs of weighting functions that yielded the most accurate classification for each distribution. It was noted that the distribution classification was not accurate for the scenario (*i.e.* sample support levels) considered, even for the EOA transformation method.

Next, Section 6.3.2 similarly conducted an exhaustive search of all pairs of weighting functions to find the pairs of weighting functions that yielded the most accurate threshold estimates for each distribution. These weightings formed the basis of the robustness analysis conducted in Section 6.3.3.

Section 6.3.3 then examined the accuracy of the threshold estimates given by the top pairs of weightings for each transformation method. The analysis was conducted for each of the distributions considered (Gaussian, K, Weibull, Pareto, Lognormal). In addition, the impact of using the sample covariance matrix was considered. Finally, the impact of excising the candidate distributions from the set of libraries was considered.

The excised libraries were formed to help quantify the capability of the COSMiC transformations in the context of a cognitive radar. To form an excised library, one of the candidate distributions was removed from the library. Threshold estimates were then formed by first generating endpoints with data distributed according to the excised distribution. These endpoints were then compared to the endpoints in the libraries which were lacking said distributions, and the best estimate of the detection threshold was given. These tests provide a preliminary estimate of the capability of the COSMiC algorithm to infer the threshold of an unknown distribution based on knowledge of related distributions.

It was found that the selection of transformation methods and weighting functions had a great deal of impact on the accuracy of the average threshold estimate. Particular attention was paid to the robustness of the estimator. In other words, could the transformation method and weighting function pairs produce an accurate threshold estimate over the full 10 dB range of possible threshold values. The Studentization transformation method used

in conjunction with the (cosine^2, sine^2) pair of weighting functions produced the most accurate, robust threshold estimate for all of the SIRV distributions with shape parameters that were examined. It was not the best threshold estimator when the Gaussian or Lognormal distributions were present. In particular, the estimate for Gaussian data using this transformation method/weighting function pair suffered an additional 2.6 dB of detection loss when compared with the best transformation method/weighting function for the Gaussian distribution (which itself suffered a 0.8 dB detection loss compared to the optimal threshold). In other words, using the Studentization transformation method used in conjunction with the (cosine^2, sine^2) pair of weighting functions yields an average detection loss of 3.41 dB for Gaussian distributed data. The average threshold for Lognormal distributed data was estimated to be 1.9 dB below the optimal threshold on average (leading to an increase in false alarm rate).

For all transformation methods and weighting pairs, removing the distribution from the library did not have an appreciable impact on the accuracy of the threshold estimate. However, using the sample covariance matrix (SCM) to form the quadratic, or generalized inner product (GIP) form of the random vector rather than the true, clairvoyantly known covariance matrix did severely degrade the threshold estimate. The poor estimate resulting from the use of the SCM is a function of both low sample suport and the difficulty of estimating the covariance matrix for SIRV data.

Next, in Section 6.4 the COSMiC method was examined in a similar manner to that of Section 6.3, but the number of weighting functions used to estimate each endpoint was increased from two to three. Section 6.4.1 exhaustively searched for the best triplets of weighting functions to perform distribution identification for each of the four transformation methods, and evaluated the results. The triplets of weighting functions that gave the lowest average threshold estimate error were found in Section 6.4.2. The robustness of the threshold estimates given by those weighting function triplets were examined in Sections 6.4.3.1-6.4.3.5 in a similar manner as was done with the pairs of weighting functions in Sections 6.3.3.1-

6.3.3.5.

However, it was found that increasing the number of weighting functions from two to three did not appreciably impact the accuracy of the results. Therefore, it was concluded that two weighting functions provided sufficient degrees of freedom to form the most accurate estimates possible for the sample support under consideration.

A discussion of the results found in Chapter 6 was given in Section 6.5, and suggestions were made for areas of improvement for the COSMiC algorithms.

Chapter 7 applied neural networks the teh same two problems considered by the COSMiC algorithm: distribution identification and threshold estimation. The beginning of Chapter 7 provided a brief background on neural networks and Section 7.1 summarized the parameters used when constructing the neural networks. The neural networks for each scenario were trained with varying numbers of hidden neurons (10, 20, and 30) and training samples ($10^2, 10^3$ and 10^4 training samples per distribution/shape parameter pair). In addition, half of the neural networks were trained using ordered inputs and the other half were trained using raw, unordered data.

In Section 7.2.1 a series of neural networks were trained to identify or classify the distribution that best fit a set of sample data. It was shown that if the covariance matrix was known, the neural networks provided a high degree of classification accuracy for most of distribution/shape parameter pairs considered. However, the networks exhibited a high rate of misclassification when Gaussian, Lognormal, or high shape parameter Weibull distributed data was tested.

The results implied that a better segmentation of training data was needed to train the networks. In addition, the distribution classification failed if the covariance matrix was used. The networks converged to approximately the same solution for all examined quantities of hidden neurons and training sample support if ordered data was used. However, the neural networks using 10 hidden neurons sometimes had difficulty converging to an effective solution. While the performance was universally poor if the sample covariance matrix (SCM) was used,

it was noted that increasing the number of hidden neurons seemed to increase the robustness of the classification to SCM effects.

Section 7.2.2 then examined the performance of neural networks that attempted to map input data to the corresponding detection threshold. In other words, the neural networks attempted to estimate the tail of the input data. Averaging over shape parameter values, the threshold estimates produced by the neural network of Section 7.2.2 were close to the true values (within $1-3$ dB) However, when examining the average estimates as a function of shape parameter, it was found that the neural networks tended to produce threshold estimates that were highly biased towards the average threshold over all distributions. Therefore, the network architecture that was used needed to be reconsidered.

Two threshold estimating neural network architectures based on a deep network concept were explored in Appendix B. However, the results were similar to those given in Section 7.2.2, and did not warrant inclusion in the main body of this work.

Section 7.3 summarized the results of Chapter 7 and gave a number of proposals for future work. In particular, it was hypothesized that increased sample support was needed to improve distribution classifier accuracy and covariance matrix estimate accuracy. Also, a bootstrapping algorithm was proposed to estimate the covariance matrix using a distribution identification neural network and the expectation-maximization algorithm of [75,114]. A new form of threshold estimation neural network was proposed to alleviate the problems shown by the neural networks of Section 7.2.2. Finally, it was proposed that the research on deep belief networks should be explored as an alternative architecture.

Chapter 8 examined the relationships between SIRVs by exploring divergences. First, Sections 8.1 and 8.2 described the Bregman and f divergences, respectively. In addition, the desirable properties of each were shown. Then Section 8.3 explored the Kullback-Leibler (KL) divergence, which has been shown to belong to both the Bregman and f classes of divergence. Section 8.4 derived a formal expression for the KL divergence between the Gaussian distribution and an arbitrary SIRV distribution as a function of the dimensionalities of the

vectors. The KL divergence between the Gaussian and the Pareto SIRV distributions was derived in Section 8.4.1 as a function of the dimensionality and the shape parameter of the Pareto, and a plot of the KL divergence was generated. Finally, Section 8.4.2 attempted to derive the KL divergence between the Gaussian distribution and the K distribution. However, the final expression did not have a closed form. In addition, the numerical instability of the resultant expression defied attempts to evaluate the divergence.

9.2 Future Work

First, it should be noted that an expansion of this work is to appear in [146].

There are numerous attractive areas of research that present themselves as a result of this work. Each of these areas increase the applicability of the techniques established here to measured data from modern radar systems. Some areas of improvement have already been stated in their respective chapters, and are re-stated here to provide a more comprehensive analysis.

For the COSMiC algorithms, the problem of fusing the output from the four transformation methods needs to be considered. It was shown that some transformations gave better accuracy than others. However, it was not shown that inaccurate transformations had no value. It may be possible for exploit patterns of biases to fuse the data. In other words, examination of the results of Section 6.3.3 suggest if the threshold estimate given by the WSOS method is lower than the estimate given by the Studentization and EOA methods, then the candidate data may be Gaussian or Pareto distributed. If the converse is true, then the data may be distributed K. If all estimates are close in value, then the data may be distributed as Weibull. This is just one example of a fusion technique. Others need to be investigated.

In addition, the COSMiC algorithm used the concept of library endpoints, parameterized by transformation method and sets of weighting functions. The impact of the number of

weighting functions used simultaneously was investigated. However, it may be useful to use pairs of pairs of weighting functions (*e.g.* (sine,cosine) and (cosine^2, sinh) simultaneously). In addition, the impact of the various weightings on the sample pdf needs to be explored in more detail (*i.e.* what is the impact of emphasizing the median and de-emphasizing the minimum and maximum values?). An initial exploration was presented in Section 5.2, but this examination needs to be expanded.

A flexible framework to adaptively increase the sample support of the distribution identification COSMiC algorithm was presented in Section 6.5, and is summarized here. First, it was noted in Section 5.4 that the expected value of the EOA endpoints were clearly separated into unique curves associated with each distribution in the library. The curves were parameterized by the values of the shape parameter, and coincided with the Gaussian endpoint as the shape parameters grew large. Therefore, it can be inferred that the disappointing performance of the EOA with respect to distribution identification shown in Chapter 6 is a function of the sample support used in the analysis.

However, it is important to note that increasing the sample support is not without its risks. Note that in all cases considered here the clutter is assumed to be homogeneous. Each of the vectors used to form the endpoints correspond to a separate range cell. Therefore, increasing the number of range cells similarly increases the risk of introducing non-homogeneous into the test set.

As such, the proposed algorithm uses a flexible set of endpoints. In other words, the endpoints of the library are generated from sets of N random vectors compressed into their quadratic form. However, if $J > 2N$ homogeneous range cells are available, then a set of $K = \left\lfloor \frac{J}{N} \right\rfloor$ endpoints may be generated. The final endpoint to be tested is then formed as the average of the K endpoints. Therefore, in the proposed scheme the pre-generated library can adapt to the amount of available data.

In addition, based on the analysis in Section 5.4 it is likely that the three non-EOA transformation methods will only yield differential based information. In other words, considered

singly each transformation method gave an ambigious mapping from endpoint space to distribution (when viewed in expectation). However, the relationships between the endpoints given by the WSOS were not compared with the endpoints of the Studentization method, and so on.

The COSMiC algorithms utilize the location of the endpoint of the linked vectors formed from the weighted order statistics. However, the shape of the linked vectors may provide further information. Therefore, future work should be expanded to consider the *vector* of weighted order statistics, rather than the *sum* of the weighted order statistics.

The robustness of the threshold estimation algorithm is greatly influenced by the wide range of shape parameters considered for each distribution. However, the detection threshold associated with the data depends on both the shape parameter and the dimensionality. Therefore, the dimensionality of reported non-Gaussian data should be considered. In other words, the threshold associated with low shape parameter data may be lower than considered here because the number of pulses in a coherent processing interval used by the measuring radar is higher than is considered here. Therefore, the library needs to be re-examined to ensure the thresholds considered are realistic.

The distribution identification neural network analysis should be rerun with greater sample support both in the form of longer data vectors and a greater number of input data vectors. The increased sample support should improve the neural network performance both through increased data support and improved covariance matrix estimation.

The expectation-maximization (EM) algorithm of [75, 114] should be incorporated into both the COSMiC and neural networking approaches. The sample support requirements of the EM algorithm should also be quantified. In addition, it has been noted that the algorithms considered here demonstrated ambiguities when the shape parameter of test data was high (*i.e.* the clutter approached the Gaussian distribution). It would be interesting to investigate the robustness of the EM algorithm to estimating the covariance matrix when an incorrect distribution is hypothesized, but both the correct and incorrect distributions have

a near Gaussian tail.

In particular, the EM algorithm should be paired with a distribution identification neural network or the EOA transformation library (if sample support is sufficient) to form a "bootstrapping" approach. In other words, the output of the distribution identification can be used to form a distribution hypothesis. If the hypothesized distribution possesses a shape parameter, distribution specific shape parameter estimation techniques can be used. The resultant distribution/shape parameter pair can then be used to inform the maximum likelihood estimation of the covariance matrix that is generated by the EM algorithm. The improved covariance matrix can then be used to re-generate the quadratic forms of the sample data, and the newly formed power estimates fed back into the distribution identification algorithm. If the distribution hypothesis is unchanged, then it is assumed that the power estimates are reliable. If not, then the process repeats. The resultant estimates can then be used in the maximal scale invariant test statistic described in [75, 114].

A new series of threshold estimating neural networks should be implemented. The output of these neural networks should be binary, and associated with "steps" in the increase in detection threshold required (indexed to the threshold of the Gaussian distribution). An equal number of training samples corresponding to each threshold step should be employed to avoid biasing the network. For example, under the current model 11 output neurons could be trained, corresponding to detection thresholds $0, 1, \ldots, 10$ dB greater than the threshold required for Gaussian distributed data.

The deep belief network (DBN) machine learning architecture should be examined. The unsupervised training step inherent in the DBN process may be adept at determining a feature extraction that has not been considered here.

The numerical integration of the Kullback-Leibler (KL) divergence between the Gaussian and the K distributions should be investigated and evaluated. In addition, it should be compared to the KL divergence between the Gaussian and Pareto distributions. In particular, the relationship between KL divergence and detection threshold should be explored.

The presence of heterogeneous data should be considered. In particular, the case of two "clutter patches" with differing distributions should be explored. In this case, the window of data used to construct the quadratic samples will start distributed according to one distribution, and then "slid" in range until all samples are drawn from the second distribution. The capability of estimating the necessary threshold should be examined and compared to current methods.

Recall from Section 3.3 that optimal detection in SIRV clutter is possible if the inverse function $h_{2L}^{-1}(q)$ is known. Therefore, it may be possible numerically estimate the inverse function for known SIRVs, and then apply the techniques established in this work to map from a measured data sample to the appropriate value of $h_{2L}^{-1}(q)$. In a similar spirit, the non-homogeneity detector (*i.e.* maximal invariant test statistic) derived in [75, 114] may be implemented if the function $h_{2L}(q)$ is known. If a mapping from a measured data sample to the appropriate value of $h_{2L}(q)$ can be established, the covariance matrix may be optimally estimated and the non-homogeneity detector implemented.

The COSMiC algorithm and associated techniques should be extended to incorporate a *learning* framework. In other words, we should extend this basic concept of a cognitive radar that selects the best model for the current situation to a system that can modify the models in its memory based on its experiences. To implement this learning framework, conditions must be established to allow the algorithm to take observed data and estimate the novelty/homogeneity of the data. When enough measured homogeneous data has been accumulated, a new endpoint is added to the library, or a new neural network is trained. This learning capability will allow fielded systems to adapt to changing conditions and provide a robust and flexible radar system.

There are several areas of research to which the COSMiC and neural network approaches can be compared

First, the COSMiC and neural network approaches should be augmented by and/or compared to the classic and current techniques for performing space-time adaptive processing

(STAP) in non-homogeneous clutter (*e.g.* [36, 147–159]). In addition, a new formation of the STAP framework, the multiple waveform STAP (MuW-STAP or μ-STAP) has been introduced in [40, 160]. The μ-STAP approach shows great promise in mitigating the effects of non-homogeneous clutter. The performance of the μ-STAP algorithm in SIRV clutter should be analyzed. In addition, the threshold estimate given by the μ-STAP algorithm should be compared to that of the COSMiC algorithm and the proposed improved threshold estimating neural network.

Finally, the SIRV clutter modelling techniques described here can be applied to improve the models and assumptions made in other areas of research. In particular, it has been noted that the clutter response of pulse agile radar is more difficult to characterize than non-pulse agile radar [161–164]. Also, these modelling techniques can be used to improve and expand the clutter model used in the design and analysis of radar-embedded communication systems [165–171].

9.3 Conclusions

Ultimately this dissertation considered the challenges faced by a cognitive radar detector. The SIRV model was shown to be an effective model for non-Gaussian clutter from both an empirical and a theoretical perspective. Three approaches towards implementing a cognitive radar detector were extensively examined and discussed. In addition, conclusions were drawn and numerous avenues of future research were given.

Two combined order statistics modelled in clutter (COSMiC) approaches were considered. Both approaches constructed libraries of candidate distributions. The points in the library were formed from weighted sums of non-linear transformations of order statistics. The first algorithm attempted to identify the distribution that best fit the sample data. The second algorithm attempted to provide a direct estimation of the optimal detection threshold associated with the sample data.

The distribution identification algorithm did not work for the parameters considered. However, it was shown that in expectation the extended Ozturk algorithm (EOA) could discriminate between all distributions that were tested. Therefore, increasing the sample support in the form of an average of endpoints may allow for effective distribution identification by the EOA.

The threshold estimation COSMiC algorithm gave accurate estimates for all distributions tested. However, the results were significantly degraded when the sample covariance matrix was used to form the quadratic form of the random vectors. It was noted that all estimation was conducted with very low sample support. In addition, the threshold estimate was negligibly affected when the distribution under test was removed from the COSMiC libraries. This result implies that a cognitive radar using the COSMiC algorithm could successfully infer a detection threshold in the face of clutter distributed according to an unknown SIRV distribution.

Two series of neural networks were trained to provide a comparison to the COSMiC algorithms. The first set of neural networks was designed to classify distributions based on a set of input data. The second set of neural networks was trained to estimate the threshold directly from the input data.

The distribution identification neural networks enjoyed more success than was produced by any of the transformation method and weighting function combinations that were explored in the context of the first COSMiC algorithm. However, it was noted that at the sample support considered the use of the sample covariance matrix greatly degraded the output of the distribution classifier.

The threshold estimation neural networks suffered from a structural flaw. At first glance, when the average threshold error was averaged over all shape parameters for each distribution, the output was relatively accurate. However, when the threshold estimate for data distributed according to each shape parameter was examined separately, it was shown that the estimate was very poor. In the end it was concluded that the threshold estimated by

the neural network was biased towards the average threshold over all the training data. Therefore, the threshold error given by the neural network was largely a function of the relationship between the threshold and shape parameter for each distribution under test.

The number of hidden neurons and training samples needed for the neural networks to converge on a final solution was not large. In addition, it was reduced by pre-processing the input data in the form of ordering. However, increasing the number of hidden neurons allowed the neural networks to produce more accurate results when the sample covariance matrix was used.

To summarize, for the sample support levels considered here the COSMiC algorithm produced more accurate estimates when estimating the detection threshold associated with a set of sample data than the neural network approach. The success of the COSMiC algorithm held true even if the distribution associated with the sample data was removed from the library. Meanwhile, the neural networks provided a higher distribution classification accuracy than the COSMiC algorithm. However, improved covariance matrix estimates are needed by the neural networks, as the distribution classification does not produce usable results under the parameters considered if the sample covariance matrix is used to form the quadratic form of the input vectors.

To improve the analysis of both approaches, it is necessary to increase the sample support with respect to the number of samples per random vector (*i.e.* number of radar pulses). For all examples discussed in Chapters 6 and 7 this number was $L = 4$. It was concluded that this level of sample support gave too few samples to characterize the modulating random variable. This lack of sample support increased the detrimental effects imposed by use of the sample covariance matrix. However, with respect to estimating the covariance matrix, endpoints of the COSMiC libraries, and input neurons of the neural networks, the ratio of number of vectors N to length of vector L should not increase beyond the $N/L = 4$ case considered here except to form a limit on the sample support required for the COSMiC distribution identification algorithm using the EOA transformation. This ratio is limited to

ensure real-world sample supports are considered.

Finally, the concept of divergence was considered. In particular, it was shown that the Kullback-Leibler (KL) divergence is the only divergence to belong to both the Bregman and f classes of divergences. In such a light, the KL was chosen to provide a measure of divergence between SIRV distributions. Following the same line of reasoning as the Ozturk algorithm, the divergence between the Gaussian and an arbitrary SIRV was shown. More specifically, the KL divergence between the Gaussian distribution and a Pareto distribution with an arbitrary shape parameter was derived. Finally, the numerical computation of the KL divergence between the Gaussian distribution and the K distribution was attempted. However, the solution was not numerically stable. Therefore, more work is needed to formally quantify the KL divergence between the SIRV and the K distribution.

In conclusion, the three approaches highlighted here provide a foundation upon which to build a cognitive radar detector. The threshold estimating COSMiC algorithm provides a method of robustly estimating the detection threshold associated with an unknown heavy tailed distribution. The neural network approaches shown give an accurate method of classifying radar clutter according to commonly measured distributions. Finally, the KL divergence provides a formal method of quantifying the divergence between the Gaussian distributions and the SIRV class of distributions that form the best candidate for a general descriptor of radar clutter.

References

[1] M. Rangaswamy, P. Chakravarthi, D. Weiner, L. Cai, H. Wang, and A. Ozturk, "Signal detection in correlated gaussian and non-gaussian radar clutter," Rome Laboratory, Tech. Rep. 93-17391, 1993.

[2] J. Metcalf, S. Blunt, and B. Himed, "A machine learning approach to distribution identification in non-gaussian clutter," in *Radar Conference, 2014 IEEE*, May 2014, pp. 0739–0744.

[3] S. Haykin, *Adaptive Filter Theory.* Prentice Hall, 2002.

[4] ——, "Signal processing: where physics and mathematics meet," *Signal Processing Magazine, IEEE*, vol. 18, no. 4, pp. 6 –7, jul 2001.

[5] K. S. Shanmugan and A. Breipohl, *Random Signals: Detection, Estimation and Data Analysis.* John Wiley & Sons, 1988.

[6] S. Watts and K. Ward, "Spatial correlation in k-distributed sea clutter," *Communications, Radar and Signal Processing, IEE Proceedings F*, vol. 134, no. 6, pp. 526 –532, october 1987.

[7] K. Sangston and K. Gerlach, "Coherent detection of radar targets in a non-gaussian background," *Aerospace and Electronic Systems, IEEE Transactions on*, vol. 30, no. 2, pp. 330 –340, apr 1994.

[8] E. Conte and M. Longo, "Characterisation of radar clutter as a spherically invariant random process," *Communications, Radar and Signal Processing, IEE Proceedings F*, vol. 134, no. 2, pp. 191 –197, april 1987.

[9] S. M. Kay, *Fundamentals of Statistical Signal Processing: Detection Theory*. Prentice Hall PTR, 1998.

[10] F. Ulaby, R. K. Moore, and A. K. Fung, *Microwave Remote Sensing: Active and Passive, Vol. I – Microwave Remote Sensing Fundamentals and Radiometry*. Addison-Wesley, 1981.

[11] G. W. Stimson, *Introduction to Airborne Radar, 2nd Ed.* Scitech Publishing, Inc., 1998.

[12] C. Hülsmeyer, "Hertzian-wave projecting and receiving apparatus adapted to indicate or give warning of the presence of a metallic body such as a ship or a train," British Patent 13 170, Sep 22, 1904.

[13] D. O'Hagan, H. Kuschel, M. Ummenhofer, J. Heckenbach, and J. Schell, "A multi-frequency hybrid passive radar concept for medium range air surveillance," *Aerospace and Electronic Systems Magazine, IEEE*, vol. 27, no. 10, pp. 6 –15, oct. 2012.

[14] K. Olsen and K. Woodbridge, "Performance of a multiband passive bistatic radar processing scheme; part i," *Aerospace and Electronic Systems Magazine, IEEE*, vol. 27, no. 10, pp. 16 –25, oct. 2012.

[15] ——, "Performance of a multiband passive bistatic radar processing scheme-part ii," *Aerospace and Electronic Systems Magazine, IEEE*, vol. 27, no. 11, pp. 4 –14, november 2012.

[16] S. Kingsley and S. Quegan, *Understanding Radar Systems*. SciTech Publishing Inc., 1999.

[17] E. Conte, A. De Maio, and C. Galdi, "Statistical analysis of real clutter at different range resolutions," *Aerospace and Electronic Systems, IEEE Transactions on*, vol. 40, no. 3, pp. 903 – 918, july 2004.

[18] S. Watts and K. Ward, "Spatial correlation in k-distributed sea clutter," *Communications, Radar and Signal Processing, IEE Proceedings F*, vol. 134, no. 6, pp. 526 –532, october 1987.

[19] S. Haykin, "Cognitive radar: a way of the future," *Signal Processing Magazine, IEEE*, vol. 23, no. 1, pp. 30–40, 2006.

[20] S. Haykin, Y. Xue, and P. Setoodeh, "Cognitive radar: Step toward bridging the gap between neuroscience and engineering," *Proceedings of the IEEE*, vol. 100, no. 11, pp. 3102–3130, 2012.

[21] J. Guerci, Ed., *Cognitive Radar: The Knowledge-Aided Fully Adaptive Approach*. Artech House, 2010.

[22] S. Haykin, Ed., *Cognitive Dynamic Systems: Perception-Action Cycle, Radar and Radio*. Cambridge Univ. Press, 2012.

[23] H. Griffiths, L. Cohen, S. Watts, E. Mokole, C. Baker, M. Wicks, and S. Blunt, "Radar spectrum engineering and management: Technical and regulatory issues," in *Proceedings of the IEEE*, Jan 2015.

[24] H. Griffiths, S. Blunt, L. Cohen, and L. Savy, "Challenge problems in spectrum engineering and waveform diversity," in *Radar Conference (RADAR), 2013 IEEE*, April 2013, pp. 1–5.

[25] G. Capraro, A. Farina, H. Griffiths, and M. Wicks, "Knowledge-based radar signal and data processing: a tutorial review," *Signal Processing Magazine, IEEE*, vol. 23, no. 1, pp. 18–29, 2006.

[26] J. Guerci and E. Baranoski, "Knowledge-aided adaptive radar at darpa: an overview," *Signal Processing Magazine, IEEE*, vol. 23, no. 1, pp. 41 – 50, jan. 2006.

[27] S. Blunt, P. McCormick, T. Higgins, and M. Rangaswamy, "Physical emission of spatially-modulated radar," *IET Radar, Sonar & Navigation*, vol. 8, no. 12, Dec 2014.

[28] ——, "Spatially-modulated radar waveforms inspired by fixational eye movement," in *Radar Conference, 2014 IEEE*, May 2014, pp. 0900–0905.

[29] T. Higgins and S. Blunt, "Analysis of range-angle coupled beamforming with frequency-diverse chirps," in *Waveform Diversity and Design Conference, 2009 International*, Feb 2009, pp. 140–144.

[30] R. Romero and N. Goodman, "Adaptive beamsteering for search-and-track application with cognitive radar network," in *Radar Conference (RADAR), 2011 IEEE*, 2011, pp. 1091–1095.

[31] M. Wicks, E. Mokole, S. Blunt, V. Amuso, and R. Schneible, Eds., *Principles of Waveform Diversity and Design.* SciTech Publishing, 2010.

[32] S. Pillai, K. Li, I. Selesnick, and B. Himed, Eds., *Waveform Diversity: Theory & Applications.* McGraw-Hill, 2011.

[33] F. Gini, A. De Maio, and L. Patton, Eds., *Waveform Design and Diversity for Advanced Radar Systems.* IET, 2012.

[34] K. Sangston, F. Gini, and M. Greco, "Coherent radar target detection in heavy-tailed compound-gaussian clutter," *Aerospace and Electronic Systems, IEEE Transactions on*, vol. 48, no. 1, pp. 64 –77, jan. 2012.

[35] K. Sangston, F. Gini, M. Greco, and A. Farina, "Structures for radar detection in compound gaussian clutter," *Aerospace and Electronic Systems, IEEE Transactions on*, vol. 35, no. 2, pp. 445 –458, apr 1999.

[36] K. Gerlach, S. Blunt, and M. Picciolo, "Robust adaptive matched filtering using the fracta algorithm," *Aerospace and Electronic Systems, IEEE Transactions on*, vol. 40, no. 3, pp. 929–945, July 2004.

[37] S. Blunt, K. Gerlach, and J. Heyer, "Hrr detector for slow-moving targets in sea clutter," *Aerospace and Electronic Systems, IEEE Transactions on*, vol. 43, no. 3, pp. 965–974, July 2007.

[38] ——, "Non-coherent detection of slow-moving targets in high-resolution sea clutter," in *Radar Conference, 2004. Proceedings of the IEEE*, April 2004, pp. 345–348.

[39] S. Blunt and K. Gerlach, "Adaptive pulse compression via mmse estimation," *Aerospace and Electronic Systems, IEEE Transactions on*, vol. 42, no. 2, pp. 572 – 584, april 2006.

[40] S. Blunt, J. Jakabosky, J. Metcalf, and J. Stiles, "Multi-waveform stap," *Radar Conference, 2013. Proceedings of the IEEE*, May 2013.

[41] W. L. Stutzman and G. A. Thiele, *Antenna Theory and Design, 2nd Ed.* John Wiley & Sons, 1998.

[42] M. A. Richards, J. A. Scheer, and W. Holm, *Principles of Modern Radar, Vol. I: Basic Principles.* Scitech Publishing Inc., 2010.

[43] J. Ward, "Space-time adaptive processing for airborne radar," Lincoln Laboratory, Tech. Rep. 1015, 1994.

[44] L. Brennan and F. Staudaher, "Subclutter visibility demonstration," Adaptive Sensors Incorporated, Tech. Rep. RL-TR-92-21, 1992.

[45] R. Klemm, "Adaptive clutter suppression for airborne phased array radars," *Microwaves, Optics and Antennas, IEE Proceedings H*, vol. 130, no. 1, pp. 125 –132, february 1983.

[46] K. J. Sangston and K. R. Gerlach, "Non-gaussian noise models and coherent detection of radar targets," Naval Research Laboratory, Tech. Rep. NRL/FR/5341-92-9367, 1992.

[47] I. Reed, J. Mallett, and L. Brennan, "Rapid convergence rate in adaptive arrays," *Aerospace and Electronic Systems, IEEE Transactions on*, vol. AES-10, no. 6, pp. 853 –863, nov. 1974.

[48] E. Kelly, "An adaptive detection algorithm," *Aerospace and Electronic Systems, IEEE Transactions on*, vol. AES-22, no. 2, pp. 115 –127, march 1986.

[49] S. M. Kay, *Fundamentals of Statistical Signal Processing: Estimation Theory*. Prentice Hall PTR, 1998.

[50] F. Robey, D. Fuhrmann, E. Kelly, and R. Nitzberg, "A cfar adaptive matched filter detector," *Aerospace and Electronic Systems, IEEE Transactions on*, vol. 28, no. 1, pp. 208 –216, jan 1992.

[51] S. Kraut, L. Scharf, and L. McWhorter, "Adaptive subspace detectors," *Signal Processing, IEEE Transactions on*, vol. 49, no. 1, pp. 1 –16, jan 2001.

[52] M. Sekine, T. Musha, Y. Tomita, T. Hagisawa, T. Irabu, and E. Kiuchi, "On weibull-distributed weather clutter," *Aerospace and Electronic Systems, IEEE Transactions on*, vol. AES-15, no. 6, pp. 824 –830, nov. 1979.

[53] E. Conte, A. De Maio, and C. Galdi, "Statistical analysis of real clutter at different range resolutions," *Aerospace and Electronic Systems, IEEE Transactions on*, vol. 40, no. 3, pp. 903 – 918, july 2004.

[54] W. Stehwien, "Statistics and correlation properties of high resolution x-band sea clutter," in *Radar Conference, 1994., Record of the 1994 IEEE National*, mar 1994, pp. 46 –51.

[55] E. Jakeman and P. Pusey, "A model for non-rayleigh sea echo," *Antennas and Propagation, IEEE Transactions on*, vol. 24, no. 6, pp. 806 – 814, nov 1976.

[56] A. Farina, A. Russo, and F. Studer, "Coherent radar detection in log-normal clutter," *Communications, Radar and Signal Processing, IEE Proceedings F*, vol. 133, no. 1, pp. 39 –53, february 1986.

[57] E. Conte and M. Longo, "Correspondence: On a coherent model for log-normal clutter," *Communications, Radar and Signal Processing, IEE Proceedings F*, vol. 134, no. 2, pp. 198 –200, april 1987.

[58] S. Watts and K. Ward, "Spatial correlation in k-distributed sea clutter," *Communications, Radar and Signal Processing, IEE Proceedings F*, vol. 134, no. 6, pp. 526 –532, october 1987.

[59] S. Watts, "Radar detection prediction in k-distributed sea clutter and thermal noise," *Aerospace and Electronic Systems, IEEE Transactions on*, vol. AES-23, no. 1, pp. 40 –45, jan. 1987.

[60] J. B. Billingsley, "Ground clutter measurements for surface-sited radar," Lincoln Laboratory, Tech. Rep. 786, 1993.

[61] G. A. Akers, "An approach to ground moving target indication using multiple resolutions of multilook synthetic aperture radar images," Ph.D. dissertation, University of Kansas, 2009.

[62] M. Slamani, "High-level adaptive signal processing architecture with applications to radar non-gaussian clutter a new approach to radar detection based on the partitioning and statistical characterization of the surveillance volume," Air Force Research Laboratory, Tech. Rep. RL-TR-95-164, 1995.

[63] J. Bergin and P. Techau, "High-fidelity site-specific radar simulation: Kassper '02 workshop datacube," ISL, Tech. Rep. ISLSCRD-TR-02-105, 2002.

[64] A. Farina, A. Russo, F. Scannapieco, and S. Barbarossa, "Theory of radar detection in coherent weibull clutter," *Communications, Radar and Signal Processing, IEE Proceedings F*, vol. 134, no. 2, pp. 174 –190, april 1987.

[65] K. J. Sangston and B. H. Cantrell, "On the problem of optimal signal detection in discrete-time, correlated, non-gaussian noise," Naval Research Laboratories, Tech. Rep. NRL Report 9177, 1989.

[66] M. Rangaswamy, D. Weiner, and A. Ozturk, "Non-gaussian random vector identification using spherically invariant random processes," *Aerospace and Electronic Systems, IEEE Transactions on*, vol. 29, no. 1, pp. 111 –124, jan 1993.

[67] E. Conte, M. Di Bisceglie, M. Longo, and M. Lops, "Canonical detection in spherically invariant noise," *Communications, IEEE Transactions on*, vol. 43, no. 234, pp. 347 –353, feb/mar/apr 1995.

[68] C. D. Richmond, "Adaptive array signal processing and performance analysis in non-gaussian environments," Ph.D. dissertation, Massachusetts Institute of Technology, 1996.

[69] A. Zoubir, V. Koivunen, Y. Chakhchoukh, and M. Muma, "Robust estimation in signal processing: A tutorial-style treatment of fundamental concepts," *Signal Processing Magazine, IEEE*, vol. 29, no. 4, pp. 61–80, July.

[70] J. Kingman, "Random walks with spherical symmetry," *Acta Math.*, vol. 109, pp. 11 –53, 1963.

[71] ——, "On random sequences with spherical symmetry," *Biometrika*, vol. 59, pp. 492 –494, 1972.

[72] K. Yao, "A representation theorem and its applications to spherically-invariant random processes," *Information Theory, IEEE Transactions on*, vol. 19, no. 5, pp. 600 – 608, sep 1973.

[73] M. Johnson, *Multivariate Statistical Simulation.* John Wiley and sons, 1987.

[74] J. Goldman, "Detection in the presence of spherically symmetric random vectors," *Information Theory, IEEE Transactions on*, vol. 22, no. 1, pp. 52 – 59, jan 1976.

[75] M. Rangaswamy, "Statistical analysis of the nonhomogeneity detector for non-gaussian interference backgrounds," *Signal Processing, IEEE Transactions on*, vol. 53, no. 6, pp. 2101 – 2111, june 2005.

[76] M. Rangaswamy, J. Michels, and D. Weiner, "Multichannel detection for correlated non-gaussian random processes based on innovations," *Signal Processing, IEEE Transactions on*, vol. 43, no. 8, pp. 1915 –1922, aug 1995.

[77] B. Picinbono, "On circularity," *Signal Processing, IEEE Transactions on*, vol. 42, no. 12, pp. 3473 –3482, dec 1994.

[78] K. Sangston, F. Gini, M. Greco, and A. Farina, "Structures for radar detection in compound gaussian clutter," *Aerospace and Electronic Systems, IEEE Transactions on*, vol. 35, no. 2, pp. 445 –458, apr 1999.

[79] S. Schwartz, "Conditional mean estimates and bayesian hypothesis testing (corresp.)," *Information Theory, IEEE Transactions on*, vol. 21, no. 6, pp. 663 – 665, nov 1975.

[80] M. Rangaswamy, D. Weiner, and A. Ozturk, "Computer generation of correlated non-gaussian radar clutter," *Aerospace and Electronic Systems, IEEE Transactions on*, vol. 31, no. 1, pp. 106 –116, jan. 1995.

[81] C. Bishop, *Pattern Recognition and Machine Learning.* Springer, 2006.

[82] B. Bratley, P. Fox, and L. Schrage, *A Guide to Simulation.* Springer-Verlag, 1987.

[83] N. Redding, "Estimating the parameters of the k distribution in the intensity domain," Defense Science and Technology Organisation, Electronics and Surveillance Research Laboratory, Tech. Rep. DSTO-TR-0839, 1999.

[84] M. Ritchie, A. Charlish, K. Woodbridge, and A. Stove, "Use of the kullback-leibler divergence in estimating clutter distributions," in *Radar Conference (RADAR), 2011 IEEE*, may 2011, pp. 751 –756.

[85] I. Gradshteiyn and I. Ryzhik, Eds., *Table of integrals, series, and products.* Academic Press, 1980.

[86] L. Wasserman, *All of Statistics: A Concise Course in Statistical Inference.* Springer, 2004.

[87] M. Greco, P. Stinco, F. Gini, and M. Rangaswamy, "Impact of sea clutter nonstationarity on disturbance covariance matrix estimation and cfar detector performance," *Aerospace and Electronic Systems, IEEE Transactions on*, vol. 46, no. 3, pp. 1502 –1513, july 2010.

[88] W. Weibull, "A statistical distribution function of wide applicability," *ASME Journal of Applied Mechanics*, pp. 293 –297, September 1951.

[89] R. R. Boothe, "The weibull distribution applied to the ground clutter backscatter coefficient," U.S. Army Missile Command, Tech. Rep. RE-TR.69-15, june 1969.

[90] J. Billingsley, A. Farina, F. Gini, M. Greco, and L. Verrazzani, "Statistical analyses of measured radar ground clutter data," *Aerospace and Electronic Systems, IEEE Transactions on*, vol. 35, no. 2, pp. 579 –593, apr 1999.

[91] G. Goldstein, "False-alarm regulation in log-normal and weibull clutter," *Aerospace and Electronic Systems, IEEE Transactions on*, vol. AES-9, no. 1, pp. 84 –92, jan. 1973.

[92] D. Schleher, "Radar detection in weibull clutter," *Aerospace and Electronic Systems, IEEE Transactions on*, vol. AES-12, no. 6, pp. 736 –743, nov. 1976.

[93] M. Di Bisceglie and C. Galdi, "Cfar detection of extended objects in high-resolution sar images," *Geoscience and Remote Sensing, IEEE Transactions on*, vol. 43, no. 4, pp. 833 – 843, april 2005.

[94] M. Farshchian and F. Posner, "The pareto distribution for low grazing angle and high resolution x-band sea clutter," in *Radar Conference, 2010 IEEE*, May 2010, pp. 789–793.

[95] G. Weinberg, "Assessing pareto fit to high-resolution high-grazing-angle sea clutter," *Electronics Letters*, vol. 47, no. 8, pp. 516–517, April 2011.

[96] ——, "Constant false alarm rate detectors for pareto clutter models," *Radar, Sonar Navigation, IET*, vol. 7, no. 2, pp. 153–163, February 2013.

[97] T. Barnard and F. Khan, "Statistical normalization of spherically invariant non-gaussian clutter," *Oceanic Engineering, IEEE Journal of*, vol. 29, no. 2, pp. 303–309, April 2004.

[98] C. Edwards and D. Penney, Eds., *Calculus with Analytic Geometry.* Prentice Hall, 1998.

[99] "NIST Digital Library of Mathematical Functions," http://dlmf.nist.gov/, Release 1.0.5 of 2012-10-01, online companion to [172]. [Online]. Available: http://dlmf.nist.gov/

[100] P. Davis and P. Rabinowitz, Eds., *Methods of Numerical Integration.* Academic Press Inc., 1984.

[101] M. Rangaswamy, B. Himed, and J. Michels, "Statistical analysis of the nonhomogeneity detector," in *Signals, Systems and Computers, 2000. Conference Record of the Thirty-Fourth Asilomar Conference on*, vol. 2, 29 2000-nov. 1 2000, pp. 1117 –1121 vol.2.

[102] ——, "Performance analysis of the nonhomogeneity detector for stap applications," in *Radar Conference, 2001. Proceedings of the 2001 IEEE*, 2001, pp. 193 –197.

[103] M. Rangaswamy, J. Michels, and B. Himed, "Statistical analysis of the nonhomogeneity detector for stap applications," *Digit. Signal Process.*, vol. 14, no. 3, 2004.

[104] V. Rohatgi, *An Introduction to Probability Theory Mathematical Statistics.* Wiley, 1976.

[105] J. Jackson and R. Moses, "A model for generating synthetic vhf sar forest clutter images," *Aerospace and Electronic Systems, IEEE Transactions on*, vol. 45, no. 3, pp. 1138–1152, July 2009.

[106] H. A. David and H. N. Nagaraja, *Ordered Statistics.* John Wiley and Sons, 2003.

[107] N. Balakrishnan and C. Rao, Eds., *Handbook of Statistics 17, Order Statistics: Applications.* Elsevier, 1998.

[108] J. Tukey, "Nonlinear (nonsuperimposable) methods for smoothing data," *Conference Records of Electronics and Aerospace Systems Convention (EASCOM)*, p. 673, 1974.

[109] A. Ozturk, "A general algorithm for univariate and multivariate goodness-of-fit tests based on graphical representation," *Communications in statistics - theory and methods*, vol. 20, no. 10, pp. 3111 –3137, 1991.

[110] A. Ozturk and E. Dudewicz, "A new statistical goodness-of-fit test based on graphical representation," *Biometrical Journal*, vol. 34, no. 4, pp. 403 –427, 1992.

[111] A. Ozturk and J. Romeu, "A new method for assessing multivariate normality with graphical applications," *Communications in statistics, simulation and computation*, vol. 21, no. 1, pp. 15 –34, 1992.

[112] A. Ozturk, "An application of a distribution identification algorithm to signal detection problems," in *Signals, Systems and Computers, 1993. 1993 Conference Record of The Twenty-Seventh Asilomar Conference on*, nov 1993, pp. 248 –252 vol.1.

[113] B. Babu, J. Torres, and W. Melvin, "Processing and evaluation of multichannel airborne radar measurements (mcarm) measured data," in *Phased Array Systems and Technology, 1996., IEEE International Symposium on*, 1996, pp. 395–399.

[114] M. Rangaswamy, J. Michels, and B. Himed, "Statistical analysis of the nonhomogeneity detector for non-gaussian interference backgrounds," in *Radar Conference, 2002. Proceedings of the IEEE*, 2002, pp. 304 – 310.

[115] W. Melvin, M. Wicks, and R. Brown, "Assessment of multichannel airborne radar measurements for analysis and design of spacetime adaptive processing architectures and algorithms," *Proc. IEEE Nat. Radar Conf.*, 1996.

[116] S. Haykin, Ed., *Neural Networks and Learning Machines*. Pearson, 2009.

[117] W. McCulloch and W. Pitts, "A logistical calculus of the ideas immanent in nervous activity," in *Bulletin of Mathematical Biophysics*, vol. 5, 1943, pp. 115–133.

[118] D. Hebb, Ed., *The Organization of Behavior: A Neurophysical Theory*. Wiley, 1949.

[119] M. Rosenblatt, "The perceptron: A probabilistic model for information storage and organization in the brain," in *Psychological Review*, vol. 65, 1958, pp. 386–408.

[120] M. Rosenblatt, Ed., *Principles of Neurodynamics*. Spartan, 1962.

[121] M. Minsky and S. Papert, Eds., *Perceptrons*. MIT Press, 1969.

[122] M. H. Beale, M. T. Hagan, and H. B. Demuth. (2014) Neural network toolbox user's guide. [Online]. Available: http://www.mathworks.com/help/pdf_doc/nnet/nnet_ug.pdf

[123] D. Yu and L. Deng, "Deep learning and its applications to signal and information processing [exploratory dsp]," *Signal Processing Magazine, IEEE*, vol. 28, no. 1, pp. 145–154, Jan 2011.

[124] L. M. Bregman, "The relaxation method of finding the common points of convex sets and its application to the solution of problems in convex programming," *USSR Computational Mathematics and Mathematical Physics*, vol. 7, pp. 200 –217, 1967.

[125] A. Banerjee, S. Merugu, I. Dhillon, and J. Ghosh, "Clustering with bregman divergences," *Journal of Machine Learning Research*, vol. 6, pp. 1705 –1749, Oct. 2005.

[126] F. Itakura and S. Saito, "A statistical method for estimation of speech spectral density and formant frequencies," *Electronic Communications Japan*, vol. 53-A, pp. 36–43, 1970.

[127] S. Kullback and R. Leibler, "On information and sufficiency," *Annals of Mathematical Statistics*, vol. 55, pp. 79–86, 1951.

[128] P. Mahalanobis, "On the generalised distance in statistics," *Proceedings of the National Institute of Sciences of India 2*, vol. 1, pp. 49–55, 1936.

[129] A. Banerjee, X. Guo, and H. Wang, "On the optimality of conditional expectation as a bregman predictor," *Information Theory, IEEE Transactions on*, vol. 51, no. 7, pp. 2664 –2669, jul 2005.

[130] S.-I. Amari, "α -divergence is unique, belonging to both f -divergence and bregman divergence classes," *Information Theory, IEEE Transactions on*, vol. 55, no. 11, pp. 4925 –4931, nov. 2009.

[131] I. Csiszár, "Eine informationstheoretische ungleichung und ihre anwendung auf den beweis der ergodizität von markoffschen ketten," *Magyar Tud. Akad. Mat. Kutat Int. Kzl.*, vol. 8, pp. 85 –108, 1963.

[132] M. S. Ali and S. Silvey, "A general class of coefficients of divergence of one distribution from another," *J. R. Statist. Soc. B*, vol. 28, pp. 131 –142, 1966.

[133] F. Liese and I. Vajda, "On divergences and informations in statistics and information theory," *Information Theory, IEEE Transactions on*, vol. 52, no. 10, pp. 4394 –4412, oct. 2006.

[134] S. Eguchi and J. Copas, "Interpreting kullback-leibler divergence with the neyman-pearson lemma," *Journal of Multivariate Analysis*, vol. 97, p. 2034–2040, oct. 2006.

[135] T. Cover and J. Thomas, *Elements of Information Theory*. Wiley-Interscience, 2006.

[136] I. Csiszár, "Why least squares and maximum entropy? an axiomatic approach to inference for linear inverse problems," *Ann. Statist.*, vol. 19, pp. 2032 –2066, 1991.

[137] M. Abramowitz and I. Stegun, *Handbook of Mathematical Functions with Formulas, Graphs, and Mathematical Tables*. Dover, 1972.

[138] E. W. Weisstein. (2014) Incomplete gamma function. [Online]. Available: http://mathworld.wolfram.com/IncompleteGammaFunction.html

[139] H. Wall, *Analytic Theory of Continued Fractions*. Chelsea, 1948.

[140] (2014) Incomplete gamma function. [Online]. Available: http://www.mathworks.com/help/matlab/ref/gammainc.html

[141] (2014) Incomplete gamma function. [Online]. Available: https://www.gnu.org/software/octave/doc/interpreter/Special-Functions.html

[142] E. Weisstein. (2015) Euler-mascheroni constant. [Online]. Available: http://mathworld.wolfram.com/Euler-MascheroniConstant.html

[143] E. T. Whittaker and G. N. Watson, Eds., *A Course in Modern Analysis, 4th ed.* Cambridge University Press, 1990.

[144] (2014) Functions of one variable. [Online]. Available: https://www.gnu.org/software/octave/doc/interpreter/Functions-of-One-Variable.html

[145] L. Shampine, "Journal of computational and applied mathematics," in *Vectorized adaptive quadrature in MATLAB*, vol. 211, 2008, pp. 131–140.

[146] J. Metcalf, S. Blunt, and B. Himed, "A machine learning approach to cognitive radar detection," accpeted at 2015 IEEE Radar Conference.

[147] W. Melvin, "Space-time adaptive radar performance in heterogeneous clutter," *Aerospace and Electronic Systems, IEEE Transactions on*, vol. 36, no. 2, pp. 621 – 633, apr 2000.

[148] A. Shackelford, K. Gerlach, and S. Blunt, "Partially adaptive stap using the fracta algorithm," *Aerospace and Electronic Systems, IEEE Transactions on*, vol. 45, no. 1, pp. 58–69, Jan 2009.

[149] S. Blunt, K. Gerlach, and M. Rangaswamy, "Stap using knowledge-aided covariance estimation and the fracta algorithm," *Aerospace and Electronic Systems, IEEE Transactions on*, vol. 42, no. 3, pp. 1043–1057, July 2006.

[150] S. Blunt and K. Gerlach, "Efficient robust amf using the fracta algorithm," *Aerospace and Electronic Systems, IEEE Transactions on*, vol. 41, no. 2, pp. 537–548, April 2005.

[151] D. Boroson, "Sample size considerations for adaptive arrays," *Aerospace and Electronic Systems, IEEE Transactions on*, vol. AES-16, no. 4, pp. 446–451, July 1980.

[152] K. Gerlach, "The effects of signal contamination on two adaptive detectors," *Aerospace and Electronic Systems, IEEE Transactions on*, vol. 31, no. 1, pp. 297–309, Jan 1995.

[153] D. J. Rabideau and A. Steinhardt, "Improved adaptive clutter cancellation through data-adaptive training," *Aerospace and Electronic Systems, IEEE Transactions on*, vol. 35, no. 3, pp. 879–891, Jul 1999.

[154] K. Gerlach, "Outlier resistant adaptive matched filtering," *Aerospace and Electronic Systems, IEEE Transactions on*, vol. 38, no. 3, pp. 885–901, Jul 2002.

[155] M. Picciolo and K. Gerlach, "Median cascaded canceller for robust adaptive array processing," *Aerospace and Electronic Systems, IEEE Transactions on*, vol. 39, no. 3, pp. 883–900, July 2003.

[156] E. Aboutanios and B. Mulgrew, "Hybrid detection approach for stap in heterogeneous clutter," *Aerospace and Electronic Systems, IEEE Transactions on*, vol. 46, no. 3, pp. 1021–1033, July 2010.

[157] O. Besson and S. Bidon, "Adaptive processing with signal contaminated training samples," *Signal Processing, IEEE Transactions on*, vol. 61, no. 17, pp. 4318–4329, Sept 2013.

[158] K. Gerlach, "Efficient reiterative censoring of robust stap using the fracta algorithm," in *Radar Conference, 2003. Proceedings of the International*, Sept 2003, pp. 57–61.

[159] S. Blunt and K. Gerlach, "Efficient robust amf using the enhanced fracta algorithm: results from kassper i ii [target detection]," in *Radar Conference, 2004. Proceedings of the IEEE*, April 2004, pp. 372–377.

[160] S. Blunt, J. Metcalf, J. Jakabosky, and B. Himed, "Sinr analysis of multi-waveform stap," in *Radar Conference, 2014 IEEE International*, Oct 2014.

[161] T. Higgins, K. Gerlach, A. Shackelford, and S. Blunt, "Aspects of non-identical multiple pulse compression," in *Radar Conference (RADAR), 2011 IEEE*, May 2011, pp. 895–900.

[162] M. Cook, S. Blunt, and J. Jakabosky, "Optimization of waveform diversity and performance for pulse-agile radar," in *Radar Conference (RADAR), 2011 IEEE*, May 2011, pp. 812–817.

[163] T. Higgins, S. Blunt, and A. Shackelford, "Time-range adaptive processing for pulse agile radar," in *Waveform Diversity and Design Conference (WDD), 2010 International*, Aug 2010, pp. 115–120.

[164] S. Blunt, M. Cook, and J. Stiles, "Embedding information into radar emissions via waveform implementation," in *Waveform Diversity and Design Conference (WDD), 2010 International*, Aug 2010, pp. 000 195–000 199.

[165] J. Metcalf, C. Sahin, S. Blunt, and M. Rangaswamy, "Analysis of symbol design strategies for intrapulse radar-embedded communications," submitted to IEEE Aerospace & Electronic Systems.

[166] S. Blunt, J. Metcalf, C. Biggs, and E. Perrins, "Performance characteristics and metrics for intra-pulse radar-embedded communication," *Selected Areas in Communications, IEEE Journal on*, vol. 29, no. 10, pp. 2057–2066, December 2011.

[167] S. Blunt, P. Yatham, and J. Stiles, "Intrapulse radar-embedded communications," *Aerospace and Electronic Systems, IEEE Transactions on*, vol. 46, no. 3, pp. 1185–1200, July 2010.

[168] J. Metcalf, S. Blunt, and E. Perrins, "Detector design and intercept metrics for intrapulse radar-embedded communications," in *MILITARY COMMUNICATIONS CONFERENCE, 2011 - MILCOM 2011*, Nov 2011, pp. 188–192.

[169] S. Blunt and J. Metcalf, "Using time reversal of multipath for intra-pulse radar-embedded communications," in *Waveform Diversity and Design Conference (WDD), 2010 International*, Aug 2010, pp. 000 155–000 158.

[170] ——, "Estimating temporal multipath via spatial selectivity: Building environmental knowledge into waveform design for radar-embedded communications," in *Electromagnetics in Advanced Applications, 2009. ICEAA '09. International Conference on*, Sept 2009, pp. 513–516.

[171] S. Blunt and P. Yantham, "Waveform design for radar-embedded communications," in *Waveform Diversity and Design Conference, 2007. International*, June 2007, pp. 214–218.

[172] F. W. J. Olver, D. W. Lozier, R. F. Boisvert, and C. W. Clark, Eds., *NIST Handbook of Mathematical Functions*. New York, NY: Cambridge University Press, 2010, print companion to [99].

[173] J. Michels, M. Rangaswamy, and B. Himed, "Performance of stap tests in compound-gaussian clutter," in *Sensor Array and Multichannel Signal Processing Workshop. 2000. Proceedings of the 2000 IEEE*, 2000, pp. 250 –255.

[174] R. Little and D. Rubin, *Statistical Analysis with Missing Data*. New York:Wiley, 1987.

[175] M. Rangaswamy and J. Michels, "Adaptive signal processing in non-gaussian noise backgrounds," in *Statistical Signal and Array Processing, 1998. Proceedings., Ninth IEEE SP Workshop on*, sep 1998, pp. 53 –56.

Appendix A

COSMiC Weighting Comparison Tables

A.1 Pairwise Distribution Identification

A.1.1 Gaussian Distributed Data

Weightings		Percentage Chosen					
1	2	Gaussian	K	Weibull	Pareto	Lognormal	Gamma Mod.
cosh	$\cosh^2$	48.1	5.2	44.2	2.5	0.0	0.0
cosh	sinh	48.1	5.2	44.2	2.5	0.0	0.0
cosh	$\sinh^2$	48.1	5.2	44.2	2.5	0.0	0.0
cosh	tanh	48.1	5.2	44.2	2.5	0.0	0.0
cosh	$\tanh^2$	48.1	5.2	44.2	2.5	0.0	0.0
sinh	$\sinh^2$	48.0	11.8	38.9	1.3	0.0	0.1
sinh	tanh	48.0	11.8	38.9	1.3	0.0	0.1
sinh	$\tanh^2$	48.0	11.8	38.9	1.3	0.0	0.1
$\cosh^2$	sinh	46.3	8.8	41.8	3.1	0.0	0.0
$\cosh^2$	$\sinh^2$	46.3	8.8	41.8	3.1	0.0	0.0

Table A.1: Distribution identification percentages of top 10 WSOS COSMiC weighting pairs for Gaussian Distributed data

Weightings		Percentage Chosen					
1	2	Gaussian	K	Weibull	Pareto	Lognormal	Gamma Mod.
$\cosh^2$	sinh	60.8	10.8	5.7	19.0	0.2	3.6
$\cosh^2$	$\sinh^2$	60.8	10.8	5.7	19.0	0.2	3.6
$\cosh^2$	tanh	60.8	10.8	5.7	19.0	0.2	3.6
$\cosh^2$	$\tanh^2$	60.8	10.8	5.7	19.0	0.2	3.6
tanh	$\tanh^2$	60.6	4.8	22.1	9.4	0.1	3.1
$\sinh^2$	tanh	60.4	4.2	11.3	19.9	0.3	3.9
$\sinh^2$	$\tanh^2$	60.4	4.2	11.3	19.9	0.3	3.9
sine^2	cosh	60.2	4.7	22.1	9.6	0.2	3.2
sine^2	$\cosh^2$	60.2	4.7	22.1	9.6	0.2	3.2
sine^2	sinh	60.2	4.7	22.1	9.6	0.2	3.2

Table A.2: Distribution identification percentages of top 10 Studentized COSMiC weighting pairs for Gaussian Distributed data

Weightings		Percentage Chosen					
1	2	Gaussian	K	Weibull	Pareto	Lognormal	Gamma Mod.
cos	$\cos^2$	46.6	2.2	37.6	11.8	0.8	1.1
cos	sine	46.6	2.2	37.6	11.8	0.8	1.1
cos	sine^2	46.6	2.2	37.6	11.8	0.8	1.1
cos	cosh	46.6	2.2	37.6	11.8	0.8	1.1
cos	$\cosh^2$	46.6	2.2	37.6	11.8	0.8	1.1
cos	sinh	46.6	2.2	37.6	11.8	0.8	1.1
cos	$\sinh^2$	46.6	2.2	37.6	11.8	0.8	1.1
cos	tanh	46.6	2.2	37.6	11.8	0.8	1.1
cos	$\tanh^2$	46.6	2.2	37.6	11.8	0.8	1.1
sine^2	cosh	38.5	2.1	32.4	20.5	5.2	1.2

Table A.3: Distribution identification percentages of top 10 EOA COSMiC weighting pairs for Gaussian Distributed data

A.1.2 K Distributed Data

Weightings		Percentage Chosen					
1	2	Gaussian	K	Weibull	Pareto	Lognormal	Gamma Mod.
cos	$\cos^2$	0.1	3.2	93.8	0.6	2.0	0.2
cos	sine	0.1	3.2	93.8	0.6	2.0	0.2
cos	sine^2	0.1	3.2	93.8	0.6	2.0	0.2
cos	cosh	0.1	3.2	93.8	0.6	2.0	0.2
cos	$\cosh^2$	0.1	3.2	93.8	0.6	2.0	0.2
cos	sinh	0.1	3.2	93.8	0.6	2.0	0.2
cos	$\sinh^2$	0.1	3.2	93.8	0.6	2.0	0.2
cos	tanh	0.1	3.2	93.8	0.6	2.0	0.2
cos	$\tanh^2$	0.1	3.2	93.8	0.6	2.0	0.2
sinh	$\sinh^2$	0.2	2.9	96.7	0.0	0.0	0.3

Table A.4: Distribution identification percentages of top 10 WSOS COSMiC weighting pairs for K Distributed data

Weightings		Percentage Chosen					
1	2	Gaussian	K	Weibull	Pareto	Lognormal	Gamma Mod.
$\cosh^2$	sinh	36.2	23.8	8.4	21.2	0.3	10.1
$\cosh^2$	$\sinh^2$	36.2	23.8	8.4	21.2	0.3	10.1
$\cosh^2$	tanh	36.2	23.8	8.4	21.2	0.3	10.1
$\cosh^2$	$\tanh^2$	36.2	23.8	8.4	21.2	0.3	10.1
tanh	$\tanh^2$	36.1	23.2	31.9	5.3	0.1	3.3
sine^2	cosh	35.8	23.1	32.0	5.5	0.2	3.4
sine^2	$\cosh^2$	35.8	23.1	32.0	5.5	0.2	3.4
sine^2	sinh	35.8	23.1	32.0	5.5	0.2	3.4
sine^2	$\sinh^2$	35.8	23.1	32.0	5.5	0.2	3.4
sine^2	tanh	35.8	23.1	32.0	5.5	0.2	3.4

Table A.5: Distribution identification percentages of top 10 Studentized COSMiC weighting pairs for K Distributed data

Weightings		Percentage Chosen					
1	2	Gaussian	K	Weibull	Pareto	Lognormal	Gamma Mod.
tanh	$\tanh^2$	17.8	20.4	37.9	15.4	3.2	5.4
sinh	$\sinh^2$	10.8	19.7	48.7	12.9	3.4	4.5
sinh	tanh	10.8	19.7	48.7	12.9	3.4	4.5
sinh	$\tanh^2$	10.8	19.7	48.7	12.9	3.4	4.5
cos	$\cos^2$	22.5	18.9	41.3	10.8	2.5	4.1
cos	sine	22.5	18.9	41.3	10.8	2.5	4.1
cos	sine^2	22.5	18.9	41.3	10.8	2.5	4.1
cos	cosh	22.5	18.9	41.3	10.8	2.5	4.1
cos	$\cosh^2$	22.5	18.9	41.3	10.8	2.5	4.1
cos	sinh	22.5	18.9	41.3	10.8	2.5	4.1

Table A.6: Distribution identification percentages of top 10 EOA COSMiC weighting pairs for K Distributed data

A.1.3 Weibull Distributed Data

Weightings		Percentage Chosen					
1	2	Gaussian	K	Weibull	Pareto	Lognormal	Gamma Mod.
sine	sine^2	4.5	11.5	65.4	12.9	2.6	3.1
sine	cosh	4.5	11.5	65.4	12.9	2.6	3.1
sine	$\cosh^2$	4.5	11.5	65.4	12.9	2.6	3.1
sine	sinh	4.5	11.5	65.4	12.9	2.6	3.1
sine	$\sinh^2$	4.5	11.5	65.4	12.9	2.6	3.1
sine	tanh	4.5	11.5	65.4	12.9	2.6	3.1
sine	$\tanh^2$	4.5	11.5	65.4	12.9	2.6	3.1
$\cos^2$	sine	4.4	10.8	65.0	13.4	3.3	3.0
$\cos^2$	sine^2	4.4	10.8	65.0	13.4	3.3	3.0
$\cos^2$	cosh	4.4	10.8	65.0	13.4	3.3	3.0

Table A.7: Distribution identification percentages of top 10 WSOS COSMiC weighting pairs for Weibull Distributed data

Weightings		Percentage Chosen					
1	2	Gaussian	K	Weibull	Pareto	Lognormal	Gamma Mod.
sine	sine^2	25.7	13.8	45.7	9.0	2.1	3.7
sine	cosh	25.7	13.8	45.7	9.0	2.1	3.7
sine	$\cosh^2$	25.7	13.8	45.7	9.0	2.1	3.7
sine	sinh	25.7	13.8	45.7	9.0	2.1	3.7
sine	$\sinh^2$	25.7	13.8	45.7	9.0	2.1	3.7
sine	tanh	25.7	13.8	45.7	9.0	2.1	3.7
sine	$\tanh^2$	25.7	13.8	45.7	9.0	2.1	3.7
cos	$\cos^2$	25.7	14.0	45.5	9.0	2.1	3.7
cos	sine	25.7	14.0	45.5	9.0	2.1	3.7
cos	sine^2	25.7	14.0	45.5	9.0	2.1	3.7

Table A.8: Distribution identification percentages of top 10 Studentized COSMiC weighting pairs for Weibull Distributed data

Weightings		Percentage Chosen					
1	2	Gaussian	K	Weibull	Pareto	Lognormal	Gamma Mod.
sinh	$\sinh^2$	12.3	13.3	54.5	13.4	2.8	3.7
sinh	tanh	12.3	13.3	54.5	13.4	2.8	3.7
sinh	$\tanh^2$	12.3	13.3	54.5	13.4	2.8	3.7
$\cosh^2$	sinh	12.5	10.8	52.8	15.5	4.6	3.8
$\cosh^2$	$\sinh^2$	12.5	10.8	52.8	15.5	4.6	3.8
$\cosh^2$	tanh	12.5	10.8	52.8	15.5	4.6	3.8
$\cosh^2$	$\tanh^2$	12.5	10.8	52.8	15.5	4.6	3.8
$\sinh^2$	tanh	15.1	11.2	48.2	16.8	4.5	4.2
$\sinh^2$	$\tanh^2$	15.1	11.2	48.2	16.8	4.5	4.2
cosh	$\cosh^2$	17.4	7.8	47.2	14.1	10.9	2.6

Table A.9: Distribution identification percentages of top 10 EOA COSMiC weighting pairs for Weibull Distributed data

A.1.4 Pareto Distributed Data

Weightings		Percentage Chosen					
1	2	Gaussian	K	Weibull	Pareto	Lognormal	Gamma Mod.
$\cos^2$	sine	17.2	9.1	39.2	31.7	1.7	1.2
$\cos^2$	sine^2	17.2	9.1	39.2	31.7	1.7	1.2
$\cos^2$	cosh	17.2	9.1	39.2	31.7	1.7	1.2
$\cos^2$	$\cosh^2$	17.2	9.1	39.2	31.7	1.7	1.2
$\cos^2$	sinh	17.2	9.1	39.2	31.7	1.7	1.2
$\cos^2$	$\sinh^2$	17.2	9.1	39.2	31.7	1.7	1.2
$\cos^2$	tanh	17.2	9.1	39.2	31.7	1.7	1.2
$\cos^2$	$\tanh^2$	17.2	9.1	39.2	31.7	1.7	1.2
sine	sine^2	17.7	10.1	38.5	30.8	1.5	1.5
sine	cosh	17.7	10.1	38.5	30.8	1.5	1.5

Table A.10: Distribution identification percentages of top 10 WSOS COSMiC weighting pairs for Pareto Distributed data

Weightings		Percentage Chosen					
1	2	Gaussian	K	Weibull	Pareto	Lognormal	Gamma Mod.
$\cosh^2$	sinh	42.6	18.4	5.9	24.0	0.3	8.8
$\cosh^2$	$\sinh^2$	42.6	18.4	5.9	24.0	0.3	8.8
$\cosh^2$	tanh	42.6	18.4	5.9	24.0	0.3	8.8
$\cosh^2$	$\tanh^2$	42.6	18.4	5.9	24.0	0.3	8.8
$\sinh^2$	tanh	42.0	14.2	17.7	16.8	0.6	8.8
$\sinh^2$	$\tanh^2$	42.0	14.2	17.7	16.8	0.6	8.8
cos	$\cos^2$	28.1	12.3	40.8	11.6	2.8	4.5
cos	sine	28.1	12.3	40.8	11.6	2.8	4.5
cos	sine^2	28.1	12.3	40.8	11.6	2.8	4.5
cos	cosh	28.1	12.3	40.8	11.6	2.8	4.5

Table A.11: Distribution identification percentages of top 10 Studentized COSMiC weighting pairs for Pareto Distributed data

Weightings		Percentage Chosen					
1	2	Gaussian	K	Weibull	Pareto	Lognormal	Gamma Mod.
sine	$sine^2$	17.2	5.9	38.0	26.8	8.1	4.0
sine	cosh	17.2	5.9	38.0	26.8	8.1	4.0
sine	cosh	17.2	5.9	38.0	26.8	8.1	4.0
sine	sinh	17.2	5.9	38.0	26.8	8.1	4.0
sine	$sinh^2$	17.2	5.9	38.0	26.8	8.1	4.0
sine	tanh	17.2	5.9	38.0	26.8	8.1	4.0
sine	$tanh^2$	17.2	5.9	38.0	26.8	8.1	4.0
cos^2	sine	20.2	5.8	35.0	23.7	11.9	3.4
cos^2	$sine^2$	20.2	5.8	35.0	23.7	11.9	3.4
cos^2	cosh	20.2	5.8	35.0	23.7	11.9	3.4

Table A.12: Distribution identification percentages of top 10 EOA COSMiC weighting pairs for Pareto Distributed data

A.1.5 Lognormal Distributed Data

Weightings		Percentage Chosen					
1	2	Gaussian	K	Weibull	Pareto	Lognormal	Gamma Mod.
cos^2	sine	5.9	14.0	23.9	40.9	10.2	5.1
cos^2	$sine^2$	5.9	14.0	23.9	40.9	10.2	5.1
cos^2	cosh	5.9	14.0	23.9	40.9	10.2	5.1
cos^2	$cosh^2$	5.9	14.0	23.9	40.9	10.2	5.1
cos^2	sinh	5.9	14.0	23.9	40.9	10.2	5.1
cos^2	$sinh^2$	5.9	14.0	23.9	40.9	10.2	5.1
cos^2	tanh	5.9	14.0	23.9	40.9	10.2	5.1
cos^2	$tanh^2$	5.9	14.0	23.9	40.9	10.2	5.1
sine	$sine^2$	7.1	15.9	21.7	40.2	9.3	5.8
sine	cosh	7.1	15.9	21.7	40.2	9.3	5.8

Table A.13: Distribution identification percentages of top 10 WSOS COSMiC weighting pairs for lognormal Distributed data

Weightings		Percentage Chosen					
1	2	Gaussian	K	Weibull	Pareto	Lognormal	Gamma Mod.
cos	$\cos^2$	6.2	40.7	39.6	4.8	2.8	5.9
cos	sine	6.2	40.7	39.6	4.8	2.8	5.9
cos	sine^2	6.2	40.7	39.6	4.8	2.8	5.9
cos	cosh	6.2	40.7	39.6	4.8	2.8	5.9
cos	$\cosh^2$	6.2	40.7	39.6	4.8	2.8	5.9
cos	sinh	6.2	40.7	39.6	4.8	2.8	5.9
cos	$\sinh^2$	6.2	40.7	39.6	4.8	2.8	5.9
cos	tanh	6.2	40.7	39.6	4.8	2.8	5.9
cos	$\tanh^2$	6.2	40.7	39.6	4.8	2.8	5.9
sine	sine^2	6.2	40.3	40.0	4.8	2.8	5.9

Table A.14: Distribution identification percentages of top 10 Studentized COSMiC weighting pairs for lognormal Distributed data

Weightings		Percentage Chosen					
1	2	Gaussian	K	Weibull	Pareto	Lognormal	Gamma Mod.
$\cos^2$	sine	5.1	22.0	29.4	11.7	23.9	7.8
$\cos^2$	sine^2	5.1	22.0	29.4	11.7	23.9	7.8
$\cos^2$	cosh	5.1	22.0	29.4	11.7	23.9	7.8
$\cos^2$	$\cosh^2$	5.1	22.0	29.4	11.7	23.9	7.8
$\cos^2$	sinh	5.1	22.0	29.4	11.7	23.9	7.8
$\cos^2$	$\sinh^2$	5.1	22.0	29.4	11.7	23.9	7.8
$\cos^2$	tanh	5.1	22.0	29.4	11.7	23.9	7.8
$\cos^2$	$\tanh^2$	5.1	22.0	29.4	11.7	23.9	7.8
sine	sine^2	4.3	21.8	26.4	16.9	20.2	10.4
sine	cosh	4.3	21.8	26.4	16.9	20.2	10.4

Table A.15: Distribution identification percentages of top 10 EOA COSMiC weighting pairs for lognormal Distributed data

A.2 Pairwise Threshold Estimation

WSOS			Studentized			Ext. Ozturk		
Weight 1	Weight 2	Avg. Err.	Weight 1	Weight 2	Avg. Err.	Weight 1	Weight 2	Avg. Err.
cos	$\tanh^2$	0.83 dB	sinh	tanh	2.92 dB	cos	$\cos^2$	3.19 dB
cos	$\sinh^2$	0.84 dB	cosh	sinh	3.02 dB	$\cos^2$	$\tanh^2$	3.28 dB
cos	tanh	0.89 dB	sinh	$\tanh^2$	3.03 dB	cos	$\tanh^2$	3.46 dB
cos	sinh	0.89 dB	cosh	tanh	3.04 dB	cos	$\sinh^2$	3.51 dB
sinh	$\sinh^2$	0.91 dB	tanh	$\tanh^2$	3.07 dB	$\cos^2$	$\sinh^2$	3.53 dB
$\sinh^2$	tanh	0.91 dB	cos	sinh	3.17 dB	cos	tanh	3.75 dB
$\sinh^2$	$\tanh^2$	0.92 dB	$\cos^2$	$\tanh^2$	3.20 dB	$\cos^2$	tanh	3.75 dB
sinh	tanh	0.96 dB	sine	tanh	3.20 dB	cos	sinh	3.80 dB
tanh	$\tanh^2$	1.00 dB	cos	cosh	3.21 dB	$\cos^2$	sinh	3.98 dB
sinh	$\tanh^2$	1.02 dB	$\cos^2$	cosh	3.22 dB	cos	sine^2	4.29 dB

Table A.16: Average threshold estimation error in dB for COSMiC with Gaussian distributed data

WSOS			Studentized			Ext. Ozturk		
Weight 1	Weight 2	Avg. Err.	Weight 1	Weight 2	Avg. Err.	Weight 1	Weight 2	Avg. Err.
cos	sine^2	3.9 dB	cosh	sinh	1.75 dB	$\cos^2$	$\tanh^2$	2.11 dB
cos	$\tanh^2$	4.2 dB	sinh	tanh	1.75 dB	cos	$\cos^2$	2.26 dB
cos	$\sinh^2$	4.8 dB	sinh	$\tanh^2$	1.79 dB	$\cos^2$	$\sinh^2$	2.34 dB
cos	sine	4.9 dB	cosh	tanh	1.89 dB	$\cos^2$	tanh	2.44 dB
cos	tanh	4.9 dB	tanh	$\tanh^2$	1.90 dB	cos	$\tanh^2$	2.49 dB
cos	$\cos^2$	5.1 dB	cosh	$\tanh^2$	1.90 dB	cos	$\sinh^2$	2.49 dB
cos	sinh	5.3 dB	cos	$\tanh^2$	1.90 dB	$\cos^2$	sinh	2.62 dB
$\sinh^2$	$\tanh^2$	5.3 dB	cos	cosh	1.92 dB	cos	tanh	2.73 dB
sine^2	$\sinh^2$	5.8 dB	cos	$\cosh^2$	1.96 dB	cos	sinh	2.77 dB
sinh	$\sinh^2$	5.8 dB	cos	$\sinh^2$	1.96 dB	$\cos^2$	cosh	2.79 dB

Table A.17: Average threshold estimation error in dB for COSMiC with K distributed data

WSOS			Studentized			Ext. Ozturk		
Weight 1	Weight 2	Avg. Err.	Weight 1	Weight 2	Avg. Err.	Weight 1	Weight 2	Avg. Err.
$\sinh^2$	$\tanh^2$	0.91 dB	cosh	sinh	1.07 dB	$\cos^2$	$\tanh^2$	1.48 dB
sinh	tanh	0.96 dB	sinh	tanh	1.08 dB	cos	$\cos^2$	1.64 dB
$\cos^2$	cosh	0.98 dB	sinh	$\tanh^2$	1.10 dB	$\cos^2$	$\sinh^2$	1.74 dB
sinh	$\sinh^2$	1.01 dB	cosh	tanh	1.22 dB	$\cos^2$	tanh	1.84 dB
$\cos^2$	$\cosh^2$	1.03 dB	tanh	$\tanh^2$	1.23 dB	cos	$\tanh^2$	1.91 dB
$\sinh^2$	tanh	1.03 dB	cos	$\tanh^2$	1.23 dB	cos	$\sinh^2$	1.92 dB
cosh	$\cosh^2$	1.09 dB	cosh	$\tanh^2$	1.24 dB	$\cos^2$	sinh	2.04 dB
sinh	$\tanh^2$	1.09 dB	cos	cosh	1.24 dB	cos	tanh	2.14 dB
sine^2	$\cosh^2$	1.10 dB	cos	$\cosh^2$	1.28 dB	$\cos^2$	cosh	2.18 dB
tanh	$\tanh^2$	1.10 dB	cos	$\sinh^2$	1.28 dB	cos	sinh	2.19 dB

Table A.18: Average threshold estimation error in dB for COSMiC with Weibull distributed data

WSOS			Studentized			Ext. Ozturk		
Weight 1	Weight 2	Avg. Err.	Weight 1	Weight 2	Avg. Err.	Weight 1	Weight 2	Avg. Err.
$\cos^2$	$\cosh^2$	-0.30 dB	sinh	tanh	1.32 dB	$\cos^2$	$\tanh^2$	1.69 dB
sine	cosh	-0.34 dB	cosh	sinh	1.34 dB	cos	$\cos^2$	1.74 dB
cos	sine	-0.34 dB	sinh	$\tanh^2$	1.38 dB	$\cos^2$	$\sinh^2$	1.92 dB
sine^2	cosh	-0.37 dB	cosh	tanh	1.46 dB	cos	$\sinh^2$	1.93 dB
sine	sinh	-0.39 dB	tanh	$\tanh^2$	1.48 dB	cos	$\tanh^2$	1.93 dB
cos	sine^2	-0.44 dB	cos	$\tanh^2$	1.52 dB	$\cos^2$	tanh	2.07 dB
sine	$\sinh^2$	-0.44 dB	cos	cosh	1.53 dB	cos	tanh	2.22 dB
sine^2	sinh	-0.46 dB	cos	sinh	1.55 dB	cos	sinh	2.25 dB
$\cos^2$	sine^2	0.44 dB	cosh	$\tanh^2$	1.57 dB	$\cos^2$	sinh	2.26 dB
cos	$\cos^2$	0.44 dB	cos	$\cosh^2$	1.58 dB	$\cos^2$	sine^2	2.54 dB

Table A.19: Average threshold estimation error in dB for COSMiC with Pareto distributed data

WSOS			Studentized			Ext. Ozturk		
Weight 1	Weight 2	Avg. Err.	Weight 1	Weight 2	Avg. Err.	Weight 1	Weight 2	Avg. Err.
sine	$\tanh^2$	-1.50 dB	$\cos^2$	sine^2	-1.88 dB	sine^2	$\sinh^2$	-0.70 dB
sine^2	$\tanh^2$	-1.54 dB	$\cos^2$	$\tanh^2$	-1.96 dB	sinh	$\tanh^2$	-0.77 dB
sine	tanh	-1.55 dB	sine^2	$\tanh^2$	-1.96 dB	sine^2	sinh	-0.82 dB
sine^2	tanh	-1.81 dB	$\cos^2$	$\sinh^2$	-1.96 dB	tanh	$\tanh^2$	-0.86 dB
sine	sine^2	-2.13 dB	$\cos^2$	$\cosh^2$	-1.96 dB	sine^2	$\tanh^2$	-0.87 dB
$\cos^2$	sine	-2.65 dB	sine^2	$\sinh^2$	-1.98 dB	sinh	tanh	-0.88 dB
$\cos^2$	sine^2	-3.24 dB	sine^2	$\cosh^2$	-1.98 dB	sine	$\sinh^2$	-1.16 dB
cos	sine	-3.30 dB	$\cos^2$	sine	-1.98 dB	sine^2	tanh	-1.24 dB
cos	sine^2	-3.33 dB	$\cos^2$	tanh	-1.99 dB	sine	$\sinh^2$	-1.28 dB
sine	$\sinh^2$	-3.68 dB	sine^2	tanh	-1.99 dB	sin	sinh	-1.32 dB

Table A.20: Average threshold estimation error in dB for COSMiC with lognormal distributed data

A.3 Tables for Distribution Identification using Triplets of Weightings

A.3.1 Gaussian Distributed Data

Weightings			Percentage Chosen					
1	2	3	Gaussian	K	Weibull	Pareto	Lognormal	Gamma Mod.
sine^2	cosh	$\cosh^2$	49.1	5.0	43.3	2.5	0.0	0.1
sine^2	cosh	sinh	49.1	5.0	43.3	2.5	0.0	0.1
sine^2	cosh	$\sinh^2$	49.1	5.0	43.3	2.5	0.0	0.1
sine^2	cosh	tanh	49.1	5.0	43.3	2.5	0.0	0.1
sine^2	cosh	$\tanh^2$	49.1	5.0	43.3	2.5	0.0	0.1
sine^2	$\cosh^2$	sinh	49.1	5.0	43.3	2.5	0.0	0.1
sine^2	$\cosh^2$	$\sinh^2$	49.1	5.0	43.3	2.5	0.0	0.1
sine^2	$\cosh^2$	tanh	49.1	5.0	43.3	2.5	0.0	0.1
sine^2	$\cosh^2$	$\tanh^2$	49.1	5.0	43.3	2.5	0.0	0.1
sine^2	sinh	$\sinh^2$	49.1	5.0	43.3	2.5	0.0	0.1

Table A.21: Distribution identification percentages of top 10 WSOS COSMiC weighting triplets for Gaussian Distributed data

Weightings			Percentage Chosen					
1	2	3	Gaussian	K	Weibull	Pareto	Lognormal	Gamma Mod.
sinh	$\sinh^2$	tanh	45.8	3.5	35.3	12.3	1.3	1.7
sinh	$\sinh^2$	$\tanh^2$	45.8	3.5	35.3	12.3	1.3	1.7
sinh	tanh	$\tanh^2$	45.8	3.5	35.3	12.3	1.3	1.7
cosh	$\cosh^2$	sinh	45.6	3.6	35.6	12.1	1.3	1.7
cosh	$\cosh^2$	$\sinh^2$	45.6	3.6	35.6	12.1	1.3	1.7
cosh	$\cosh^2$	tanh	45.6	3.6	35.6	12.1	1.3	1.7
cosh	$\cosh^2$	$\tanh^2$	45.6	3.6	35.6	12.1	1.3	1.7
cosh	sinh	$\sinh^2$	45.6	3.6	35.6	12.1	1.3	1.7
cosh	sinh	tanh	45.6	3.6	35.6	12.1	1.3	1.7
cosh	sinh	$\tanh^2$	45.6	3.6	35.6	12.1	1.3	1.7

Table A.22: Distribution identification percentages of top 10 Studentized COSMiC weighting triplets for Gaussian Distributed data

Weightings			Percentage Chosen					
1	2	3	Gaussian	K	Weibull	Pareto	Lognormal	Gamma Mod.
$\sinh^2$	tanh	$\tanh^2$	42.9	2.8	39.9	12.3	0.9	1.2
sine	sine^2	cosh	41.0	2.3	30.6	20.8	4.0	1.3
sine	sine^2	$\cosh^2$	41.0	2.3	30.6	20.8	4.0	1.3
sine	sine^2	sinh	41.0	2.3	30.6	20.8	4.0	1.3
sine	sine^2	$\sinh^2$	41.0	2.3	30.6	20.8	4.0	1.3
sine	sine^2	tanh	41.0	2.3	30.6	20.8	4.0	1.3
sine	sine^2	$\tanh^2$	41.0	2.3	30.6	20.8	4.0	1.3
sine	cosh	$\cosh^2$	41.0	2.3	30.6	20.8	4.0	1.3
sine	cosh	sinh	41.0	2.3	30.6	20.8	4.0	1.3
sine	cosh	$\sinh^2$	41.0	2.3	30.6	20.8	4.0	1.3

Table A.23: Distribution identification percentages of top 10 EOA COSMiC weighting triplets for Gaussian Distributed data

A.3.2 K Distributed Data

Weightings			Percentage Chosen					
1	2	3	Gaussian	K	Weibull	Pareto	Lognormal	Gamma Mod.
$\sinh^2$	tanh	$\tanh^2$	0.1	3.1	96.6	0.0	0.0	0.2
$\cosh^2$	sinh	$\sinh^2$	0.2	3.0	96.6	0.0	0.0	0.2
$\cosh^2$	sinh	tanh	0.2	3.0	96.6	0.0	0.0	0.2
$\cosh^2$	sinh	$\tanh^2$	0.2	3.0	96.6	0.0	0.0	0.2
$\cosh^2$	$\sinh^2$	tanh	0.2	3.0	96.6	0.0	0.0	0.2
$\cosh^2$	$\sinh^2$	$\tanh^2$	0.2	3.0	96.6	0.0	0.0	0.2
$\cosh^2$	tanh	$\tanh^2$	0.2	3.0	96.6	0.0	0.0	0.2
sinh	$\sinh^2$	tanh	0.2	2.9	96.7	0.0	0.0	0.2
sinh	$\sinh^2$	$\tanh^2$	0.2	2.9	96.7	0.0	0.0	0.2
sinh	tanh	$\tanh^2$	0.2	2.9	96.7	0.0	0.0	0.2

Table A.24: Distribution identification percentages of top 10 WSOS COSMiC weighting triplets for K Distributed data

Weightings			Percentage Chosen					
1	2	3	Gaussian	K	Weibull	Pareto	Lognormal	Gamma Mod.
cos	$\cos^2$	sine	22.2	22.1	41.4	8.6	2.1	3.7
cos	$\cos^2$	sine^2	22.2	22.1	41.4	8.6	2.1	3.7
cos	$\cos^2$	cosh	22.2	22.1	41.4	8.6	2.1	3.7
cos	$\cos^2$	$\cosh^2$	22.2	22.1	41.4	8.6	2.1	3.7
cos	$\cos^2$	sinh	22.2	22.1	41.4	8.6	2.1	3.7
cos	$\cos^2$	$\sinh^2$	22.2	22.1	41.4	8.6	2.1	3.7
cos	$\cos^2$	tanh	22.2	22.1	41.4	8.6	2.1	3.7
cos	$\cos^2$	$\tanh^2$	22.2	22.1	41.4	8.6	2.1	3.7
cos	sine	sine^2	22.2	22.1	41.4	8.6	2.1	3.7
cos	sine	cosh	22.2	22.1	41.4	8.6	2.1	3.7

Table A.25: Distribution identification percentages of top 10 Studentized COSMiC weighting triplets for K Distributed data

Weightings			Percentage Chosen					
1	2	3	Gaussian	K	Weibull	Pareto	Lognormal	Gamma Mod.
$\sinh^2$	tanh	$\tanh^2$	21.3	18.6	41.5	11.4	3.0	4.2
$\cosh^2$	sinh	$\sinh^2$	18.2	17.9	45.8	10.7	3.2	4.0
$\cosh^2$	sinh	tanh	18.2	17.9	45.8	10.7	3.2	4.0
$\cosh^2$	sinh	$\tanh^2$	18.2	17.9	45.8	10.7	3.2	4.0
$\cosh^2$	$\sinh^2$	tanh	18.2	17.9	45.8	10.7	3.2	4.0
$\cosh^2$	$\sinh^2$	$\tanh^2$	18.2	17.9	45.8	10.7	3.2	4.0
$\cosh^2$	tanh	$\tanh^2$	18.2	17.9	45.8	10.7	3.2	4.0
sinh	$\sinh^2$	tanh	17.8	17.5	43.3	12.9	4.1	4.4
sinh	$\sinh^2$	$\tanh^2$	17.8	17.5	43.3	12.9	4.1	4.4
sinh	tanh	$\tanh^2$	17.8	17.5	43.3	12.9	4.1	4.4

Table A.26: Distribution identification percentages of top 10 EOA COSMiC weighting triplets for K Distributed data

A.3.3 Weibull Distributed Data

Weightings			Percentage Chosen					
1	2	3	Gaussian	K	Weibull	Pareto	Lognormal	Gamma Mod.
sine	sine^2	cosh	12.7	18.7	64.9	2.0	0.1	1.6
sine	sine^2	$\cosh^2$	12.7	18.7	64.9	2.0	0.1	1.6
sine	sine^2	sinh	12.7	18.7	64.9	2.0	0.1	1.6
sine	sine^2	$\sinh^2$	12.7	18.7	64.9	2.0	0.1	1.6
sine	sine^2	tanh	12.7	18.7	64.9	2.0	0.1	1.6
sine	sine^2	$\tanh^2$	12.7	18.7	64.9	2.0	0.1	1.6
sine	cosh	$\cosh^2$	12.7	18.7	64.9	2.0	0.1	1.6
sine	cosh	sinh	12.7	18.7	64.9	2.0	0.1	1.6
sine	cosh	$\sinh^2$	12.7	18.7	64.9	2.0	0.1	1.6
sine	cosh	tanh	12.7	18.7	64.9	2.0	0.1	1.6

Table A.27: Distribution identification percentages of top 10 WSOS COSMiC weighting triplets for Weibull Distributed data

Weightings			Percentage Chosen					
1	2	3	Gaussian	K	Weibull	Pareto	Lognormal	Gamma Mod.
sine^2	cosh	cosh^2	24.6	13.8	47.6	8.4	1.9	3.6
sine^2	cosh	sinh	24.6	13.8	47.6	8.4	1.9	3.6
sine^2	cosh	sinh^2	24.6	13.8	47.6	8.4	1.9	3.6
sine^2	cosh	tanh	24.6	13.8	47.6	8.4	1.9	3.6
sine^2	cosh	tanh^2	24.6	13.8	47.6	8.4	1.9	3.6
sine^2	cosh^2	sinh	24.6	13.8	47.6	8.4	1.9	3.6
sine^2	cosh^2	sinh^2	24.6	13.8	47.6	8.4	1.9	3.6
sine^2	cosh^2	tanh	24.6	13.8	47.6	8.4	1.9	3.6
sine^2	cosh^2	tanh^2	24.6	13.8	47.6	8.4	1.9	3.6
sine^2	sinh	sinh^2	24.6	13.8	47.6	8.4	1.9	3.6

Table A.28: Distribution identification percentages of top 10 Studentized COSMiC weighting triplets for Weibull Distributed data

Weightings			Percentage Chosen					
1	2	3	Gaussian	K	Weibull	Pareto	Lognormal	Gamma Mod.
cosh	cosh^2	sinh	16.9	9.4	51.9	13.1	4.5	4.1
cosh	cosh^2	sinh^2	16.9	9.4	51.9	13.1	4.5	4.1
cosh	cosh^2	tanh	16.9	9.4	51.9	13.1	4.5	4.1
cosh	cosh^2	tanh^2	16.9	9.4	51.9	13.1	4.5	4.1
cosh	sinh	sinh^2	16.9	9.4	51.9	13.1	4.5	4.1
cosh	sinh	tanh	16.9	9.4	51.9	13.1	4.5	4.1
cosh	sinh	tanh^2	16.9	9.4	51.9	13.1	4.5	4.1
cosh	sinh^2	tanh	16.9	9.4	51.9	13.1	4.5	4.1
cosh	sinh^2	tanh^2	16.9	9.4	51.9	13.1	4.5	4.1
cosh	tanh	tanh^2	16.9	9.4	51.9	13.1	4.5	4.1

Table A.29: Distribution identification percentages of top 10 EOA COSMiC weighting triplets for Weibull Distributed data

A.3.4 Pareto Distributed Data

Weightings			Percentage Chosen					
1	2	3	Gaussian	K	Weibull	Pareto	Lognormal	Gamma Mod.
cos	$\cos^2$	sine	24.6	8.5	38.9	24.2	1.3	2.5
cos	$\cos^2$	sine^2	24.6	8.5	38.9	24.2	1.3	2.5
cos	$\cos^2$	cosh	24.6	8.5	38.9	24.2	1.3	2.5
cos	$\cos^2$	$\cosh^2$	24.6	8.5	38.9	24.2	1.3	2.5
cos	$\cos^2$	sinh	24.6	8.5	38.9	24.2	1.3	2.5
cos	$\cos^2$	$\sinh^2$	24.6	8.5	38.9	24.2	1.3	2.5
cos	$\cos^2$	tanh	24.6	8.5	38.9	24.2	1.3	2.5
cos	$\cos^2$	$\tanh^2$	24.6	8.5	38.9	24.2	1.3	2.5
cos	sine	sine^2	24.6	8.5	38.9	24.2	1.3	2.5
cos	sine	cosh	24.6	8.5	38.9	24.2	1.3	2.5s

Table A.30: Distribution identification percentages of top 10 WSOS COSMiC weighting triplets for Pareto Distributed data

Weightings			Percentage Chosen					
1	2	3	Gaussian	K	Weibull	Pareto	Lognormal	Gamma Mod.
$\cos^2$	sine	sine^2	26.3	11.8	42.5	11.8	3.0	4.6
$\cos^2$	sine	cosh	26.3	11.8	42.5	11.8	3.0	4.6
$\cos^2$	sine	$\cosh^2$	26.3	11.8	42.5	11.8	3.0	4.6
$\cos^2$	sine	sinh	26.3	11.8	42.5	11.8	3.0	4.6
$\cos^2$	sine	$\sinh^2$	26.3	11.8	42.5	11.8	3.0	4.6
$\cos^2$	sine	tanh	26.3	11.8	42.5	11.8	3.0	4.6
$\cos^2$	sine	$\tanh^2$	26.3	11.8	42.5	11.8	3.0	4.6
$\cos^2$	sine^2	cosh	26.3	11.8	42.5	11.8	3.0	4.6
$\cos^2$	sine^2	$\cosh^2$	26.3	11.8	42.5	11.8	3.0	4.6
$\cos^2$	sine^2	sinh	26.3	11.8	42.5	11.8	3.0	4.6

Table A.31: Distribution identification percentages of top 10 Studentized COSMiC weighting triplets for Pareto Distributed data

Weightings			Percentage Chosen					
1	2	3	Gaussian	K	Weibull	Pareto	Lognormal	Gamma Mod.
$\cos^2$	sine	sine^2	20.0	7.2	38.4	22.8	7.2	4.4
$\cos^2$	sine	cosh	20.0	7.2	38.4	22.8	7.2	4.4
$\cos^2$	sine	$\cosh^2$	20.0	7.2	38.4	22.8	7.2	4.4
$\cos^2$	sine	sinh	20.0	7.2	38.4	22.8	7.2	4.4
$\cos^2$	sine	$\sinh^2$	20.0	7.2	38.4	22.8	7.2	4.4
$\cos^2$	sine	tanh	20.0	7.2	38.4	22.8	7.2	4.4
$\cos^2$	sine	$\tanh^2$	20.0	7.2	38.4	22.8	7.2	4.4
$\cos^2$	sine^2	cosh	20.0	7.2	38.4	22.8	7.2	4.4
$\cos^2$	sine^2	$\cosh^2$	20.0	7.2	38.4	22.8	7.2	4.4
$\cos^2$	sine^2	sinh	20.0	7.2	38.4	22.8	7.2	4.4

Table A.32: Distribution identification percentages of top 10 EOA COSMiC weighting triplets for Pareto Distributed data

A.3.5 Lognormal Distributed Data

Weightings			Percentage Chosen					
1	2	3	Gaussian	K	Weibull	Pareto	Lognormal	Gamma Mod.
cos	$\cos^2$	sine	12.6	8.3	27.6	34.5	6.7	10.3
cos	$\cos^2$	sine^2	12.6	8.3	27.6	34.5	6.7	10.3
cos	$\cos^2$	cosh	12.6	8.3	27.6	34.5	6.7	10.3
cos	$\cos^2$	$\cosh^2$	12.6	8.3	27.6	34.5	6.7	10.3
cos	$\cos^2$	sinh	12.6	8.3	27.6	34.5	6.7	10.3
cos	$\cos^2$	$\sinh^2$	12.6	8.3	27.6	34.5	6.7	10.3
cos	$\cos^2$	tanh	12.6	8.3	27.6	34.5	6.7	10.3
cos	$\cos^2$	$\tanh^2$	12.6	8.3	27.6	34.5	6.7	10.3
cos	sine	sine^2	12.6	8.3	27.6	34.5	6.7	10.3
cos	sine	cosh	12.6	8.3	27.6	34.5	6.7	10.3

Table A.33: Distribution identification percentages of top 10 WSOS COSMiC weighting triplets for lognormal Distributed data

Weightings			Percentage Chosen					
1	2	3	Gaussian	K	Weibull	Pareto	Lognormal	Gamma Mod.
$\cos^2$	sine	sine^2	5.0	41.9	38.5	4.9	3.4	6.3
$\cos^2$	sine	cosh	5.0	41.9	38.5	4.9	3.4	6.3
$\cos^2$	sine	$\cosh^2$	5.0	41.9	38.5	4.9	3.4	6.3
$\cos^2$	sine	sinh	5.0	41.9	38.5	4.9	3.4	6.3
$\cos^2$	sine	$\sinh^2$	5.0	41.9	38.5	4.9	3.4	6.3
$\cos^2$	sine	tanh	5.0	41.9	38.5	4.9	3.4	6.3
$\cos^2$	sine	$\tanh^2$	5.0	41.9	38.5	4.9	3.4	6.3
$\cos^2$	sine^2	cosh	5.0	41.9	38.5	4.9	3.4	6.3
$\cos^2$	sine^2	$\cosh^2$	5.0	41.9	38.5	4.9	3.4	6.3
$\cos^2$	sine^2	sinh	5.0	41.9	38.5	4.9	3.4	6.3

Table A.34: Distribution identification percentages of top 10 Studentized COSMiC weighting triplets for lognormal Distributed data

Weightings			Percentage Chosen					
1	2	3	Gaussian	K	Weibull	Pareto	Lognormal	Gamma Mod.
cos	$\cos^2$	sine	5.6	30.7	31.7	10.9	12.8	8.3
cos	$\cos^2$	sine^2	5.6	30.7	31.7	10.9	12.8	8.3
cos	$\cos^2$	cosh	5.6	30.7	31.7	10.9	12.8	8.3
cos	$\cos^2$	$\cosh^2$	5.6	30.7	31.7	10.9	12.8	8.3
cos	$\cos^2$	sinh	5.6	30.7	31.7	10.9	12.8	8.3
cos	$\cos^2$	$\sinh^2$	5.6	30.7	31.7	10.9	12.8	8.3
cos	$\cos^2$	tanh	5.6	30.7	31.7	10.9	12.8	8.3
cos	$\cos^2$	$\tanh^2$	5.6	30.7	31.7	10.9	12.8	8.3
cos	sine	sine^2	5.6	30.7	31.7	10.9	12.8	8.3
cos	sine	cosh	5.6	30.7	31.7	10.9	12.8	8.3

Table A.35: Distribution identification percentages of top 10 EOA COSMiC weighting triplets for lognormal Distributed data

A.4 Tables for Threshold Estimation using Triplets of Weightings

Weight 1	Weight 2	Weight 3	Avg. Error (dB)
cos	$\sinh^2$	$\tanh^2$	0.76 dB
cos	tanh	$\tanh^2$	0.78 dB
cos	sinh	$\tanh^2$	0.81 dB
cos	$\sinh^2$	tanh	0.82 dB
cos	sinh	$\sinh^2$	0.82 dB
cos	sinh	tanh	0.83 dB
sinh	$\sinh^2$	$\tanh^2$	0.90 dB
$\sinh^2$	tanh	$\tanh^2$	0.90 dB
cos	$\cos^2$	sinh	0.92 dB
sinh	$\sinh^2$	tanh	0.92 dB

Table A.36: Error in threshold estimation for WSOS method with Gaussian distributed data

Weight 1	Weight 2	Weight 3	Avg. Error (dB)
cos	sinh	$\tanh^2$	2.77 dB
sinh	tanh	$\tanh^2$	2.85 dB
cosh	sinh	tanh	2.85 dB
cos	cosh	sinh	2.86 dB
cosh	sinh	$\tanh^2$	2.90 dB
cos	sinh	tanh	2.99 dB
cos	tanh	$\tanh^2$	3.01 dB
cosh	tanh	$\tanh^2$	3.02 dB
cos	cosh	tanh	3.02 dB
cos	$\cosh^2$	sinh	3.03 dB

Table A.37: Error in threshold estimation for studentized method with Gaussian distributed data

Weight 1	Weight 2	Weight 3	Avg. Error (dB)
cos	$\cos^2$	$\tanh^2$	3.28 dB
cos	$\cos^2$	$\sinh^2$	3.35 dB
cos	$\cos^2$	tanh	3.49 dB
cos	$\cos^2$	sinh	3.55 dB
$\cos^2$	$\sinh^2$	$\tanh^2$	3.59 dB
cos	$\sinh^2$	$\tanh^2$	3.60 dB
$\cos^2$	tanh	$\tanh^2$	3.74 dB
cos	$\cos^2$	sine^2	3.76 dB
cos	$\sinh^2$	tanh	3.83 dB
cos	tanh	$\tanh^2$	3.85 dB

Table A.38: Error in threshold estimation for EOA method with Gaussian distributed data

Weight 1	Weight 2	Weight 3	Avg. Error (dB)
cos	sine^2	$\tanh^2$	4.40 dB
cos	$\sinh^2$	$\tanh^2$	4.94 dB
cos	sine^2	$\sinh^2$	4.94 dB
cos	sine	sine^2	5.05 dB
cos	$\cos^2$	$\tanh^2$	5.07 dB
cos	tanh	$\tanh^2$	5.09 dB
cos	$\cos^2$	sine^2	5.13 dB
cos	sine^2	tanh	5.14 dB
cos	sine	$\tanh^2$	5.14 dB
cos	$\cos^2$	$\sinh^2$	5.24 dB

Table A.39: Error in threshold estimation for WSOS method with K distributed data

Weight 1	Weight 2	Weight 3	Avg. Error (dB)
cos	sinh	$\tanh^2$	1.64 dB
cosh	sinh	$\tanh^2$	1.73 dB
cos	cosh	sinh	1.73 dB
sinh	tanh	$\tanh^2$	1.74 dB
cosh	sinh	tanh	1.76 dB
cos	$\cosh^2$	sinh	1.86 dB
cos	sinh	$\sinh^2$	1.86 dB
cos	sinh	tanh	1.86 dB
cosh	tanh	$\tanh^2$	1.86 dB
$\cosh^2$	sinh	tanh	1.87 dB

Table A.40: Error in threshold estimation for Studentized method with K distributed data

Weight 1	Weight 2	Weight 3	Avg. Error (dB)
cos	$\cos^2$	$\tanh^2$	2.28 dB
cos	$\cos^2$	$\sinh^2$	2.34 dB
$\cos^2$	$\sinh^2$	$\tanh^2$	2.41 dB
cos	$\cos^2$	tanh	2.43 dB
cos	$\cos^2$	sinh	2.48 dB
cos	$\sinh^2$	$\tanh^2$	2.52 dB
$\cos^2$	tanh	$\tanh^2$	2.52 dB
$\cos^2$	$\sinh^2$	tanh	2.63 dB
cos	$\cos^2$	sine^2	2.66 dB
$\cos^2$	sinh	$\tanh^2$	2.68 dB

Table A.41: Error in threshold estimation for EOA method with K distributed data

Weight 1	Weight 2	Weight 3	Avg. Error (dB)
$\cos^2$	cosh	$\cosh^2$	1.01 dB
sinh	$\sinh^2$	$\tanh^2$	1.02 dB
sinh	$\sinh^2$	tanh	1.04 dB
$\sinh^2$	tanh	$\tanh^2$	1.04 dB
$\cosh^2$	sinh	$\sinh^2$	1.05 dB
cos	$\sinh^2$	tanh	1.05 dB
sinh	tanh	$\tanh^2$	1.05 dB
$\cos^2$	$\cosh^2$	$\sinh^2$	1.06 dB
$\cos^2$	cosh	tanh	1.06 dB
cosh	$\cosh^2$	tanh	1.06 dB

Table A.42: Error in threshold estimation for WSOS method with Weibull distributed data

Weight 1	Weight 2	Weight 3	Avg. Error (dB)
cos	sinh	$\tanh^2$	0.98 dB
cosh	sinh	$\tanh^2$	1.09 dB
cos	cosh	sinh	1.09 dB
sinh	tanh	$\tanh^2$	1.12 dB
cosh	sinh	tanh	1.15 dB
cos	sinh	tanh	1.22 dB
cos	$\cosh^2$	sinh	1.23 dB
cos	sinh	$\sinh^2$	1.23 dB
cos	cosh	tanh	1.25 dB
cos	cosh	$\tanh^2$	1.25 dB

Table A.43: Error in threshold estimation for Studentized method with Weibull distributed data

Weight 1	Weight 2	Weight 3	Avg. Error (dB)
cos	$\cos^2$	$\tanh^2$	1.74 dB
cos	$\cos^2$	$\sinh^2$	1.81 dB
cos	$\cos^2$	tanh	1.88 dB
$\cos^2$	$\sinh^2$	$\tanh^2$	1.88 dB
cos	$\cos^2$	sinh	1.94 dB
$\cos^2$	tanh	$\tanh^2$	1.97 dB
cos	$\sinh^2$	$\tanh^2$	2.03 dB
$\cos^2$	$\sinh^2$	tanh	2.11 dB
cos	$\cos^2$	sine^2	2.13 dB
$\cos^2$	sinh	$\tanh^2$	2.15 dB

Table A.44: Error in threshold estimation for EOA method with Weibull distributed data

Weight 1	Weight 2	Weight 3	Avg. Error (dB)
$\cos^2$	sine^2	$\tanh^2$	0.06 dB
sine^2	tanh	$\tanh^2$	-0.08 dB
$\cos^2$	$\sinh^2$	tanh	-0.10 dB
$\cos^2$	sine	tanh	-0.11 dB
$\cos^2$	sine	$\tanh^2$	0.15 dB
$\cos^2$	sine^2	tanh	-0.16 dB
$\cos^2$	$\cosh^2$	tanh	-0.20 dB
sine	tanh	$\tanh^2$	0.21 dB
$\cos^2$	sinh	$\sinh^2$	0.23 dB
cos	sine	sine^2	0.25 dB

Table A.45: Error in threshold estimation for WSOS method with Pareto distributed data

Weight 1	Weight 2	Weight 3	Avg. Error (dB)
cos	sinh	$\tanh^2$	1.27 dB
cos	cosh	sinh	1.36 dB
cosh	sinh	$\tanh^2$	1.37 dB
sinh	tanh	$\tanh^2$	1.37 dB
cosh	sinh	tanh	1.38 dB
cosh	tanh	$\tanh^2$	1.50 dB
cos	sinh	tanh	1.50 dB
cos	$\cosh^2$	sinh	1.51 dB
cos	sinh	$\sinh^2$	1.51 dB
cos	cosh	tanh	1.52 dB

Table A.46: Error in threshold estimation for studentized method with Pareto distributed data

Weight 1	Weight 2	Weight 3	Avg. Error (dB)
cos	$\cos^2$	$\tanh^2$	1.81 dB
cos	$\cos^2$	$\sinh^2$	1.87 dB
cos	$\cos^2$	tanh	1.99 dB
cos	$\sinh^2$	$\tanh^2$	2.01 dB
$\cos^2$	$\sinh^2$	$\tanh^2$	2.03 dB
cos	$\cos^2$	sinh	2.05 dB
$\cos^2$	tanh	$\tanh^2$	2.19 dB
cos	$\sinh^2$	tanh	2.24 dB
cos	tanh	$\tanh^2$	2.26 dB
cos	sinh	$\sinh^2$	2.27 dB

Table A.47: Error in threshold estimation for EOA method with Pareto distributed data

Weight 1	Weight 2	Weight 3	Avg. Error (dB)
sine	sine^2	tanh	-1.40 dB
sine	sine^2	$\tanh^2$	-1.47 dB
sine	sine^2	cosh	-1.73 dB
sine	sine^2	sinh	-1.86 dB
$\cos^2$	sine	sine^2	-2.01 dB
cos	sine	sine^2	-2.27 dB
sine	sine^2	$\sinh^2$	-2.38 dB
sine	tanh	$\tanh^2$	-2.58 dB
sine^2	tanh	$\tanh^2$	-2.99 dB
$\cos^2$	sine	$\tanh^2$	-3.13 dB

Table A.48: Error in threshold estimation for WSOS method with lognormal distributed data

Weight 1	Weight 2	Weight 3	Avg. Error (dB)
$\cos^2$	$\cosh^2$	$\sinh^2$	-1.86 dB
$\cos^2$	cosh	$\sinh^2$	-1.92 dB
$\cos^2$	cosh	$\cosh^2$	-1.92 dB
sine^2	cosh	$\sinh^2$	-1.92 dB
sine^2	cosh	$\cosh^2$	-1.92 dB
sine^2	$\cosh^2$	$\sinh^2$	-1.92 dB
$\cos^2$	tanh	$\tanh^2$	-1.93 dB
sine^2	tanh	$\tanh^2$	-1.93 dB
$\cos^2$	$\sinh^2$	$\tanh^2$	-1.94 dB
$\cos^2$	$\cosh^2$	$\tanh^2$	-1.94 dB

Table A.49: Error in threshold estimation for studentized method with lognormal distributed data

Weight 1	Weight 2	Weight 3	Avg. Error (dB)
sine^2	sinh^2	tanh^2	-0.67 dB
sine^2	sinh	sinh^2	-0.69 dB
sinh	sinh^2	tanh	-0.72 dB
sine^2	sinh	tanh^2	-0.73 dB
sine^2	sinh^2	tanh	-0.74 dB
sine^2	sinh	tanh	-0.87 dB
sinh	tanh	tanh^2	-0.93 dB
sine^2	tanh	tanh^2	-0.95 dB
sine	sinh	sinh^2	-1.14 dB
sine	sinh^2	tanh	-1.21 dB

Table A.50: Error in threshold estimation for EOA method with lognormal distributed data

Appendix B

Deep Belief Network Strategies

A deep machine learning architecture is defined as a system "composed of many layers of non-linear processing stages, where each layer's outputs are fed to its immediate higher layer as the input" [123]. It should be noted that the commonly used deep strategies are typically characterized by an unsupervised pre-training step for feature extraction [123]. The most commonly encountered deep structure is the deep belief net (DBN) [116, 123].

As the desired feature space here is already known and well quantified, we chose to use a deep structure composed of layers of individually trained neural networks. In other words, the difficulty here is not in the dimensionality of the feature space (*i.e.* in the number of parameters) to be learned, but in the ambiguity and low sample support inherent in the problem. The desired classes of data are known and easily generated. For these reasons we choose to do the stacking of the processing layers manually.

Note that when the true covariance matrix is known, the distribution identification neural networks were accurate for a large number of test cases. In addition, the test cases that did not yield accurate classification corresponded to data with a large shape parameter. In the large shape parameter regime, the data becomes increasingly close (as the shape parameter increases) to Gaussian distributed. This trait is shared by all of the SIRV distributions examined here. In addition, there were questions raised by the imbalance in training data

used to train the neural networks. For example, out of the 153 distribution/shape parameter pairs that were used to train each neural network, 65 of the pairs belonged the Pareto distribution. Using a deep neural network can help to counteract that imbalance in data points to prevent overtraining. For these reasons, we examine two deep neural networks here.

The first deep neural network is explored in Section B.1 and is formed from a distribution identification neural network followed by six threshold estimating neural networks tailored for each candidate distribution. The second deep neural network is explored in Section B.1 and introduces a shape parameter estimating neural network preceding the threshold estimation neural networks for the K, Weibull, Pareto, and GM distributions. These two deep networks are explored in more detail in their respective sections.

B.1 Two Stage Threshold Estimating Deep Network

The first deep neural network examined uses a distribution identifying neural network followed by a set of six threshold estimating neural networks (corresponding to each of the distributions used to train and test the networks). The output of the distribution identifying neural network is fed into a selector, which feeds the input data into the neural network associated with the distribution chosen by the distribution identification neural network. The deep network structure is illustrated in Figure B.1.

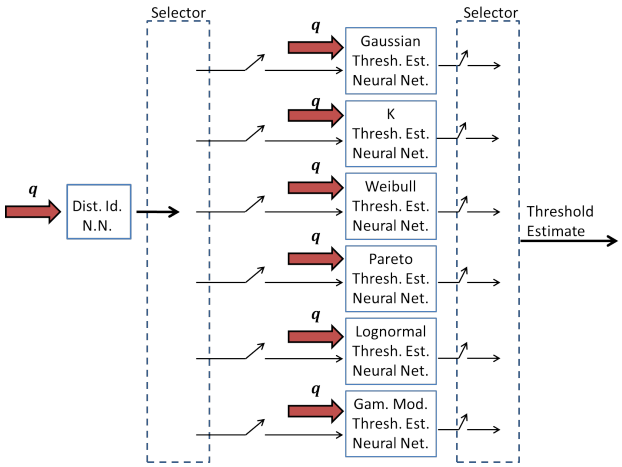

Figure B.1: Deep neural network for threshold estimation

Note that the training parameters over the two layers of neural networks are held constant. In other words, if a distribution identification neural network has 10 hidden neurons and was trained with 10^3 samples per distribution/shape parameter pair, all threshold estimation neural networks associated with the distribution identification neural network have 10 hidden neurons and are trained with 10^3 samples per shape parameter. The number of shape parameters considered per distribution is the same as was considered in Chapter 7. Continuing the above example, the threshold estimation neural network associated with the Pareto distribution has 10 hidden neurons and was trained with 65×10^3 total training samples. The parameters of the neural network itself (*i.e.* number of hidden neurons, number of training samples used, ordering of data) is the same as was described in Section 7.1.

In addition, when the distribution under test is excised from the training data for the distribution identification neural network, the corresponding threshold estimation neural network is removed from the selector's options. Sections B.1.1-B.1.5 examine the threshold estimation accuracy for each of the candidate distributions, and compare the results to the accuracy of the corresponding neural networks shown in Sections 7.2.2.1-7.2.2.5.

B.1.1 Threshold Estimation of Gaussian Data with a Deep Neural Network

Table B.1 gives the average threshold estimate error for the deep neural networks when Gaussian data is present. Comparing Table B.1 to 7.13, the deep approach performs similarly when the CCM is used. However, it appears that there is an ≈ 0.3 dB improvement in estimation error when the SCM is used in the deep approach.

		Unordered Data			Ordered Data		
HN	Samples	Full	Excised	Δ_{full} (Δ_{excised})	Full	Excised	Δ_{full} (Δ_{excised})
10	10^2	5.1 (5.1)	5.1 (5.1)	0.0 (0.0)	2.9 (1.5)	2.9 (1.5)	-1.4 (-1.4)
10	10^3	5.1 (5.1)	5.1 (5.1)	0.0 (0.0)	3.2 (1.8)	3.2 (1.8)	-1.4 (-1.4)
10	10^4	5.0 (5.0)	5.0 (5.0)	0.0 (0.0)	3.0 (1.9)	3.0 (1.9)	-1.1 (-1.1)
20	10^2	3.1 (1.8)	3.1 (1.8)	-1.3 (-1.3)	3.2 (1.9)	3.2 (1.9)	-1.3 (-1.3)
20	10^3	3.1 (1.7)	3.1 (1.7)	-1.3 (-1.3)	3.2 (1.8)	3.2 (1.8)	-1.3 (-1.3)
20	10^4	5.2 (5.2)	5.2 (5.2)	0.0 (0.0)	3.1 (1.9)	3.1 (1.9)	-1.3 (-1.3)
30	10^2	3.2 (1.9)	3.3 (1.9)	-1.4 (-1.4)	3.2 (1.9)	3.2 (1.9)	-1.3 (-1.3)
30	10^3	3.1 (1.7)	3.1 (1.7)	-1.5 (-1.5)	3.0 (1.5)	3.0 (1.5)	-1.5 (-1.5)
30	10^4	3.2 (2.0)	3.2 (2.0)	-1.2 (-1.2)	3.2 (2.0)	3.2 (2.0)	-1.2 (-1.2)

Table B.1: Average Threshold Error (dB) when Gaussian data is fed into a two layer neural network

B.1.2 Threshold Estimation of K Data with a Deep Neural Network

Table B.2 summarizes the threshold error estimates for K distributed data, averaged over shape parameter when the various deep neural networks are used. Note that comparing Table B.2 to Table 7.14, the two groups of neural networks perform similarly. However, in general the deep neural networks provide a slightly lower estimate error when the SCM is used.

		Unordered Data			Ordered Data		
HN	Samples	Full	Excised	Δ_{full} (Δ_{excised})	Full	Excised	Δ_{full} (Δ_{excised})
10	10^2	2.2 (2.5)	2.8 (2.5)	0.2 (-0.3)	2.4 (2.0)	3.9 (1.7)	-0.3 (-2.1)
10	10^3	2.5 (2.3)	4.7 (2.3)	-0.2 (-2.4)	2.4 (2.4)	3.0 (1.9)	0.0 (-1.2)
10	10^4	2.5 (2.2)	4.4 (2.2)	-0.2 (-2.2)	2.3 (2.0)	3.5 (1.8)	-0.3 (-1.7)
20	10^2	2.3 (2.1)	3.2 (1.8)	-0.2 (-1.4)	2.3 (2.0)	2.9 (2.1)	-0.2 (-0.8)
20	10^3	2.3 (1.8)	3.6 (1.8)	-0.5 (-1.8)	2.3 (1.9)	4.7 (1.8)	-0.4 (-2.9)
20	10^4	2.7 (2.4)	4.4 (2.4)	-0.3 (-2.0)	2.3 (2.0)	3.6 (1.8)	-0.3 (-1.8)
30	10^2	2.4 (2.4)	3.4 (2.0)	0.0 (-1.4)	2.3 (2.4)	3.0 (2.2)	0.1 (-0.8)
30	10^3	2.3 (2.0)	4.0 (1.9)	-0.3 (-2.1)	2.3 (1.9)	1.3 (1.8)	-0.4 (0.5)
30	10^4	2.3 (2.1)	3.5 (1.9)	-0.3 (-1.6)	2.3 (2.0)	3.8 (1.8)	-0.3 (-2.0)

Table B.2: Average Threshold Error (dB) when K data is fed into a two layer neural network

Figures B.2a-B.5c expand the results of Table B.2 to show the estimation accuracy of the deep neural networks as a function of shape parameter. Comparing Figures B.2a-B.5c to Figures 7.11a-7.14c, there is little apparent improvement in using the deep architecture to identify K distributed clutter.

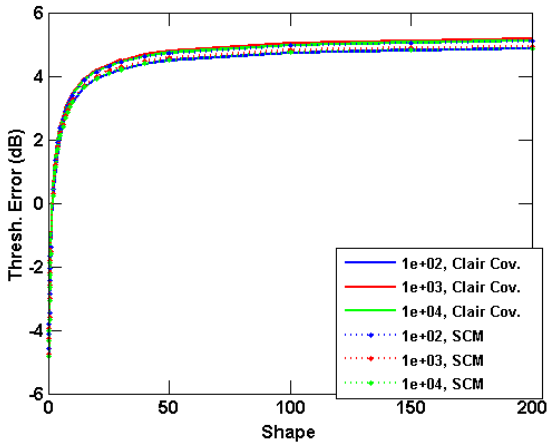

(a) Threshold error (in dB) for varying training sample support w/CCM (solid) and SCM (dotted) with 10 hidden neurons

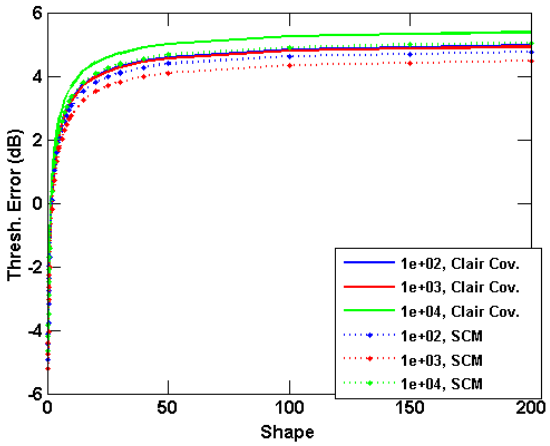

(b) Threshold error (in dB) for varying training sample support w/CCM (solid) and SCM (dotted) with 20 hidden neurons

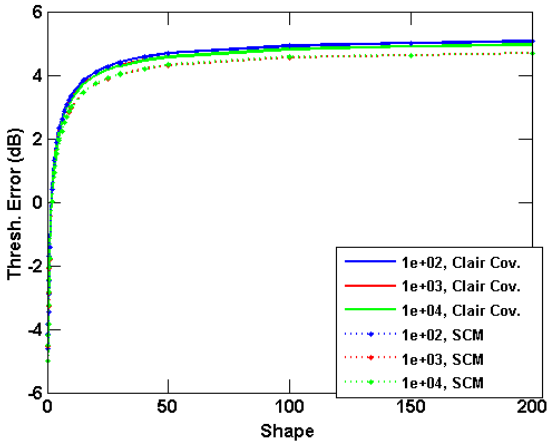

(c) Threshold error (in dB) for varying training sample support w/CCM (solid) and SCM (dotted) with 30 hidden neurons

Figure B.2: Threshold estimation by a deep neural network for unordered K distributed data

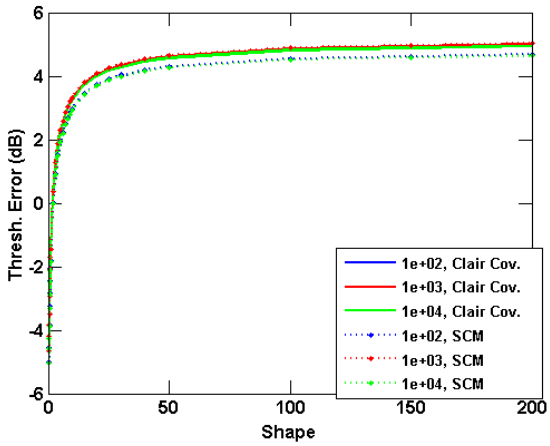

(a) Threshold error (in dB) for varying training sample support w/CCM (solid) and SCM (dotted) with 10 hidden neurons

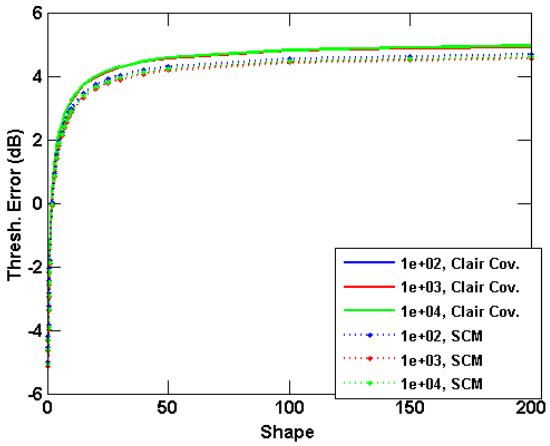

(b) Threshold error (in dB) for varying training sample support w/CCM (solid) and SCM (dotted) with 20 hidden neurons

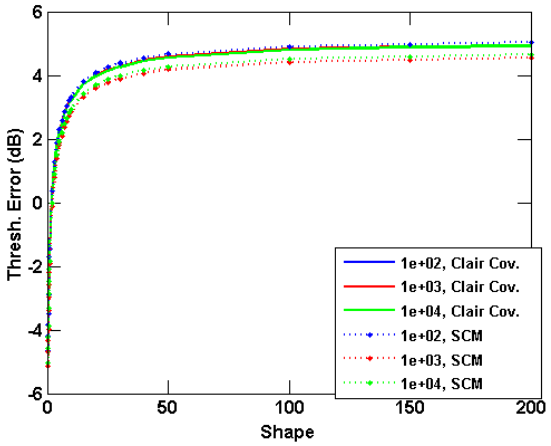

(c) Threshold error (in dB) for varying training sample support w/CCM (solid) and SCM (dotted) with 30 hidden neurons

Figure B.3: Threshold estimation by a deep neural network for ordered K distributed data

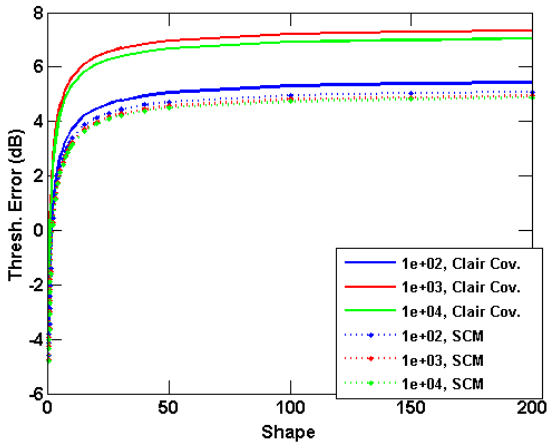

(a) Threshold error (in dB) for varying training sample support w/CCM (solid) and SCM (dotted) with 10 hidden neurons

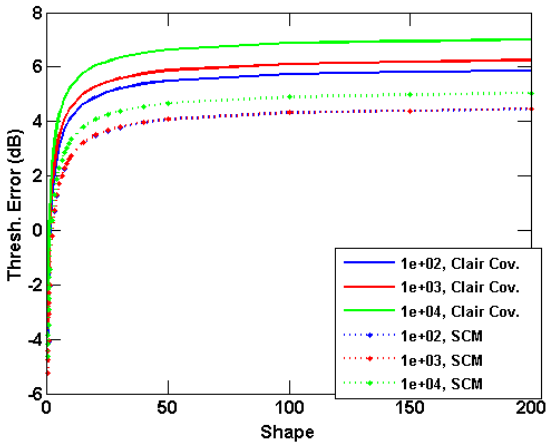

(b) Threshold error (in dB) for varying training sample support w/CCM (solid) and SCM (dotted) with 20 hidden neurons

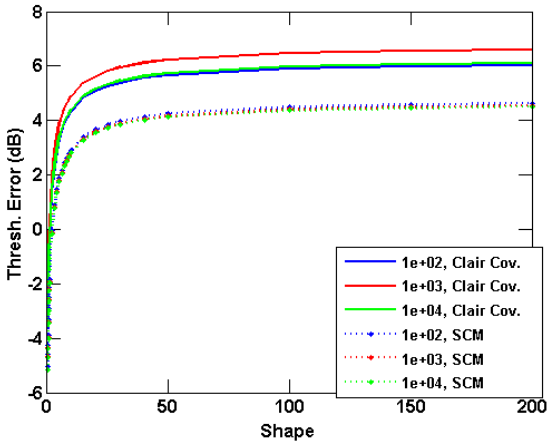

(c) Threshold error (in dB) for varying training sample support w/CCM (solid) and SCM (dotted) with 30 hidden neurons

Figure B.4: Threshold estimation by a deep neural network for unordered K distributed data, K data not included in training data

However, from comparing Figures B.5a-B.5c to 7.14a-7.14c, it appears that when the K distribution is omitted from ordered training data, using a deep neural network allows the individual neural networks to better converge to a top tier solution. However, the convergence properties are not monotonic with respect to training sample support.

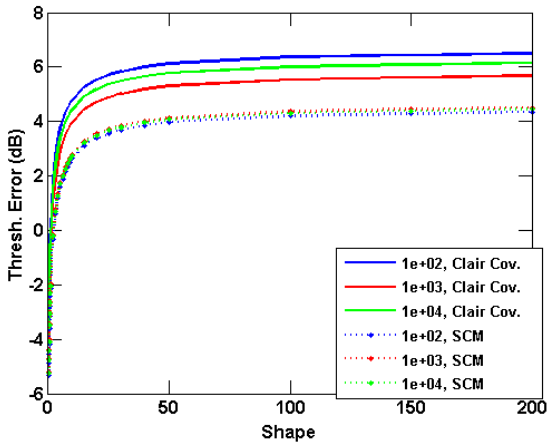

(a) Threshold error (in dB) for varying training sample support w/CCM (solid) and SCM (dotted) with 10 hidden neurons

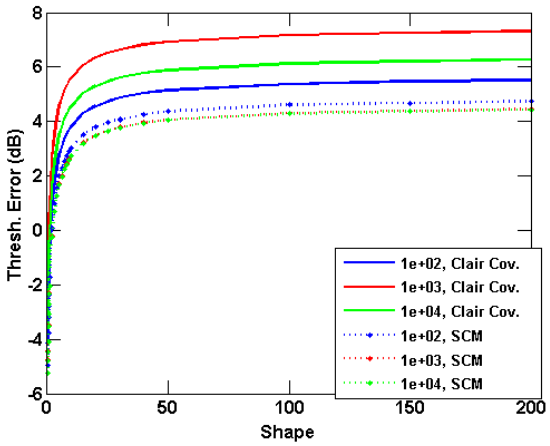

(b) Threshold error (in dB) for varying training sample support w/CCM (solid) and SCM (dotted) with 20 hidden neurons

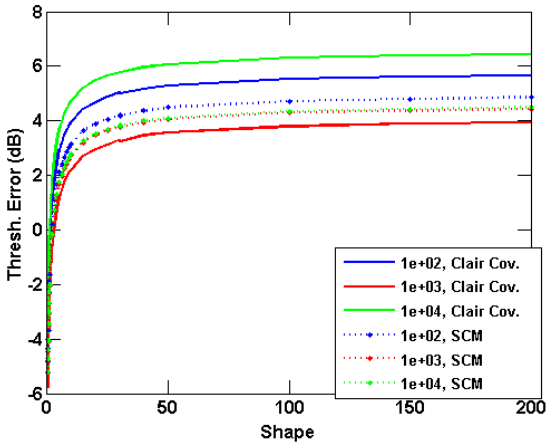

(c) Threshold error (in dB) for varying training sample support w/CCM (solid) and SCM (dotted) with 30 hidden neurons

Figure B.5: Threshold estimation by a deep neural network for ordered K distributed data, K data not included in training data

B.1.3 Threshold Estimation of Weibull Data with a Deep Neural Network

Table B.3 shows the average threshold estimation accuracy when Weibull data is fed into the deep neural networks. Comparing the results of Table B.3 to 7.15, the deep architecture does not offer a discernible improvement.

		Unordered Data			Ordered Data		
HN	Samples	Full	Excised	Δ_{full} (Δ_{excised})	Full	Excised	Δ_{full} (Δ_{excised})
10	10^2	2.3 (2.1)	2.4 (2.1)	-0.2 (-0.2)	3.0 (2.1)	3.3 (2.5)	-1.0 (-0.8)
10	10^3	2.2 (2.0)	2.2 (2.0)	-0.2 (-0.2)	3.2 (2.4)	3.4 (2.8)	-0.8 (-0.6)
10	10^4	2.0 (1.9)	2.0 (1.9)	-0.1 (-0.1)	3.0 (1.7)	3.4 (2.8)	-1.2 (-0.6)
20	10^2	3.0 (2.1)	3.3 (2.7)	-1.0 (-0.7)	3.0 (2.0)	3.3 (2.7)	-1.1 (-0.7)
20	10^3	2.9 (1.8)	3.4 (2.8)	-1.1 (-0.7)	2.9 (1.7)	3.3 (2.7)	-1.2 (-0.7)
20	10^4	2.4 (2.1)	2.4 (2.1)	-0.3 (-0.3)	3.0 (1.7)	3.5 (2.8)	-1.2 (-0.6)
30	10^2	3.2 (2.4)	3.4 (2.7)	-0.8 (-0.7)	3.1 (2.3)	3.4 (2.7)	-0.8 (-0.7)
30	10^3	3.1 (2.0)	3.5 (2.8)	-1.1 (-0.7)	2.9 (1.7)	3.4 (2.7)	-1.2 (-0.7)
30	10^4	3.0 (1.8)	3.4 (2.8)	-1.2 (-0.6)	3.0 (1.8)	3.5 (2.9)	-1.2 (-0.6)

Table B.3: Average Threshold Error (dB) when Weibull data is fed into a two layer neural network

Figures B.6a-B.9c provide the results of Table B.3 broken down as a function of shape parameter. Comparing Figures B.6a-B.9c to Figures 7.15a-7.18c, the behaviour and accuracy of the deep neural networks are similar to the behaviour and accuracy of the neural networks examined in Section 7.2.2.

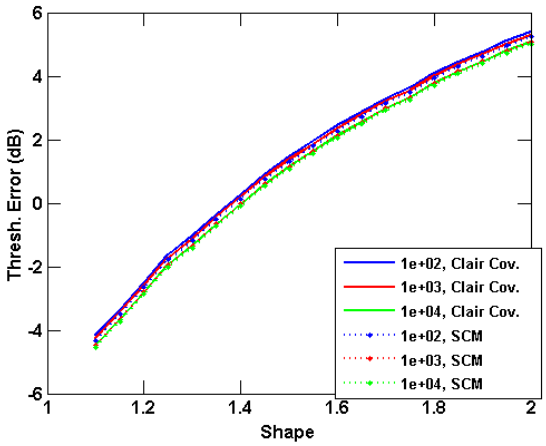

(a) Threshold error (in dB) for varying training sample support w/CCM (solid) and SCM (dotted) with 10 hidden neurons

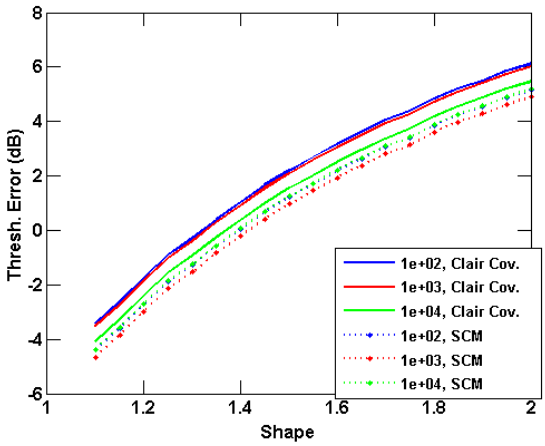

(b) Threshold error (in dB) for varying training sample support w/CCM (solid) and SCM (dotted) with 20 hidden neurons

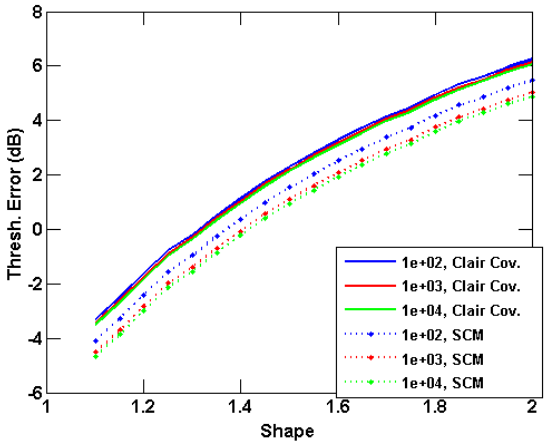

(c) Threshold error (in dB) for varying training sample support w/CCM (solid) and SCM (dotted) with 30 hidden neurons

Figure B.6: Threshold estimation by a deep neural network for unordered Weibull distributed data

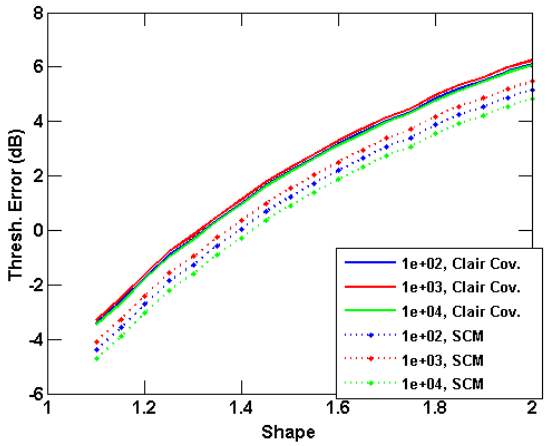

(a) Threshold error (in dB) for varying training sample support w/CCM (solid) and SCM (dotted) with 10 hidden neurons

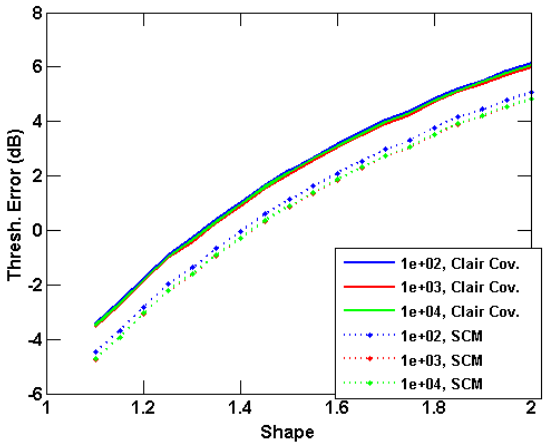

(b) Threshold error (in dB) for varying training sample support w/CCM (solid) and SCM (dotted) with 20 hidden neurons

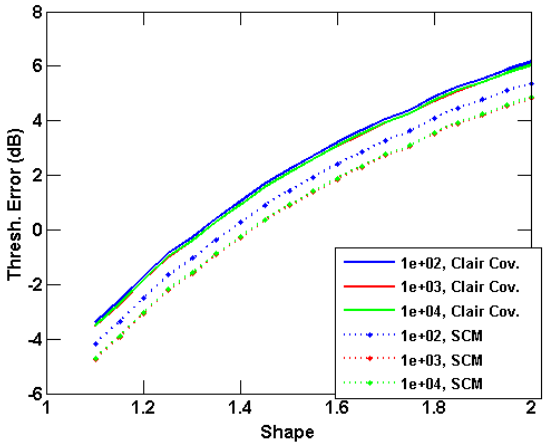

(c) Threshold error (in dB) for varying training sample support w/CCM (solid) and SCM (dotted) with 30 hidden neurons

Figure B.7: Threshold estimation by a deep neural network for ordered Weibull distributed data

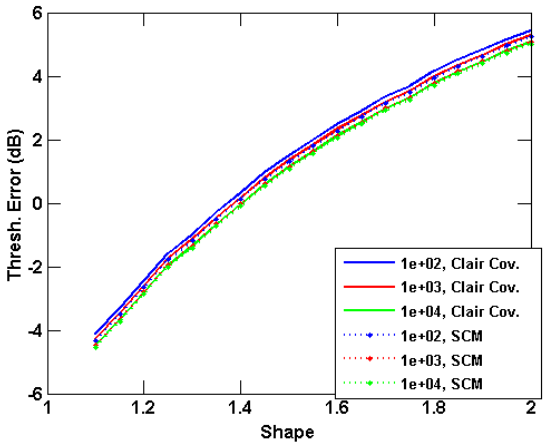

(a) Threshold error (in dB) for varying training sample support w/CCM (solid) and SCM (dotted) with 10 hidden neurons

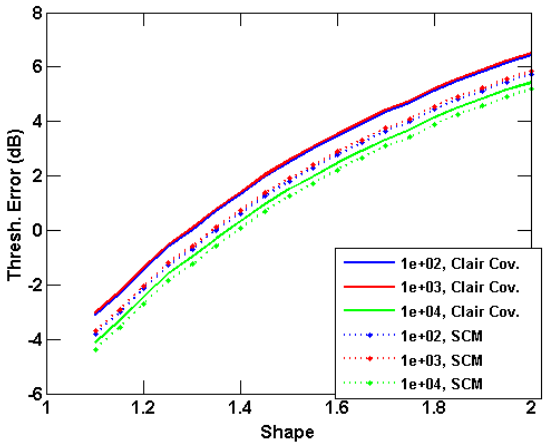

(b) Threshold error (in dB) for varying training sample support w/CCM (solid) and SCM (dotted) with 20 hidden neurons

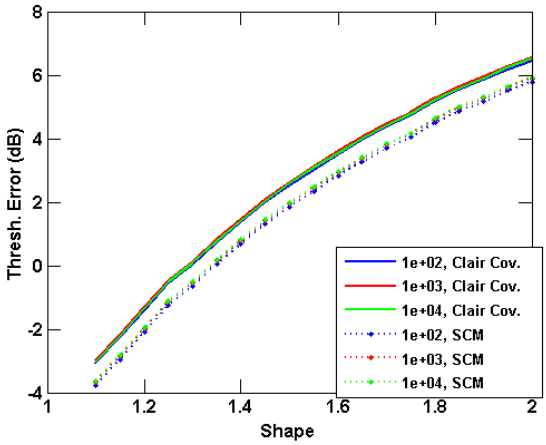

(c) Threshold error (in dB) for varying training sample support w/CCM (solid) and SCM (dotted) with 30 hidden neurons

Figure B.8: Threshold estimation by a deep neural network for unordered Weibull distributed data, Weibull data not included in training data

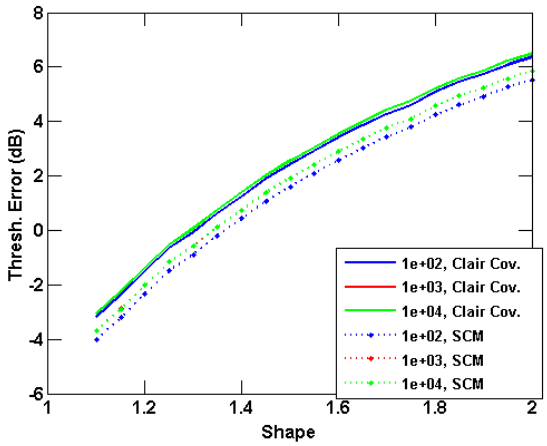

(a) Threshold error (in dB) for varying training sample support w/CCM (solid) and SCM (dotted) with 10 hidden neurons

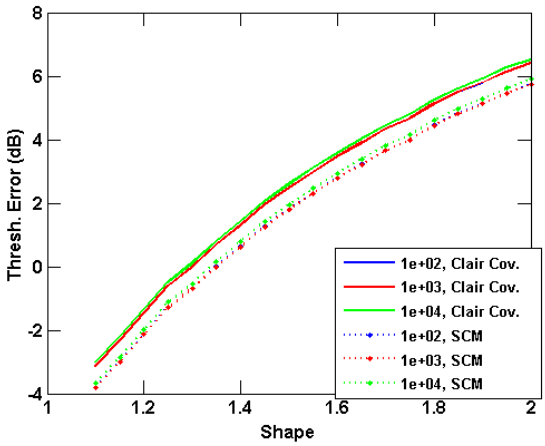

(b) Threshold error (in dB) for varying training sample support w/CCM (solid) and SCM (dotted) with 20 hidden neurons

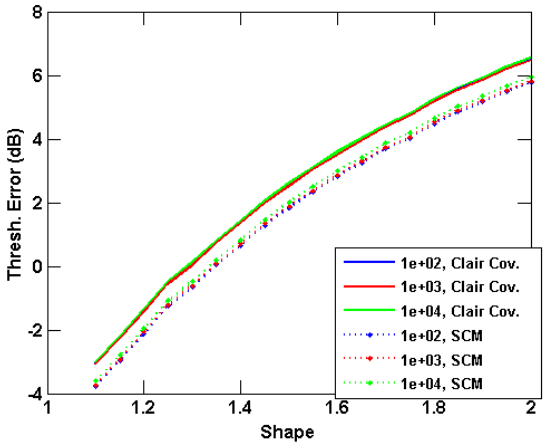

(c) Threshold error (in dB) for varying training sample support w/CCM (solid) and SCM (dotted) with 30 hidden neurons

Figure B.9: Threshold estimation by a deep neural network for ordered Weibull distributed data, Weibull data not included in training data

B.1.4 Threshold Estimation of Pareto Data with a Deep Neural Network

Table B.4 shows the average threshold estimation accuracy of the deep neural networks when Pareto data is tested. Comparing Tables B.4 and 7.16 the deep neural network approach considered here does not offer any consistent benefit when Pareto data is present.

		Unordered Data			Ordered Data		
HN	Samples	Full	Excised	Δ_{full} (Δ_{excised})	Full	Excised	Δ_{full} (Δ_{excised})
10	10^2	2.4 (2.3)	3.3 (3.2)	-0.1 (-0.1)	2.0 (0.1)	0.8 (-0.6)	-1.9 (-1.4)
10	10^3	2.3 (2.3)	3.6 (3.6)	0.0 (0.0)	2.0 (0.3)	1.2 (0.4)	-1.7 (-0.8)
10	10^4	2.2 (2.2)	3.6 (3.6)	0.0 (0.0)	2.0 (0.2)	1.2 (0.4)	-1.8 (-0.8)
20	10^2	2.0 (0.2)	0.9(-0.6)	-1.8 (-1.5)	2.1 (0.3)	0.7 (-0.7)	-1.8 (-1.4)
20	10^3	2.0 (0.2)	0.9(-0.6)	-1.8 (-1.5)	2.0 (0.4)	1.0 (-0.3)	-1.6 (-1.3)
20	10^4	2.3 (2.3)	1.6 (1.3)	0.0 (-0.3)	2.0 (0.3)	1.0 (0.3)	-1.7 (-1.3)
30	10^2	2.0 (0.4)	1.1 (0.3)	-1.6 (-0.9)	2.0 (0.3)	1.0 (-0.1)	-1.6 (-1.1)
30	10^3	2.0 (0.2)	1.0 (-0.3)	-1.8 (-1.3)	2.0 (0.2)	0.9 (-0.5)	-1.8 (-1.5)
30	10^4	2.0 (0.4)	1.0 (-0.2)	-1.6 (-1.2)	2.0 (0.4)	1.0 (-0.3)	-1.6 (-1.3)

Table B.4: Average Threshold Error (dB) when Pareto data is fed into a two layer neural network

Figures B.10a-B.13c explore the results shown in Table B.4. Comparing Figures B.10a-B.13c to Figures 7.19a-7.22c, the deep neural network approach does not offer any consistent improvement.

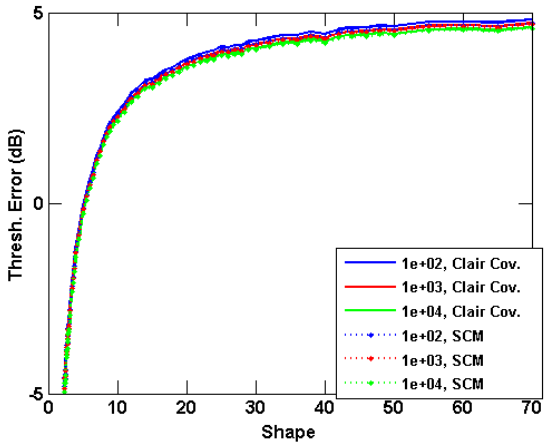

(a) Threshold error (in dB) for varying training sample support w/CCM (solid) and SCM (dotted) with 10 hidden neurons

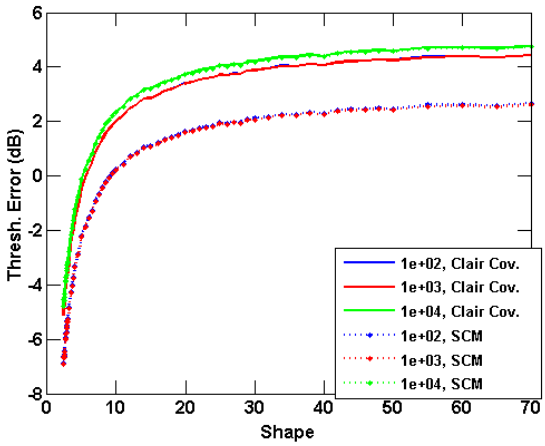

(b) Threshold error (in dB) for varying training sample support w/CCM (solid) and SCM (dotted) with 20 hidden neurons

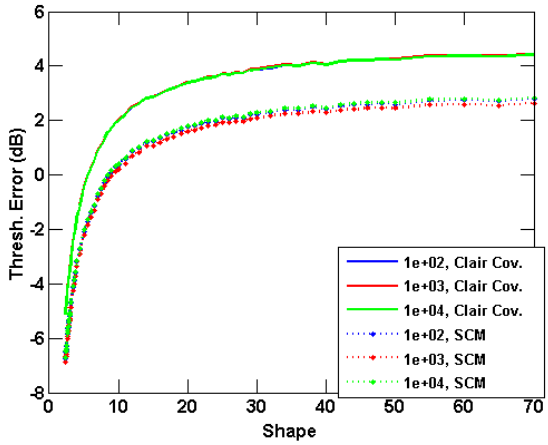

(c) Threshold error (in dB) for varying training sample support w/CCM (solid) and SCM (dotted) with 30 hidden neurons

Figure B.10: Threshold estimation by a deep neural network for unordered Pareto distributed data

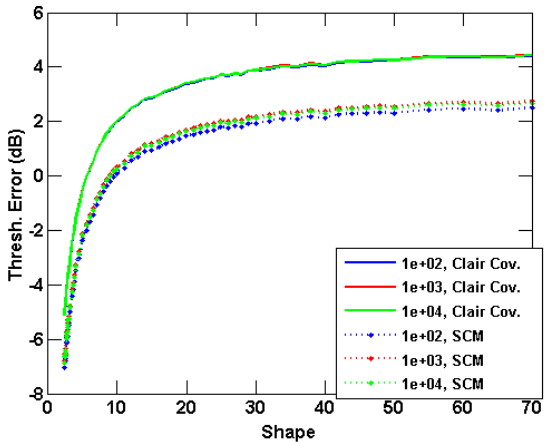

(a) Threshold error (in dB) for varying training sample support w/CCM (solid) and SCM (dotted) with 10 hidden neurons

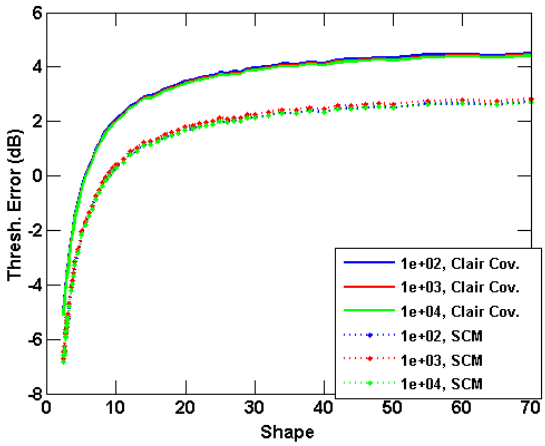

(b) Threshold error (in dB) for varying training sample support w/CCM (solid) and SCM (dotted) with 20 hidden neurons

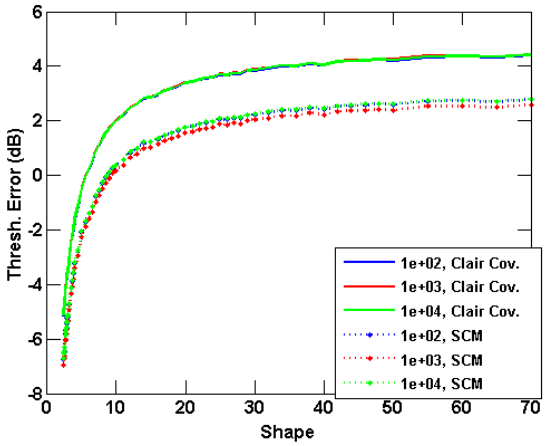

(c) Threshold error (in dB) for varying training sample support w/CCM (solid) and SCM (dotted) with 30 hidden neurons

Figure B.11: Threshold estimation by a deep neural network for ordered Pareto distributed data

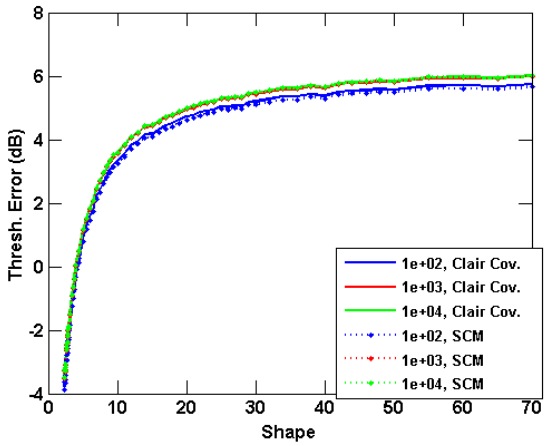

(a) Threshold error (in dB) for varying training sample support w/CCM (solid) and SCM (dotted) with 10 hidden neurons

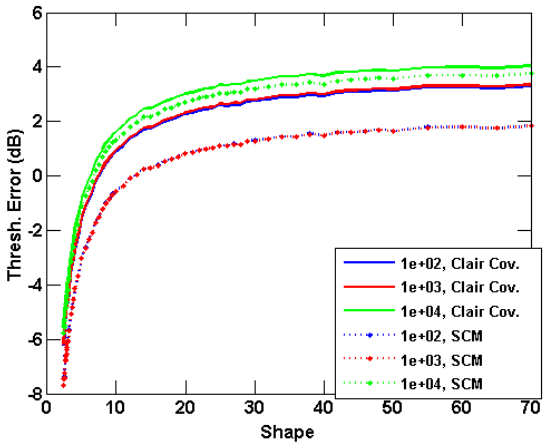

(b) Threshold error (in dB) for varying training sample support w/CCM (solid) and SCM (dotted) with 20 hidden neurons

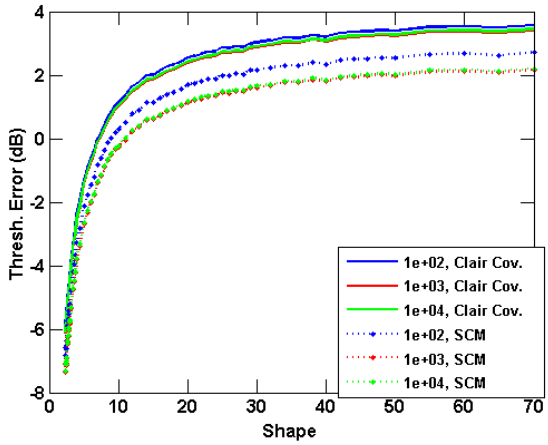

(c) Threshold error (in dB) for varying training sample support w/CCM (solid) and SCM (dotted) with 30 hidden neurons

Figure B.12: Threshold estimation by a deep neural network for unordered Pareto distributed data, Pareto data not included in training data

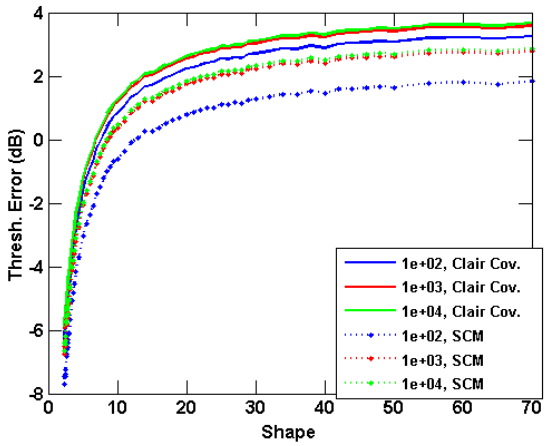

(a) Threshold error (in dB) for varying training sample support w/CCM (solid) and SCM (dotted) with 10 hidden neurons

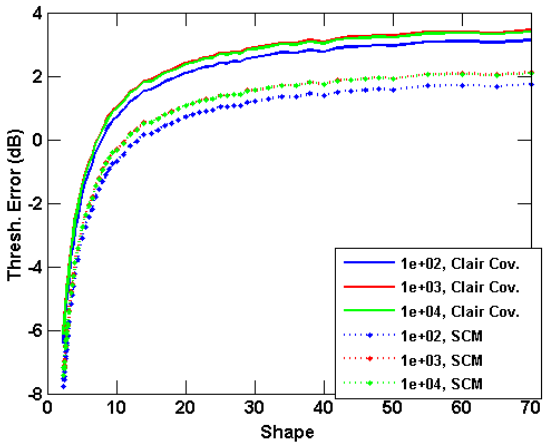

(b) Threshold error (in dB) for varying training sample support w/CCM (solid) and SCM (dotted) with 20 hidden neurons

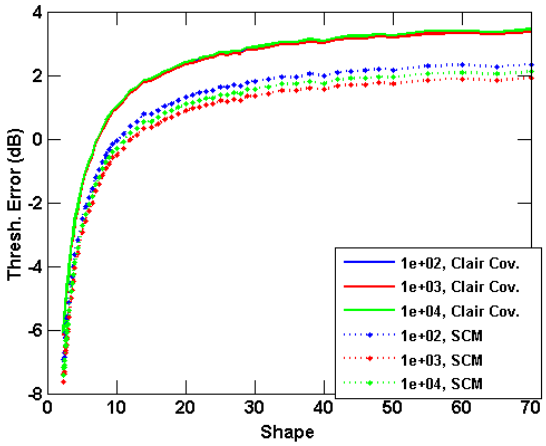

(c) Threshold error (in dB) for varying training sample support w/CCM (solid) and SCM (dotted) with 30 hidden neurons

Figure B.13: Threshold estimation by a deep neural network for ordered Pareto distributed data, Pareto data not included in training data

B.1.5 Threshold Estimation of Lognormal Data with a Deep Neural Network

Table B.5 shows the average threshold estimation error when Lognormal data is tested with the deep neural network approach shown in Figure B.1. Comparing Table B.5 to Table 7.17, the deep approach resulted in certain networks yielding minor improvements in

accuracy ($\approx 0.1 - 0.3$ dB). However, given the results explored in the rest of this section, this minor improvement cannot be considered statistically significant. More likely, the noted improvement may be a function of the convergence properties of neural networks, rather than a benefit of the deep approach considered here.

		Unordered Data			Ordered Data		
HN	Samples	Full	Excised	Δ_{full} (Δ_{excised})	Full	Excised	Δ_{full} (Δ_{excised})
10	10^2	-4.7 (-5.0)	-4.7 (-5.0)	-0.3 (-0.3)	-3.2 (-5.4)	-3.3 (-5.4)	-2.2 (-2.2)
10	10^3	-4.9 (-5.1)	-5.0 (-5.1)	-0.2 (-0.2)	-3.4 (-5.3)	-3.4 (-5.3)	-1.9 (-1.9)
10	10^4	-5.1 (-5.2)	-5.1 (-5.2)	-0.1 (-0.1)	-3.2 (-5.3)	-3.2 (-5.3)	-2.1 (-2.1)
20	10^2	-3.3 (-5.3)	-3.4 (-5.3)	-2.0 (-1.9)	-3.2 (-5.3)	-3.3 (-5.3)	-2.1 (-2.0)
20	10^3	-3.3 (-5.3)	-3.4 (-5.4)	-2.0 (-2.0)	-3.3 (-5.1)	-3.3 (-5.2)	-1.8 (-1.9)
20	10^4	-4.9 (-5.0)	-4.9 (-5.0)	-0.2 (-0.2)	-3.3 (-5.3)	-3.3 (-5.3)	-2.0 (-2.0)
30	10^2	-3.6 (-5.3)	-3.7 (-5.3)	-1.7 (-1.6)	-3.5 (-5.3)	-3.5 (-5.3)	-1.8 (-1.8)
30	10^3	-3.3 (-5.3)	-3.4 (-5.4)	-2.0 (-2.0)	-3.3 (-5.3)	-3.3 (-5.3)	-2.0 (-2.1)
30	10^4	-3.4 (-5.2)	-3.4 (-5.2)	-1.8 (-1.7)	-3.4 (-5.3)	-3.4 (-5.2)	-1.9 (-1.9)

Table B.5: Average Threshold Error (dB) when lognormal data is fed into a two layer neural network

B.2 Three Stage Threshold Estimating Deep Network

The second deep neural network under consideration is a modification of the neural network considered in Section B.1. In particular, a set of shape parameter estimating neural networks is trained and inserted as a preceding layer to the threshold estimation neural networks corresponding to distributions with shape parameters (*i.e.* K, Weibull, Pareto, and Gamma Modulated (GM)). The shape parameter estimate is then added to the vector of input data for the threshold estimating neural networks. The deep neural network architecture under consideration is illustrated in Figures B.14-B.16.

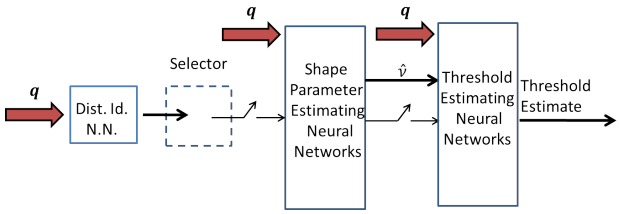

Figure B.14: Deep neural network for threshold estimation

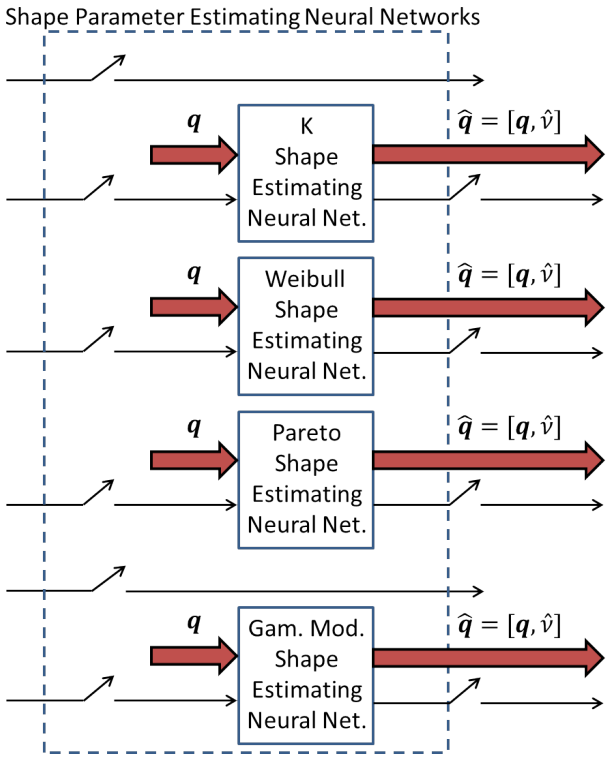

Figure B.15: Deep neural network - shape parameter estimating neural networks

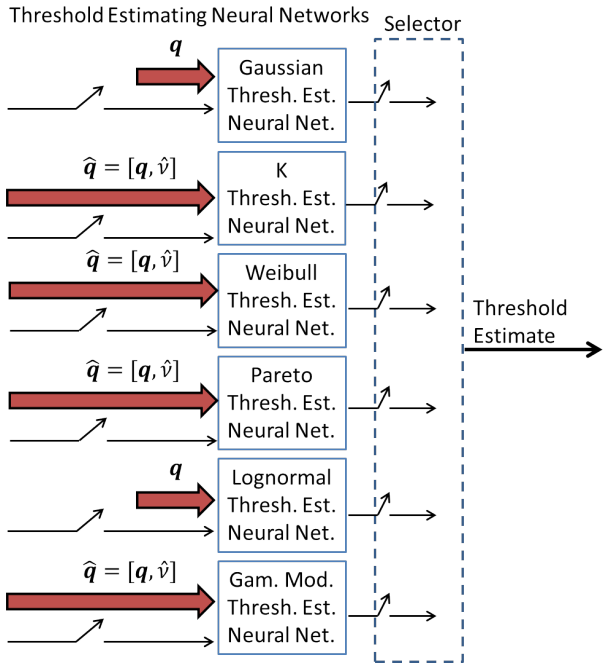

Figure B.16: Deep neural network for threshold estimation - threshold estimating neural networks with augmented input

The performance of the collection of deep neural networks with the architecture shown in Figures B.14-B.16 is examined on a distribution by distribution basis in Sections B.2.1-B.2.5. The parameters of the neural network itself (*i.e.* number of hidden neurons, number of training samples used, ordering of data) is the same as was described in Section 7.1.

B.2.1 Threshold Estimation of Gaussian Data with a Deep Neural Network

Table B.6 summarizes the performance of the deeep neural networks under consideration when Gaussian data is tested. Comparing Table B.6 to 7.13, the deep approach offers significant reduction (1.5-4 dB) in detection loss compared to the single layer threshold estimating neural networks. The resultant detection loss is robust to use of the SCM, with less than half a dB in difference between average estimates given by the data sets using CCM and the data sets using the SCM.

		Unordered Data			Ordered Data		
HN	Samples	Full	Excised	Δ_{full} (Δ_{excised})	Full	Excised	Δ_{full} (Δ_{excised})
10	10^2	1.2 (1.2)	1.2 (1.2)	0.0 (0.0)	1.2 (1.3)	1.2 (1.3)	0.1 (0.1)
10	10^3	0.7 (0.8)	0.7 (0.8)	0.1 (0.1)	1.4 (1.2)	1.4 (1.2)	-0.2 (-0.2)
10	10^4	1.9 (1.9)	1.9 (1.9)	0.0 (0.0)	1.2 (0.9)	1.2 (0.9)	-0.3 (-0.3)
20	10^2	1.1 (1.1)	1.1 (1.1)	0.0 (0.0)	1.3 (1.1)	1.3 (1.1)	-0.3 (-0.3)
20	10^3	1.4 (1.5)	1.4 (1.5)	0.0 (0.0)	1.3 (0.9)	1.3 (0.9)	-0.4 (-0.4)
20	10^4	1.5 (1.5)	1.5 (1.5)	0.0 (0.0)	1.2 (1.0)	1.2 (1.0)	-0.2 (-0.2)
30	10^2	1.4 (1.4)	1.4 (1.4)	0.0 (0.0)	1.2 (1.0)	1.2 (1.0)	-0.2 (-0.2)
30	10^3	1.3 (1.1)	1.3 (1.1)	-0.2 (-0.2)	1.4 (1.1)	1.4 (1.1)	-0.3 (-0.3)
30	10^4	1.2 (1.0)	1.2 (1.0)	-0.2 (-0.2)	1.3 (1.2)	1.3 (1.2)	-0.2 (-0.2)

Table B.6: Average Threshold Error (dB) when Gaussian data is fed into a multiple layer neural network

B.2.2 Threshold Estimation of K Data with a Deep Neural Network

The performance of the deep neural network architecture shown in Figures B.14-B.16 for K distributed data is summarized in Table B.7. Comparing Table B.7 to Table 7.14, a wide variety of average estimate errors are given. Some of the averages (*e.g.* the neural networks with 10 hidden neurons trained with 10^3 training samples per shape parameter value) were biased towards an increase in false alarm. Overall, in this case the solution the neural networks converged to was highly variable. This is in contrast to the previous neural networking results, where the networks converged to solutions that were very similar to each other (*i.e.* generating threshold averages within 1-2 dB of each other).

		Unordered Data			Ordered Data		
HN	Samples	Full	Excised	Δ_{full} (Δ_{excised})	Full	Excised	Δ_{full} (Δ_{excised})
10	10^2	-3.1 (-1.7)	-8.9 (-1.7)	1.4 (7.3)	2.3 (1.5)	2.5 (1.0)	-0.8 (-1.5)
10	10^3	-9.9 (-2.2)	4.5 (-2.2)	7.7 (-6.7)	2.1 (1.4)	8.3 (0.9)	-0.6 (-7.5)
10	10^4	-3.0 (-0.9)	4.0 (-0.9)	2.1 (-4.9)	2.0 (1.1)	3.4 (0.8)	-0.9 (-2.5)
20	10^2	2.1 (1.4)	4.0 (1.0)	-0.7 (-3.0)	2.3 (1.3)	8.8 (1.7)	-0.9 (-7.0)
20	10^3	2.1 (1.0)	2.7 (1.0)	-1.1 (-1.6)	2.0 (1.0)	3.2 (-0.8)	-1.1 (-2.4)
20	10^4	-0.9 (-1.3)	4.5 (-1.3)	-0.4 (-5.8)	2.1 (1.0)	3.7 (0.8)	-1.1 (-3.0)
30	10^2	2.5 (1.8)	4.1 (1.2)	-0.7 (-2.9)	2.3 (1.4)	4.0 (1.1)	-0.9 (-2.9)
30	10^3	2.1 (1.2)	3.7 (1.1)	-0.9 (-2.6)	2.2 (1.1)	4.7 (0.9)	-1.1 (-3.8)
30	10^4	2.0 (1.0)	3.4 (0.8)	-1.0 (-2.6)	1.9 (1.1)	3.0 (0.8)	-0.9 (-2.2)

Table B.7: Average Threshold Error (dB) when K data is fed into a multiple layer neural network

Figures B.17a-B.20c illustrate the average results of Table B.7 as a function of shape parameter. Comparing Figures B.17a-B.20c to Figures 7.11a-7.14c, the deep network architecture under consideration is more sensitive to the use of the CCM. In addition, the results are less consistent as a function of network construction parameters (*i.e.* number of hidden neurons, number of training samples used). However, most of the average estimates are similar to those shown in Section 7.2.2 for the threshold estimation neural networks.

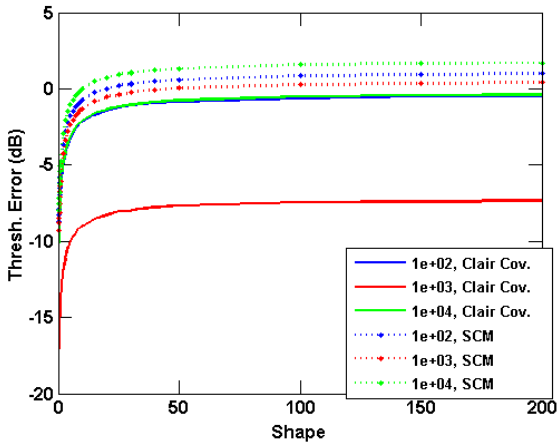

(a) Threshold error (in dB) for varying training sample support w/CCM (solid) and SCM (dotted) with 10 hidden neurons

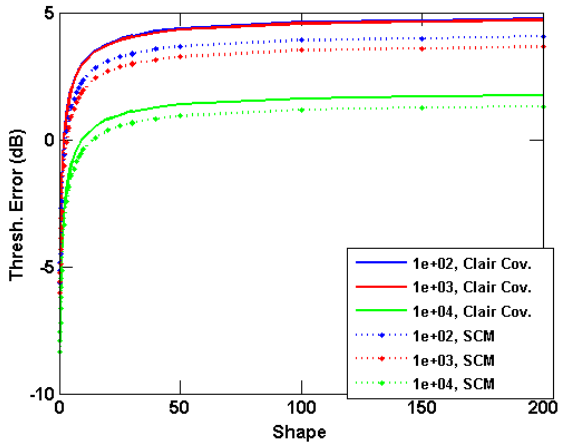

(b) Threshold error (in dB) for varying training sample support w/CCM (solid) and SCM (dotted) with 20 hidden neurons

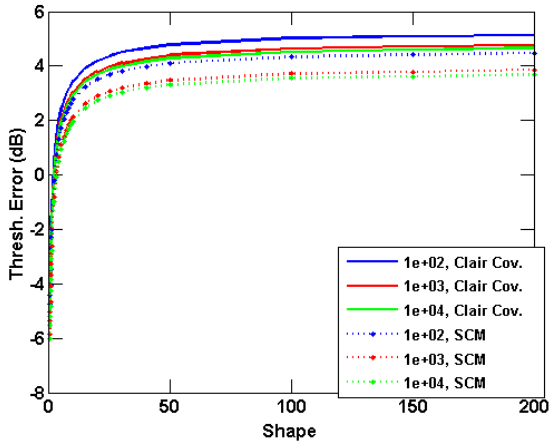

(c) Threshold error (in dB) for varying training sample support w/CCM (solid) and SCM (dotted) with 30 hidden neurons

Figure B.17: Threshold estimation by a three stage deep neural network for unordered K distributed data

It is interesting to note that the neural networks constructed with 20 hidden neurons and trained with 10^4 unordered sets of data per shape parameter give the best average results for the K distribution of all neural networks considered in this work. When examined as a function of shape parameter, this network gives the best average threshold estimate accuracy at medium to high shape parameter K distributed data. However, it yields the least accurate results noted for low shape parameter data, resulting in a threshold 8 dB too low for the

shape parameter value $\nu = 0.3$.

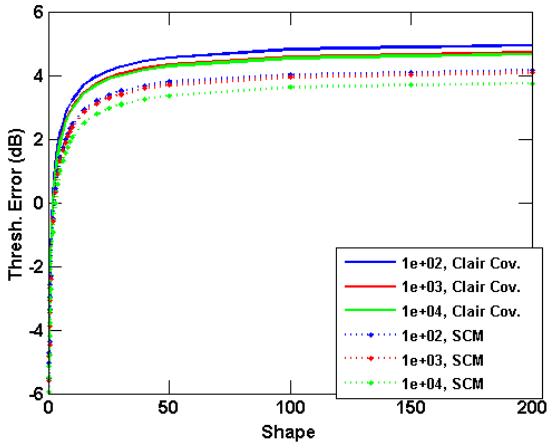

(a) Threshold error (in dB) for varying training sample support w/CCM (solid) and SCM (dotted) with 10 hidden neurons

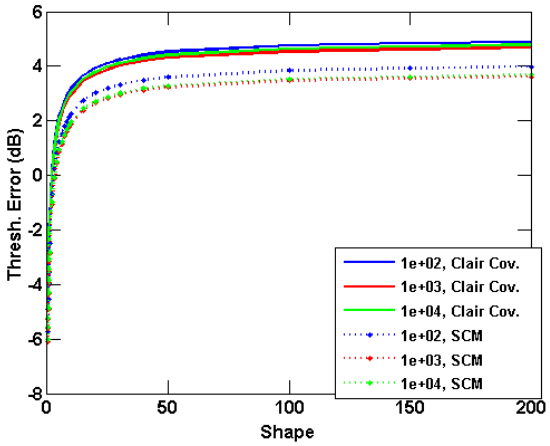

(b) Threshold error (in dB) for varying training sample support w/CCM (solid) and SCM (dotted) with 20 hidden neurons

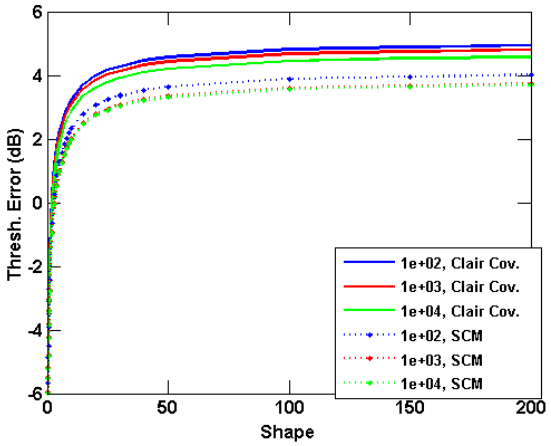

(c) Threshold error (in dB) for varying training sample support w/CCM (solid) and SCM (dotted) with 30 hidden neurons

Figure B.18: Threshold estimation by a three stage deep neural network for ordered K distributed data

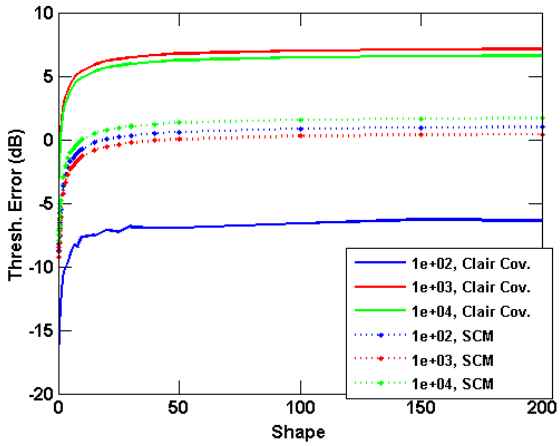

(a) Threshold error (in dB) for varying training sample support w/CCM (solid) and SCM (dotted) with 10 hidden neurons

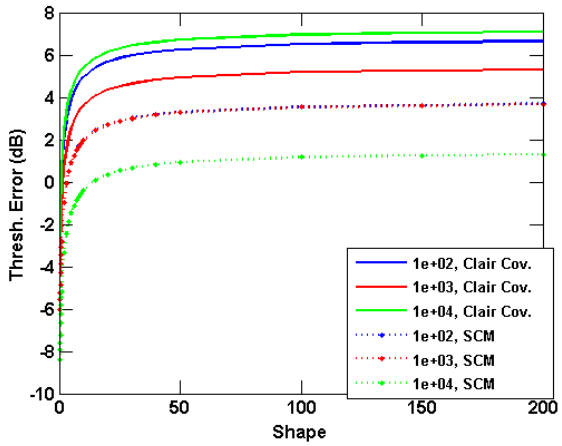

(b) Threshold error (in dB) for varying training sample support w/CCM (solid) and SCM (dotted) with 20 hidden neurons

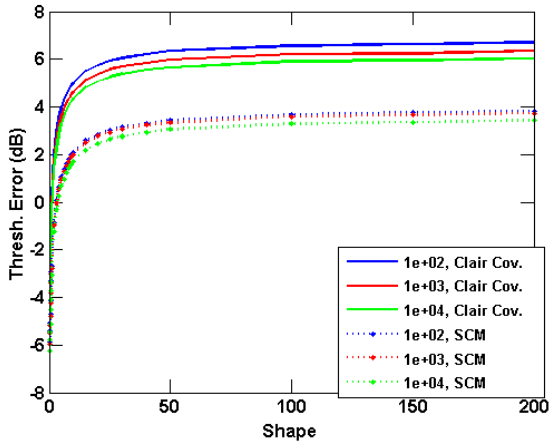

(c) Threshold error (in dB) for varying training sample support w/CCM (solid) and SCM (dotted) with 30 hidden neurons

Figure B.19: Threshold estimation by a three stage deep neural network for unordered K distributed data, K data not included in training data

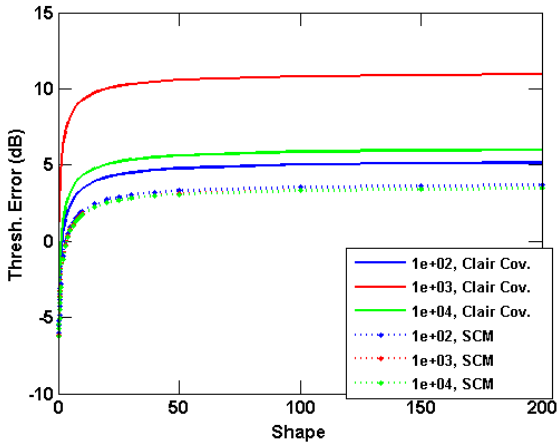

(a) Threshold error (in dB) for varying training sample support w/CCM (solid) and SCM (dotted) with 10 hidden neurons

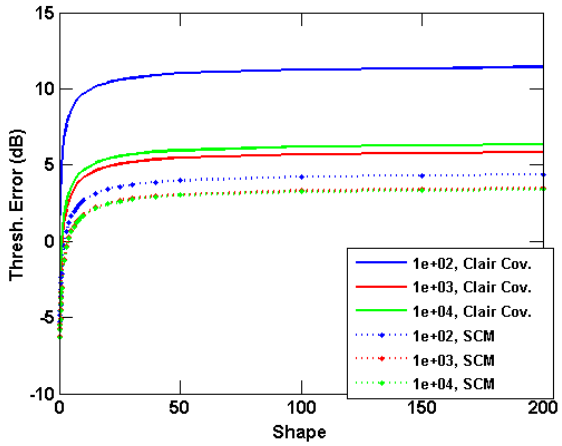

(b) Threshold error (in dB) for varying training sample support w/CCM (solid) and SCM (dotted) with 20 hidden neurons

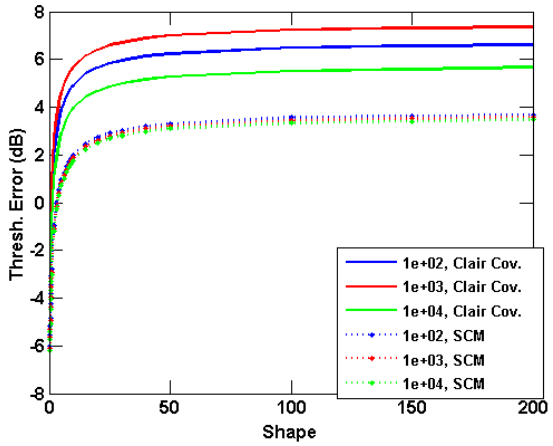

(c) Threshold error (in dB) for varying training sample support w/CCM (solid) and SCM (dotted) with 30 hidden neurons

Figure B.20: Threshold estimation by a three stage deep neural network for ordered K distributed data, K data not included in training data

B.2.3 Threshold Estimation of Weibull Data with a Deep Neural Network

Table B.8 examines the average threshold error when Weibull distributed data is tested by the deep neural networks under consideration. Unlike the results shown in Table 7.15, the here results vary greatly from neural network to neural network.

		Unordered Data			Ordered Data		
HN	Samples	Full	Excised	Δ_{full} (Δ_{excised})	Full	Excised	Δ_{full} (Δ_{excised})
10	10^2	-2.6 (-2.0)	-2.3 (-2.0)	0.6 (0.3)	2.3 (1.3)	2.6 (1.9)	-1.0 (-0.7)
10	10^3	-3.3 (-2.5)	-3.4 (-2.5)	0.8 (0.8)	2.3 (1.3)	2.6 (1.7)	-1.0 (-1.0)
10	10^4	-1.7 (-1.2)	-1.7 (-1.2)	0.4 (0.4)	2.2 (0.8)	2.7 (2.0)	-1.4 (-0.7)
20	10^2	2.2 (1.1)	2.6 (1.8)	-1.2 (-0.8)	2.3 (1.0)	2.6 (1.7)	-1.3 (-0.9)
20	10^3	2.1 (0.7)	2.5 (1.7)	-1.4 (-0.8)	2.1 (0.7)	2.7 (1.8)	-1.5 (-0.9)
20	10^4	-1.3 (-1.6)	-1.4 (-1.6)	-0.3 (-0.3)	2.2 (0.7)	2.7 (1.9)	-1.5 (-0.8)
30	10^2	2.5 (1.6)	2.8 (2.1)	-0.9 (-0.7)	2.6 (1.3)	3.0 (1.8)	-1.2 (-1.1)
30	10^3	2.3 (0.9)	2.8 (1.7)	-1.4 (-1.0)	2.2 (0.7)	2.6 (1.7)	-1.5 (-0.9)
30	10^4	2.1 (0.7)	2.6 (1.6)	-1.5 (-1.0)	2.1 (0.7)	2.7 (1.9)	-1.4 (-0.8)

Table B.8: Average Threshold Error (dB) when Weibull data is fed into a multiple layer neural network

Figures B.21a-B.24c show the results of Table B.8 as a function of shape parameter. Note that the nature of the threshold estimate error to shape parameter curves associated with each neural network do not vary greatly, only the bias. As was initially shown in Table B.8, the neural networks converged to a variety of solutions when compared to the networks examined in Section 7.2.2.3. In addition, the SCM makes a greater impact here than when the networks of Section 7.2.2.3 are employed.

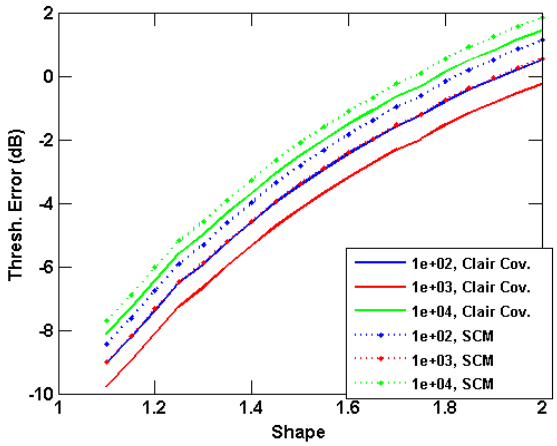

(a) Threshold error (in dB) for varying training sample support w/CCM (solid) and SCM (dotted) with 10 hidden neurons

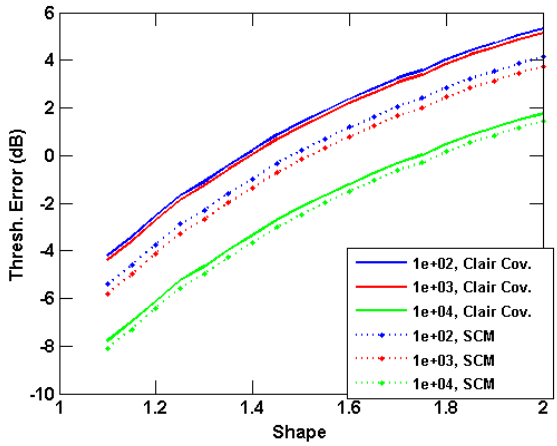

(b) Threshold error (in dB) for varying training sample support w/CCM (solid) and SCM (dotted) with 20 hidden neurons

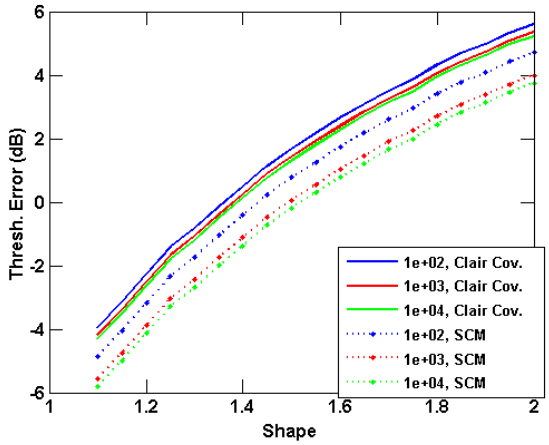

(c) Threshold error (in dB) for varying training sample support w/CCM (solid) and SCM (dotted) with 30 hidden neurons

Figure B.21: Threshold estimation by a three stage deep neural network for unordered Weibull distributed data

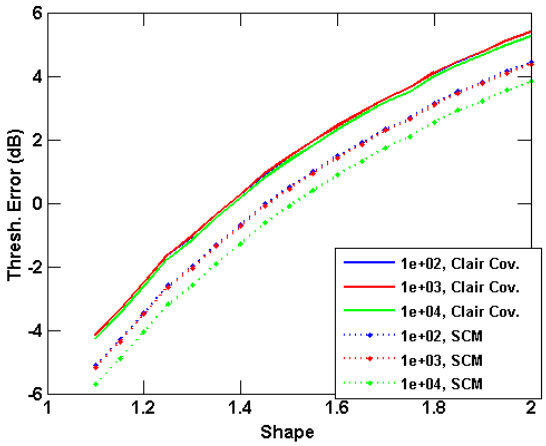

(a) Threshold error (in dB) for varying training sample support w/CCM (solid) and SCM (dotted) with 10 hidden neurons

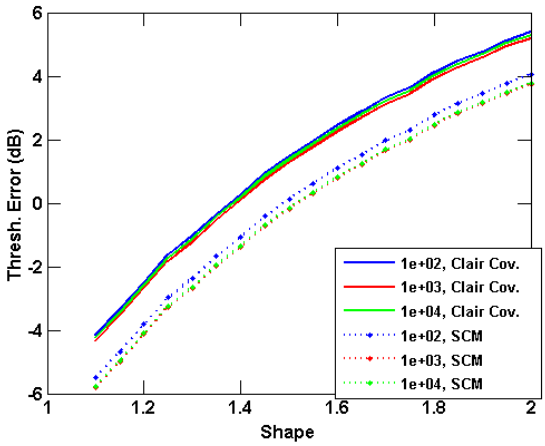

(b) Threshold error (in dB) for varying training sample support w/CCM (solid) and SCM (dotted) with 20 hidden neurons

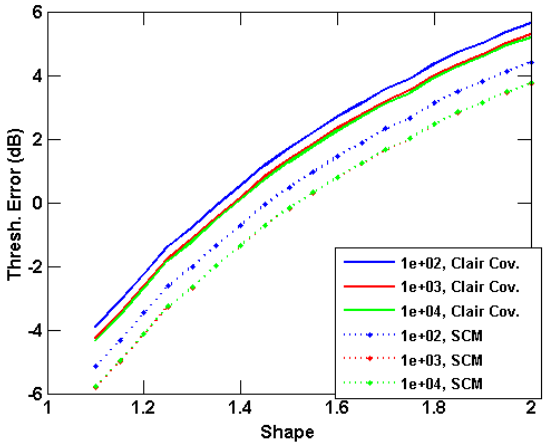

(c) Threshold error (in dB) for varying training sample support w/CCM (solid) and SCM (dotted) with 30 hidden neurons

Figure B.22: Threshold estimation by a three stage deep neural network for ordered Weibull distributed data

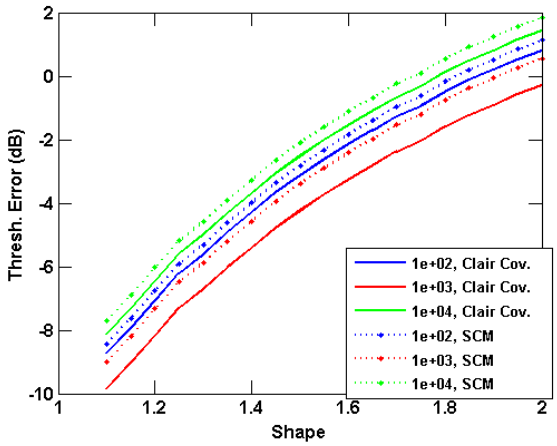

(a) Threshold error (in dB) for varying training sample support w/CCM (solid) and SCM (dotted) with 10 hidden neurons

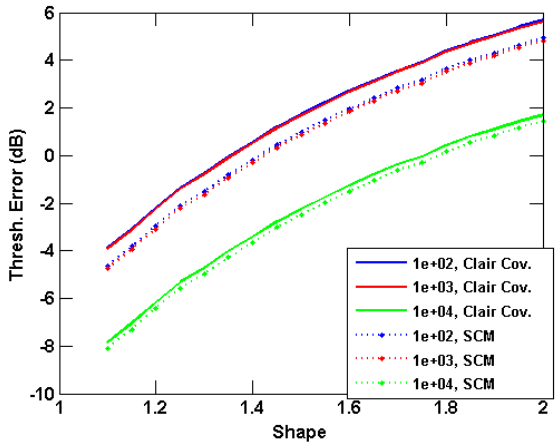

(b) Threshold error (in dB) for varying training sample support w/CCM (solid) and SCM (dotted) with 20 hidden neurons

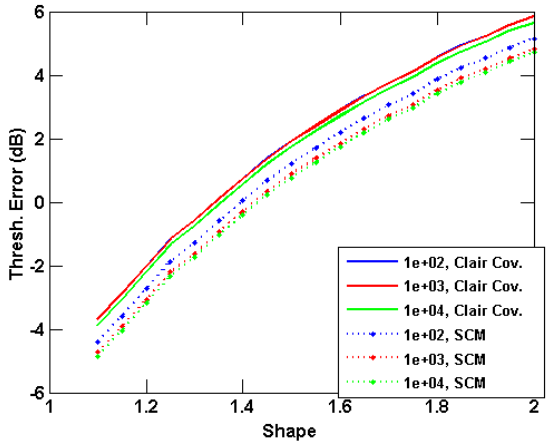

(c) Threshold error (in dB) for varying training sample support w/CCM (solid) and SCM (dotted) with 30 hidden neurons

Figure B.23: Threshold estimation by a three stage deep neural network for unordered Weibull distributed data, Weibull data not included in training data

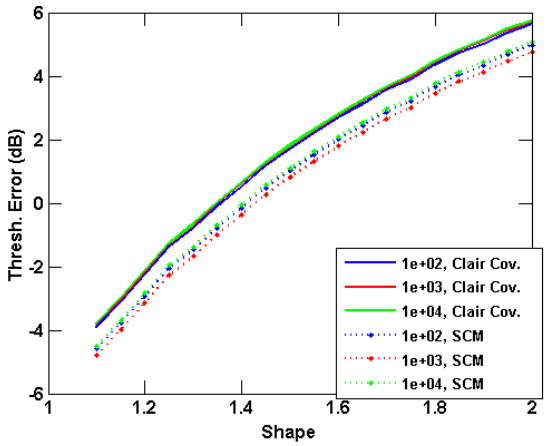

(a) Threshold error (in dB) for varying training sample support w/CCM (solid) and SCM (dotted) with 10 hidden neurons

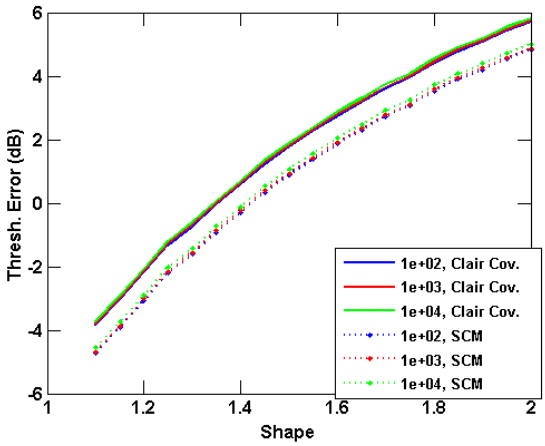

(b) Threshold error (in dB) for varying training sample support w/CCM (solid) and SCM (dotted) with 20 hidden neurons

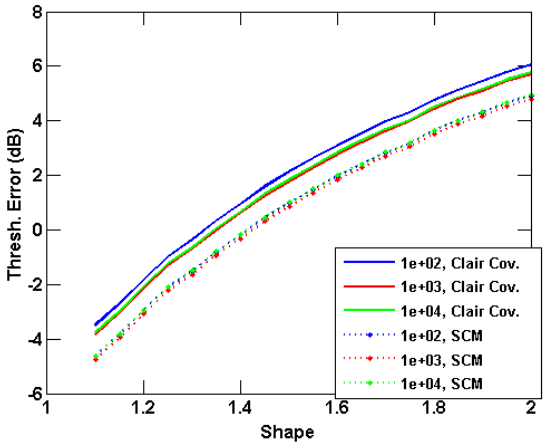

(c) Threshold error (in dB) for varying training sample support w/CCM (solid) and SCM (dotted) with 30 hidden neurons

Figure B.24: Threshold estimation by a three stage deep neural network for ordered Weibull distributed data, Weibull data not included in training data

B.2.4 Threshold Estimation of Pareto Data with a Deep Neural Network

Table B.9 shows the average threshold estimation error when Pareto distributed training data is used with the deep neural networks shown in Figures B.14-B.16. Comparing to the results shown in Table 7.16, the neural networks trained here largely produce average

thresholds that are below the desired threshold.

		Unordered Data			Ordered Data		
HN	Samples	Full	Excised	Δ_{full} (Δ_{excised})	Full	Excised	Δ_{full} (Δ_{excised})
10	10^2	-1.7 (-1.7)	2.4 (2.4)	0.1 (0.0)	-0.4 (-1.5)	0.7 (-0.3)	-1.1 (-1.0)
10	10^3	-2.2 (-2.1)	2.3 (2.2)	0.1 (-0.1)	-0.2 (-1.3)	0.9 (0.1)	-1.1 (-0.7)
10	10^4	-1.0 (-1.0)	2.3 (2.4)	0.0 (0.1)	-0.3 (-1.5)	0.9 (0.2)	-1.2 (-0.7)
20	10^2	-0.6 (-1.7)	0.8 (-0.2)	-1.1 (-1.0)	0.0 (-1.4)	0.9 (0.1)	-1.4 (-0.8)
20	10^3	-0.6 (-1.4)	0.7 (-0.4)	-0.8 (-1.1)	-0.1 (-1.5)	0.8 (-0.3)	-1.3 (-1.0)
20	10^4	-1.4 (-1.3)	2.4 (2.4)	0.0 (0.0)	0.1 (-1.5)	0.7 (-0.4)	-1.5 (-1.1)
30	10^2	0.1 (-1.3)	0.7 (0.1)	-1.4 (-0.6)	0.5 (-2.1)	0.8 (-0.1)	-2.6 (-0.8)
30	10^3	0.1 (-1.4)	0.8 (-0.3)	-1.5 (-1.0)	-0.3 (-1.4)	0.7 (-0.4)	-1.1 (-1.1)
30	10^4	-0.4 (-1.5)	0.8 (-0.3)	-1.1 (-1.0)	-0.5 (-1.4)	0.7 (-0.3)	-0.9 (-1.0)

Table B.9: Average Threshold Error (dB) when Pareto data is fed into a multiple layer neural network

Figures B.25a-B.28c show the results of Table B.9 as a function of shape parameter. It is clear that none of the neural networks trained show a desired degree of accuracy as a function of shape parameter.

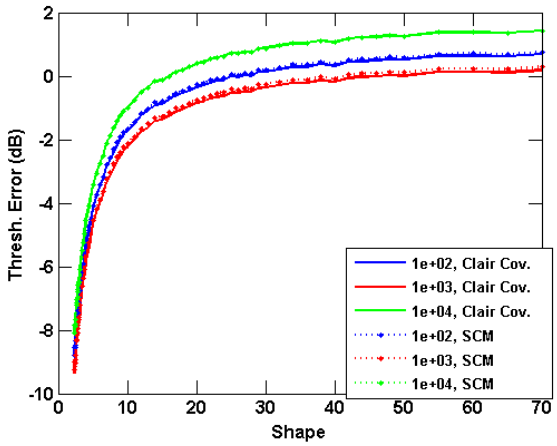

(a) Threshold error (in dB) for varying training sample support w/CCM (solid) and SCM (dotted) with 10 hidden neurons

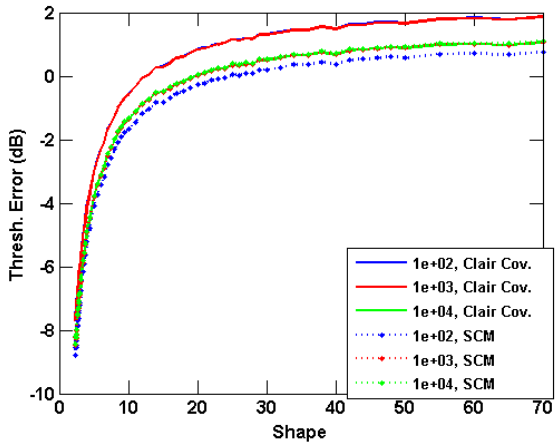

(b) Threshold error (in dB) for varying training sample support w/CCM (solid) and SCM (dotted) with 20 hidden neurons

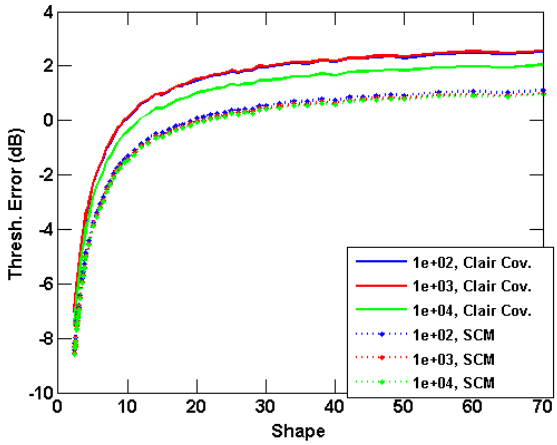

(c) Threshold error (in dB) for varying training sample support w/CCM (solid) and SCM (dotted) with 30 hidden neurons

Figure B.25: Threshold estimation by a three stage deep neural network for unordered Pareto distributed data

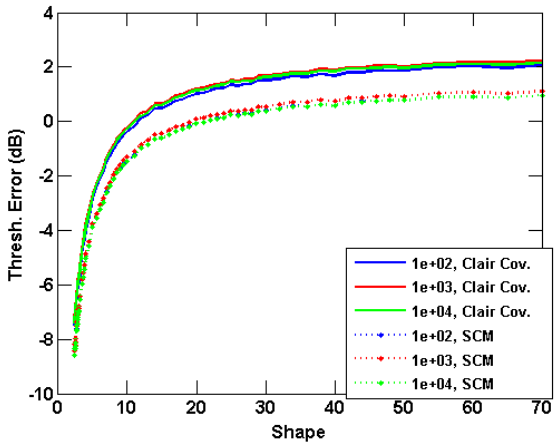

(a) Threshold error (in dB) for varying training sample support w/CCM (solid) and SCM (dotted) with 10 hidden neurons

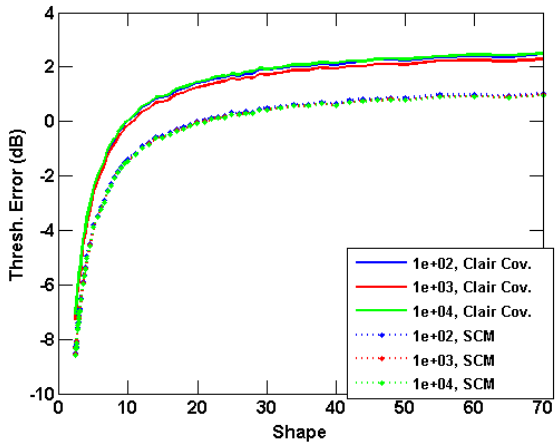

(b) Threshold error (in dB) for varying training sample support w/CCM (solid) and SCM (dotted) with 20 hidden neurons

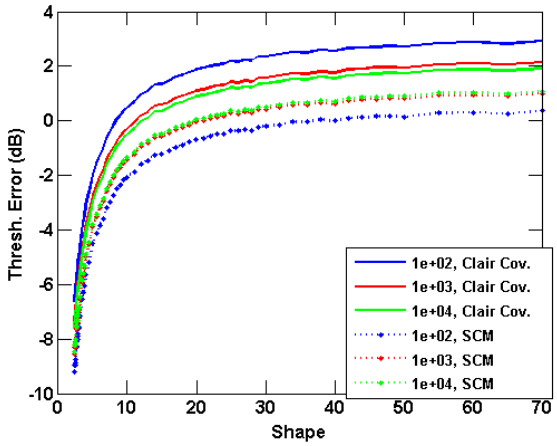

(c) Threshold error (in dB) for varying training sample support w/CCM (solid) and SCM (dotted) with 30 hidden neurons

Figure B.26: Threshold estimation by a three stage deep neural network for ordered Pareto distributed data

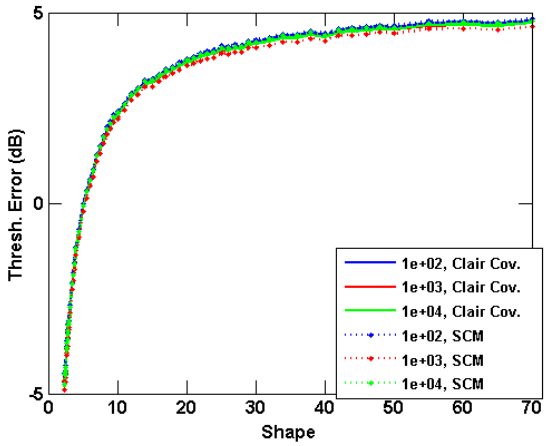

(a) Threshold error (in dB) for varying training sample support w/CCM (solid) and SCM (dotted) with 10 hidden neurons

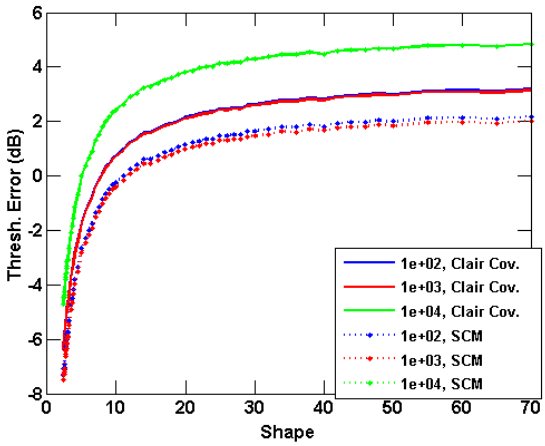

(b) Threshold error (in dB) for varying training sample support w/CCM (solid) and SCM (dotted) with 20 hidden neurons

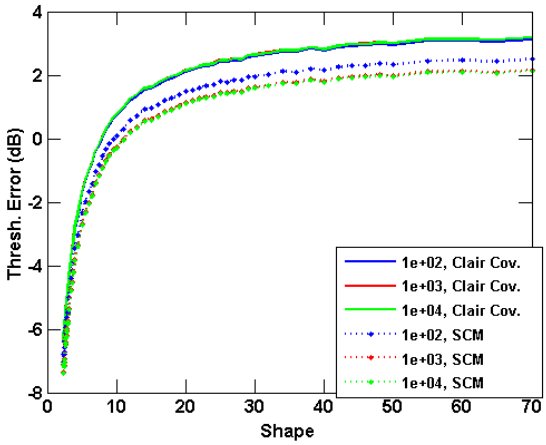

(c) Threshold error (in dB) for varying training sample support w/CCM (solid) and SCM (dotted) with 30 hidden neurons

Figure B.27: Threshold estimation by a three stage deep neural network for unordered Pareto distributed data, Pareto data not included in training data

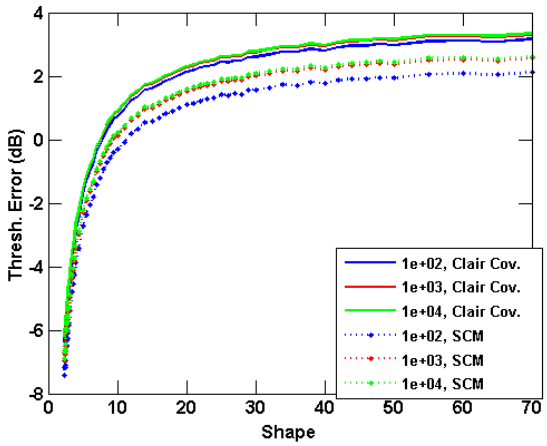

(a) Threshold error (in dB) for varying training sample support w/CCM (solid) and SCM (dotted) with 10 hidden neurons

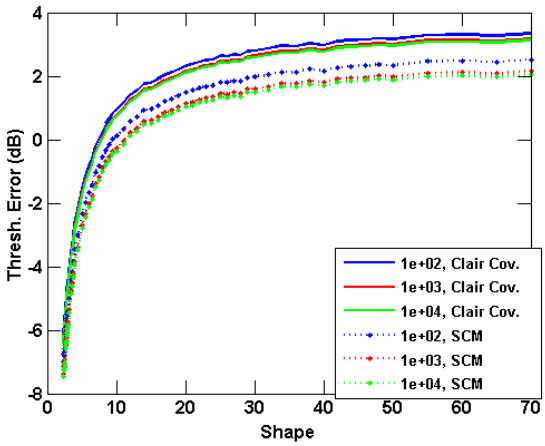

(b) Threshold error (in dB) for varying training sample support w/CCM (solid) and SCM (dotted) with 20 hidden neurons

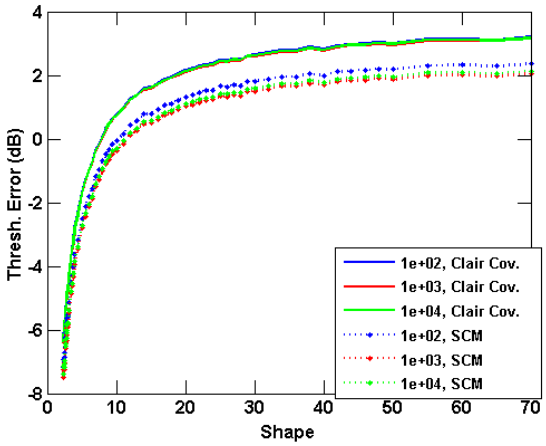

(c) Threshold error (in dB) for varying training sample support w/CCM (solid) and SCM (dotted) with 30 hidden neurons

Figure B.28: Threshold estimation by a three stage deep neural network for ordered Pareto distributed data, Pareto data not included in training data

B.2.5 Threshold Estimation of Lognormal Data with a Deep Neural Network

The performance of the neural networks under consideration of this section for Lognormal distributed test data is summarized in Table B.10. The average error results shown in Table B.10 are largely much worse (*i.e.* 3-5 dB less accurate) than those shown in Table 7.17.

However, ordering the data leads to a much lower threshold error for these deep neural networks when Lognormal data is tested.

		Unordered Data			Ordered Data		
HN	Samples	Full	Excised	Δ_{full} (Δ_{excised})	Full	Excised	Δ_{full} (Δ_{excised})
10	10^2	-9.1 (-9.1)	-8.9 (-9.1)	0.0 (-0.2)	-4.4 (-7.9)	-4.7 (-8.1)	-3.5 (-3.3)
10	10^3	-9.9 (-9.7)	-9.9 (-9.7)	0.2 (0.2)	-4.0 (-7.8)	-4.1 (-7.8)	-3.9 (-3.7)
10	10^4	-8.3 (-8.4)	-8.4 (-8.4)	-0.0 (0.0)	-4.0 (-7.7)	-4.3 (-7.7)	-3.6 (-3.4)
20	10^2	-4.5 (-8.5)	-4.7 (-8.5)	-4.0 (-3.8)	-4.2 (-8.0)	-4.4 (-7.9)	-3.8 (-3.5)
20	10^3	-4.5 (-8.5)	-4.9 (-8.5)	-4.0 (-3.6)	-3.9 (-7.9)	-3.8 (-7.9)	-4.0 (-4.1)
20	10^4	-8.7 (-8.8)	-8.7 (-8.8)	-0.0 (-0.0)	-3.2 (-7.9)	-3.2 (-7.9)	-4.7 (-4.7)
30	10^2	-3.7 (-8.2)	-4.1 (-8.2)	-4.5 (-4.2)	-4.1 (-6.9)	-4.0 (-6.8)	-2.8 (-2.9)
30	10^3	-3.5 (-7.9)	-3.3 (-7.8)	-4.4 (-4.5)	-4.4 (-8.2)	-4.3 (-8.2)	-3.8 (-3.9)
30	10^4	-4.8 (-7.8)	-5.1 (-7.8)	-3.0 (-2.7)	-5.4 (-7.8)	-5.2 (-7.8)	-2.4 (-2.6)

Table B.10: Average Threshold Error (dB) when lognormal data is fed into a multiple layer neural network

Appendix C

Current Literature Applying Covariance Matrix Estimation to SIRV Data

In this chapter two current radar signal processing approaches are discussed provide both justification to some of the techniques discussed in this work, as well as promising lines of inquiry that will serve as a basis for future work. First, the non-homogeneity detector of [75, 114] is discussed. This detector provides a SIRV based, scale invariant detector that can provide improved resilience to false alarms in non-Gaussian clutter. Second, the practical implications of sea clutter non-stationarity is explored via a discussion of the results of [87]. Both of these works provide illumination on current approaches of estimating the covariance matrix of measured SIRV data.

C.1 Non-Homogeneity Detection

Here we have developed the SIRV framework as a natural fit to the radar clutter modeling problem. The heavy-tailed nature of measured radar clutter data is assumed to be produced by modulating the random variable V with a Gaussian distributed complex random vector $\tilde{Z}$. This heavy tail causes increased false alarms and causes the scaling of test and secondary data to vary.

A radar system uses training data derived from cells near the cell under test (CUT). Therefore, even for Gaussian distributed clutter, it is common for training data and the test data to vary in scale. The maximal scale invariant test statistic was developed in [51, 173] and is often called the normalized adaptive matched filter (NAMF). This test statistic is given as

$$\Lambda_{\text{NAMF}} = \frac{\left|\mathbf{p}^H \hat{\mathbf{\Sigma}}^{-1} \mathbf{y}\right|}{\left[\mathbf{p}^H \hat{\mathbf{\Sigma}}^{-1} \mathbf{p}\right] \left[\mathbf{y}^H \hat{\mathbf{\Sigma}}^{-1} \mathbf{y}\right]} \tag{C.1}$$

where $\mathbf{p}$ is the Doppler or spatio-Doppler steering vector, $\hat{\mathbf{\Sigma}}^{-1}$ is the inverse of the sample covariance matrix, and $\mathbf{y}$ is the received complex sampled measurements.

While the NAMF is invariant to scale between the test and training data, it is not necessarily invariant to different scaling for each training data vector. Therefore, when the NAMF was extended to the SIRV framework in [75, 114], the estimation of the covariance matrix was a concern. Note that each training data vector is modulated by a different instantiation of the random variable V. Denote the training data by the collection of N length L complex valued SIRVs indexed as $\mathbf{y}_i, \quad i = 1, \ldots, N$. Let the sample quadratic form be defined as

$$\hat{q}_i = \mathbf{y_i}^H \hat{\mathbf{\Sigma}}^{-1} \mathbf{y_i}. \tag{C.2}$$

The maximum likelihood estimation of the covariance matrix is [75, 114, 174, 175]

$$\hat{\mathbf{\Sigma}}^{-1} = \frac{1}{N} \sum_{i=1}^{N} c_i \mathbf{y}_i \mathbf{y}_i^H \tag{C.3}$$

where

$$c_i = \frac{-h'_{2L}(\hat{q}_i)}{h_{2L}(\hat{q}_i)} \tag{C.4}$$

and $h'_{2L}(q)$ is the derivative of the function $h_{2L}(q)$. Recall that the function $h_{2L}(q)$ is unique

to each SIRV and is given by (3.27), repeated here

$$h_{2L}(q) = \int_0^\infty v^{-L} \exp(-\frac{p}{v^2}) f_V(v) \mathrm{d}v. \tag{C.5}$$

Using the dummy variable w, recall that

$$\begin{aligned} h'_{2L}(w) &= \frac{\partial h_{2L}(w)}{\partial w} \\ &= -h_{2L+2}(w). \end{aligned} \tag{C.6}$$

Notice that c_i is given by substituting (C.2) in (C.4), and so requires $\hat{\mathbf{\Sigma}}^{-1}$. However, from (C.3), the definition of $\hat{\mathbf{\Sigma}}^{-1}$ likewise requires c_i! It was suggested in [174] to solve this quandary through use of the iterative expectation-maximization algorithm. Further, notice that the maximum likelihood estimation of the covariance matrix also requires knowledge of the function $h_{2L}(q)$. If this function is not known *a priori*, it must be estimated.

If the sample covariance matrix can be determined, the pdf of the NAMF can be shown to be [75, 114]

$$f_{\mathrm{NAMF}}(r) = \int_0^1 \frac{K(1-\gamma) f_\Gamma(\gamma) \mathrm{d}\gamma}{\left[1 + (1-\gamma)\frac{r}{1-r}\right]^{K+1}} \frac{1}{(1-r)^2} \tag{C.7}$$

where $K = N - L + 1$,

$$f_\Gamma(\gamma) = \frac{1}{\beta(K+1, L+1)} \gamma^K (1-\gamma)^{L-2}, \quad 0 \le \gamma \le 1 \tag{C.8}$$

and the Beta function $\beta(a, b)$ is defined in (5.3).

As defined in [75, 114], a non-homogeneity detector (NHD) for SIRV distributed data operates under the hypothesis test

$$\begin{aligned} \mathcal{H}_0 : &\quad \Lambda_{\mathrm{NAMF}} \text{ is statistically consistent with } f_{\mathrm{NAMF}}(r) \\ \mathcal{H}_1 : &\quad \Lambda_{\mathrm{NAMF}} \text{ is not statistically consistent with } f_{\mathrm{NAMF}}(r). \end{aligned} \tag{C.9}$$

Therefore, if a target is present the test and primary data vectors will not be statistically consistent and $\mathcal{H}_1$ will be true. In [75, 114] the NHD is compared to the generalized inner product (GIP) non-homogeneity detector of [101–103] using both simulated K distributed data and measured data from the multichannel airborne radar measurement (MCARM) program [115]. The GIP assumes Gaussianity of both the training and testing data, so the SIRV based approach appears to suffer from a much lower rate of false alarm for K distributed and measured clutter.

The NHD presented in [75, 114] requires accurate estimation of the function $h_{2L}(q)$ and sufficient sample support to estimate the covariance matrix. Therefore, the underlying SIRV must be identified before the maximal, scale invariant property of the NHD may be utilized. As discussed in Section 5.4, distribution identification of SIRVs is one of the two goals of the COSMiC algorithm. Therefore, a two step algorithm may be employed where the COSMiC algorithm is first used to estimate the SIRV, and the non-homogeneity detector of [75, 114] can then be used to determine the presence of a target.

C.2 Investigating the Impact of Measured Sea Clutter Non-Stationarity

In a recent work the practical implications of target detection in sea clutter was examined [87]. As mentioned in Section C.1, maximum likelihood estimation of SIRV data requires knowledge of the function $h_{2L}(q)$. To work around this problem, [87] used three different covariance matrix estimators: the traditional sample covariance matrix (SCM), normalized sample covariance matrix (NSCM), and a fixed point (FP) technique. For the purposes of this work the implementation details of the two latter covariance matrix estimators are not of interest. For their definitions and details of their implementation, see [87].

The measured data used by [87] was generated from two ground-based radars that overlooked the ocean. Each of these data sets provided a long dwell time (60 seconds) over a

constant set of range cells. Therefore, the spatial and temporal non-stationarities of the sea clutter could be isolated. The power spectral density of the data was estimated via a Welch periodogram [3, 87]. The spectral content of the clutter was found to vary with respect to range cell as well as time. However, the clutter power was consistently strongest close to zero Doppler. The data was fit to the K distribution and the shape parameter was estimated via the method of moments (MoM) technique that was defined at the end of Section 3.5. The shape parameter of the distribution varied with respect to both time and polarization.

Finally, the practical implications of target detection in non-stationary data was considered. To generate the detection threshold, three average covariance matrices were generated (corresponding to the three techniques under consideration), and Monte Carlo simulation was employed using the mean value of the estimated shape parameter. The resultant probability of false alarm was then found from the (spectrally) transformed sampled data. The NSCM and FP methods provided false alarm rates close to the desired rate at frequencies far from the peak of the clutter power. Close to the clutter power, the resultant false alarm was higher than desired. When the SCM is used, the false alarms exceed the desired frequency only at the peak of the clutter spectral power. However, the detection threshold is set so that the probability of false alarm is equal to the desired probability. If the rate of false alarm encountered is *lower* than desired, the threshold is then too large. A higher threshold leads to a lower probability of detection. This relation is shown for both simulated and measured data in [87].

In [87] the difficulty of setting a detection threshold in non-Gaussian, non-stationary clutter is explored. In addition, they use Doppler processing to cancel clutter, which we have not explored up to this point. Recall that under the closure property of SIRVs, a linear transform on a vector that follows a SIRV distribution yields a vector with the same underlying characteristic pdf (*i.e.* modulating variable) and a different covariance matrix. Therefore, the normalized threshold will not change after Doppler processing, but the clutter will be canceled to some degree. We will extend our work to include Doppler processing.